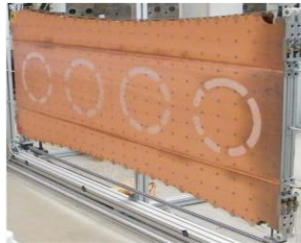
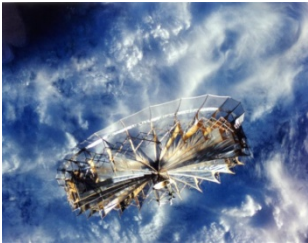


ISBN 978-9941-0-7008-2

The 2nd International Scientific Conference

Advanced Lightweight Structures and Reflector Antennas

Proceedings



**October 1-3, 2014
Tbilisi, Georgia**

The objectives of the conference are:

- To present the state of the art and explore innovative approaches for advanced lightweight structures and reflector antennas
- To share the expertise between space and ground approaches for lightweight structures
- To demonstrate recent space structures

The conference will particularly facilitate exchange of opinions and challenges in creation and development of Large Deployable Structures and Antenna Reflectors technologies, current initiatives especially in Europe and further steps. To achieve this, experts from the leading industries and academia have been brought together from all over the world.

SUPPORTING ORGANIZATIONS:



European Space Agency, ESA, the Netherlands



Technische Universitaet Muenchen, Germany



Large Space Structures UG, LSS, Germany



Ministry of Science and Education, Georgia



Georgian Technical University, Georgia



Georgian National Academy of Science, Georgia



EMCoS Consultations and Software, Georgia



Caucasus Space Ltd., Georgia



Rustavi 2, Broadcasting Company, Georgia

TABLE OF CONTENTS

Committees

Wednesday October 1, 2014

Session 1 – Large Deployable Antenna Reflectors

Session 2 – Large Deployable Reflectors

Session 3 – Radio Frequency and Mechanical Aspects

Thursday October 2, 2014

Session 4 – Mechanical, Thermal, RF Testing

Session 5 – Tensioned Membranes and Networks/Form Finding

Session 6 – Large Deployable Space Structures

Friday October 3, 2014

Session 7 – Shape Morphing, Transformation, Control

Session 8 – Materials and Manufacturing Technology

Session 9 – Membrane & Inflatable Space Structures

Session 10 – Poster Session –Lightweight Structures

CONFERENCE ORGANIZING COMMITTEE

Leri Datashvili (Technische Universität München, Germany)
 Nodar Tsignadze (Georgian Technical University, Georgia)
 Horst Baier (Technische Universität München, Germany)
 Elguja Medzmariashvili (Georgian Technical University, Georgia)

TECHNICAL COMMITTEE

Anatoly Alpatov (Institute of Technical Mechanics, Ukraine)
 Horst Baier (Technische Universität München, Germany)
 Rafael Bureo (ESA-ESTEC, the Netherlands)
 Kai-Uwe Bletzinger (Technische Universität München, Germany)
 Leri Datashvili (Technische Universität München, Germany)
 Jose Encinar (Universidad Politecnica de Madrid, Spain)
 Torben Henriksen, (ESA-ESTEC, the Netherlands)
 Christian Hühne, (German Aerospace Center (DLR, Germany)
 Kees van t Klooster (ESA-ESTEC, The Netherlands)
 Philippe Lepeltier (Thales Alenia Space, France)
 Cyril Mangenot (ESA-ESTEC, the Netherlands)
 Elgudja Medzmariashvili, (GTU, Georgia)
 Alberto Meschini (Thales Alenia Space – Italia)
 Norbert Nathrath (NTP, Germany)
 Satoru Ozawa (Japan Aerospace Exploration Agency, Japan)
 Sergio Pellegrino (California Institute of Technology, USA)
 Julian Santiago-Prowald (ESA-ESTEC, the Netherlands)
 Manfred Schmid (Astrium GmbH Satellites, Germany)
 Lorenzo Scialino, (Space Engineering S.p.A., Italy)
 Lucio Scolamiero (ESA-ESTEC, the Netherlands)
 Constantinos Stavrinidis (ESA-ESTEC, the Netherlands)
 Marco Straubel, (DLR, Germany)
 Huifeng Tan (Harbin Institute of Technology, China)
 Mark Thomson (Jet Propulsion Laboratory, USA)
 Shota Tserodze (Georgian Technical University, Georgia)
 Nodar Tsignadze (Georgian Technical University, Georgia)

CONFERENCE SECRETARIATE

68/B Kostava str., 0171, Tbilisi, Georgia

Tel.: + 995 32 / 233 09 36; + 995 32 / 236 52 39

Fax: + 995 32 / 36 52 37

E-mail: conf.icssem@gtu.ge

Wednesday

October 1, 2014

Session 1 – Large Deployable Antenna Reflectors

Advanced Architectures of Large Space Deployable Mesh Reflectors: from Medium to Very Large Sizes

Leri Datashvili, Nikoloz Maghaldadze, Julian Pauw, Stephan Endler, Horst Baier, Lali Gigineshvili Large Space Structures UG, Garching, Germany7

New Constructions of Lightweight Deployable Reflectors

E. Medzmariashvili⁽¹⁾, Julian Santiago-Prowald, Cyril Mangenot, Horst Baier, Leri Datashvili, Nodar Tsignadze, Lorenzo Scialino, kees Van't Klooster, Guram Bedukadze, Mikheil Janikashvili, Otar Tusishvili, Ludmila Philipenko, Nikoloz Medzmariashvili, Ariadna Jakhua

⁽¹⁾Institute of Constructions, Special Systems and Engineering Maintenance of Georgian Technical University, GEORGIA21

The Development of a Novel Large Deployable Antenna Reflector concept

*Alberto Meschini, Riccardo Rigato, Davide Scarozza
Thales-Alenia-Space, Italy26*

Design Concept of Large Deployable Reflector for Next Generation L-Band SAR Satellite

*Satoru OZAWA
Japan Aerospace Exploration Agency, Tsukuba Space Center, Sengen, Tsukuba, Ibaraki, JAPAN49*

Large Antenna Working Group: Status of Activities

*Julian Santiago Prowald, Cyril Mangenot
European Space Agency / ESTEC, the Netherlands52*

Session 2 – Large Deployable Reflectors

Radiometer Antenna Architecture for Oceanography Applications

Kees Van't Klooster⁽¹⁾, Cecilia Cappelin, Knud Pontoppidan, Per Heighwood Nielsen, Niels Skou, Sten Schmidl Søjbjerg, Marianna Ivashina, Oleg Lupikov, Alexander Ihle

⁽¹⁾ European Space Agency / ESTEC, the Netherlands61

Dimensional Stability and Shape-Accuracy of Shell-Membrane Reflecting Surfaces Made Of Fiber-Reinforced Elastomers

Leri Datashvili⁽¹⁾, Horst Baier, Stephan Endler, Nikoloz Maghaldadze, Mathias Friemel, Tao Luo, Gunar Reinicke, Guram Bedukadze, Konstantin Chkhikvadze, E. Medzmariashvili, N. Tsignadze, Alex Ihle, Julian Santiago-Prowald

⁽¹⁾ Institute of Lightweight Structures, Technische Universität München, Garching, GERMANY69

TALC, A 20m Thin Aperture Light Collector for Infra Red Observations in Space

Gilles Durand⁽¹⁾, Marc Sauvage, Jérôme Amiaux, Vincent Révéret, Louis.rodrique, Pierre Chanial, Samuel Ronayette, Loris Scola, Michael Carty, Matthis Durand, Lancelot Durand, Michel Berthe, Aymeric Bonnet, Sébastien

*Correia, Pascal Bultel⁽¹⁾
Laboratoire AIM, CEA/Irfu, CNRS/INSU, Université Paris Diderot, France79*

New Design of a Transformable Mechanical Cone System with V-Folded Bars

Sh. Tserodze⁽¹⁾, J. Santiago Prowald, V. Gogilashvili, K. Chkhikvadze, N. Tsignadze, A. Chapodze, M. Nikoladze

⁽¹⁾Institute of Constructions, Special Systems and Engineering Maintenance of Georgian Technical University, GEORGIA89

Session 3 – Radio Frequency and Mechanical Aspects

Edge Currents Modeling in Problems Related to Optimization of High Frequency Antenna Systems

D. Karkashadze, F. Bogdanov, R. Jobava, G. Gabriadze
EMCoS Consulting and Software, Tbilisi, Georgia 99

Sidelobe Level Reduction of Faceted Mesh Reflector Antenna Using Phyllotactic Arrangements

Jean-Christophe Angevain ⁽¹⁾, Gonçalo Rodrigues, Julian Santiago Prowald, Cyril Mangelot, Leri Datashvili
⁽¹⁾*European Space Agency / ESTEC, the Netherlands* 106

Application of ACA Algorithm and BICGSTAB Solver for Acceleration of MOM Computations of Large Scale Problems

G. Gabriadze, V. Tskhovrebashvili, F. Bogdanov, P. Tsereteli, R. Jobava
EMCoS Consulting and Software, Tbilisi, Georgia 116

Thursday

October 2, 2014

Session 4 – Mechanical, Thermal, RF Testing

Some Problems in Ground Testing of Large Space Lightweight Structures

Guram Bedukadze ⁽¹⁾, Leri Datashvili
⁽¹⁾*Georgian Technical University, Tbilisi, GEORGIA* 123

Novel Large Deployable Antenna Backing Structure Breadboard Test Campaign

V. Fraux, J. R. Reveles, M. Lawton,
Oxford Space Systems Ltd, Harwell, United Kingdom 131

Structure Analysis of Inflatable Solar Sails

Wei Jianzheng, Ma Ruiqiang, Tan Hui Feng, Song Bo and Liu Yufei
Harbin Institute of Technology, CHINA 138

Alternative Thermoelastic Deformation Measurement Techniques for Space Structures in Laboratory Conditions

Friemel, Matthias; Maghaldadze, Nikoloz; Baier, Horst; Datashvili, Leri
Institute of Lightweight Structures, Technische Universität München, Garching, GERMANY 146

Antenna Testing: Thermo-Vacuum and Combined Thermal-Near Field Test Solutions

Leonardo Alemanno, Fabrizio Rinalducci Angelantoni
Test Technologies S.r.l. ITALY 154

Session 5 – Tensioned Membranes and Networks/Form Finding

Variation of Reference Strategy - A Novel Approach for Generating Optimized Cutting Patterns of Membrane Structures

Kai-Uwe Bletzinger, Armin Widhammer, Falko Dieringer
Institute of Structural Analysis, Technische Universität München, München, GERMANY 159

Efficient Automated Resizing of a Deployable Membrane SAR Antenna

Marco Straubel, Christian Hühne, Michael Sinapius. Institute of Composite Structures and Adaptive Systems, German Aerospace Agency - DLR, Braunschweig, Germany 169

Structural Characterization and Modeling of Metallic Mesh Material for Large Deployable Reflectors

G. L. Scialino ⁽¹⁾, P. Salvini, M. Migliorelli, E. Pennestrì, P.P. Valentini, K. van't Klooster, J. Santiago Prowald, G. Rodrigues, Y. Gloy
⁽¹⁾*Space Engineering S.p.A, Rome, Italy* 182

Design and Calculation of the Surface of Space Parabolic Antenna on the Basis of Discrete Conception

Elguja Medzmariashvili, David Patariaia ⁽¹⁾, George Baliashvili, Edisher Tsotseria, Giorgi Nozadze ⁽¹⁾
Mining Institut, Tbilisi, GEORGIA193

Session 6 – Large Deployable Space Structures

Successful Starshade Petal Deployment Tolerance Verification in Support of NASA's Technology Development for Exoplanet Missions

M. Thomson, D. Webb, N. J. Kasdin, D. Lisman, S. Shaklan, E. Cady, G. W. Marks, A. Lo
Jet Propulsion Laboratory - JPL, California Institute of Technology/NASA, USA200

Ultralight Deformable Mirrors for Large Aperture Space Telescopes

Sergio Pellegrino
Graduate Aerospace Laboratories, California Institute of Technology, Pasadena, USA214

Deployable Structures in the CubeSat Program MOVE

M. Langer⁽¹⁾, C. Olthoff, L. Datashvili, H. Baier, N. Maghaldadze, U. Walter
1) Institute of Astronautics, Technische Universität München, Garching, GERMANY224

Friday

October 3, 2014

Session 7 – Shape Morphing, Transformation, Control

Pre-manufacturing Estimation and Post-manufacturing Compensation of Induced Shape Errors of Fiber Composite Structures

Horst Baier
Institute of Lightweight Structures, Technische Universität München, Garching, GERMANY234

Overview of 3D and Planar Bar Linkages for Space Deployable Structures

Julian Santiago Prowald, Rafafael Bureo Dacal, Torben Henriksen
European Space Agency / ESTEC, the Netherlands244

Conceptual Design of Deployable Composite Reflector of an X-Band Satellite Payload

Omer Soykasap, Sukru Karakaya, Ahmet Gayretli, and Yelda Akcin,
Afyon Kocatepe University, Afyonkarahisar, Turkey254

Active Shape Control of Reconfigurable Antenna Reflectors

Gonçalo Rodrigues, Jean-Christophe Angevain and Julian Santiago-Prowald
European Space Agency / ESTEC, the Netherlands264

Modelling of Mechanical Shock Induced by Deployment of Appendages

J. R. Reveles , V. Fraux , M. Lawton
Oxford Space Systems Ltd, Harwell, United Kingdom272

Session 8 – Materials and Manufacturing Technology

Dual Gridded Reflectors - Technology Developments over 30 Years

N. Nathrath,
NTP Consultancy, München, Germany281

Manufacturing Process Simulation for a High Precision Composite Reflector

Liangyu Liu, Houfei Fang, Yang Zhou, Yongbin Wu, Xiaobin Mang, Yangqing Hou
Shanghai YS Information Technology Co., Ltd., Shanghai, China291

A Novel Press-bending Forming Shell Structure for Parabolic Cylinder Reflectors

Huifeng Tan, Liuyi Yang, Rongrong Xu, Xilin Luo, Hao Liu

Harbin Institute of Technology, CHINA300

Hybrid Fiber Reinforced Polymer Composites for Lightweight Structures

N.M. Chikhradze, G.S. Abashidze, G.I. Baliashvili, G.B. Pkhaladze, D.T. Tsverava

Mining Institut, Tbilisi, GEORGIA306

Enhancement of the Electro-Magnetic Behavior of Flexible Fiber Composite Materials by Surface Coating

Endler, S⁽¹⁾, Datashvili, L., Baier, H., Roose, S.

⁽¹⁾ Institute of Lightweight Structures, Technische Universität München, Garching, GERMANY316

Session 9 – Membrane & Inflatable Space Structures

A Hybrid Inflatable Boom/Rigid Hinge Membrane Cylindrical Reflector

Lin Guo Chang, Luo Xi Lin, Du Juan, Tan Hui Feng,

Harbin Institute of Technology, CHINA326

Lightweight Inflatable Structures for Thermal Protection during Re-entry. State of the Art and Future Perspectives for their Development

Marco Adami, Lorenzo Fiore, Luciano Battocchio

Sekur Space & Technology, Caselle Torinese (TO) – Italy331

Design Analysis of an Inflatable Satellite Communication Reflector

He Huang, Fu-ling Guan, Houfei Fang

College of Civil Engineering and Architecture, Zhejiang University, Hangzhou, China341

Improving the Inflatable Parabolic Reflector

Geuskens F., Vermij G., Ording B.

Dutch Space, an EADS Astrium Company, Leiden, the Netherlands350

Satellite Inflatable Deorbiting Equipment for LEO Spacecrafts

B. Rasse, P. Damilano, C. Dupuy

Airbus Defence and Space, Saint Médard-en-Jalles Cedex, France361

Session 10 – Poster Session – Lightweight Structures

Erection Cycle of Deployable Space Reflectors Using the Functional and Technological Screen Mesh

M. Sanikidze, E. Medzmariashvili, G. Gratiashvili, O. Tusishvili, N. Medzmariashvili, M. Janikashvili

The Institute of Structures, Special Systems and Engineering Maintenance of Georgian Technical University371

Structure of Lightweight Reflector Using the Principle of “Tension Architecture”

Nikoloz Medzmariashvili, George Medzmariashvili

The Institute of Structures, Special Systems and Engineering Maintenance of Georgian Technical University384

Conical V-fold Bar Ring with Flexible Pre-stressed Center

E. Medzmariashvili, N. Tsignadze, J. Santiago Prowald, L. Datashvili, O. Tusishvili, G. Phavlenishvili(1)

(1)The Institute of Structures, Special Systems and Engineering Maintenance of Georgian Technical University391

ADVANCED ARCHITECTURES OF LARGE SPACE DEPLOYABLE MESH REFLECTORS: FROM MEDIUM TO VERY LARGE SIZES

Leri Datashvili, Nikoloz Maghaldadze, Julian Pauw, Stephan Endler, Horst Baier, Lali Gigineishvili

Large Space Structures (LSS) UG, Römerhofweg 51C, 85748 Garching b. München, Germany

Email: leri.datashvili@largespace.de

ABSTRACT

LSS UG is currently developing a large deployable reflector (LDR) technology under an ESA project aiming at LDR concepts with sizes up to 18 m diameter. Medium - 6 m and large - 12 m class LDRs have been designed for different radio frequency ranges for telecommunication and earth observation missions complying with stringent space and functionality requirements. Scalability of the selected architecture has been successfully demonstrated for the required 4 to 18 m diameter range. For example, the mentioned 12 m class LDR design, which easily fulfils Biomass mission requirements and fits into the European VEGA launcher fairing, is getting mature for practical implementation. Recent investigations of similar architectures of LDRs show the ability of a growth far above 30 m diameters with no remarkable modifications of the original concept. Two types of ring architectures have been analysed as a support structure for a reflecting surface: rings with cylindrical and with conical shapes. Both ring types make use of the same deployment concept as the 12 m LDR. The scalability feature of the proposed ring architectures and the demonstrated feasibility of very large diameters prove their high growth potential in combination with novel highly scalable cable network architectures proposed. These networks are able to overcome the limits of the conventional ones in terms of achievable overall LDR dimensions.

Demonstration of the high scalability of the LDR architectures is supported by promising results of numerical FEM and form finding optimization analyses on 20 m and 30 m diameter LDRs presented in this paper.

1. INTRODUCTION

Referring to the study in [1], reflectors utilizing peripheral deployable ring structures to support an RF-surface have been identified as the most promising direction for the development of large deployable reflector technologies. This type of spaceborne reflectors has an excellent potential for telecommunication and earth observation applications in the aperture diameter range of 4-30 meter due to a high potential of scalability. Moreover, the technology of LDRs with a deployable ring load-bearing structure is advantageous in terms of the ratio of stowed and deployed diameters.

Tensioned cable network concepts used by this kind of reflectors give a considerable advantage in development of a lightweight technology of mesh reflectors with large sizes [2]. Large deployable reflector (LDR) examples flown in space by Harris [3], [22] and Northrop Grumman [4], [5] have proven this.

The original AstroMesh concept shows a better scalability allowing a greater diversity of applications as compared to the diversity of concepts from Harris. However, it had a number of limitations related to the package dimensions promoting a variety of design modifications for the support rings [23] in order to realize different size diameters. For very large diameter LDRs, the rings are equipped with additional deployable extensions for in-height folding/deploying of the ring in order to accommodate the large increase of the deployed height due to conventional networks design.

Studies performed under ESA projects, which are summarized in [9] and [10], identified the most promising ring architectures allowing the realization of very large diameters with no remarkable modification of the ring concept. The ring proposed in [11], which is under further development at LSS, is characterized by demonstrating the feature of high scalability due to the high deployed/folded diameter ratio combined with a low mass. Moreover, the ratio of deployed and folded heights equates to 1, which is an advantageous feature as compared to the known designs of rings from e.g. Georgian Mesh Reflector [2] and AstroMesh [4], [5], being much smaller than 1.

Further on, the scalability feature of the reflector structures is enhanced by the use of an innovative highly scalable cable network from [20] and is one of the main topics of this study.

2. DERIVATION OF MAIN BUILDING BLOCKS FOR LARGE AND VERY LARGE REFLECTORS

Reflector concepts with peripheral ring supported cable networks can be split into the following building blocks: deployable ring structure, cable network approximating a paraboloid and RF-reflective surface, as shown in Fig. 1.

Two types of ring architectures are discussed in this paper: The ring can have either a prismatic shape (also called cylindrical) or a pyramidal shape (also called conical). Both of these ring architectures are based on pantographs. On the one hand, cylindrical ring structures are advantageous in terms of manufacturing due to their symmetric shape. On the other hand, rings with the conical shape have a higher stiffness and can lead to a possible mass reduction compromising the through-height symmetry.

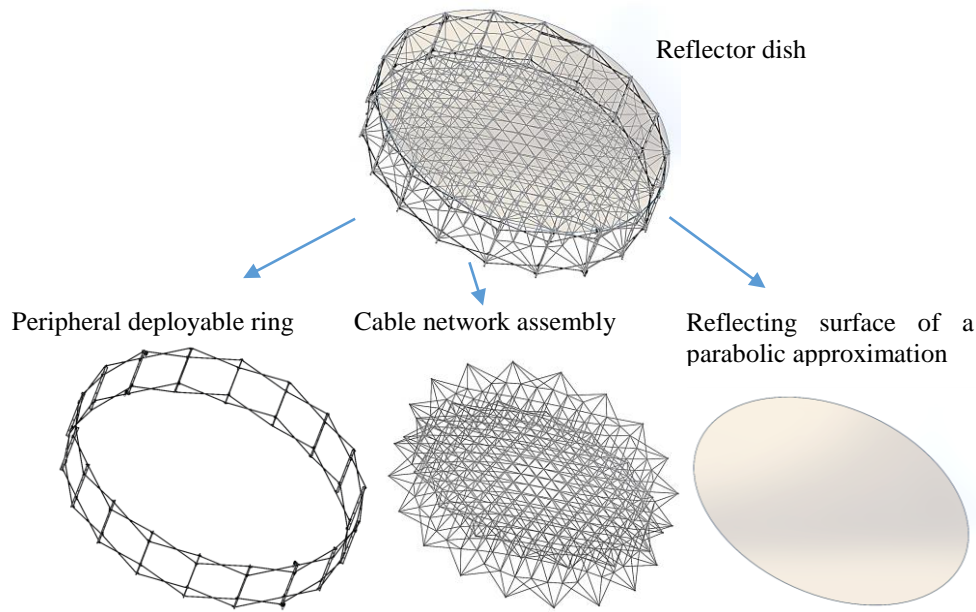


Fig. 1. Main building blocks of a large deployable reflector: CAD design of a 5 m LDR

The most important building block of an LDR in terms of antenna functionality is the reflecting surface. RF requirements yield to the necessity of high accuracy and dimensional stability of the shape of the reflecting surface. At the same time, the utilized materials shall have good stowage properties. Among different types of materials being reviewed in the literature two alternative solutions, which satisfy the stringent requirements, can be identified: knitted metal meshes and carbon fiber-reinforced silicones (CFRS), which are topic of current investigations [13], [14], [15]. A knitted metal mesh as a reflective surface for deployable spaceborne reflectors has the most eminent flight heritage, the material gives an excellent stowage possibility. In order to achieve high precision and sufficient RF performance of the reflecting surface the metal mesh needs to be tensioned. The required tension causes a surface accuracy degradation due to a so called “pillow effect”. In order to reduce this effect different types of tensioned cable networks are used leading to a faceted approximation of a parabolic surface. Setting a certain factor between the tension of the cable network and the mesh, the pillow effect can be significantly reduced to the almost pure faceting error [15]. The main features of the CFRS shell-membrane are that an RF surface made of this material does not require tensioning and that a high accuracy double curved reflecting surface can be manufactured. Application of this technology for LDRs loosens stiffness requirements of the peripheral ring structure. Thus lighter ring structures can be designed and manufactured. This technology removes the facet size requirement of the cable network because they are decoupled in terms of surface accuracy, consequently, much lighter and simpler cable networks can be utilized as they do only need to stiffen the peripheral ring [9], [10], [13], [14] [15].

The shape and stability of the reflecting surface is provided by a next building block of LDRs: A cable network. Conventional cable networks consist of a front and a rear cable net with (triangular) facets and tension ties connecting them. This concept is known as the tension truss antenna and was proposed by [24]. Functionality and reliability of this concept have been successfully proven on orbit many times. Irrespective of considerable flight heritage of this concept, it has some limitations in terms of scalability.

Cable network and ring dimensions are interconnected in this case. A high deepness of the parabolic surface (even more than 4 m) for large aperture diameters and small focal lengths lead to larger heights of the ring structures. This fact

causes the increase of the package size and in some cases package dimensions can exceed the available payload envelope of the launchers. In order to overcome these drawbacks highly scalable network designs have been proposed in [20]. The concept of highly scalable networks is demonstrated in two versions in Fig. 2. Both versions are based on a composition of tension and compression members in the cable network assembly, thus giving an opportunity to decouple the sizes of the ring and the cable network assembly: the ring height is defined independently from the depth of the parabola. The comparison shows a clear geometrical advantage of the highly scalable networks (Fig. 2), which enables a significant reduction of the required ring height as compared to the conventional networks. The introduction of the compression members in the cable network assembly gives the opportunity to realize shaped deployable reflective surfaces as well.

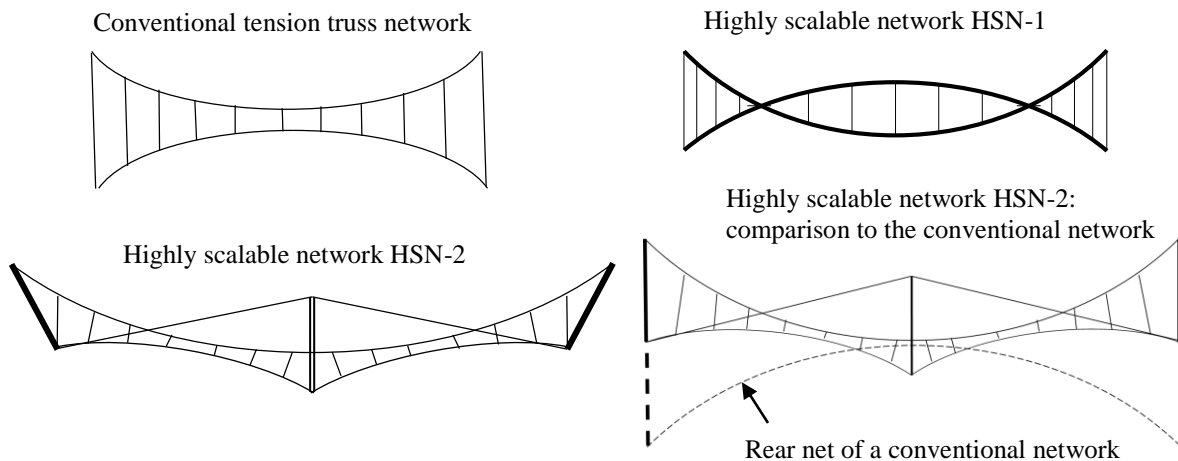


Fig. 2. Principles of highly scalable network designs from [20]

The building blocks described above combine advanced architectures of LDRs and give an excellent opportunity for scaling. Additionally, they can be used as modules for reaching very large diameters. The particular concepts of each building block can be interchanged without any significant design and technology modification.

Cable network and peripheral ring structure designs are addressed in detail in the following sections. They mainly aim at mesh LDRs.

2.1. Advanced highly scalable cable network architectures for mesh LDRs

Designing a tensioned cable network for a LDR structure is a classical form-finding task. The goal of this task is to find an equilibrium shape of the tensioned cable network with minimal deviations from the ideal paraboloid in respect to some constraints. These constraints are like uniform force distribution in the cables and ties, uniform force densities (the ratio of a cable's tension to its length), a needed force distribution, needed cable lengths, a specific positioning of intersection points cables among others. The design of the cable length under a certain limit contributes to a required shape accuracy of the radio frequency (RF) reflective surface. There are two methods of form finding used at LSS which are applicable to this problem, a force density method (FDM) by Linkwitz and Schek [16] and a dynamic relaxation method (DR) originated by Day [17].

The cable network assembly can be split up into three components for convenience: front cable network, rear cable network and their interconnecting elements (tension or compression members). Different combinations of these elements will give either a symmetric or an asymmetric cable networks of conventional or HSN designs.

Design of the cable network is mainly driven by the RF requirements. The higher frequency band is that is required for the reflector the smaller the facet sizes shall be kept for the design. A Ka-band targeted RF surface requires cable network facet sizes smaller than 200 mm. A respectively optimized front cable network of an off-axis reflector with 24 interface points to a peripheral ring structure is shown in Fig. 3-a as an example. A cable network design example with a limiting facet size of 500 mm for L-band application is depicted in Fig. 3-b.

Symmetric cable network assemblies are simpler, because the front and rear cable networks are identical and the optimization problem can be reduced to the front cable network only. Moreover, manufacturing simplifications can also be observed. Symmetric cable networks can only be designed for cylindrical load bearing rings. Depending on the geometrical parameters of the peripheral ring symmetric assemblies utilizing both types of interconnecting elements can be designed. Intersected cable networks have a higher potential for scalability because the ring and the cable network geometry can be decoupled in this case.

Depending on the supporting ring structure, asymmetric cable network assemblies need to be designed in some cases. Asymmetry is caused by the shape difference of the rear and front sides. Asymmetric designs are applicable to the cylindrical and conical ring structures.

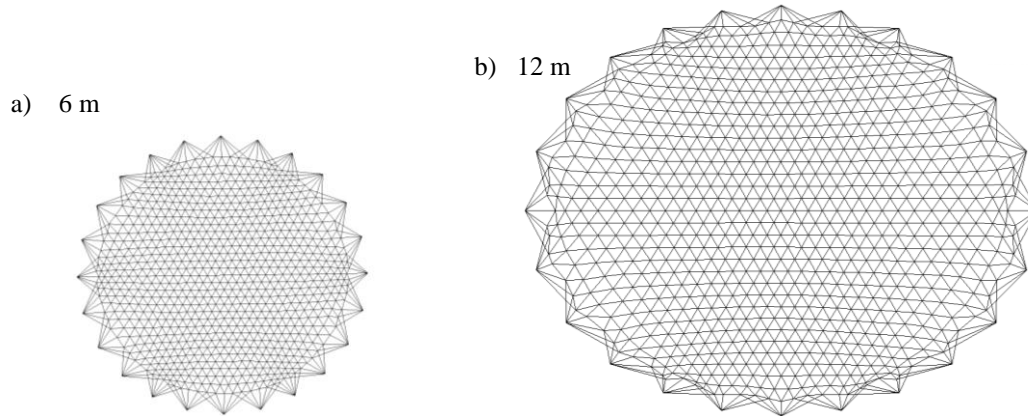


Fig. 3. Optimized front cable networks of 6 m (a) and 12 m (b) aperture diameter off-axis reflectors

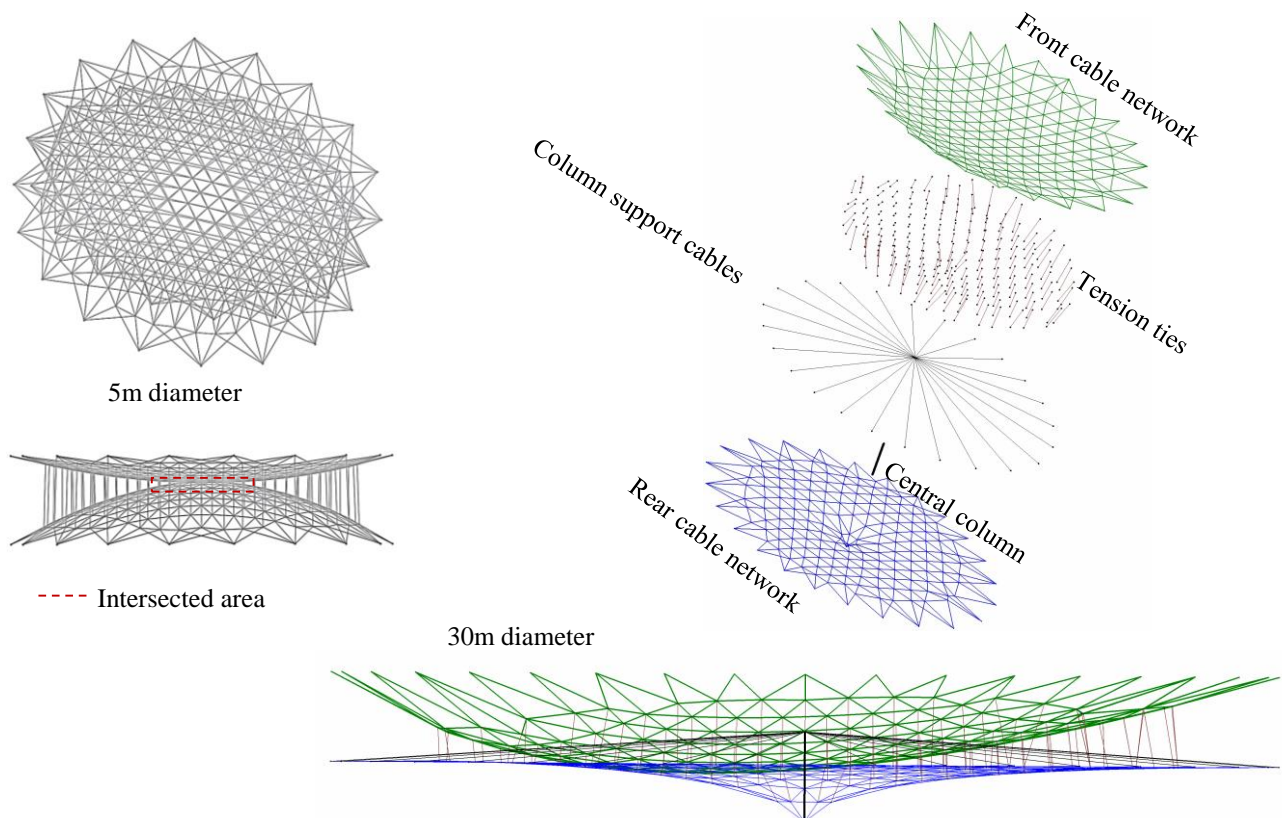


Fig. 4. Examples of optimized highly scalable networks; 5 m HSN-1 (left), 30 m HSN-2, exploded view (right)

Utilization of both, compression and tension members for interconnection of the front and rear networks, is possible. Because front and rear networks have different shapes, a complete network assembly needs to be considered in the

optimization procedure. Another challenge of the asymmetric design is the implementation of the compression members in the form finding method. The developed tools, which are based on the form finding methods mentioned above, give the opportunity to incorporate the compressed members and allow for performing an optimization with the related design variables. Examples of optimized asymmetric highly scalable cable networks are shown in Fig. 4.

2.2. Advanced deployable ring architectures

The need to transport large reflectors into orbit makes foldability of the structure a necessary requirement for accommodation in launchers. The operational configuration of the reflectors is achieved after a deployment procedure. A variety of deployable structures can be found in the literature, all of them are based on different types of foldable modules composed of interconnected hinged rods (linkages) [11]. One of the basic elements is a composition of two rods interconnected with a revolute joint forming a planar scissor pair. Combination of these planar scissor elements forms a pantograph type linkage. Foldable systems based on these elements give excellent packaging features and yield the possibility of a reliable deployment. In this section, closed loop ring structures based on different types of pantographs are presented. Two different types of planar scissor pairs are defined according to [11]: scissor pairs inscribed in a rectangle (Fig. 5 left) and scissor pairs inscribed in an arbitrary quadrilateral (Fig. 5 right). The general foldability condition described in [11] for such interconnected hinged rod ideal systems leads to the following geometric condition: $a + b - c - d = 0$. This condition is automatically fulfilled for rectangular modules, because of equal lengths. For arbitrary quadrilaterals the scissor pairs have to be constructed in a way that this condition is fulfilled. In the following sections, two different deployable ring designs based on both types of the above mentioned pantographs are presented.

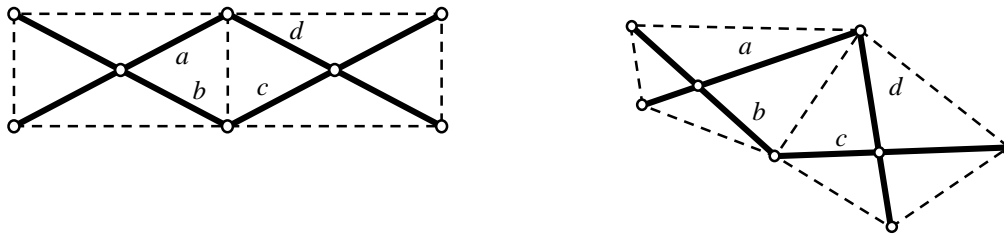


Fig. 5. Scissor pairs inscribed in rectangles (left), scissor pairs inscribed in arbitrary quadrilaterals (right)

2.2.1. A deployable ring based on a shifted double pantograph architecture

In the concept of a shifted double pantograph architecture, the ring is composed by two regular polygons inscribed in two concentric ellipses. In the height direction the polygons are expanded to form faceted cylindrical surfaces. A scissor pair composes each facet of both of the cylindrical surfaces. Upper and lower edges of the scissor pairs are fixed on the vertical posts, while inner ends are rolling on the vertical posts for folding and deployment. The fact that the ring is based on regular polygons gives the opportunity to design identical scissor pairs inscribed in a rectangle for inner and outer rings. Furthermore, the foldability condition is automatically fulfilled. During deployment, the outer and the inner vertical posts are always located on the concentric ellipses and distances between them remain constant.

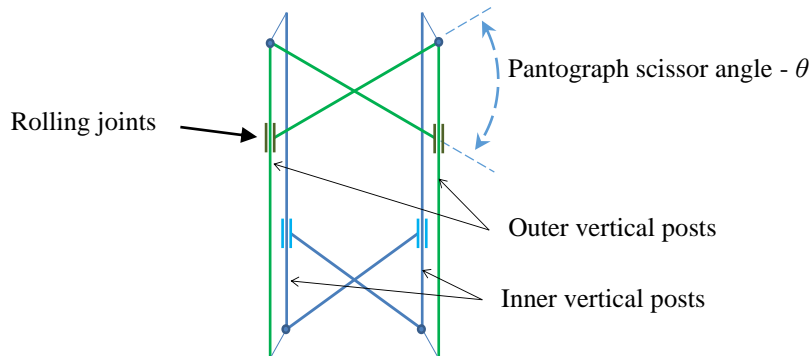


Fig. 6. Basic idea of the shifted double pantograph ring [11], [8]

Two functional demonstrators have been built and tested in order to prove the feasibility of the concept. In order to analyze and prove the good repeatability of the ring geometry photogrammetry based measurements have been performed in fully deployed configuration for five deployments together with three reference measurements. A 1.6m

diameter functional breadboard was used for these investigations. The measurement results summarized in Table 1 give a clear evidence of an excellent repeatability of the shape of the structure including the optimized cable network.

The second manufactured and tested demonstrator has a diameter of 6m. Deployment reliability of the concept has been successfully demonstrated and proved throughout many deployments. The deployment sequence of the ring is shown in Fig. 7.

Table 1. Deployment repeatability of the 1.6m functional breadboard [11]

	3 Reference Measurements			Measurements after each of 5 Deployments				
Mean radius [mm]	799.638			799.637				
STD [mm]	0.0199			0.0230				
Absolute difference from mean value. [mm]	-0.011	0.028	-0.017	0.029	0.001	-0.009	0.037	0.019



Fig. 7. Deployment of a 6m diameter functional demonstrator based on a shifted double pantograph ring

2.2.2. A lightweight deployable ring based on a single pantograph and W-fold bars

In this section a conically shaped ring architecture is presented. The idea of a ring structure with a conical shape is driven by the fact that a conical framework has naturally a higher stiffness in comparison to a cylindrical one. As offset LDRs are considered, a faceted elliptic cone is a possible ring configuration. A regular or an irregular polygon inscribed in an aperture boundary ellipse can be considered. In the height direction, the faceted elliptic cone is cut with a plane parallel to the aperture plane. As a result, a ring structure with a conical shape is acquired. Each facet of the ring has a trapezoidal shape and naturally has a higher stiffness than a rectangular one. Each facet of the ring consists of a scissor on the upper or lower side and a horizontal bar (parallel to the bases of the trapezoid) on the opposite side [20]. In this case, two sections of the ring have to be considered due to the fact that two sections are forming one foldable module with two pantographs on top side and W-fold bars on the bottom, as shown in Fig. 8.

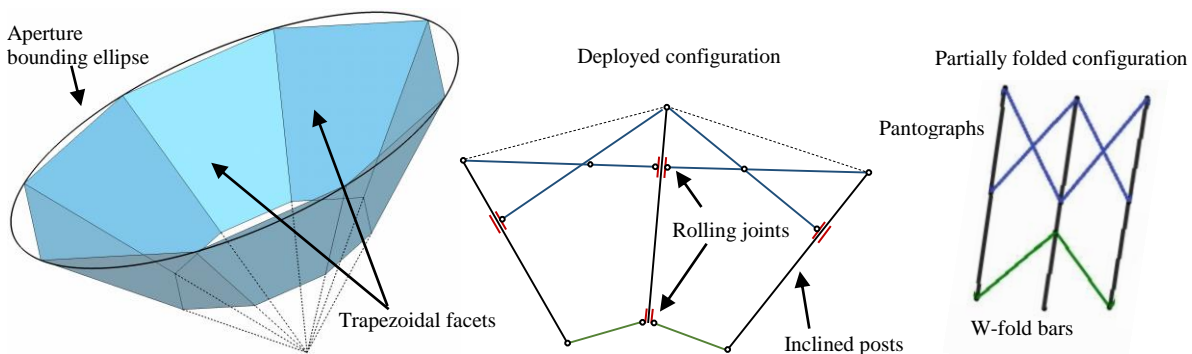


Fig. 8. Shape of an elliptic conical ring (left) and composition of a section of the conical ring (right)

Due to the elliptic shape of the reflecting surface, the trapezoids do have different shapes in a quarter. This leads to the necessity of non-identical scissor pairs. Additionally, all pantographs of the ring shall fulfil the foldability condition described above. The foldability condition for this type of pantographic structures can be represented graphically. A general geometric construction method of two-dimensional structures composed of scissor pairs has been presented in [21]. A scissor pair with lengths a and b is considered. In order to connect this unit with another scissor pair with lengths c and d so that foldability condition $a + b - c - d = 0$ is fulfilled leads to the fact that both intersecting points of scissor pairs have to be located on an ellipse. The foci of this ellipse are located on the intersection points of two compatible scissor pairs. Every intersection point of the scissor pairs that lies on this ellipse will fulfil the foldability condition [21]. For the case of a conical ring, this method can be extended to the three dimensional case. All scissor pairs having their intersection points located on an ellipsoid and ends in foci will satisfy the foldability condition. This three dimensional construction method has been utilized for the single pantograph ring and is shown in Fig. 9 for a half faceted elliptic cone with pantographs on the rear side.

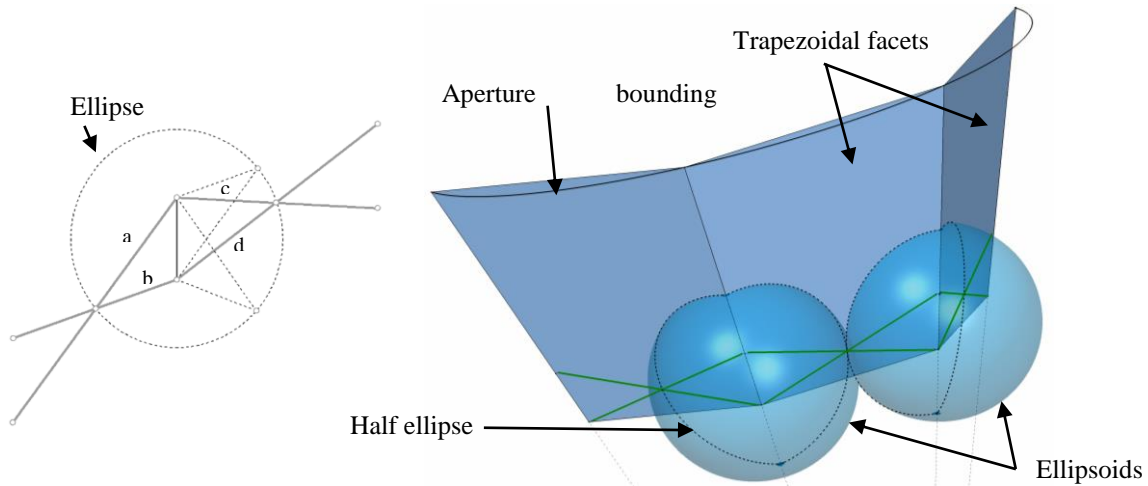


Fig. 9. Geometric 2D interpretation (left) [21] and 3D interpretation of foldability the condition (right)

3. STIFFNESS AND MASS CHARACTERIZATION OF ADVANCED LDR ARCHITECTURES

Finite element method (FEM) analyses have been performed to evaluate the structural performance of the different concepts of reflector dishes. Parametric FE models of the conical and cylindrical reflector dishes have been established with the FEM software ANSYS. The goal of the performed FE analysis is to investigate and characterize the structure in terms of deployed and stowed stiffness, stability under cable network pre-stress load, thermo-elastic stability and accuracy assessment among others and final dimensioning of structural parts for flight models. Then dimensioning of the structural parts takes the sufficient critical load factor (>3) derived from the prestress and the worst thermal loads into account.

The goal of this chapter is to demonstrate that the stiffness of the LDR architectures in deployed state is able to satisfy the modal safety requirements. By using the earlier introduced scaling methods, this can also be achieved for diameters up to 30 m. A dynamic modal behaviour of reflector dishes has been investigated with a mass margin of 20% added to the reflector's calculated masses for all presented modal analyses. The modal analyses have been performed under consideration of the cable network pre-tensioning load case.

Established parametric FE models of the conical and cylindrical reflector dishes are similar in terms of the used materials, joints, and structural elements. The complete FE model of the cylindrical reflector dish is shown in Fig. 10. The nomenclature introduced, as shown in the figure, is used in this paper.

Pantograph bars and vertical posts are represented by CFRP tubes in the FE model. All hinges have been modelled as multipoint constraint elements with the needed rotational degrees of freedom, which are available in the FE software ANSYS. The masses of each joint have been modelled with mass elements in an appropriate position based on the values from CAD models. All FE models have the same support fixations modelled by fixing the first vertical post at top and bottom points and the neighboring vertical posts top points' translational degrees of freedom. This kind of fixation simulates a designed attachment to the arm and gives a quick possibility for the assessment of the reflector's stiffness.

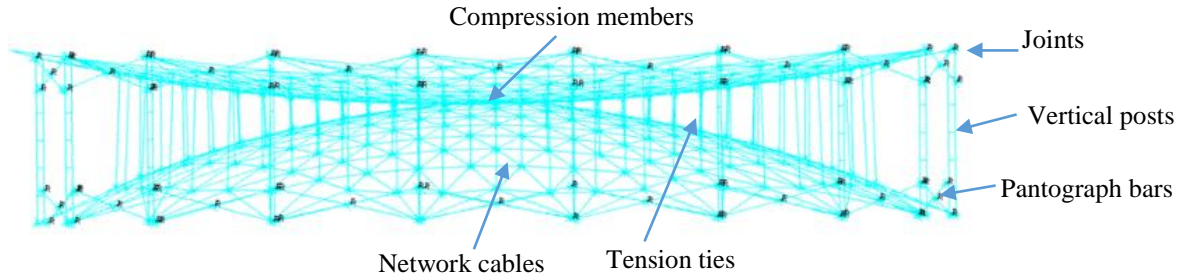


Fig. 10. Exemplary FE model of a LDR with a cylindrical peripheral ring

3.1. 8 to 18 m class LDRs

The performance of the LDRs based on cylindrical and conical peripheral rings is evaluated in terms of stiffness and stability behaviour. A 12m design is used as example for reflectors of the 8 to 18m class. The performed parametric studies provide a basis for the comparison of the different configurations of the LDR concept. Both of the architectures are based on the initial reflector parameters given in Table 2. The resulting reflecting surface geometry has a depth of 1.2 m and an elliptic shape in the aperture plane with the following characteristic dimensions: major axis=15 m, minor axis=12 m.

Table 2. Reference reflector parameters of LDRs of large family

Parameter	Value
Reflector projected circular aperture diameter [m]	12
Reflector focal length [m]	6
Reflector offset [m]	3

3.1.1. Cylindrical architecture with shifted double pantograph ring

The reference design of the LDR based on the shifted double pantograph cylindrical ring is shown in Fig. 11. This architecture uses the intersected cable network concept HSN-1. The three main parameters that influencing the ring design are the number of sections, the ring height (H) and the pantograph scissor angle θ (see Fig. 11). A ring with 24 sections, a scissor angle θ of 25° and a ring height of 2250 mm is considered as reference design for the cylindrical reflector.

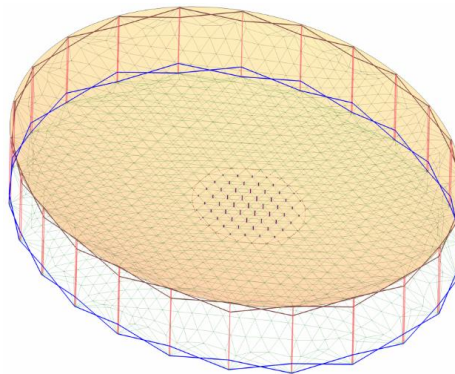


Fig. 11. CAD reference design of a reflector dish based on the cylindrical shifted double pantograph ring and HSN-1

Fig. 12 depicts the first two mode shapes and the respective Eigen-frequencies of the reference configuration of the cylindrical reflector dish. The reference design fully satisfies the stiffness requirements. The first mode shapes are an out of plane cantilever bending mode and a twisting mode relative to the major axis of the aperture ellipse. The corresponding frequencies are 0.527 Hz and 0.676 Hz.

The influence of the main parameters of the peripheral ring on the modal behaviour of the reflector dish has been analysed. The scissor angle θ (see Fig. 6) influences the ring stiffness most. Therefore, a parametric study of reflector dish's modal behaviour dependant on the angle θ has been performed. The number of ring sections and the ring height have been kept constant. The Eigen-frequency results of the performed study are shown in Fig. 13 along with the corresponding masses of the reflector.

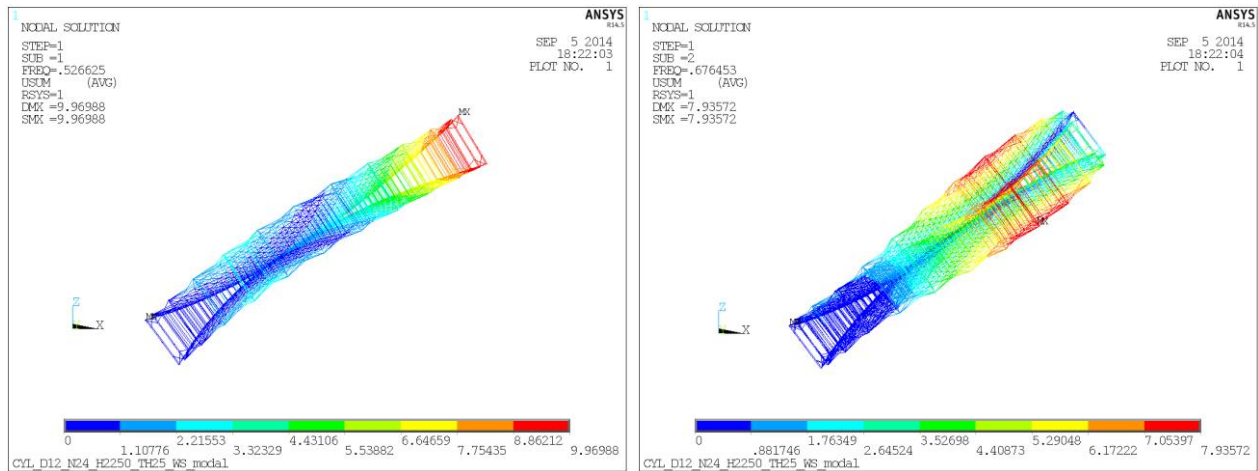


Fig. 12. First two mode shapes of the cylindrical reflector dish

From the graphs in Fig. 13 it can be concluded that the cylindrical LDR architecture based on the double pantograph ring has a high potential of stiffness increase with an insignificant impact on the total dish mass. The first two mode shapes in the complete analysed range of the pantograph angle are an out-of-plane cantilever bending mode and a twisting mode. The first Eigen frequency increases up to an angle at which the ends of the top and the bottom pantograph bars meet in the middle of the height, forming a “quasi-truss” structure. A value of 1,373 Hz at $\theta=66^\circ$ can be yielded. The further increase of the angle causes a decrease of the stiffness of the structure. From this analysis, one can conclude that the stiffness of the ring shows high sensitivity to the effective shear stiffness of the section. This fact is confirmed by a subsequent study of the stiffness of the structure incorporating diagonal stiffening cables. These stiffening cables give constant shear stiffness to the ring and result in a constant first Eigen-frequency, while the angle change does not yield the previously seen effect anymore (Fig. 14).

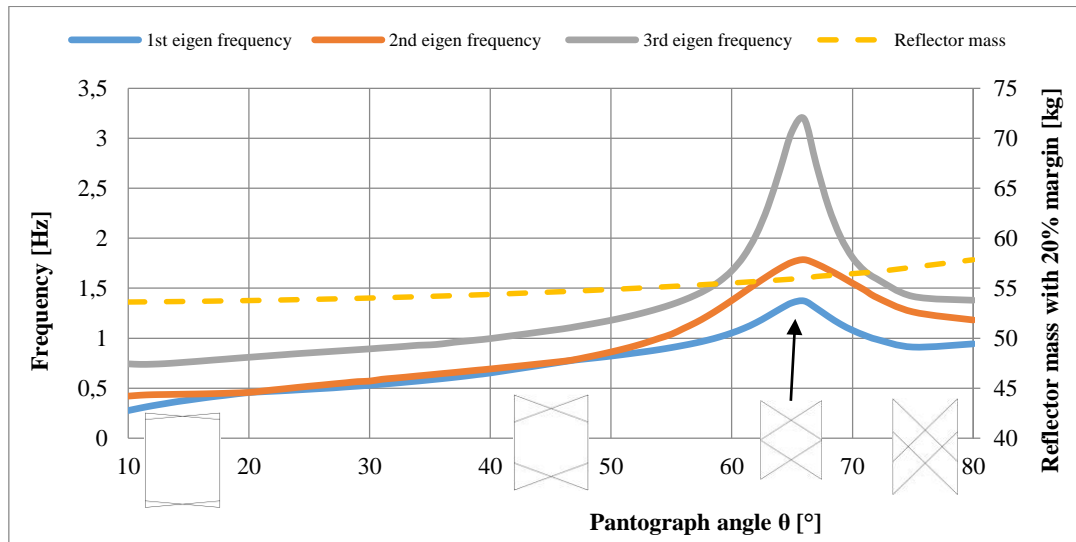


Fig. 13. Influence of pantograph scissor angle θ on the first three Eigen-frequencies and the mass of the LDR

The influence of the scissor angle on the modal frequencies is characteristic for all the pantograph rings discussed below. A further parameter that influences the modal behaviour of the reflector dish is the mounting type of the reflector. Three different mounting types are feasible without changing the concept of the boom to reflector dish interface. The ring can be supported on the second and third neighbouring vertical posts instead of the first one being a

reference. Analyses have been performed for all three configurations with the reference parameters of the reflector dish. The results of the performed analyses show the influence of the moved position of the mounting point: the first mode is a bending mode and the corresponding frequencies are increased by approximately 0.1 Hz.

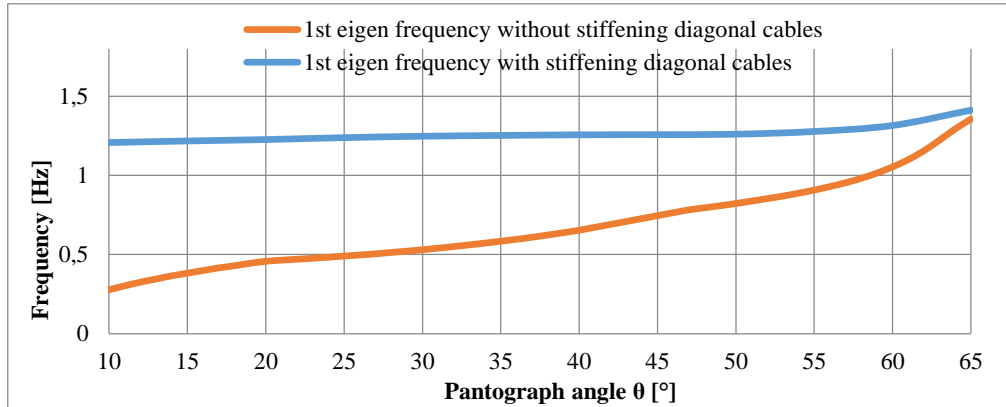


Fig. 14. Influence of pantograph scissor angle θ on the first Eigen-frequencies of the LDR in the case of section without and with diagonal stiffening cables

3.1.2. Conical architecture with a single pantograph ring and W-fold bars

The CAD design of an LDR based on the single pantograph conical ring is shown in Fig. 15. An asymmetric cable network assembly is utilized in this analysis case. The configuration of the ring structure is defined by the parameters shown in Fig. 15: the number of sections of the ring, the conical ring height H and the conicity angle α . On the section level the geometry of the ring is only defined by the pantograph scissor angle θ . The method of pantograph construction for the elliptic conical rings, as described in section 2.2.2, has been implemented in the parametric FE model. Thus, all pantographs satisfy the foldability condition. The number of sections, equal to the number of facets of the faceted elliptic pyramid created by the ring, is set to 24 in order to keep the architecture comparable with the cylindrical ring design. The scissor angle θ has been set to 40° as a reference value.

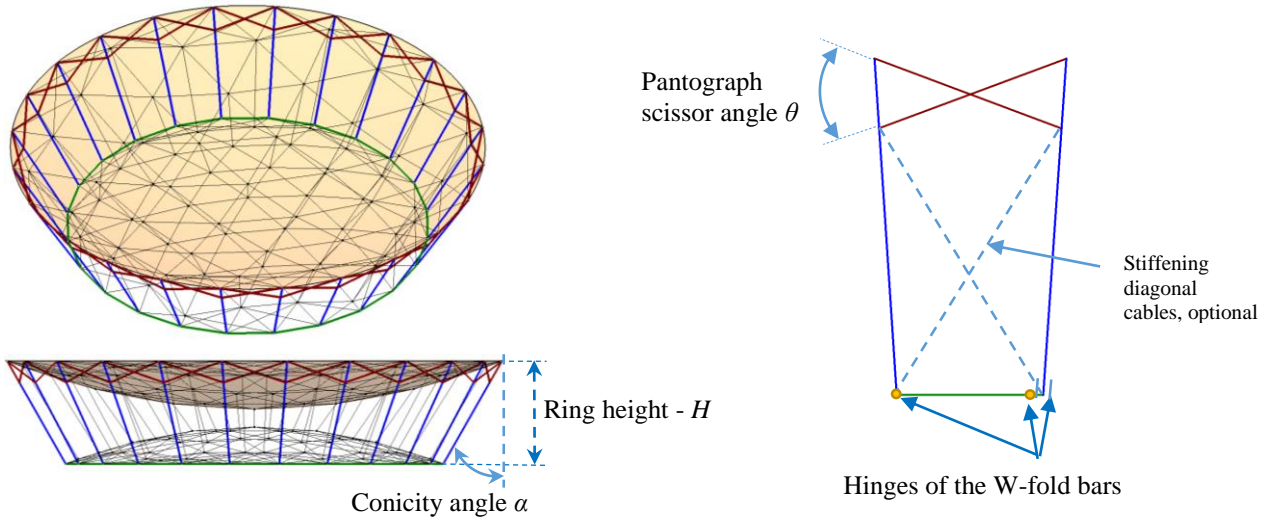


Fig. 15. CAD design of a reflector dish based on the conical single pantograph ring and an asymmetric cable network; design parameters of the conical ring

The parametric studies have been performed by varying the main parameters of the ring and investigating their influence on the modal behaviour of the structure. The conicity angle α (see Fig. 15) is one of the parameters that have a main influence on the stiffness of the reflector dish. The influence of the conicity angle change is expressed by the reduction of the effective cone height more than by the improvement of the 3D stiffness behaviour. The ring section height has not been considered as a free parameter but has been derived from the foldability condition. As mentioned above, the scissor angle increase yields higher natural frequencies of the reflector. Another very promising aspect of the

single pantograph design is that the mass of the reflector dish is about 20% less compared to the double pantograph reflector design. The introduction of diagonal stiffening cables causes a frequency increase up to the very high values. The influence of the scissor angle diminishes in configurations with diagonal stiffening cables.

The influence of the support type on the modal behaviour of the reflector is similar to the behaviour observed for the cylindrical reflectors: The Eigen-frequencies remarkably increase when the support points are moved from the first neighbouring posts to the second and to the third neighbouring posts.

3.2. 18 to 35 m class LDRs

Reflectors with dishes of 20 m and 30 m projected aperture diameter have been considered as a reference for characterization of stiffness for the 18 – 35 m class LDRs, known as very large size reflectors. The reflector configurations are based on the parameters listed in Table 3. The resulting reflective surfaces have a large depth and a highly extended elliptical aperture. This is done intentionally in order to examine the extreme configurations of the reflectors. Mentionable is the fact that in the case of 30 m diameter the depth of the reflector surface is larger than 4 m. The use of conventional cable network assemblies would require the height of the deployed ring to be in the range or larger than 8 m. Even if the package dimensions of the stowed configuration of the reflector would fit in the dynamic envelope of the available launchers, the structural requirements of such a ring are far beyond current state of the art. The highly scalable cable networks HSN-1 and HSN-2 (see Fig. 4) enable a high scalability of the concepts, thus of the technology. The shifted double pantograph ring has been analysed for very large sizes.

Table 3. Reference reflector parameters of LDRs of very large family

Parameter	Value	
Reflector projected circular aperture diameter [m]	20	30
Reflector focal length [m]	6	9
Reflector offset [m]	3	3

For the 20m reflector dish, a ring with 24 sections has been utilized. For the 30m one, 36 sections are needed in order to keep ring height below 4m (4 m is considered as an approximate limit of the package height). The design option with stiffening cables has been chosen for these analyses. The performed structural analyses follow the same sequence as for the 12 m reflector: after the form finding and optimization analysis of the highly scalable networks and the incorporation of them into the FE models, first a prestress and then modal analysis have been performed.

The modal analysis results for 20 m and 30 m reflector dishes are presented in Fig. 16. The first mode shapes at 0.485 Hz and 0.225Hz respectively are shown. The achieved results are very promising for LDRs of this class. Moreover, these designs take into account the structural stability as well.

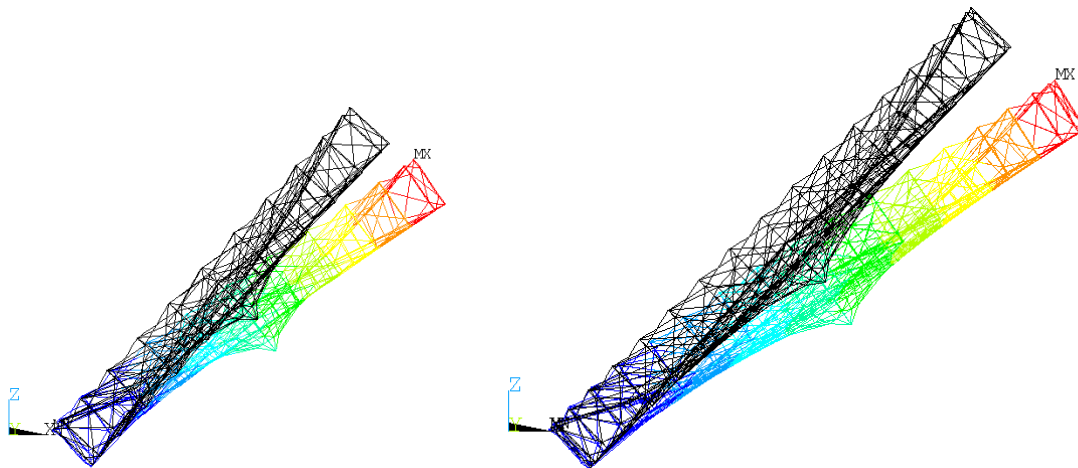


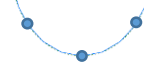


Fig. 16. First mode shapes of 20m (left) and 30m (right) aperture diameter reflector dish

Different support types can be utilized to increase the first Eigen-frequencies in these cases as well. The first Eigen-frequencies' dependence on the support types are listed in Table 4 for both reflector dishes. Note that for both LDRs and all support types the first mode shape is a bending mode and that the second mode is a twisting mode.

Table 4. Influence of support type on the first two Eigen-frequencies of 20 and 30m diameter LDRs

	Eigen-frequency , [Hz]	In plane support types		
		First neighboring vertical posts	Second neighboring vertical posts	Third neighboring vertical posts
		 (S1)	 (S2)	 (S3)
20m diameter	First	0,485	0,607	0,614
	Second	0,519	0,612	0,774
30m diameter	First	0,225	0,262	0,323
	Second	0,235	0,306	0,351

As it can be observed from the table, a helpful increase of the natural frequencies can be achieved by moving the mount points to the next neighboring posts.

3.3. Summary of LDR classes

Basic properties of the LDRs classes are summarized in Table 5. Medium size LDRs are presented by 6m and 5m aperture diameter reflector dishes targeting Ka and C bands respectively, both based on cylindrical rings. Large size LDRs are represented by 12m diameter reflector dishes targeting X and L bands with cylindrically and conically shaped rings. 20 m and 30 m aperture diameter reflectors based on cylindrical single and double pantograph rings represent very large size reflectors class in this paper.

Table 5. Characteristics of the designed and analyzed LDRs of different classes

LDR classes	Projected aperture diameter [m]	Frequency band	F/D	Areal density (reflector dish) [kg/m ²]	Stowed diameter [m]	Stowed height [m]	First Eigen-frequency, deployed [Hz]
Medium 4 - 8 m	5	Up to Ka	1	0,99	0,44	1,08	1
	6		1	0,81			1,5
Large 8 - 18 m	12	Up to X	0,5	0,39	0,54	2,25	Up to 1,4
	12		0,5	0,32	0,54	3,4	Up to 1,5
Very large 18 to 35 m	20	Up to S	0,3	0,31	0,7	3,6	0,48-0,61
	30		0,3	0,26	0,85	4	0,22-0,32

4. CONCLUSIONS

The basics of the ring and cable network architectures have been presented in this paper. It is shown that highly scalable cable networks according to [20] give a possibility of scaling the LDR technology from 4 to 35 m with no conceptual change.

The stiffness assessment of the reference designs from all the LDR classes show that the followed concept of shifted double or single pantograph will meet the flight hardware requirements with 20% of mass advantage for the latter one.

Reflectors for the Ka band can be realized with smaller diameters. The reflectors with diameters up to 30 m of the presented architecture fulfil the requirements for up to S band applications.

REFERENCES

- [1]. Mangelot, C., et al.: Large Antenna Working Group, ESA Final Report, TEC-EEA/2010.595/CM (2010)
- [2]. Datashvili, L., Review and Evaluation of the Existing Designs / Technologies for Space Large Deployable Apertures. *International Scientific Conference on Advanced Lightweight Structures and Reflector Antennas*, 14 - 16 October 2009, Tbilisi, Georgia, 2009
- [3]. "Harris deployable antennas", http://download.harris.com/app/public_download.asp?fid=463
- [4]. Thomson, M. W., "The AstroMesh deployable reflector", In *IUTAM-IASS Symposium on Deployable Structures: Theory and Applications* (Cambridge, UK, 6–9 September 1998), S. Pellegrino and S. D. Guest, Eds., Kluwer Academic Publishers, Dordrecht, The Netherlands, 2000, pp. 435–446.
- [5]. M. W. Thomson, "Astromesh deployable reflectors for Ku and Ka band commercial satellites", AIAA-2002-2032.
- [6]. Santiago-Prowald, J., Such Taboada, M.: Innovative deployable reflector design. In: 33rd ESA Antenna Workshop, October 2011 ESA-ESTEC, Noordwijk, The Netherlands.
- [7]. Santiago-Prowald, J. & Baier, H., "Advances in deployable structures and surfaces for large apertures in space", *CEAS Space Journal*, Springer Vienna, 2013, 5, 89-115
- [8]. Datashvili, L.; Endler, S.; Wei, B.; Baier, H.; Langer, H.; Friemel, M.; Tsignadze, N. & Santiago-Prowald, J., "Study of mechanical architectures of large deployable space antenna apertures: from design to tests", *CEAS Space Journal*, Springer Vienna, 2013, vol. 5, pp. 169-184
- [9]. Datashvili, L.; Baier, H.: "Derivation of Different Types of Antenna Reflectors from the Principle of Highly Flexible Structures", *European Conference on Antennas and Propagation 8.*, The Hague, The Netherlands, 2014
- [10]. Datashvili, L.; Maghaldadze, N.; Ender, S.; Pauw, J.; He, P. ; Baier, H.; Ihle, A.; Prowald, J. S.: "Advances in Mechanical Architectures of Large Precision Space Apertures", *European Conference on Spacecraft Structures, Materials & Environmental Testing*, 2014
- [11]. Datashvili, L.: "Foldability of hinged-rod systems applicable to deployable space structures", *CEAS Space Journal* (5), 2013, S. 157 - 168
- [12]. Wei, B.; Magner, D.; Endler, S.; Datashvili, L.: "High precision large space structures: challenges in cable networks design". *International Conference on Textile Composites and Inflatable Structures, Structural Membranes*, CIMNE 2013, München, 2013
- [13]. Datashvili, L.; Baier, H.; Wehrle, E.; Kuhn, T.; Hoffmann, J.: "Large Shell-Membrane Space Reflectors". 51st AIAA/ASME/ASCE/AHS/ASC Structures, Structural Dynamics, and Materials Conference, 12 - 15 April 2010 2010, Orlando, Florida, USA, 2010
- [14]. Datashvili, L.; Baier, H.: "Space Applicable Antenna Reflectors with Flexible Shell-membrane Reflecting Surface". *International Scientific Conference on Advanced Lightweight Structures and Reflector Antennas*, 14 - 16 October 2009, Tbilisi, Georgia, 2009
- [15]. Datashvili, L.; Baier, H.; Schimitschek, J.; Lang, M.; Huber, M.: "High Precision Large Deployable Space Reflector Based on Pillow-Effect-Free Technology". 48th AIAA/ASME/ASCE/AHS/ASC Structures, Structural Dynamics, and Materials Conference, 2007
- [16]. Eastwood Im, Mark Thomson, Houfei Fang, James C. Pearson, James Moore and John K. Lin, "Prospects of Large Deployable Reflector Antennas for a New Generation of Geostationary Doppler Weather Radar Satellites", AIAA SPACE 2007 Conference & Exposition, Long Beach, California.
- [17]. H.-J. Schek, "The force density method for form finding and computation of general networks", *Journal of Computer methods on applied mechanics and engineering*, volume 3 (1974) 115-134.
- [18]. M. R. Barnes, "Form finding and analysis of tension structures by dynamic relaxation", *International Journal of space structures*, Vol. 14, No.2, 1999.
- [19]. Datashvili, L.; Maghaldadze, N.; Ender, S.; Pauw, J.; He, P. ; Baier, H.; Ihle, A.; Prowald, J. S.: "Advances in Mechanical Architectures of Large Precision Space Apertures", *European Conference on Spacecraft Structures, Materials & Environmental Testing*, 2014
- [20]. L. Datashvili, "Deployable Space Reflector", Georgian Patent Application ID: 12873/01, 19.10.2012
- [21]. Niels De Temmerman, "Design and Analysis of Deployable Bar Structures for Mobile Architectural Applications", PHD Thesis, Vrije Universiteit Brussel, 2007

- [22]. Dennis Semler, Ann Tulintseff, Rodney Sorrell, James Marshburn, “Design, Integration, and Deployment of the TerreStar 18-meter Reflector”, 28th AIAA International Communications Satellite Systems Conference (ICSSC-2010), 30 August - 2 September 2010, Anaheim, California
- [23]. <http://www.northropgrumman.com/BusinessVentures/AstroAerospace/Products/Pages/AstroMesh.aspx>
- [24]. K. Miura, Y. Miyazaki (1990). “Concept of the tension truss antenna”, AIAA J, 28 (1990), pp. 1098–1104

NEW CONSTRUCTIONS OF LIGHTWEIGHT DEPLOYABLE REFLECTORS

E. Medzmariashvili⁽¹⁾, Julian Santiago-Prowald⁽²⁾, Cyril Mangenot⁽²⁾, Horst Baier⁽³⁾, Leri Datashvili⁽³⁾, Nodar Tsignadze⁽¹⁾, Lorenzo Scialino⁽⁴⁾, Kees Van't Klooster⁽²⁾, Guram Bedukadze⁽¹⁾, Mikheil Janikashvili⁽¹⁾, Otar Tusishvili⁽¹⁾, Ludmila Philipenko⁽¹⁾, Nikoloz Medzmariashvili⁽¹⁾, Ariadna Jakhua⁽¹⁾

⁽¹⁾*Institute of Constructions, Special Systems and Engineering Maintenance of Georgian Technical University*
#68b Kostava St. 0172 Tbilisi, Georgia
Email: medzmariashvili@gtu.ge; icssem@gtu.ge

⁽²⁾*European Space Agency - ESTEC*
Keperlaan 1, 2200AG, Noorwijk, The Netherlands
Email: Julian.Santiago.Prowald@esa.int, Cyril.Mangenot@esa.int, Kees.van.t.Klooster@esa.int

⁽³⁾*Munich Technical University – Institute of Lightweight Structures*
Boltzmannstrasse 15, 85747, Garching, Germany
Email: datashvili@llb.mw.tum.de; baier@tum.de

⁽⁴⁾*Space Engineering S.P.A*
Via dei Berio 91, 00155 Roma, Italy
Email: lorenzo.scialino@space.it

ABSTRACT

Creation of large size, lightweight, rigid and precision reflectors is the problem that still remains in the field of space antennas. In recent years, a voluminous work has been being conducted jointly by the European Space Agency, Munich Technical University and Georgian Technical University aiming at finding out a new structural design. The structures of the rings having a new design circular double pantograph, conical V-fold bars, unfolding springs and electrical motors, and of the flexible, geometrically unchangeable center have been elaborated and theoretically and experimentally studied within the scope of the work. The researches and tests revealed pros and cons of the new constructions. In their entirety, the structures are rigid, precision, lightweight and are capable of controlling and managing the transforming processes.

1. INTRODUCTION

The new scheme of deployable space reflector was created on the base of the logic of stretched architecture, have been elaborated their design principles, have been designed, manufactured and tested their demonstrators and functional models [1][2][3][4][5].

Reflectors build according two main schemes of finished transformation's deployable ring were reviewed within the scope of the work:

- Pantographic deployable bearing ring with tensioning, flexible center is locate in two lines;
- V fold bar deployable bearing ring with tensioning, flexible center.

2. PANTOGRAPHIC DEPLOYABLE BEARING RING WITH TENSIONING, FLEXIBLE CENTER IS LOCATE IN TWO LINES

Let us have a look at the deployable reflector antenna ring structure, each section of which has equal length load-bearing rods-levers arranged in a cross-like fashion that intersect in a central cylindrical unit. The lever ends are fixed in posts by means of cylindrical units. The edge cylindrical units are motionless with respect to a post. The intrinsic units are "slidable" in the direction of the post, which determines the deployment and folding of the ring (fig 1).

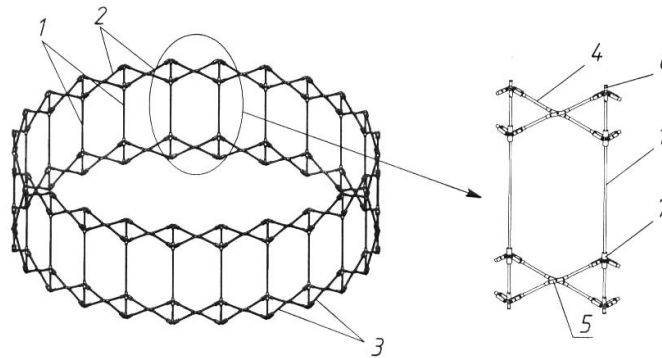


Fig. 1 – Constructional scheme of 4 meter deployable ring model and one section

1 – Vertical bar; 2 – upper pantographic structure; 3 – lower pantographic structure; 4 – separate pantographic levers; 5 – central cylindrical joint intersecting of pantographic levers; 6 – joints performed with cylindrical nodes that are fastening the ends of adjacent pantographic levers located at the end of the vertical bar; 7 – sliding joint located at the vertical bar that fastens adjacent levers with cylindrical joints.

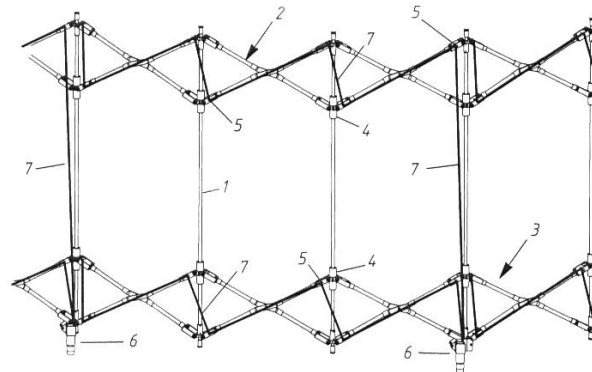


Fig. 2 – Structural diagram of the four meter deploying ring model and of a single section

1 – Vertical bar; 2 – upper pantographic structure; 3 – lower pantographic structure; 4 – joints sliding on the vertical bar; 5 – rollers located at the end of levers, joints; 6 – motors; 7 – ring deployable bearing cable

The units which are “slidable” along a post are moved by a deploying cable that passes over them and motionless units and passes through the units disposed on each subsequent post and finally it coils on a rotary shaft of an electrical drive, while its another end is fixed in a motionless cylindrical unit being disposed several next posts apart fig. 2.

According to the project the triangular cell shape cable nets are fastened in lower joints of vertical bar and regulating joints according to the height at the top of vertical bar, in 4 meter ring.

Their corresponding joints are connected with tensioners that are equipped with length compensating springs. Fig 3 displays the scheme of placements of vertical bars and fastening with its peripheral joints at the end of vertical bars.

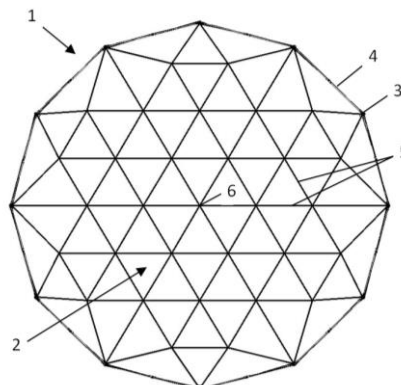


Fig. 3 – Top view of tensioned net and with its peripheral joints on the ends of its post

1 – ring; 2 – tensioned mesh; 3 – joints above the vertical bars; 4 – pantographs between the vertical bars; 5 – flexible rods of mesh; 6 – joints of mesh

Presented constructional principles became bases for project of 4 meter deployable space reflector, its views in unfolded state and in folded transportation package shown in fig. 4.

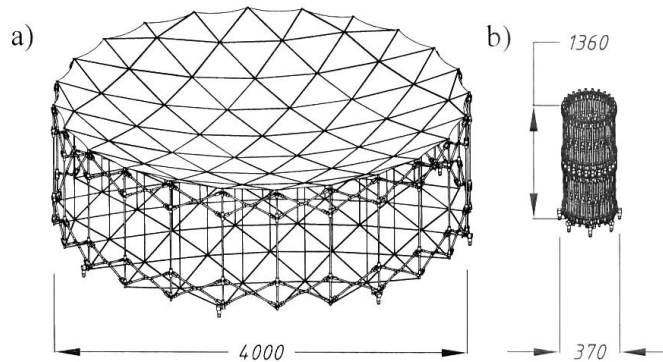


Fig. 4 - 4 meter deployable space reflector, its views in unfolded state (a) and in folded transportation package(b).

The aim of experimental researches was to find out how the real functional technical characteristics of presented design of reflector corresponds to projected one, and also to determine those specific issues that requires special attentions for farther improvement of construction.

Montage and test of reflector been performed on stand, that particularly provided imitation of gravity compensating condition (fig 5).



Fig 5 – functional model of 4 meter deployable reflector

The main purpose of experiment was to study deployment transformation, to reach accurate geometry of approximate surface of reflector's screen and its repetition (also with high accuracy) on different stages of deployment. The experimental research with above mentioned aims included the research of following questions:

- Control, management and reliability of reflector deployment;
- Velocity of deployment;
- Variation of force in deployable cables during the deployment;
- Electricity consumed by motors during the deployment;
- Spread of force in cables of fully deployed ring;
- Spread of force in tensioners of reflecting mesh;
- Force actuating in support and back mesh of reflector;
- Forces in elements of pantograph;
- Geometry of reflector and repetition;
- Eigenfrequencies

As experimental researches showed, during the entire process of deployment, except the last stage of deployment, when flexible center starts its deployment, the ends of pantograph are moving along the post with insignificant force, what causes deployment. This effect in model been reached with that that the “slidable” displacement of joints in the direction of the post is performed using the longitudinal bearings. It gives possibility to change sliding friction on to the rolling friction that causes fewer expenses regarding the friction (fig 6).



Fig.6 “slidable” displacement of joints in the direction of the post that is performed using the longitudinal bearings

Based on the analyses of created functional breadboard and materials of performed theoretical and experimental researches the following graph presents the dependence between diameter of reflector and the weight of flying option of reflector with flexible, tensioned center and double pantograph with unfolding ring. This graph shows that the weight of reflector with “space” performance is less than the weight of created functional model (fig 7).

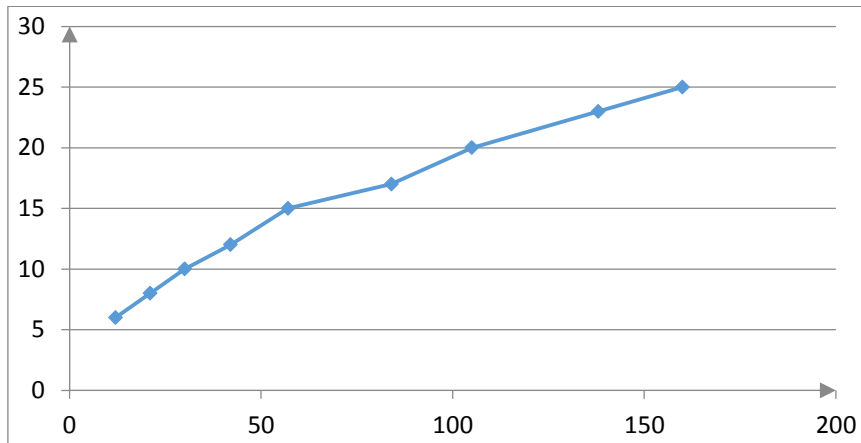


Fig 7 The weights of double pantograph reflector

3. V FOLD BAR DEPLOYABLE BEARING RING WITH TENSIONING, FLEXIBLE CENTER

Now let's discuss deployable space reflector with flexible tensioned center and with ring having the shape of truncated pyramid that is deployable by the V-fold bar springs.

The mentioned reflector was created on the bases of the scheme that was presented by specialists of European Space agency. It was realized jointly by the specialists of Georgian Technical University, Munich Technical University and Space Engineering.

The main purpose of reflector's creation was to design modular large deployable space reflector in future. Creation of reflector was a main purpose to design large modular deployable space reflector in future and to use springs as an energetic bases of reflector's deployment. Motors are used to control and manage deployment process, and to tension deployment stabilizing cable system.

6 meter space structure with truncated cone shape, with V-fold bars and springs, and with tensioned center was redesigned created and tested on the bases of the mentioned logic.

The general views of the reflector antenna having "V-fold bars" in deployed and transportable states can be seen in fig 8.

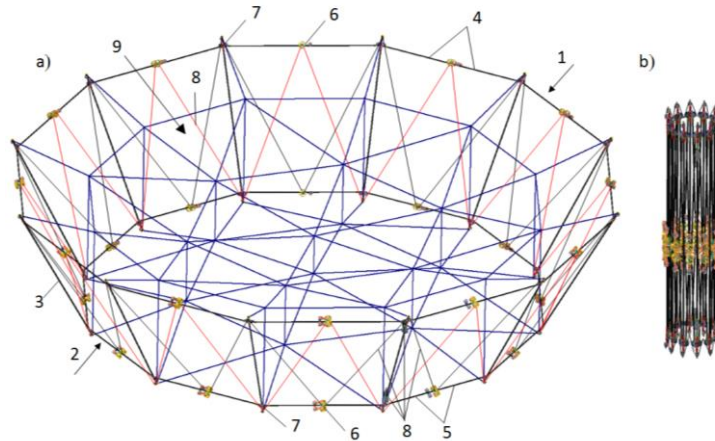


**Fig. 8 - General view of the construction
a) in the deployed state and b) in folded state.**

1 – upper ring; 2 – lower ring; 3 – vertical bar; 4 – V-fold bar of upper ring; 5 – V-fold bar of lower ring; 6 – unfolding mechanism; 7 – synchronizing mechanism; 8 – deployment stabilizing mechanism; 9 – central part

The central part comprises the following:

- Functional and technological elastic meshes;
- Vertical or inclined tensioners for connecting them;
- Reflecting mesh located at the bottom of the functional mesh – screen of reflector.

A kinematical diagram of deployment/folding of a single section of the space reflector antenna load-bearing ring and its geometrical parameters are shown in fig. 9.

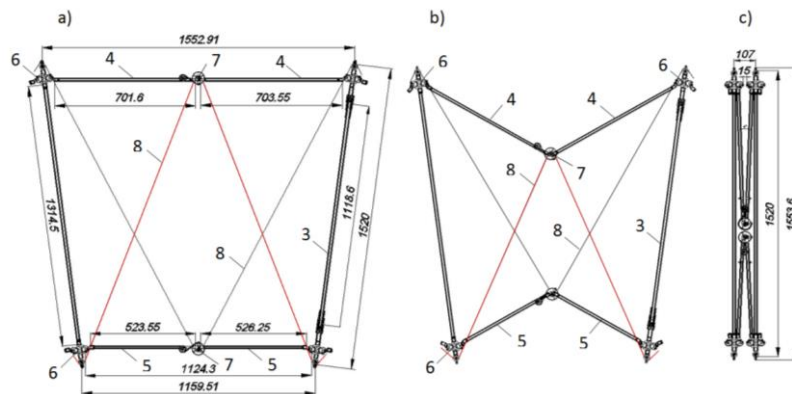


Fig. 9 Kinematical diagram of deployment/folding of the load-bearing ring single section.

Deployed state; b) Partially folded state; c) Folded state; 3 Post; 4. V-fold bars of the upper ring; 5. V-fold bars of the lower ring; 6 Synchronization mechanism; 7. Hinge with permanent force spring deployment mechanisms; 8. Deployment stabilization system.

The deployment of the load-bearing ring is effectuated by permanent moment flat springs.

Due to the symmetrical distribution of forces, coupled permanent moment spring mechanisms are used on each pair of V-fold bars (fig. 10).

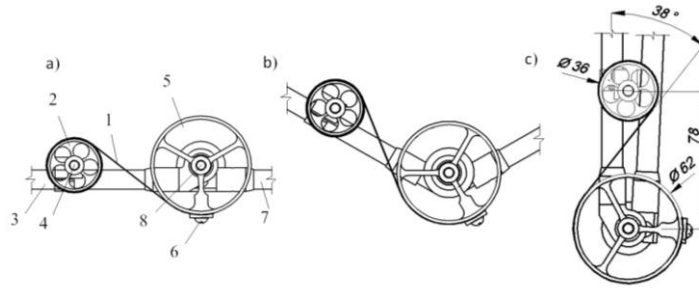


Fig. 10. Permanent moment spring deployment mechanism.

Deployed state; b) Partially folded state; c) Folded state; 1. Spring; 2. Small drum; 3. Left V-fold bar; 4. Rotary axis; 5. Coiling drum; 6. Bolt; 7. Right V-fold bar; 8. Motionless axis.

The horizontal rods are interconnected by means of synchronous transmission mechanisms, which allow simultaneous motion of the levers contained in the upper and lower rings.

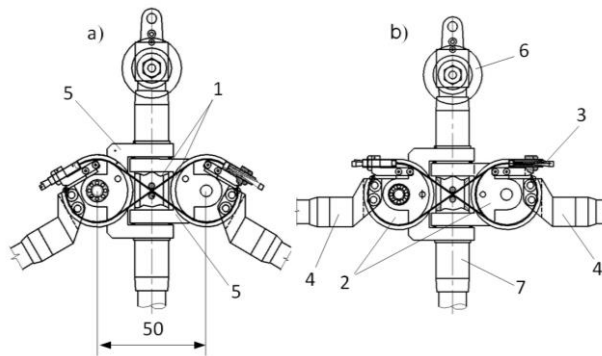


Fig. 11. Synchronization mechanism.

a – Partially folded state; b) – Deployed state;
1. Cable; 2. Guide roller; 3. Cable stretching device. 4. V-fold bars; 5. Articulates 6. Rollers. 7. Post

Levers can be rapidly turned around the synchronizing mechanism during the deployment. It will be caused from forces actuated by the springs. It will cause an impact effect in last moment. To avoid this we used levers' deployment reducing cable system that easily follows the deployment process and actuated by motors (fig 12).

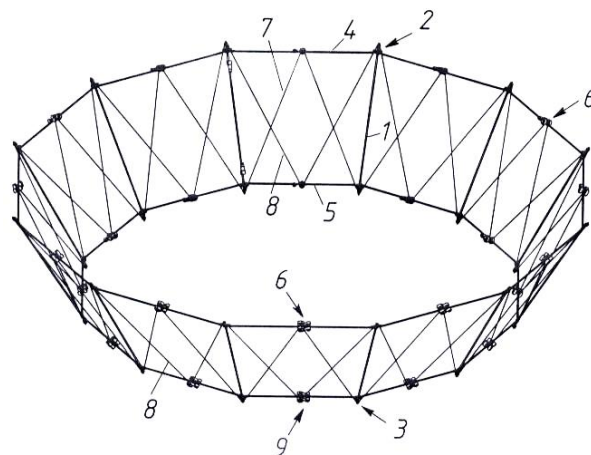


Fig 12. stabilizing system of deployable bearing ring

1- Post, 2 and 3 - the upper and bottom joints; 4 and 5 – levers of Upper and bottom V-Fold bars; 6 - Joint with ring unfolding spring and with roller for stabilizing cables; 7 – Stabilizing cable for the deployment of upper V-fold bar; 8 - Stabilizing cable for the deployment of bottom V-fold bar; 9 – V-fold bar unifying joint.

Two motors are used in reflector. One motor service to the deployment reduction of upper V-fold bars and the other serves to the lower ones. Motors are switch off when levers are in vertical condition. Functional model of reflector was manufactured during its researching stage. The maximum diameter of reflector is 6000 mm and its weight reached 16 kg.

The functional model of reflector was hanged mechanically in offloading stand. Should be mentioned that constructional scheme with V-fold bars and with springs⁰ required satisfaction of lots of conditions of weightlessness. By the work of stabilizing system deployment time of reflector was 9÷11 minutes (fig 13).



Fig 13 – Deployable space reflector with V-fold bar, Springs and flexible, tensioned center

After several deployments of reflector can be said that during each different deployment stages the geometrical shape of reflector are not similar. It is caused by the different forces actuated in different sections of stabilizing system; it stipulates variation of form of deployable ring. Herewith, its form at the last stage of deployment and final fixation completely in accordance with its design geometry. The mentioned defects mostly in middle stage of deployment mainly conditioned with the deployment spring system in V-fold bars (fig 14 a) and deployment stabilizing electromechanical system (fig 14b), they both are simultaneously functioning in reflector.

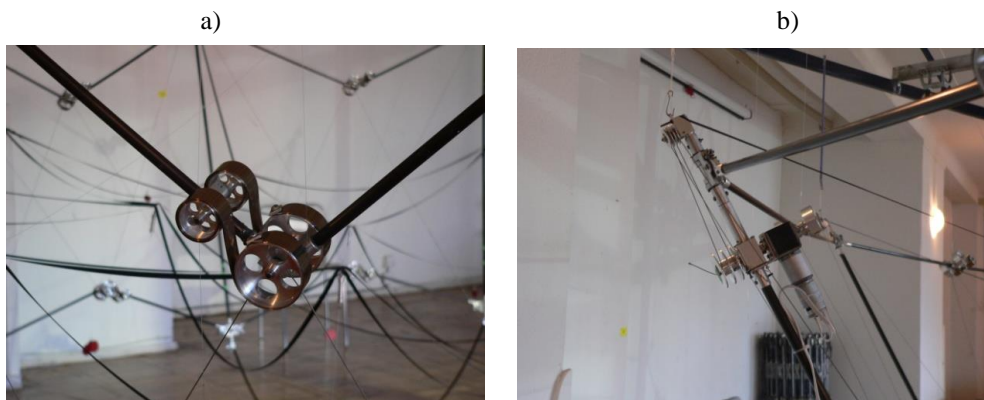


Fig 14 – Joints of deployable reflector
a - Joint with constant force spring; b – joint with motor.

4. CONCLUSION

We have discussed modified option of functional model with different deployment and stabilizing conditions on the results of the experimental researches and theoretical analyses of the functional model of deployable reflector with flexible, tensioned center and ring with electromechanical system and deployment V-fold bar and springs having truncated cone shape.

Here can be mentioned that discussed scheme of V-fold bar and experimental construction that is created on its base are fully satisfying the requirements and creates new perspective to create new modification.

5. REFERENCES

- [1]. E. medzmariashvili, Sh. Tserodze, V. Gogilashvili. New Variant of the Large Deployable Ring-Shaped Space Antenna. *Space Communications* 22 (2009) 41-48.
- [2]. E. Medzmariashvili, N Tsignadze, Sh. Tserodze, J. Santiago-Prowald; C. Mangelot, C.G.M. Van't Klooster, H. Baier, M. Janikashvili. Design of Reflector with Double Pantograph and Flexible Center. *Proceedings of ESA Antenna Workshop on Large Deployable Antennas*. 2-3 October 2012. ESTEC, Noordwijk, The Netherlands.
- [3]. E. Medzmariashvili, N. Medzmariashvili. Constructive Logic of Reflector Created with Double Pantograph Deployable Load-Bearing Ring. *Proceedings of ESA Antenna Workshop on Large Deployable Antennas*. 2-3 October 2012. ESTEC, Noordwijk, The Netherlands.
- [4]. E. Medzmariashvili, Sh. Tserodze, O. Tusishvili, N. Tsignadze, J. Santiago-Prowald, C.G.M. Van't Klooster, N. Medzmariashvili. Mechanical Supporting Ring Structures *CEAS Space Journal of European Aerospace Societies*. ISSN 1868-2502. Published online. June 2013
- [5]. E. Medzmariashvili, N. Medzmariashvili, O Tusishvili, N. Tsignadze, J. Santiago-Prowalds, C. Magenot, H. Baier, L. Scialino, L. Philipenko. The possible Options of Conical V-fold Bar Ring's Deployment with Flexible Pre-Stressed Center. *CEAS Space Journal of European Aerospace Societies*. ISSN 1868-2502. Published online. June 2013

THE DEVELOPMENT OF A NOVEL LARGE DEPLOYABLE ANTENNA REFLECTOR CONCEPT

Alberto Meschini⁽¹⁾, Riccardo Rigato⁽¹⁾, Davide Scarozza⁽¹⁾

⁽¹⁾*Thales Alenia Space - Via Saccomuro 24, 00131 Roma - Italy,*
alberto.meschini@thalesaleniaspace.com
riccardo.rigato@thalesaleniaspace.com
davide.scarozza@thalesaleniaspace.com

ABSTRACT

Thales Alenia Space Italy developed and patented a Large Deployable Reflector concept based on modular and scalable cells. This novel LDR, that presents fully innovative structural and kinematic concepts, converged into the development of a meshed LDR, in the range of 5 to 18 meters to be used for future TLC/EO and Navigation missions, within the ESA 'Innovative, Scalable, Large Deployable Antenna Reflector' AO/1-7217/NL/CP contract. A reduced scale LDR bread-board has been developed to demonstrate the validity of the kinematic approach and successfully deployed. The critical component bread-boarding to support the manufacturing of a 6 m diameter demonstrator, which includes a full scale cell, has been successfully achieved. Definition of masses, envelope, structural and thermal performance are on-going activities, currently to the level of a Preliminary Design Review. All technologies involved in the development will remain within the Europe borders.

1. INTRODUCTION

The proposed innovative reflector [1], is based on a scalable, modular and deployable polygonal-like structure based on tetrahedral building block elements (Fig. 1). The reflector is edge connected to the deployment arm and hence to the S/C by means of the 'Connecting Arm' through rotary actuators that provide deployment and trimming functions according to mission requirements. The reflector plus the connecting arm form the 'Reflector Dish' assembly. A detailed description of the elements and the functional feature of the reflector module are reported hereafter.

2. SCALABLE, DEPLOYABLE REFLECTOR STRUCTURE MODULE DESCRIPTION

The principal element constituting the reflector module is the expandable tetrahedron which is a (isosceles or equilateral) triangular base pyramid with variable base to height aspect ratio. The reflector module is made of a certain number N (6, 7, 8, ...) of tetrahedral building blocks (Fig. 2) two by two having identical dimensions with respect to reflector optics offset plane (with the exception of the tetrahedrons lying on the offset plane). The reflector front view looks like a star built around an irregular polygon but still symmetric with respect to the offset plane. The selected configuration for the study, C-band 6 meter diameter, is based on 7 tetrahedrons because offers a good compromise between stowed envelope and mass. The reflector module geometry (that is the triangle bases) is established starting from the dimensions of the reflector aperture, an ellipse, having two main axes the minor of the two being the reflector projected diameter. The tetrahedron aspect ratios are determined, by means of a skeleton model, on the basis of the reflector projected diameter, F/D and clearance by imposing that the length of one side of each tetrahedron base is constant all around reflector aperture. When the reflector is fully deployed, the N tetrahedron's bases do not lie on the same plane. Tetrahedrons are rotated such to have their external vertex lying on a cone tangent to the edge of the parabolic reflector aperture. The rotation rule is such that, when rotated, the tetrahedron vertexes form an offset polygon frame parallel with respect to the one with the tetrahedron lying on a plane. The reflector module is made of N tetrahedral building blocks that because of imposed geometrical conditions have the same stowed height. The tetrahedrons are connected each other by means of the so called 'triple joints' which allow the tetrahedrons to expand and to rotate around one side of the base to cope with the cone tangent to the parabola. The reflector structure is closed by the crowning linkage that connects the vertex of the N tetrahedrons. The deployment of the reflector structure occurs by passive means that is springs and is speed regulated by dampers suitably positioned. The deployment is synchronized by mechanical means. An expandable connecting arm connects the reflector assembly to the deployment arm. This reflector structure concept allows the reflector diameter scaling by simply varying the length of the involved linear elements while the radial envelope is theoretically not dependent upon module dimension. The topology, number of deployable elements and the number, location and function of the deployment mechanisms remains unchanged when the reflector is scaled up or down (Fig. 3). This concept is valid in principle since, due to instability issues, when increasing linear elements the moment of inertia of the struts shall be increased accordingly as well as driving torque and stiffness of mechanisms. Hence, it can be stated that the cross section of the stowed reflector increases slightly along with reflector diameter while the stowed height is proportional to reflector diameter.

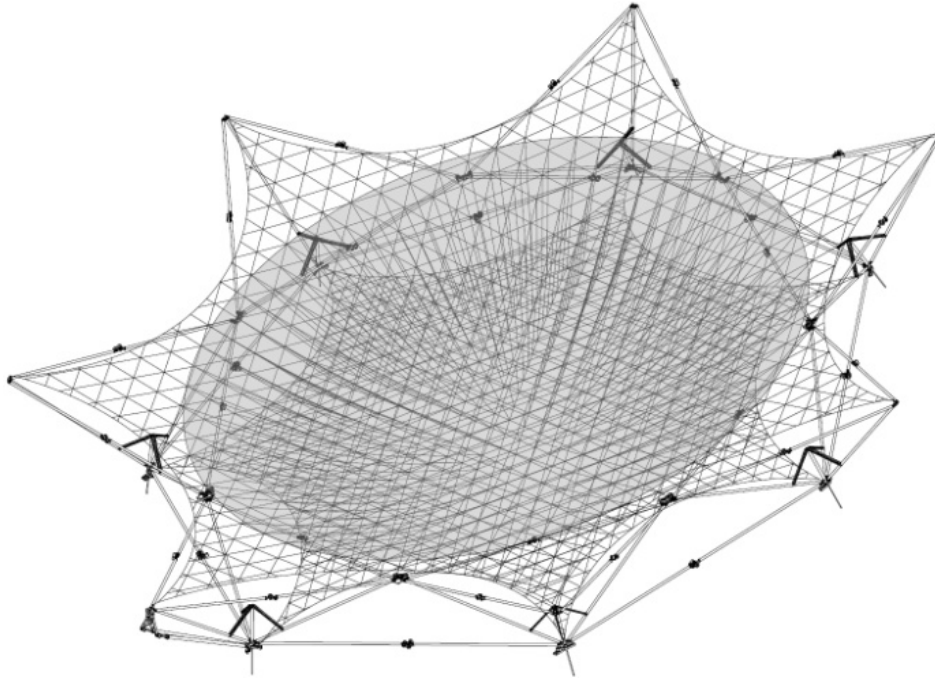


Fig. 1. Modular, scalable reflector dish (#7 modules)

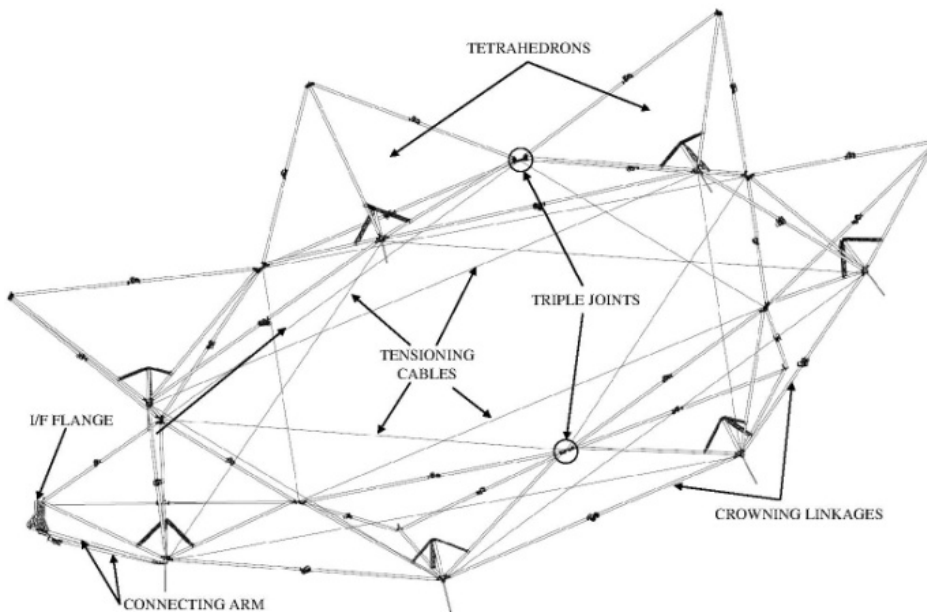


Fig. 2. Deployed reflector dish structure

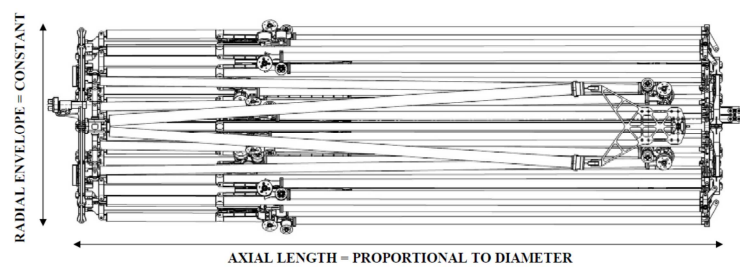


Fig. 3. Stowed reflector module theoretical rules

3. REFLECTOR DISH ELEMENTS

3.1. Expandable tetrahedral building block

The tetrahedron, that is the main building block of the LDR, has a compact envelope with a very small cross section when stowed and is able to expand to form a stable and stiff 3D structure. The main elements that constitute the expandable tetrahedron are:

- 3 Foldable ribs
- 3 Foldable compasses
- 1 Central hub hinge
- 1 Central cylinder (linear damper)
- 3 Levers
- 3 Swivel hinges

The deployment is synchronized (Fig. 4), thus the axial symmetry during deployment is maintained by means of the central cylinder. The central cylinder behaves also as a damper that is able to control the deployment speed. The foldable compasses, driven by the 180° constant torque hinges, provide an axial thrust that increases progressively when the tetrahedron is reaching the final position. This feature is very useful for the overall structure deployment margin. The swivel hinges, derived from [2], are based on collar joints and allow the correct kinematic link between the compasses and the ribs. The deployment kinematic is fully correct and the tetrahedron results in a one Degree of Freedom system (mobility 1); spherical joints, typically affected by radial and axial play, are not used.

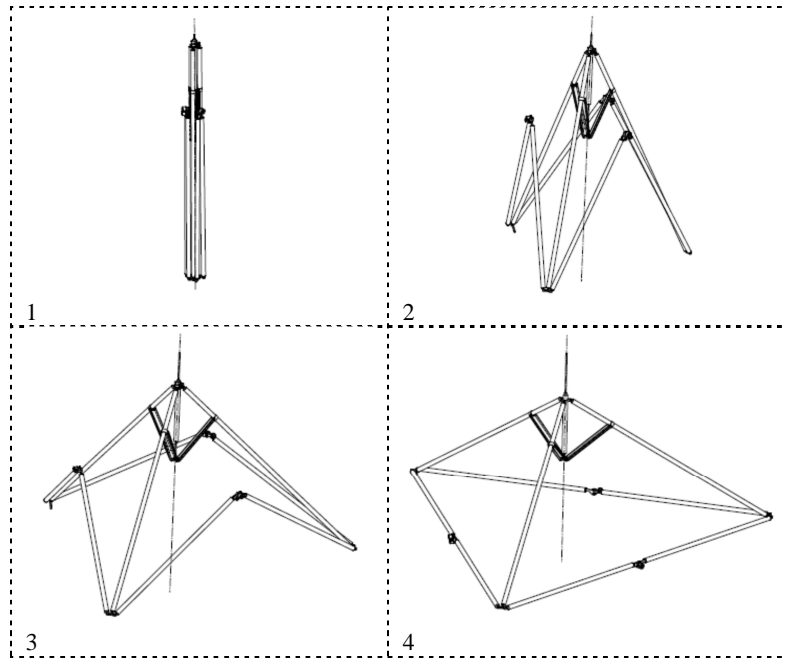


Fig. 4. Tetrahedron expansion sequence

3.2. Crowning Linkage

The crowning linkage connects the vertexes of the N tetrahedrons in order to close the module structure. Each linkage is made of a foldable compass made of two struts and driven by a 180° dampened constant torque hinge. The compass follows the tetrahedron but when this finishes its deployment it allows the tetrahedron to rotate around one side of their triangular base. The crowning linkage is longer than the distance between the vertexes of two adjacent tetrahedrons when their bases are coplanar that is before the tetrahedron rotation. The compass provides an axial thrust that increases progressively when the two struts get aligned (Fig. 5). This is a key feature for the overall structure deployment margin.

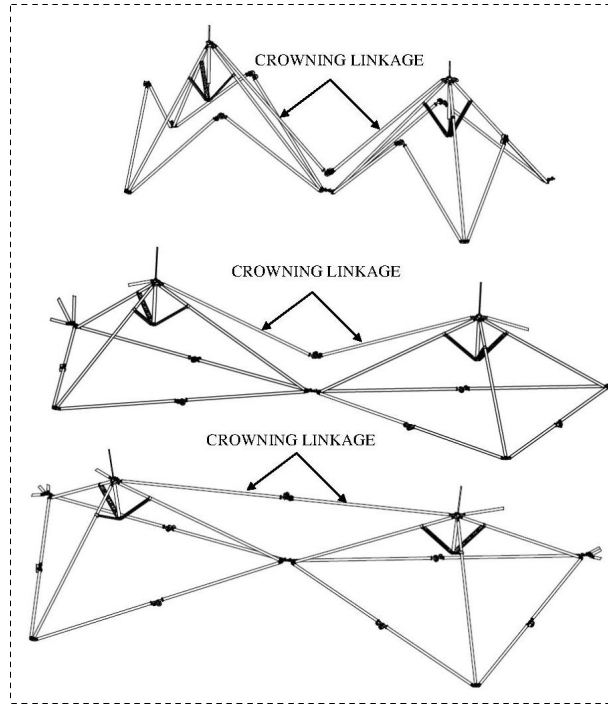


Fig. 5. Crowning linkage deployment sequence

3.3. Triple joint

The triple joint is the key component that allows the connection of two adjacent tetrahedrons in all the reflector module phases that is stowage and deployment. The triple joint exhibits the following features:

- Connects the tetrahedrons when in stowed condition
- Allows the tetrahedrons to expand up to the final stable condition
- Allow the tetrahedron to rotate around one side of the triangular base to match with the cone tangent to the parabolic reflector
- Secure the final tetrahedrons position to the required angle by positive latching
- Provide the interface for the front tensioning cables

3.4. Tensioning Cables

The deployed module structure is uniquely determined, without the need of tensioning cables, since all the structure degrees of freedom are constrained. However, the structure is made of flexible strut elements and hence the final stiffness can be reached by a proper cable system (Fig. 6) that shall be pre-tensioned by the module structure thrust. In principle it would be possible to remove the tensioning cable since the front and rear nets behaves as a cable system. This point will be addressed for the detailed reflector design.

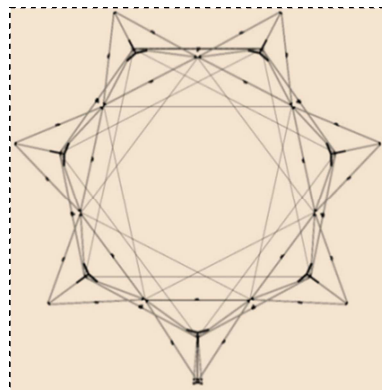


Fig. 6. Tensioning cables layout

3.5. Damping systems

The module deployment speed is controlled by dampers. Two types of dampers, rotary and linear, are used:

- Linear damper for Tetrahedron
- Rotary damper for Crowning linkage

3.6. Hold-down systems

The reflector dish package is maintained in the stowed condition by means of the Secondary Hold-down and Release Mechanisms (SHRM) which is made of two separable belts located at the reflector Front and Rear extremities.

3.7. Synchronization systems

3.7.1. Tetrahedron synchronization

The tetrahedron behaves like a three rib umbrella. The deployment is synchronized by means of the central cylinder (a liner guide) and three levers thus axial symmetry is always guaranteed along with the deployment.

3.7.2. Crowning linkage synchronization

The crowning linkages connect the vertexes of the N tetrahedrons and hence form an irregular polygon. In the first phase of deployment this polygon expands since tetrahedrons are fully deployed but still in plane. In the second phase the polygon reaches its final shape together with the tetrahedron rotation. A short lever connects and synchronizes the crowning linkages such to leave the tetrahedrons free to rotate around one side of their triangular base without introducing torsion into the crowning linkage polygon. On the other hand, rotation of tetrahedrons shall be congruent with crowning linkage expansion. It shall be noted that the N crowning linkage sections deploy in seven vertical planes, which are linked, each other, by means of the synchronization lever.

3.7.3. Tetrahedron rotation synchronization

The rotation of the tetrahedrons, around the inner side of their bases, can occur at any moment of the deployment with the only constraints of the crowning linkage as described in §3.7.2. The deployment strategy can limit the tetrahedron rotation degrees of freedom by releasing the reflector SHRM in two steps that is:

- Step A release of Rear SHRM
- Step B release of Front SHRM

After the release of the Rear SHRM the reflector appears as shown in Fig. 7. At this point the stowed tetrahedrons reach their maximum rotation consistent with the crowning linkage and cannot anymore return to their initial position. This strategy eliminates 6 degrees of freedom to the overall reflector kinematics thus improving the robustness of the deployment. After the release of the Front SHRM the reflector appears as shown in Fig. 8.

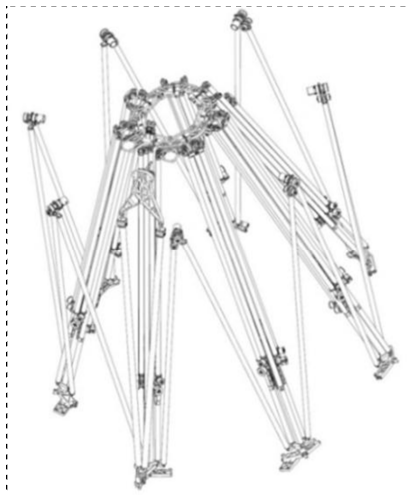


Fig. 7. Tetrahedron rotation after Rear SHRM release



Fig. 8. Tetrahedron expansion after Front SHRM release

3.8. Connecting Arm

The Connecting Arm is a collapsible structure that connects the tetrahedron #1 to the deployment arm. It is linked on one side to the tetrahedron vertex and on the other side to the tetrahedron swivel, suitably modified to be connected to the arm flange. The connecting arm deployment is activated by the SHRM release and is synchronized with the tetrahedron deployment.

3.9. Mesh-net tensioning system

When the module structure is fully rigid, all latches engaged and the cables well tensioned, that is at the end of the deployment, it is ready to allow for the mesh/net tensioning. This approach decouples the module structure geometry from the mesh/net shape achievement. The decoupling of the two mechanical systems is as better as the module to mesh/net stiffness ratio is high. The mesh/net tensioning is achieved by means of the Net Tensioning (linear) Actuator (NTA) embedded in the external rib of the tetrahedron (Fig. 9). TAS-I has wide experience in developing actuators [3] and in particular linear actuators; about fifty LA's have been successfully flown up to date. The front and rear nets are connected with spring loaded ties at the intersection of the net strips.

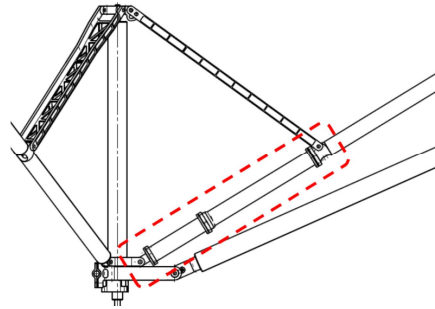


Fig. 9. Net Tensioning Actuator location

3.10. Miniaturized Boom Hinges

The Miniaturized Boom Hinge (both dampened and un-dampened) has been specifically conceived to connect and deploy long and flexible booms (up to 2.5 meters) to be used for the LDR deployable structure. The MBH is a self-standing unit with two output flanges supported by journal bearings. The MBH is motorized by constant torque springs which provide constant torque all over the deployment angle. The MBH provides stiffness and strength and behaves as a structural connection between the adjacent booms. The MBH deployed configuration is secured by positive latching. Torque Margin is largely positive within the operative environmental conditions.

4. REFLECTOR DISH PERFORMANCE

4.1. Reflector dish stowed configuration

The stowed reflector dish package for a 6 m aperture, C-band is quite compact and can be embarked also on small S/C (Fig. 10).

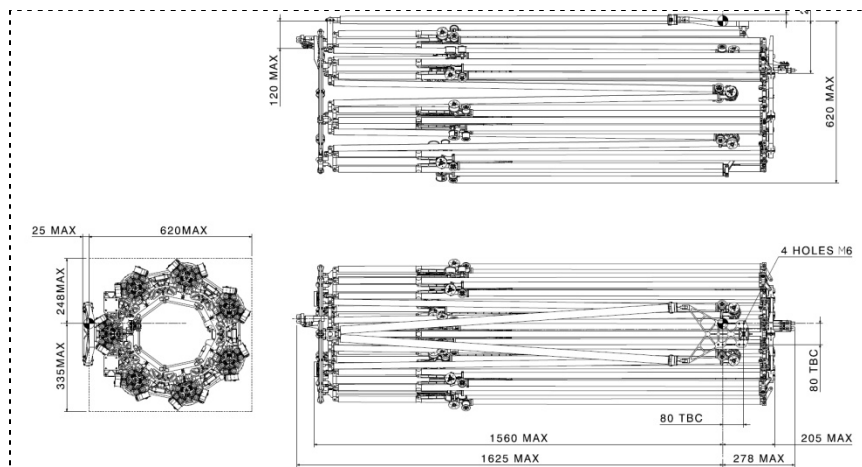


Fig. 10. Reflector dish (6 m) stowed dimensions

4.2. Structural analyses

A detailed Finite Element Model (Fig. 11) of the stowed reflector dish has been developed to verify stiffness and strength of the baseline mechanical design and launch restraint system. The structural analyses confirmed the adequacy of the integrated Hold-down and Release Mechanism approach. In particular the detailed modal and stress analyses demonstrated that an intermediate belt is not necessary to anchor the reflector package to the S/C body.

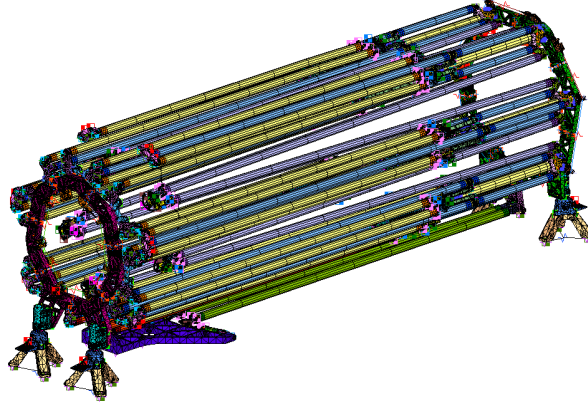


Fig. 11. Stowed Reflector dish Finite Element Model

4.3. Dynamic analyses

A detailed multi body model of the reflector dish has been built. The model is fully consistent with the CAD model geometry and hence with all the kinematic rules. The multi body analyses, performed with the Adams code, allowed the verification of the spring torque and damping rate distribution, the deployment evolution, torque's and contact forces in all the hinges of the structure. The Mesh/Net assembly have not been simulated yet. The full reflector dish deployment simulation has been achieved considering all local flexibilities and friction contributions (Fig. 12).

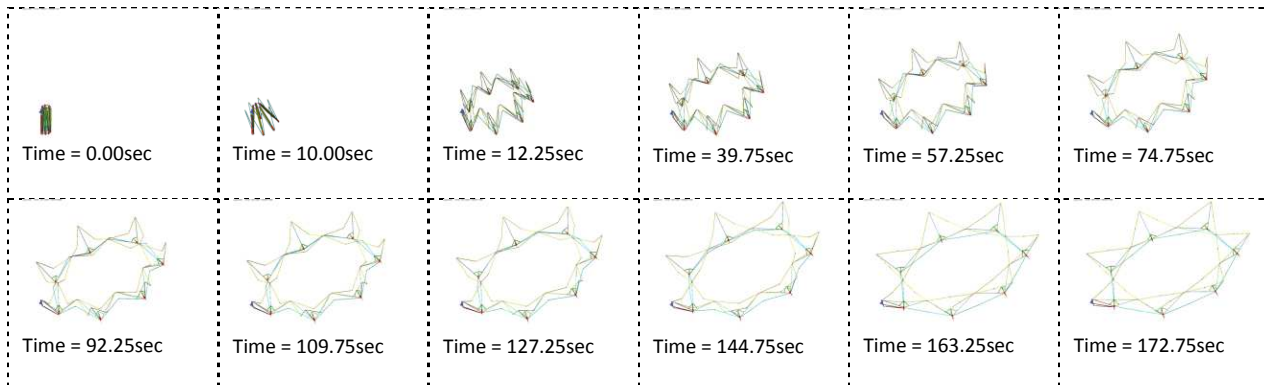


Fig. 12. Reflector dish deployment dynamic simulation

5. REFLECTOR ASSEMBLY

5.1. Assembly Definition

The reflector assembly is made of:

- Reflector dish which includes the Connecting arm
- Primary Hold-down and Release Mechanisms (PHRM)
- Deployment boom or arm
- Deployment rotary actuators (minimum two)

The proposed LDR configuration is based on the combined Primary and Secondary Hold-down and Release Mechanisms design approach. In particular, the SHRM constitutes an integral part of the PHRM because provides I/F's for four Fixed Hold-down and Release Mechanisms (FHRM) that restraint the whole reflector package directly to the S/C wall. This approach should eliminate the belt to restraint the reflector package toward the S/C with mass and

complexity advantages. The whole load path between reflector dish package and S/C will pass through the four FHRM's, directly connected to the front and rear SHRM belts (Fig. 13). The detailed modal and stress analyses demonstrated the validity of this approach.

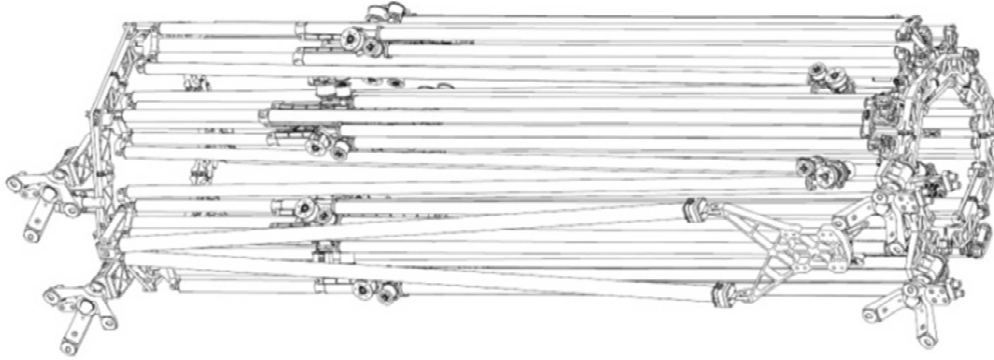


Fig. 13. Reflector assembly (6 m) without arm

5.2. Dynamic Simulation

The multi-body model of a 6m, C-band LDR assembly has been developed and the deployment simulation on board a mini satellite embarked on Vega has been carried out (Fig. 14).

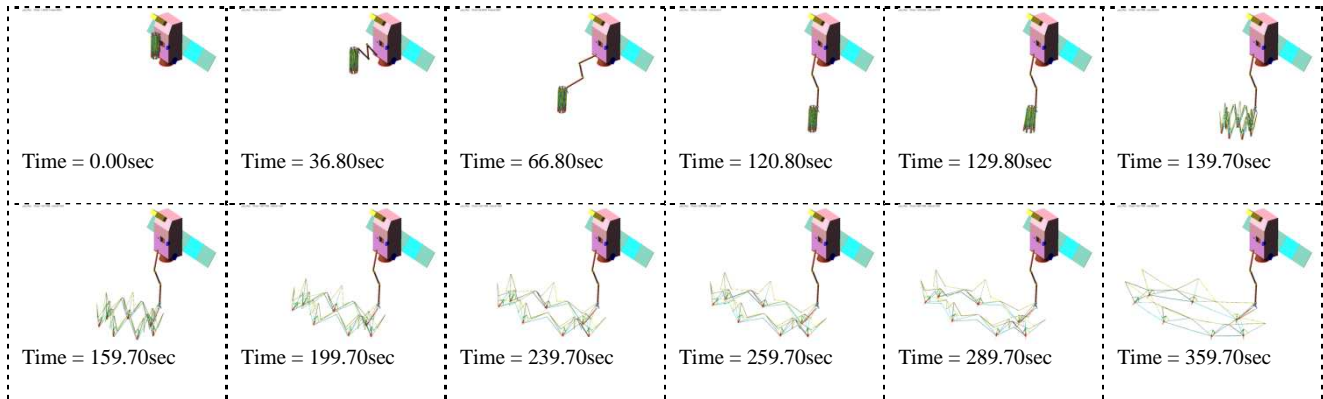


Fig. 14. LDR deployment on board a mini satellite

5.3. S/C accommodation

The proposed modular and scalable cells LDR concept can be easily embarked either on board mini (Fig. 15) and medium size class S/C buses (Fig. 16-17). Beside the small stowed envelope feature, the following main advantages can be evidenced:

- Simple interface with the S/C (no protrusions)
- Simple and reliable Primary Hold-down system (four FHRM's)
- No Hold-down and Release Belt
- Short deployment boom (because of the attachment to the tetrahedron vertex)
- Boom outside from primary feed pattern (as above)

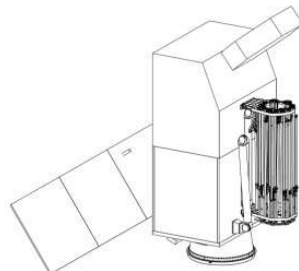


Fig. 15. Reflector assembly (6 m) on board mini S/C

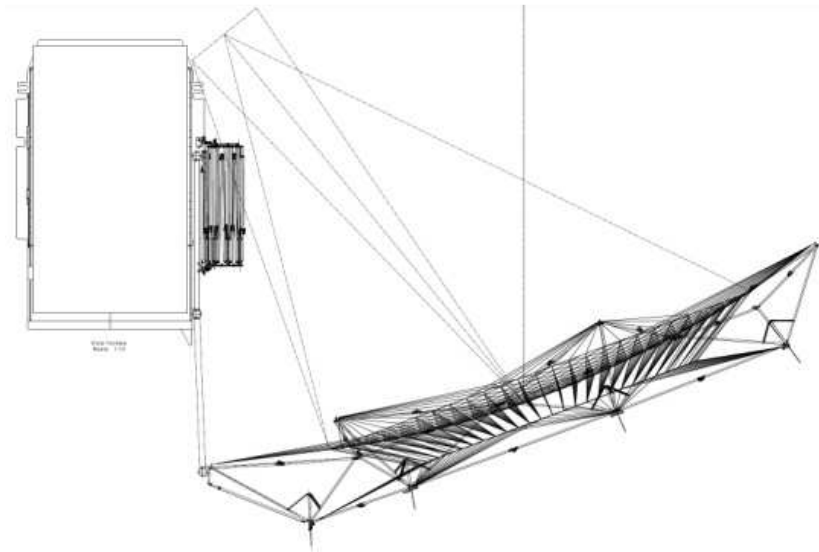


Fig. 16. Reflector assembly (6 m) on board SB B2

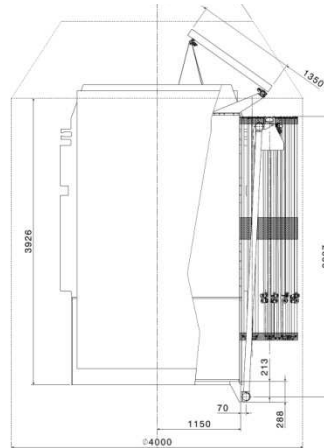


Fig. 17. LDR (12 m) on board SB B2/Ariane 5 Sylva 5

5.4. Scalability assessment

The reflector structure concept herein described allows for the reflector diameter scaling by simply varying the length of the involved linear elements while the radial envelope is lowly dependent upon module size.

Once the number of cells has been selected, the topology, number of deployable elements and the number, location and function of the deployment mechanisms remains unchanged when the reflector is scaled up or down. This concept is valid only in principle mainly because of these points:

- when increasing linear elements the moment of inertia of the linear elements (struts) shall be increased accordingly to limit deformation induced by the hinge spring torque
- driving torque shall be increased at least linearly to have constant separation force at strut extremity
- stiffness and hence mass and envelope of mechanisms shall be increased

A scaling rule has been established to determine the strut diameter and hinge torque such to guarantee linearly increasing separation forces and the same flexibility to strut length ratio. Starting from the reflector skeleton for each reflector family, number of cells and taking into account the strut diameter and spring torque requirements it is possible to establish, as a first order of magnitude, the reflector dish stowed envelope (Tab. 1).

Tab. 1. Stowed envelope versus reflector family

	D = 6m C-band	D = 12 m L-band
Number of cells N	Axial length [mm]	
6	2070	4280
7	1730	3560
8	1490	3060
	Lateral envelope [mm]	
6	570 x 550	960 x 930
7	600 x 580	980 x 950
8	620 x 600	1010 x 980

Using a CAD skeleton model the reflector configuration (Fig. 18) can be quickly achieved by simply input the reflector optics parameters (diameter, focal length and clearance). At the moment three different models have been developed that is one per number of cells.

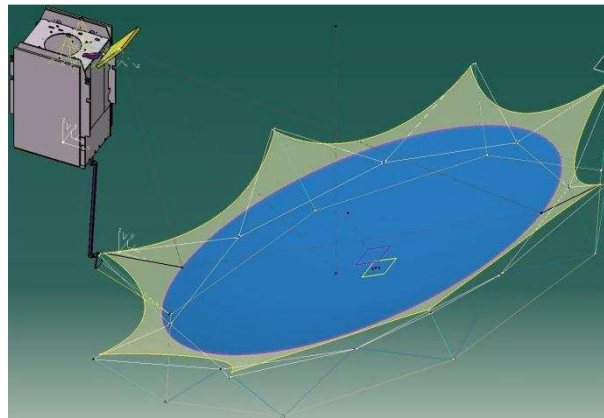


Fig. 18. LDR (12 m) on board SB B2 (skeleton model)

6. REFLECTOR DISH BREADBOARDING

6.1. Reduced size reflector

A reduced size reflector ($d = 1.5$ m) has been designed and manufactured to demonstrate the correctness of the deployment kinematic approach. The following differences with respect to the real LDR configuration have to be evidenced:

- Circular aperture instead of elliptical
- Helical springs instead of leaf springs
- Torque 5 times smaller than required
- No damping
- No connecting arm
- No mesh and net

The deployment tests have been performed both in cup-up and cup-down (Fig. 19) configurations using a simplified zero g device. Tests were successful for both. Considering the weakness of the springs the test has to be considered highly successful. The deployment has been manually controlled by means of a wire. The reduced size LDR demonstrator confirmed the robustness of the deployment kinematic approach.

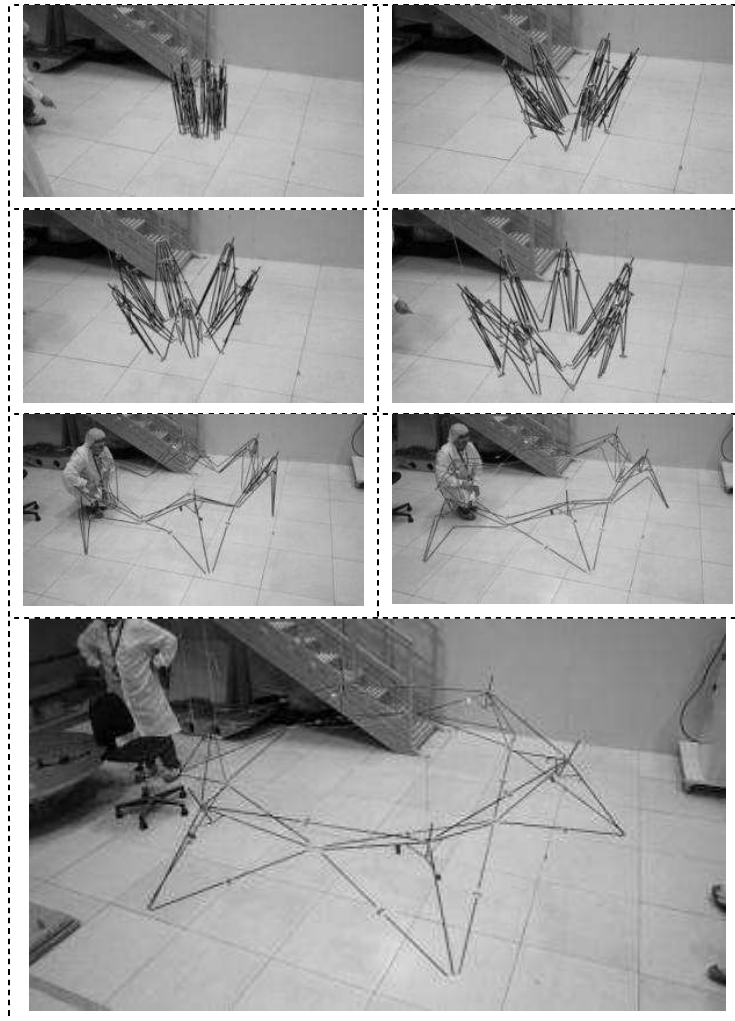


Fig. 19. Deployment sequence of 1.5 m diameter BB

6.2. Tetrahedron plus Connecting Arm

The tetrahedron and connecting arm of the 6 m diameter, C-band reflector have been bread-boarded to verify the deployment features of the assembly and the latching engagement of hinges and connecting arm. The test results are fully satisfactory and in particular:

- Mass is as expected
- Deployment is repeatable and reliable
- Deployment is always successful with vertex downward and without mass compensation (Fig. 20)
- Deployment with vertex upward needs gravity compensation because of the I/F flange mass (this should not apply at reflector level because of the interaction between tetrahedrons)
- Connecting Arm latches get easily engaged at the end of deployment
- Experimental modal analysis, performed with clamped I/F flanges provides good results quite in line with the predictions (Fig. 21)

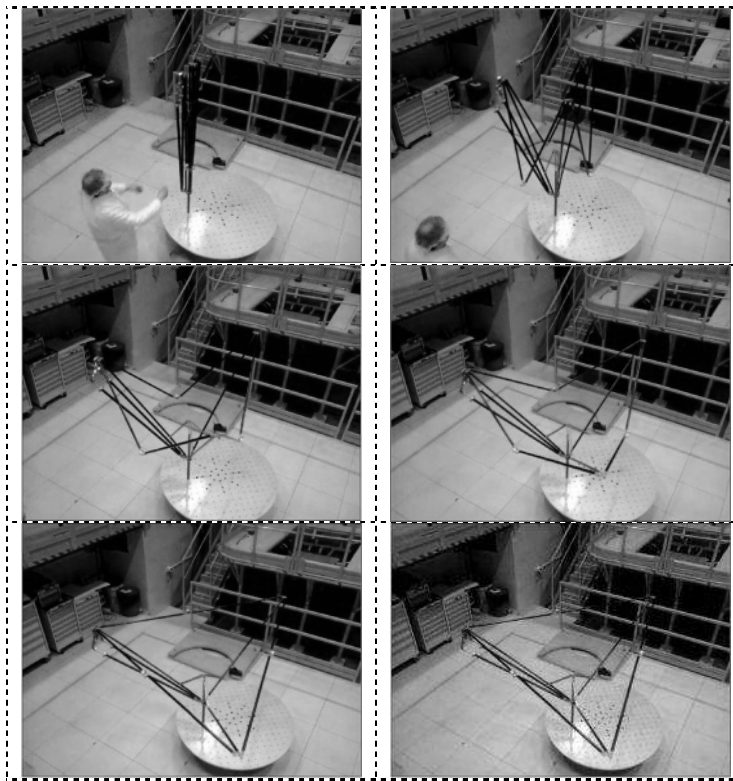


Fig. 20. Tetrahedron & Connecting arm deployment

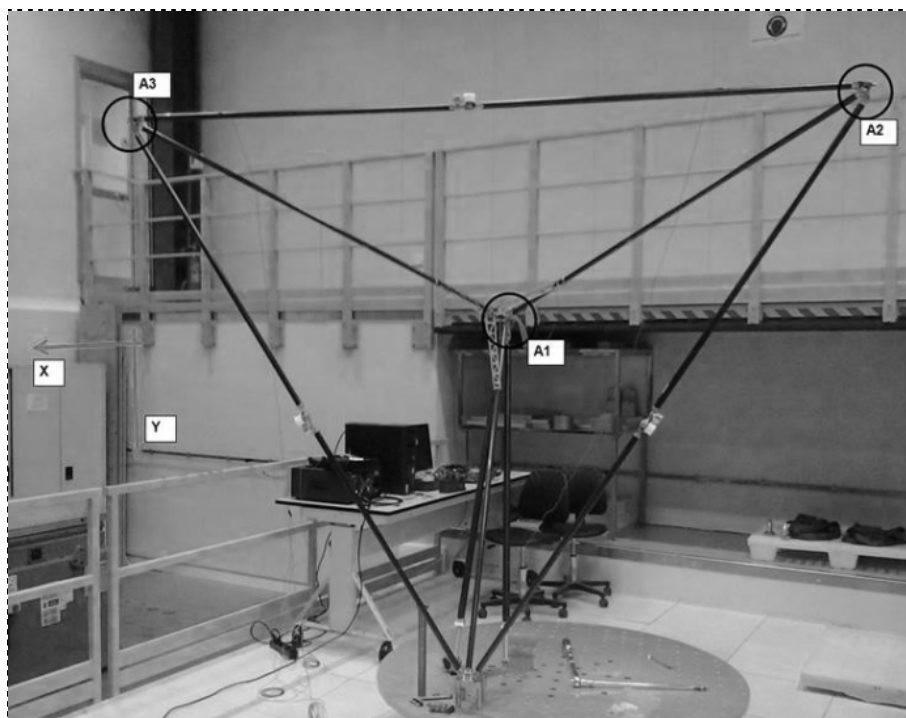


Fig. 21. Experimental modal analysis on tetrahedron

6.3. Miniaturized Boom Hinges

The bread-boarding of both dampened and un-dampened MBH's is fully satisfactory and all performances are in line with the requirements and in particular:

- Mass is fully satisfactory
- Minimum torque is always guaranteed
- Torque margin is widely positive

However, friction torque is slightly higher than expected and could be easily reduced with a better manufacturing tolerance management.

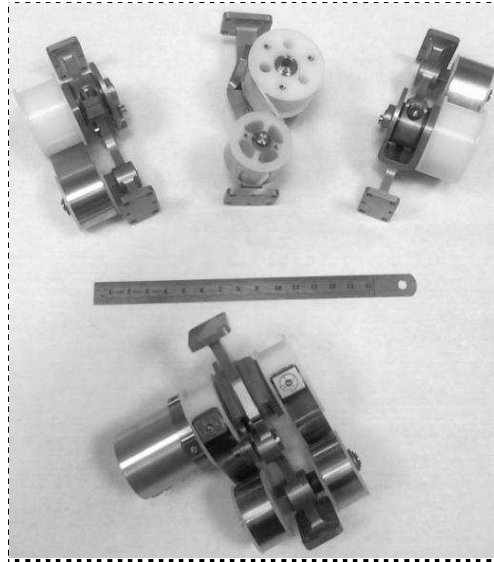


Fig. 22. Reflector hinges bread-boarding

6.4. Crowning linkage

One sector of the crowning linkage of the 6 m diameter, C-band reflector has been bread-boarded. It consists of the following elements:

- One Dampened MBH
- Two CFRP struts
- Fittings to MBH
- Fittings to Tetrahedron vertex

The expected mass of the crowning linkage is within tolerances. Manual deployment tests have been performed to confirm that the linkage is not sensitive to gravity. No problems have been evidenced during integration of the linkage. Alignment of end fittings is good confirming the integration process.

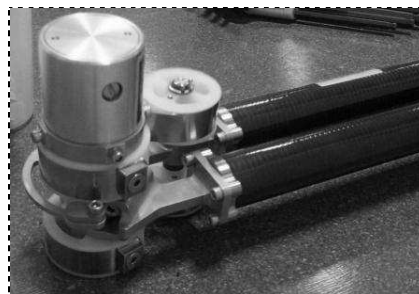


Fig. 23. Portion of crowning linkage with MBH

6.4. Linear Damper (cylinder)

The bread-boarding of the linear damper is fully satisfactory and performance in line with the requirements and in particular:

- Mass is fully satisfactory with a significant reduction with respect to prediction
- Damping rate is adjustable within the required tolerances
- External damping rate setting has been implemented



Fig. 24. Linear Damper (cylinder) bread-board

7. CONCLUSIONS

The preliminary LDR design and bread-boarding activities are considered fully successful and next step will be the manufacturing of the 6 m diameter reflector dish demonstrator.

REFERENCES

- [1]. A. Meschini, R. Rigato, D. Scarozza, "Large Deployable Antenna Reflector for a Satellite Antenna" Patent Application N. PCT/IB2013/059894, 04 November 2013.
- [2]. A. Meschini; "Actuation Mechanism with Three-dimensional Rectilinear Guide"; US Patent #2008/0258987 A1, October 23, 2008.
- [3]. A. Meschini, "Antenna mechanism systems overview from production series to novel developments", 28th ESA Antenna Workshop on Space Antenna Systems and Technologies, Noordwijk, The Netherlands 31 May-3 June 2005.

ACKNOWLEDGEMENTS

Acknowledgements, for the precious help received, shall be given to Lucio Scolamiero, who managed the ESA study up to the Critical Component Review, Gonalo Rodrigues, the present ESA study technical manager and Maurizio Milano the TAS-I program manager.

DESIGN CONCEPT OF LARGE DEPLOYABLE REFLECTOR FOR NEXT GENERATION L-BAND SAR SATELLITE

Satoru OZAWA⁽¹⁾

⁽¹⁾*Japan Aerospace Exploration Agency
Tsukuba Space Center*

*2-1-1 Sengen, Tsukuba, Ibaraki, Japan 305-8505
email:ozawa.satoru@jaxa.jp*

ABSTRACT

In recent years, the importance of SAR (synthetic aperture radar) has risen due to its capacity to observe a wide area of the earth regardless of climate or local sun time of the observation area. JAXA, or Japan Aerospace Exploration Agency, has researched and developed L-band SAR satellites and utilized their observation data for science researches and practical applications such as emergency relief during disasters. For next generation SAR program, or ALOS-Next, the users of researches and applications demand (i) expansion of swath width of observation area, (ii) preservation or improvement of resolution, and (iii) improvement of radiometry performance and SAR image quality. However, due to the nature of conventional planar phased array antennas, it is difficult to satisfy these demands simply by extending traditional SAR technologies. To overcome these limitations, JAXA has decided to employ LDR (large deployable reflectors). This paper describes a design concept of LDR for ALOS-Next satellite.

1. INTRODUCTION

JAXA, Japan Aerospace Exploration Agency, has launched an earth observation satellite ALOS-2 on May 24th 2014. ALOS-2 is a follow-up program of ALOS that had contributed to cartography, regional observation, disaster monitoring, and resource surveys since its launch in 2006. Along with ALOS, ALOS-2 also has a planar type phased array antenna, PALSAR-2, is 3 m x 9 m rectangular shape and a SAR (synthetic aperture radar) that can achieve 3 m resolution at maximum with a swath of 50 km using L-band signal. The satellite has already started clipping images of the earth such as green forests hills around Mt. Fuji, and a growing island Nishi no Shima[1].

Before the launch of ALOS-2, JAXA kicked off an investigation for ALOS-Next program with DLR, the German Aerospace Center. The ALOS-Next is, as its name would suggest, a successor of the ALOS-2 earth observation mission and designed to perform ALOS/ALOS-2 mission, as well as to observe essential climate variables such as biosphere (forest biomass, forest degradation, disturbance type, agro forestry), geosphere/lithosphere (volcanic eruptions), hydrosphere (ocean currents, soil moisture), cryosphere (polar ice and snow cover, permafrost). To accomplish such a wide range of mission, JAXA and DLR decided to employ an antenna system with 15 m diameter large deployable reflectors instead of phased array antennas.

JAXA has been developing and researching large deployable reflectors. ETS-VIII (the engineering test satellite viii) is a mobile communication satellite, launched in 2006 and has two large deployable reflectors for the communication between the geostationary satellite and small user terminals. The reflectors were made from segmented modules, forming an ellipse reflector, 19 m in major axis, 17 m in minor axis, and were the largest reflectors in the world at the time of launch on Dec 18th, 2006. The large deployable reflector for reception was successfully deployed on the 25th and the one for transmission on the 26th. The deployment profile and reflector surface accuracy were confirmed to satisfy the requirements through the in-orbit experiments after the launch. Its communication performances were also confirmed by experiments with small user terminals.

After the launch of ETS-VIII, JAXA continued researching LDRs for extending their diameter and making them lighter to realize 30 m class reflectors. Whereas the ETS-VIII LDR uses umbrella type deployable mechanism, the enlarged LDR employs foldable umbrella mechanism, or tri-fold deployable mechanism[2]. The tri-fold deployable reflector has then obtained three times longer ribs and half weight density in comparison to the ETS-VIII LDR. The 30 m class reflector consists of 7 segmented modules of the tri-fold reflectors.

A reflector for the ALOS-Next mission is of tri-fold deployable reflectors and composed of a single module, not a multi-module, because 15 m is small enough to be formed by a single reflector.

This paper introduces designs of JAXA's conventional LDRs to confirm tri-fold mechanisms and multi-module reflectors, describes a concept of the ALOS-Next LDR, shows structural analysis results and discusses an applicability of the tri-fold deployable reflectors to ALOS-Next mission.

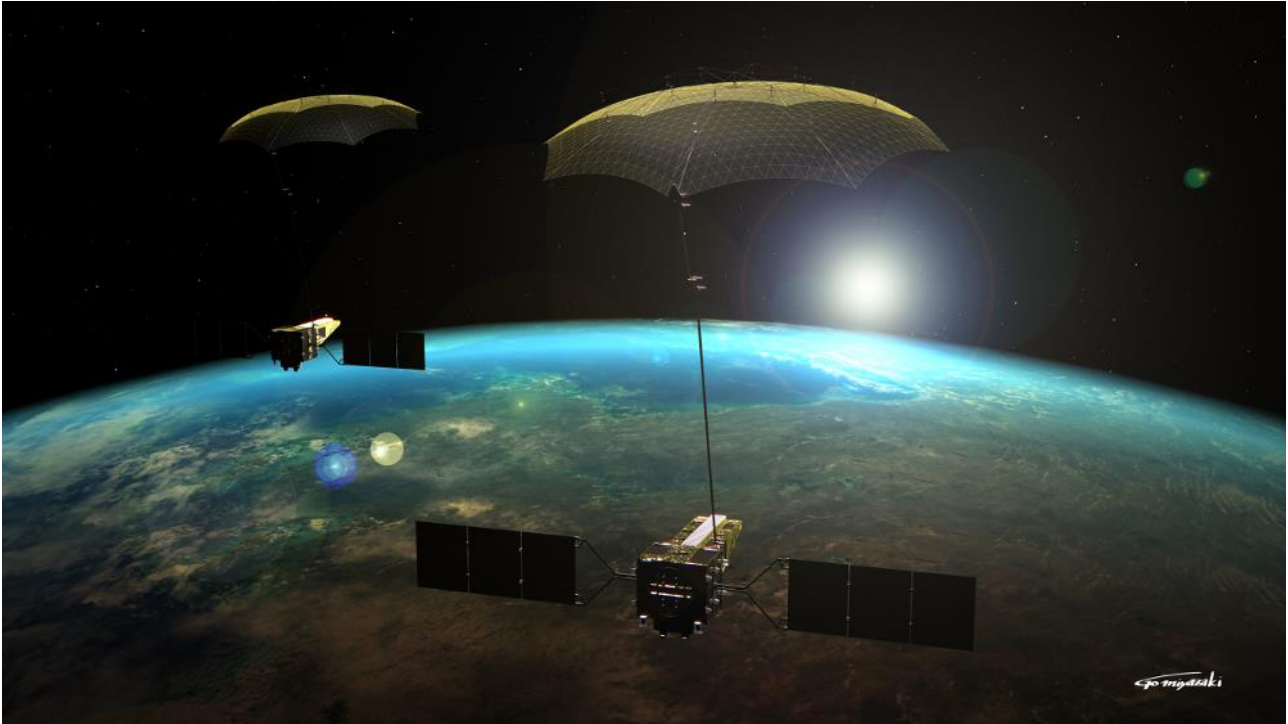


Fig. 1. Artist's rendering of ALOS-Next mission

2. ALOS-NEXT MISSION

The ALOS-Next is illustrated in Fig. 2. The satellite has a 15 m diameter LDR connected to the body with a boom. A feed array is attached to the opposite side of the reflector. It consists of 24 feeds and is driven by a DBF (digital beam former) unit. Two solar array paddles are connected to the satellite body and generates electric power for the satellite. The satellite will be placed into a sun synchronous orbit at the altitude of 780 km.

Its mission is to observe the Earth surface with L-band SAR technique. With a strip map mode, the satellite acquires 350 km wide image with 3 m resolution. The SAR sends off radio signals and receives back scatter from the ground. By processing the received signal, one can get the Earth picture. Fig. 3 is an example of SAR image. This is the first image acquired by ALOS-2 and is similar to images taken by optical sensors. The ALOS-Next can take a picture of the whole surface of the Earth every 8 days.

Conservative SAR systems can achieve either wide swath or high resolution but not both. For the wide swath it uses scan SAR but this degrades the resolution, and for the high resolution it uses strip-map but for the narrow swath. With the LDR and the DBF, the ALOS-Next realizes the two at the same time: a wide observation swath of 350 km and a high resolution of 3 m.

The concept of the ALOS-Next observation scheme is shown in Fig. 4[3]. With 15 m diameter reflector, the ground beam area is almost 15 km. The satellite is equipped with 24 feeds to achieve the 350 km observation swath. At the transmission, the satellite illuminates 350 km at the same time by emitting the radio wave from all the feeds. The back scattering signal returns continuously from the ground from near to far. The return signal is very narrow, hits the feeds from the one side to the other and can be received at the high gain with the use of LDR. Finally, the satellite achieves a wide swath and high resolution at the same time.

Fig. 5 shows the comparison with ALOS-2. At the high resolution mode (strip map mode), ALOS-2 observes only a 50 km width. ALOS-Next can observe a 350 km width. This capacity means, for example, that all of east Japan can be observed in one scan in the event of an earthquake.

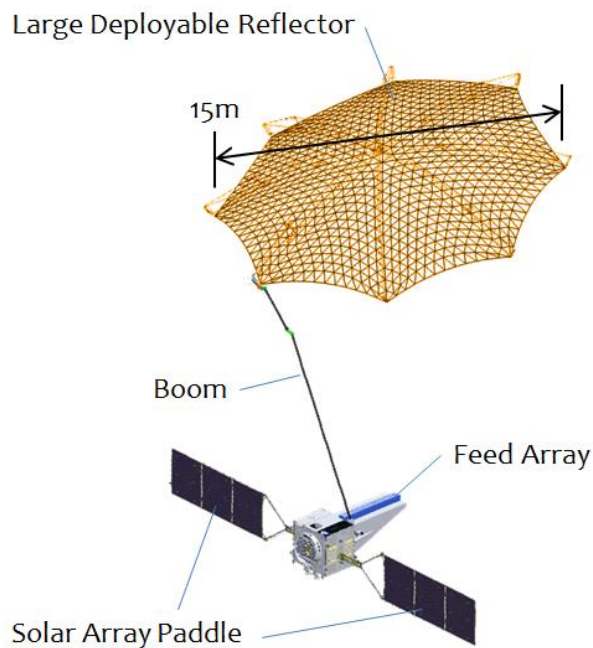


Fig. 2. In-orbit configuration of ALOS-Next



Fig. 3. Example of SAR image

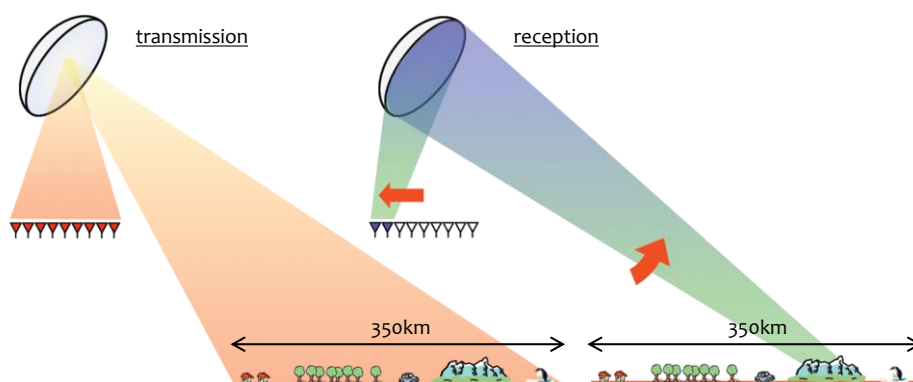


Fig. 4. Observation concept of LDR and DBF

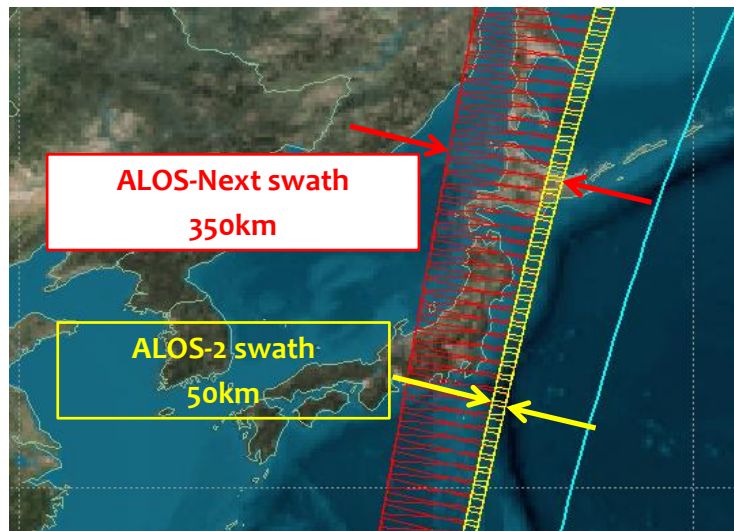


Fig. 5. Comparison of ALOS-Next observation swath with ALOS-2 in 3 m resolution strip map mode

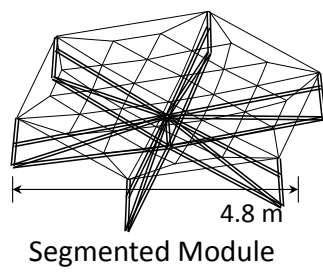
3. LARGE DEPLOYABLE REFLECTORS

The ALOS-Next mission requires a 15 m diameter reflector for L-band. As Fig. 2 shows, the reflector is mounted on the top of the satellite with a boom and so must be very light to suppress beam pointing errors caused by satellite controls. JAXA's latest LDR design can meet this requirement.

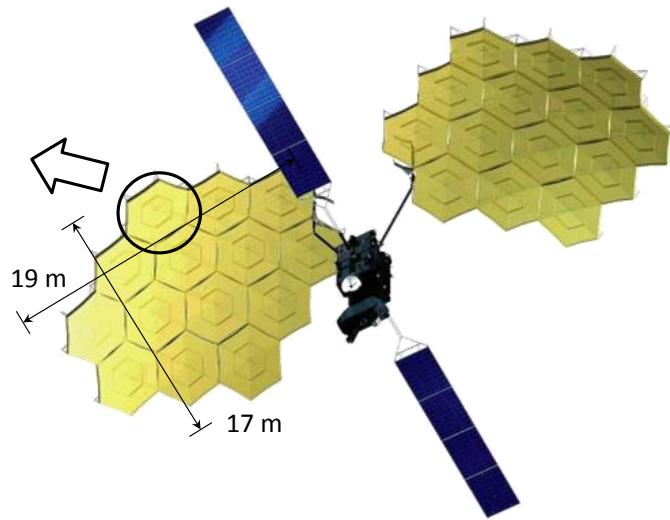
The research and development of LDR in JAXA started from the ETS-VIII project. The in-orbit image of ETS-VIII is shown in Fig. 6. This is a mobile communication satellite to realize a communication between the ground and the orbit with handheld user terminals. The satellite consists of two LDRs for transmission and reception. The ETS-VIII was launched in 2006 and successfully deployed the LDRs. The reflector is for S-band and requires 2.5 mm rms. It sizes 19 m x 17 m and is composed from 14 segmented modules. Each module is hexagonal in shape and made from deployable truss. At every slider springs are installed and drive the reflector deployment. By deploying all the segmented module in synchronization, the whole reflector deploys. The deployed LDRs in-orbit are shown in Fig. 7. The reflector's surface accuracy, pointing accuracy and beam patterns were confirmed to meet the requirements by in-orbit tests after launch.

As a follow-up program of ETS-VIII, JAXA studied a next generation mobile communication satellite aiming to realize communications with small user terminals whose size and power are equivalent to cellular phones used in ground network. To accomplish this, the satellite requires 30 m reflectors. The satellite with a 30 m reflector is shown in Fig. 8. The number of modules is changed to 7 segmented modules from 14 of the ETS-VIII. The module design is also changed to tri-fold deployable reflector.

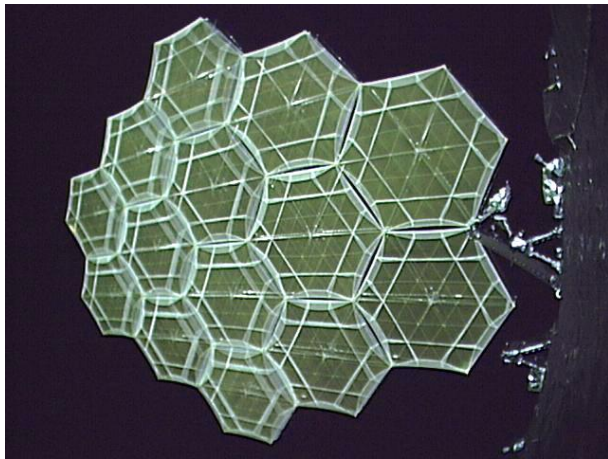
The tri-fold deployable reflector is designed to realize 30 m diameter. With the design, the segmented module expands its diameter to 14.4 m of tri-fold reflector from 4.8 m of the ETS-VIII. The unit structure of tri-fold deployable reflector is tri-fold deployable truss. Same as the ETS-VIII LDR, springs are installed in sliders and drives the deployment. The movement of sliders are controlled by a motor and control cables. While the diameter is three times larger than the previous design, the reflector weight is half. Practicality of the tri-fold deployable reflector was confirmed through its design, analyses and structural and deployment tests. Fig. 9 are pictures taken during the deployment test.



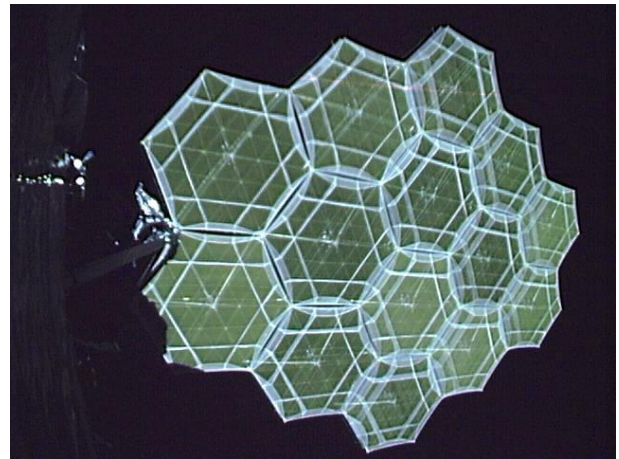
(a) Segmented module of LDR



(b) In-orbit image of ETS-VIII

Fig. 6. Configuration of LDRs for ETS-VIII

(a) LDR for reception



(b) LDR for transmission

Fig. 7. Deployed LDR pictures taken in-orbit

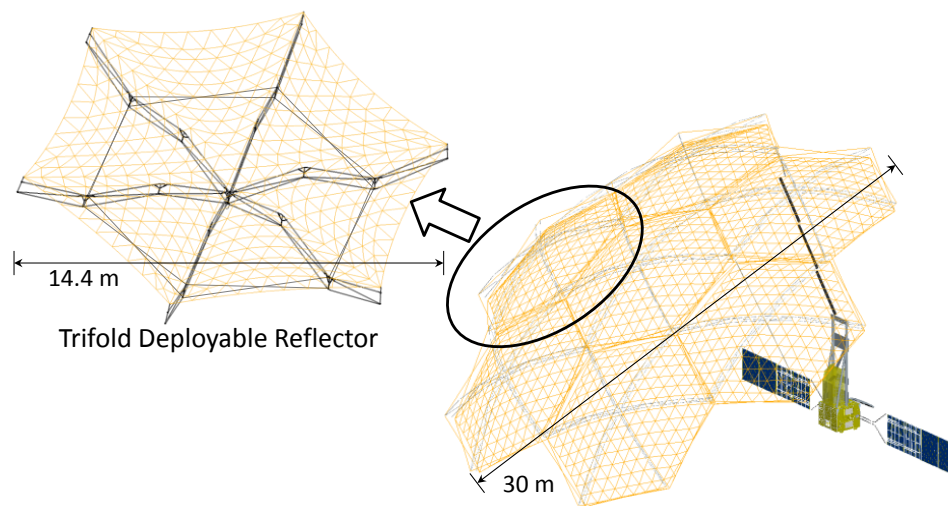


Fig. 8. Mobile communication satellite with enlarged LDR



(a) Beginning of deployment



(b) 30% deployed



(c) Fully deployed

Fig. 9. Deployment ground test of enlarged LDR

4. DESIGN CONCEPT OF LDR FOR ALOS-NEXT

As written in Chapter 2, the ALOS-Next mission requires 15 m diameter reflector. For this purpose, JAXA employed tri-fold deployable reflector because the mission also requires a stability of antenna beam pointing and a lighter antenna is an advantage.

An overview of the reflector is shown in Fig. 10. While the segmented module of 30 m reflector is hexagonal in shape, the ALOS-Next reflector is octagonal. In addition, co-trusses are attached between the ribs to have a round shape. The reflector is composed of a reflector surface, cable network and support structure. The reflector surface is made from metal mesh and reflects RF signal. Cable network is to connect the reflector surface and support structure and to form parabolic shape. The support structure is made from eight of tri-fold deployable truss, and can do the deployment motion by moving its sliders.

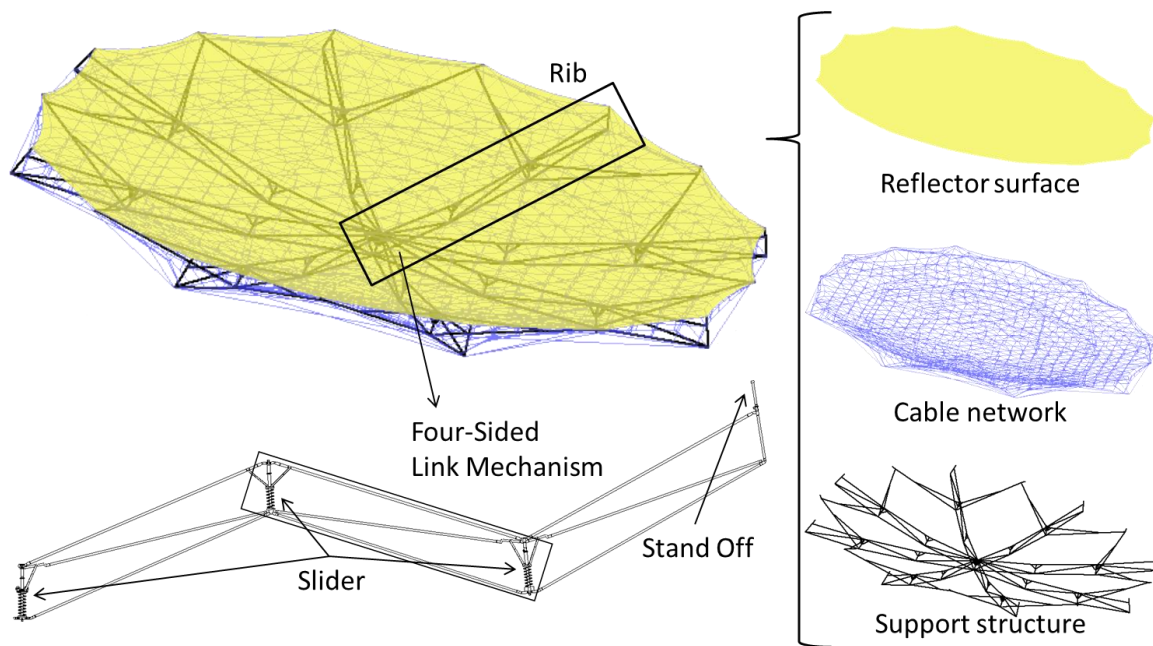


Fig. 10. LDR for ALOS-Next, its deployable mechanism and its layers

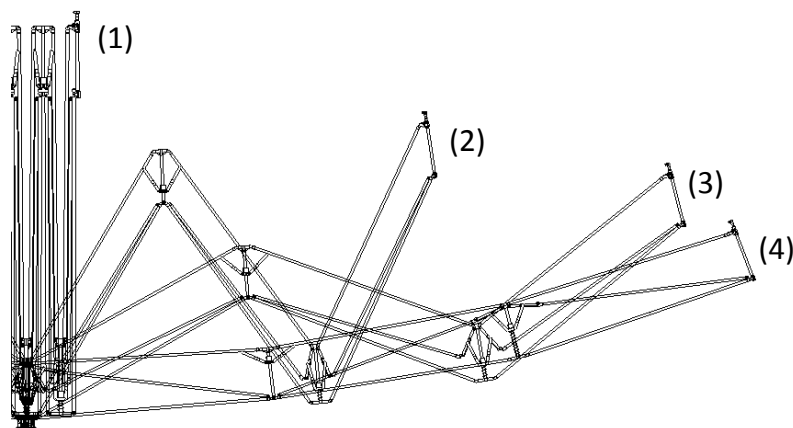


Fig. 11. Deployment sequence of tri-fold deployable truss

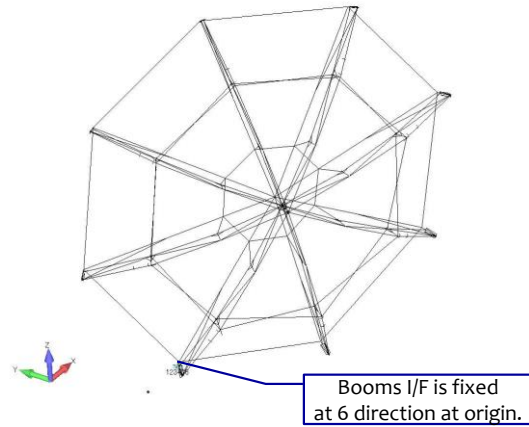


Fig. 12. Boundary condition of structural modal analysis

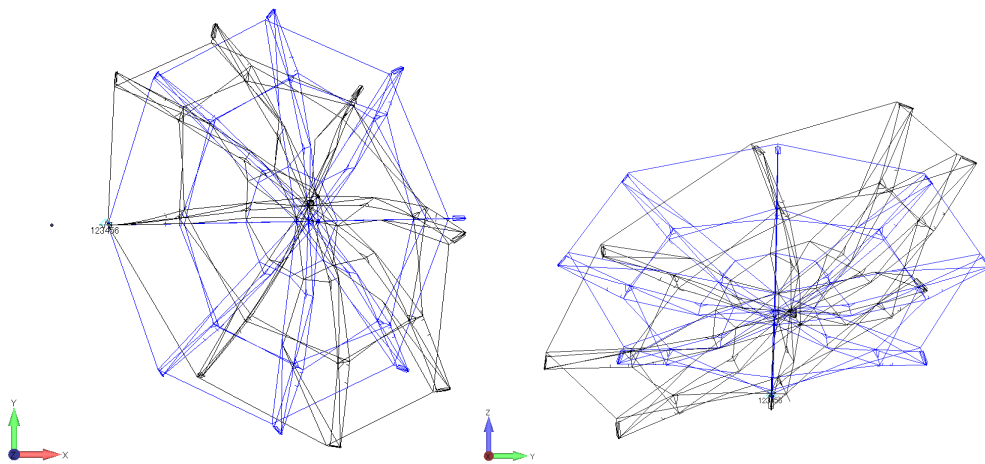


Fig. 13. First mode shape

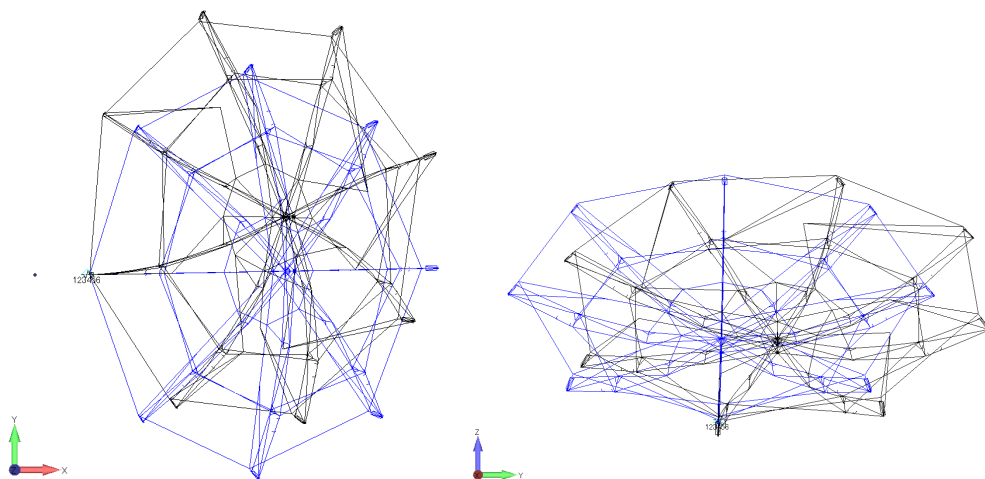


Fig. 14. Second mode shape

Fig. 11 shows the deployment sequence of tri-fold deployable truss. At the stowed configuration, the truss stands vertical as pile of beams at the position (1). As the sliders move by springs installed at every slider, the truss deploys from the position (2) to (4) and finally is deployed to the position (4).

To check the structural performance, model analyses were carried out. Fig. 12 shows the model and boundary condition used in the analysis. The boom design is not yet fixed and, therefore for the analysis, the boom / reflector interface is fixed. Fig. 13 shows the structural first mode obtained by the analysis. In the first mode the reflector rotates around x axis and angles the beam direction to azimuth direction. This mode is to be suppressed by modifying the truss member between the boom / reflector interface and the center of reflector. The second mode is rotation about z axis. This mode is also to be suppressed by the modification for the first mode.

5. CONCLUSION

The next generation L-band SAR program “ALOS-Next” employs large deployable reflectors as its antenna system and confirms that it is feasible to mount the reflectors. The tri-fold deployable reflector used for ALOS-Next inherits deployable truss design and so is reliable. It is different from the ETS-VIII in that the reflector is designed as single module. Structural analyses for the concept design of the reflector show some future challenges towards the satellite system definition.

REFERENCES

- [1]. First Image Data Acquisition by DAICHI-2 (ALOS-2), http://global.jaxa.jp/press/2014/06/20140627_daichi2.html
- [2]. S. Ozawa, K. Shintate, and A. Tsujihata, “Trifold Deployable Reflector,” Workshop on Large Deployable Antennas, Noordwijk, the Netherlands, October 2012.
- [3]. A. Moreira, “German Spaceborne Radar Program: TerraSAR-X, TanDEM-X and Beyond,” 1st German/Japanese Science and Application Workshop for Next Generation SAR, Tokyo, Japan, June 2013.

ACKNOWLEDGEMENTS

The author thanks members of the large deployable reflector design team from NEC for their technical suggestions to our research project.

LARGE ANTENNA WORKING GROUP: STATUS OF ACTIVITIES

Julian Santiago-Prowald and Cyril Mangenot

European Space Agency –ESTEC

Keplerlaan 1, 2200AG, Noordwijk, The Netherlands

Email: Julian.Santiago.Prowald@esa.int, Cyril.Mangenot@esa.int

ABSTRACT

The first edition of the International Conference on Advanced Lightweight Structures and Reflector Antennas took place in Tbilisi in 2009. That event provided a wide and deep overview of the state of the art in deployable structures technologies for space engineering. It was obviously based on the heritage of the Georgian Technical University that lead to the first Georgian space object. Also the evolution of deployable architectures were presented, as well as the state of the art in US, Russia, Japan and Europe. At the time, it was clear that European technologies in this specialized field had not been developed at the same pace as other ones. Following the initiative of the Electrical and Mechanical departments of ESA, a working group on Large Deployable Antennas (LAWG) was initiated, involving the participation of applications directorates, mainly Earth Observation and Telecommunications. In this paper, the activities coordinated by the LAWG are briefly presented. These activities involve technology demonstration as well as system level studies for the establishment of requirements and roadmaps.

1. INTRODUCTION

The background of deployable antenna structures in the European context is extensive and goes back several decades [1]. The first development activities intended for flight hardware were initiated by ESA with the Contraves' 12 m inflatable reflector and the 5 m aperture Unfurlable Mesh Antenna developed by MBB in the early 80s. The latter is in essence a hinged-rib antenna architecture. Despite all the efforts, industrial developments were discontinued in spite of the incipient commercial interest at the time, leaving the field free to non-European products to capture the telecommunications and institutional markets.



Fig. 1. MBB Unfurlable Mesh Reflector during deployment testing (Courtesy of EADS Astrium and ESA).

Another example of European developments is the ERA 9 m antenna (Fig. 2) by Aerospatiale, now Airbus Defence and Space. The structure is based on a truss of deployable triangular prism elements supporting the metal wire mesh. Each lateral facet of the prism is a six-bar linkage that unfolds into a parallelogram with unfolding diagonal rods made themselves with articulated links. It was flown in 1988 on the MIR station.

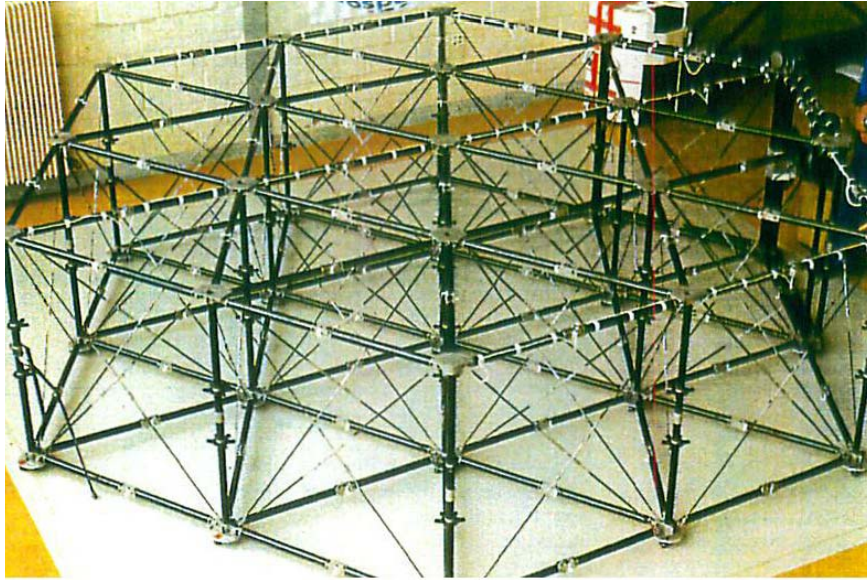


Fig. 2. Structure deployment test of ERA 9 m antenna (Courtesy of Airbus DS).

Pantographic structures and associated technologies have been conceived and developed since the early 80s for the Soviet space programs, originating at the Georgian Technical University (GTU). The flight model of a ring architecture consisting of a 5.5 m aperture double pantograph structure with radially tensed membrane ribs was deployed on the MIR station in 1999. This design and the development team contributed significantly to ESA's 12 m Large Deployable Antenna (LDA) development, within the ARTES 5 program (Fig. 3). The concept of the ring structure relied on a single circular pantograph equipped with radial outer lever extensions. These extensions produced the 14.7 by 12 m elliptical aperture starting from the 10 m circular ring. The design followed largely the architecture of the MIR antenna experiment of GTU, updated with full carbon-composite tubes and tapes. The mass of the reflector was 57 kg overall, although the necessary deployable boom was the largest contributor to the total mass due to its length and stiffness requirement. However, even if the LDA fulfilled the requirements with only a few exception, the design was discarded for future developments due to potential performance issues with the outer levers and the limitations introduced by the central interface.

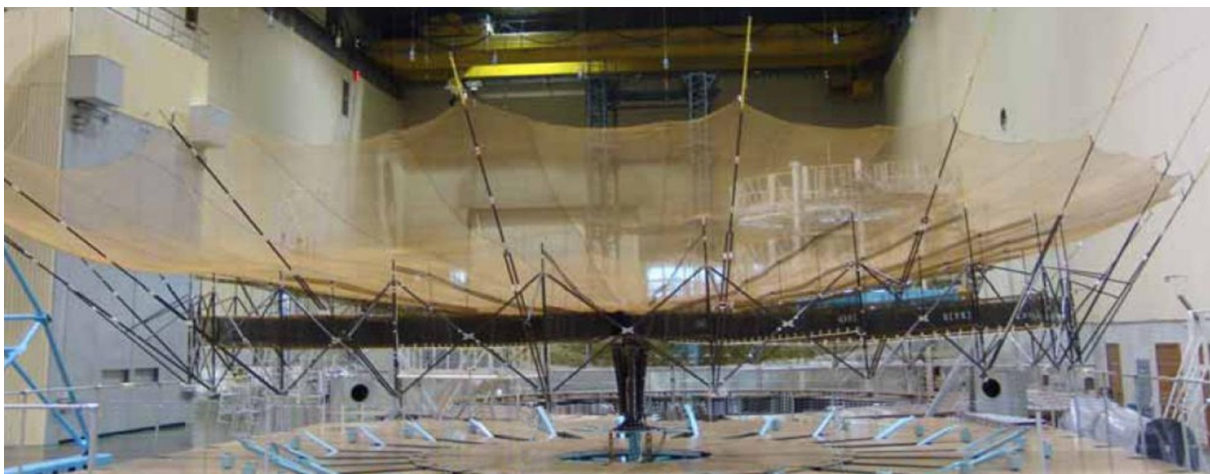


Fig. 3. Large Deployable Antenna EQM in deployed configuration (Courtesy of TAS-I, NPO-EGS and ESA).

Five years ago the first edition of the conference *Advanced Lightweight Structures and Reflector Antennas* took place in Tbilisi. That event provided a wide and deep overview of the state of the art in deployable structures technologies for space. It was obviously based on the heritage of the Georgian Technical University that led to the first Georgian space object. Also the evolution of these architectures were presented, as well as the state of the art in US, Russia, Japan and Europe. At the time, it was clear that European technologies in this specialized field had not been developed at the same pace as other ones. Shortly after, thanks to the initiative of the Electrical and Mechanical departments of D/TEC in ESA, a working group on Large Deployable Antennas (LAWG) was initiated, involving the participation of applications directorates, mainly Earth Observation and Telecommunications. Among other conclusions, the Working Group found that the large antenna market reachable by potential European providers was larger than initially estimated, in addition to the significance and diversity of the missions that could benefit from European developments in this field. It was also concluded that Europe was in a weak position in terms of IPR and therefore it was recommended that actions should be undertaken to improve that picture. The message was taken by the technical members of the WG.

As a result, a roadmap was proposed for developments covering the three identified families of reflector products over the two aperture ranges (4-7 m and 6-18 m), and also very important, the first patents were filed by ESA, securing new ideas. The first technical development initiated in mid-2010 was the small activity involving universities with a proven tradition in space deployable structures. Several concepts were evaluated and the final selection allowed developing two demonstrators of 6 m aperture: a double-pantograph ring (evolved from the Georgian heritage of pantographic rings) and a new architecture called afterwards the conical ring, based on V-folding struts. Both were developed in an intense and short time by GTU and TUM and presented at the 2012 ESA Large Deployable Antenna Workshop. In the meantime, the IPR base has been enlarged both at ESA and European industry.

Other activities, coordinated by the LAWG and included in the Harmonisation of Telecom Reflector Antennas roadmap, were also initiated. For instance, a remarkable effort was deployed in the GSP framework (RESTEO). In the study it was concluded that it is possible to exploit common deployable structures technologies for the needs of both Earth Observation and Telecommunications missions. Also a very interesting design of constant torque hinge was demonstrated.

Development activities thereafter have been initiated in the TRP programme, building on the initial ones and allowing to consolidate the concepts and preparing for higher technology readiness level. These are ongoing and progressing at the moment and include architecture consolidation studies (SCALABLE) and reflecting surface technology developments (MESH and LABUM). Also very important, system level activities are initiated in the frame of ARTES 1 (LARREQ), in order to accommodate the European technologies on existing and future platforms, allowing hence to prepare a European integrated solution to the needs of large apertures. The efforts are now converging to the ARTES 5 programme with activities for technology (MESURA) and test methods (RF and deployment tests mainly). The developments are still ongoing, and steadily reaching a TRL acceptable for first flight activities.

2. OUTCOMES OF PRECURSOR TECHNOLOGY DEVELOPMENT ACTIVITIES

The TAHARA study was initiated by ESA (before the establishment of the LAWG) with LLB - Technical University of Munich and DSL - University of Cambridge, both among the reference players in Europe in the field of deployable structures for space applications. The activity provided a global overview of the state of the art in 2005 and allowed to gather detailed insight into available technologies and an open-minded perspective. The activity introduced also improvements in the knowledge of spring-back composite shell constructions in terms of non-linear analytical methods for CFRP materials and an evolved design of the Stiffened Spring-Back Reflector [2], which included an edge stiffener with dedicated slits for folding.

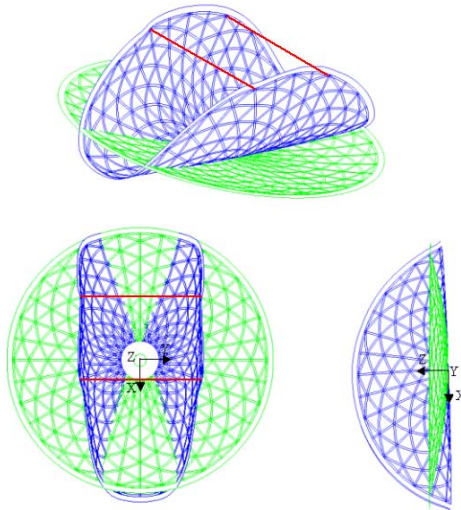


Fig. 4. Stiffened Spring-Back Reflector design of DSL-University of Cambridge [2].

TAHARA provided also a remarkable technology development of a new composite material, called CFRS (Carbon Fibre Reinforced Silicone). The unique characteristic of CFRS is the elastic behaviour of the silicone matrix in combination to the Carbon fibre fabric, providing both high deformability under actuation, intrinsic stiffness under environmental perturbations and high thermal stability. The continuation of the TAHARA study was devoted to increasing the technology readiness level of the CFRS. It was demonstrated that the material itself provided good results for highly deformable shell-membranes with high thermal stability and preserving their shape and integrity under mechanical and thermal loads, including thermal vacuum cycling. Later work in other activities has also shown that CFRS endures radiation without significant degradation and can provide good Passive Intermodulation performances.

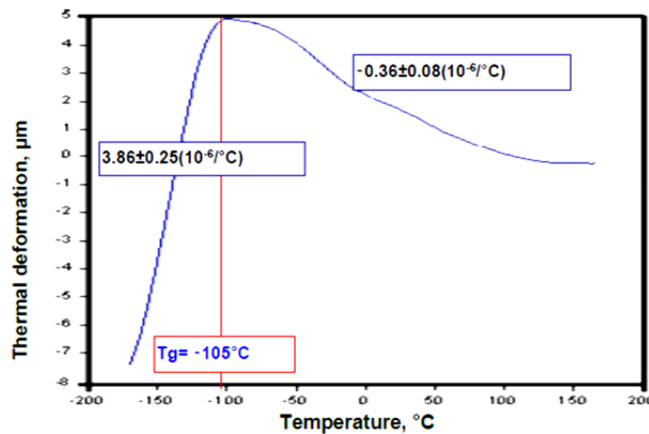


Fig. 5. Thermal expansion properties of CFRS versus temperature (LLB-TUM). Values in figure correspond to average CTE in the temperature range.

The SAFIRS study, implemented within the Innovation Triangle Initiative, was initiated as a further development from TAHARA, for a first trial of the integration of a CFRS surface with folding stiffeners into a deployable backing structure. In fact the reflector concept was first designed within the activities of TAHARA, although the demonstrator was finally manufactured and tested in this study. The deployable structure was a simplified realisation of radial pantographic ribs, to some extent similar to the HALCA antenna radial structure, in a small scale. In a further step in this study, the hybrid material CFRS/CFRP was developed as well. This happened in parallel to another study by TUM using an umbrella-type rigid ribs reflector, FLAME, which was deployed and measured in parabolic flights. Even if SAFIRS showed feasibility of the concept, it was designed for a central interface. Later studies using the CFRS have

evolved into a different architecture favouring the lateral interface. This is however not seen as a limitation of the material or the concept, just another architecture of the reflector assembly.

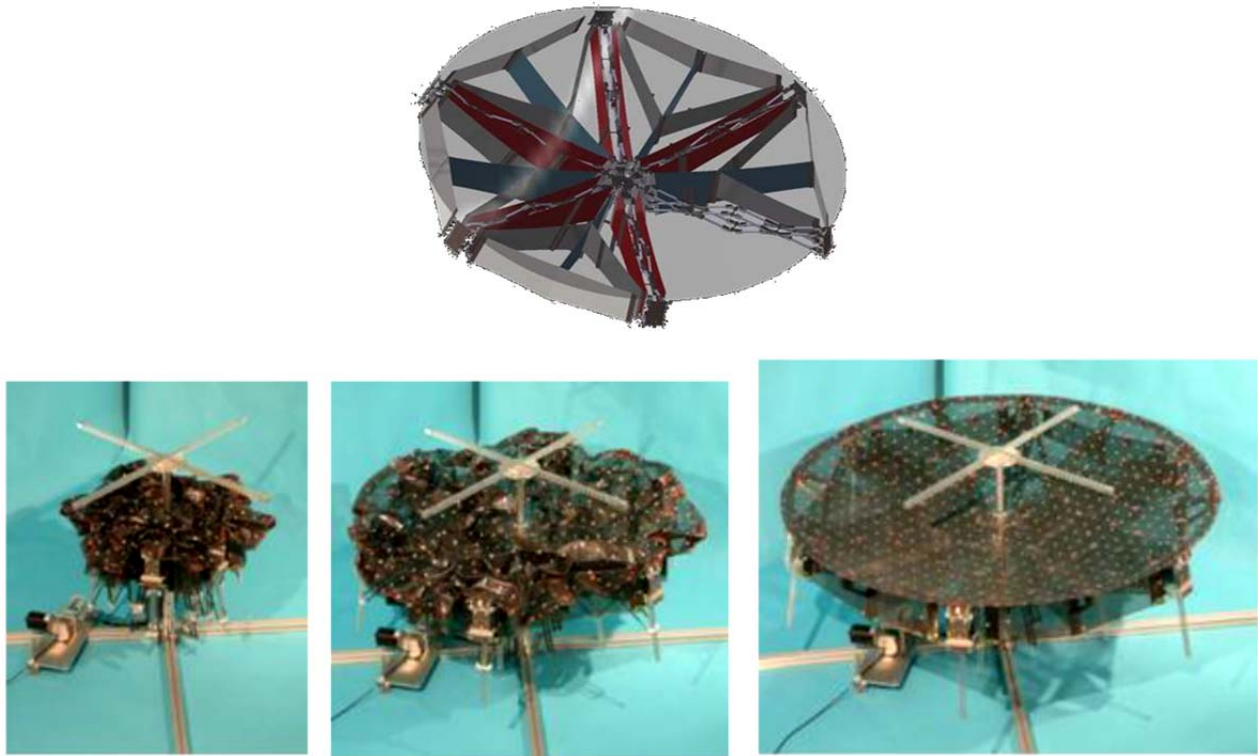


Fig. 6. SAFIRS demonstrator, CAD and test model during deployment (LLB-TUM).

Following the 2009 Conference in Tbilisi, the LAWG was established within ESA [1]. The mandate of the working group was mainly to identify the space missions/applications, markets and technologies related to the large deployable antennas, giving recommendations on the way forward within ESA. These recommendations were not only of programmatic nature, but also addressed the preferred antenna architectures to be developed. As an immediate consequence of the final report a new study was initiated, devoted to the development of new ideas following the recommendations on the technical lines to follow by the LAWG. The TALDES study (Technical Assessment of Large Deployable Structures) was initiated in 2010 with LLB-TUM for exploring further the potential of pantographic structures, and the participation of the Georgian Technical University due to their vast and deep heritage and experience in the MIR experiment.

The TALDES study focussed on the structural building blocks of large deployable antenna reflectors, considering two characteristic sizes: 4-8 m and 8-25 m projected apertures. Two demonstrators of a peripheral ring structure were built and tested, both of 6 m aperture, fully functional in terms of kinematics and actuation and representative of the mass and stiffness of a flight unit. Both were presented in the October 2012 Large Deployable Antenna Workshop at ESTEC. Following the principles of the Tension-Truss architecture of Miura and Miyazaki [3], they were equipped with a network in the centre made of extensible tape, although not necessarily representative of the final concepts to be implemented in future models. One of the rings is constructed as a cylindrical double pantograph ring with crossing (also called shifted) pantographs. The second ring transforms from a compact cylindrical package into a conical ring, and is constructed with V-folding bars. It is based on ESA patents 568 and 621, demonstrating two motorisation options, i.e. electrical and spring actuation.



Fig. 7. Deployment tests of the TALDES 6 m double pantograph ring demonstrator of LLB-TUM (Photo ESA/A. Le Floc'h) and the 6 m conical ring of GTU (photo GTU). Both developed under ESA study.

In parallel to the TALDES study, another ITI activity was initiated with ABSL in the UK to develop a ring based on the hybrid Sarrus-pantograph concept, starting from ESA patent 568. The development allowed to demonstrate the kinematics and the actuation of this variant in a different industrial environment. Actuators are in this case DC motors integrated inside 3 of the vertical bars for driving the upper pantograph in addition to springs in the V-folds. The ring has a slight fixed conical angle which can affect the stowage ratio although not significantly. The demonstrator has been submitted to a large number of deployments without major problems, therefore reliability is considered as comparable to the double pantograph ring. Further work would be necessary to progress in terms of readiness level. After the development was finalised in 2013, the activities on this concept are now continued by the spin-off company Oxford Space Systems.

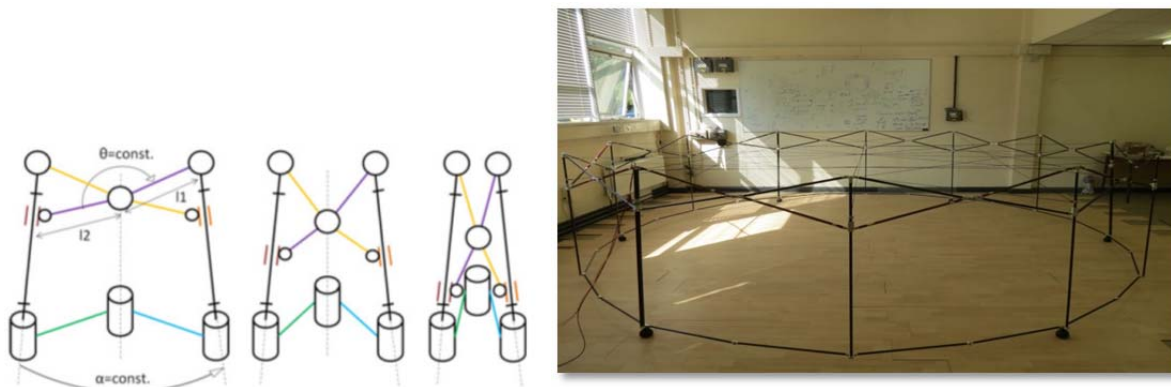


Fig. 8. Hybrid Sarrus-pantograph cell employed in the 4-m circular ring (courtesy of ABSL).

Within the GSP programme, the RESTEO study largely helped to assess needs and related requirements of large reflector antennas for both Telecom and Earth Observation future missions [4]. The study was conducted by Space Engineering of Rome with the participation of HPS and LLB-TUM of Munich. It deepened in RF, mechanical, thermal and satellite accommodation aspects considering the commonality and differences of the applications. Investigation of compliance for all antenna and reflector requirements was completed and resulted in selecting two architectures of peripheral rings, namely the two concepts demonstrated by TALDES, as the two candidates for further development in Europe. The study was concluded in 2012.

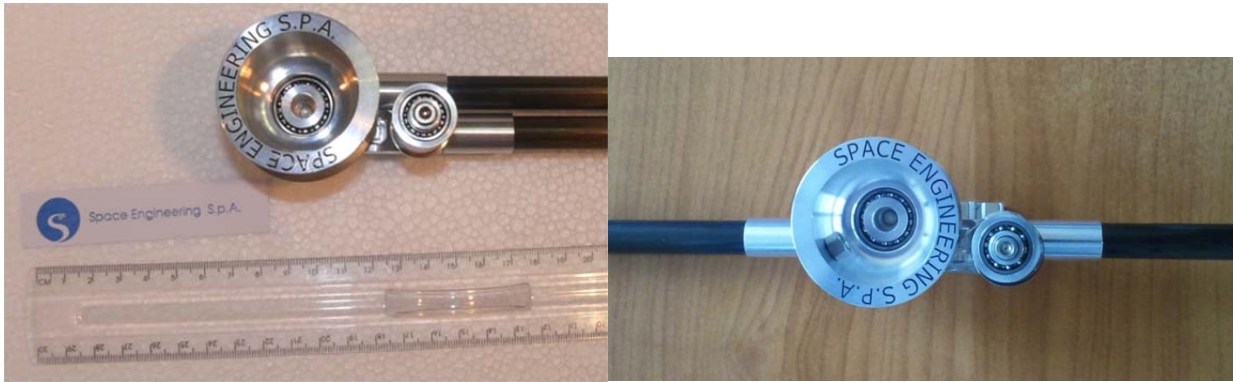


Fig. 9. Constant Torque spring actuated hinge developed by Space Engineering under ESA study.

As a continuation of RESTEO, additional work was performed in coordination with the TALDES team to develop a constant-torque 180 degree actuator, compatible with the V-folding bars. It is a robust and reliable design of spring-actuated hinge, demonstrated at breadboard level but with flight representative design and construction. It is modular in the provision of torque, which can range from 1 to 5 Nm without major impact in dimensions or mass. It is foreseen to include a damper inside the drum in future developments [4].

Most of these activities, especially after the LAWG roadmap consolidation, have been carried in parallel and under the roadmaps outlined by the LAWG as well as the Harmonisation of Telecommunications Reflector Antennas. It has to be mentioned that despite the controlled funding, they have resulted in very relevant progress in the state of the art and the knowledge of the technologies and the products. They have created the basis for activities in the TRP and ARTES programmes, as their natural continuation for increasing the technology readiness level, the qualification status and the progress towards integration in space system. These activities are described in section 3.

3. RUNNING AND PLANNED ACTIVITIES

The ARTES 5.1 activity MESURA (Medium Size Unfurlable Reflector Antenna), initiated in September 2011 with Astrium ST of Les Mureaux, now Airbus DS, and Thales Alenia Space as subcontractor, is devoted to adapting the well-known foldable tips concept to current telecommunications missions requirements with apertures in the range of 4 to 7 m. The targeted operational frequency bands range from C to Ka. The selected concept relies on solid CFRP parts with dedicated deployment and hold-down mechanisms. One of the major challenges is accommodating the large reflector on a large spacecraft bus and the smallest compatible fairings of commercially competitive launchers in single and dual launch configurations. Phase 1 has concluded successfully, by identifying candidate mission scenarios, selecting candidate platforms and the corresponding launcher fairing envelopes, screening of mechanisms concepts and structural materials. This has led to a design of structures and deployment concept that fulfils the accommodation, RF, mechanical and thermal requirements. A preliminary design of the demonstrator of phase 2 has been performed and will be manufactured and tested. The planned date for the end of the activity is within the first quarter of 2015, allowing for a potential qualification for flight within 2016.

The TRP activity LABUM (Large Apertures Based on Ultrastable Membranes) has been running since 2012 under contract with LLB-TUM and is progressing towards the demonstration phase. The main objective is the feasibility demonstration of thermo-elastically stable membranes or shell-membranes for the generation of large apertures in the range of 5 to 50 m. Thus the focus is on the shape stability in orbit. In particular, the shell-membrane technology selected is based on the CFRS material, which has the particular feature of not requiring pretension to generate a parabolic or shaped reflecting surface. Phase 1 of the study has concluded with a consolidated design of the shell-membrane structure suitable for flight. The interfaces between the shell-membrane surfaces and the deployable structure, which are designed following space telescopes concepts that create a quasi-static suspension of the surface, have deserved special attention. Also the gravity compensation devices and methods for on-ground testing have required special efforts, considering in particular the architecture of the membrane. The preliminary design of the demonstrator and gravity off-loading are available. Phase 2 is progressing to the detailed design of the 5 m demonstrator

and the preparation of the thermal-distortions test in a sun-simulation vacuum chamber, including the effect of shadows. This activity is considered as a milestone for the potential evolution of this technology of shell-membranes. In case of no unexpected material behaviour and the fulfilment of the expected performances, a new generation of antenna reflectors will be conceived after all the efforts invested in new materials and structural architectures developments. It is worth mentioning that CFRS is finding its way in other applications as well, such as mechanical reshaping of antennas and ground terminals [5].

The activity SCALABLE (Innovative Scalable Large Deployable Antenna Reflector) was approved for implementation in the TRP programme with the objective of developing deployable structures for large antenna reflectors with the particular requirement of providing a scalable design in the range of 4 to 18 m aperture. A starting point of this study was clearly the outcomes of the RESTEO GSP study, already pre-selecting two European technologies suitable for that purpose. However, the SoW called for an open competition of innovative solutions. Two parallel contracts were awarded, one to the team of HPS with LSS of Munich as subcontractor (TUM spin off) and another one to Thales Alenia Space of Italy. The two architectures under development are complementary ideas. The HPS/LSS design is an evolution of the double-pantograph architecture, which includes significant improvements in the possibility of creating a conical ring and especially the network and metal mesh integration. The network design is considered as a key factor versus existing commercial products, closing hence the open points from the TALDES study in terms of detailed implementation of the mesh and its performances. In addition to the mass/stiffness and reliability aspects already addressed in TALDES, this concept would provide a definitive answer to the shape stability and capability of shaping the mesh not only to the parabolic surface, with an innovative solution. At this point in time the study with HPS/LSS has achieved successful closure of the phase 1. Meanwhile, the TASI concept builds on a certain degree of modularity as the answer to scalability, using deployable tetrahedra as unit cells. It relies on the TASI constant torque hinges for actuation. The activity is focussing on deployment reliability as the key aspect, and the progress in mass, stiffness and stability performances are being addressed deeply.

The TRP activity MESH, with Space Engineering of Rome as prime contractor and the important contributions of ITA (textile institute of the University of Aachen), University of Rome 'Tor Vergata' and University of Pavia. It is devoted to the definition of a European metal mesh industrial process. Strangely enough, even if the material source of Tungsten guided wire and the warp knitting machines are European, there is not yet a fully established industrial production of this sort of mesh with the required performances. Alternatives exist commercially, although not yet with the materials and performances required for the applications addressed, such as in Ka band. The study has traded off stitches and process parameters to cover the needs of reflection losses and depolarisation, taking care of the mechanical stiffness, strength and anisotropy and especially passive intermodulation. A further particular development within MESH has taken place for the mechanical characterisation taking into account bi-tensional state measurements, using and improving concepts from the textile industry. However, a major effort is obviously invested in the establishment of the mesh knitting process parameters, in particular the production of the suitable yarn and the stitch in the required size. Special attention is given to the yarn production with triple wire, as was the case of the LDA development. At the moment the work is focussed in freezing the process parameters.

The ARTES 1 study LARREQ (Large Aperture Antennas and Associated Reflector Requirements) is a system level activity devoted to analysing the accommodation of at least two European developments on at least one European spacecraft platform. All critical system aspects shall be investigated, as encountered during the different mission phases, including launcher accommodation, AOCS, RF performances and compatibility, mechanical and thermal behaviour. This shall lead to the elaboration of a combined development plan, especially for the interfaces, and the identification of all the actions to be performed either at reflector or platform level to prepare the commercial applications using large reflectors. At this point in time the contract has been recently awarded and work is planned to start in fall 2014. The expectation is that this activity will clear the way of European technologies to be embarked on European platforms addressing thus the major issues of technological dependence and transnational regulations.

Building on the LAWG roadmap and the significant activity resulting from it, a new ARTES 5.1 study is being implemented for addressing one of the key aspects that, as lesson learned from prior experience, has been deemed critical: on-ground testing. This activity, dealing mainly with RF and deployment testing methods has been approved in the ARTES workplan and will be initiated within 2014. The objective is to develop test methods for the verification of large unfurlable reflector up to 12 m projected aperture. This shall include test methods for key performances such as

deployment, surface accuracy, thermo-elastic stability, RF and Passive Intermodulation. Also analytical methods and tools for test predictions and correlation shall be established and a demonstration of test methods by employing suitable ground support equipment will be performed.

4. CONCLUSIONS

Activities initiated by ESA on large deployable antennas have been summarised. More activities concerning deployable structures are being prepared and implemented ESA-wide, not only for antennas, also for other equipment such as solar generators and solar sails, and not only for telecommunications and Earth observation, also for scientific missions. The ones presented in the paper have focussed on the antenna-related technologies and mostly for telecommunications and Earth observation as the major drivers of the deployable structures field. As a final remark, it has to be mentioned that synergies, commonalities and harmonisation of these activities are always taken into account in order to optimise the resources put in place by member countries and incorporating the inputs provided by national agencies.

5. REFERENCES

- [1] Mangenot, C., et al., Large Antenna Working Group. Final Report, ESA, September 2010.
- [2] Datashvili, L., et al., TAHARA Study CCN1 Final Report. May 2005.
- [3] Miura, K., Miyazaki, Y., Concept of the Tension Truss Antenna, AIAA J. 28(6), 1098–1104, 1990.
- [4] Scialino, L., et al., Large Deployable Reflectors for Telecom and Earth Observation Applications, CEAS Space Journal, Vol. 5, Number 3-4, 2013, DOI 10.1007/s12567-013-0044-7.
- [5] Rodrigues, G., Angevain, J.C. and Santiago-Prowald, J., Shape Optimisation of Reconfigurable Antenna Reflectors, CEAS Space Journal, Vol. 5, Number 3-4, 2013, DOI 10.1007/s12567-013-0038-5.

ACKNOWLEDGEMENTS

The authors wish to thank all contributors to the large antenna working group activities.

RADIOMETER ANTENNA ARCHITECTURE FOR OCEANOGRAPHY APPLICATIONS

Kees van 't Klooster⁽¹⁾, Cecilia Cappelin⁽²⁾, Knud Pontoppidan⁽²⁾, Per Heighwood Nielsen⁽²⁾, Niels Skou⁽³⁾, Sten Schmidl Søjbjerg⁽³⁾, Marianna Ivashina⁽⁴⁾, Oleg Lupikov⁽⁴⁾, Alexander Ihle⁽⁵⁾

⁽¹⁾*Estec, Keplerlaan 1, 2201AZ Noordwijk, Netherlands*

Kees.van.t.klooster@esa.int

⁽²⁾*Ticra, Læderstræde 34, 2. DK-1201 Copenhagen K Denmark*

CC@ticra.com, KP@ticra.com

⁽³⁾*Denmark Technical University, Ørsted's Plads Building 348, room 124, 2800 Kgs. Lyngby, Denmark*

NS@space.dtu.dk, SSS@space.dtu.dk

⁽⁴⁾*Chalmers University E-building, Hörsalsvägen 9-11, SE-412 96 Göteborg, Sweden*

marianna.ivashina@chalmers.se, oleg.iupikov@chalmers.se

⁽⁵⁾*HPS GmbH, Hofmannstraße 25-27, 81379 München, Germany*

Ihle@hps-gmbh.com

ABSTRACT

Antennas for microwave remote sensing instruments require large apertures for sensitivity, depending on requirements. (Phased) Array antennas and large reflectors are used, both for active or passive instruments. Recently the 7th ESA Explorer mission Biomass was selected. It will use a deployable parabolic reflector to be embarked on a not so big spacecraft for Low Earth Orbit (LEO) exploiting a feed-array. Also new architectures for radiometers are investigated. Antenna architectures will appear, using focal arrays combined with a large reflector. Such approach is already followed for terrestrial radio-astronomy in preparation for future Square Kilometre Array (SKA). Advances in integrated circuitry, both for RF frontends and processing circuitry, permit a needed lower power consumption, allowing eventually space applications. It is expected that multiple-beam multi-frequency radiometer instruments for space will appear and use such technology developments. The paper provides a short overview of past activities – even radio-astronomy - and gives recent information from an ESA study on radiometry developments, addressing the shaped toroidal reflector antenna with focal plane array.

1. INTRODUCTION

Microwave remote sensing from Space requires accurate instrumentation. An antenna as transducer is an important part of the instrument. RF properties of the antenna have to be known with absolute accuracy, implying precision in many facets, including mechanical realisation and its relation to RF performances. The antenna is often the largest contributor in the overall instrument accuracy budget. In order to handle weak signals with high accuracy, large effective apertures are needed, both for active (radar) as well as passive (radiometry) remote sensing. Large, de-facto deployable antennas are needed for such applications. Remote sensing can be considered to include both Earth observation and radio astronomy tasks. A short review below presents some past activities in ESA. Information is given about the recent selection of the 7th ESA Earth Explorer. In the remaining part, new radiometer architectures for oceanography are addressed, with a focus on a large reflector in combination with a focal plane array. Some material is already presented in [19, 20, and 21]. This paper here is descriptive in nature, more results are forthcoming.

- Radio Astronomy Antennas. Extremely high resolution applications in Very Long Baseline Interferometry (VLBI) require a space-based radio telescope to act with Earth based radio telescopes. The Japanese project Halca [24] did realise it for a first time. Radio-Astron [10], now more than 3 years in orbit, showed results with records in resolution.

Unique “stand-alone” observations have to be made from Space for those wavelengths, for which the atmosphere and ionosphere of the Earth prevent terrestrial work (predominantly very low and very high frequency bands). Two studies have been carried out on Space VLBI in the past for ESA, supported by international science teams. The first study made it to a Phase A (Quasat, in late 80's). After this study Huygens-Cassini mission was selected (it is interesting to mention that successful localisation results were reported about the landing of Huygens on Titan, thanks to Earth-based VLBI: a precise landing trajectory on Titan was determined).

Critical technologies have been investigated for QUASAT, like a multi-frequency dual-polarised feed and inflatable antenna (as selected reflector candidate). A 6 mØ symmetric prime-fed reflector model (scaling 1:3) was realised and tested before/after folding exercises (Fig.1) in lab environment. RF performances were predicted, with measured RF feed results and measured precise geometrical reflector data as input [1]. Secondary patterns showed effects of the rms

reflector surface accuracy. Rms values were obtained from theodolite measurements before/after packaging (0.99 and 1.13 mm rms respectively, against 0.7 mm spec).

Recently an inflatable reflector design was reported [3] and particular deformations were described (W-deviations). Although the design [3] has a striking comparability with the 6mØ Quasat model [1], we have not observed such deviations, which would lead to much larger pattern distortions than observed.

The Quasat reflector investigations included self-rigidisation by proper treatment, to allow eventual de-pressurisation in space as desirable against (micro) meteorites. In a broader context a 3 mØ and 12mØ offset reflector have been investigated. The 12 mØ inflatable offset reflector was realised with telecommunication applications in mind. The 12m model was never fully tested under space conditions. Geometrical assessment resulted in ~3mm rms and L-band multiple beam capabilities were derived for telecommunication tasks [17]. The program for inflatable reflectors was abandoned. One reason was, that large thin shell inflatable reflector antennas have a criticality concerning buckling aspects (observed in a shuttle experiment also). Adaptation of new technologies and modelling techniques might be able to bring inflatable technology forward again, however buckling aspects and thermal environments remain critical, leading to problems for thin shell shaped inflatable reflector antennas. Feed studies in ESA covered multi-frequency feeds and wide-band corrugated feeds [1, 2, 6, 27] and led also to spin-off applications, like multi-frequency feed for radar-altimeters, reflector assessment techniques for testing during thermal vacuum tests, etc.

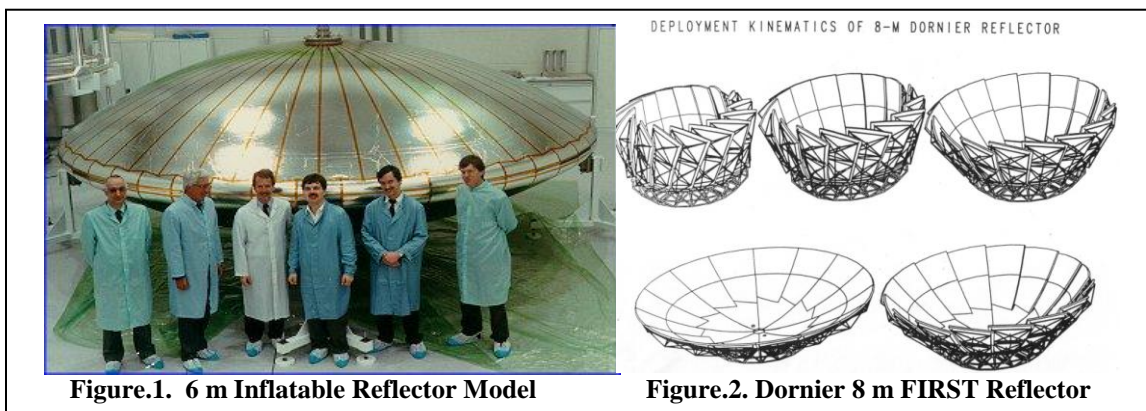


Figure.1. 6 m Inflatable Reflector Model

Figure.2. Dornier 8 m FIRST Reflector

In early 90's a joint ESA-Roscosmos study addressed the "International VLBI Satellite –IVS". A 25 mØ deployable solid panel reflector antenna was considered (in concept comparable to RadioAstron antenna). It should be launched in a canister on the Energya-rocket (instead of the Buran – impressive). See [4] for a description and antenna aspects [5]. Associated RF studies dealt with low cross-polar wide bandwidth dual polarised feeds [6]. IVS should be able to satisfy both VLBI- and stand-alone observations. Stand-alone observation require a very clean pattern (less the case for VLBI). This has been revisited later in studies like Arise [25] and in a recent paper [15] on the basis of the Astro-mesh reflector.

Early ESA technology studies for realisation of a Far Infrared Radio Telescope (FIRST, mid 80's) led to a development of a demonstration panel with 4μ rms, as needed for such telescope in Fig.2. An inclined panel hinge attachment is observed, to be operated for deployment in a synchronised manner. Such concept was further investigated for Dornier Daisy and MEA design (offset) [7] for telecommunication with a model qualified. One can see some technology solutions back in other programs, like a mentioned panel hinging to allow denser packaging during launch.

RadioAstron program continued a long period since early 80's. It was launched 18 July 2011. Successful deployment of the 10 mØ antenna was reported 5 days later. Radio Astron also has panels (27) hinged under an angle to a central section. Records in resolution VLBI results with baselines larger than the Earth diameter are reported [10].

Quasi solid panel configurations (call it hybrid) were initially investigated in [8], but not taken forward. The 8 mØ FIRST program was abandoned. Later it was revived with 3 mØ non-deployable fixed radio telescope for Herschel. The renamed mission Herschel was launched in 2009. Herschel mission is completed now, because the last on-board helium for detector-cooling has been used [9].

Astro Space Centre of Lebedev Institute studies a MM and Far Infrared instrument for the Millimetron program [10], which received further attention after successful RadioAstron launch and its first results. A deployable 10 meter antenna is needed, to operate at ultra-low temperature [11]. A low-loss, cooled, accurately configured deployable reflector antenna is needed, which is a major task to be realised and one of (if not the most) the critical items for Millimetron.

-Antennas for Earth Observation Instruments. ESA has a backlog in active remote sensing with ERS 1 and 2 and Envisat program. More recently Sentinel 1 was launched, which forms now a part of the Copernicus program. Relevant descriptive information is found in [12]. A selection was made in 2013 for the 7th Earth Explored mission [13] out of

been three competitive Phase A studies. Satellites for these missions operate from a Low Earth Polar Orbit (LEO). Two active (Synthetic Aperture Radar) microwave missions and a passive mission have been competing [13].

- Biomass will operate a SAR in UHF at 435 MHz ($\lambda \approx 70$ cm), with a reflector antenna with $\sim 11\text{m}$ aperture. A USA supplier is envisaged for a deployable reflector antenna. Small platform and launcher with constraints lead to interesting accommodation and antenna aspects. The reflector, although $\sim 11\text{m}$ has electrical sizing (λ) not much different from an offset-reflector antenna used for a Ku-band satellite terminal at home for reception of TV channels. The antenna – an instrument sensor - has to operate very accurately, putting strong demands on reflector stability and feed assembly (RF, polarisation properties, stability), platform accommodation and interconnection. See [13] for more info.
- CoReH2O mission, although not selected, was planned with a spacecraft SAR mission with a deployable, solid reflector antenna, operating in X and Ku-band for instrument radar functionality (SAR modes) [13]. Such type of mission might well be revisited for comparable or other tasks. It has an interesting dual polarised multiple feed solution, providing with the reflector a coverage of 100km wide strip along-track (ScanSAR is used).
- PREMIER, although not selected, was planned for investigations of atmospheric properties exploiting limb-sounding. An infrared and a millimetre wave limb-sounder was envisaged, with for the latter a 0.8×1.6 m solid main reflector in a dual reflector assembly, illuminated by a quasi-optical network around 340 GHz (upper and lower band). It would provide multiple beam coverage of a 22 km vertical range at some 3200 km distance from the satellite just above the horizon of the Earth [13]. A reflector surface accuracy smaller than 10μ rms is needed and reference material includes heritage to the flying ODIN satellite [14].

The Biomass mission has been selected with its large deployable reflector antenna with a reflector supplier from USA. The status of the NASA mission SMAP is followed with interest, carrying for the first time a 6 mØ mesh reflector operating in L-band, deployable and functioning in LEO with an intriguing conical scanning mission configuration. The parabolic reflector of SMAP is used as a rotating reflector assembly, with the feed platform kept fixed (feed aperture directed away from nadir). The satellite is very special with its rotating reflector a precise conical scanning [16].

In general the considered reflector configurations had a symmetric parabolic or an offset parabolic shape. Symmetric parabolic reflectors may find application for space based radio telescope as element in a VLBI network. For radio telescopes doing single dish observations, the side-lobe performances more demanding. A symmetrical dual reflector antenna has been considered for IVS [5]. Patterns must be accurate. Asymmetric configuration cannot be used in telecommunication applications because of demanding pattern and side-lobe requirements and polarisation purity. An offset configuration has to be used with critical mechanical/structural aspects due to an absence of circular symmetry.

In the following we consider a different reflector geometry, namely a shaped toroidal offset reflector, envisaged to be used for radiometry tasks with high sensitivity for oceanography applications in a push-broom configuration.

2. RADIOMETRY FOR OCEANOGRAPHY APPLICATIONS

Radiometer requirements for oceanography applications are demanding. High sensitivity is important with radiometric resolution, spatial resolution, pattern and polarisation cleanliness and capability to measure near to coastlines. Antenna patterns should have a good sampling function capability or beam-efficiency to reduce effects from disturbing signals incoming via side-lobes. Such disturbances can come from more warmer land areas, coming in through side-lobes when near to coast lines. Higher resolution is requested. It implies small footprints and thus, with a satellite platform moving with a speed of several km/sec, a short integration time for the radiometer. Larger apertures provide better sensitivity but with the reduced integration time, a scanning or multiple-beam architecture might be needed.

Three general schemes for coverage are presented in Fig.2 respectively conical scanning, push-broom coverage and across track scanning. The third scheme can include 1D scanning, multiple beam as well as 1D correlation techniques (interferometer), using line sources within the antenna aperture. The number of front-ends can be reduced for such configuration and selected on a basis of finding the appropriate balance between applying minimum redundancy considerations and the best situation when filling an aperture for a required sensitivity [22]. Synthesised antenna pattern performances using correlation have to satisfy requirements like sensitivity or distance to coast-line. In a scheme for across track scanning, we observe a resolution degradation when going off-nadir.

The global interest is to have a short revisit time over the same target area. Associated coverage requirements dictate the width of the useful swath, schematically indicated in Fig.2. The conical scan arrangement allows for a wide coverage, but it has lower sensitivity. It is due to available integration time with a rotating antenna beam scanning in a spiralling sense over the coverage. Adding more beams would allow better sensitivity, at a cost of complexity in an already complex mission architecture with fixed feed assembly and a rotating reflector. Multiple feed horns can provide better sensitivity. One could further replace feed horns by a focal plane array and realise even better illumination capability,

having more patterns with a smoother pattern overlap. It is still limited due to accommodation constraints given physical limitations in the focal region of an instrument with rotating reflector. The precise combination must be used with a synchronised satellite movement and spin-rate of reflector connected with precise coverage and resolution. It has consequences for available coverage and sensitivity of the radiometer instrument. For frequency bands considered here (higher than L-band, SMAP [16]), the use of multiple feeds or alternatively a focal plane array is desirable [21].

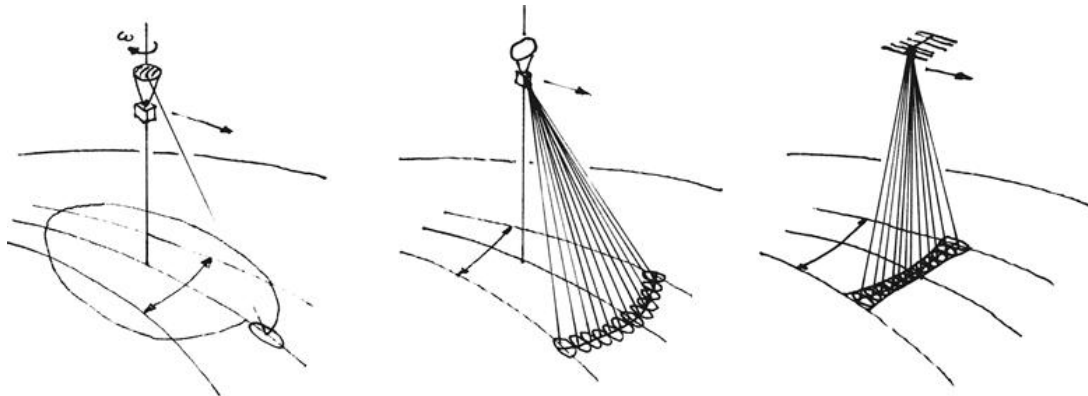


Fig. 2. Conical scanning coverage, multiple beam push-broom coverage, multiple beam coverage across-track.

The push-broom architecture uses a toroidal parabolic reflector and a set of feeds or – as recently shown and investigated [19,20] – a focal plane array, to adapt to excitation distributions needed for separate beam-efficient beams for coverage. The radiometric sensitivity is better by almost an order of magnitude compared to a conical scanning radiometer. The separate beams can be configured on a conical surface, ensuring identical incidence on the Earth surface to ensure good polarisation responses for all beams. Such scenario was addressed already [18], with a single feed for a beam. As noted, the feed horns for the beams are positioned on an arc in a focal plane. A demonstrator was realised. Potter horns were used located at interlaced arcs in the focal plane, to realise the necessary adjacent beams from the toroidal parabolic reflector with low overlap. The demonstrator was realised at 37 GHz with a 1 meter sized reflector. In general: once a reflector for a push-broom is deployed, there is no more movement, which is an advantage.

Recently an ESA study was initiated on improved radiometer instruments targeting oceanography applications. It was requested to combine and improve the good antenna expertise, expertise on large reflector antennas and on focal plane arrays (readily underway for future Square KM array for radio astronomy). TICRA took a lead in this study and arrived at promising novel results which will –no doubt – be taken forward in a not too far future. An enthusiastic team included participants involved in radiometry, radio astronomy antennas and in large deployable reflector antennas. Within the study the push broom radiometer configuration was selected for more investigations, due to its high sensitivity.

The rotationally symmetric feed horns provided a coverage with resolution on the ground with a shape slightly deviating from desirable ones and not-perfect beam efficiency with systematic side-lobes (problem with the error signal when coming close to a coastline). In the recent study the application of focal plane arrays allowed to correct for that and to generate better beam shapes with good patterns even with a shaped toroidal parabolic reflector antenna. Densely sampled focal plane arrays instead of single feed elements offer such a potential in principle: a realisation of efficient antenna patterns and further control of polarisation as needed.

3. ON REQUIREMENTS

The oceanography community has interest in high-precision sea-surface temperature (SST) and ocean vector winds (OVW) with high resolution (spatially and radiometric). Conical scanning and push broom radiometer scenarios have been studied in ESA and find applications in operational missions like METOP [12]. Resolution, pattern cleanliness and related to that the a minimum distance to coast are important. Fig.3 shows tentative requirements for a radiometer (C, X, Ku) targeting break-through compared to available instrumentation with fixed reflectors (an ESA study Microwat [23] investigated this already). For 17 GHz one could consider a mesh reflector. OVW requires accurate polarimetry, S3 and S4 means 3rd and 4th Stokes parameter. Some results will be shown in the actual presentation.

4. PUSH BROOM ANTENNA INVESTIGATIONS

Resolution requirements lead to an initial aperture sizing of ~5 mØ for a conical scanner and to 5x7.5m toroidal reflector for the case of a push broom. Distance to coast has been analysed taking an assumed distinct step-function of 100 K in an observed radiometric temperature distribution, like when moving over a coastline and later by optimisation

Freq. [GHz]	Band width [MHz]	Polarization	Sensitivity [K]	Bias [K]	Resolution [km]	Dist.to coast [km]
6.9	300	V, H	0.30	0.25	20	5-15
10.65	100	V, H S_3, S_4	0.22 0.22	0.25 0.25	20 20	5-15 5-15
18.7	200	V, H S_3, S_4	0.25 0.25	0.25 0.25	10 10	5-15 5-15

Fig. 3. Requirements for Band Radiometer (C, X and Ku-band)

under constraints of power captured within a solid angle, compared to power captured within a hemisphere. The three frequency bands considered are relatively narrow band and well separated. Measures have to be taken to protect against interference, when looking downward to the Earth from a satellite. As described in the study [19,20,21], application of a densely packed focal plane array can enhance sensitivity, both for conical scanner and for the push-broom, but a conical scanner has reduced space in its focal area to hoist a focal plane array and has from the onset less sensitivity than a push broom configuration [21]. We focus now further on the push-broom scenario.

The sizing of the focal plane three-band array is visualised in Fig.4. The number of pencil beams relates linearly to a coverage required and so does the sizing of the focal plane array. Derivation of array element excitations for each beam follows from optimisation to realise a needed focal plane distribution to produce a clean beam. A complex field distribution is needed in the plane for the focal array for each single beam. Analyses have been carried out both by Tica and by Chalmers University. Both approaches have evolved into comparable results [19,20]. Optimisation scenarios require testing for pattern cleanliness, with importance to the distance to coast. Fig. 4 shows a scenario for a push broom reflector, with an incoming (Gaussian) beam of rays to determine the focal plane distribution.

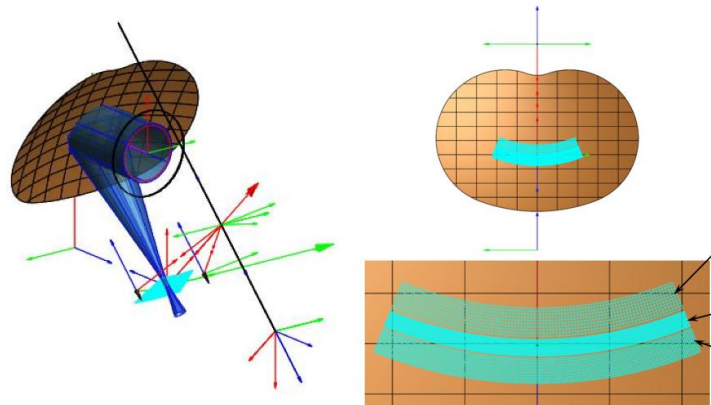


Fig. 4 Push broom toroidal reflector and focal plane array for three different frequency bands.

With promising results reported [19,20] further improved results have led to focal plane array performances and sizing for the three frequency bands. Accommodation requirements have not been considered, but in the work a tentative sizing has been considered for a coverage capability of about 600 km, simply to avoid deployment for the feed system. The element distance has been considered with about 0.7 to 0.75λ spacing (crossed dipole elements, mutual coupling accounted for as for strip dipoles at this stage). Analysis including mutual coupling must be carried out to secure a precise focal field description for two polarisations for the element selected "conf.icssem@gtu.ge" <conf.icssem@gtu.ge>, and with that a precise antenna pattern description. A "good" element choice and associated analysis is important for this. The focal plane array must have the necessary (complex) focal plane distribution to secure an accurate dual-polarised antenna pattern with good beam efficiency (complying with distance to coast requirements). The original antenna pattern [18] had a shoulder in its pattern, thus its beam efficiency was not optimum. This can be improved by a properly excited focal plane array, with indicatively 7 by 22 elements to provide the focal field distribution for a beam. Indicatively a total nr of elements results for a desired coverage, with all separate beams connected to subsets of elements in the array with one column shifted. The number of elements is large indeed. Each dual polarised element is connected to two receivers, followed by A/D conversion to get digital signals for further processing for appropriate multiple beam formation. Power consumption for such a large number of elements is today an obvious issue, for space applications out of the question, but exciting improvements are underway in terrestrial developments to make such scenarios possible with feasible power constraints even for space applications.

5. DEPLOYABLE SHAPED TOROIDAL PARABOLIC REFLECTOR

The selected toroidal reflector shape is obtained by rotation of a parabolic curve about an axis parallel to the direction from a feed to the reflector, see [18]. Following an initial trade-off of parameter settings a 5x7.5 m reflector resulted (for ~600 km swath from ~800km orbit). The focal array has its elements in rows along an arc in a plane (Fig. 4).

The toroidal shaped reflector has been investigated for feasibility by HPS, known for expertise in large deployable reflector antennas. At first glance it looks like the well-known Astro-mesh reflector [15, 16]. There are differences, including the (dual and elliptical) annular pantograph, integral design of opposite non-symmetric webs with force density method (FDM) for support a of toroidal (not a parabolic) reflector shape with kidney-like perimeter, with consequences for some limited remaining residual forces to be fine-tuned along the reflector perimeter

The overall mechanical configuration is shown in Fig. 5. A dual- pantograph in elliptical annular configuration supports as a stiff peripheral ring two opposite interconnected tension nets, one having a desirable shape to support the reflector. The desirable shape is found using the FDM with a solution iteratively arrived at with proprietary HPS processing. The net supporting a reflector causes triangular facets to appear in the case of a metal mesh. Alternatively if it can be configured to support a carbon Fibre Reinforced Silicone (CFRS) reflector, the triangular faceting is less pronounced than for the very elastic metal mesh. This needs to be further optimised, but it is an important subject.

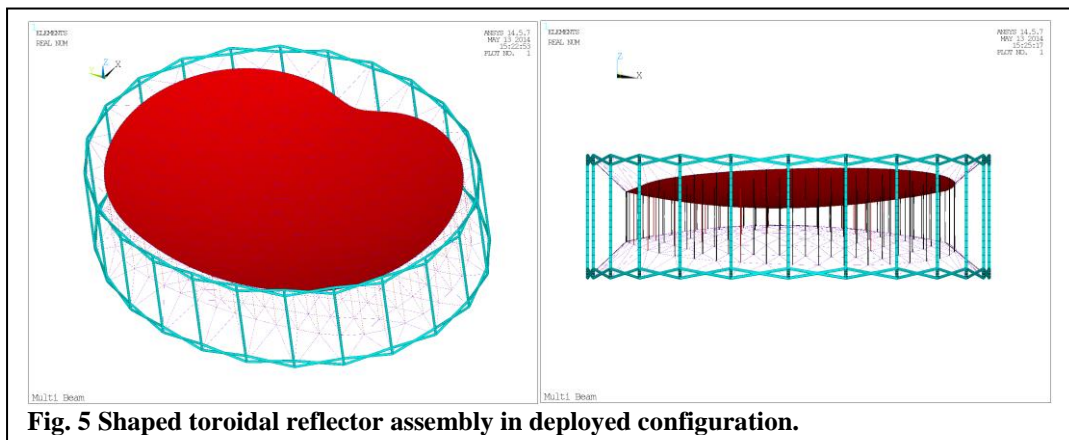


Fig. 5 Shaped toroidal reflector assembly in deployed configuration.

An initial finite element model has been established for static and modal analysis. Attention has been given to a pretension of upper and lower band nets and interconnects. A CFRS configuration as alternative needs further iteration but has advantages. With initial representative assumptions taken, a mass for the reflector of near to 45 kg resulted (no thermal hardware) and first eigenmode slightly above 0.64 Hz (metal mesh assumed).

Static deformation of the net assembly has been evaluated after application of pretension. Residual unbalances in tension forces have to be handled with care, potentially resulting in slight deformation due to nodal displacements of the net, as observed in analyses. However its effect is small and can be in part recovered during assembly. The upper net supports a reflecting metal mesh. Analysis has been done to reduce effects of periodicity due to systematic triangular faceted openings in the supporting band net. This gives rise to specific grating lobes in the secondary antenna pattern. This is not desirable for a radiometer antenna. Analysis showed that sides of the triangular facets should be less than around 10 cm (related to 17.2 GHz) and so directly related to the nr of bands in the net. Perturbing/randomising of triangular facets to support a mesh may look like a consideration at first glance. However, it is difficult to implement and for a radiometric application, one must be careful: grating lobes are smeared out, but a radiometric signal is a result of integration over an angular side-lobe sector. It can well be a situation (in LEO orbit) that a radiometric contribution from a grating lobe is comparable to the integrated signal over a wider angular sector of such a dispersed grating lobe.

Metal mesh as reflector material is realised on knitting machines with finite needle spacing. Such mesh has some electromagnetic transparency, especially at higher frequencies (compare it to an inductive screen). The radiometer (offset configuration) has eventually an additional incoming radiometric signal through the reflecting mesh, but coming from cold space with a low (radio) background temperature of a few Kelvin in the microwave regime. Nevertheless a dense metal mesh is desirable, requiring a knitting process with a large number of small openings per unit area.

CFRS reflector material is about to be tested for a space environment in ESA studies. CFRS allows to be shaped on a mandrel and after curing has some memory effect. It is slightly heavier than knitted mesh (mass/unit surface area) and can be folded. When deployed in space, it goes to its initial desirable shape. CFRS material looks also promisingly concerning absence of triangular facets (shape better realised, effect of triangular facets reduced compared to the metal

mesh). For ultra-precise radiometer reflectors a metallisation of CFRS is necessary to reduce loss, otherwise loss due to the reflection from carbon fibres is higher (than metal mesh) and may vary with environmental temperature variations/gradients, especially at higher frequency. Ohmic loss of 0.05 dB leads to ~1% contribution in observed radiometric temperature, which is a deviation impacting on radiometer performances.

Thermal analyses for the reflector assembly have been carried out with initial assumptions for thermal conductivities, absorption α and emissivity ε for applied materials. A maximum and minimum temperature of +55° C and -40° C respectively was found for a typical Low Earth Orbit scenario. It is known to be more severe for the geostationary orbit. Thermal elastic deformations have been obtained for a structural model, taking into account the thermal loads. The resulting shape deformation has been fed into RF analyses. A very small impact on RF radiometer antenna pattern has been found for a selected set of parameters.

6. CONCLUDING REMARKS

Following an introduction with information about past radio astronomy and remote sensing projects and the recent selection of the 7th Earth Explorer mission for Earth Observation, we addressed the radiometer for oceanography tasks.

A large reflectors with a focal plane array is a likely direction to be applied for future sensitive radiometers.

Such arrays allow to provide a replacement for single or multiple feed horns (to increase sensitivity) and they can realise desirable focal plane distributions for a provision of more clean antenna patterns than separate feed-horns even if the reflector is shaped (in which case further adaptation is known and possible).

The push-broom antenna configuration has been revisited in this context. A properly excited focal plane array can provide improved antenna patterns compared to the patterns achieved in [18].

Application today of focal plane arrays is too power hungry for space applications, but reliable indications are available, that the necessary power consumption can come down by an order of magnitude.

With efforts ongoing for developments for RF frontend circuitry, the required power will come down, allowing digital processing for the multiple beams needed, without beam forming circuitry with loss and with many interconnects.

A large 5x7.5 m toroidal parabolic reflector has been investigated for feasibility by HPS, exploiting the available knowledge and processes at HPS. Such technology is enabling and it is not the only (European) one. A design has been made for a reflector configuration, relying on an elliptical annular support ring with a dual pantograph, it supports two opposite nets, one of which carries a reflector mesh. An initial structural model was derived. A finite element model was realised to derive first eigenmodes and for structural analysis.

A modest claim can be made, that a push broom antenna configuration has been revisited and advanced in its capability and might be applied successfully for oceanography radiometer tasks, under some possible conditions, that

- A precisely shaped toroidal deployable reflector design as investigated is realised. Progress is well underway in related areas of large deployable reflector antennas, for instance at HPS.
- Advantages can be taken from availability of other technologies like CFRS, provided it is very good reflecting.
- A focal plane array is configured, exploiting appropriate field matching to allow good pattern correction as needed with a shaped toroidal reflector, satisfying the radiometer beam pattern requirements. A resulting high sensitive radiometer design is prone to interferences and precautions have to be taken [21].
- Analyses are carried out to select, analyse and realise precisely (with mutual coupling and tolerances) the dual polarised array elements, positioned in a finite sized array. Analysis is possible with available tools nowadays.
- There is the availability of very low power circuitry, thus reducing the required power for larger focal plane arrays with RF front end dual polarised receivers, A/D circuitry and low power processing capability. Very interesting progress is underway, with [26] just as an example.

A push broom radiometer has potentially an order of magnitude higher sensitivity than a conical scanning radiometer. However, the conical scanning radiometer has a wider coverage capability, thus lower revisit time, but lower sensitivity.

REFERENCES

- [1]. K. van 't Klooster, W. Rits, E. Pagana, P.G. Mantica, M.C. Bernasconi, *An Inflatable Parabolic Reflector Antenna: Its Realisation and Electrical Predictions*, ESA Journal, 1990, Vol. 14 and presented at "International Meeting on Mirror Antenna Constructions", Riga, Latvia, 6-9 September 1990.
- [2]. D. Savini, G. Figlia, A. v. Ardenne, K. van 't Klooster, *A Triple Frequency Feed for the Quasat Antenna*, IEEE AP Symposium, 1988, Syracuse.
- [3]. Huifeng Tan, Lina Mao, Changguo Wang, *Shape Analysis and Optimisation of Inflatable Membrane*, 1st Conference on Advanced Light Weight Structures and Reflector Antennas, 2009, Tbilisi

- [4]. *IVS, An ESA Assessment Study*, ESA SCI (91)2,
- [5]. C.G.M. van 't Klooster, *Space VLBI, A Proposed Antenna Configuration for the Radio Astronomy Satellite IVS*, Proc. 2nd ICEAA Conference, Turin, 1991, pp267-270.
- [6]. C.G.M. van 't Klooster, *Feed Developments for Astronomy Satellites in Europe*, Multi-Feed Systems for Radio Telescopes. ASP Conf Series, Vol 75, 1995, p347.
- [7]. B.Abt, H. Wollenhaupt, *A Deployable 30/20 GHz Multibeam Offset Antenna*, AIAA 10th Communication Satellite Systems Conference, March 84, AIAA-84-0658.
- [8]. S.D. Guest, S. Pellegrino, *A New Concept for Solid Surface Deployable Antennas*, Acta Astronautica, Vol 38, No 2 p103, 1995. Also <http://www-civ.eng.cam.ac.uk/dsl/publications/Solid.surface.dep.antennas.pdf>.
- [9]. <http://sci.esa.int/herschel/>
- [10]. *RadioAstron and Millimetron*, <http://asc-lebedev.ru>.
- [11]. *Теплозащита для Миллиметрона*, p10, <http://www.iss-reshetnev.ru/images/File/newspaper/2014/361.pdf>
- [12]. http://www.esa.int/Our_Activities/Observing_the_Earth
- [13]. http://www.esa.int/Our_Activities/Observing_the_Earth/The_Living_Planet_Programme/Earth_Explorers/Future_missions.
- [14]. <https://directory.eoportal.org/web/eoportal/satellite-missions/o/odin>
- [15]. G.Marks, C.Lillie, S.Kuehn, Northrop Grumman Aerospace Systems, USA. *Application of the Astromesh Reflector to Astrophysics Missions (86 GHz Cosmic Microwave Background)*, ESA Antenna Workshop 2011, Estec, Noordwijk, The Netherlands.
- [16]. M.Mobrem, E.Keay, G.Marks, *Development of the Large Aperture Reflector/Boom Assembly for the SMAP Spacecraft*, Astro Aerospace, Northrop Grumman Aerospace Systems, USA, ESA Antenna Workshop 2012, Estec, Noordwijk, The Netherlands.
- [17]. D. Savini, P. Besso, Tatalias, K. van 't Klooster, W. Rits, *Electrical Performances of an Inflatable Reflector for Land-Mobile Communications*, IEE ICAP Conference 1991, York, UK, 1991.
- [18]. P.H. Nielsen, K. Pontoppidan, J. Heeboel, B. Le Stradic, *Design, Manufacture and Test of a Pushbroom Radiometer*, IEE, ICAP Conference, York, UK, 1988.
- [19]. C. Cappellin, K.Pontoppidan, P. Nielsen, N.Skou, S.S.Søbjærg, M.Ivashina, O.Iupikov, A.Ihle, D.Hartmann, K.van 't Klooster, *Novel Multi-Beam Radiometers for Accurate Ocean Surveillance*, EuCAP2014, The Hague, NL, April 2014, 4 p.
- [20]. O.Iupikov, M.Ivashina, K.Pontoppidan, P.H.Nielsen, C.Cappellin, N.Skou, S.S.Søbjærg, A.Ihle, D.Hartmann, K.v. 't Klooster, *Dense Focal Plane Arrays for Push-Broom Satellite Radiometers*, EuCAP2014, The Hague NL, Apr 2014.
- [21]. N.Skou, S.S.Søbjærg, S.S.Kristensen, C.Cappellin, K.Pontoppidan, M.Ivashina, A.Ihle, K.van 't Klooster, *Future Spaceborne Ocean Missions, using High Sensitivity Multiple Beam Radiometers*, IGARSS Conference, IEEE 2014, Quebec Canada.
- [22]. A.Moffet, *Minimum Redundancy Linear Antennas*, IEEE, Trans Ant and Prop. March 1968.
- [23]. http://due.esrin.esa.int/stse/projects/stse_project.php?id=134
- [24]. <http://www.isas.ac.jp/e/enterp/missions/halca/index.shtml>
- [25]. <http://adsabs.harvard.edu/full/2000aprs.conf..261M>
- [26]. P.J.A. Harpe, B Bűsze, K. Philips, H. de Groot, *A 0.47-1.6 mW 5-bit-1GS/s Time Interleaved ADC for Low-Power UWB Radios*, IEEE Journ. Of Solid State Circuits, Vol.47. No 7, July 2012.
- [27]. Y. Beniguel, A. Berthon, C. van 't Klooster, L. Costes, *Design Realisation and Measurements of a High Performance Wide-Band Corrugated Horn*, IEEE, TAP, Vol53, No 11, Nov. 2005.

-oO-0-Oo-

DIMENSIONAL STABILITY AND SHAPE-ACCURACY OF SHELL-MEMBRANE REFLECTING SURFACES MADE OF FIBRE-REINFORCED ELASTOMERS

**L. Datashvili⁽¹⁾, Horst Baier⁽¹⁾, Stephan Endler⁽¹⁾, Nikoloz Maghaldadze⁽¹⁾,
Mathias Friemel⁽¹⁾, Tao Luo⁽¹⁾, Gunar Reinicke⁽¹⁾, Guram Bedukadze⁽²⁾, Konstantin Chkhikvadze⁽²⁾,
E. Medzmariashvili⁽²⁾, Nodar Tsignadze⁽²⁾, Alexander Ihle⁽³⁾, Julian Santiago-Prowald⁽⁴⁾**

⁽¹⁾*Institute of Lightweight Structures, Technische Universität München
Boltzmannstr. 15, 85748 Garching, Germany, Email: datashvili@tum.de*

⁽²⁾*Institute of Constructions, Special Systems and Engineering Maintenance, Georgian Technical University
#68b Kostava St., 0171 Tbilisi, Georgia, Email: tsignadze@gtu.ge*

⁽³⁾*High Performance Space Structure Systems, HPS GmbH
Hofmannstraße 25-27, 81379 München Germany, Email: ihle@hps-gmbh.com*

⁽⁴⁾*TEC-MSS Structures Section, European Space Agency / ESTEC
Keplerlaan 1, 2201 AZ Noordwijk, the Netherlands, Email: Julian.santiago.prowald@esa.int*

ABSTRACT

A shell-membrane reflecting surface made of a carbon fiber reinforced silicone (CFRS) composite material is a possible candidate for large deployable reflectors for replacement of a knitted metal mesh. Knowing the very low CTE of the material measured on a specimen level there is a large interest to prove the thermo-elastic dimensional stability and high shape accuracy of the material on a large-scale LDR structure. The study of stability of the CFRS shell-membrane reflecting surface is subject of a current ESA/LLB project LABUM. As the CFRS composite material will be subjected to high temperature variations in orbit, like from -200°C to +100°C, it is mandatory to develop a deformation prediction tool which will take into account the glass transition temperature of the silicone (~ -105°C) and its temperature dependent properties. Above this temperature, the silicone is flexible and, therefore, the CFRS is characterized with high stability, while below the T_g the silicone stiffens and all the material properties change significantly. An established numerical FE model allows making thermo-elastic deformation (TED) predictions taking into account these temperature dependent material properties. A proper modeling of the material flexural properties, which has a significant influence on TED results due to high flexibility of the material, is another important aspect addressed in the paper. Results of numerical and experimental investigations of stability of the material through the scaled laboratory models of LDR enabled the next level of numerical study of a medium size LDR, as well as planning of experimental investigations in a thermal vacuum chamber simulating orbital temperature loads and measurement of deformations.

1. INTRODUCTION

A shell-membrane reflecting surface made of a carbon fiber reinforced silicone (CFRS) composite material development progress and status have been reported in numerous papers [4] to [18]. CFRS offers quite a few mechanical, radio frequency (RF) and thermo-elastic advantages over the conventional knitted metal mesh used in many large deployable reflectors (LDR) flown in orbit. These advantages of the CFRS are related to the non-pre-stressed and doubly curved construction, high dimensional stability and superior RF properties suitable for high frequencies with very good passive intermodulation performance among others. LDR mechanical designs can benefit based on the above-mentioned: they can be designed lighter and cable networks can be simplified or removed completely, which are mandatory for the meshes. To further develop and advance the material technology readiness level (TRL) ESA has initiated a project LABUM aiming the high dimensional stability and high surface accuracy demonstration of CFRS.

Deployment tests were performed and surface shape repeatability proved on the shell-membrane reflector breadboard consisting of a double pantograph deployable ring as a back structure and a reflecting surface of CFRS shell-membrane. The breadboard folding and deployment have been performed utilizing a so-called “rolled-umbrella” folding pattern for the shell-membrane. Deployment sequence of the 1.6 m breadboard is shown in Fig. 1.

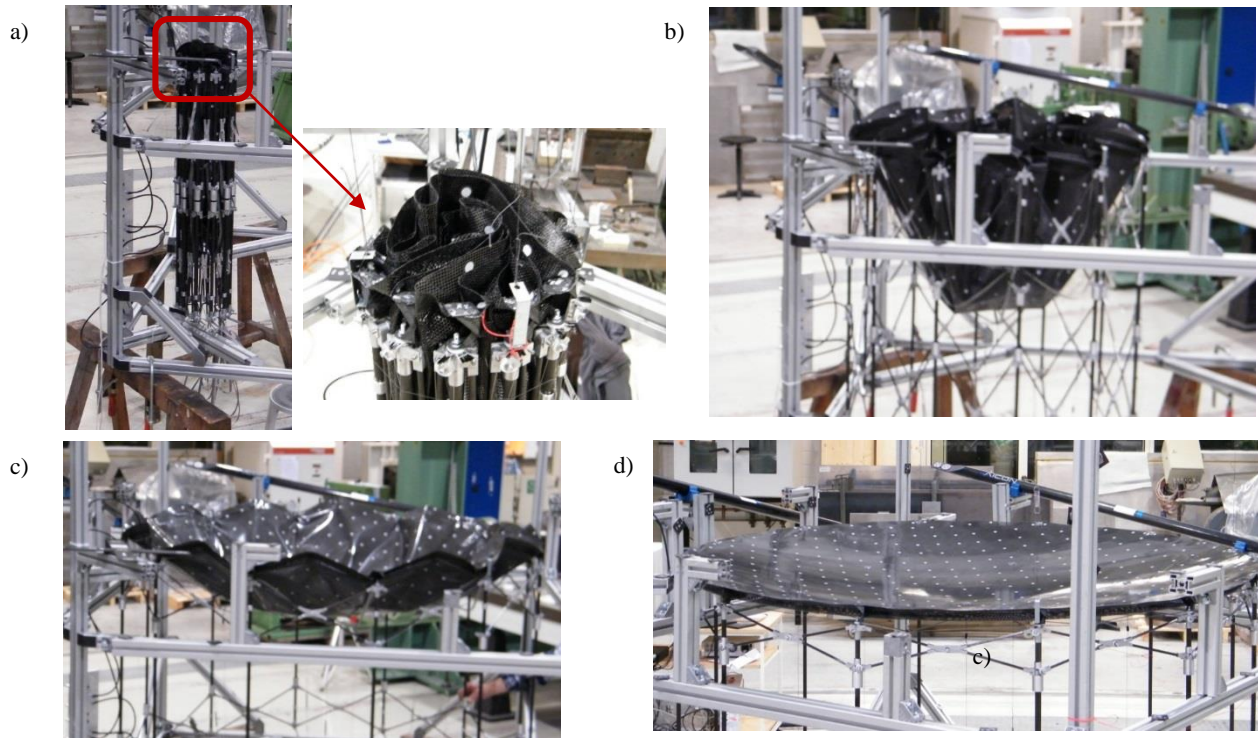


Fig. 1. Deployment sequence of the shell-membrane reflector breadboard a) stowed configuration b) and c) partly deployed configurations d) fully deployed configuration.

The shape measurements have been performed before and after each folding/deployment cycle using photogrammetry measurement system. Comparison of the measured surface shapes to the reference shape show high repeatability of the shape; namely, a relative change of the RMS of shape deviations from the best fit paraboloid remain in a $\pm 3\%$ range and the focal length of the best fit paraboloid varies in less than $\pm 0.05\%$ range.

Current results in bread boarding and respective shape measurements in the laboratory conditions discussed below indicate that promising results shall be expected through its testing in the relevant environment of large space simulator (LSS) of ETS. A thermo-elastic deformation (TED) prediction method as well as a TED measurement method are addressed and obtained results are discussed for the 5 m demonstrator as well as for the breadboard. For accurate deformation prediction, a FE numerical tool is established in ANSYS, which takes into account measured and estimated nonlinear material properties related to the temperature change. Then predictions of TED in a full -200°C to $+130^{\circ}\text{C}$ temperature range are possible. TV chamber tests will be performed for verification of the prediction tools and prove of stability of the shell-membrane RF surface of a large scale.

2. DESIGN ASPECTS OF THE SHELL-MEMBRANE LDRS

2.1. Large deployable reflector designs

Targeted LDR size with CFRS shell-membrane reflecting surface is from 4 m to 12 m, although much larger diameters can also be realized. For the purpose, two different ring structures have been innovated designed and will be followed in next stages [1]. The first one is based on a conical V-fold ring structure shown in Fig. 2a, [2], [3] and the other - on a cylindrical shifted double pantograph ring Fig. 2b [13].

The both concepts exhibit sufficiently high performance and high scalability for following not only the shell-membrane LDRs development but also metal mesh LDRs. The conical ring based LDR has a higher stiffness due to its conicity, so it can be directly applied for the shell-membrane reflecting surface to provide deployment and support to it. In case of the use of any kind of simplified cable networks, both ring concepts will show similar stiffness properties, both concepts are followed therefore.

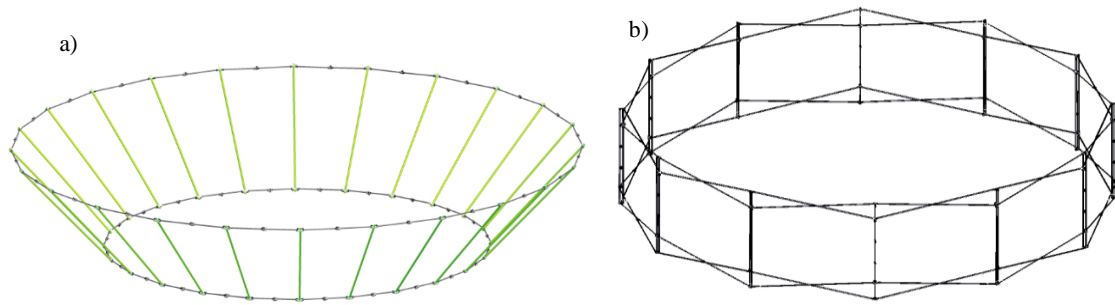


Fig. 2. LDR deployable rings: (a) a conical V-fold, (b) a double shifted pantograph

For the design of the shell-membrane reflector demonstrator, which will be subjected to the large space simulator (LSS) thermal-vacuum (TV) chamber tests the conical ring design is followed. However, a non-deployable ring structure is adapted for the tests while the goal of the tests is prove of thermo-elastic stability of the shell-membrane.

2.2. Design of the shell-membrane reflector demonstrator

The shell-membrane reflector demonstrator consist of the conical truss framework, a CFRS reflecting surface and an interface structure between the truss ring and the surface. Fig. 3 gives a final CAD design of the demonstrator.

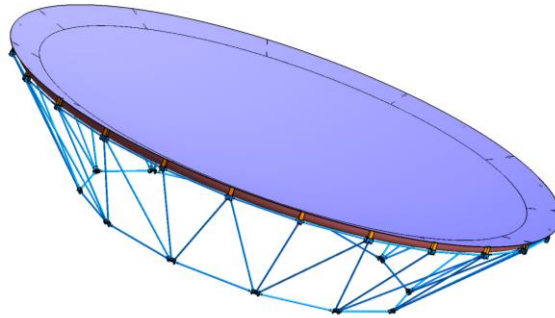


Fig. 3. Conical ring supported shell-membrane reflector demonstrator design

As the demonstrator will be tested in the LSS, all the materials used in the design are space applicable. Metal joints connect CFRP tubes at the truss nodes. A special design of the interface supports are adapted. This serves for decoupling thermo-elastic deformations of the ring and the surface (Fig. 4, a). For shell-membrane edge stiffening, an omega shaped CFRS ring is used.

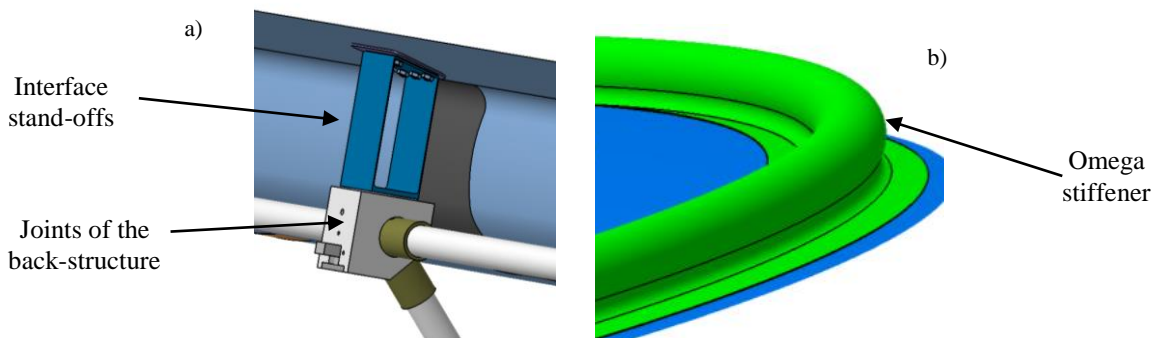


Fig. 4. Details of the demonstrator design: (a) metal joint of the truss, CFRS surface and an interface stand-off, (b) omega-shaped stiffening ring of the shell-membrane surface

3. NUMERICAL ANALYSIS OF THE SHELL-MEMBRANE DEMONSTRATOR AND TED PREDICTIONS

Based on the results of thermo-elastic measurements, an updated FE model has been established and used for deformation predictions of the demonstrator. Some basics of the FE modeling and analysis results are discussed in this chapter.

3.1. Modelling of the CFRS Composite Material

For finite element (FE) modelling, a proper model of the CFRS material has been derived based on extensive mechanical and thermo-elastic tests performed on CFRS specimens with single and multi-layers. General tendency is that the measured tensile modulus usually overestimates flexural stiffness of a single layer CFRS. For modelling of the correct flexural stiffness of the single layer composite a simple method is adapted: a single composite layer is modelled with three layers like a sandwich as shown in Fig. 5. By adjusting the material properties of its mid effective layer and taking the outer layers of pure matrix, the both flexural and tensile properties of the full composite fit to the measured values.

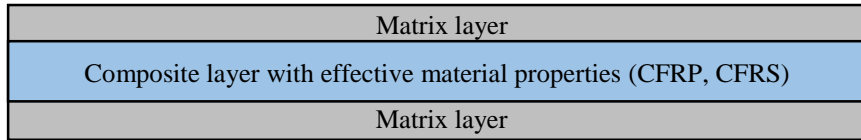


Fig. 5. The Sandwich Composite Model of CFRS Layer

Material properties of the silicone itself are highly temperature dependent. Both the stiffness and the CTE of silicone change a lot when temperature drops below its glass transition temperature $T_g = -105^\circ\text{C}$. CTE of the silicone drops down about three times (Fig. 6), while the tensile modulus increases on about three orders of magnitude.

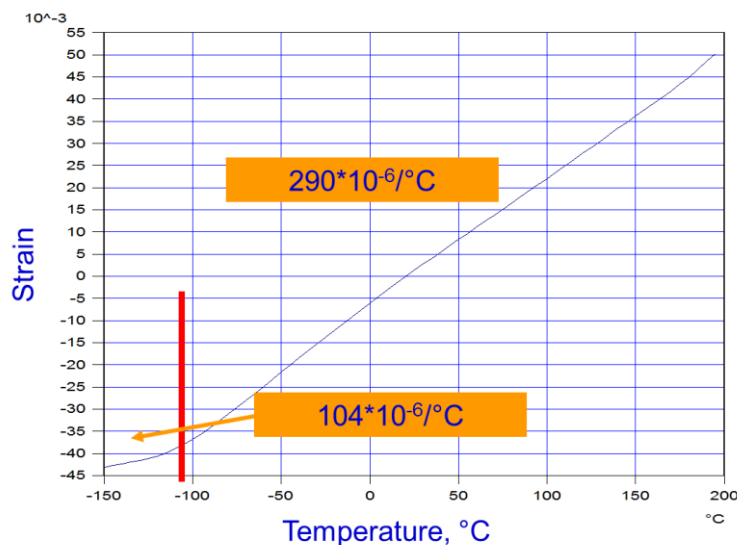


Fig. 6. Thermal expansion and CTEs of the silicone

Due to these changes, CFRS composite material stiffness and strength properties are highly dependent on temperatures. Correct modelling of these temperature dependent properties is a precondition of the proper TED prediction.

3.2. FE Model and load cases

A FE model of the shell-membrane demonstrator is shown in Fig. 7. It is constructed with the following parts: reflecting surface with omega ring reinforcement, conical back-structure, interface stand-offs and suspension ropes.

Shell finite elements are used for modelling of the CFRS shell-membrane surface. Metal joints and interface stands are modelled using shell and solid finite elements, while back-structure truss CFRP tubes and suspension ropes use beam finite elements. Ropes are constrained for the displacements in a gravity direction. Additionally a single point is fixed on a conical truss.

This approach allows analysing the demonstrator structure at several load steps:

- Gravity load at room temperature (RT). The back structure will be suspended with an angle $\theta = 20^\circ$ to vertical direction. The distorted shape under this load is considered as a reference
- Gravity load and uniform temperature load - cooling down to -220°C , below the T_g . However, the shape of the reflecting surface is assessed at the temperatures of -100°C and -185°C . The first temperature corresponds to the

approximate load at low earth orbit and to the limit of high flexibility of CFRS, while the latter one is about 15°C below the lowest temperature of the LSS TV chamber and is identified as a worst-case load.

- Gravity load and uniform temperature load - heating up to +130°C. This load corresponds to the maximally heated demonstrator in the chamber with margins.
- Temperature loading between -220°C, -100°C, and +130°C, for examining the orbital behaviour of the reflector

These load cases enable full characterization of the LDR demonstrator and preparation of the chamber tests.

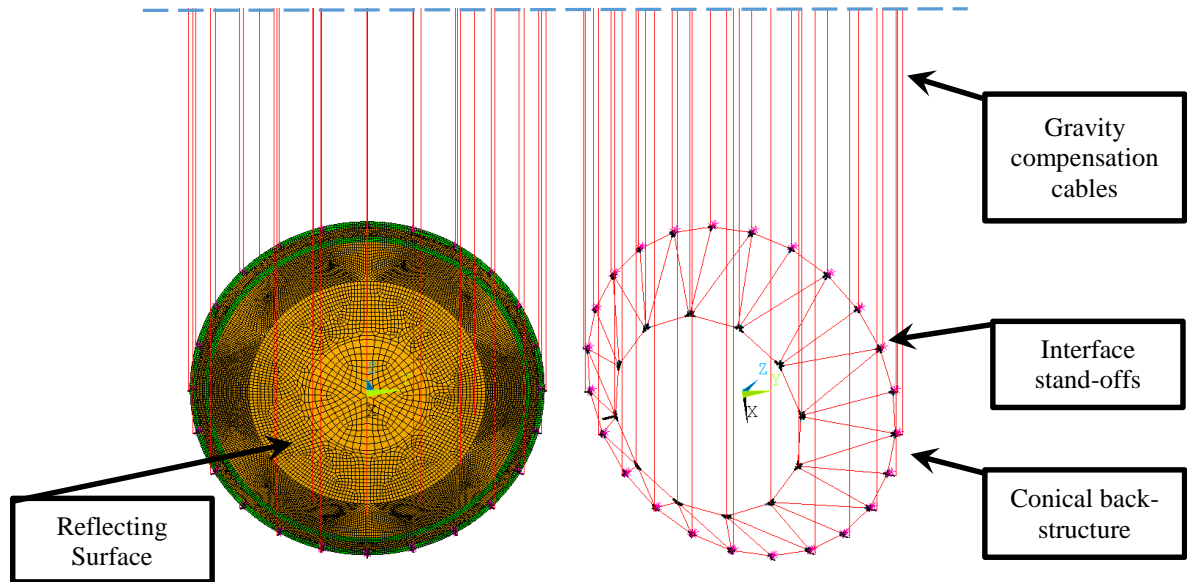


Fig. 7. FE model of the reflector demonstrator

3.3. Detailed shape analysis of the CFRS shell-membrane reflecting surface

Main contributor in degradation of the RF performance of the reflector are out-of-plane deformations. These deformations are referred as U_z deformations in the text below. Minimum and maximum out-of-plane deformations, as well as mean value, standard deviation and best-fit RMS accuracy of the reflecting surface under the different load cases are given in Table 1 for the area suspected inside the omega ring. Corresponding shape deviation plots are shown in Fig. 8. It is remarkable, that all the RMS results given in the table for all load cases are significantly low even including the gravity deformations. Orbit related deformations caused only by temperature change are even lower.

Table 1: Out-of-plane deformation of the CFRS reflecting surface inside of the omega stiffener

Load	Max. [mm]	Min. [mm]	Mean value [mm]	Standard deviation [mm]	Best fit RMS accuracy, [mm]	Focal Length of the best fit paraboloid, [mm]
Gravity at RT	-1,082	-2,284	-1,747	0,300	0.1811	4998.6824
Gravity load and -100°C	0,894	-0,947	0,260	0,394	0.16113	5003.0604
Gravity load and -185°C	4,319	2,502	3,843	0,257	0.13456	4992.6266
Gravity load and +130°C	-0,552	-2,078	-1,357	0,290	0.18872	4998.2613
RT (nominal)	0	0	0	0	0	5000.000
-100°C	2,163	1,766	2,075	0,054	0.027484	4997.5465
-185°C	4,824	3,489	4,508	0,209	0.10488	4991.5214
+130°C	0,851	0,660	0,754	0,022	0.012655	4999.8685

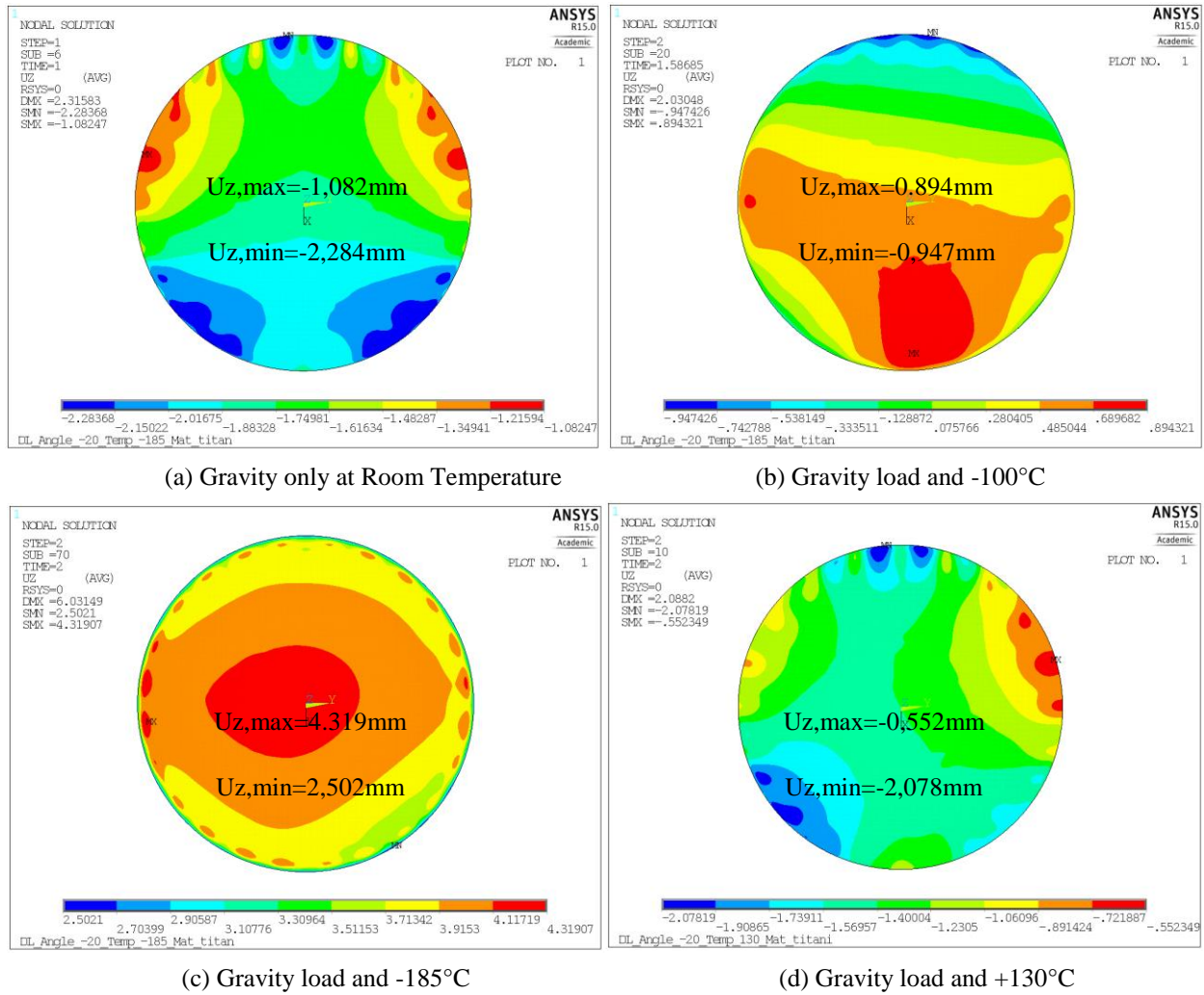


Fig. 8. Out-of-plane deformation of double layer CFRS reflecting surface under different load cases

Deformation analysis results for a full temperature range for gravity and temperature loads are summarized in Fig. 9 and for temperature loads only in Fig. 10. The latter figure demonstrates a narrow band between minimum and maximum U_z deformations throughout the temperatures above the T_g of the silicone, while below the T_g the deformation band width increases slightly. Fig. 9 shows similar trends with a larger shift between the minimum and maximum U_z deformations already at RT corresponding to the gravity loads, which is then maintained almost through the full temperature load.

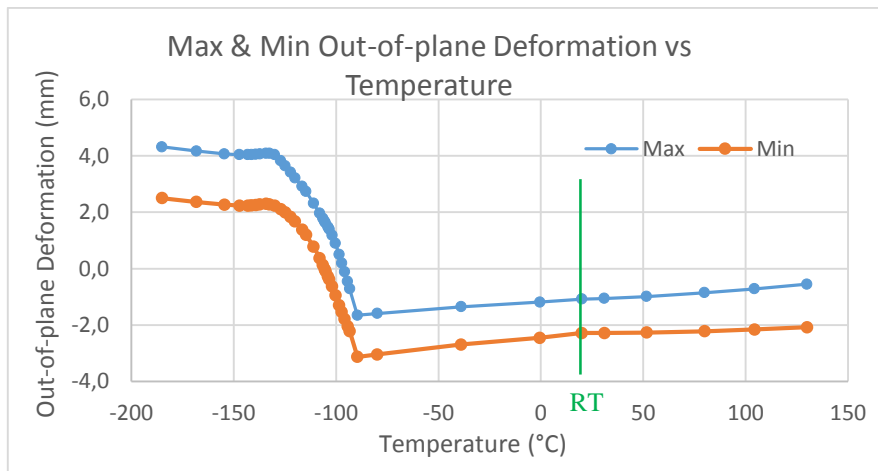


Fig. 9. Maximum and minimum U_z deformation of the surface (Gravity & Temperature Load)

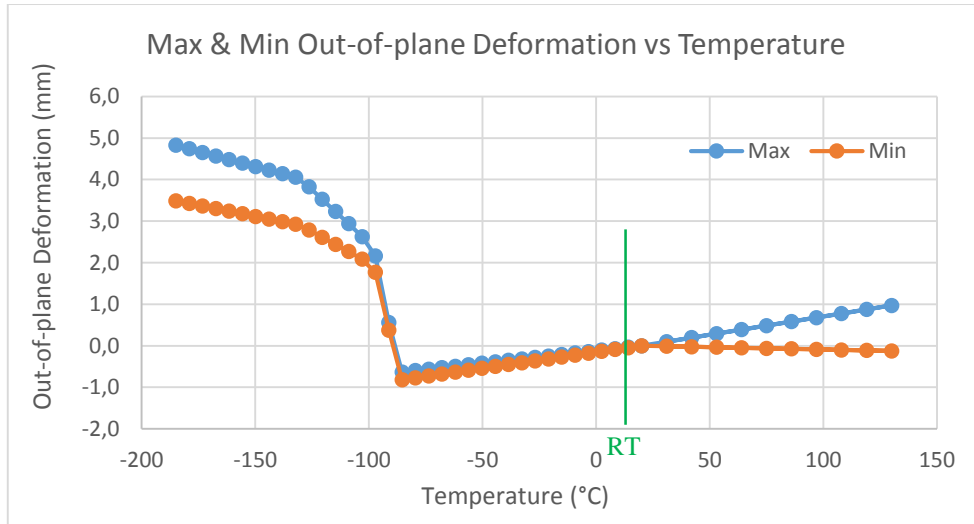


Fig. 10. Maximum and minimum Uz deformation of the surface (Temperature Load only)

4. ACCURACY AND TED MEASUREMENTS OF THE DEPLOYABLE REFLECTOR

In order to prepare TED tests of the demonstrator in the TV chamber, all the methods, tools and approaches have been developed and elaborated through testing of the breadboard (BB) in the laboratory conditions.

For the thermo-elastic deformation measurements of the BB of 1.6 m, two different heating systems were applied:

- TED-measurement with heating of the complete front side of the BB using a halogen-array with twelve lamps of 1kW power per each (Fig. 11):
- TED-measurement with partially heated front side of the BB using a single lamp that is directed at the centre of the antenna from the back side of the BB

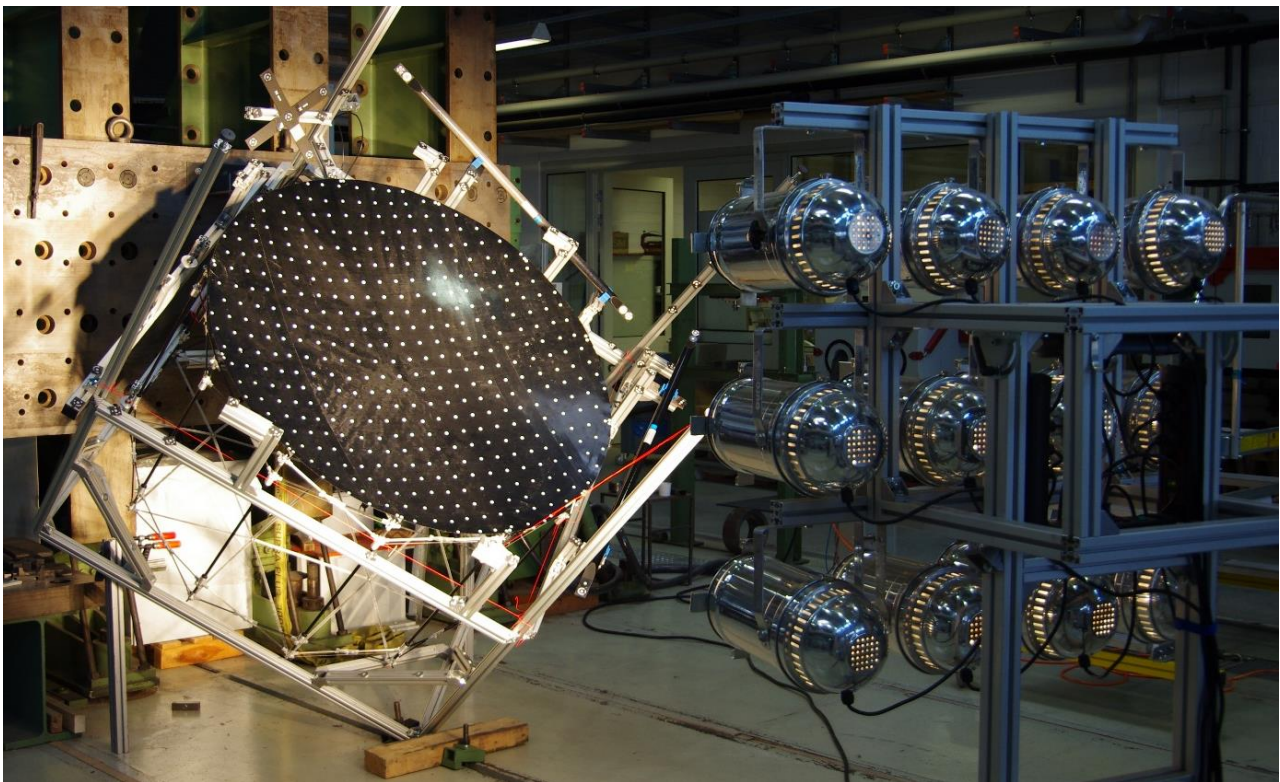


Fig. 11. Test setup for thermo-elastic deformation (TED) measurement of the BB front side.

To achieve a good distribution of the temperature field when using the complete array, each of the lamps is adjusted prior to the measurements to point at a distinct position of the surface. The temperature field on the BB is monitored using three different sensors. The temperatures on the back-structure are monitored with thermocouples and the temperatures on the surface are monitored using a thermography-camera. The thermography camera is calibrated with an additional thermocouple attached to the surface point that is visible to the thermography camera. For additional measurements a calibrated handheld laser thermometer is used.

The temperature measurements showed that the surface temperature reaches its maximum of about 100°C in the centre of the surface after one minute for the setup with all twelve lamps in use. The temperature plots (see Fig. 12) show that the temperature is higher at the centre and drops to RT at the rim. There has been observed distortion in temperature distribution that was caused by the front strut creating shadows on the surface for both the lamp-radiation and the thermography camera. The temperature measurements on parts of the backstructure show a rise in temperature of only 1.6°C , as most parts are behind the surface in its shadow.

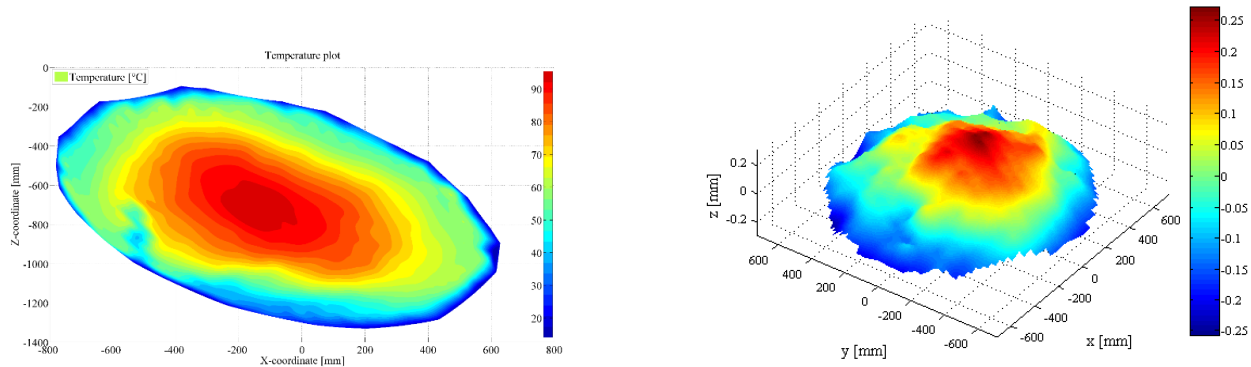


Fig. 12. Temperature plot of surface at elevated temperature (left). Comparison of surface at elevated temperature with reference surface (right).

For the TED measurements, the reflector shape is measured in cold (room temperature) and hot (see Fig. 11 and Fig. 12) conditions using the photogrammetry system. The photogrammetry data is then used for finding the best-fit RMS accuracies for the shell membrane in each measurement case. In Fig. 13 results of best fitting of all the shape measurement data are plotted for the cold and hot cases. The RMS and focal length values are given as relative changes compared to the references. As it can be seen, the relative change in best-fit RMS is insignificant and is less than 0.1%. The focal length changes on about 2 mm from reference to hot and back, and gives always almost the same values respectively as can be observed from the figure.

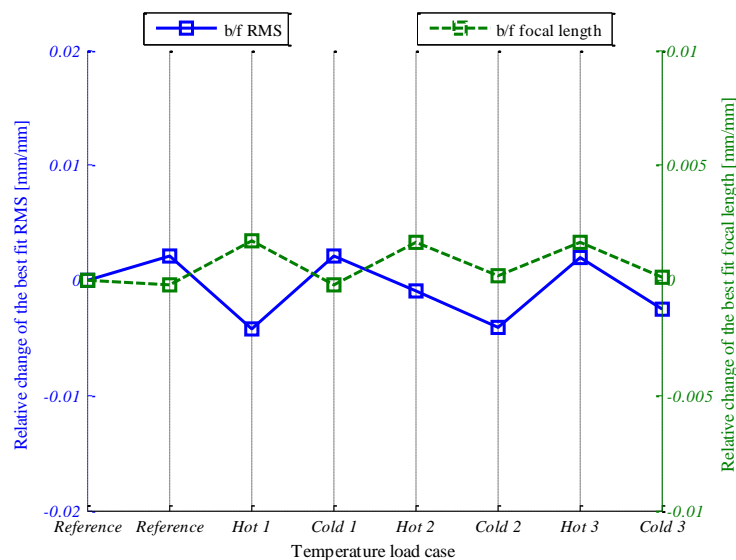


Fig. 13. Relative changes of the best fit RMS and focal length due to temperature cycling load case. Reference measurements were performed at room temperature and correspond to the cold cases.

5. CONCLUSIONS AND OUTLOOK

Shell-membrane reflector demonstrator design and analysis have been presented in this paper. Performed numerical nonlinear analyses of the shape of the demonstrator, which take into account temperature dependent material properties of the CFRS shell-membrane and large deformations, show promising results of the surface shape accuracy even with extreme temperature gradients.

Presented results allow initiation of the manufacturing steps of the reflector to be tested inside of the LSS TV chamber. The shell-membrane RF surface lamination will be performed on the mold (Fig. 14, left) specially designed and manufactured for the CFRS. Developed mold technology allows cheap and lightweight design and can be realized in much larger sizes.

A TV chamber test configuration of the demonstrator is shown on the right in Fig. 14.

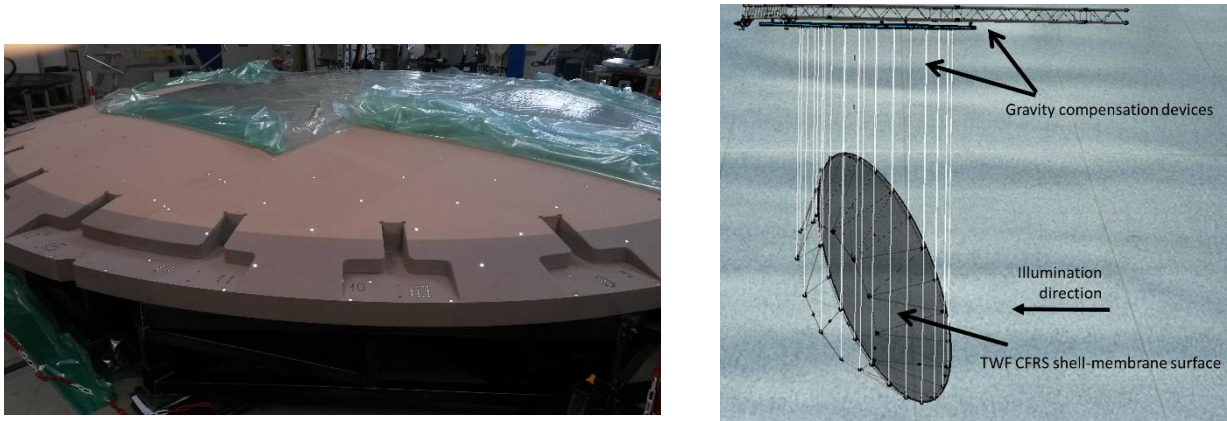


Fig. 14. High accuracy mold and 5 m demonstrator test configuration in the TV chamber

REFERENCES

- [1]. http://www.esa.int/TEC/Structures/SEM4NF91M9H_1.html
- [2]. Santiago-Prowald, J., Such Taboada, M.: Innovative deployable reflector design. In: 33rd ESA Antenna Workshop, October 2011 ESA-ESTEC, Noordwijk, The Netherlands
- [3]. Santiago-Prowald, J. & Baier, H. "Advances in deployable structures and surfaces for large apertures" *CEAS Space Journal*, Springer Vienna, 2013, 5, 89-115H.
- [4]. Baier, L. Datashvili, Z. Gogava, E. Medzmariashvili, V. Montuori: Building blocks of large deployable precision membrane reflectors, In: Proceedings of the 42nd AIAA/ASME structures, structural dynamics and materials conference, AIAA paper no. 2001-1478, April 2001, Seattle. DOI: 10.2514/6.2001-1478.
- [5]. L. Datashvili, "Multifunctional and Dimensionally Stable Flexible Fibre Composites for Space Applications", *Journal of the International Academy of Astronautics "Acta Astronautica"*, 2009 (special issue: Glasgow)
- [6]. L. Datashvili, H. Baier, "Flexible Fiber Composites for Space Structures", chapter in the book "*Fiber-Reinforced Composites*", Edited by G. Chang, pp. 605-640, ISBN: 978-1-61470-303-7 (hardcover), 2012, Nova Science Publishers, NY, USA
- [7]. L. Datashvili, H. Baier, "Shell-Membrane Reflecting Surface Material for Deployable and Transformable Space Reflectors", *Proc. ESA Conf. on Antennas*, Noordwijk, Mai 2008
- [8]. L. Datashvili, H. Baier, L. da Rocha-Schmidt, "Multi-scale Analysis of Structures made of Triaxially Woven Fabric Composites with Stiff and Flexible Matrix Materials", *proceedings of the 52th AIAA/ASME/ASCE/AHS/ASC Structures, Structural Dynamics, and Materials Conference* 2011, Denver
- [9]. L. Datashvili, H. Baier, E. Wehrle, T. Kuhn and J. Hoffmann, "Large Shell-Membrane Space Reflectors", In proc.: *51st AIAA/ASME/ASCE/AHS/ASC Structures, Structural Dynamics, and Materials Conference*, 2010. DOI: 10.2514/6.2010-2504.
- [10]. L. Datashvili, H. Baier, „Derivation of Different Types of Antenna Reflectors from the Principle of Highly Flexible Structures”, *Proceedings of the EuCAP 2014 - The 8th European Conference on Antennas and Propagation, The Hague*, The Netherlands, 6 – 11 April, 2014

- [11]. L. Datashvili, H. Baier, J. Schimitschek, M. Lang, and M. Huber, "High Precision Large Deployable Space Reflector Based On Pillow-Effect-Free Technology"; AIAA-2007-2186 *Proceedings of the 48th AIAA/ASME/ASCE/AHS/ASC Structures, Structural Dynamics, and Materials Conference*, 23 - 26 Apr 2007, Honolulu, Hawaii
- [12]. Leri Datashvili, Nikoloz Maghaldadze, Stephan Endler, Julian Pauw, Peng He, Horst Baier, Alexander Ihle, Julian Santiago Prowald, "Advances in Mechanical Architectures of Large Precision Space Apertures", *Proceedings of the European Conference on Spacecraft Structures, Materials & Environmental Testing*, 01 – 04 April, 2014, Braunschweig, Germany
- [13]. Datashvili, L. "Foldability of hinged-rod systems applicable to deployable space structures", *CEAS Space Journal*, Springer, 2013, 5, 157-168
- [14]. L. Datashvili, "Review and Evaluation of the Existing Designs/Technologies for Space Large Deployable Apertures", *proceedings of the International Scientific Conference "Advanced Lightweight Structures and Reflector Antennas"*, 14-16 October 2009 Tbilisi, Georgia.
- [15]. Wei, B.; Magner, D.; Endler, S.; Datashvili, L.: High precision large space structures: challenges in cable networks design. International Conference on Textile Composites and Inflatable Structures, Structural Membranes, CIMNE 2013, München, Germany.
- [16]. L. Datashvili, H. Baier, "Large Membrane Reflectors" *Proceedings of the 3rd European Conference on Antennas and Propagation - EuCAP 2009*, 23-27 March 2009, Berlin, Germany.
- [17]. L. Datashvili, H. Baier, "Precision Deployable Shell-Membrane Antenna Reflector for Space Applications", *Proceedings of the 59th International Astronautical Congress 2008*, Glasgow, Scotland
- [18]. L. Datashvili, M. Lang, M. Huber, H. Baier, "Accuracy Study of a Space Deployable Antenna Reflecting Surface Under 0g and 1g Conditions"; *Deutscher Luft- und Raumfahrtkongress 2006*, 06.-10.11.2006, Braunschweig, Deutschland, published in the proceedings of 2007, band III-IV

ACKNOWLEDGEMENTS

The company Wacker Silicones, Germany, is gratefully acknowledged for a continues support in shell-membrane technology development.

The staff of the workshop of LLB is acknowledged for their strong support in the project. Special thanks go to Mr. Bernhard Lerch and Mr. Ludwig Krämer.

TALC, A 20m Thin Aperture Light Collector for infra red observations in space

Gilles Durand^a, Marc Sauvage^a, Jérôme Amiaux^a, Vincent Révéret^a, Louis.rodrique^a, Pierre Chanial^c,
Samuel Ronayette^a, Loris Scola^d, Michael Carty^d, Matthis Durand^f, Lancelot Durand^g, Michel
Berthe^a, Aymeric Bonnet, Sébastien Correia^b, Pascal Bultel^h

^aLaboratoire AIM, CEA/Irfu, CNRS/INSU, Université Paris Diderot; France
durandgs@cea.fr, marc.sauvage@cea.fr, jerome.amiaux@cea.fr, vincent.revere@cea.fr, Louis.rodriquez@cea.fr,
samuel.ronayette@cea.fr, michel.berthe@cea.fr

^bINSA Lyon, GMD; France

aymeric.bonnet@insa-lyon.fr, sebastien.correia@insa-lyon.fr

^cAPC, Astroparticule et Cosmologie, Université Paris Diderot; France
chanial@apc.univ-paris7.fr

^dCEA/DSM/Irfu/SIS, France

loris.scola@cea.fr, michael.carty@cea.fr

^fIUT Cachan, GMP; France

matthisdurand@gmail.com

^gIUT Ville d'Avray; France

durand.lancelot@gmail.com

^hCentre National d'Etudes Spatiales, Launchers Directorate; France
pascal.bultel@cnes.fr

ABSTRACT

TALC, Thin Aperture Light Collector is a 20 m **space observatory** project exploring some unconventional optical solutions (between the single dish and the interferometer) allowing the resolving power of a classical 27 m telescope. With TALC, the principle is to remove the central part of the prime mirror dish, cut the remaining ring into 24 sectors and store them on top of one-another. The aim of this far infrared telescope is to explore the 600 μm to 30 μm region. With this approach we have shown that we can store a ring-telescope of outer diameter 20m and segments thickness of 0.25m inside the fairing of Ariane 5 or Ariane 6. The general structure is the one of a bicycle wheel, whereas the inner sides of the segments are in compression to each other and play the role of a rim. The segments are linked to each other using a pantograph scissor system that let the segments extend from a pile of parallel dishes to a parabolic ring keeping high stiffness at all time during the deployment. The inner corners of the segments are linked to a central axis using spokes as in a bicycle wheel. The secondary mirror and the instrument box are built as a solid unit fixed at the extremity of the main axis. The tensegrity analysis of this structure shows a very high stiffness to mass ratio, resulting into 3 Hz Eigen frequency. The segments will consist of two composite skins and honeycomb CFRP structure build by replica process. Solid segments will be compared to deformable segments using oriented shear of the rear surface using ceramic PZT fibres. The adjustment of the length of the spokes and the relative position of the side of neighbour segments let control the phasing of the entire primary mirror. The telescope is cooled by natural radiation. It is protected from sun radiation by a deployable or inflatable solar screen, loosely linked to the telescope. The telescope is oriented using inertia wheels and plasma jets. This telescope will carry a wide field bolometer camera and a high resolution spectrometer to be operated at 0.3K. This telescope may be launched with an Ariane 6 rocket up to 800 km altitude, and use a plasma stage to reach the Lagrange 2 point within 18 month. The plasma propulsion stage is part of a commercial vehicle used for communication satellites that also includes solar panels, orientation system and communication. The guide-line for development of this telescope is to use similar techniques and serial subsystems developed for the satellite industry. Using serial commercial vehicle and building a telescope using large number of replicated similar parts is the way to think the construction as a object built in serial for costs reduction.

Keywords: Thin Aperture Light Collector, Deployable space telescope, Sub-millimeter telescope, Passive cooling, Tera-hertz telescope, Bolometer camera

INTRODUCTION

TALC is a 20 m space observatory project exploring some unconventional optical solutions (between the single dish and the interferometer) allowing the resolving power of 27 m telescope in the range of 100 μm to 600 μm . The light collection surface is 20 times larger than the Herschel mirror, giving access to very faint and/or distant sources. With an unconventional optical design comes the necessity to combine data acquisition with unconventional data processing techniques, which are being developed today, based on the notions of sparsity in astronomical signals.

On the optical side, an annular telescope gives access to a higher resolution as compare to a filled telescope of the same diameter. Telescopes or interferometer have limitations in sensitivity and resolution. While an observation time may be increased to observe fainter objects, it will not give access to better angular resolution. For this reason TALC gives the preference to resolution at the cost of loosing sensitivity as compare to a filled telescope of the same diameter. Given a given area of mirrors, a ring telescope will have a larger diameter than a filled telescope that results into direct improvement of the diffraction limit. The PSF of telescope with a central obstruction of half its surface has 70% of its power outside of the main beam, while the first zero of the d'Airy pattern is situated at 0.8 times the angle of the one of a filled telescope of same diameter. With appropriate inversion, we have shown that the angular separation of the half obscured telescope is 20% narrower than the one a filled telescope of same diameter. (Paper of Marc Sauvage, Pierre Chanial)¹

On the mechanical side, it is simple to build a stiff wheel structure with stretched spokes and compressed rim as invented by Jules Truffault in 1875 with it the first modern bicycle wheel. This tensegrity axi-symmetric structure gives access to the one of the stiffest light-weighted structure. As a result, the big wheels are the largest mobile structures built in the world as for example the Singapore wheel with 150 m diameter.



Figure 1. Singapore flying wheel 150m diameter.

In our case, the rim consists of the serial of the inner sides of the mirror segments linked by knee joints. Two sets of spokes are pulling these knees towards the extremities of a central mast. Single pistons installed between the outer corners of adjacent segments suffice to control the orientation of the segments as petals of a flower. As a result this annular telescope does not require an additional support structure: the axis of the telescope, the set of mirrors and the spokes constitute the structure. Moreover the tilt and piston of the segments may be tuned by adjustment of the length of the spokes and the distance between adjacent mirrors. The figures shown here show how to stack 24 segments of diameter 4m. Using the fairing of Ariane 5 or Ariane 6 with inner diameter of 5.2m, 16 segments give also access to a 20m telescope.

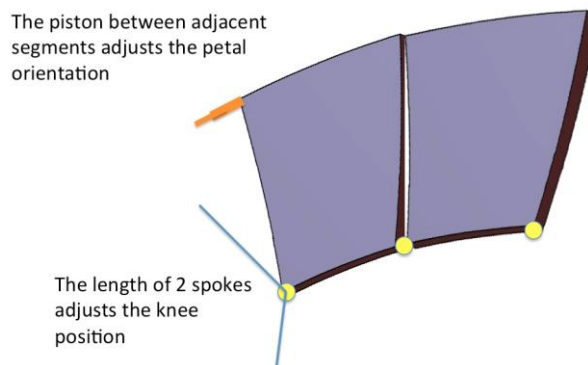


Figure 2. Piston, Tip Tilt adjustment of the segments

Deployment.

The segmented mirrors are stored inside the fairing as a pile of dishes. Such a stack offers the ultimate segment stiffness, since the entire stacked volume is occupied with their reinforcement lightweight structure. The segments are linked to each other with a scissor system such as a scissor lift. The axis and length of these scissors are designed to allow a scotched yoke movement from a stack of dishes up to a large ring of adjacent segments in the shape of a parabola. One branch of the scissor is part of each mirror, the other branch toggles during the extension. The instrument case and the M2 mirror constitute a solid block. Before the start of the deployment of the segments, this block is positioned at the top of the central mast. The set of spokes are stretched by extension of the mast while a spring-loaded mechanism extends the segments from each other. At start of deployment, a launching track still to be designed is used to force the set of mirrors to extend on either side from the central position, in order to keep all spokes stretched at all times. In the midrange, both the launching track and the spokes keep the mirrors along their trajectory. At the end of the deployment the spokes are driving the trajectory to complete the movement until the 2 mirrors at extreme positions meet and are compressed to each other.

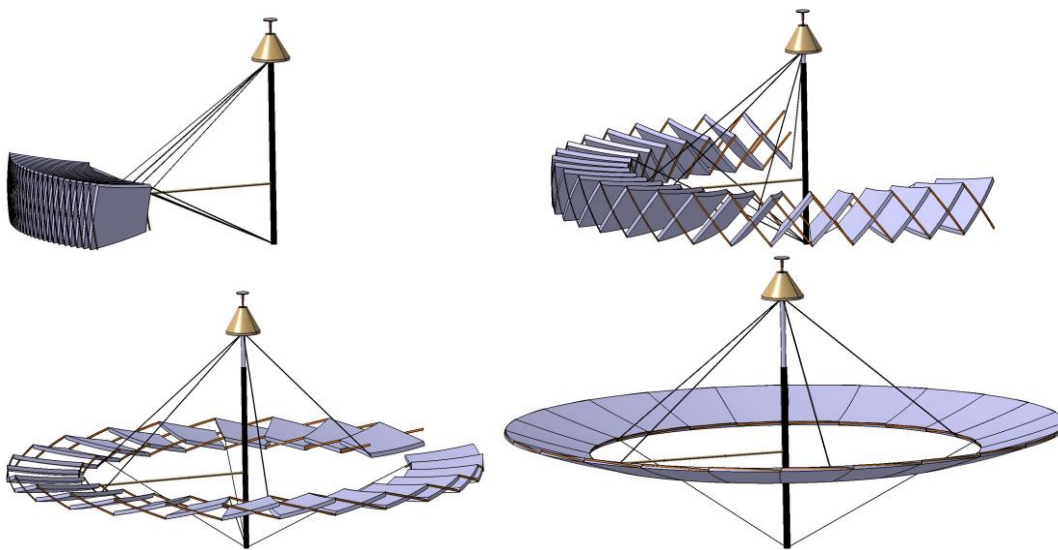


Figure 3. At start of the deployment a launching track is used to force the set of mirrors to extend on either side from the central mirror. At the end of the deployment the spokes hold the entire wheel.

Our simulations and the construction of a 4m prototype have shown that a synchronization rod shall be installed between the inner and the outer toggling scissors, in order to give stiffness to the ensemble of mirrors during its extension. The smaller inner scissor should be linked to the larger external scissor by means of a connecting rod. As a result the toggling link between the segments are C shaped arches that surrounds $\frac{3}{4}$ of the segments when they are stacked. When the mirror is deployed, the synchronization rods are stored at the rear of the parabolic mirror.

Recent update on the deployment mechanism:

We have found an updated axis system that includes knee bearings instead of axis, that allows to stack the pile of segments parallel to each other, thus allowing a much better use of the space inside the fairing. We will use this optimised stacking to make the segments thicker, in order improve the shape without active control. We will next calculate the stiffness of the set of partially deployed structure at each stage. Eigen frequency and damping at all the stages of the deployment will be performed in order to simulate the real deployment including the friction at knees and oscillations during the process. In an advanced status of the project, we will build a set of 3 segments and test the mechanical deployment in cryogenic conditions for a great number of cycles.

A configuration Excel data sheet has been created to include all design parameters. This sheet is linked to the Catia and Nastran files, in order to update all simulations, kinematic and mechanical behaviour for concurrent engineering system analysis. It will be used as well for the optic and thermal model.

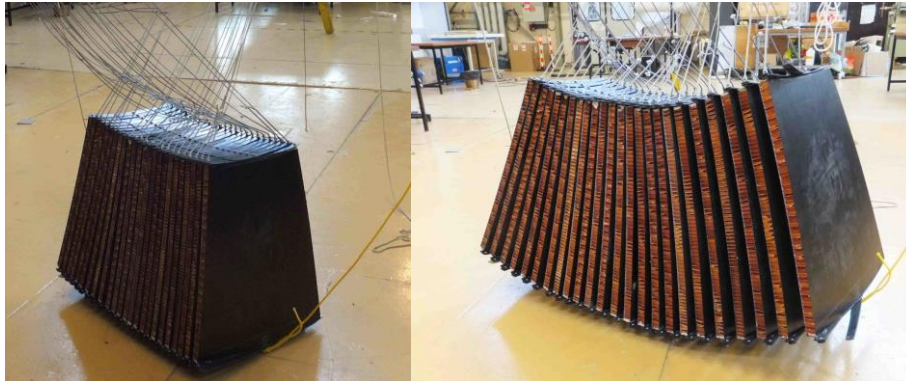


Figure 4. On this model scale 1/5, the segments are built with skins of pre-impregnated UD carbon epoxy on Nomex honeycomb. The model weights 36 kg for 4 meter diameter.



Figure 5. The scissors are made of pre-impregnated UD carbon epoxy. We learned that a synchronization system is needed between the inner and outer scissors to help the pack of segments extend on a predictable trajectory. In the next model the toggling scissors will be tubular. The inner and outer scissors will be built as a single piece in shape of C.

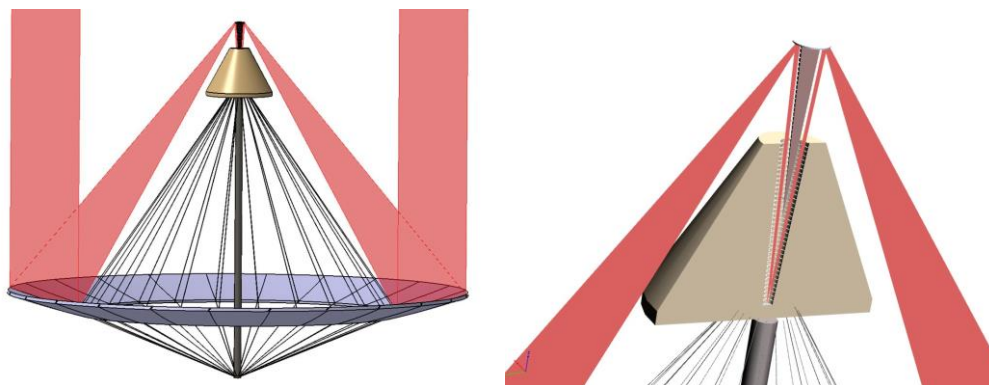


Figure 6. Cut of the TALC, the pupil is unobstructed outside of the instrument case. The spokes follow a route in parallel to the light between M2 and M3. Within the instrument case large baffles are installed between the outside of the beam and the cone that blocks the central pupil area.

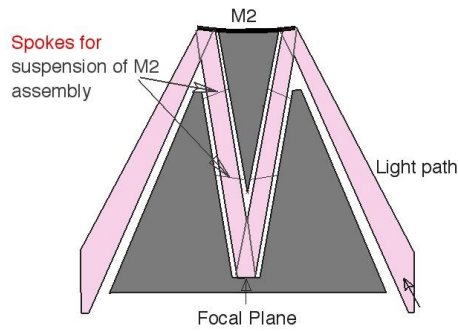


Figure 7. The cone that supports M2 is secured within the instrument case by 6 spokes or laminated transparent film. The obstruction of the pupil is very limited.

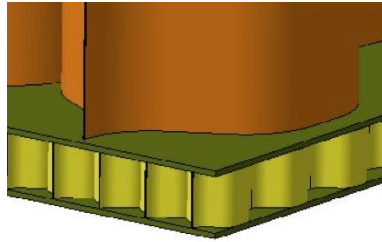


Figure 8. The segments of mirrors are 25 cm Thick. They consist of a carbon honeycomb core in sandwich between composite skins. In order to limit the footprint of the large cell honeycomb core, the skin on the mirror side consists itself of a carbon honeycomb sandwich 10mm thick cells + CFRP UD skins. The skin at the rear of the mirror is monolithic. It is equipped with PZT uniaxial pads arranged in triangle, in order to fine tune the mirror shape.

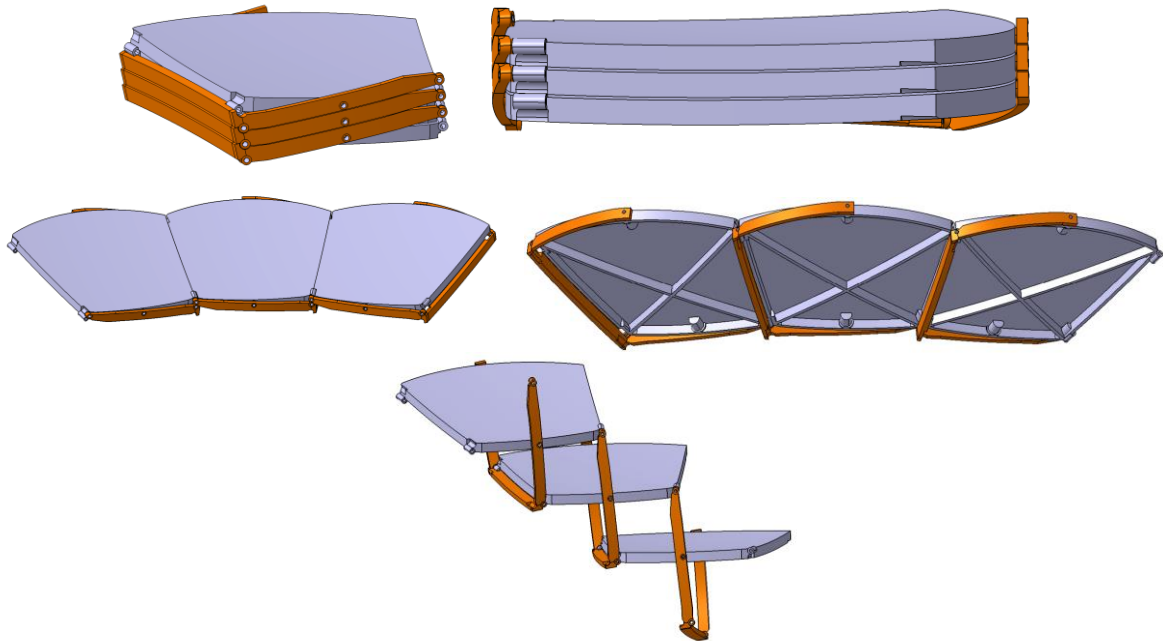


Figure 9: Model of the deployable structure for 3D printing to show the deploying principal. The kinematic model has evolved until the mirrors are stacked parallel inside the fairing. They deploy towards a parabolic position. All segments and scissors are linked to each other so as to deploy under a unique degree of freedom. The spokes are used to fine tune the segments to their final position.

Baseline: passive segments. The design of the panels is at a very preliminary status. Most promising is to build the segments by replica on a steel polished mould. A first layer of nano-laminated metal reflective surface is first deposited at vacuum or electrodeposit. 70 layers of ultrathin carbon UD 25 gr/m² are stacked at angles of 15°. A porous

honeycomb core with 3mm step and 10mm thickness will be placed and be covered with similar layers of UD carbon fibre. This ensemble will be cured. The rear skin composite skin is built as a multilayer UD at 15°. After completion of these two composite skins, the main structure will be built by assembling the front and rear skins on both sides of a carbon honeycomb with porous larger cells. The structure will be cured and unmoulded. This structure has been used for our dynamic model.

Construction of active segments: We do not know if the segments may be built within the required shape or if an active control within the segment is necessary. In the case such a control is necessary to reshape the segment, we expect to use piezo-actuators within the rear skin of the segments. By stretching or extending locally the rear skin in the given directions, it will be possible to reshape local part of each segment.^{3,4} Uniaxial piezo pads arranged in triangle pattern parallel to the rear skin would allow local shape control. We envisage to use uniaxial piezo pads that consist of ceramic PZT-5 square micro fibres. These piezo pads provide high stiffness and a range of elongation of 1800 ppm.

<http://www.wired.com/2007/12/micro-fiber-com/>

Since these piezo-actuators behave as electric capacitors, many pads may be driven by a single amplifier and be multiplexed to polarise each one at a time. Each pad memorises the voltage during a scan and therefore the actual constraint between refreshing writing cycles. This process does not dissipate power. The mirrors may be cooled down by heat radiation down to 30K.

Dissipation of vibrations at launch:

As a free outcome, the microfiber piezo pads could also be used as vibration damping system during launch. Such pads are used as anti-vibration systems for the blades of helicopters while they are connected to dissipative electric resistors. This is of prime interest since the carbon fibre honeycomb structure of the panels do not develop any damping, which could result in high vibration stress at launch.

Stiffness of the ring telescope: We have simulated the Eigen-frequencies for a free flying ensemble telescope + instrument Disconnected from the vehicule and solar shield. This represents the case of a telescope linked to the satellite using a flexible arm. We tested several configurations of cables honeycomb structures, masts and spokes at various pre-stress within a total mass of 2.5 tons. We could obtain the lowest Eigen-frequencies above 3 Hz. This structure might be damped passively or actively if necessary. In the deployed status, all articulation shall use flex pivots to provide a pure elastic behaviour.

The calculations of the Eigen-frequencies has been performed for the following conditions :

Upper cables diameter 2.5mm pre-stressed 182 N

Lower cables diameter 4mm pre-stressed 300 N

Compression on the mast 3500 N

Length of the mast in the axis of the telescope : 12 .7 m

Diameter of the mast : 230*250 mm,

Weight of the mast : 400 kg

Mass M2 + instrument :1500 kg

Segments: 24 segments at 10 kg/ m2

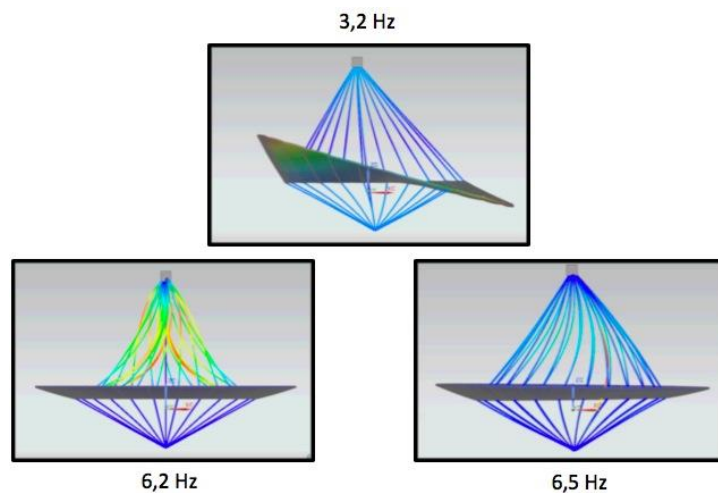


Figure 10. The lowest Eigen-frequencies are shown after trimming of the mass of mast, spokes and segments. The pre-stress on the spokes is related to the pre-stress calculated on the inner side of the segments at their construction. In this case, the telescope is considered as free flying as compare to the rest of the satellite.

Actuators for the control of the position of the mirrors. The coarse position of one point of each segment will be sensed using a fish eye reflector and interferometer distance sensor for coarse adjustment of the mirrors in piston to the focus. A wave front sensor using an infrared star will be used to sense the error orientation of each segment. The spokes length and the pistons to trim the petal orientations will be adjusted with piezo actuators.

V-Groove sun shield

Since the mirror is too large to be cooled down actively, it is preferred to install TALC behind a V-groove shield in order to reach a thermal equilibrium as low as possible. During the next system analysis we will compare two sorts of sun shields. For a V-Groove rigidly connected to the telescope, as it is the case for the JWST, the reliability is improved since there are no movements between the thermal shield and the telescope. The shield must be built wide enough to keep TALC in the shadow of the telescope while the whole satellite is rotated away from the pointing transverse to the sun. Due to the size of TALC, such a sun shield would cover ten times the one of the JWST ie 21m * 14m. In another design, the V-Groove sun shield is built as a circular axi-symmetric structure at a size just larger than the projection of the telescope in all orientations. The shield is kept aligned to the sun at all times. The mast in the axis of the telescope is articulated to the mast that holds the telescope away from the sunshield. In this case the size of the V-Groove could be decreased to 28 meters in diameter at wider angles between the layers. Lower temperature would be obtained as compare to a shield toggling to the sun.

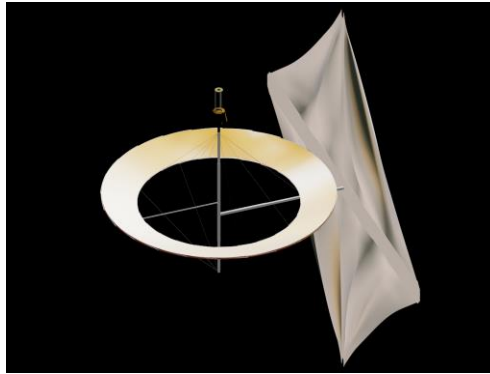


Figure 11. TALC represented with a preliminary solar shield at the time of the study of the deployment of the telescope

We have simulated the time constant of a V-groove consisting of 5 layers of aluminized Kapton to reach a stable temperature without a telescope in its shadow. Next step is to add the telescope with pure passive cooling in order to estimate the temperature gradients and time constants using pure radiating cooling.

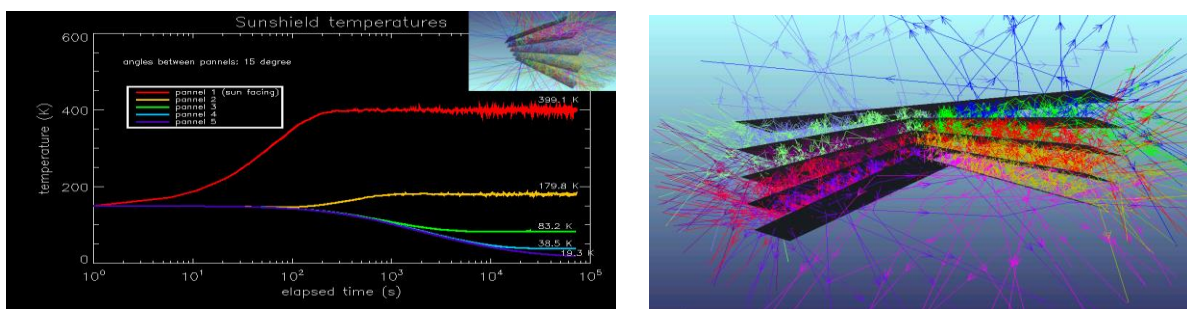


Figure 12. Study case of the cooling down of a V-groove stack, without hardware in its shadow. Initial temperature was set to 150K, the curves represent the change of temperature of the layers versus time in seconds.

Cooling system for the detector and instrument case. In order to allow for a life-time of TALC in the range of 10 to 15 years, cryo-coolers will be preferred to a tank of liquid helium. The 30 Hz compressor of the cryo-cooler will be installed on the warm side of the sunshield. The radiative cold source shall be installed just next to the compressor. Behind the sunshield, there will be no additional cold sources. A long counter-flow heat exchanger built with tubes into tubes will be extending from will cross the sun shield, extend along the masts and reach the Joule Thomson valve at the

location of the two or three stage He4 and He3 sorption coolers near the detectors. Temperatures below 0.25K will cool the bolometers as in the case of the PACS camera of Herschel.

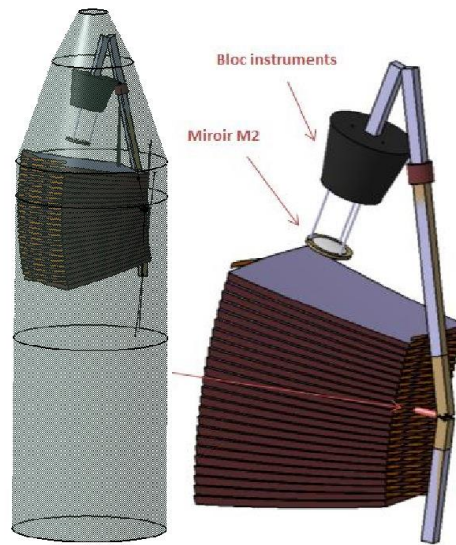


Figure 13. Former version of Talc with segments not yet parallel, folded inside Ariane 5 fairing. The masts consist of telescopic tubes and knees. The flexible spokes are not shown. During the launch, the spokes are kept protected inside a dedicated sock.

Launching rocket

The total weight of the Instrument + telescope + mast + sun-shield + cryocooler is 4.2 tons. The vehicle including solar panels, inertia wheels, telecom, jet gas orientation system is 1.2 tons.

Launch with ARIANE 5: TALC was optimized to fit the fairing of Ariane 5 with a diameter of 5.4m. The total weight to be launched to Lagrange 2 is 6 tons. Ariane 5 ECA may launch TALC directly to Lagrange 2 point as in the case of the 6.2 tons JWST.

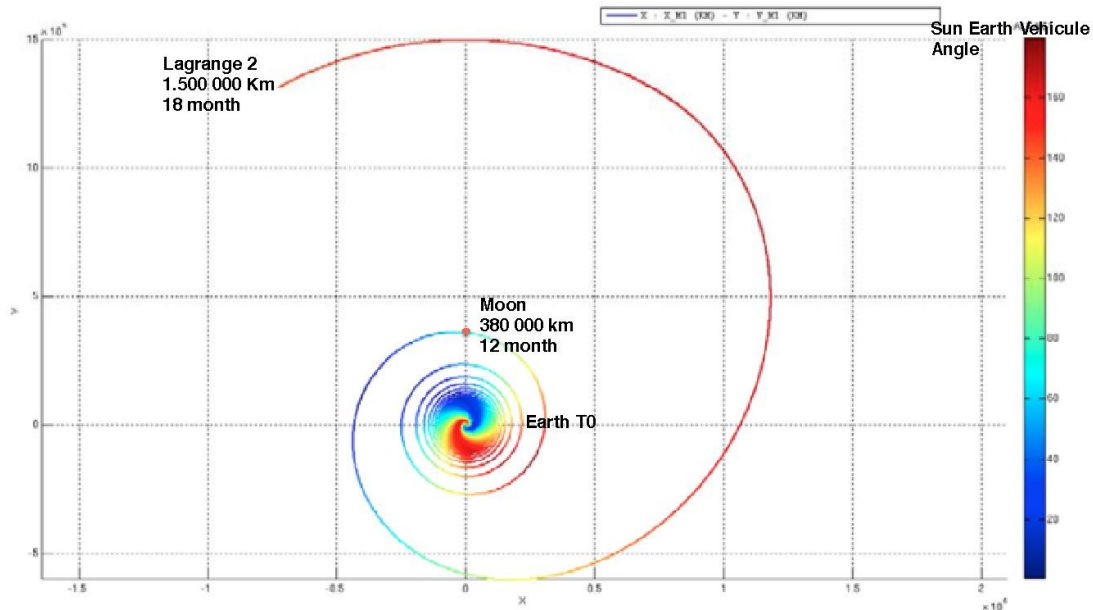


Figure 14. Mission profile – LEO to L2 transfer of TALC with an electric kick-stage (AIRBUS & CNES)

Launch with ARIANE 6 + Electric propulsion kick-stage : this is a promising alternative to heavy launchers such as ARIANE 5. The size of the fairing is kept identical, but scientific payload is injected in LEO or MEO. The implemented advanced propulsion is based on SNECMA HET engines developed for the coming NEOSAT generation satcoms. thus reducing costs. Total TALC mass after launcher separation is to exceed 9 tons, which includes scientific payload, stage

working as mission spacecraft, necessary xenon fuel, communication means. The electric kick-stage is to transfer TALC's 4.2 tons instruments from LEO/MEO to final L2 position. Injection orbit is to be optimized to ensure mission safety. Moon vicinity can be managed with additional chemical propulsion. After TALC full commissioning at L2 point the propulsion module will be used for energy supply, coarse orientation and fine tuning of orientation with its reaction wheels. The main antenna for astronomical data will be stowed retracted, sun shield will be deployed first. The telescope will be deployed later at cold in order to avoid reflected light from the sun.

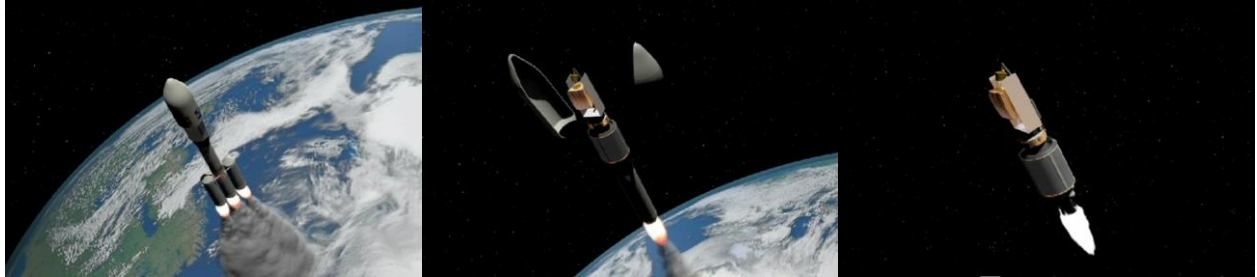


Figure 15. The 2 solid stages and the hydrogen / oxygen VINCI stage

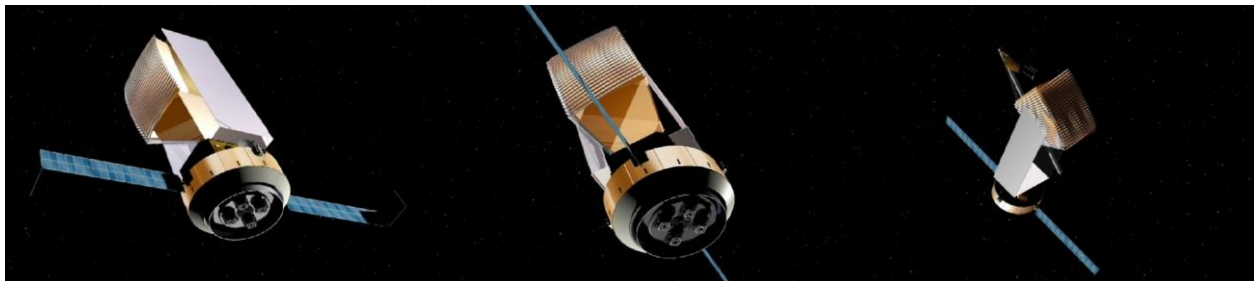


Figure 16. Electric kick-stage used as mission spacecraft to support TALC observatory deployment

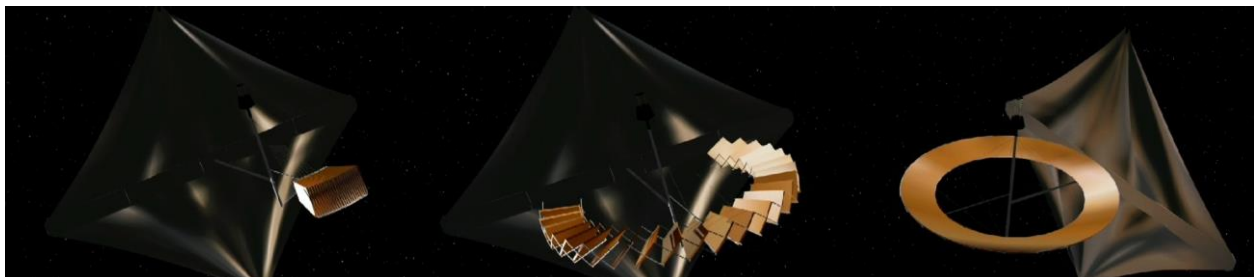


Figure 17. Deployment of the sun shield and the telescope

Size of TALC There is no direct proportion between the size of the fairing and the size of the telescope since other numbers of mirrors of different thickness could be chosen. We have proposed a 20m telescope as a demonstrator. It may be considered as a pathfinder to larger annular telescopes using the same wheel structure. Larger annular telescope designed for smaller wavelength will require additional control systems.

GOING TOWARDS A H2020 PROGRAM:

Since the SPIE conference at Montreal 2014 we have understood that TALC might be a good pathfinder towards visible space telescope for astrophysics and earth observation.

We discovered the maturation of active control mirrors using piezo-actuators at the rear of composite.

We propose to build within 3 years:

- A spherical stainless steel mould at scale 1/3 of the segment, polished to visible wavelengths.
- Use the technique described above to build a carbon honeycomb mirror at the thickness of TALC (25cm) in order to check the surface quality and stability that can be reached.
- Build a similar mirror equipped with active microfiber axial correcting pads with the aim to reach 3 μm RMS on the surface. Further on, we will work on basis of best effort in order to estimate which ultimate RMS surface quality can be reached.

- Build a mirror at the thickness of TALC equipped with isotropic pzt films to check the efficiency of this technique cheaper to build.
- Build 3 mirrors at scale 1/3 of TALC segments, in order to test the repeatability of positioning of segments of TALC next to each other. A great number of cycles will be performed on a subsystem of 3 mirrors + scissors, until we reach reliability and smoothness in the movement and locking system.
- Inside a cryostat at 77K with size $\phi 3.5\text{m}$, H3.5m demonstrate the repeatability of the positioning of 3 segments relative to each other. Check the stability of the segments at cryogenic temperature. (Vacuum enclosure, vacuum pumps and LN2 precooling available at CEA Saclay.)
- Build an optical control system to check the mirror quality at room and cryogenic temperatures.

The next step beyond JWST is as follows: we propose to demonstrate that structures larger than what may be tested inside a single cryostat on earth may be modelled and tested as serial subunits.

- Develop the coarse positioning measuring system (using cat eyes and metrology by multi-wavelength laser interferometry)
- Develop a fine OPL control of the mirror shape

REFERENCES

- [1] M. Sauvage: This conference [9143-42] The science case and data processing strategy for the Thinned Aperture Light Collector (TALC): a project for a 20 m far-infrared space telescope.
- [2] P. Bultel: "ADVANCED PROPULSION TO OBTAIN PERFORMANT AND FLEXIBLE LAUNCHERS STAGES". 1st ASTech Paris Exploration Conference 17-19th December 2012.
- [3] A. Zuccaro Marchi 2014 Spie Montreal conference [9151-115] Active optics for space applications: an ESA perspective
- [4] J.Steeves 2014 Spie Montreal conference [9151-4] Design, fabrication and testing of active carbon shell mirrors for space telescope applications
- [5] <http://sem-proceedings.com/20i/sem.org-IMAC-XX-Conf-S13P03-An-Overview-Composite-Actuators-with-Piezoceramic-Fibers.pdf>
- [6] <http://www.smart-material.com/MFC-product-main.html>

NEW DESIGN OF A TRANSFORMABLE MECHANICAL CONE SYSTEM WITH V-FOLDING RODS

Sh. Tserodze⁽¹⁾, J. Santiago Prowald⁽²⁾, V. Gogilashvili⁽¹⁾, K. Chkhikvadze⁽¹⁾,
N. Tsignadze⁽¹⁾, A. Chapodze⁽¹⁾, M. Nikoladze⁽¹⁾

*Institute of Constructions, Special Systems and Engineering Maintenance of GTU;
68b Kostava St. 0175, Tbilisi, Georgia;
Emails: Tserodze@gtu.ge, Tsignadze@gtu.ge*

*European Space Agency, ESTEC – Structures Section,
Keplerlaan 1, 2200 AG, Noordwijk, The Netherlands.
Email: Julian.santiago.prowald@esa.int*

ABSTRACT

A new closed-chain deployable system is presented, which during transformation keeps on deploying until it reaches the conical shape [2, 3, 4]. In conformity with the technical specifications, individual parts of the system perform the simultaneous motion in the radial direction. The main motion of the system produced by geometric constraints is studied, i.e. we consider the degree of structural motion. Parametric degrees of freedom caused by technological errors, modes of motion, types of load or deployment velocity are not taken into consideration at this stage. The kinematic analysis of the system is performed for the regulated structural component which can be regarded as a model of the kinematics of the system as a whole. A peculiar feature of the structure presented in the paper is that, as compared with analogous structures, for connecting the sections with one another there is no need of using additional synchronization devices in both belts simultaneously. The kinematic analysis has been carried out on the structural elements of regular joints, which represent the kinematics of the system as a whole. This structural mechanism is a differential lever mechanism, the driving elements of which enable us to obtain the desired law of motion of a characteristic link. Therefore we can construct the function of position of the lever mechanism and also the kinematic functions of transmission. For the preliminary investigation of the structure and making possible changes in it we have constructed a mathematical model by means of the ANSYS software using the Ansys Parametric Design Language. The DOFs of the hinges are simulated in local coordinate systems and are as much as possible approximated to the real model. Calculations are performed for various kinds of loads and appropriate results are obtained.

1. INTRODUCTION

The development of new designs of space deployable antenna reflectors is a topic of high interest. In the present paper, we present a conical deployable structure with folding rods [3]. A noteworthy feature of the structure is its light weight which has been achieved due to the logic of the design itself and the optimization of structural components. This means that due to high dynamic characteristics and strength reserves of the system, it can be designed with a minimal number of elements and minimal cross-section values. As a load-bearing ring we have chosen a cone-shaped hinged system with folding rods. To equate the degree of kinematic motion to one, we have invented an original scheme of connection of sections with one another. As a result the structure has become quite simple and reliable.

The proposed system is light-weight, rigid and is characterized by accurate geometrical parameters, which is the mandatory condition for the reflecting surface of the structure to have good performance.

In this paper, we also present a design modification that has no synchronization elements and is distinguished by natural synchronization at the time of deployment – however we do not touch upon this issue here since it is the subject of future investigation.

2. GENERAL VIEW OF THE STRUCTURE AND ITS CONSTITUENT ELEMENTS

The proposed structure consists of hexagonal (conditionally) hinged-rod chains of different dimensions, which are interlinked by means of struts. The chains are interconnected through cylindrical hinges which are set in the central parts of the corner brackets rotating in the radial direction (Fig. 1).

For their part, the upper and lower kinematic chains are the rods connected by cylindrical hinges. The ends of the folding rods are connected in the circular direction by outermost and central cylindrical hinges. The outermost cylindrical hinges are attached to the bracket ends, whereas the central cylindrical hinges are located directly at the places of rods folding.

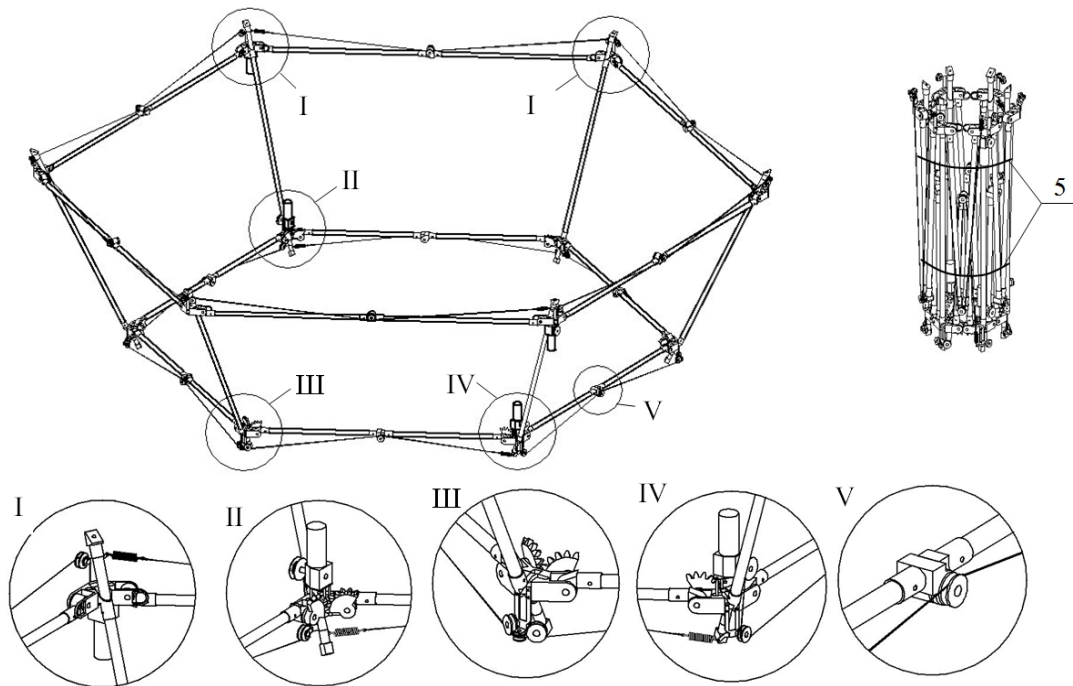


Fig. 1. The general view and structural components

During transformation, the folding rods of each section shift in the radial direction, simultaneously unfolding in the vertical plane, whereas the struts connecting the upper and the lower belt deflect also in the radial direction. Below we show the deployment stages of one section for the standard and the shifted variant. In the case of the shifted variant, the height of the stowed package and, accordingly, the number of sections will be essentially less (Fig. 2).

For the synchronous deployment of the system it suffices to mount synchronization devices on the lower belt. In our case, the synchronization mechanism consists of a pair of gear-wheels which are installed on the axes connecting the brackets and V-folding rods from the inner side of the reflector. They are rigidly fixed at the ends of the folding rods by means of additional pins and rotate together with them.

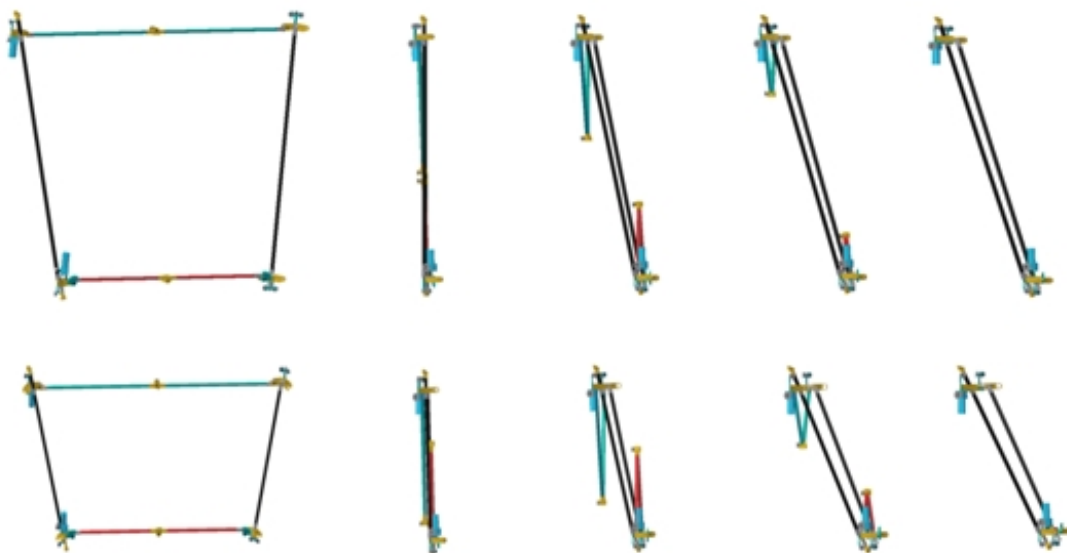


Fig. 2. Deployment stages of one section for the standard and shifted variants

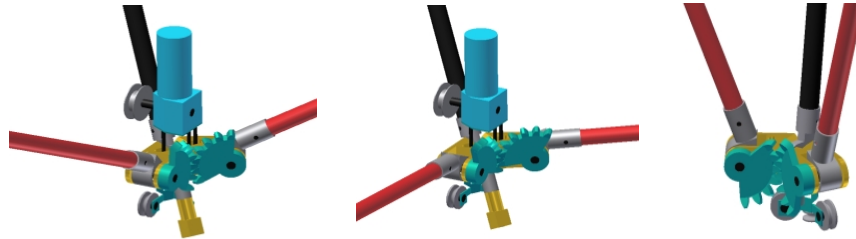


Fig. 3. Positions of the gear-wheel mechanism of synchronization of the lower belt with an electric drive and without it

To illustrate the efficient operation of the proposed system, let us consider its kinematic scheme. Since during the transformation of the system, the brackets remain in their horizontal position, they can carry the deployment electric drives (Fig. 3). An advantage of the proposed deployment mechanism, as compared with the existing ones [2, 4], is that it is fixed not to the struts, but to the main brackets.

As a result the deployment system is able to rotate in the radial direction together with the main brackets, thereby preventing v-fold rods from falling-out at the last deployment stage (Figs. 1, 4).

3. PROBLEMS OF GEOMETRICAL INVARIABILITY OF ONE SECTION

Let us consider one section of the load-bearing ring with unfolding ropes and electric motors in the fully deployed and stowed states of the structure. First we will consider the problem of geometrical compliance of the section in its plane (Fig. 4 a)

When the fully deployed system is in the stressed state, main brackets 1 not subjected to the action of braces 2 are in the horizontal position. Accordingly, the axes passing through the upper and lower hinges X_{up} and X_{low} are parallel to one another and are in the horizontal position, too. The normal X_{per} to the plane of the section is the axis deflecting from the axes X_{up} and X_{low} by an angle α . Therefore, theoretically, it can be asserted that the section is geometrically stable in its plane (Fig. 4 a).

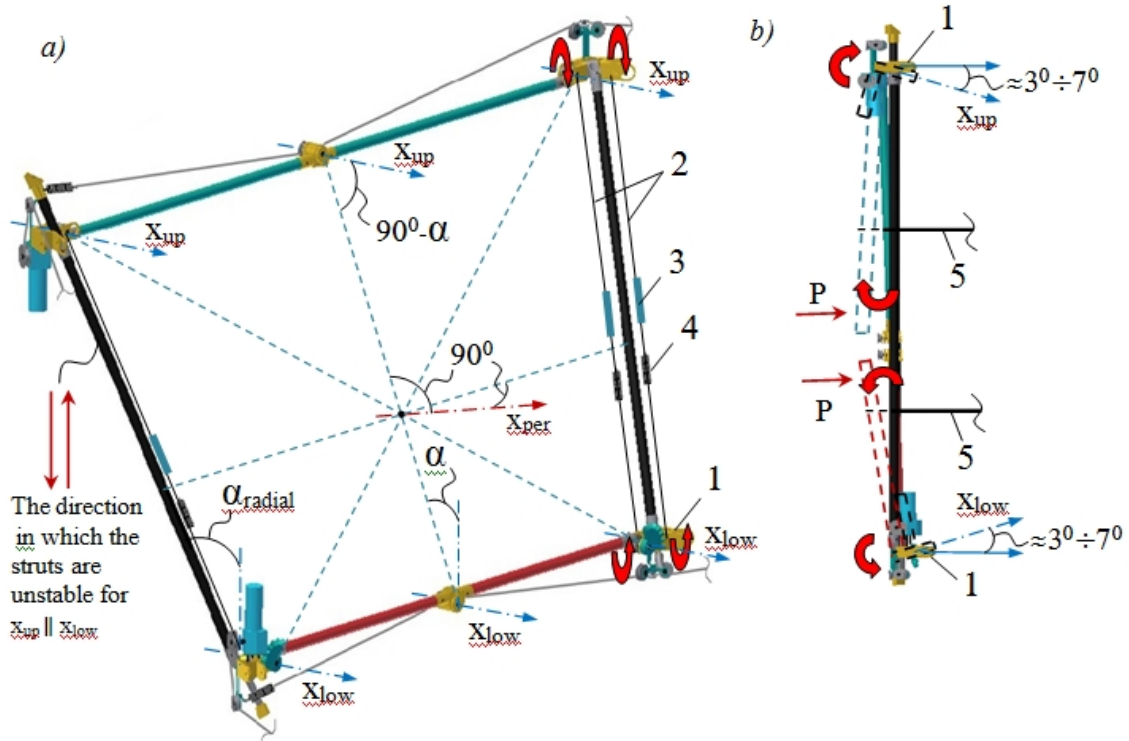


Fig. 4. The section in the stressed state

As to the stability of struts in the vertical direction in the absence of synchronization elements (gear-wheels), this is questionable because $X_{up} \parallel X_{low}$, which means that the shift of the struts in the vertical direction is not restricted (Fig. 4 a).

To solve this problem it is necessary to fulfill the condition $X_{up} \nparallel X_{low}$. For this, the elements of the main brackets located at the strut ends are joined by means of braces 2. The braces incorporate springs 4 and length regulating devices 3.

The tensioning of the paired braces makes the brackets slightly change the angle by rotating in the radial direction. Accordingly, the electric drives, guiding rollers, deploying ropes and V-folding rods together with central hinges, which the brackets carry, will rotate, too. As a result the condition $X_{up} \nparallel X_{low}$ will be satisfied, i.e. the upper and the lower belt rotate by a small angle from the horizontal plane in the mutually opposite directions (Fig. 4 b).

To receive a compactly stowed package, the bending rods can be forcibly fixed in the vertical position by means of ropes 5 (Fig. 1), i.e. in the stowed position the main brackets will pass to the horizontal position as a result of the extension of braces 2 and the tensioning of springs 4.

The deployment of the system (stowed package) starts right after ropes 5 are released and, in consequence, the V-folding rods pop out and change insignificantly the angle. During transformation, the tilt of the rods preserves, thereby restricting the shift of the struts in the vertical direction (Fig. 4 b). In that case, no synchronization elements are needed and the design of the structure becomes even more simplified.

We have constructed the model of a single-belt cone structure with brackets turned inside out, which clearly demonstrates the positioning of the V-folding rods during transformation (Fig. 5).



Fig. 5. The single-belt cone structure with brackets turned inside out

The scheme shown in Fig. 4 is an innovation and needs further investigation. Our discussion here is limited to the preliminary study of the modification shown in Fig. 1.

4. STRUCTURAL PECULIARITIES OF THE CHAIN SYSTEM

The studies show that from the standpoint of dynamics it is advisable to decrease the degree of mobility of the chain system to an optimal level – this can be done by increasing the number of drives or by installing additional linking devices or by using both techniques simultaneously [1].

Let us consider the transformable system with many degrees of freedom. The conditional structural scheme is shown in Fig. 6. It is assumed in the first approximation that the system is in equilibrium and the struts move in the radial direction.

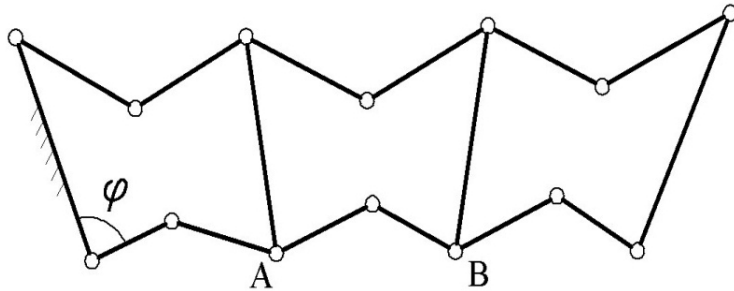


Fig.. 6. The double-layer kinematic system

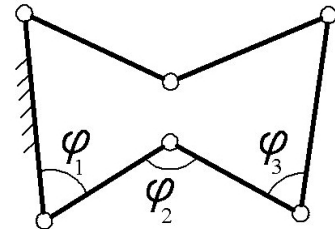


Fig. 7. The driving chain

In the considered scheme, the number of links is $n=15$, the kinematic pair with one mobility $p_1=18$, then the degree of relative movement is $w = 9$. If this scheme has one driving element with generalized parameter φ , then eight degrees of freedom play the role of regulating coordinates (relative coordinates of five links of the lower layer and three connecting struts).

For one section shown in Fig. 7 we obtain $n=5$, $p_1=6$, $w = 9$. In that case, the defining parameters of mechanism position functions will be $\varphi_1, \varphi_2, \varphi_3$. If φ_1 is the coordinate of the driving element, then φ_2 and φ_3 will be relative regulating coordinates. For the symmetric system $\varphi_1 = \varphi_3$.

If additional links (say, in the form of gear-wheel or rope transmission) are installed in the components A and B of the kinematic scheme, then in the system with three sections and one drive (Fig. 6) there remain six regulating coordinates. Analogously, the system shown in Fig. 7 can be reduced to the system shown in Fig. 8, which consists of one driving group ($n=6$, $p_1=8$, $p_2=1$, $w = 1$) and two adjoined groups for which $n=5$, $p_1=7$, $p_2=1$, $w = 0$.

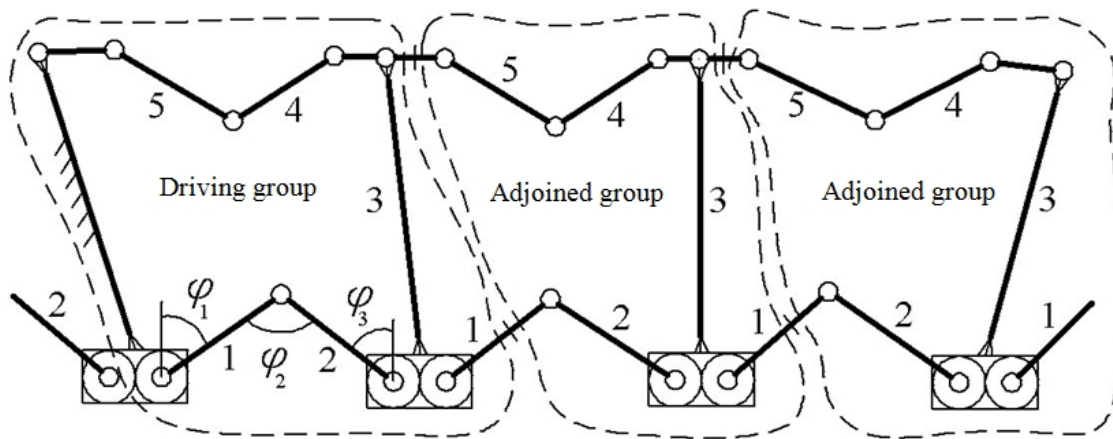


Fig. 8. The kinematic scheme of the reduced cone chain system;
Drive group, adjoined groups

The upper and lower layers have rope transmissions and the lower layer is additionally provided with a gearing mechanism.

5. GEOMETRY AND KINEMATIC ANALYSIS OF THE BLOCK SCHEME OF A TRANSFORMABLE CONE CHAIN STRUCTURE

We consider the chain system with closed contour, which during transformation keeps on deploying until it reaches the conical shape. In conformity with the technical specifications, individual parts of the system perform simultaneous motion in the radial direction. We mean only the main motion of the system produced by geometric constraints, i.e. we consider the degree of structural motion. Parametric degrees of freedom caused by technological errors, modes of motion, type of load or deployment velocity are not taken into consideration at this stage.

The kinematic analysis of the system is performed for the regular joint of the structural element, which fully reflects the whole system kinematics (Fig. 9). The struts of the mechanism move in radial directions, whereas the V-folding rods are set in motion in the vertical planes by means of spring- drives and step motors.

The initial parameters of the considered structural element are as follows:

Number of regular structural groups (number of sections), n ;

Outer radius of the upper base of the imaginary truncated pyramid, R ;

Outer radius of the lower base of the imaginary truncated pyramid, r ;

Height of the imaginary truncated pyramid, H ;

The tilt of the face of the imaginary truncated pyramid from the plane of bending rods, δ ;

Lengths of mechanism links - ℓ_1 , ℓ_2 and L ;

Variable parameters of the system R , r , h_1 , h_2 , δ , γ , β .

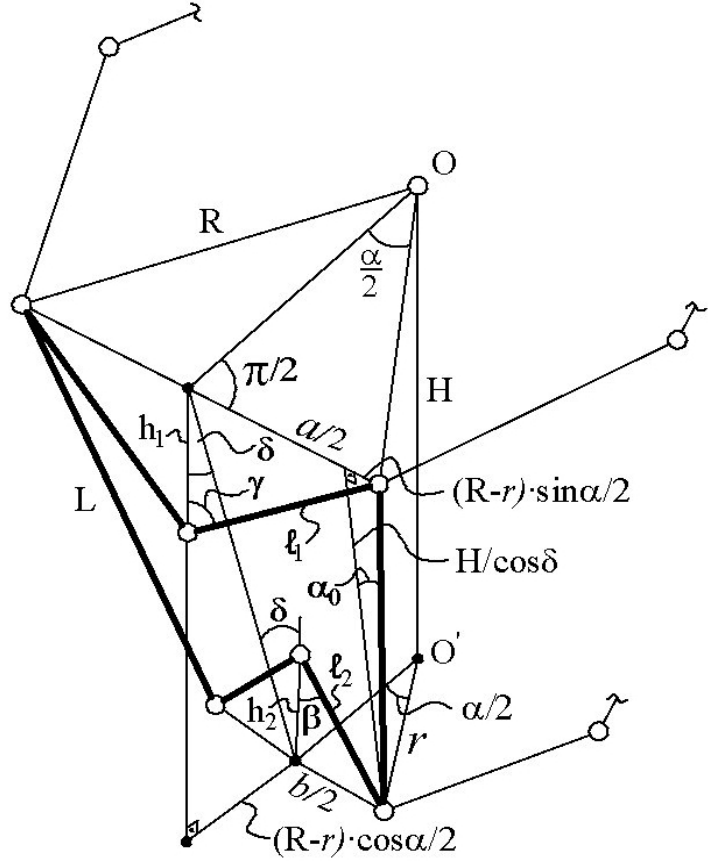


Fig. 9. The kinematic diagram of the chain system

As seen from Fig. 4, the structural element is a spatial differential lever mechanism with three relative degrees of freedom. By means of three driving elements we can obtain the needed law of motion of the working components with the desired regulation level.

The constant and variable parameters of the considered system have the form:

$$\alpha = 2\pi/n; \quad R = \frac{\ell_1 \cdot \sin \gamma}{\sin \frac{\alpha}{2}}; \quad r = \frac{\ell_2 \cdot \sin \beta}{\sin \frac{\alpha}{2}}; \quad h_1 = \ell_1 \cdot \cos \gamma; \quad h_2 = \ell_2 \cdot \cos \beta;$$

$$\delta = \arctg \frac{(R-r) \cdot \cos \frac{\alpha}{2}}{H}; \quad \alpha_0 = \arctg \frac{(R-r) \cdot \sin \frac{\alpha}{2}}{H} \cdot \cos \delta; \quad \cos \alpha_0 = \frac{H}{L \cdot \cos \delta};$$

$$(R-r) \cdot \sin \frac{\alpha}{2} = L \sin \cdot \alpha_0.$$

Where the angles γ , β and α_0 are the generalized parameters by means of which we define the function of position of the proposed mechanism. The graph of functions will be constructed according to a given law of motion of driving elements of the mechanism.

6. PRELIMINARY STRUCTURAL CALCULATIONS AND POSSIBLE RESULTS

For the preliminary investigation of the structure and making possible changes in it we have constructed the mathematical model using the ANSYS software using the Ansys Parametric Design Language (Fig. 10).

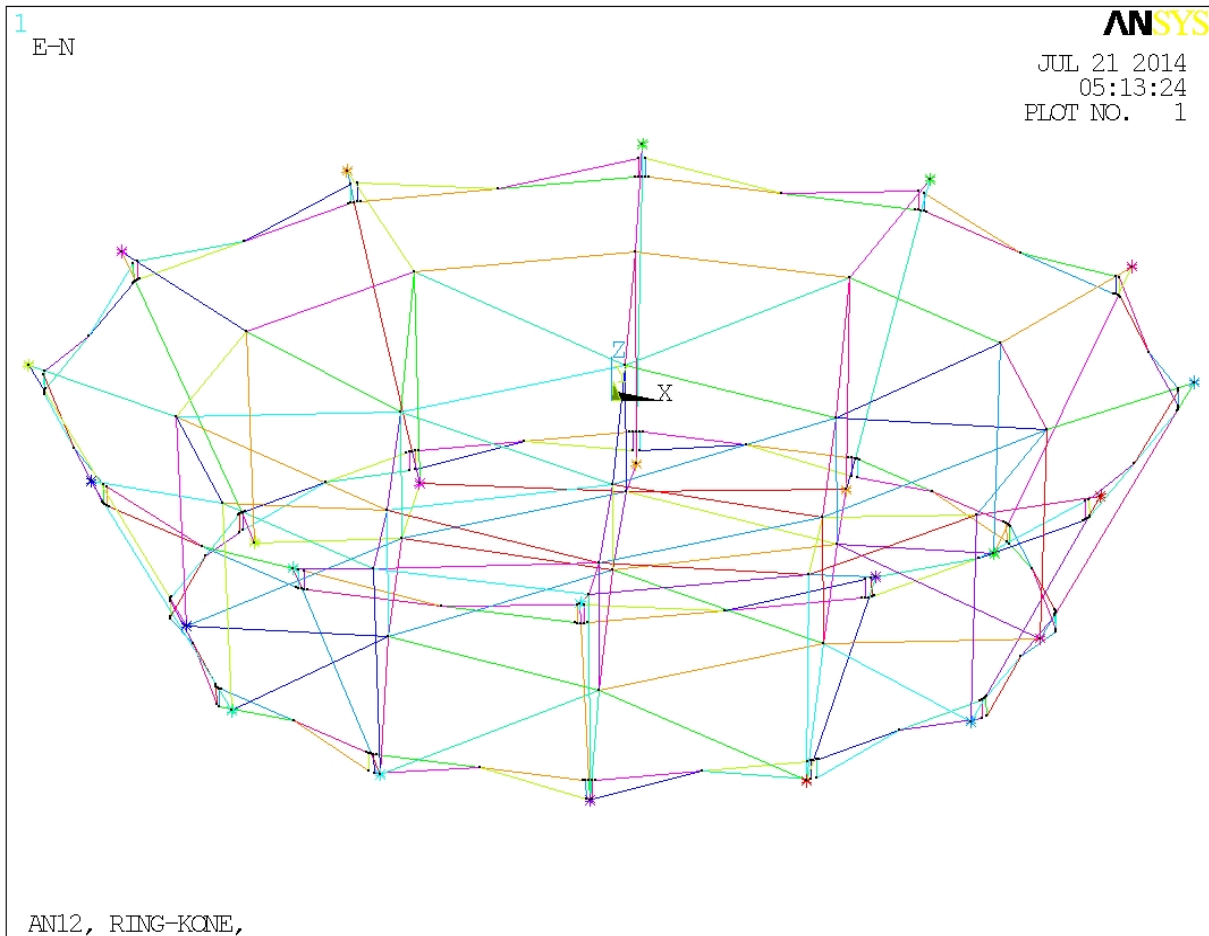


Fig. 10. The mathematical model of the structure with the lower mesh fastened to the strut ends

The degrees of freedom of the hinges are simulated in local coordinate systems and are as much as possible approximated to the real model.

As to the central part, in our case we use the variant developed under the supervision of Dr. J. Santiago Prowald (ESA) and studied jointly with us (ESA contract number: 4000102096/10/NL/PA) [3]. More exactly, the central part consists of vertical tension ties connecting the lower stabilizing mesh and the upper functional one. The meshes have triangular cells and are made of black-reinforced plastic bands. The central part of the upper surface is identical to the lower one, the only difference being that additional linear bands are used for connecting the upper mesh to the upper ends of the struts.

Furthermore, the lower ends of the peripheral tension ties are directly fastened to the lower ends of the struts. This might lead to unwanted shifts (see the general view of the mathematical model in Fig. 10).

The investigation of the stressed-deformed state of the structure shows that in order to reduce unwanted shifts and rotations to a minimum it is better to fasten the meshes directly to the rings (to the main brackets). However because of design peculiarities this can be done only for the lower mesh.

Besides, it is more appropriate if in the final reflector deployment stage the central hinges of V-folding rods and the radial hinges of struts will be in the fixed state.

Total displacements in the components of the reflector with the lower mesh attachment to the lower ring are shown in Fig. 11. Actually, the lower mesh is positioned a little higher because it is fastened directly to the brackets and not to the lower ends of struts. Thus displacements are reduced to a minimum.

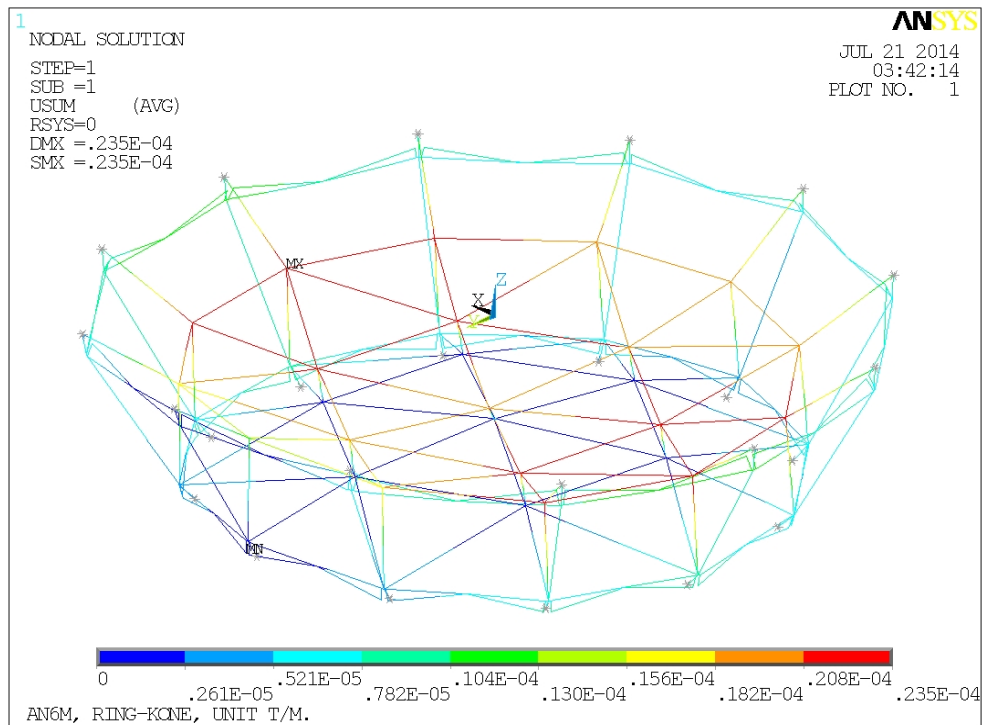


Fig. 11. Total displacements in the components of the reflector with the mesh attached to the lower ring

Figs. 12, 13 show forces acting on the tension ties and elements of the upper mesh after making the above-mentioned changes.

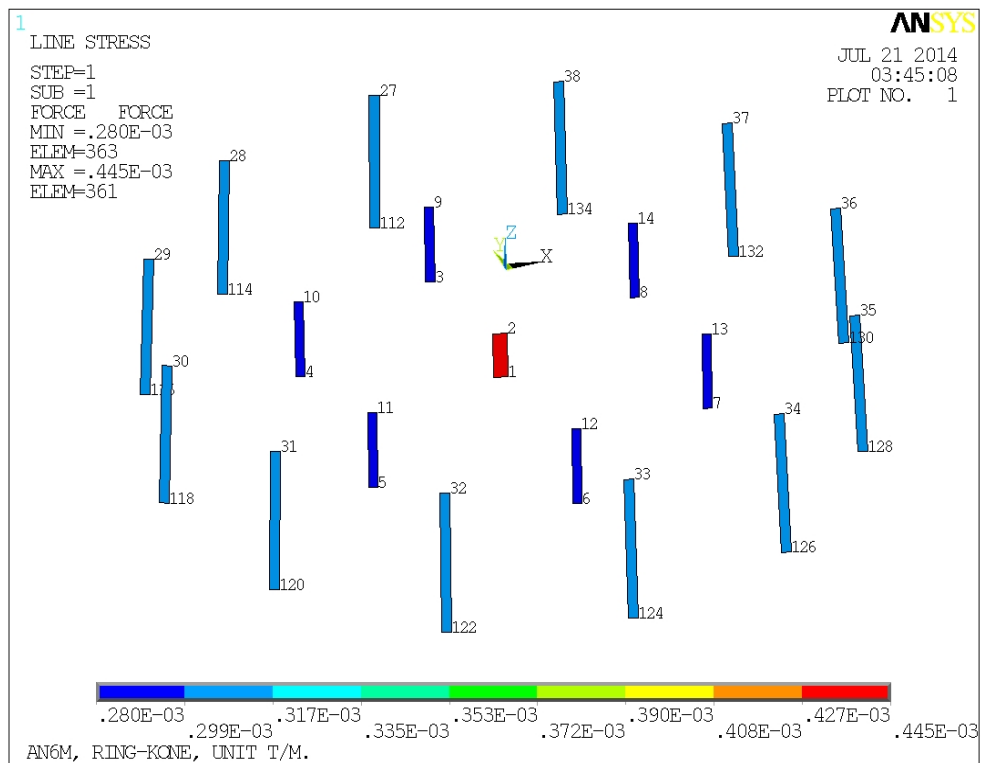


Fig. 12. Forces applied to the tension ties

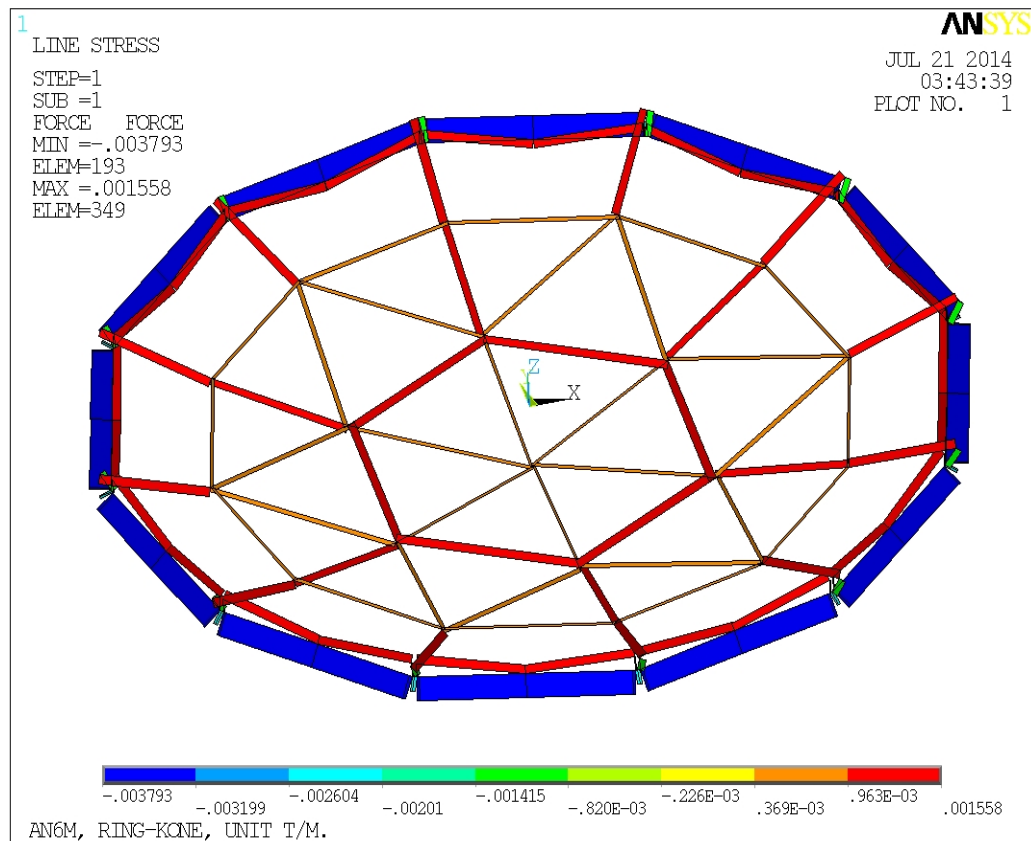


Fig. 13. Tensioned elements of the upper tape mesh

Since the upper mesh is fastened to the upper ends of struts, the latter may have unwanted bends. To prevent them, it is necessary to increase the strut rigidity.

At the final stage of our structural calculations, we define natural oscillation frequencies and shapes of the proposed structure. Appropriate masses are applied to the opposite strut ends, while one of the struts is used for fastening, Figs. 14, 15.

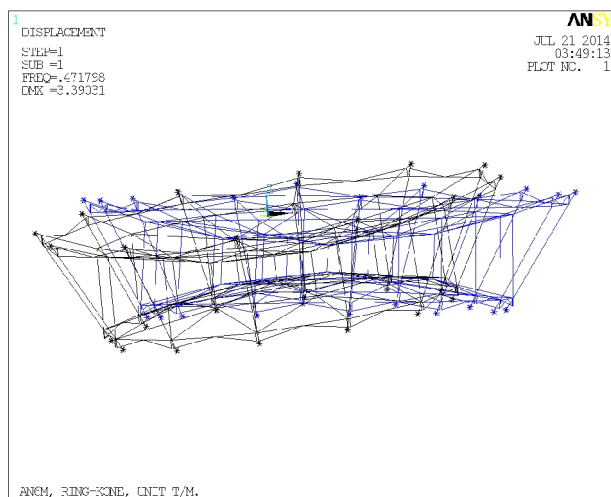


Fig.. 14. First shape

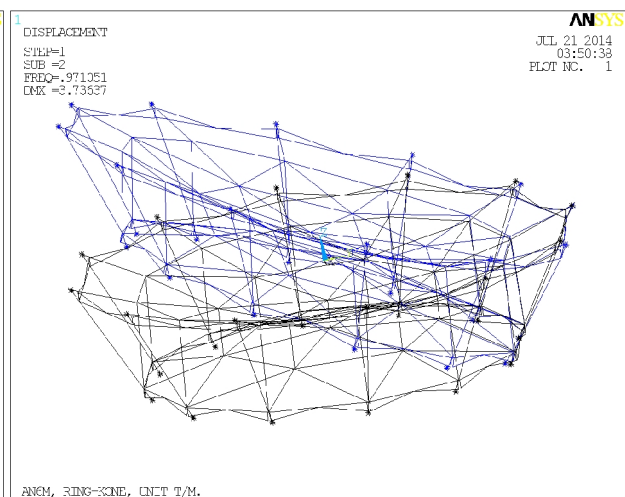


Fig. 15. Second shape

The table below contains the first five numerical eigenfrequencies values of the system. The obtained results prove that the structure is sufficiently rigid. Displacements of the components are minimal and the system in the working state retains its shape.

SET	TIME/FREQ	LOAD STEP	SUBSTEP
1	0.47180	1	1
2	0.97105	1	2
3	1.5476	1	3
4	2.2571	1	4
5	3.5054	1	5

7. CONCLUSION

We present a new design of a closed-chain deployable cone system with V-folding rods, which is an evolution of prior designs demonstrated previously [3], and discuss the structural schemes of transformable systems and their block diagrams. Structural analysis is carried out taking into account the character of structural components (elements). Relative degrees of mobility of systems are established, which control the deployment of systems until it reaches the design position. A law of the process of unfolding is established in conformity with geometrical and kinematic specifications, taking into consideration the degree of regulation.

A method is proposed for the kinematic analysis of the system that takes into account its structural peculiar properties. The geometry of the block diagram is discussed and the kinematic analysis of the cone transformable system is carried out – the obtained data allow one to determine the function of position of the whole system and to evaluate the process of its deployment.

Based on the theoretical analysis, appropriate changes have been made in the construction. We have determined forces acting on the elements. A sufficiently rigid structure has been created. It has been established that all elements of the central part are tensioned, while displacements are minimal. Therefore we can make a conclusion that the structure is efficient in operation and its further investigation inspires interest.

which is an evolution of prior designs demonstrated previously

REFERENCES

- [1]. Levitski N.I. "Theory of Machines and Mechanisms". Moscow, Nauka, 592 p., 1990. (In Russian).
- [2]. Sh. Tserodze, J. Santiago Prowald, van't Klooster C.G.M., E. Logacheva. "Spatial Double Conical Ring-Shaped Reflector for Space Based Application". Proceedings of 33rd ESA Antenna Workshop "Challenges for Space Antenna Systems". 18 - 21 October 2011. ESTEC, Noordwijk, The Netherlands.
- [3]. Sh. Tserodze, E. Medzmariashvili, N. Tsignadze, O. Tusishvili, J. Santiago-Prowald, H. Baier, L. Scialino, C. Manganot. "The structure of conical reflector with v-fold bar's deployable ring". Proceedings of InterNational Scientific Conference "Workshop on large deployable antennas". 2-3 October 2012. ESTEC, Noordwijk, The Netherlands.
- [4]. E. Medzmariashvili, Sh. Tserodze, V. Gogilashvili, A. Sarchimelia, K. Chkhikvadze, N. Siradze, N. Tsignadze, M. Sanikidze, M. Nikoladze, G. Datunashvili. "New variant of the deployable ring-shaped space antenna reflector". IOS Press, "Space Communications", An International Journal, Impact Factor: 0.08, #1 (22), pp. 41-48, october 2009. <http://iospress.metapress.com/content/k13638701327>

EDGE CURRENTS MODELLING IN PROBLEMS RELATED TO OPTIMIZATION OF HIGH FREQUENCY ANTENNA SYSTEMS

D. Karkashadze^(1,2), F. Bogdanov^(1,3), R. Jobava⁽¹⁾, G. Gabriadze^(1,2)

⁽¹⁾EMCoS Ltd, 27 Pekin str., 0160 Tbilisi, Georgia

⁽²⁾Tbilisi State University, 1 Chavchavadze Ave., 0179 Tbilisi, Georgia

⁽³⁾Georgian Technical University, 77 Kostava str., 0175 Tbilisi, Georgia

⁽⁴⁾Georgian University of The Patriarchate, 53a Chavchavadze Ave., 0162 Tbilisi, Georgia

Email: david.karkashadze@emcos.ge

ABSTRACT

Over the past 40-50 years, research in the field of high-frequency (HF) wave scattering from various objects with complex geometry and material filling, was focused on methods accounting edge diffraction effects accurately, using high-frequency asymptotic techniques (Geometrical Theory of Edge Diffraction GTD, Physical Theory of Diffraction PTD, Method of Physical Optics PO, Method of equivalent currents MEC). It can be shown, that these methods usually generate the most simple calculation formulas, but give inaccurate results outside backscattering direction. This paper proposes a hybrid method based on MoM, PO and modified MEC, which takes into account contribution of electric and magnetic edge currents into the scattered field. It is shown that, in contrast to the methods outlined above, the values of proposed edge currents are independent on the direction of radiation.

1. INTRODUCTION

Optimization of antenna systems is impossible without efficient numerical method for direct calculation of antenna characteristics and radiated fields. Over the past 40-50 years, research in the field of high-frequency (HF) wave scattering from various objects with complex geometry and material filling, was focused on several key areas. Among them we should mention:

- Methods for a more accurate accounting of diffraction effects on the edges of the scatterer using high-frequency asymptotic methods, such as Keller's Geometrical Theory of Edge Diffraction (GTD), Physical Theory of Diffraction (PTD), method of Physical Optics (PO) [1];
- Method of equivalent currents (MEC), proposed by Ryan and Peters [4] and generalized by Knott, Senior [5] and Michaeli [6];
- Hybrid methods, combining with both numerical (MoM, MAS, EFIE, MFIE) and high-frequency asymptotic methods (GTD, PTD, PO, MEC).

In the early 80s, many works were devoted to a comparative analysis of these methods to identify the most accurate and universal method. For instance, the work of Knott and Senior [7] provides a detailed analysis of the positive and negative aspects of each of these methods. In particular, it is shown that the methods, based on GTD and standard PO, generate the most simple calculation formulas, but give inaccurate results outside backscattering direction. Keller's or Ufimtsev's theories, using approximations of diffraction on the edge, improve the results of GTD and standard PO just outside the boundary of light and shade. The most efficient method is MEC, which has no the above restriction, but equivalent currents used in the method, actually are unphysical and depend on the observation direction of the scattered field. This fact greatly complicates creation of the optimal numerical algorithm and the software for engineering calculations. Thus, by the end of 80-ies, development of foundations of listed high frequency scattering techniques for perfectly conducting bodies was finished, and so far, new works were focused on improvement of the theory for non-perfectly wedges, impedance bodies and optimal computation of integrals occurring in these methods [8].

This paper proposes a hybrid method, based on MoM, PO and modified MEC. In this method, the special MoM-type basis functions for free edges are introduced, which allow taking into account the contribution of electric and magnetic edge currents to the scattered field, calculated by the method of induced electromotive force (emf). It is shown that, in contrast to the methods outlined in [1], the proposed method introduced modified edge currents which not depend on the direction of radiation. On the base of these modifications, a calculation core for simulation and optimization of the characteristics of antenna systems is developed.

Based on a comparison of different methods for solving the problem of scattering by the bodies of complex configuration and large electrical size, we demonstrate the effectiveness and flexibility of the algorithm for engineering calculations.

2. EDGE CURRENT BASIS FUNCTION AND METHOD OF INDUCED ELECTROMOTIVE FORCE (EMF)

Modified method of equivalent edge currents, presented in this paper, is based on physically accurate description of interaction between radiation from the edge and the rest part of the scattering surface. Such description requires modelling of edge current flow into the nearby surface elements and vice versa. Modelling of these phenomena is performed using surface-to-wire basis functions.

It is well-known that, to properly describe the current flow in surface-to-wire junctions and its radiated HF EM field (Fig. 1), special basis function (BS) should be constructed. Also, to describe the currents along the edges, additional electric (EBS) and magnetic (MBS) basis functions should be introduced.

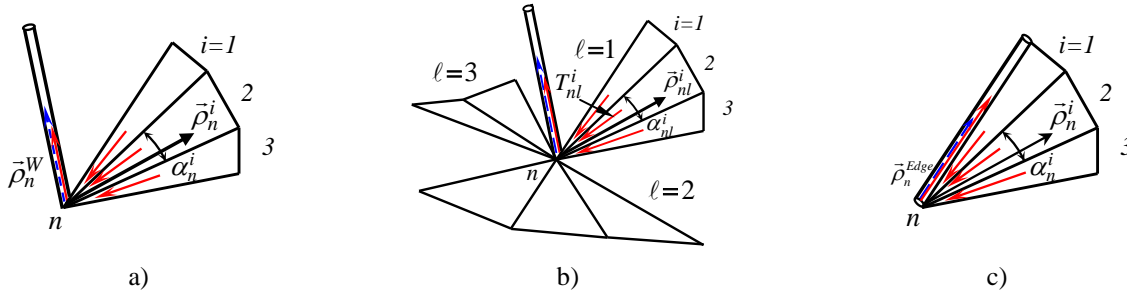


Fig. 1. Illustration of basis function: (a) - with one group of triangles; (b) – with l groups of triangles , (c) - with one group of triangles and corresponding edge, dashed arrow for magnetic edge currents and solid one for electric edge currents.

The surface-to-wire BS for triangulated geometries has been first introduced in [11]. However, this BS, applied separately for each junction triangle and junction segment, though exhibits the proper $1/\rho$ singular current behaviour near the attachment point, creates a varying charge density within the junction triangle. The more suitable surface-to-wire BS, involving all triangles around the junction wire, have been proposed in [12]. If all the junction triangles are adjoined via common edges, such as in Fig. 1(a), then this BS function, both for surface-to-wire junction of Fig. 1 (a), (b) and electric edges Fig. 1(c), can be easily rewritten as:

$$\vec{f}_n^{electric}(\vec{r}) = \begin{cases} -\frac{\alpha_n^i}{2A_n^i\alpha_n^{tot}} \frac{\left[1 - \left(1 - \zeta_n^i\right)^2\right]}{\left(1 - \zeta_n^i\right)^2} (\vec{r} - \vec{r}_n), & \vec{r} \text{ in } T_n^i, \\ -\frac{1}{2\pi a_n l_n} (\vec{r} - \vec{r}_n), & \vec{r} \text{ on } W_n, \\ -\frac{1}{\pi t_n l_n} (\vec{r} - \vec{r}_n), & \vec{r} \text{ on } Edge_n \end{cases} \quad (1)$$

where ζ_n^i is normalized area coordinate of the current point in i -th triangle T_n^i associated with n -th node, A_n^i is an area of i -th triangle, a_n is radius of wire segment W_n of length l_n , t_n is thickness of edge $Edge_n$ of length l_n , α_n^i is an angle between the two edges of T_n^i , α_n^{tot} is a total angle between the ending triangle edges.

In additional MBS can be introduced as:

$$\vec{f}_n^{magnetic}(\vec{r}) = \begin{cases} \frac{1}{2\pi a_n^+ l_n^+}(\vec{r} - \vec{r}_n^+), & \vec{r} \text{ on } W_n^+ \\ -\frac{1}{2\pi a_n^- l_n^-}(\vec{r} - \vec{r}_n^-), & \vec{r} \text{ on } W_n^- \end{cases} \quad (2)$$

defined on a pair of adjacent wire segments W_n^\pm of radii a_n^\pm and lengths l_n^\pm , where r_n^\pm is position vectors of the remote segment endpoints.

Using introduced basis function (1-2) MoM coefficients of electric and magnetic currents I_n^{elect} and I_n^{magn} can be found using method of Induced Electromotive Force (emf). For this, on the first stage, scattering of initial field by PEC surface is obtained. On the second stage, solution of previous stage is used for determination of electric and magnetic edge currents of PEC surface:

$$\begin{aligned} Z_{nn}^E \cdot I_n^{elect} &= \vec{E}_\tau^{tot}(n); \\ Z_{nn}^H \cdot I_n^{magn} &= \vec{H}_\tau^{tot}(n), \end{aligned} \quad (3)$$

where n is an ID of free edge on the given PEC surface; $\vec{E}_\tau^{tot}(n)$ is an average value of tangential component of electric field on n -th edge and on the junction triangles. This field is obtained on the first stage of solution. $\vec{H}_\tau^{tot}(n)$ is corresponding total magnetic field. Z_{nn}^E is diagonal element of MoM impedance matrix, responsible for electric self-influence of the portion of surface, representing surface-to-wire junction. Z_{nn}^H is diagonal element of the MoM impedance matrix defining magnetic self-influence of the wire segments with magnetic current. Described approach can be an alternative to modified MoM with special basis functions (1) and (2) for edges.

Definition of matrix elements $Z_{nn}^{E,H}$ implies that these elements contain information about wire radiuses, however, these radiuses are not determined by geometry of the problem explicitly and some additional assumptions are needed. When thickness of metal sheets is defined, edge wire radius naturally is defined as half of this thickness. For infinitely thin surfaces, thickness of edge wires should be defined empirically based on numerical experiments.

3. NUMERICAL RESULTS

It is obvious that impact of edge currents on scattered EM field depends on polarization, direction of incidence, and mutual positioning of edges and observation points. In order to check influence of edge currents on results, we used MoM as a reference with well segmented edge triangles.

Fig. 2(a) shows model of helicopter with average edge length $l=0.12$ m. Wavelength of incident plane wave is chosen as $\lambda=0.428$ m. In order to get correct results, triangulation along edges should be improved to reach approximately $l=\lambda/10$. Fig. 2(b) shows appropriate model with average free edge length $l=0.03$ m.

Such modification of triangulation increases the number of unknowns from 14,512 for model in Fig. 2(a) to 37,303 for model in Fig. 2(b).

MEC approach hybridized with method of induced emf, presented in the previous section, allows to drastically reduce the number of unknowns required to ensure a reasonable degree of accuracy. Fig. 3 shows scattering cross section (SCS) for helicopter, calculated in three different cases:

- SCS in meridian plane from MoM solution of plane wave scattering on the triangulated helicopter model (a) with total numbers of triangles $N=9,940$;
- SCS in meridian plane from MoM solution of plane wave scattering on the helicopter model (b) with meshed free edges and total numbers of triangles $N=25,941$;
- SCS in meridian plane from MoM solution using equivalent electric edge currents (3) for plane wave scattering on the helicopter model (a).

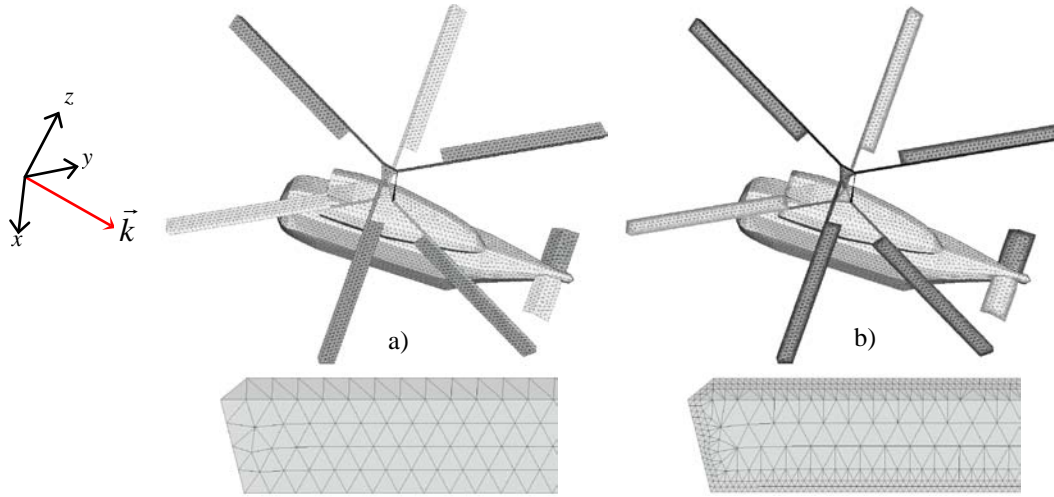


Fig. 2. Triangulated model of helicopter: a) Model with $N=9,940$ total number of triangles, free edge average length $l=0.12\text{m}$; b) Model with meshed free edge for $N=25,941$ total number of triangles, free edge average length $l=0.03\text{m}$

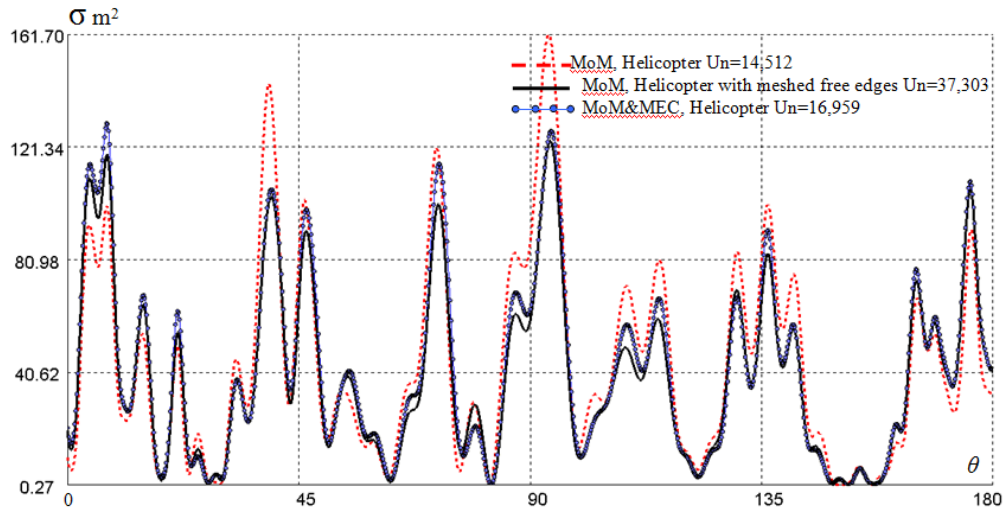


Fig. 3. Scattering Cross-Section (σ) versus to meridian coordinate θ (wavelength $\lambda=0.428\text{m}$): a) Dashed - MoM solution of plane wave scattering on the triangulated helicopter model with 14,512 unknowns; b) Solid - MoM solution of plane wave scattering on the triangulated helicopter model with meshed free edges 37,303 unknowns; c) Rounded - MoM solution using equivalent electric edge currents (3) for plane wave scattering on the triangulated helicopter model (a) with 16,959 unknowns.

In this example, the frontal irradiation and electric field polarization being parallel to the plane of the propellers of the helicopter (wavelength $\lambda = 0.428\text{m}$) provides the largest contribution of electrical edge currents in the SCS of the object. We can see that impact of edge currents is dependent on observation angle and reaches 30%-35% for $\theta \approx 30^\circ$ and $\theta \approx 95^\circ$ angles of meridian coordinates. It is obvious that edge currents improve accuracy of MoM solution and do not require addition discretization of the edges.

The following example on the Fig. 4 for an illustration of influence of edge currents on the classical solution of Physical Optics approach and on the Zero-order approximation from Magnetic Field Integral Equation (MFIE) solution. Here results of dependence meridian components of electric field from spherical coordinate θ for the four various cases are displayed:

- Full MoM solution for “Magellan spacecraft” triangulated model, when total number of triangles on the spacecraft body is $N_{tot}=146159$ and on the antenna $N_a=59128$. Antenna irradiated from electric dipole located in focal point of this antenna for frequency $f=1.0$ GHz;
- Conventional PO solution for the same model as in a) but for simplified model of antenna with $N_a=2916$;
- Correction of conventional PO solution with Modified Method of Equivalent Edge Currents (MMEEC) for the same model as in b).
- Zero-order approximation from Magnetic Field Integral Equation (MFIE) solution for the same model as in a).

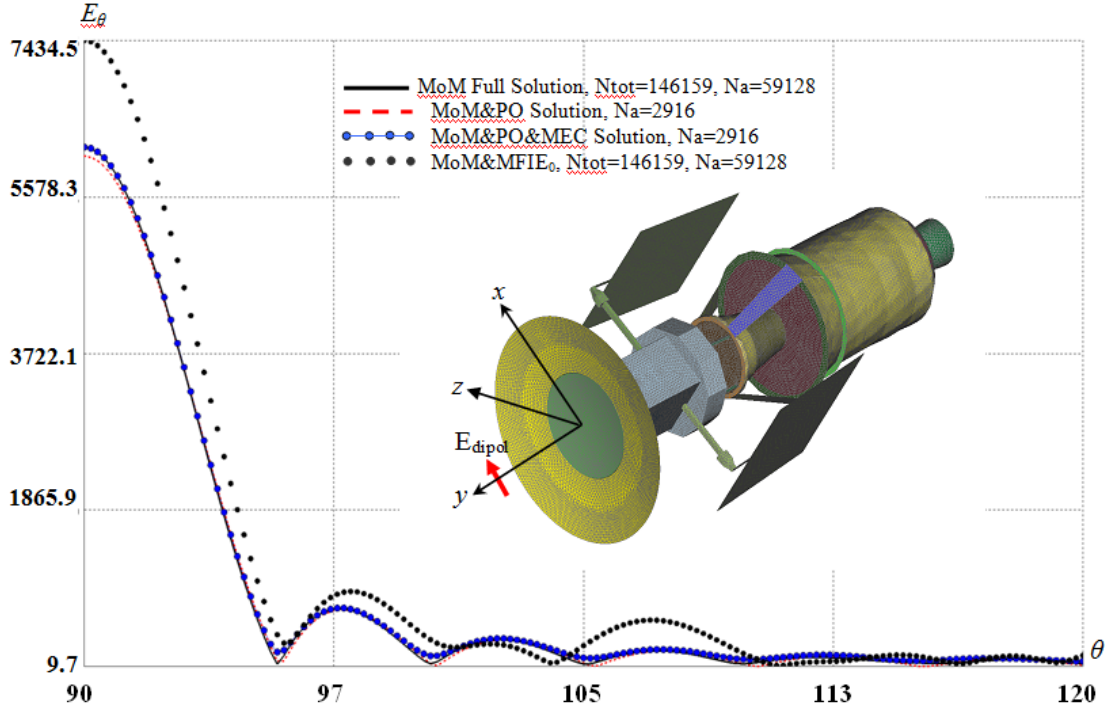


Fig. 4. Triangulated Model of “Magellan spacecraft” with parabolic antenna irradiated from electric dipole located in focal point of this antenna: a) Solid - meridian component of scattered electric field versus to coordinate θ from full MoM solution; b) Dashed – PO solution; c) Thin solid with circles – PO solution correction with MEC; d) Circle - Zero-order approximation from MFIE solution.

From [15], surface density of current in approach of Physical Optics the is defined as follows:

$$\vec{J}^{PO}(s) = \begin{cases} 2 [\vec{n}(s) \times \vec{H}^i(s)], & \text{illuminated area} \\ 0, & \text{shaded area} \end{cases}, \quad (4)$$

where \vec{n} is the external normal to the given body surface and \vec{H}^i is the incident magnetic field.

Surface density of current on the shaded party of a body is supposed equal to zero. It is obvious, that actually, the real current induced on a body surface will differ (owing to a surface curvature) from \vec{J}^{PO} current. Exact expression for density of this surface current is defined as follows:

$$\vec{J}(s) = \vec{J}^{PO}(s) + \vec{J}^I(s), \quad (5)$$

Where \vec{J}^I is a surface density of the additional current as result of presence of any curvature of the given surface.

This density of an additional current is comparable to Physical Optics current, only on wavelength distances from corresponding surface edges. Thus, if the sizes of a body considerably exceed of wavelength, this additional currents occupy rather small part of given surface and slightly influence on the classical solution of Physical Optics.

Exactly such situation is realized in the given example, and it is clearly visible from the comparison of cases a) and b). Besides, the given antenna completely shades the main part of body of this spacecraft, therefore full MoM solution does

not differ from the corresponding solution for the isolated antennas. In addition, the method MEEC c) amend the small correction in classical PO solution b), because the basic body of spacecraft is in the shadow zone of antenna and that this incident field poorly shines the edges of an given antenna.

From the given results we can see, that the solution based on the zero-order approximation of Magnetic Field Integral Equation (MFIE) c) are strongly differ from PO solution b) for full model (spacecraft + antenna), but completely agreed with the results for the isolated antenna.

For an explanation of this result it is necessary to draft consider the procedure of zero-order approximation technique in Magnetic Field Integral Equation. The standard MFIE for PEC surfaces

$$\frac{1}{2} \vec{J}(s') - \frac{1}{4\pi} \vec{n}(s') \times \int_s \vec{J}(s) \times \nabla G(R) dS = \vec{n}(s') \times \vec{H}^i(s'), \quad (6)$$

rewritten for the triangulated surfaces is defined as follows:

$$\vec{J}(T_n) - \sum_{m=1}^N \left[\vec{n}_n \times \frac{1}{2\pi} \int_{T_m} \vec{J}(T_m) \times \nabla G(r_{s_n}, r_{s_m}) dT_m \right] = 2 \left[\vec{n}_n \times \vec{H}^i(T_n) \right]. \quad (7)$$

The zero-order approximation of solution of the given equation can be written down in the following form:

$$\vec{J}^{(0)}(T_n) = \frac{1}{1 - \frac{\alpha_n}{2\pi}} \left[\vec{n} \times \vec{H}^i(T_n) \right], \quad (8)$$

where α_n is inner angle between facets of triangle pair and $H^i(T_n)$ - average value of incident magnetic field strength on the given pair of triangles.

As we can see, zero-order approximation of Magnetic Field Integral Equation (8) completely coincides with PO solution (4) only on the smooth, shined PEC surface.

Thus, scattered EM field in zero-order approximation are calculated using all spacecraft surface currents (8) (spacecraft + antenna) against to PO solution b), being a principal cause of a divergence of corresponding results.

Besides, the solution of integrated equation (6) in the form (8), is differs from corresponding PO currents in the form (4) and current (3) from MMEEC solution. Its contain in explicit form dependence of surface current on the values of inner angle, which is correct only for closed PEC scatterers (from specificity MFIE).

All above results are obtained using only electric edge currents. Additional usage of magnetic currents can improve presented results.

4. REFERENCES

- [1]. J.B. Keller, "Diffraction by an aperture", J. Appl. Phys., vol. 28, no.4, pp. 426-444, Apr. 1957.
- [2]. P.Ya. Ufimtsev, "An approximate calculation of the diffraction of plane electromagnetic waves at certain metallic bodies", Journal of Technical Physics, 1957, vol. 27, №8, p. 1840-1849 (in Russian).
- [3]. V.A. Fok, Problems of diffraction and propagation of electromagnetic waves. M.: Sov. Radio, 1970 (in Russian).
- [4]. C.E. Ryan, L. Peters, "Evaluation of edge-diffracted fields including equivalent currents for the caustic regions", IEEE Trans. Antennas Propagat., vol. AP-17, pp. 292-299, 1969.
- [5]. E.F. Knott, T.B.A. Senior, "Equivalent currents for a ring discontinuity", IEEE Trans. Antennas Propagat., vol. AP-21, pp. 693-695, 1973.
- [6]. A. Michaeli, "Equivalent currents for arbitrary aspects of observation", IEEE Trans. Antennas Propagat., vol. AP-23, no. 3, pp. 693-695, Mar. 1973.
- [7]. E.F. Knott, T.B.A. Senior, "Comparison of three high-frequency diffraction techniques", Proc. IEEE, vol. 62, pp. 1468-1474, 1974.
- [8]. G. Pelosi, Y. Rahmat-Samii, J.L. Volakis, "High-Frequency Techniques in Diffraction Theory: ", IEEE Antennas & Propagation Magazine, Vol. 55, no. 4, pp. 32-40, August 2013.
- [9]. P. L. Christiansen, N. Chr. Albertsen, O. Breinbjerg, "50 years J.B. Keller's Geometrical Theory of Diffraction", IEEE Antennas & Propagation Magazine, Vol. 55, no. 4, pp. 32-40, August 2013.

- [10]. P.H. Pathak, G. Carluccio, M. Albani, "The Uniform Geometrical Theory of Diffraction and Some of its Application", IEEE Antennas & Propagation Magazine, Vol. 55, no. 4, pp. 41-69, August 2013.
- [11]. S. M. Rao, "Electromagnetic scattering and radiation of arbitrarily shaped surfaces by triangular patch modeling," Ph.D. dissertation, Univ. Mississippi, Oxford, 1980.
- [12]. S.U. Hwu and D.R. Wilton, Electromagnetic scattering and radiation by arbitrary configurations of conducting bodies and wires, tech. rep. 87-17, San Diego State University, May 1988.
- [13]. S. U. Hwu, D. R. Wilton, and S. M. Rao, "Electromagnetic scattering and radiation by arbitrary conducting wire/surface configurations," in Proc. IEEE Int. Symp. on Antennas Propag., Jun. 1988, vol. 26, pp. 890–893.
- [14]. Faik Bogdanov, Roman Jobava, Irina Chochia, Development, Validation and Application of Node Triangle Joint Basis Functions in MoM Implementations for Triangulated Geometries, Proceedings of 7th European Conference on Antenna and Propagation (EUCAP-2013), Catalog number CFP1377B-USB, Gothenburg, Sweden, April 2013, pp. 189-193.
- [15]. P.Ya. Ufimtsev, "Method of edge waves in the physical theory of diffraction", Izd.-vo Sov. Radio, 1962.

Sidelobe level reduction of faceted mesh reflector antenna using phyllotactic arrangements

Jean-Christophe Angevain ⁽¹⁾, Gonçalo Rodrigues ⁽¹⁾, Julian Santiago Prowald ⁽¹⁾, Cyril Mangenot ⁽¹⁾, Leri Datashvili ⁽²⁾

⁽¹⁾ESTEC, European Space Agency,
Keplerlaan 1, 2200AG Noordwijk Zh, The Netherlands
Email: Jean.Christophe.Angevain@esa.int

⁽²⁾ Lehrstuhl für Leichtbau, Technische Universität München,
Boltzmannstraße 15, 85748 Garching, Germany
Email: Datashvili@llb.mw.tum.de

ABSTRACT

Mesh reflector antennas made of multiple quasi-flat facets arranged with a regular lattice are, under certain conditions, known to generate high level sidelobes, called faceting lobes. This paper investigates some deterministic ways to reduce the faceting sidelobes of mesh reflector antenna by applying phyllotactic arrangements to the supporting net of the mesh reflector surface. This nature-inspired arrangement is derived from a spiral pattern with a Fibonacci sequence, and is known to be irregular.

1. INTRODUCTION

Mesh reflector antennas made of multiple quasi-flat facets arranged with a regular lattice are known to generate high level sidelobes, called faceting lobes. The location of these faceting lobes depends on the periodicity of the adjacent facets, expressed in terms of wavelength. The faceting lobes are also sometimes called grating lobes by analogy with the antenna array theory, where the individual reflector facets could be seen as the radiating elements of an antenna array. The condition of appearance of these lobes in the visible region remains the same as for the antenna array theory with the periodic spacing exceeding one wavelength. As a consequence, for low frequency bands, this periodicity does not have any effect since such faceting lobes are out of the visible region. This is no longer the case when the operating frequency increases and the corresponding wavelength is less than the periodic spacing.

The reduction of sidelobes level for mesh reflector antennas is of importance from the system performance point of view. This is particularly true for telecommunication payloads or Earth observation and scientific microwave instrument systems where interference levels arising from the antenna sidelobes need to be kept as low as possible with respect to the useful or the observed signal.

This paper investigates some deterministic ways to reduce the faceting sidelobes of mesh reflector antenna by applying phyllotactic arrangements to the faceting of the reflector surface. Indeed, this type of arrangement called phyllotactic can be observed in Botany for instance in the spatial distribution of the seeds inside a sunflower or the scales inside a pine cone. This type of nature-inspired arrangement is inferred from a spiral pattern with Fibonacci sequence. In this paper, the reflector parabolic surface is fitted by an aperiodic distribution of triangular flat facets following a phyllotactic arrangement. This aperiodic spatial distribution with a uniform or a non-uniform density of facets allows reducing the faceting sidelobes level as demonstrated by the RF simulations performed on both the periodic and the phyllotactic arrangement of facets on the mesh reflector surface.

Besides the RF analysis, the mechanical feasibility constraints imposed by such an irregular arrangement on the structural design are assessed. The challenges regarding the mechanical compatibility and manufacturing aspects are also discussed. In particular, the feasibility of achieving a predictable equilibrium of geometry and internal forces distribution in the tensioned net is preliminary studied using form finding tools, and the way forward to reduce manufacture complexity and cost is identified.

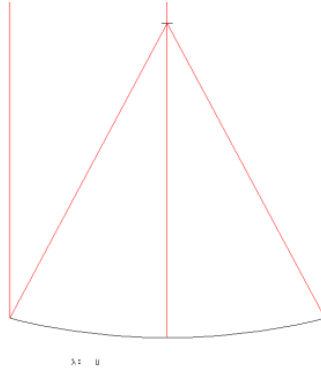
2. EFFECT OF FACET PERIODICITY OF MESH REFLECTOR

2.1. Antenna Geometry

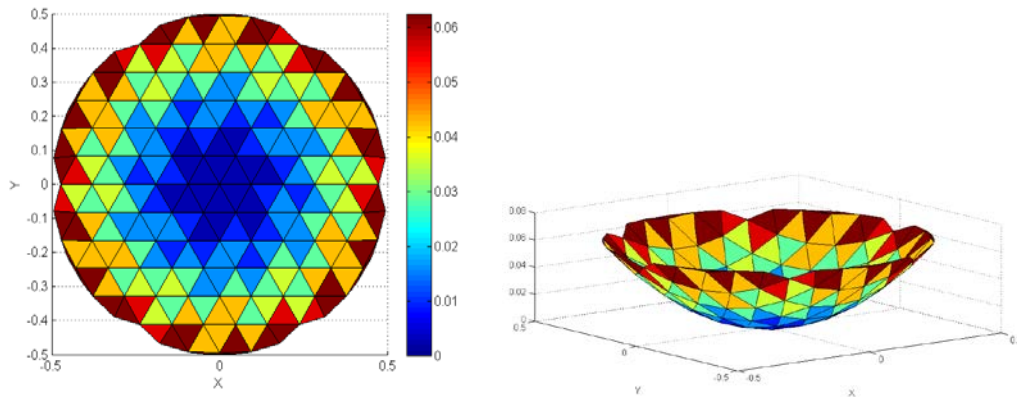
For sake of simplicity, a center fed reflector antenna is analyzed in this paper where feed blockage is neglected. The reflector antenna geometry is shown in Table 1, and depicted in Fig. 1. The feed illumination is Gaussian with a taper of -12 dB at the edge of the reflector.

Table 1. Antenna Geometry

Reflector Geometry	[meters]	[wavelengths] assuming $f=50GHz$
Projected Area Diameter	1	166.67
Focal Length	0.977	162.83
Clearance	0	0

**Fig. 1. Reflector Antenna Geometry**

The antenna consists of a mesh reflector that is assumed to be with flat triangular facets arranged in a regular lattice as depicted in Fig. 2. The mesh reflector consists of 222 triangular facets and the length of the side of each equilateral triangle is 95 mm.

**Fig. 2. Mesh reflector with a periodic arrangement of triangular facets (left: top view, right: side view)**

The surface accuracy of the mesh reflector is 0.170 mm after best-fitting the surface to an ideal solid parabolic reflector.

2.2. Antenna performances with a periodic lattice

The antenna performances of the mesh reflector with triangular facets are compared to the ones obtained with a solid parabolic reflector. As expected, faceting lobes are observed in the visible angular domain, as illustrated in Fig. 3 and Fig. 4. These lobes are periodically located along radial lines in the uv-plane, as expected from a triangular lattice with a six-fold rotational symmetry.

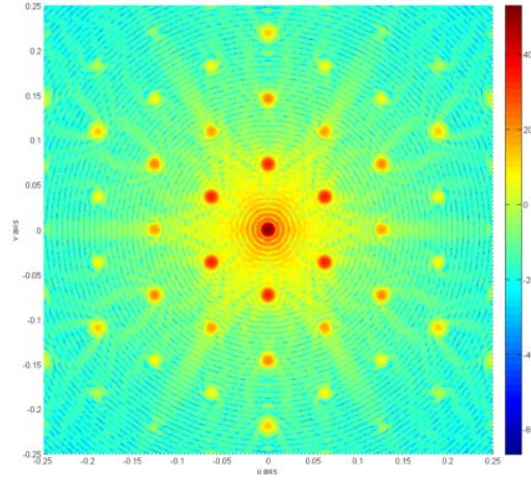


Fig. 3. Co-polarization pattern of a mesh reflector antenna with triangular facets in uv plane

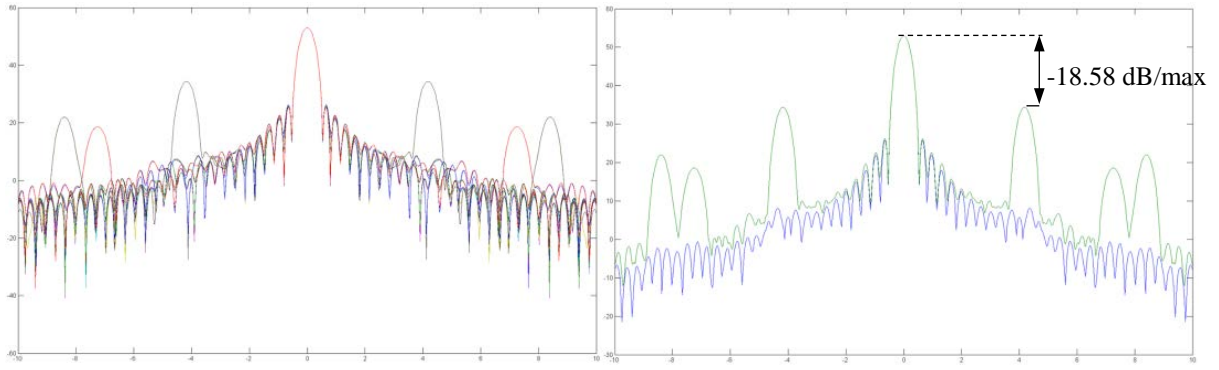


Fig. 4. Co-polarization pattern phi-cuts of a mesh reflector antenna with triangular facets (Left: Superimposition of 24 pattern phi-cuts, Right: Maximum envelope and average pattern phi-cuts)

3. MESH REFLECTOR WITH PHYLLOTACTIC ARRANGEMENTS

3.1. Mesh reflector and antenna geometry

In order to reduce the level of faceting sidelobes, it is proposed to arrange the facets of mesh reflector by using a phyllotactic arrangement. This deterministic nature-inspired and aperiodic arrangement is already known from the antenna array theory to reduce sidelobes [1], [2]. The triangular facets are constructed as follows:

The circular aperture of radius R_0 is sampled with N points $M_k, k \in \{1, \dots, N\}$, which have the following Cartesian coordinates:

$$M_k \begin{cases} x_k = R_0 \sqrt{\frac{k}{N}} \cos(2\pi k / \varphi^2) \\ y_k = R_0 \sqrt{\frac{k}{N}} \sin(2\pi k / \varphi^2) \\ z_k = \frac{x_k^2 + y_k^2}{4F} \end{cases} \quad (1)$$

where $\varphi = \frac{1+\sqrt{5}}{2}$ is the golden number inferred from the Fibonacci sequence and F is the focal length.

A Delaunay triangulation is then applied to this set of N points in order to form each elementary triangular facet of the mesh reflector, as illustrated in Fig. 5.

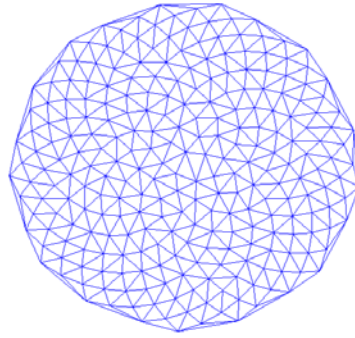


Fig. 5. Top view of triangular facets of a mesh reflector

The antenna geometry is chosen to be similar to the one described in Table 1 so that it is possible to compare the performance of the mesh reflector with an aperiodic lattice to the one with a periodic lattice. The number of points is selected in such a way that the number of triangles is similar to the mesh reflector with a periodic lattice. The number of points is 140 and the number of triangles is 265.

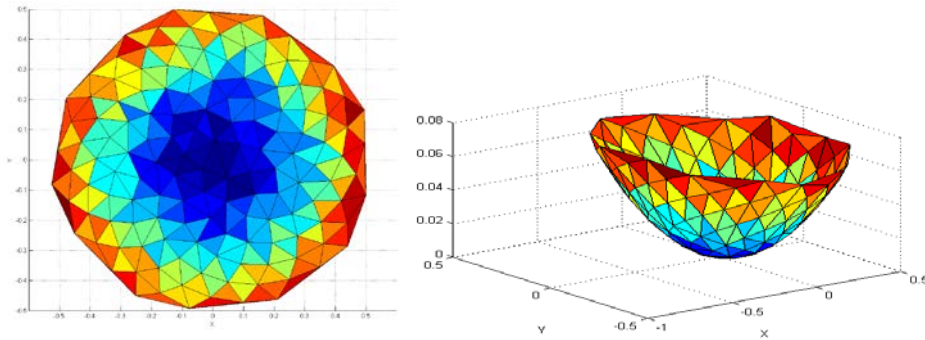


Fig. 6. Mesh reflector with an aperiodic arrangement of triangular facets (Left: Top view, Right: Side view)

The surface accuracy of the mesh reflector with a phyllotactic arrangement is 0.237 mm after best-fitting the surface to an ideal solid parabolic reflector.

3.2. Antenna performances for a mesh reflector with a phyllotactic arrangement

The co-polarization pattern of the mesh reflector is shown in Fig. 7 and Fig. 8. One can remark that, as expected, the faceting lobes have strongly vanished. One can also note that, as expected from the lower surface accuracy, the antenna peak directivity and the associated aperture efficiency are slightly degraded. It shall be pointed out that the faceting sidelobe vanishing translate into an increase of the sidelobe pattern averaged over the azimuth cuts of the antenna radiation pattern as shown in Fig. 7 where two sidelobe rings are visible in the uv-plane, and also as illustrated in Fig. 8.

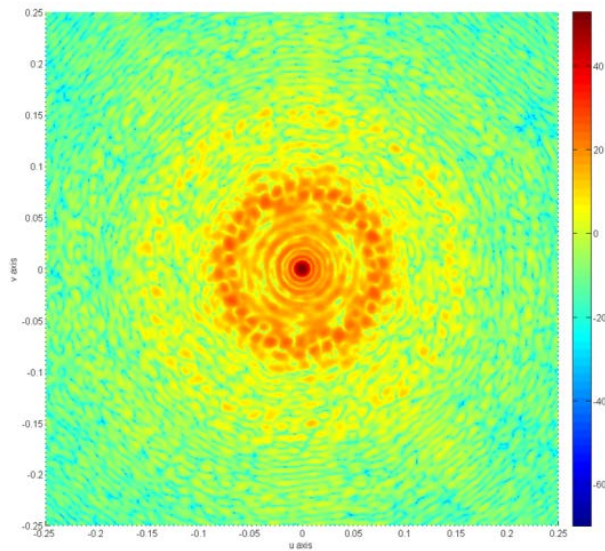


Fig. 7. Co-polarization pattern of mesh reflector antenna with a phyllotactic arrangement in uv plane

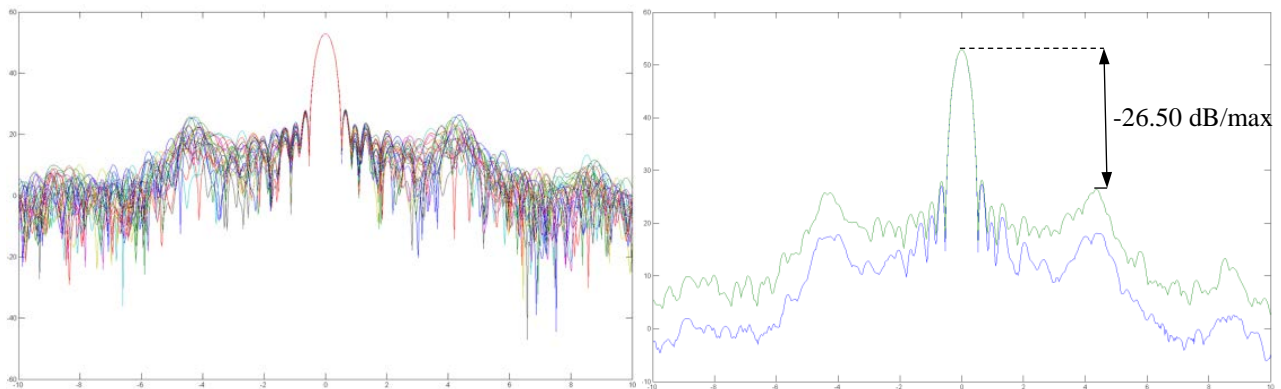


Fig. 8. Co-polarization pattern phi-cuts of mesh reflector antenna with a phyllotactic arrangement (Left: Superimposition of 24 pattern phi-cuts, Right: Maximum envelope and average pattern phi-cuts)

Table 2. Summary of the RF performances of a mesh reflector antenna with a periodic and with a phyllotactic arrangement of triangular facets

Antenna Performances	Solid reflector	Mesh reflector with a periodic arrangement	Mesh reflector with a phyllotactic arrangement	Units
Peak Directivity	53.42	52.96	52.87	dBi
Aperture efficiency	80.1	72.1	70.6	%
First sidelobe level	-27.44	-26.72	-24.70	dB/max
Maximum sidelobe level @ $\sim \pm 4^\circ$ (*)	-49.90	-18.58	-26.50	dB/max

(*): Angle where faceting lobes are maximum

3.3. Impact of a non-uniform density of triangular facets

In order to get the best reflector surface accuracy in the central part of the reflector where the field amplitude is the strongest, a phyllotactic arrangement with a non-uniform density of triangular facets has been analysed with small facets in the central area and larger ones at the periphery of the reflector surface. This is depicted in Fig. 9. A similar methodology to the one described in section 3.1 is used, where the N vertices M_k of the triangular facets are distributed as follows for each $k \in \{1, \dots, N\}$:

$$M_k \begin{cases} x_k = R_0 \left(\frac{k}{N}\right)^{1/Q} \cos(2\pi k/\varphi^2) \\ y_k = R_0 \left(\frac{k}{N}\right)^{1/Q} \sin(2\pi k/\varphi^2) \\ z_k = \frac{x_k^2 + y_k^2}{4F} \end{cases} \quad (2)$$

assuming the index of n th-root $Q=1.4$, and of R_0 the radius of the circular aperture

The number of points and triangular facets are kept identical to the ones in section 3.1. The surface accuracy after geometrical best-fit is 0.332 mm.

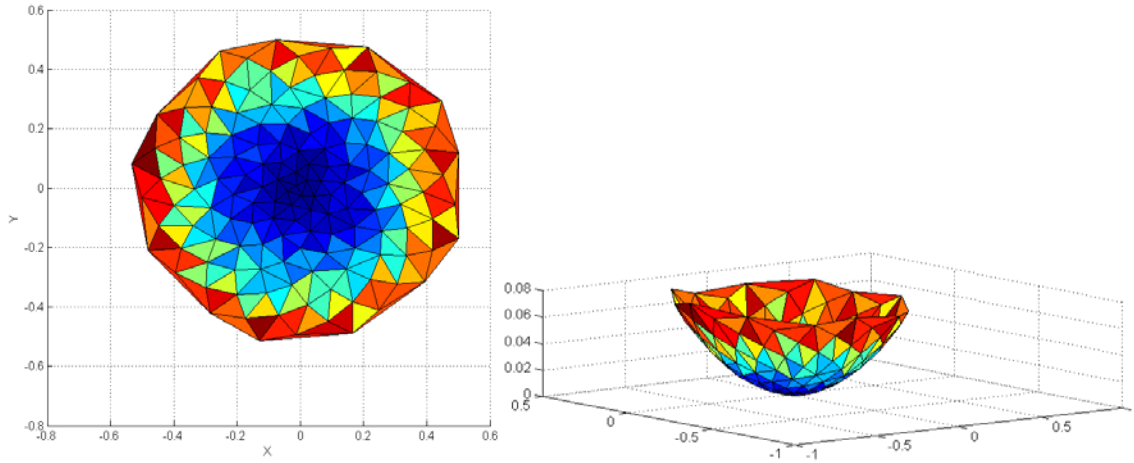


Fig. 9. Mesh reflector with a phyllotactic arrangement of triangular facets with a non-uniform density (Left: Top view, Right: Side view)

The performances obtained with such an arrangement shows that the level of far-out sidelobes in the vicinity of $\theta \sim \pm 4^\circ$ are further decreased, as illustrated in Fig. 10, Fig. 11 and presented in Table 1. However the peak directivity and the associated aperture efficiency are degraded. Furthermore, we can observe in Fig. 11 that the main lobe shape exhibits some “shoulders” which are resulting from the merge of the main lobe and the first sidelobes due to the reflector surface distortions.

Table 3. Summary of the RF performances of a mesh reflector antenna with a phyllotactic arrangement of triangular facets with a uniform and a non-uniform density

Antenna Performances	Mesh reflector with phyllotactic arrangement (uniform density)	Mesh reflector with phyllotactic arrangement (non-uniform density)	Units
Peak Directivity	52.87	52.52	dBi
Aperture efficiency	70.6	65.1	%
Maximum sidelobe level @ $\sim \pm 4^\circ$ (*)	-26.50	-28.04	dB/max

(*): Angle where faceting lobes are maximum

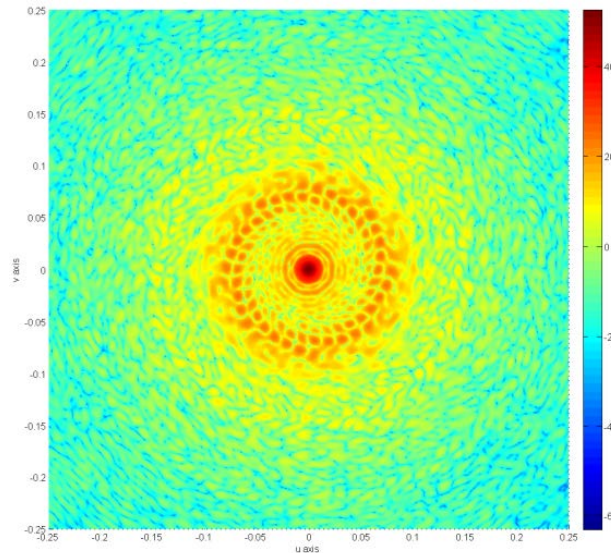


Fig. 10. Co-polarization pattern of a mesh reflector antenna with a non-uniform phyllotactic arrangement

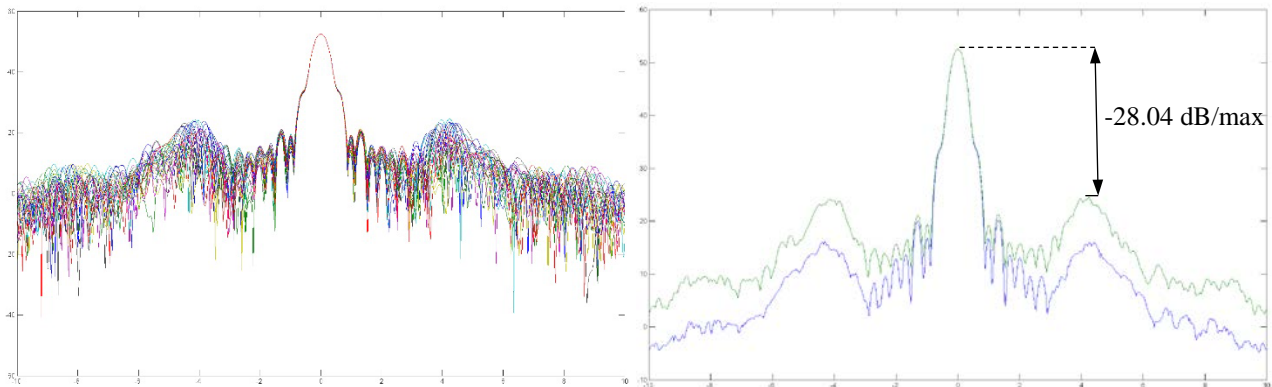


Fig. 11. Co-polarization pattern phi-cuts of a mesh reflector antenna with a non-uniform phyllotactic arrangement (Left: Superimposition of 24 pattern phi-cuts, Right: Maximum envelope and average pattern phi-cuts)

4. MECHANICAL FEASIBILITY AND MANUFACTURING CONSTRAINTS

4.1. Mechanical Feasibility Constraints

The design of a cable net system exhibits a very strong interaction between its geometry and stress/force distribution. Therefore, the phyllotactic arrangement was analysed from a mechanical point-of-view in order to guarantee the force equilibrium at each vertex of the triangular faces.

In a first investigation, an iterative form-finding, departing from the phyllotactic arrangement with uniform density of triangular facets, was performed with the Force Density Method similarly to [3]. The resulting distribution of the triangular facets is shown in Fig. 12, in which a surface accuracy of 0.619 mm could be obtained after a geometrical best fit to the paraboloid.

The electrical performances of the balanced cable net were also computed and are presented in Fig. 13, Fig. 14 and Table 3. The capability for the faceting sidelobe suppression is maintained by this first-shot in hardware implementation, even despite a slight degradation of both the peak gain and the first sidelobes. The far-out sidelobes level at $\theta \sim \pm 4^\circ$ is nevertheless further reduced.

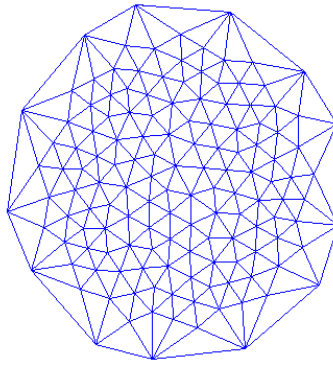


Fig. 12. Top view of triangular facets of a cable net approximating a phyllotactic arrangement and exhibiting force equilibrium

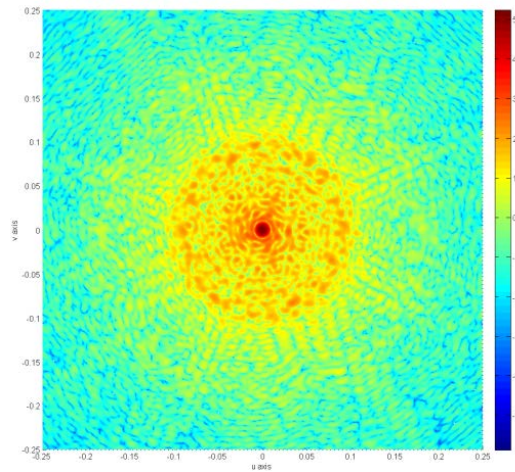


Fig. 13. Co-polarization pattern of a mesh reflector antenna with a post-processed phyllotactic arrangement taking into account force equilibrium constraints

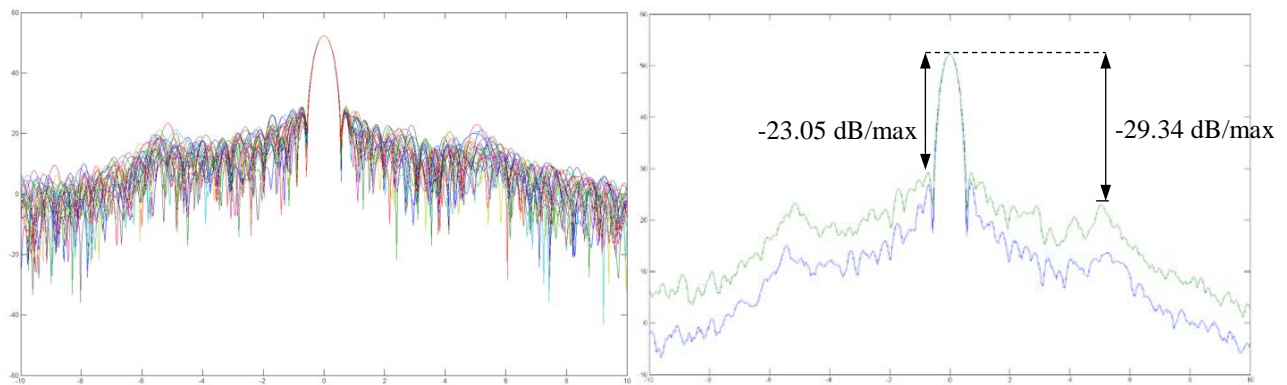


Fig. 14. Co-polarization pattern phi-cuts of a mesh reflector antenna with a post-processed phyllotactic arrangement taking into account force equilibrium constraints (Left: Superimposition of 24 pattern phi-cuts, Right: Maximum envelope and average pattern phi-cuts)

Table 4. Summary of RF performances of a mesh reflector antenna with a phyllotactic arrangement of triangular facets with and without force equilibrium constraints

Antenna Performances	Mesh reflector with a phyllotactic arrangement (uniform density and without constraints)	Mesh reflector with a phyllotactic arrangement taking into account force equilibrium constraints	Units
Peak Directivity	52.87	52.29	dBi
Aperture efficiency	70.6	61.8	%
First sidelobe level	-24.70	-23.05	dB/max
Maximum sidelobe level @ $\sim \pm 4^\circ$ (*)	-26.50	-29.34	dB/max

(*): Angle where faceting lobes are maximum

It shall be stressed out that this force equilibrium constraint at each vertex of the triangular facets, ie at each mechanical node of the tensioned net, result into a non-uniform distribution of internal forces. As an additional constraint to be investigated next is finding a uniform or quasi uniform distribution force in the net in order to achieve equilibrium, keep positive tension under the orbital loads and thus guarantee the form of the reflector mesh. It is believed that a coupled mechanical-RF optimisation will help to obtain a good compromise between RF performance and the abovementioned force constraints.

4.2. Manufacturing Constraints

In manufacturing practice, it is observed that a uniform distribution of tensions in the cable net gives simplified manufacturing process and a good quality of final tensioning of the net. Simplicity of the manufacturing process has been demonstrated on a reflector breadboard [4], [5]. Manufacturing, assembling, and final stable tensioning of the nets required remarkably low effort thanks to uniform force distribution and related manufacturing process.

In order to achieve high mechanical / RF performance of the cable net and the reflector in whole with removed sidelobes, one would need to allow some force variation in the cables. Then an upper threshold shall be imposed on the admissible tension levels for minimizing the deflection of the support structure and a lower threshold for ensuring shape stability (positive cable tension), minimum level of possible mesh pillowing and adequate PIM performance of the reflecting surface. The enhancement of the tension distribution of the cable net will constitute a next step, incorporating these constraints in a coupled RF-mechanical optimization.

Another manufacturing constraint of such nets is related to a curvilinear shape of a single cable combined out of many straight parts. This factor may impose requirements to all of the following: the cable material, the shape of its cross-section and the joint design. In a conventional tensioned cable nets each cable has a form close to the straight line. Because of straightness, the joints of cables are much simpler, while with the curved cables joints design needs to be reconsidered.

5. CONCLUSION

The first investigations presented in this paper demonstrate that the phyllotactic arrangement of triangular facets of a mesh reflector enable reducing the faceting sidelobes that are typical of a regular arrangement of facets. It is also observed that the peak directivity and the associated aperture efficiency are marginally impacted by the irregular arrangement of facets.

Other design constraints such as the mechanical feasibility and the manufacturing need to be further refined. The impact of the mechanical constraint of force equilibrium at each node of the mesh has been preliminary assessed on the phyllotactic arrangement of triangular facets combining a cable net. This shows a degradation of the peak gain of 0.6dB with respect to a phyllotactic configuration without any constraints, a significant increase of the first sidelobes and a slight decrease of the sidelobes in the angular domain where the faceting lobes are appearing. A more elaborated coupled RF/mechanical optimization would be required to further enhance these performance and take into consideration other essential mechanical constraints such as a uniform or quasi-uniform distribution of internal forces in the tensioned net of cables.

REFERENCES

- [1]. D. W. Boeringer, "Phased array including a logarithmic spiral lattice of uniformly spaced radiating and receiving elements", Northrop Grumman Corp. Patent, Patent No: US6433754, 13 August 2002
- [2]. M. C. Vigano, G. Toso, G. Caille, C. Mangenot, I. E. Lager,; "Spatial density tapered sunflower antenna array", 3rd European Conference on Antenna and Propagation EUCAP 2009
- [3]. B. Wei, L. Datashvili, "Cable Web Design for Precision Large Deployable Reflectors", Workshop on Large Deployable Antennas, 2-3 October, 2012, Noordwijk, The Netherlands.
- [4]. Datashvili, L.: "Foldability of hinged-rod systems applicable to deployable space structures." CEAS Space Journal (5), 2013, S. 157 - 168
- [5]. Datashvili, L.; Endler, S.; Wei, B.; Baier, H.; Langer, H.; Friemel, M.; Tsignadze, N.; Santiago-Prowald, J.: "Study of mechanical architectures of large deployable space antenna apertures: from design to tests." CEAS Space Journal (5), 2013, S. 169-184

APPLICATION OF ACA ALGORITHM AND BICGSTAB SOLVER FOR ACCELERATION OF MOM COMPUTATIONS OF LARGE SCALE EM PROBLEMS

G.Gabriadze^(1,2), V.Tskhovrebashvili^(1,2), F.Bogdanov^(1,3), P.Tsereteli^(1,4), R.Jobava⁽¹⁾

(1)EMCoS Ltd, 27 Pekin str., 0160 Tbilisi, Georgia

(2) Tbilisi State University, 1 Chavchavdze Ave., 0179 Tbilisi, Georgia

(3) Georgian Technical University, 77 Kostava str., 0175 Tbilisi, Georgia

(4) Georgian University of The Patriarchate, 53a Chavchavadze Ave., 0162 Tbilisi, Georgia

Email: giga.gabriadze@emcos.com

ABSTRACT

The given paper describes the application of ACA (Adaptive Cross Approximation) algorithm for acceleration of MoM solution of large scale and complex EM problems. Iterative solutions are very practical for such cases. One of such solutions is MLFMM (Multilevel Fast Multipole Method), which has been successfully used in the past years. As an alternative, we consider ACA algorithm to reduce required memory for matrix storage, to speed up calculation time of matrix elements and matrix-vector-product operation. This technique starts with presenting the MoM matrix in hierarchical form and identifying near and far-field interaction sub-blocks. Near-field blocks are calculated directly, while far-field blocks are decomposed via ACA, requiring significantly less memory. After ACA decomposition, linear system is solved iteratively, using BICGSTAB (Biconjugate Gradient Stabilized) iterative solver. In order to improve convergence of iterative process SPAI (Sparse Approximate Inverse) preconditioner is applied. To demonstrate performance and applicability of described technique, two numerical experiments are presented: a) calculation of radiation pattern of Naval ship mounted Yagi-Uda antenna operating at 430MHz, and b) calculation of radiation pattern of Magellan spacecraft high gain reflector antenna operating at 3GHz. Based on these calculations, we show that ACA calculation is much faster than direct solution, while accuracy is quite acceptable.

1. INTRODUCTION

The method of moments (MoM) is one of the most widespread and generally used techniques for solving electromagnetic radiation and scattering problems [1]. It solves discretized EFIE (Electric Field Integral Equation), MFIE (Magnetic Field Integral Equation) or CFIE (Combined Field Integral Equation) equations, which finally lead to the solution of linear system of equations:

$$Ax = b \quad (1)$$

Here A is impedance matrix, x is the unknown current distribution and b is the known right-hand-side. The most general techniques to solve such system use matrix Gauss elimination or LU decomposition methods, which require a predictable amount of resources in terms of time $O(N^3)$ and storage $O(N^2)$, where N denotes size of linear equations.

The size of linear equations N depends on discretization factor of the integration boundary. Generally, surface geometries are presented using triangles, while wires are represented using line segments. To achieve satisfactory results, at least several triangles/segments should be used per wavelength. When the frequency of the task is high compared to the dimension of geometry, N reaches a high value and often it becomes impossible to find solution using even most powerful computers.

One of the promising ways to solve linear equations with large number of unknowns is the usage of iterative solvers. Iterative solvers give an approximation of solution with a given accuracy. Main property of iterative solutions is that only the matrix-vector-product operation is needed. There are a lot of popular, so-called, Krylov subspace methods: Conjugate Gradient, MINRES, GMRES, QMR, BICGSTAB, etc., which can easily be implemented into MoM based solvers [2].

Several techniques like FMM (Fast Multipole method), MLFMM (Multi Level Fast Multipole method), AIM (Adaptive Integral Method), ACA (Adaptive Cross Approximation) algorithms are widely applied in order to speed up matrix-vector-product operation and to reduce memory requirements of iterative solver [3][4].

In the given paper we present the application of ACA technique [4][5][6], used for acceleration of MoM solver, aiming to calculate scattering and radiation from electrically large EM problems. For solution of the system, iterative solver BICGSTAB (Biconjugate Gradient Stabilized) [7][8] is used and SPAI (Sparse Approximate Inverse) is applied as preconditioner to speed up convergence rate of solver [9][10].

To demonstrate performance and applicability of described approach, two numerical experiments are presented: a) calculation of radiation pattern of Naval ship mounted Yagi-Uda antenna operating at 430MHz and b) calculation of radiation pattern of Magellan spacecraft high gain reflector antenna operating at 3GHz. Calculation accuracy, time and used memory are compared with direct solutions.

2. THEORETICAL BACKGROUND

2.1. Adaptive Cross Approximation

Each A_{ij} entry of MoM matrix A represents interaction between i and j boundary elements. Therefore, it is always possible to choose groups on boundary with weak interaction, for example, geometrically far positioned groups. Generally, corresponding matrix block is close to some low rank matrix and can be approximated by ACA technique [4].

The hierarchical matrix representation is used for choosing "well-separated" boundary groups [11]. First, geometrical domain is recursively partitioned according to some geometrical criteria, e.g. geometrical domain with ten elements {1,2,3,4,5,6,7,8,9,10} in the Fig. 1 is partitioned into two clusters: {1,2,3,4,5} and {6,7,8,9,10}. Then cluster {1,2,3,4,5} is split into new clusters: {1,2} and {3,4,5}, correspondingly cluster {6,7,8,9,10} is divided into clusters: {6,7,8} and {9,10}. As a result, the cluster tree is constructed (see Fig. 2). Next, cluster pairs, which are geometrically well-separated, are labelled as "RK blocks" (Rank Low), while cluster pairs, which are not well separated, are marked as "full blocks". This procedure begins from the upper level of cluster and is applied hierarchically to all clusters at following generations, until the finest level is reached. In such manner, we obtain matrix in hierarchical form, containing a set of blocs of various sizes (see Fig. 3), "RK blocks" are coloured with white, while "full blocks" are coloured with gray.

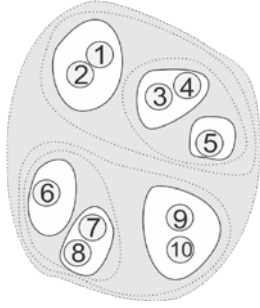


Fig. 1. Geometrical domain

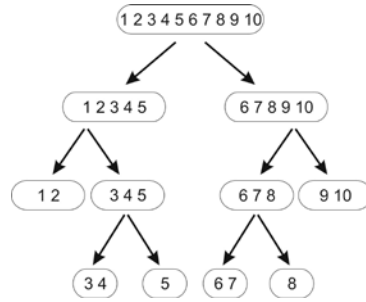


Fig. 2. Cluster tree

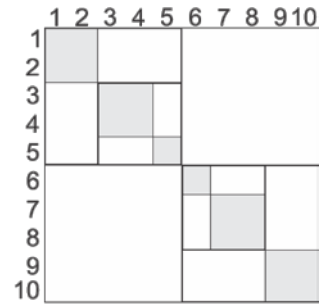


Fig. 3. Hierarchical Matrix

Once "RK blocks" are identified, it is time to approximate them by low-rank matrixes. Let Z_{mn} represent interaction between far positioned element groups. Using ACA decomposition Z_{mn} can be approximated by low rank matrixes U_{mk} and V_{kn} , where $k \ll m, n$ is effective rank of the matrix Z_{mn} see Fig. 4. The goal of ACA is to achieve $\|Z_{mn} - U_{mk} \times V_{kn}\| \leq \varepsilon \|Z_{mn}\|$ for a given tolerance ε . Here $\|\cdot\|$ denotes Frobenius norm of a matrix. Therefore, instead of storing entire $m \times n$ elements, the algorithm requires to store only $(m+n)k$ elements. In such way, all RK blocks are decomposed and totally compressed matrix is received (see Fig. 5).

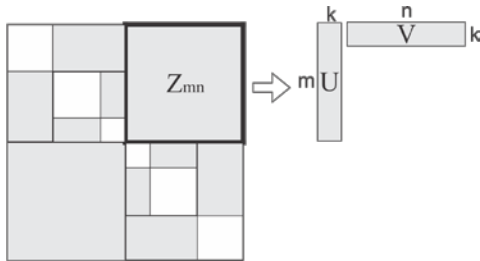


Fig. 4. ACA decomposition of RK block

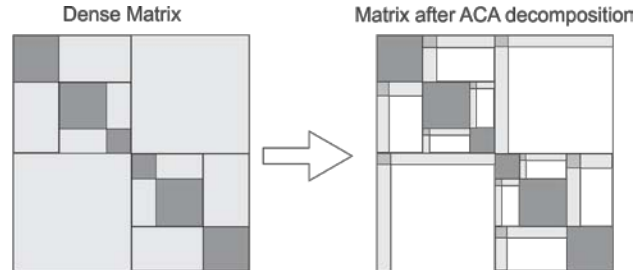


Fig. 5. Matrix compression using ACA

2.2. Iterative Solvers and Preconditioning

An iterative solver for linear system (1) calculates a set of approximate solutions x^i to exact answer x , each with a decreased error, using matrix A repeatedly and without changing it. The advantage of this method compared to direct solution is the feasibility of achieving the needed accuracy in a small number of iterations and finding a solution close enough to x . It should be noted as well, that main disadvantage of iterative solvers is related to poor convergence in the most practical situations.

To speed up the convergence of iterative solver, transformation of the system (1) into different system with more favorable properties is needed. This procedure is known as preconditioning, and a matrix, that affects such transformation, is called preconditioner [9]:

$$MAx = Mb \quad (2)$$

Here M is preconditioner. The linear system (2) has the same solution as (1) but converges faster in case of successful preconditioning. In most cases M is some approximation of the matrix A^{-1} . There are two main requirements for preconditioner: first, the preconditioned system should be easy to solve and second, preconditioner itself should be cheap to construct and apply [9]. One of such preconditioners is Sparse Approximate Inverse (SPAI) [10].

SPAI is sparse matrix M , which minimizes $\|I - \tilde{A}M\|$ subject. Here I is an identity matrix and \tilde{A} is a sparse approximation of A matrix. Because of sparsity, this problem decouples into N independent least squares problems, for each column of M with number of unknowns equal to the number of nonzero entries in current column of M .

$$\|I - \tilde{A}M\| = \sum_{j=1}^N \|e_j - \tilde{A}m_j\| \quad (3)$$

Here e_j is the j th unit vector and m_j is the j th column of M . For each fixed j we consider the set $J = \{i\}$, which specifies nonzero pattern of m_j . Then only J columns of \tilde{A} are need for calculation of m_j . Let $\tilde{A}(:, J)$ be the submatrix of \tilde{A} formed from such columns, and let I be the set of indices of nonzero rows of $\tilde{A}(:, J)$. Then we can restrict our attention to the matrix $\hat{A} = \tilde{A}(I, J)$, to the unknowns vector $\hat{m}_j = m_j(J)$ and to the right-hand side $\hat{e}_j = e_j(J)$. Once J and I are known, nonzero entries in m_j can be computed by solving the unconstrained least squares problem $\min \|\hat{e}_j - \hat{A}\hat{m}_j\|$. Schematically calculation of SPAI is presented in Fig. 6 and Fig. 7.

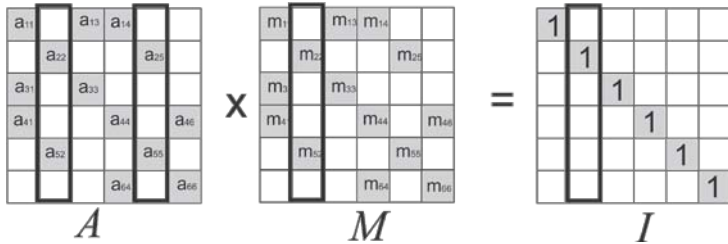


Fig. 6. Calculation of 2th column of M matrix

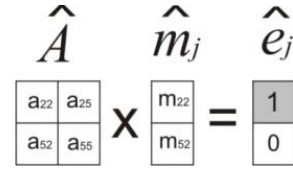


Fig. 7. Unconstrained least squares problem

Choice of sparsity patterns for \tilde{A} and M matrixes is the most important part of SPAI construction. In our case, choice of these patterns is similar to “Full blocks” in hierarchical matrix (see Fig. 3), but the size of the boxes at finest level is much smaller. Besides that, box sizes for M matrix is twice bigger than box sizes for \tilde{A} .

3. NUMERICAL EXPERIMENTS

In this section we show some numerical examples that demonstrate effectiveness of described algorithm. To check accuracy and speed gain of described algorithm, the same models are recalculated using direct solutions. In all computations tolerance for ACA compression is set to $1e-3$ and box size at finest level of clustering is set to $\lambda/4$ or minimum 256 elements. Two boxes are considered well separated (corresponding to RK block), if distance between them is more than $0.75 \times \text{box dimension}$. Accuracy for BICGSTAB solver is set to $3e-3$ and $\lambda/4$ or minimum 4 elements are chosen for SPAI pattern. ACA calculations are performed on computer with 48 cores (AMD 2.49GHz) 128GB RAM, while direct simulations are performed on 48 cores (Intel 2GHz) 256GB RAM. Because of not enough memory, all direct calculations went in out-of-core mode.

3.1. Yagi-Uda Antenna on Naval Ship

Investigation of optimal antenna position, analysis of near/far fields generated by antennas placed on large structures (like ships, aircrafts, etc.) plays important role in onboard antennas design and installation. This application demonstrates analysis of Yagi-Uda antenna mounted on naval ship and operating at 430MHz frequency.

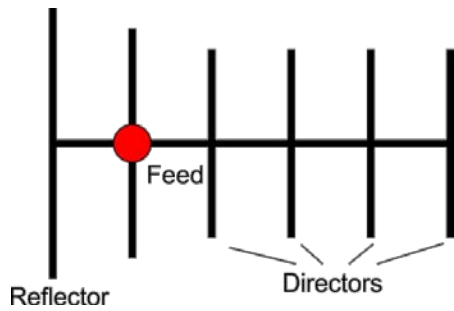


Fig. 8. Yagi-Uda Antenna

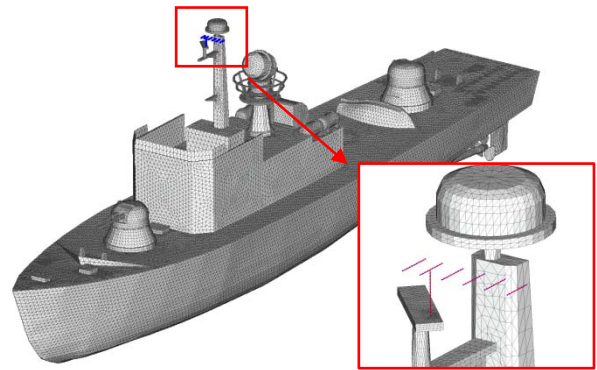


Fig. 9. Yagi-Uda Antenna on Naval Ship

Length of the ship is 39.5m, width - 7.3m and height 12.9m. Wavelength at 430MHz equals 70cm and average size of triangles - 5cm. Such triangulation size leads to 90,885 triangles, corresponding to 136,696 unknowns and 285,124MB memory for matrix storage. Near field and far field distributions are calculated and analyzed. To check accuracy, ACA results are compared with direct solution results. Comparison show, that ACA results are very close to direct solution results (see Fig. 12 and Fig. 13).

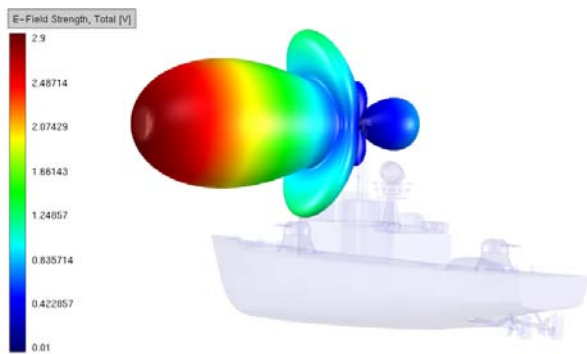


Fig. 10. Radiation pattern of Yagi in free space

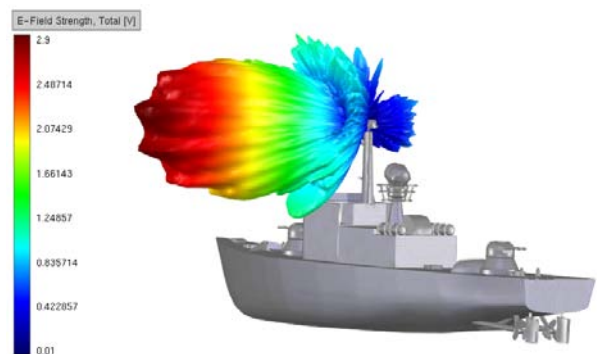


Fig. 11. Radiation pattern of Yagi mounted on mast

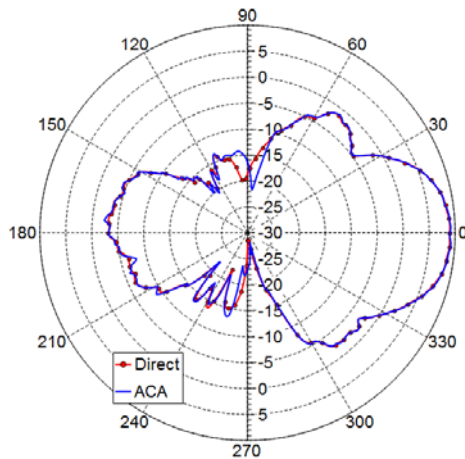


Fig. 12. Total electric field [dBV/m], horizontal plane

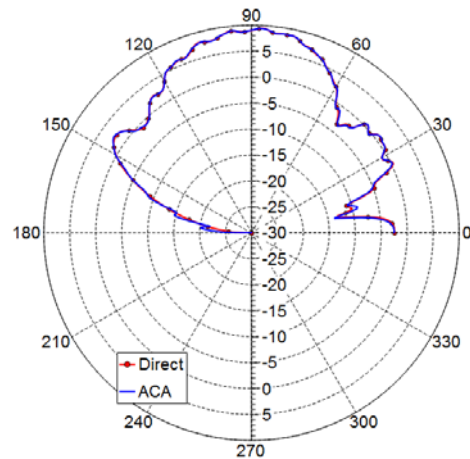


Fig. 13. Total electric field [dBV/m], vertical plane

In Fig. 14 and Fig. 15 cluster boxes for levels 5, 8 and 10 and hierarchical matrix for given model is presented.

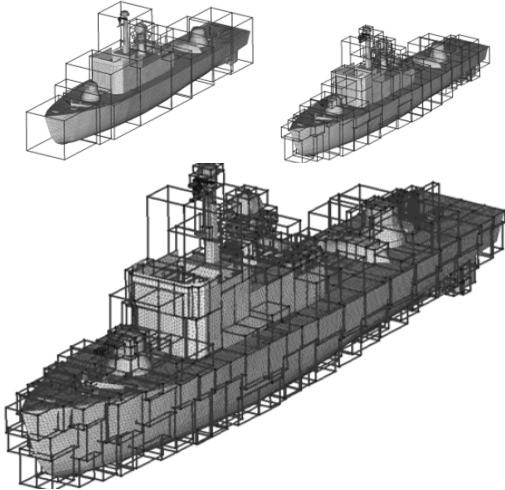


Fig. 14. Clustering boxes for level 5, level 8 and level 10

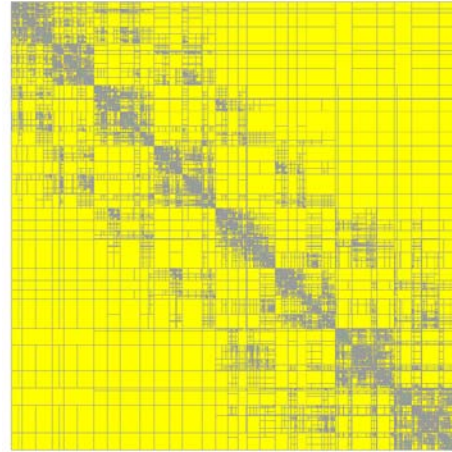


Fig. 15. RK blocks include 97.75% of matrix. Achieved compression equals 92.95%

Portion of full blocks and RK blocks are 2.25% and 97.75% correspondingly. Totally, 22,956.903MB is required for matrix storage after ACA decomposition. This corresponds to 91.95% compression. In addition, 157.562MB is required for SPAI preconditioner storage, with 0.11% density. ACA matrix filling, SPAI calculation and BICGSATB solving takes 12.09 minutes, while for matrix filling and solving, direct solution needs 443.26 minutes (37 times longer). Detailed information of performance is shown in the following tables.

Table 1. ACA performance

Portion of full blocks	2.25%
Portion of RK blocks	97.75%
Compression	91.95%
SPAI density	0.11%
Iterations	32

Table 2. Comparison with direct solution

	ACA	Direct
Filling time [min]	5.47	42.72
Preconditioning [min]	2.23	0.00
Solving time [min]	4.38	400.54
Total time [hr]	0:12:05	7:23:33
Memory [MB]	23,274.96	285,124.00

3.2. Magellan Spacecraft Simulation

This application demonstrates Magellan spacecraft simulations at 3GHz. It is fed by horn antenna pattern. Far field pattern of a horn antenna is calculated and is used as a specialized incident field source for Magellan high gain antenna.

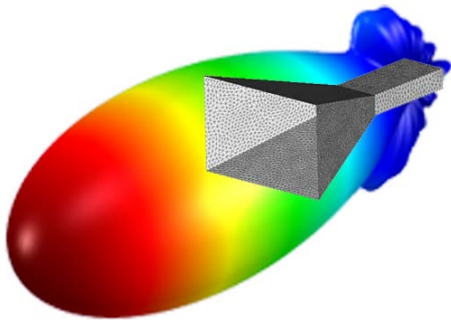


Fig. 16. Horn antenna radiation at 3GHz

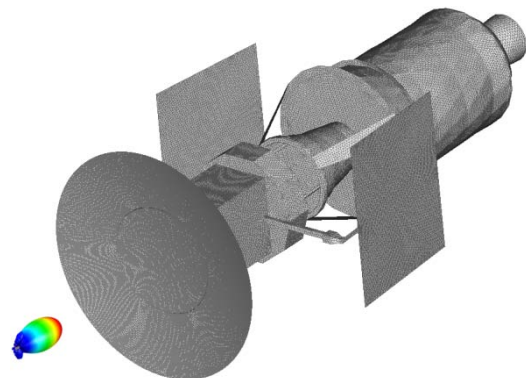


Fig. 17. Magellan spacecraft. Its high gain reflector antenna is fed by horn antenna radiation

Magellan spacecraft is about 10m long and diameter of its high gain reflector antenna is about 3.7m. Wavelength at 3GHz is 10cm, average size of triangles - 3cm and total number of triangles -146,159. Such triangulation gives 218,626 unknowns and 729,332.68MB memory for direct MoM solution.

In Fig. 18 and Fig. 19, comparison of far field pattern calculated using ACA and direct solutions are shown. It is seen that results are in good agreement with each other.

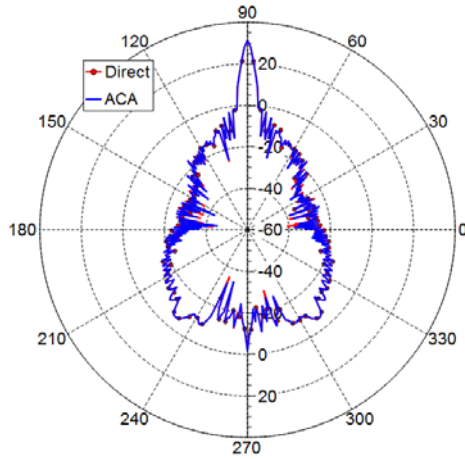


Fig. 18. Total electric field [dBV/m], horizontal plane

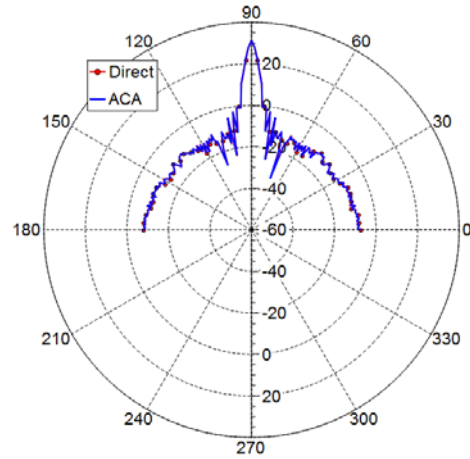


Fig. 19. Total electric field [dBV/m], vertical plane

In the next figures corresponding cluster boxes and hierarchical matrix are presented. Portion of "Full blocks" and "RK blocks" are 2.11% and 97.89% correspondingly.

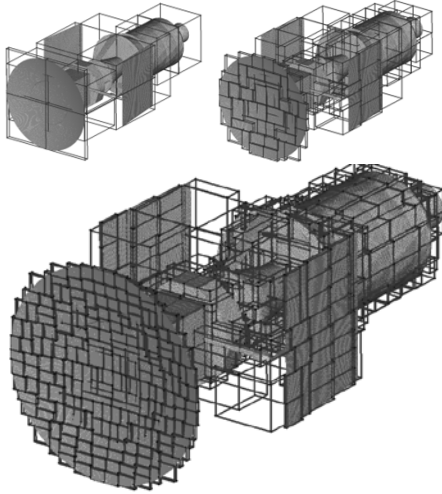


Fig. 20. Clustering boxes for level 5, level 8 and level 10

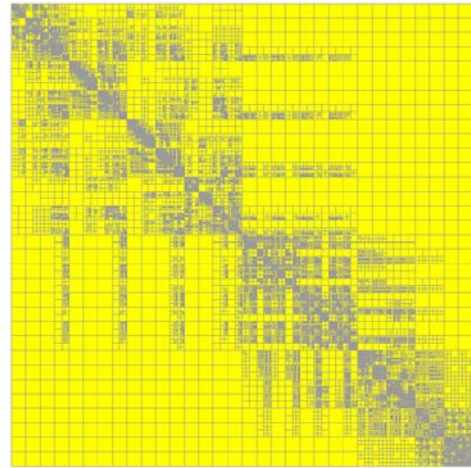


Fig. 21. RK blocks include 97.89% of matrix. Achieved compression equals 92.34%

After ACA decomposition, 5,5870.700MB is required to store matrix. This corresponds to 92.34% compression. In addition, 108.42MB is required for SPAI preconditioner storage, with 0.03% density. ACA matrix filling, SPAI calculation and BICGSATB solving needs 25.41 minutes, while for matrix filling and solving, direct solution takes 1384.85 minutes (55 times longer). Detailed information of performance is shown in the following tables.

Table 3. ACA performance

Portion of full blocks	2.11%
Portion of RK blocks	97.89%
Compression	92.34%
SPAI density	0.03%
Iterations	29

Table 4. Comparison with direct solution

	ACA	Direct
Filling time [min]	17.11	104.09
Preconditioning [min]	2.04	-
Solving time [min]	6.26	1280.75
Total time [hr]	0:25	23:04
Memory [MB]	56,091.76	729,332.68

4. CONCLUSIONS

ACA technique and iterative solver is applied to MoM solution for electrically large problems. We can see from the results, that usage of iterative solver and ACA compression gives a significant gain in both, used memory and calculation time, and accuracy is quite acceptable. Also, computational speed gain grows with increase of number of unknowns. It can be said, that for antenna radiation problems, discussed technique is very effective and applicable.

5. REFERENCES

- [1]. R.F. Harrington, J.L. Harrington, "Field computation by moment methods", Oxford University Press ©1996
- [2]. Henk A. van der Vorst, "Iterative Methods For Large Linear Systems", June 24, 2002
- [3]. B. Carpentieri, I. S. Duff, L. Giraud and G. Sylvand "Combining fast multipole techniques and an approximate inverse preconditioner for large electromagnetism calculations". *SIAM J. SCI. COMPUT.* vol. 27, no. 3, pp. 774–792
- [4]. K. Zhao, M. Vouvakis and J. Lee, "The Adaptive Cross Approximation Algorithm for Accelerated Method of Moment Computations of EMC Problems," *IEEE Trans. on EMC*, vol. 47, no. 4, pp. 763-773, November 2005
- [5]. S. Kurz, O. Rain, S Rjasanow, "The adaptive cross-approximation technique for the 3D boundary-element method", *IEEE Trans. magn.*, vol. 38, no. 2, pp.421-424, March 2002
- [6]. G. Gabriadze, F. Bogdanov, P. Tsereteli, R. Jobava, E. Yavolovskaya, "ACA method and SPAI preconditioner for acceleration BICGSTAB solver in MoM based solver TriD", Direct and Inverse Problems of Electromagnetic and Acoustic Wave Theory (DIPED), 2011 XVth International Seminar/Workshop, 26-29 Sept. 2011, pp. 151-155.
- [7]. G.Sleijpen and H.van der Vorst, "Maintaining convergence properties of BiCGstab methods in finite precision arithmetic", *Numerical Algorithms*, 10(1995),pp. 203-223
- [8]. G.Sleijpen and H.van der Vorst, "Reliable updated residuals in hybrid BiCG methods", *Computing*, 56(1996), pp.141-163
- [9]. Michele Benzi, "Preconditioning Techniques for Large Linear Systems: A Survey", *Journal of Computational Physics* 182, 418–477 (2002)
- [10]. M. Benzi, M. Tuma, "A sparse approximate inverse preconditioner for nonsymmetric linear systems", *SIAM J. Sci. Comput.* vol. 19, no. 3, pp. 968–994, May 1998
- [11]. Steffen Borm, Lars Grasedyck, Wolfgang Hackbusch, "Hierarchical Matrices", April 21, 2005

SOME PROBLEMS IN GROUND TESTING OF LARGE SPACE LIGHTWEIGHT STRUCTURES

Guram Bedukadze⁽¹⁾, Leri Datashvili⁽²⁾

⁽¹⁾ *Georgian Technical University, Kostava 68 b, Tbilisi, Georgia,*
E-mail: beduk_saxli@yahoo.com

⁽²⁾ *Large Space Structures (LSS) UG, Römerhofweg 51C, Garching, Germany,*
E-mail: leri.datashvili@largespace.de

ABSTRACT

Testing of large deployable space structures on ground is related to the number of challenges caused by the size. RF and deployment tests, shape accuracy measurements under different simulated environments, stiffness tests of large antenna reflectors need special facilities with properly designed gravity compensation systems.

The paper describes methods and challenges of gravity compensation for deployment, stiffness and shape accuracy tests of lightweight large deployable structures including antenna reflectors

1. INTRODUCTION

Large deployable structures (LDS), and transmit-receive large deployable antenna reflectors (LDR) among them are important components of space satellite systems.

Trying to create such structures, designers target a minimum structural weight through the application of lightweight materials and minimizing cross-sections of the elements. Although gravity is absent, any space structure is subjected to the different environmental loading in orbit. These are large temperature gradients, deep vacuum and radiation, dynamic orbital and launch loads among others.

An orbital reliable radio frequency (RF) functionality during the full lifetime of the LDR depends not only on RF properties of the surface but also on its mechanical properties like stiffness, strength, surface accuracy, reliability of deployment, resistance to radiation and some other factors. Designing space structures according to these factors require not only analytical and numerical predictions but also numerous ground experimental investigations and tests for validation of those mechanical properties among others.

Besides investigations and full characterization of the used structural materials in terms of mechanical, thermo-elastic, thermo-optical properties and characterization of their stability and resistance under vacuum and radiation conditions, the following specific tests shall be performed on full size deployable structures

- Deployment of the structure, control of kinematic processes, finding, characterization and/or removing of parasitic influences during deployment for more accurate simulation of the orbital deployment.
- Definition of the power budget needed for reliable deployment with a defined margin and study of variation of the required power budget;
- Measurement and evaluation of forces and deformations in the members of the structure during and after the deployment;
- Deployed (and stowed) modal experimental analysis of stiffness;
- Measurement of shape accuracy and repeatability.

These tests are significant set of tests for large size structures, while they require complex ground support and test equipment. In order to have reliable results in ground experiments and tests, a maximum approximation of orbital conditions is required. For this purpose gravity compensation systems (GCS), thermal-vacuum chambers, solar simulators, vibration equipment, and other special purpose test facilities shall be designed built and utilized. Development and use of such test facilities imply some prerequisites most important of which are associated to the size and the required qualification level of the test object.

2. GRAVITY COMPENSATION AND MICRO GRAVITY

There are number of methods for simulating orbital gravity conditions reducing gravity effects during on-ground experiments of space structures. These are a free fall (e.g. ground-based drop facilities), a 0g parabolic flight (also a kind of a free fall), neutral buoyancy in a water or an air environment and mechanical gravity compensation.

Zero-g parabolic flights are mainly used for training of astronauts and it approximates the weightlessness in a best way. The use of this method for LDS is limited by the size of the free space in planes and the duration of micro-gravity. However, there are examples of micro-gravity deployment and shape accuracy tests in planes. For example, ETS VIII reflector deployment [1], a zero gravity deployment test of a DLR bi-stable boom [14], a deployment and shape accuracy test of a shell-membrane LDR demonstrator developed by TUM [12] (see Fig. 1). Parabolic flight time giving micro gravity conditions equates to about 22 s. Several tens of such micro gravity conditions can be created during a single parabolic flight.



Fig. 1. ETS VIII reflector, Japan (left), a deployable inflatable boom, DLR (middle), and a shell-membrane deployable LDR, LLB/TUM (right) tests under micro-gravity environment of an Airbus A300 zero-g flight

A duration of a free fall zero gravity in drop facilities (specially built free fall towers and vertical tunnels) are limited in time that is about five Seconds [2]. For example, free fall time in the deepest (145 m) vertical tunnel at NASA's Zero Gravity Research Facility is only 5.18 s. These kind of facilities are best suited for the deceleration tests of the satellite structures.

Hidrobuoyancy is one of the most effective methods for simulation of the micro-gravity conditions of free space environment. This method is widely used for training of astronauts. Application of buoyancy methods for deployment of LDRs is limited due to high drag induced by the water environment. Mentionable is the fact, that the method can be applied as a gravity compensation in some special cases of deployable truss and latticed structures. A clear example of application of hidrobuoyancy method for gravity compensation is the test conducted by Georgian Technical University (GTU) shown in Fig. 2.

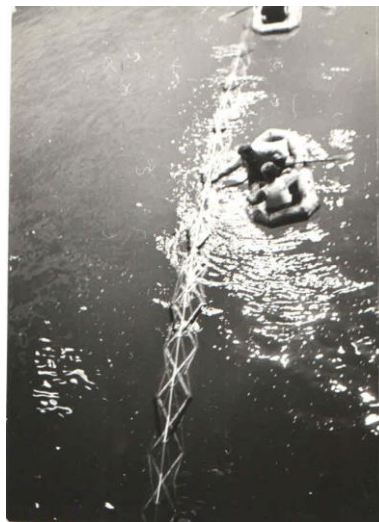


Fig. 2. Deployment of a truss structure with a triangular cross section at GTU

A truss structure of 18m length in deployed configuration with a triangular cross section has been deployed in a 40 m diameter tank in the water. The weight of the structure was compensated via floating tubes. The performed test clearly indicates the high influence of the drag on the deployment process. In the case of mechanical method for gravity compensation the structure has been deployed in 6 seconds, while the full deployment took more than one minute in the case of hidrobuoyancy (see Fig. 2). In most structural applications hidrobuoyancy is not suitable due to criticality of moisture uptake by the structure and complications of its drying.

In some special cases zero gravity environment for ultra-lightweight objects can be simulated via balloons filled with light gas. This method is also a case of buoyancy method but in air environment [10]. A negative aspect of this method is again the drag induced by air.

Due to the above mentioned limitations, mechanical systems are mostly used for offloading and simulation of near-zero gravity conditions for ultra-lightweight structures of large sizes. In most of gravity compensation structures developed by the leading research centres worldwide the gravity force of test objects is compensated by springs or counterweights, which are interconnected via a system of cables, carts moving on rails/guides and pulleys.

A GCS for solar panel deployment shown in Fig. 3 [3, 4] uses a suspension via springs, while GCS in Fig. 4 [5] is based on counterweights. In contrast to the previous system several guides are used for an umbrella type deployment scheme of the reflector.

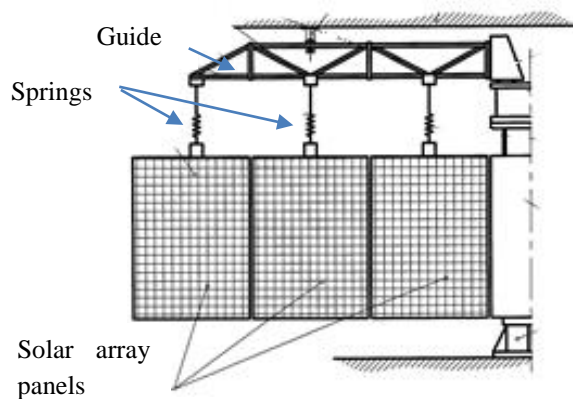


Fig. 3. Mechanical suspension GCS used for solar panel deployment

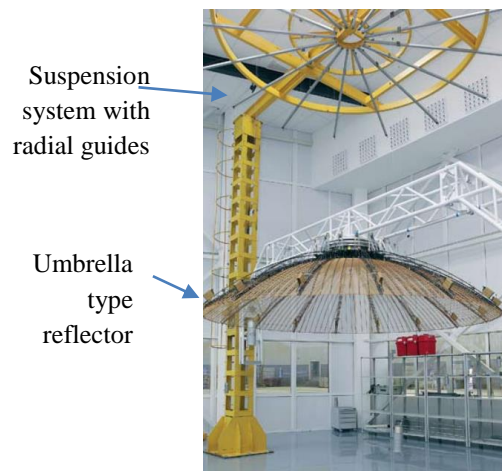


Fig. 4. Mechanical GCS with counterweights used for testing of a large deployable reflector

Fig. 5 shows other examples of structures of offloading systems based on the weight compensation [6].



Fig. 5. Mechanical GCS used for testing of a large deployable reflector

Springs used for suspension in GCS together with a guide allow for a horizontal movement freedom of the test object. Like in the example given in Fig. 3, parts of the structure can move freely in the horizontal direction therefore gravity influence is minimized. Counterweights used in the GCS allow additional vertical freedom of the structure, giving an advantage, although double weight will have some negative influence, e.g. during dynamic tests, to be taken into account.

Constant force springs can add a vertical movement capacity to the spring suspension systems. Some active control systems are also used to extend suspension systems to the vertical movement freedom of the test object. In any case, suspension cable length with springs or with counterweights plays significant role: the longer the better decoupling of the suspension system from the GCS itself.

In the 80s of last century three test rigs have been developed and built by the Institute of Structures, Special Systems and Engineering Maintenance (formerly Institute for Space Constructions) of GTU. These served as an assembly jig and a test bench for deployable space reflectors up to 30m in diameter. The GCS was based on the mechanical method and was composed of radially guiding rails with freely movable carts and pulleys (see Fig. 6).



Fig. 6. Deployment of a 30m diameter reflector on a mechanical GCS developed by GTU

Similar GCS was designed manufactured and utilized during the pre-flight tests of the Georgian mesh reflector flown on board of the space station MIR in 1999.

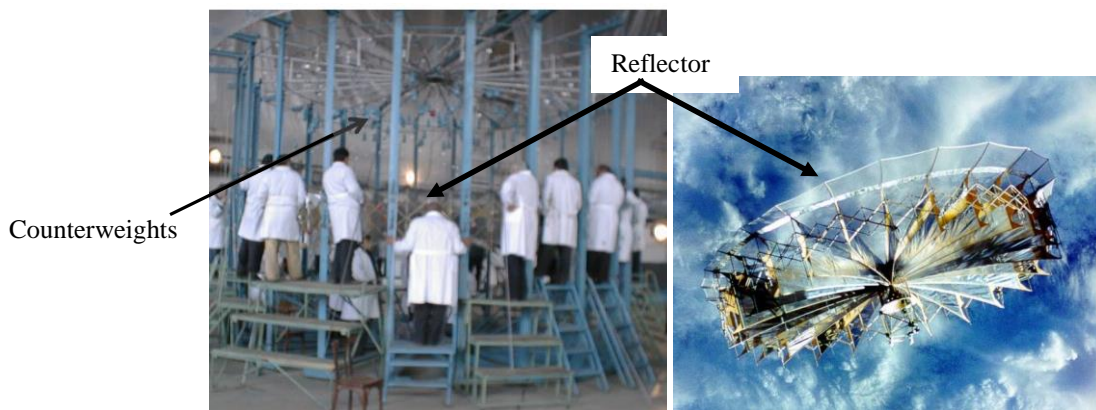


Fig. 7. Georgian Mesh Reflector under a mechanical GCS and in orbit weightlessness

All the compensation systems based on above-mentioned principle have the same characteristic problem, namely friction forces in the pulleys and bearings, having a negative influence on the free deployment of the structure. There are several methods to reduce the effect of friction: double or triple bearings, magnetic and pneumatic active supports for example. A rather complex and expensive electro-mechanical system has been developed in Russia. The system consists of special load cells (load measuring devices), which transmit the tension of the cable and its inclination for any moment of deployment. The data is then post-processed via computer and vertical and horizontal actuators are actuated for decreasing of deviations caused by friction to minimum [7].

Another interesting method of frictionless movement is the use of air tracks. An example of frictionless movement using an air track is shown in Fig. 8 [8]. A guide with a closed triangular cross section is equipped with a certain small holes pattern, an air compressor creating an air flow is connected to the tube. As a result a small frictionless on the guide moving platform is acquired. The idea is also utilized in some transportation methods and in some attractions (see Fig. 8) [9].

On-ground deployment testing of LDSs is related to one more problem, namely measurement of the deformations and stresses arising during the deployment. A special care has to be taken by choosing of measurement technique for this kind of structures in order to avoid deformations induced by measuring devices and their communication cables.

It can be concluded, that development of this type of complex and expensive structures is only worth for qualification tests. For the early stages of development of deployable structures and for feasibility study of concepts much simpler structures can be utilized.

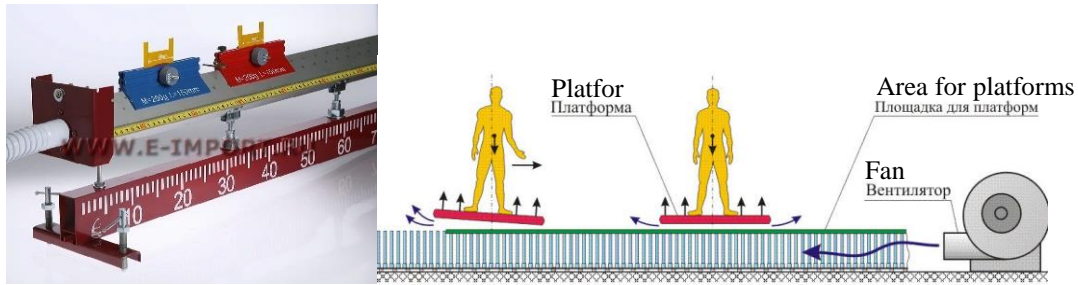


Fig. 8. Air track as a gravity compensation system

A simple and effective solution for gravity compensation is used in a deployable structure developed at LLB TUM [15]. A demonstrator of a large deployable reflector is deployed on the floor by special spherical balls attached to the structure (Fig. 9).

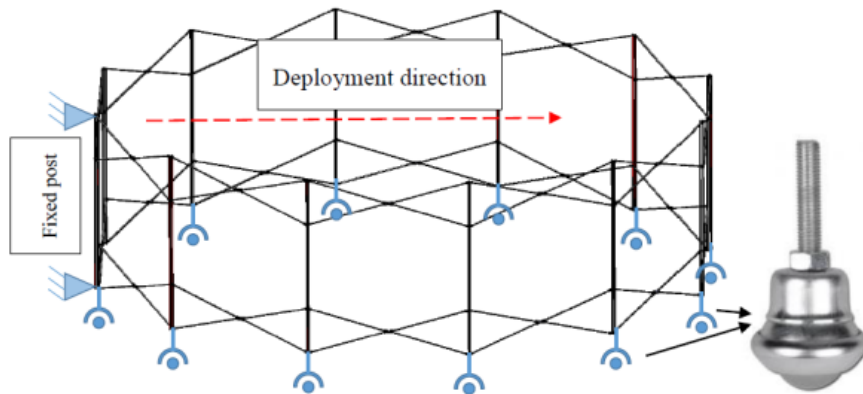


Fig. 9. Rolling ball concept for gravity compensation structure

Anyway, in orbit deployment and functionality test (Fig. 7, right) is the best “simulated” weightless environment but it is also most expensive one.

3. SHAPE ACCURACY MEASUREMENT METHODS

The reflective surfaces of LDRs are mostly made of very thin shell-membranes or knitted metal wire meshes. These materials show a high sensitivity to mechanical loads, thus only non-contact measurement methods for shape measurements of this kind of structures can be utilized. To this kind of methods geodesic, photogrammetric and lased based methods can be highlighted.

Some time ago the geodesic methods have been widely used for shape measurements of reflecting surfaces. Fig. 10 shows an example of geodesic measurement method [11].

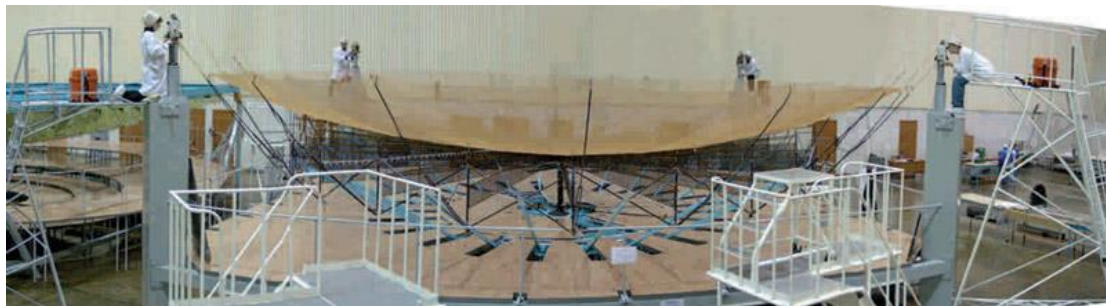


Fig. 10. Geodesic shape measurement method for reflecting surfaces

The shape of a 4m aperture diameter LDR breadboard developed by GTU has also been measured utilizing a geodesic measurement technique. High accuracy electronic levelers have been used. An auxiliary fixed basis system consisting of four rigid metal towers has been built around the test rig in order to make this measurement possible (Fig. 11).



Fig. 11. Shape measurement using tacheometers mounted on rigid towers

A special care has to be taken while measuring shapes of reflecting surfaces made of thin shell-membranes or knitted meshes, in order to take into account deformations induced by the gravity. Gravity compensation of a highly flexible shell-membrane or of metal mesh is almost impossible without introduction of large deviations in shape measurements. In order to subtract gravity deformations of metal mesh the shape of the reflecting surface has been measured in two positions relatively to gravity vector: cup up and cup down positions have been measured. Acquired data gives an opportunity to subtract the gravity induced deformations and predict the reflecting surface shape under zero gravity conditions. The method can be utilized if high shape repeatability has been proven with several measurements after folding and deployment of the reflector.

Nowadays photogrammetry (also called videogrammetry) measurement system is widely used for shape accuracy measurements. Fig. 12 shows an example of shape measurement of reflecting surfaces using a photogrammetry system at TUM involving a camera system (single or multi cameras), two scale bars, a coordinate cross and coded and non-coded retro-reflective markers.

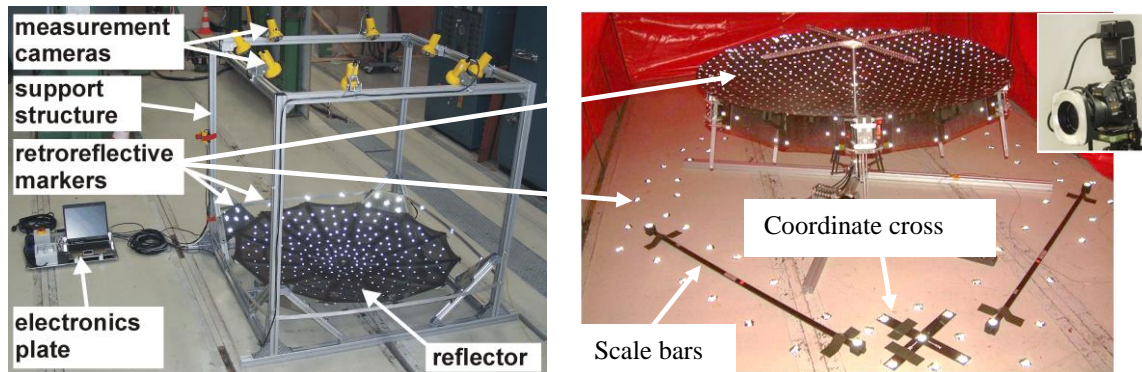


Fig. 12. Shape measurements using photogrammetry: measured with 8 synchronized camera system during the zero-g flight (left), measured with a single moving camera (right)

Measurement accuracy of the photogrammetry system is in the range of $10\mu\text{m/m}$, although for larger diameters large size calibrated scale bars are required for keeping the high accuracy of the measurement. Markers can be of different types: along with the retro-reflective markers contrast markers are also used, while fully non-contact photogrammetry measurements involve dot-projection techniques. The latter type of markers enable photogrammetry measurements of extremely thin lightweight membrane structures (of non-diffuse surfaces) even there are methods for transparent

membranes dot-projection. The limitation of this type of markers relates to the impossibility of tracking of the deformation of a single point through the different deformed states, while reflective markers enable point tracking.

Laser radar is a new technique of fast measurements of very large sizes. Up to 30 m distance (60 m in diameter) can be measured with the same accuracy of $10\mu\text{m/m}$. It gives a full image of the object and is very useful to measure any local shape deviation. This technique is preferred nowadays for shape measurements for fast measurement and short data post-processing time with less effort although it is one of the most expensive measurement system.



Fig. 13. Laser radar measurement system from Nikon Metrology

Some peculiarities of GCS systems arise during the on-ground experimental modal analysis of lightweight deployable structures. One has to deal with double amount of structural weight or additional stiffnesses of the suspension springs for the modes representing out-of-plane (vertical direction) oscillations. Horizontal oscillations will have a minimum influence. Assessment of the influence of counterweights used for gravity compensation can be done by multiplying the measured frequency by $\sqrt{2}$ since the mass of the elastic systems is doubled by the counterweights. In addition, taking into account frictions in the pulleys stiffness of the cables (springs) is required for precision assessment of the Eigen frequency in deployed configuration (a so called orbital stiffness). A different type of GCS has been designed for overcoming these problems using so called flying beams [13] (see Fig. 14).

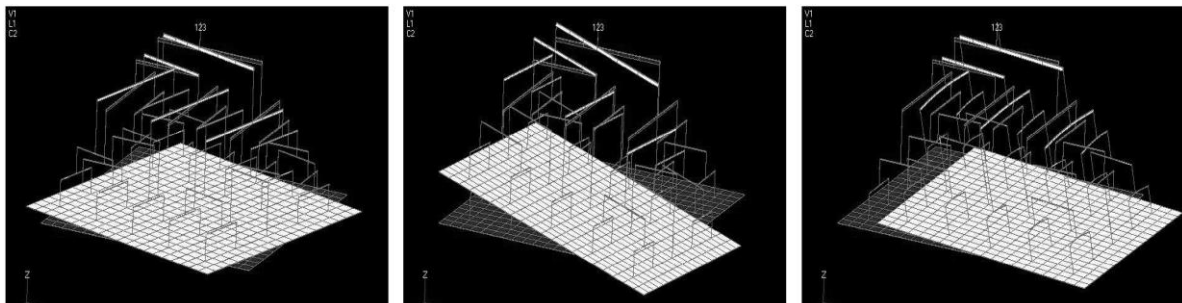


Fig. 14. Flying beam concept for gravity compensation

This method can be effectively applied for dynamic tests in free-free conditions, while shall be applied with caution for deployment tests while there is a high risk of arising folding and deployment problems in the case of application for large size deployable structures.

4. CONCLUSIONS

On-ground testing of large space structures is connected to many specific problems for simulating approximated space environment. In this paper the methods of mechanical testing of large deployable lightweight structures in a simulated micro-gravity conditions are summarized with emphases on deployment, stiffness and accuracy tests.

The following gravity compensation methods have been addressed:

Free fall methods:

- Parabolic zero-g flights
- Free fall towers

Buoyancy methods

- Hydro-buoyancy
- Air buoyancy

Mechanical methods

- Counterweights and related
- Springs suspension
- Constant force/torque springs
- Combined springs and counterweights

Active methods

- Magnetic
- Pneumatic
- Electro-mechanical

In orbit testing in weightlessness

RF testing of LDRs will most likely need similar systems as deployment tests for gravity compensation with additional care about minimizing the influence of GCS on the RF properties of a test article.

REFERENCES

- [1]. <http://global.jaxa.jp/projects/sat/ets8/topics.html>
- [2]. http://en.wikipedia.org/wiki/File:Zero_Gravity_Facility_-_GPN-2000-001454.jpg
- [3]. <http://bankpatentov.ru/node/482293>
- [4]. <http://www.findpatent.ru/patent/237/2376217.html> (RU 2376217)
- [5]. <http://www.iss-reshetnev.ru/images/File/newspaper/2011/255.pdf> Сибирский Спутник, 5№14(255),10 мая, 2011
- [6]. <http://gopressa.ru/pressa/pdf/1624/1624-1.pdf> «НПО ПМ – Малое конструкторское бюро» как дочернее предприятие ФГУП «Научно-производственное объединение прикладной механики имени академика М. Ф. Решетнёва» (сегодня ОАО «Информационные спутниковые системы» имени академика М. Ф. Решетнёва)
- [7]. <http://www.iss-reshetnev.ru/images/File/magazin/2009/m7-screen.pdf>, Журнал «Информационные спутниковые системы» №7, 2009г, (ОАО «ИСС» РЕШЕТНЁВ). Система Обезвешивания Крупногабаритных Рефлекторов
- [8]. <http://www.e-import.ru/index.php?page=579>
- [9]. http://www.ski.ru/static/750/2_32101.html
- [10]. В.А.Тарасов, Д.В.Чугуев МГТУ им. Н.Э.Баумана „Методика Обеспечения Требуемых Геометрических Параметров Мало жестких Конструкций Ркт В Процессе Их Обезвешивания При Помощи Воздушных Шаров“, <http://www.ihst.ru/~akm/3019t.pdf>
- [11]. <http://promgeo.com/services/astro>
- [12]. Datashvili, L.; Lang,M.; Huber,M.; Baier,H.: Accuracy study of a space deployable antenna reflecting surface under 0G and 1G conditions. In: DGLR Jahrbuch Bd. III 2006. DGLR, 2006
- [13]. Greschik, Gyula, and W. Keith Belvin. "High-fidelity gravity offloading system for free-free vibration testing." *Journal of Spacecraft and Rockets* 44.1 (2007): 132-142.
- [14]. Marco Straubel, Joachim Block, Michael Sinapius, and Christian Hühne, "Deployable Composite Booms for Various Gossamer Space Structures", 52nd AIAA/ASME/ASCE/AHS/ASC Structures, Structural Dynamics and Materials Conference, 4 - 7 April 2011, Denver, Colorado, USA, <http://enu.kz/repository/2011/AIAA-2011-2023.pdf>
- [15]. Datashvili, L. "Foldability of hinged-rod systems applicable to deployable space structures", *CEAS Space Journal*, Springer, 2013, 5, 157-168

ACKNOWLEDGEMENT

Authors would like to thank Mr. N. Maghaldadze, LSS, for his assistance.

NOVEL LARGE DEPLOYABLE ANTENNA BACKING STRUCTURE BREADBOARD TEST CAMPAIGN

V. Fraux⁽¹⁾, J. R. Reveles⁽²⁾, M. Lawton⁽³⁾

^(1,2,3) *Oxford Space Systems Ltd, Harwell, OX11 0QX, UK*

⁽¹⁾ vincent.fraux@oxfordspacesystems.com

⁽²⁾ juan.reveles@oxfordspacesystems.com

⁽³⁾ mike.lawton@oxfordspacesystems.com

ABSTRACT:

The Oxford Space Systems (OSS) deployable structures team undertook the development of a novel outer ring mechanism suitable for a Large Deployable Antenna (LDA) capable of supporting both a Carbon Fibre Reinforced Silicon (CFRS) reflector surface as well as a more conventional metal mesh. This led to the realisation of a 4 metre diameter breadboard (BB) demonstrator of the deployable backing structure. The purpose of the breadboard was to validate and demonstrate the kinematics of the chosen concept together with some of the key benefits of the selected deployable ring structure. The concept selected for the structure is an adaptation of the Sarrus mechanism with a pantograph adjusted to maintain a constant angle between the neighbouring vertical bars and therefore maintain a constant pyramid angle. Although the conical version of the Sarrus concept is more complex, it is stiffer than the prismatic version. Crucially, it also allows modularity as long as the ring maintains a hexagonal shape. The OSS LDA structure is a ring comprising 12 facets, synchronised via the pantograph and actuated via 3 vertical active members containing embedded actuators. Additionally, all 'V' joints and scissor joints are spring loaded to ensure the deployment loads are well distributed throughout the structure and the deployed configuration is maintained. The breadboard structure weighs 7.0kg and deploys from a minimum diameter of 0.23m to 4m. When the structure is stowed, an internal cylindrical volume of 0.18m diameter is achieved to allow the storage of the reflector surface material and supporting cable network.

Several tests were conducted on the completed breadboard. This paper provides a summary of the testing activities and results for the LDA BB. The BB performed very well in terms of mass, volume, deployment time, power, kinematics, repeatability and in-plane stiffness. The successful deployment test of the BB demonstrates the kinematics, the ability to tension a cable network and repeatability of 0.02mm from the centre of the structure. It deploys in 5 minutes 21 seconds with an average power of 6W. The BB can be readily stowed in a similar amount of time with little or no manual intervention.

The stiffness of the structure was measured and show a free-free in-plane natural frequency of 1.3Hz and a fixed-free in-plane frequency of 0.8Hz.

The LDA structure BB test campaign has proven the viability, competitive performance and robustness of the novel LDA concept developed by the OSS team.

1 INTRODUCTION

The Oxford Space Systems (OSS) deployable structures team undertook the development of a novel outer ring mechanism suitable for a Large Deployable Antenna (LDA) capable of supporting both a Carbon Fibre Reinforced Silicon (CFRS) reflector surface as well as a more conventional metal mesh. This led to the realisation of a 4 metre diameter breadboard (BB) demonstrator of the deployable backing structure (Fig 1). The purpose of the breadboard was to validate and demonstrate the kinematics of the chosen concept together with some of the key benefits of the selected deployable ring structure. The concept selected for the structure is an adaptation of the Sarrus mechanism with a pantograph adjusted to maintain a constant angle between the neighbouring vertical bars and therefore maintain a constant pyramid angle. Although the conical version of the Sarrus concept is more complex, it is stiffer than the prismatic version. Crucially, it also allows modularity as long as the ring maintains a hexagonal shape. The OSS LDA structure is a ring comprising 12 facets, synchronised via the pantograph and actuated via 3 vertical active members containing embedded actuators. Additionally, all 'V' joints and scissor joints are spring loaded to ensure the deployment loads are well spread throughout the structure and the deployed configuration is maintained. The breadboard structure weighs 7.0kg and deploys from a minimum diameter of 0.23m to 4m. When the structure is stowed, an internal cylindrical volume of 0.18m diameter is achieved to allow the storage of the reflector surface material and supporting cable network. Several tests were conducted on the breadboard with a low cost approach to determine the viability of the concept.

This paper provides a summary of the low cost testing activities and results for the LDA BB developed and built by the OSS team

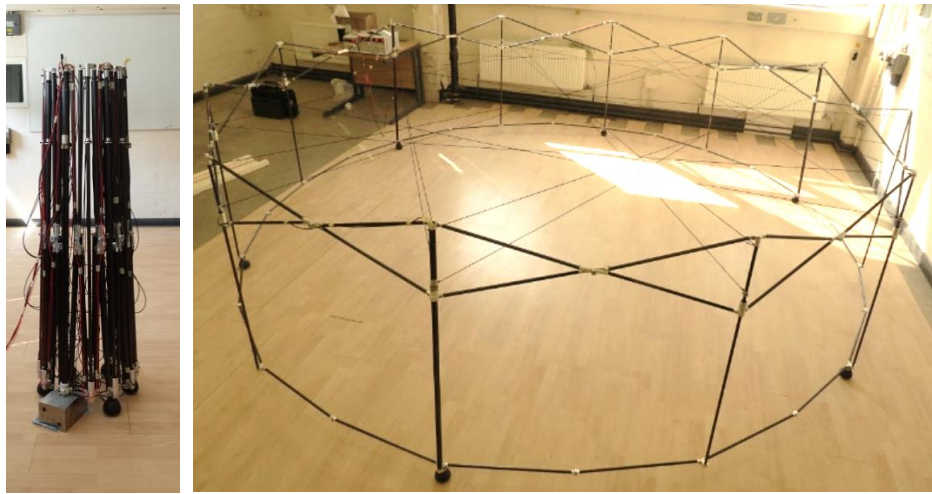


Fig. 1: LDA 4m BB in stowed and deployed configuration

2 BUDGETS

Table 1 shows the budgets measured on the BB. The deployed diameter shown is the average diameter measure from 5 deployments.

Table 1: Budgets measured on BB

Budget	Dimension measured or (estimated)	Margin	Dimension including margin
LDA Structure (incl. actuators) mass	7.0 kg	-	7.0 kg
4m Shell-membrane	(6.300 kg)	20%	7.560 kg
Total mass	-	-	14.56 kg
Deployed top diameter	3.953 m	-	3.953 m
Stowed top diameter	0.23 m	-	0.23 m
Stowed bottom diameter	0.33 m	-	0.33 m
Stowed internal diameter	0.18 m	-	0.18 m
Height	1.07 m	-	1.07 m
Deployment time	321 s	-	321 s

3 DEPLOYMENT REPEATABILITY TEST

The repeatability test is to determine if the structure, when fully deployed, comes to rest in a repeatable and predictable position when stowed and deployed a number of times from a fixed datum. The test comprised the same deployment sequence of the structure during 5 events, with measurement of the position of the vertical members (via optical targets and a short range theodolite) after each deployment. The data was then analysed to determine how repeatable the structure was in terms of the maximum variance in position between full deployments and time of deployment. Additionally, the

power consumption was monitored for the three first deployment to determine the repeatability of the power profile of the three actuators.

For the deployment, the LDA is mounted on 6 evenly spread spherical wheels for gravity compensation on a laminate flooring to minimise the friction with the floor. An elastic cord network is attached to the structure to deliver a 7 g/cm tension mimicking the elasticity of the reflector surface. One of the active members is maintained in position on the floor by a heavy steel fixed support (Fig 2).

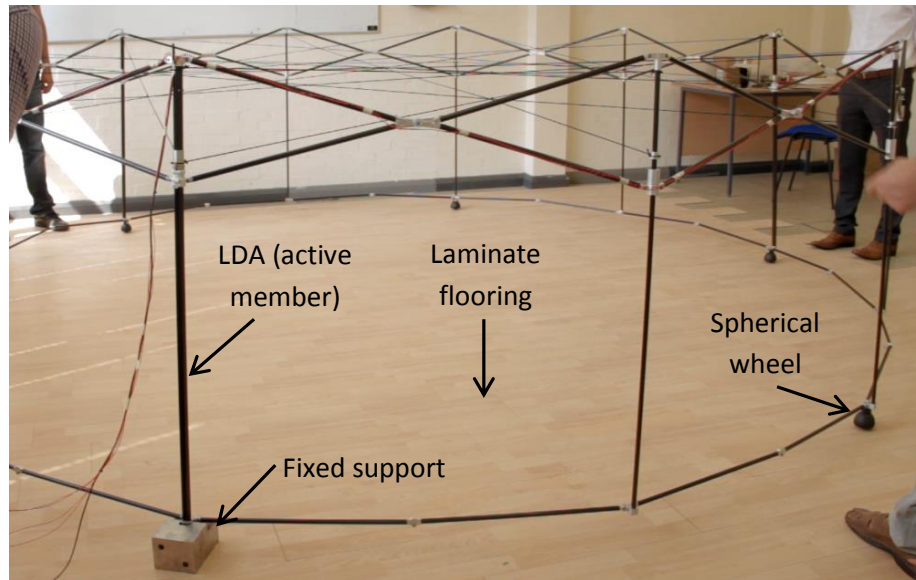


Fig. 2: LDA deployment setup

The 3 actuators (Unit 1, Unit 2 and Unit 3) are independently connected to dedicated power supplies with current limitation. The maximum power that can be drawn by the actuators is limited to 5W in order to prevent possible overheating or damage to the structure in case of jamming.

Optical targets are placed at the top of each vertical member (Fig 3) to measure their 3D position using a theodolite.

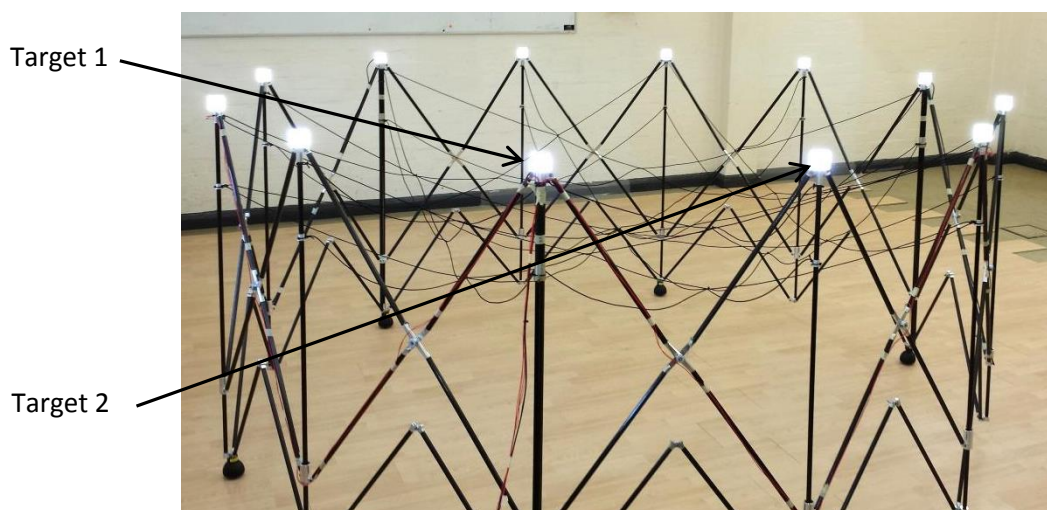


Fig. 3: LDA with optical target mounted at the top of each vertical member

The BB was successfully and smoothly deployed 5 times without any form of jamming. The data collected from the measurements of the optical targets position after each of the 5 deployments was analysed to determine the repeatability. Table 2 shows the calculated distance of each target from target 1. Targets 5, 6, 7 & 8, being the furthest away from Target 1, are predictably the one with the highest repeatability error: up to $\pm 14\text{mm}$.

Table 2: Repeatability test, vertical members distance from target 1

REPEATABILITY - distance from target 1 (m)									
	Deploy. 1	Deploy. 2	Deploy. 3	Deploy. 4	Deploy. 5	Min.	Max.	Average	error ($\pm\text{mm}$)
Target 1	0.000	0.000	0.000	0.000	0.000	0.000	0.000	0.000	0.000
Target 2	1.047	1.047	1.049	1.047	1.049	1.047	1.049	1.048	0.001
Target 3	1.937	1.946	1.940	1.937	1.940	1.937	1.946	1.940	0.005
Target 4	2.746	2.743	2.736	2.742	2.749	2.736	2.749	2.743	0.008
Target 5	3.333	3.337	3.318	3.329	3.337	3.318	3.337	3.331	0.013
Target 6	3.761	3.767	3.746	3.765	3.760	3.746	3.767	3.760	0.014
Target 7	3.859	3.860	3.847	3.871	3.856	3.847	3.871	3.859	0.012
Target 8	3.763	3.767	3.763	3.780	3.758	3.758	3.780	3.766	0.014
Target 9	3.339	3.344	3.345	3.353	3.338	3.338	3.353	3.344	0.009
Target 10	2.757	2.760	2.758	2.759	2.753	2.753	2.760	2.757	0.004
Target 11	1.948	1.937	1.947	1.939	1.950	1.937	1.950	1.944	0.008
Target 12	1.047	1.051	1.048	1.050	1.049	1.047	1.051	1.049	0.002
Center	1.902	1.906	1.896	1.909	1.901	1.896	1.909	1.903	0.007

Table 3 shows the calculated distance of each target from the calculated centre of the LDA structure, a different way of estimating the repeatability of the deployment. The maximum repeatability error of vertical member position measured over 5 deployments is $\pm 10\text{mm}$. The mean radius of the structure has an outstanding repeatability of $\pm 1\text{mm}$.

Table 3: Repeatability test, vertical members distance from the center of the structure

REPEATABILITY - distance from centre (m)									
	Deploy. 1	Deploy. 2	Deploy. 3	Deploy. 4	Deploy. 5	Min.	Max.	Average	Delta
Target 1	1.902	1.906	1.896	1.909	1.901	1.896	1.909	1.903	0.007
Target 2	1.982	1.981	1.984	1.989	1.977	1.977	1.989	1.983	0.006
Target 3	1.993	1.988	2.005	1.993	1.995	1.988	2.005	1.995	0.010
Target 4	2.017	2.014	2.019	2.010	2.020	2.010	2.020	2.016	0.006
Target 5	1.952	1.952	1.946	1.942	1.957	1.942	1.957	1.950	0.008
Target 6	1.993	1.994	1.983	1.989	1.992	1.983	1.994	1.990	0.007
Target 7	1.957	1.954	1.951	1.961	1.955	1.951	1.961	1.956	0.005
Target 8	1.992	1.994	1.998	2.002	1.989	1.989	2.002	1.995	0.007
Target 9	1.956	1.958	1.967	1.960	1.958	1.956	1.967	1.960	0.007
Target 10	2.020	2.019	2.023	2.012	2.022	2.012	2.023	2.019	0.007
Target 11	1.995	1.990	1.989	1.981	2.001	1.981	2.001	1.991	0.010
Target 12	1.965	1.966	1.954	1.961	1.964	1.954	1.966	1.962	0.008
Center	0.000	0.000	0.000	0.000	0.000	0.000	0.000	0.000	0.000
Mean rad.	1.977	1.976	1.976	1.976	1.978	1.976	1.978	1.977	0.001

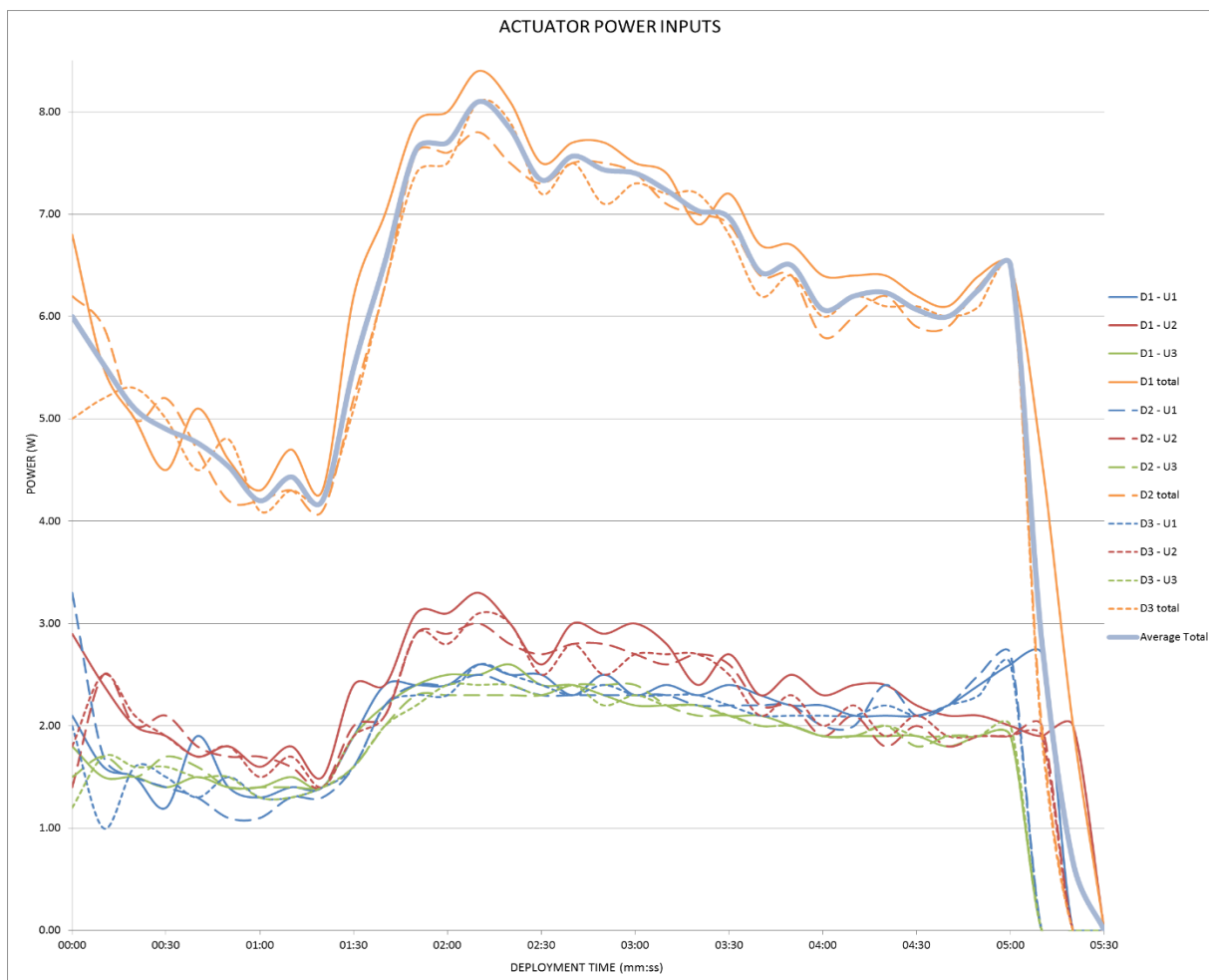
Table 4 shows the deployment times measured for the 5 deployments. The average time is 5min 21s while the difference between the shortest and the longest recorded time is 7s.

Table 4: Repeatability test, deployment time

Deployment time (mm:ss)							
Dep. 1	Dep. 2	Dep. 3	Dep. 4	Dep. 5	Min	Max	Delta
05:24	05:17	05:18	05:22	05:23	05:17	05:24	00:07
Average deployment time					05:21		

In order to understand the power consumption, distribution and evolution of the deploying structure, the current supplied to the actuators has been monitored for the first, second and third deployments. The current was recorded for each actuator (unit 1, 2 and 3) every 10s during the said deployments and the calculated power was plotted against time in Fig 4.

The actuator power appears consistent over the 3 deployment events. Unit 2 power consumption (in red) is slightly higher than unit 1 (in blue) and 3 (in green); nevertheless all follow the same profile. The total power for each deployment (in orange, sum of 3 units) shows consistency. The maximum total power recorded was 8.40W. The thick light blue line on Fig 4 is the average total power over the 3 deployments.

**Fig. 4: Actuators (U1, U2 & U3) power supply during 3 deployments (D1, D2 & D3)**

4 STRUCTURAL TEST

In order to quantify the stiffness of the LDA BB, a static and a dynamic test were performed.

4.1 Static Test

The principle of the static test is to apply a static load to the structure and measure the deflection. The static load is applied radially inward and outward to the structure at the top of the 7th vertical member, directly opposite to the fixed active member (1st member, refer to Figure 2). The load is applied using calibrated weights and a simple cable and pulley system to ensure repeatability in the direction and magnitude of the force applied. The displacement of the 7th member when a load is applied is measured using the theodolite and reflective targets and compared to the original position. The test is performed with 5N and 10N loads twice and the average of the 2 outward loading test results together with the 2 inwards pulling test results are calculated and illustrated by the graph in Fig 5.

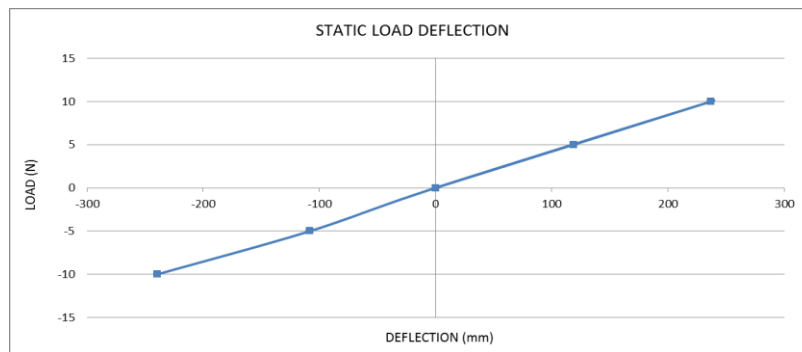


Fig. 5: Static test result graph

4.2 Dynamic Test

A dynamic test was conducted on the LDA to estimate the in-plane natural frequency in its deployed configuration. To conduct this test with a low cost approach, the BB was suspended above the ground using a 6 branch support structure and manually stressed and released to produce a response (Fig 6). The response was filmed and then analysed to extract the frequency via the number of oscillations and time. Two type of dynamic test were run:

- a Free-Free test for the in-plane mode frequency, performed 3 times and,
- a Fixed-Free test for the in-plane mode frequency, performed 5 times due to low quality of the response.

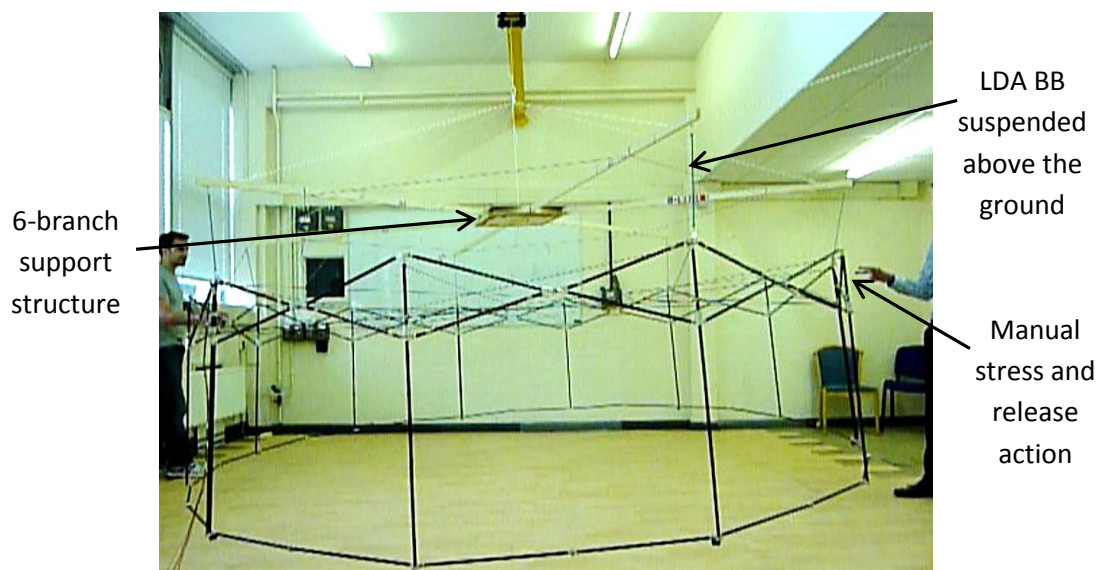


Fig 6: Dynamic test setup

The in-plane frequencies measured from the dynamic tests are reported in Table 5. The average frequency for the Free-Free configuration is 1.34Hz while the Fixed-Free configuration frequency is 0.8Hz.

Table 5: Dynamic test data

Free- free						
Time start		Time Stop		time (s)	Number of oscillation	Frequency (Hz)
Min	s	Min	s			
0	0.00	0	2.40	2.40	3	1.250
0	2.43	0	3.80	1.37	2	1.460
0	3.81	0	6.10	2.29	3	1.310
Average						1.34
Fixed - free						
Time start		Time Stop		time (s)	Number of oscillation	Frequency (Hz)
Min	s	Min	s			
0	0.00	0	6.70	6.70	5	0.746
0	6.71	0	14.33	7.62	6	0.787
0	14.34	0	20.77	6.43	5	0.778
0	20.78	0	27.00	6.22	5	0.804
0	27.01	0	31.63	4.62	4	0.866
Average						0.80

5 CONCLUSION

This paper reflects on the successful low-cost test campaign of the LDA backing structure BB built by the Oxford Space Systems (OSS) team.

The BB displays competitive mass, volume, deployment time, power, kinematics, repeatability and stiffness characteristics. The successful deployment test of the BB demonstrates the kinematics, the ability to tension a cable network and show a repeatability of 0.02mm from the centre of the structure. The structure achieves full deployment in 5 minutes 21 seconds with an average power of 6W. The BB can be readily stowed in a similar amount of time.

The stiffness of the structure was measured and show a Free-Free natural frequency of 1.3Hz and a fixed-free frequency of 0.8Hz.

The LDA structure BB test campaign has proven the viability, competitive performance and robustness of the novel LDA concept developed by the OSS team and provides a confident base upon which to progress the OSS design

REFERENCES

- [1]. C. Mangelot, J. Saniago-Prowald, K. Van T'Klooster, et al, *Large Reflector Antenna Working Group - Final Report*, ESTEC, 2010.
- [2]. L. Datashvili, H. Baier, E. Wehrle, T. Kuhn, J. Hoffmann, *Large Shell-Membrane Space Reflectors*, 51st AIAA/ASME/ASCE/AHS/ASC Structures, Structural Dynamics, and Materials Conference, AIAA 2010-2504, Orlando, (2010).
- [3]. V. Fraux, J. R. Reveles, M. Lawton, Z. You, *Novel Large Deployable Antenna Backing Structure Concepts for Foldable Reflectors*, CEAS Space Journal, Vol. 5, Issue 3-4, pp 195-201, (2013).

STRUCTURE ANALYSIS OF INFLATABLE SOLAR SAILS

Wei Jianzheng⁽¹⁾, Ma Ruiqiang⁽¹⁾, Tan Huifeng⁽¹⁾, Song Bo⁽¹⁾, Liu Yufei⁽²⁾

⁽¹⁾ *Science and Technology on Advanced Composites in Special Environments Laboratory*
Harbin Institute of Technology, Harbin 150080, China
Email: weijz@163.com

⁽²⁾ *Qian Xuesen Laboratory of Space Technology*
China Aerospace Science and Technology Corporation, Beijing 100094, China
Email: liuyufeihi@sina.com

ABSTRACT

According to the difficulty to solve the statics problem of the flexible solar sail structure which consists of the central control panel, inflatable boom, sail surface and other components, the displacement distribution of inflatable boom under gas pressure was analysed and the displacement of its ends was obtained first in this paper. Then, the static properties of the whole solar sail structure was analysed by that the displacement of the ends of inflatable boom as the boundary condition. Finally, the effecting law of the inflation pressure and the connection of the sail surface edge and inflatable boom on the vibration characteristics of the solar sail were studied. The results show that the structural modal frequency is approximately linear increase with the increase of inflation pressure; the vibration frequencies of the solar sail structure significantly increase by linking the inflatable boom and sail surface edge. So, the research in this paper is useful for the design of the solar sail structure.

Keyword: Solar sail; inflatable boom; mode; vibration characteristic;

1. INTRODUCTION

Solar sailing is a form of in-space propulsion that has yet to be demonstrated in free-flying form but continues to gain interest by those in the space community Government labs, private organizations, and academic circles alike have invested in developing the technologies necessary to enable this propellant-free source of spacecraft thrust.

The National Aeronautics and Space Administration^{[1][2]} (NASA), the Europeans^[3], and most recently notable the Japan Aerospace Exploration Agency^[4] have all dedicated resources to developing large solar sail technologies. A recent collaboration between the NASA Marshall Spaceflight Center and the Air Force Research Laboratory (AFRL) has yielded a small, 10m², solar sail free-flyer that packages into a 3 Unit Cubesat known as NanoSail-D^[5]. In 2010, AFRL has described a major portion of a test and analysis campaign designed to demonstrate that the FURL solar sail is ready for flight qualification. Through both structural analysis predictions and testing of material strengths, deployment motions, and deployed shape, the architecture was demonstrated to be analyzable and robust^[6]. Hiraku Sakamoto et.al proposes a method to store a large solar-sail membrane while ensuring repeatability of its stored configuration. The feasibility and effectiveness of the method is verified through a series of sail-storage experiments using 10m-size membranes. Large membranes used as a solar sail should be stored compactly to save the launch volume^[7]. Such a solar sail can be considered as a rigid-flexible multibody system mainly composed of a spinning central rigid hub, a number of flexible thin tethers, sail membranes, and tip masses. A simplified interplanetary kite-craft accelerated by radiation of the Sun (IKAROS) model is established in this study by using the absolute-coordinate-based (ACB) method that combines the natural coordinate formulation describing the central rigid hub and the absolute nodal coordinate formulation describing flexible parts^[8].

Solar radiation pressure, the physical source of solar sail thrust, is certainly not a new phenomenon. For decades spacecraft designers have considered the added force effects that a large, filled, reflective appendage might impart to the host spacecraft due to the reflection of sunlight photons. However, actually implementing a dedicated appendage for such a purpose has been rarely realized. Small solar sails may not be capable of soaring the distant, unexplored reaches of our solar system like has been envisioned for kilometer-sized systems. But small sails may soon serve an important function closer to home on earth-orbiting satellites. A dedicated, small sailcraft payload on thruster-laden spacecraft can greatly enhance the maneuverability of the host craft by providing a propellant-free source of thrust that can be quickly turned on or off.

2. THE FINITE ELEMENT MODEL OF THE SOLAR SAIL

In order to provide the acceleration of the spacecraft, the solar sail structure requires a large enough area for the weak sunlight pressure. However, it would require a large storage volume and larger transportation load if only use the traditional structure. Aiming at the actual instance that improving space transportation capabilities is more difficult, the solar sail structure which was designed consisting of a reflective sail membrane, a deployable sail support structure, and an attitude control subsystem. The storage area only is 0.01 times less than the expanded area of the solar soil structure. The air pump is used as the power source of the structure, and drives the inflatable booms to develop, which bring along the sail surface expand. The structural model and size parameters is shown in Fig. 1.

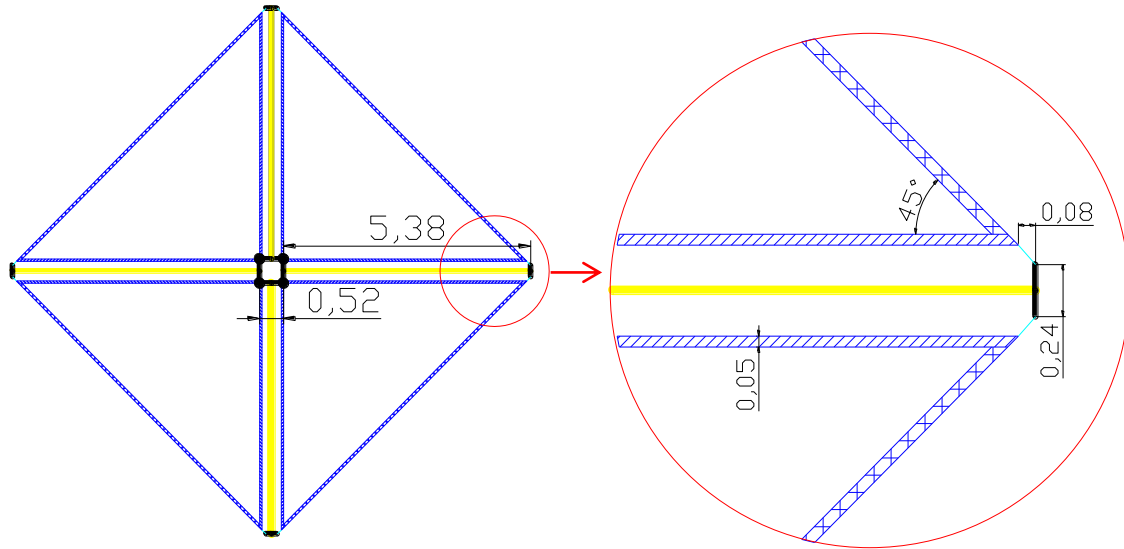


Fig. 1. The model of the solar sail structure (Unit: m)

The inflatable booms on the solar sail structure need some gas pressure to support the sail surface. Meanwhile, it would bring the inflatable booms and sail surface some stress. Therefore, the stiffening effect of stress under pressure needs to be considered for the calculation of the vibration characteristics of a solar. The vibration equation of the solar sail structure under the inflatable pressure can be described as follows:

$$M\ddot{U} + K_s U = Q \quad (1)$$

Where M is the mass matrix of sail structure, K_s is the solar sail structure stiffness matrix which is corrected by prestressed S , and Q is external excitation force.

The above equation can be normalized:

$$(K_s - \omega^2 M)\phi = 0 \quad (2)$$

Where ϕ is the modal shape matrix; and the above equation can be solved by block Lanczos iteration method.

For the analysis of the vibration characteristics of the solar sails structure, the stress and displacement of the solar sail structure under inflated pressure was calculated in the first place. The consideration for the solar sail nonlinear problems that consist of rigid-flexible coupling and large deformation is essential for the static analysis due to the solar sail structure have low density, low frequency, equal eigenfrequency and close eigenfrequency. Therefore, the implicit finite element method is not easy to converge for this nonlinear problem. An analytic method of fractional steps was used for the static analysis of the solar sail in this paper. The first step is that the deformation of inflatable booms under gas pressure is calculated using the Newton-Raphson nonlinear iteration, and the displacement of the connection that connecting the sail surface and the inflatable boom. Then, this displacement as the boundary condition, the static properties of the solar sail structure is calculated, and the displacement and stress distribution of the whole solar soil structure are obtained. Finally, based on the deformation configuration and the prestressed stiffening effect, the modal frequencies and mode shapes of the solar sail structure is calculated by the Lanczos iterative method. The flowchart of this method is shown in Fig. 2 .

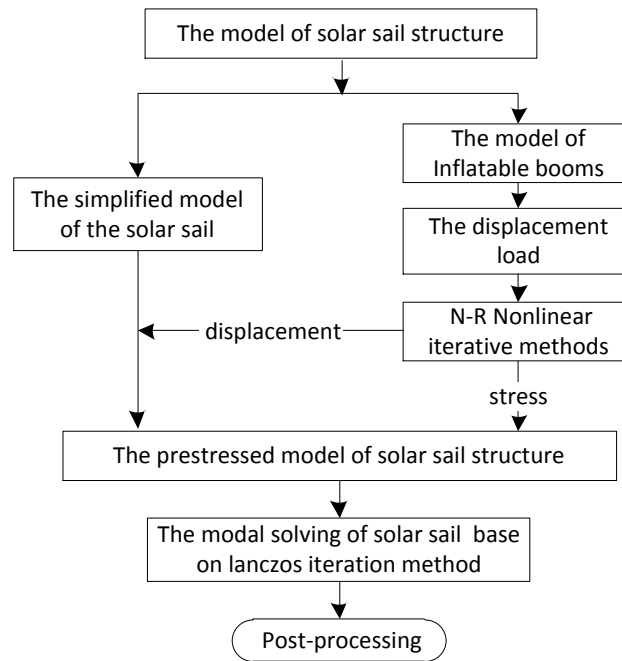


Fig. 2. The flowchart of the calculation of the vibration characteristics of the solar sail

In this paper, the inflatable booms of the solar soil structure consist of aluminum membranes, fastening tape and bi-stable thin shell structure of carbon fibers which ensure the stability of the state of being curled and extend. The fastening tap can ensure the stability of the inflatable expansion, and make certain the soil surface unfolding successfully. The thickness of the aluminum membranes is 0.14mm; the flexible bi-stable thin shell of carbon fibers is 0.35mm; the approximate booms of the end of inflatable extended arms for the suture 0.3mm. The aluminum membrane with the surface density $m=252\text{g/m}^2$, the young's modulus $E=10\text{GPa}$ and Poisson $\nu=0.33$ is considered. The finite element model of the part of inflatable booms and a quarter of the whole solar sail structure is shown in Fig. 2. There are 26996 shell 181 elements about the inflatable boom. A quarter of the solar sail structure has 83245 elements, which include 82633 membrane elements for sail surface, 560 beam elements for the inflatable boom, and 30 beam elements, 14 rope elements and 8 pole elements for the other parts. The cross section and material properties of the inflatable boom were chosen to ensure the model has an equivalent stiffness with the realistic structure.

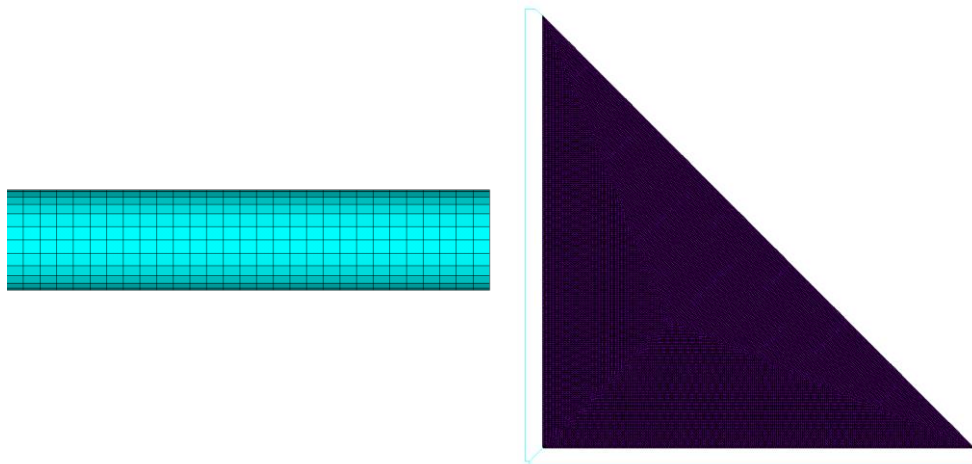


Fig. 3. The finite element model of the part of inflatable booms and a quarter of the whole solar sail structure

3. THE ANALYSIS OF THE STATIC MECHANICAL PROPERTIES OF THE SOLAR SAIL

According to the analysis method of the vibration characteristics of the solar sail structure, it is necessary to analyze the mechanical properties of the inflatable booms firstly. In this paper, based on the finite element method, the static mechanical properties of inflatable booms is analyzed under the gas pressure from 2.5KPa to 10KPa, and the

change law of the displacement of its ends and the maximum stress with the inflation pressure is obtained and plotted in Fig. 4. The results indicate that the inflatable boom is in the linear elastic stage when the inflatable pressure at 0 to 10KPa. With the increase of the inflation pressure, the displacement of the tip of the boom increase in slope of 0.05, and the maximum stress of boom increase in a non-linear, the non-linear equation can be fitted to:

$$\sigma_{\max} = -0.027P^2 + 1.213P + 0.027$$

Where σ_{\max} is the maximum stresses of the inflatable booms, the unit is MPa; P is the inflatable pressure, the unit is KPa.

When inflatable pressure increases to 10Kpa, the maximum stress of the inflatable boom is 9.42MPa and occurs at the joint connecting carbon fiber bi-stable rollable shell and aluminum film. Moreover, the stress of aluminum film is greater than the carbon fiber shell structure.

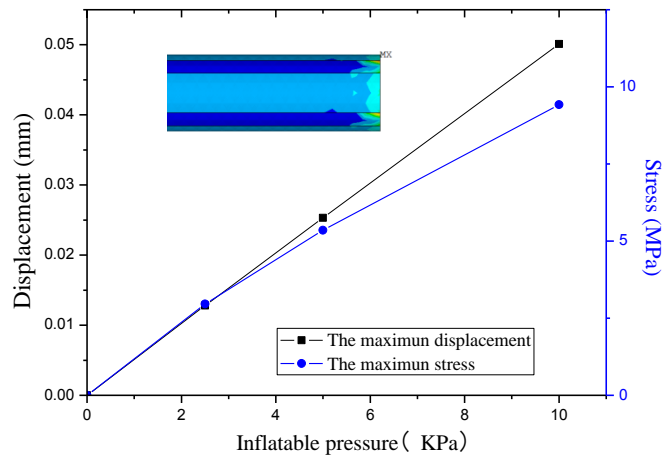


Fig. 4. The change curve of the maximum stress and displacement with the inflation pressure

The displacement and stress distribution of the solar sail structure are shown in Fig. 5. The solution show that the maximum displacement of the solar sail structure is 0.0501mm and occurs at the ends of the inflatable boom, and the maximum stress is 9.42MPa on the inflatable boom. Furthermore, the maximum stress of the sail surface occurs at the position link to the rope, and the value is 2.1MPa. This indicates that the connections require appropriate reinforcement.

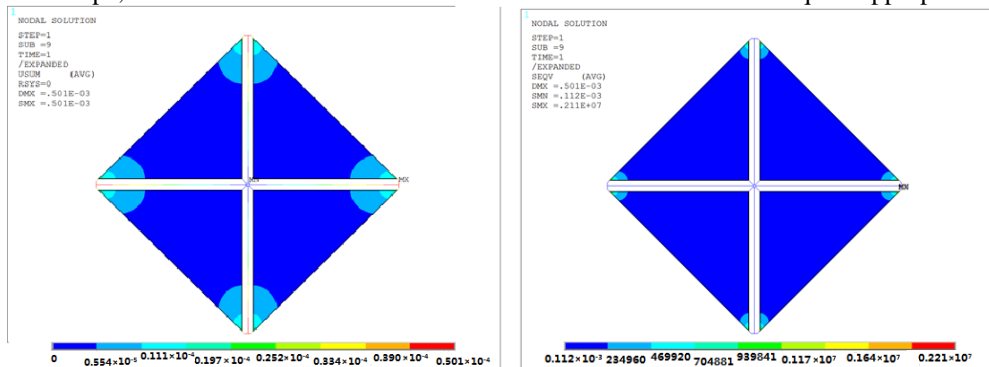


Fig. 5. The cloud pictures of displacement and stress in inflatable 10KPa

4. THE VIBRATION ANALYSIS OF SOLAR SAILS STRUCTURE

Based on the configuration and the stress distribution under the pressure in the inflatable booms, the modal frequency of solar sail structure was solved by lanczos iteration method in this paper. The rule of the changes of the modal frequency of solar sail structure with the pressure in the inflatable booms was obtained and plotted in fig. 5. The result show that the first three order modal frequencies of the structure slightly increased with the rise of the inflation pressure. The fundamental frequency of the solar sail structure increase 0.0019 HZ from 0.0043 HZ to 0.0062 HZ for the Inflation pressure from 2.5 KPa to 10 KPa. The fig.5 glance that the first 3 order modal frequencies are less than

0.012 HZ, and the adjacent modal frequencies is less than 0.004 HZ, which suggests the solar sail belongs to a typical low frequency, intensive frequency structure.

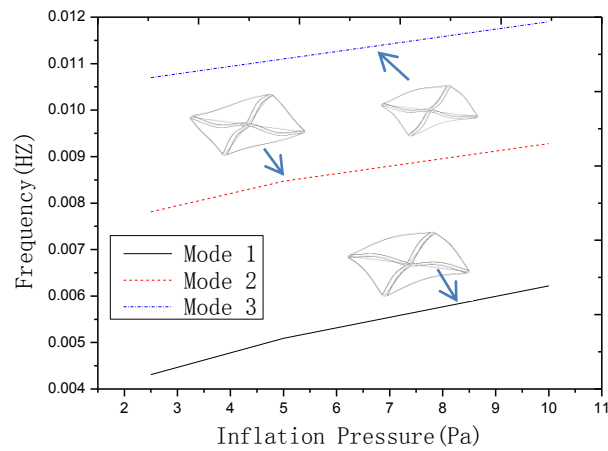


Fig. 6. The change laws of the first three modes of the solar sail with the inflation pressure

Moreover, it can be seen from Table 1 that the first six modes shapes are the vibration of the sail surface structure and the inflatable booms almost stationary. The stiffness of the sail could be improved if connected inflatable booms and the sail by some rope as shown in Fig. 7. To compare the modal frequency of the solar sail and the modified solar sail structure based on the finite element method, the effecting law of rope connecting on vibration frequency of the solar sail is obtained. Take the case of inflation pressure 10 KPa as example, the effecting law of rope connecting on the first 6 order modes of the structure is shown in Fig. 8. The result shows the modal frequency of the modified structure has increased significantly. The fundamental frequency rises nearly 16 times from 0.0063 HZ to 0.0063 HZ. Furthermore, the second and third modal frequencies of the structure also increase 15.7 and 11.8 times respectively. Thus, the conclusion that connecting inflatable booms and edges of the sail through corsages can improve the modal frequency of the solar sail is obtained.

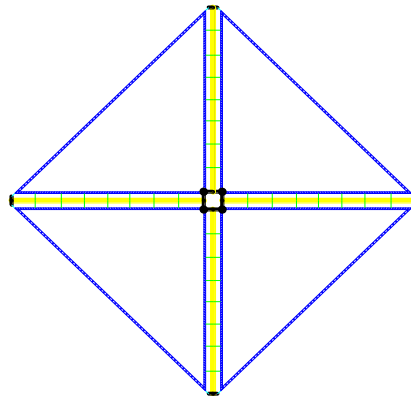


Fig. 7 The modal of the modified solar sail structure

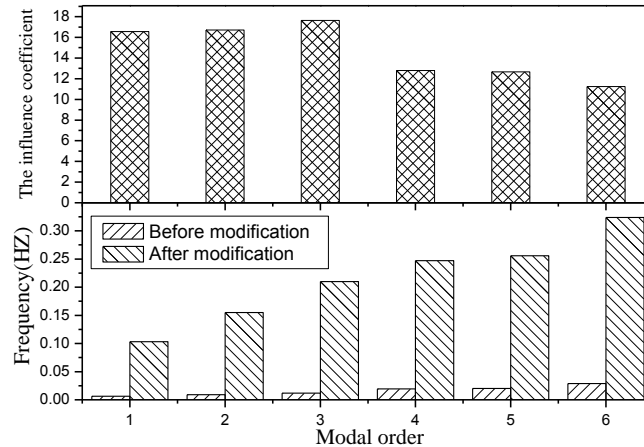
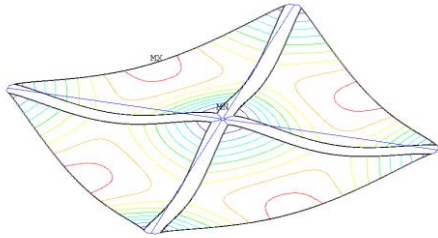
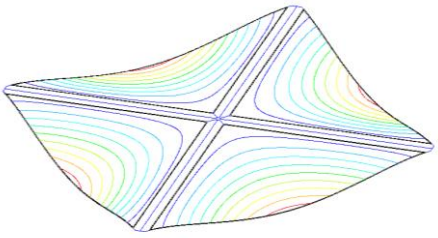
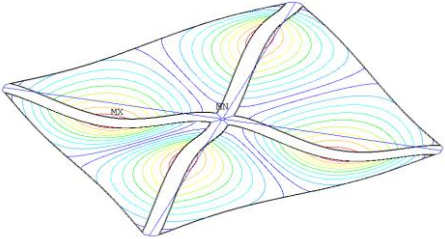
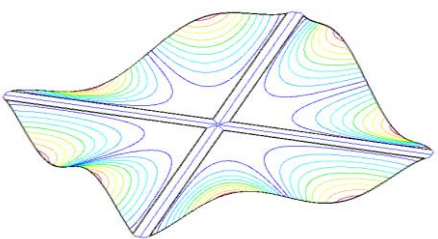
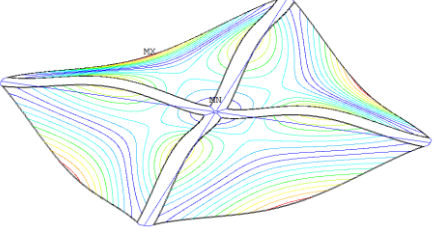
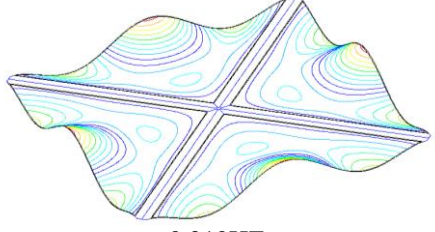
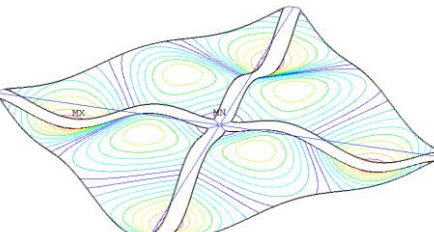
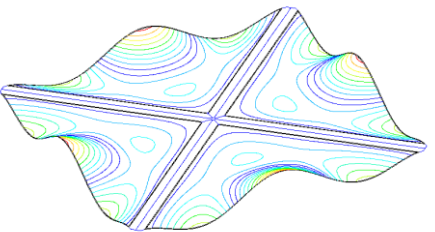
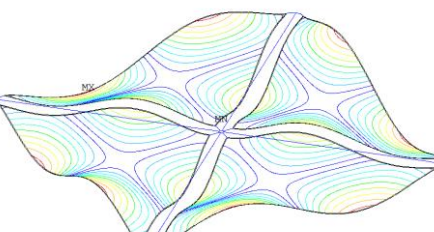
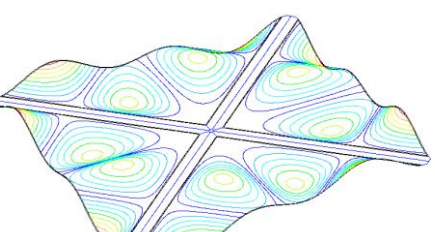


Fig. 8. The effecting law of rope connecting on the solar sail vibration frequency

Table 1 witness that the modal shapes of the solar sail structure under the 10 KPa inflation pressure. The solution shows the first six modes of sail structure is a vibration of sail surface. The first order mode is the vibration of the outside edges of the solar sail structure and drives the whole sail surface vibrate; the second order modal shapes is the vibration of the two edges of sail surface near the inflatable booms; the third order modal shapes is the vibration of the outside edges and the edges near the inflatable booms of soil surface. When connecting the edges of the sail and the inflatable boom by the rope, the vibration of the edges of the sail near the inflatable boom is not easy inspired. Correspondingly, the first order mode is the vibration of the outside edges of the solar sail structure; the structure has been divided into two parts and vibrates up and down independently in the second order mode; the third order mode is the vibration of the center of edges and the reverse vibration of the two sides of the edges. The foregoing analysis shows that the natural frequency of the solar sail structure substantial increase through connecting inflatable booms and the sail.

Table 1. The modal shape of the solar sail structure under the inflation pressure of 10KPa

Modal order	The solar sail structure	
1		
	0.00622HZ	0.103HZ
2		
	0.00928HZ	0.155HZ

3	 <p style="text-align: center;">0.0119HZ</p>	 <p style="text-align: center;">0.210HZ</p>
4	 <p style="text-align: center;">0.1193HZ</p>	 <p style="text-align: center;">0.247HZ</p>
5	 <p style="text-align: center;">0.0202HZ</p>	 <p style="text-align: center;">0.256HZ</p>

CONCLUSIONS

It is necessary to study the structural vibration characteristics for the existence of the dynamic loads, such as the attitude adjustment of the aircraft and the solar wind in the working environment of the solar sail. The static characteristic of the solar sail under the inflation pressure has been analyzed in this paper. The solutions show that both of the maximum stress and displacement appear at the end of the inflatable extended arm. With the increase of the gas pressure, the maximum displacement a linear change in 0.05 slopes, but the maximum stress follows a nonlinear change. Furthermore, the vibrational character of the solar sail has been studied base on the configuration of the deformed solar sail structure and the stress distribution. The solutions indicate that the first three order modal frequencies approximately follow a linear rise, and the modal shapes remain constant. The first six modal shapes of sail structure is a vibration of sail surface. The first three order modal frequencies are less than 0.012 HZ when the gas pressure from 0 to 10KPa. That is to say the solar sail belongs to a typical low frequency, intensive frequency structure. Besides, the fundamental frequencies of the sail rise nearly 16 times by connecting the sail surface and inflatable booms. So, the research in this paper can provide a reference for the design of the solar sail.

REFERENCE

- [1] Murphy, D., "Validation of a Scalable Solar Sailcraft System," Journal of Spacecraft and Rockets, Vol.44 No. 4, pp. 797-808, 2007.
- [2] Sleight, D., Mann, T., Lichodziejewski, D., Derbes, B., "Structural Analysis and Test Correlation of a 20-Meter Inflation-Deployed Solar Sail," 47th AIAA Structures, Structural Dynamics, and Materials Conference, 2006-1706, Newport, Rhode Island, 2006.
- [3] Lappas, V., Mengali, G., Quarta, A., Fernandez, J., Schmidt, T., Wie, B., "Practical Systems Design for an Earth-Magnetotail-Monitoring Solar Sail Mission," Journal of Spacecraft and Rockets, Vol. 46 No. 2, pp. 381-393, 2009.

- [4] Furuya, H., Inoue, Y.,, “Dynamic Properties of Rotationally Skew Fold Membrane for Spinning Solar Sail”,47th AIAA Structures, Structural Dynamics, and Materials Conference, 2006-1980, Newport, Rhode Island, 2006.
- [5] Whorton, M., Heaton, A., Pinson, R., Laue, G., Adams, C., “NanoSail-D: The First Flight Demonstration of Solar Sails for Nanosatellites,” 22nd AIAA/USU Conference on Small Satellites, SSC08-X-1, Logan, Utah. 2008.
- [6] Jeremy A. B., Emil V. A., “Verification of a Retractable Solar Sail in a Thermal-Vacuum Environment,” 51st AIAA/ASME/ASCE/AHS/ASC Structures, Structural Dynamics, and Materials Conference, 12-15 April 2010, Orlando, Florida, AIAA-2010-2585.
- [7] Hiraku S., Shogo K., Yasutaka S., Hiroshi F., et.al. “Repeatability of Stored Configuration of a Large Solar Sail with Non-negligible Thickness”, 54th AIAA/ASME/ASCE/AHS/ASC Structures, Structural Dynamics, and Materials Conference April 8-11, 2013, Boston, Massachusetts, AIAA-2013-1804.
- [8] Jiang Z., Qiang T., Hai Y. H., “Deployment dynamics of a simplified spinning IKAROS solar sail via absolute coordinate based method,” Acta Mechanica Sinica ,vol.29 No.1,pp.132–142, 2013.

ACKNOWLEDGEMENTS

We thank Prof. Wang Li and Cheng Zhengai in Qian Xuesen Laboratory of Space Technology, Beijing, China.

ALTERNATIVE THERMO-ELASTIC DEFORMATION MEASUREMENT TECHNIQUES FOR SPACE STRUCTURES IN LABORATORY CONDITIONS

Matthias Friemel, Nikoloz Maghaldadze, Horst Baier, Leri Datashvili

TU München – Institute of Lightweight Structures

Boltzmannstr. 15

85747 Garching (Germany)

Email: friemel@tum.de

ABSTRACT

This report discusses two alternative measurement techniques for thermo-elastic deformation (TED) measurements in laboratory conditions for specimen and demonstrator sized objects. The setups used for both methods and the workflow for the measurements as well as each systems applicability for different materials is discussed. After the description of the measurement techniques an overview of the thermo-elastic deformation measurements that have been performed with these systems is given. The presented TED test campaigns include measurements of solid CFRP reflector antennas and flexible shell-membrane antennas with diameters up to 1.6m. After the presentation of the performed measurements, the challenges for TED measurements of a 5m diameter demonstrator of a reflector antenna in laboratory conditions are discussed.

1. INTRODUCTION

The requirements for the dimensional stability and surface accuracy of structural components of spacecraft, such as antenna reflectors used for telecommunication and science missions, are increasing continuously [1]. In case of antenna reflectors even small changes of the antenna geometry can reduce the antenna gain, the signal quality, or affect the pointing stability of the antenna.

Depending on their orbit, space structures will face high numbers of thermal cycles that can go into thousands, with temperature amplitudes of -200°C up to +120°C, again depending on their orbit and – if applicable – type of thermal control. With the help of modern FE-tools [2], thermal in-orbit simulation is possible, but the results still need to be verified by performing a thermal vacuum test within the expected maximum and minimum temperatures and monitoring the structures geometry. Depending on the size of the object and the measurement technique used for the deformation measurement, these tests can be challenging and expensive and therefore can only be performed on the flight hardware.

For missions and projects that use new materials and construction techniques, measurement of the thermo-elastic behaviour throughout the development process of the structure can help to detect problems with the used materials and design flaws. To be able to perform thermo-elastic deformation (TED) measurements throughout the development process of the structure, two test setups have been implemented, that are capable of measuring TEDs on component level and on the final structure. These set ups use a combination of optical measurement techniques for determining the temperature field and the temperature induced deformation. A halogen lamp array is used to create the temperature field that is causing the deformation. During the post processing the temperatures at each node of the deformation field are calculated and can be used to correlate the results from the measurement with the FE models, or as an input for the temperature loads in FE-tools.

2. TEST SETUP FOR MEASUREMENTS ON SPECIMEN AND COMPONENT LEVEL

The test setup for measuring thermo-elastic deformations on specimen level consists of a support frame for mounting the specimen and a heat source for creation of the temperature field. The frame is divided in two parts. The outer part is made from Aluminium profiles and is used to mount the heat source, the thermal shielding that is protecting the optical measurement systems and the additional measurement systems. The inner part which is used to fix the specimen to the testbed is made out of Invar36 to minimize temperature effects on the measurement, as the small CTE (2×10^{-6} 1/K) of this alloy ensures that temperature induced elongations of the support structure are kept to the minimum. Additionally the Invar36 structure is covered with a layer of aluminium foil to reduce the amount of heat that is transferred into the support structure by the heat source.

The heat source used for this setup is a set of four halogen lamps with 1kW power per lamp. The power output of the lamps can be adjusted in 1% steps to be able to control the temperature field generated by the heat source. The halogen lamps are mounted on the aluminium part of the support structure and can be adjusted to guarantee an even illumination

of the specimen. The temperature of the structure can be measured using a thermography camera that is calibrated by an additional thermocouple in the line of sight of the thermography camera, or with a set of thermocouples.

The deformation of the measuring object can be recorded using an Aicon DPA Pro photogrammetry system with an accuracy of $10\text{ }\mu\text{m/m}$ and a GOM Aramis optical 3D Deformation Analysis system which has an accuracy of 10^{-4} of the measurement area. For the photogrammetry measurements the object is fitted with a grid of photogrammetry markers. Using the coordinates of these markers it is possible to compare the specimen's geometric data at room temperature and at elevated temperatures. For the measurements with the optical 3D Deformation Analysis system the specimen is equipped with a black and white pattern that can be sprayed to the specimen's surface. The measurement area can be adapted to the expected behaviour of the specimen, using bigger measurement areas for specimen with higher deformations and smaller areas for specimen with small deformations. Another benefit of using the optical 3D Deformation Analysis system in combination with the photogrammetry is that the measured strain field can be located with high accuracy as the coordinates of the edges are defined by the photogrammetry targets. Therefore it is also possible to combine the results from several measurements to get the strain data for the full structure as long as the maximum temperature is not changed during the measurements.

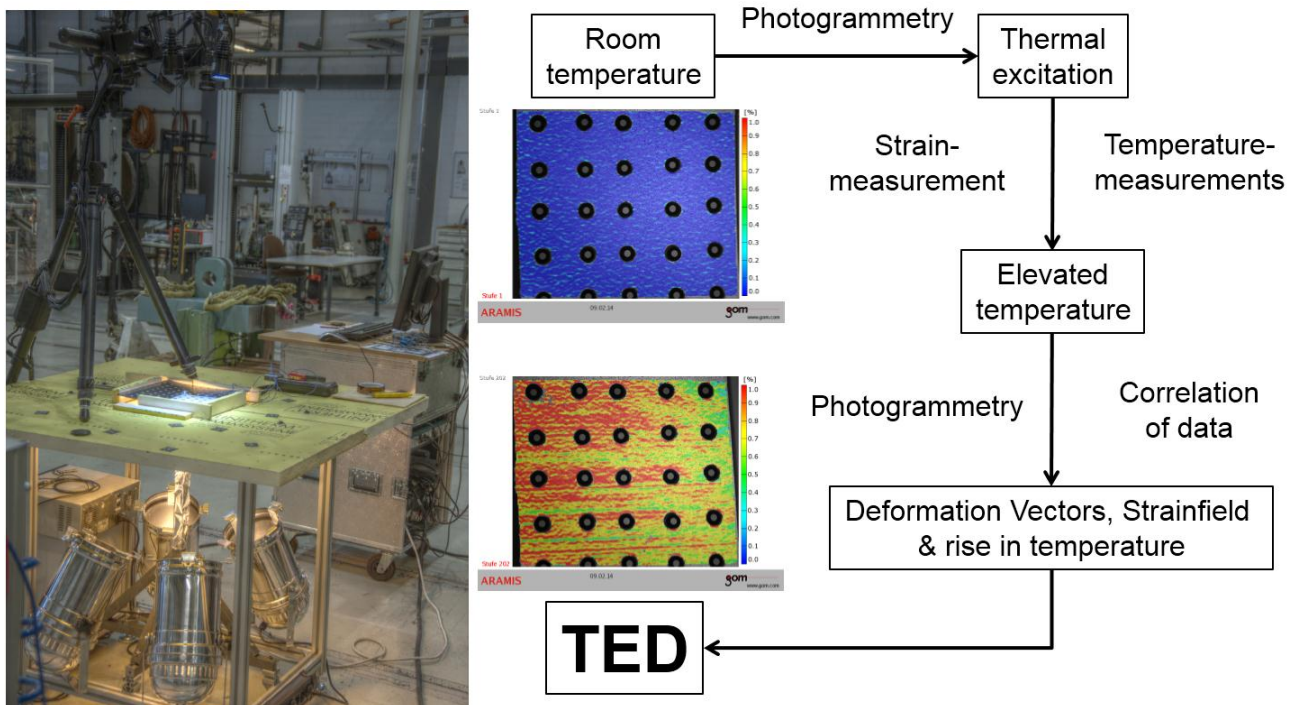


Fig. 1 - Test setup for specimen and specimen sized objects with workflow for measuring thermo-elastic deformations

3. TEST SETUP FOR MEASUREMENTS ON DEMONSTRATOR LEVEL

For the measurements on demonstrator level the setup is adapted with respect to the requirements for heating and deformation measurement. The thermal excitation of the structure is achieved using an array of twelve stage lamps with a power of 1kW each. The lamps are mounted on a support structure and can be adjusted in height and inclination to guarantee an evenly distributed illumination of the structure. The power output of the array can be adjusted in 1% steps thus guaranteeing a well-defined temperature regulation.

An Aicon DPA Pro photogrammetry system is used to determine the objects geometry at the different temperature levels. Therefore the measuring object is fitted with a grid of non-coded photogrammetry markers and coded markers and scale-bars are placed near the object for orientation and improvement of the measurement accuracy. Depending on the size of the device under test, the coded markers and scales that are used for orientation of the photogrammetry system can be mounted to an Invar frame to minimize the influence of temperature raise on the measurement accuracy.

The temperature of the measuring object is monitored using a thermography camera. The thermography cameras temperature values are adjusted to an additional thermocouple that is fixed to a part of the object that is in the line of sight

of the thermography camera thus preventing measurement errors related to optical effects – e.g. reflection of the halogen array on the measured object.

The following picture describes the complete measurement process for a thermo-elastic deformation measurement on demonstrator level:

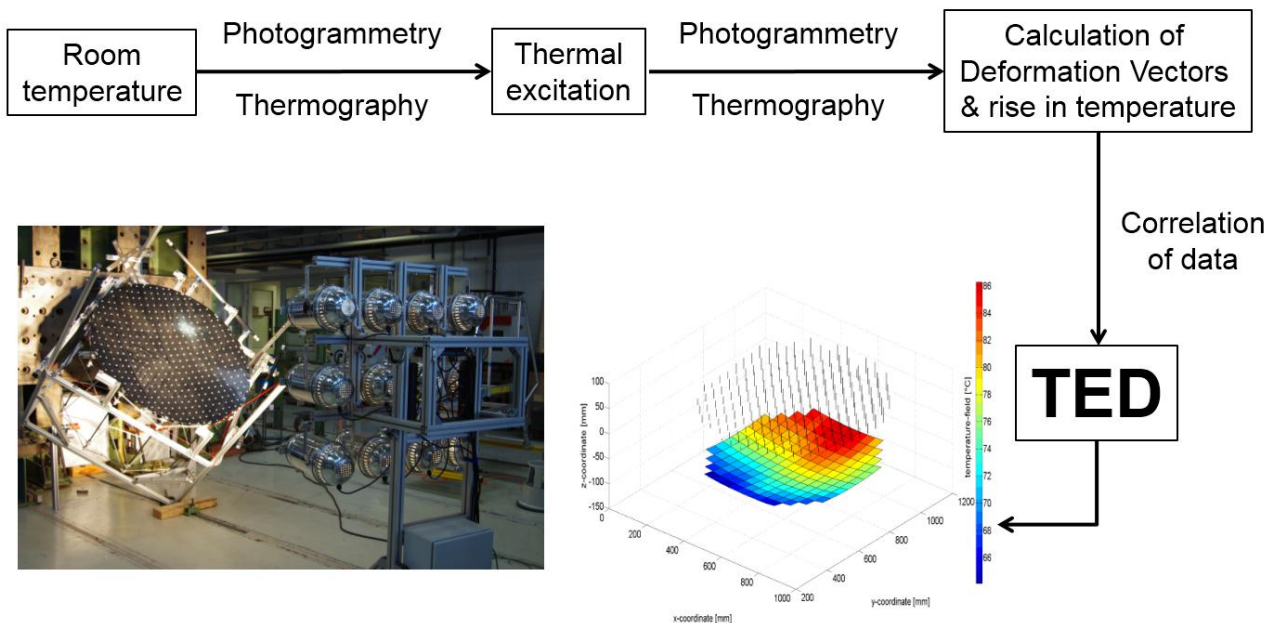


Fig. 2 - Exemplary test setup and measurement procedure for thermo-elastic deformation measurements on demonstrator level

At the beginning of the measurement the objects geometry and temperature field is recorded at room temperature thus creating a reference that the following measurements will be compared to. After the initial measurement the halogen array is set up to achieve the desired illumination of the measuring object and the power is set to the desired level. The temperature field is measured throughout the heating process using the thermography camera. As soon as the temperatures on the structure have reached constant values, the geometry of the heated object is measured using the photogrammetry system. When compared with the setup for specimen sized objects which is capable of creating very high temperatures creating measureable TEDs even for thick specimens with very small CTEs and absorptivity α , the setup for demonstrator sized objects is better suited for thin materials with high absorptivity and higher CTEs.

4. POST PROCESSING OF THE MEASUREMENT DATA

For the post processing it is necessary to calculate the exact temperature change for the tested specimen. The temperature data recorded with the thermocouple(s) can be used without any further work. The data from the thermography scans needs additional post processing before use. The temperature scan is adapted to the data recorded with the thermocouples that are visible in the scans. In the next step the temperatures at the photogrammetric markers are calculated. Due to the retro reflective surface-coating, the markers can be identified in the thermography scans. The temperature at the marker is then calculated by interpolating the temperature data in the area next to the markers.

In the next step the data from the photogrammetry measurements is used to calculate the deformation vectors for each marker, by combining the room temperature geometry and the geometry at elevated temperature and calculating the distances between the identical points in both datasets. This data is complemented with the temperature delta at each measured point to create the thermo-elastic deformation chart for the measured structure.

For the measurements that include the optical 3D Deformation Analysis system the post processing is basically the same when it comes to the temperature and photogrammetry data. For the optical 3D Deformation Analysis data the deformation and strain data of each picture set needs to be evaluated. Using the GOM Aramis system it is possible to add temperature data to the measurement by feeding a thermocouple into the recording channel of the measurement system. Depending on the area monitored by the system the data from a single thermocouple can already be enough. If the area of interest is bigger, the data from the thermography scan can be used to get the temperature field for each picture set.

As it is possible to get the data for each photogrammetry marker on the specimens' surface or, in case of using the optical 3D Deformation Analysis system – for a certain area that is defined by a set of photogrammetry markers, the data from the measurements can be used to correlate FE models with the real system.

5. EXEMPLARY THERMO-ELASTIC DEFORMATION MEASUREMENTS

Until now measurements have been performed with both systems using different materials. These measurements include a CFRP plate with an asymmetric layup resulting in a saddle form of the plate at room temperature that will flatten out with increasing temperatures. The measurements on this plate have been performed with the test setup for the specimen sized objects. The setup for demonstrator sized objects has been used for TED measurements of several reflector antennas demonstrators with diameters ranging from 0.8m to 1.6m diameter including CFRP material and carbon fiber reinforced silicone (CFRS) material.



Fig. 3 - TED measurement of a CFRP plate with asymmetric layup

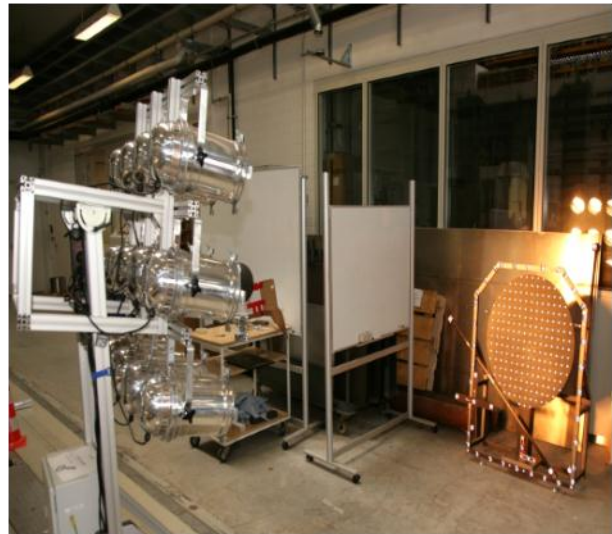


Fig. 4 - TED measurement of a 0.8m diameter CFRP reflector antenna demonstrator in an Invar36 support frame

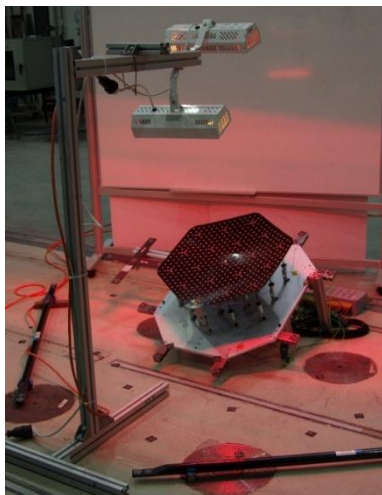


Fig. 5 - TED measurement of a CFRS reflector antenna demonstrator with variable shape

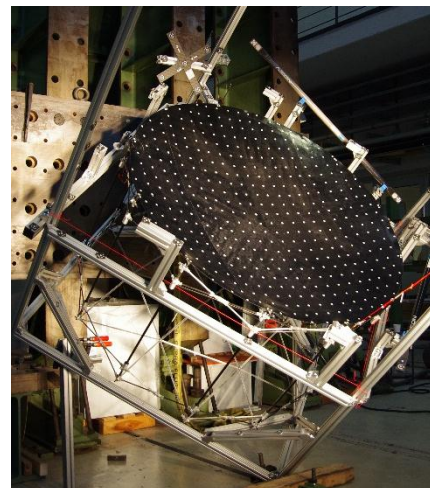


Fig. 6 - TED measurement of a CFRS large deployable antenna reflector demonstrator with 1.6m diameter (LABUM)

The setup for the specimen sized objects has been tested using a 300 x 300 mm CFRP plate with an asymmetric layup (Fig. 5), resulting in a test object that is curved in two directions at room temperature due to the asymmetric layup and will be flat when reaching the curing temperature. The plate has been fitted with a 10 x 10 grid of photogrammetry markers to be able to get sufficient geometry data. For the measurements with the optical 3D Deformation Analysis system one quadrant of the plate has been equipped with the required black and white pattern. A set of thermocouples has been installed on the top and the bottom of the plate to monitor the temperatures and to be able to adapt the temperature plots recorded with the thermography system (Fig. 8).



Fig. 7 TED setup for the CFRP plate

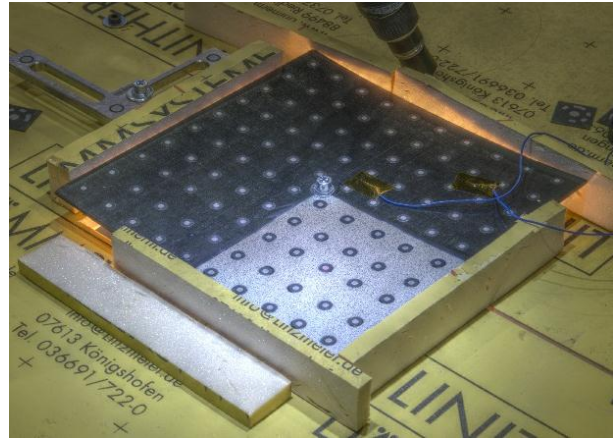


Fig. 8 Detailed view of the CFRP plate with the optical pattern for the 3D deformation analysis system and thermocouples

The halogen lamps have been operated at 25 percent of their maximum output to create the temperature field (Fig. 9). As can be seen in the temperature plot, the temperature distribution is homogenous on the whole plate with only minor distortions on the edges due to convection. The maximum temperature in the centre of the plate reaches 140°C in this configuration. The test results show that both measurement systems are capable of detecting the deformation of the CFRP plate due to the raise in temperature. Additionally it is possible to measure the strain field in each direction of the plate and to visualize the deformation field when using the optical 3D Deformation Analysis system.

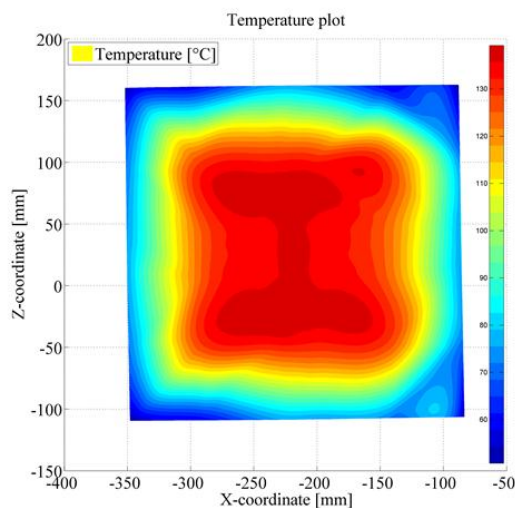


Fig. 9 Temperature field on the CFRP plate with the maximum temperature of 140°C in the center of the plate

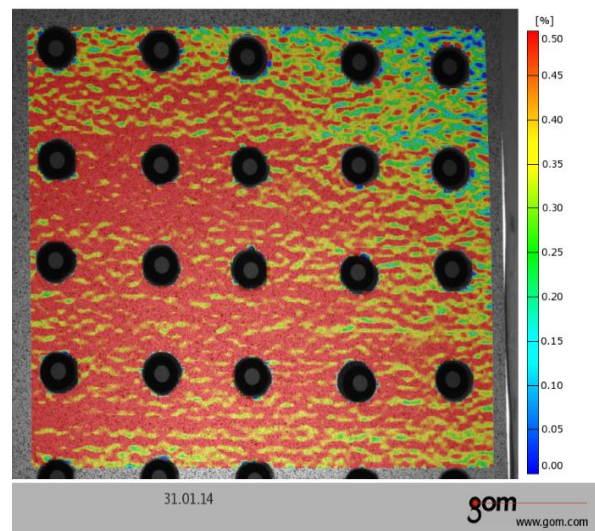


Fig. 10 Strain field in x-direction after reaching the maximum temperature of 140°C

Two different measurements have been performed on the LABUM demonstrator which is a breadboard of a large deployable reflector antenna with the RF surface being fabricated from biaxial CFRS material and a diameter of 1.6m. The first TED measurement's goal was to characterize the reflectors behaviour at elevated temperatures. Therefore, the reflector surface has been illuminated with the full halogen array from the front side as can be seen in Fig. 11. The maximum temperature in the centre of the surface has been 100°C , decreasing from the centre outwards to room temperature on the edges. A plot of the achieved temperature distribution is given in Fig. 13. The temperature plot shows two sections with reduced temperatures which are related to the mounting of the demonstrator for this tests. One of the struts that is extending from the support is blocking the thermography cameras view causing the first section with reduced temperatures. The same strut is also creating a shadow on the reflector surface due to the positioning of the halogen array, hereby reducing the temperatures on the surface in the shadowed section.

The second measurement uses only a single lamp that is illuminating the surface from its back (Fig. 12) while pointing at the centre of the reflector surface. The goal of this measurement was to find out if a partial heating of the surface can be detected with the setup in use. The temperature distribution for this test is given in Fig. 14. With the single lamp at the back of the surface the distance between heat source and reflector is only 300 mm resulting in much higher temperatures of the surface ($T_{\text{max}} = 140^{\circ}\text{C}$) but also in a much smaller heated area. The thermography scan also shows that the heat transfer rate within the surface material is minimal, as the outer parts temperature is not influenced by the heating, except for the part that is lying above the heat source and is heated due to convective heat transfer.

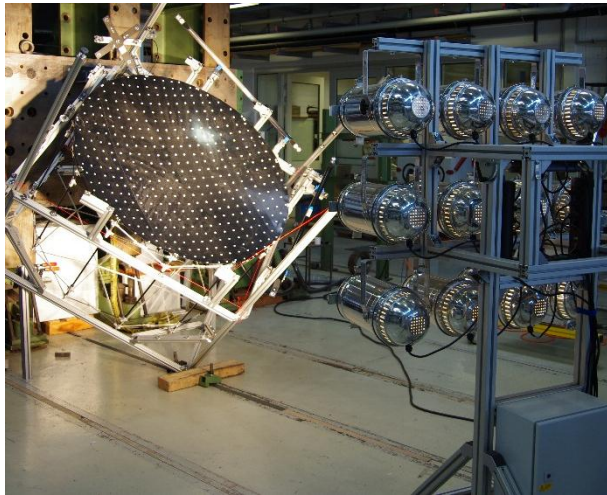


Fig. 11 Setup for the TED measurement with full illumination of the front side of the LABUM antenna

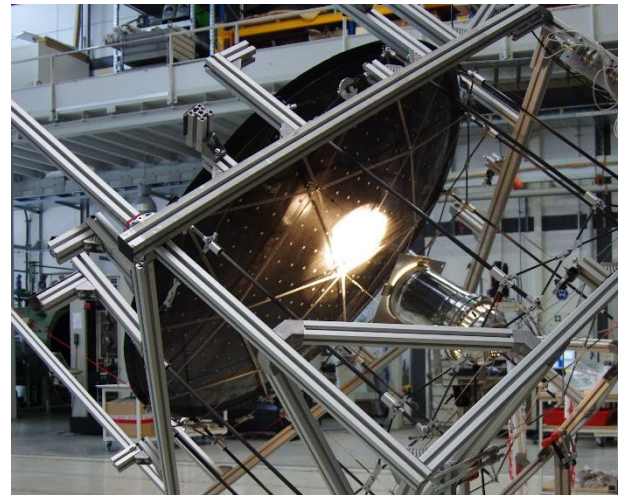


Fig. 12 Setup for the TED measurement with partial illumination of the backside of the LABUM antenna

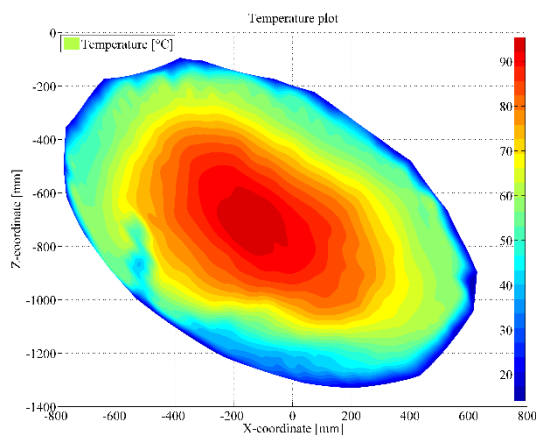


Fig. 13 Temperature field of the front side of the LABUM antenna with full illumination of the front side

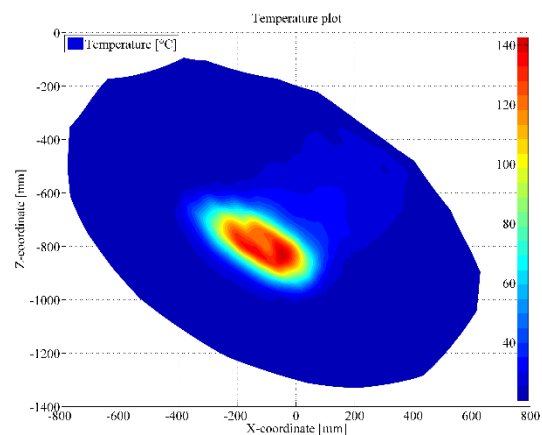


Fig. 14 Temperature field of the backside of the LABUM antenna with spot illumination of the back side

Fig. 15 and Fig. 16 show the resulting best-fit deformations of the surface z-coordinates due to the raise in temperatures for both of the previously discussed measurements. In case of the full surface heating the whole reflector antenna is affected with the maximum deformation in the centre of the surface where the temperature maximum is. In case of the spot heating the deformation plot shows that the maximum deformation is in the area that has been heated. The area above the heated spot is also affected, whereas the rest of the surface does not show any deformation due to the heating which correlates with the thermal imaging that has shown, that the temperature does not change for the lower part of the reflector.

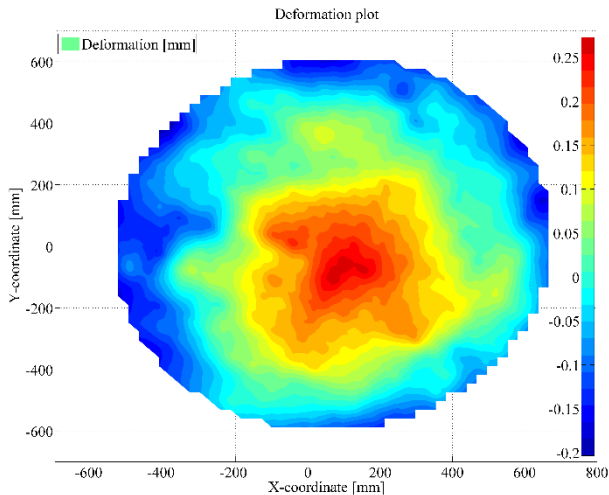


Fig. 15 Best-fit z-deformation of the antenna surface for the full surface illumination

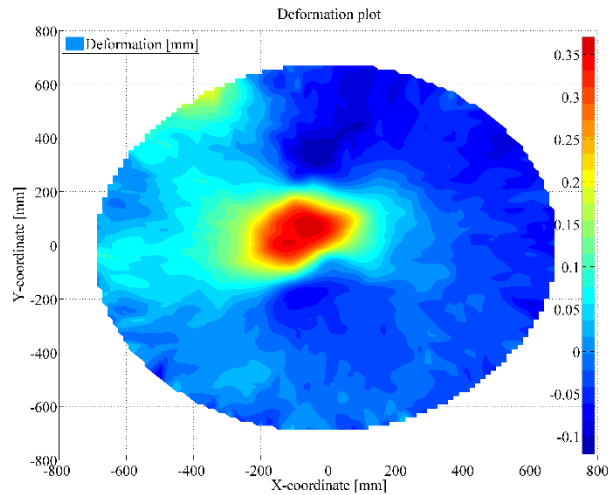


Fig. 16 Best-fit z-deformation of the antenna surface for the spot illumination

6. OUTLOOK ON LABUM 5M DIAMETR MEASUREMENT CHALLENGES

As has already been shown the presented TED measurement setups and methods have been tested on objects with up to 1.6 m diameter successfully. In the near future a TED measurement has to be performed on demonstrator of a 5 meter diameter CFRS LDR that will be fabricated at the Institute of Lightweight structures and later on be tested at LSS facilities in the Netherlands to prove the dimensional stability of the reflecting surface in simulated orbital conditions. One of the main challenges in measuring on object of this size in laboratory conditions is of course the accuracy of the measurement system itself. For objects with sizes below two meters it is never a problem to have all scales in at least a few pictures of the photogrammetry measurement. With a five meter object this is no longer possible, resulting in the need for longer scale bars to increase the system accuracy. Another challenge is the need for coded photogrammetry markers that need to be distributed all over the surface to allow recombination of single pictures during the post processing. These markers must neither be stiff or heavy as this will influence the shape and behaviour of the antenna during the measurements in the LSS chamber, they also have to be compatible with the CFRS CTE as a CTE mismatch of these components will cause an additional deformation of the reflector surface at hot and cold temperatures. They cannot be taken from the standard suppliers as the CFRS silicone surface is causing problems with standard adhesives – especially when going to cold temperatures.

For the heating of the reflector it is not possible to illuminate the whole surface of the antenna and to achieve a desirable temperature raise of about 60°C. Therefore the only possibility is to perform a spot measurement as has been shown for the LABUM tests in chapter 5 earlier.

7. CONCLUSION

Two test setups for measuring thermo-elastic deformations on specimen and demonstrator sized geometries have been presented. Both setups have been tested using different materials, geometries and heat sources. It has been shown that the setup for bigger objects is capable of measuring TEDs especially for the tested CFRS structures. Tests on a CFRP structure showed that the system is able to detect temperature induced deformations but is limited by the maximum achievable temperature especially for materials with very low CTEs. The test setup for the specimen sized geometries is better suited

for materials with low CTEs as the maximum achievable temperatures are higher and the additional use of the optical 3D Deformation Analysis system allows for measuring smaller sectors of the tested specimen with very high resolution. Further investigations will concentrate on integrating a Rayleigh based fiber optical measurement system into the test setup for the specimen sized geometries as the use of this system allows measuring temperatures and strain with a single fiber on different location of the specimen.

ACKNOWLEDGMENTS

This work has been supported by the German Federal Ministry for Economy and Technology (Bundesministerium für Wirtschaft und Technologie BMWi) in cooperation with the German Aerospace Center (DLR) and by ESTEC/ESA.

REFERENCES

- [1]. Santiago Prowald, J.; Baier, H.: Advances in large apertures for space. CEAS Space Journal, POI 10.1007/s 12567-013-0048-3 2013, 2013
- [2]. Stute, T.; Sippel, R., "Ultra Lightweight Composite Mirrors for Optical Application" in Proc. of SPIE Vol. 3132 Optomechanical Design and Precision Instruments, edited by Alson E. Hatheway, (SPIE, Bellingham, WA, 1997)
- [3]. William A. Imbriale, Steven (Shichang) Gao, Luigi Boccia, 'Space Antenna Handbook', John Wiley & Sons, Ltd, 2012
- [4]. Estler, Edmundson, Peggs, Parker, 'Large-Scale Metrology – An Update', CIRP Annals – Manufacturing Technology, Volume 51, Issue 2, 2002
- [5]. X. Maldaque. Infrared Methodology and Technology. Gordon and Breach Science Publishers. 1994
- [6]. Datashvili, L.; Baier, H.: Derivation of Different Types of Antenna Reflectors from the Principle of Highly Flexible Structures. European Conference on Antennas and Propagation [8., The Hague, The Netherlands, 2014], 2014
- [7]. Friemel, M.; Baier, H.; Datashvili, L.: New Experimental Techniques for Mechanical and Thermo-Elastic Characterization of Antenna Reflector Materials and Structures. 33rd ESA Antenna Workshop 2011, Noordwijk, 2011

ANTENNA TESTING: THERMO-VACUUM AND COMBINED THERMAL-NEAR FIELD TEST SOLUTIONS

Prepared by Leonardo Alemanno ⁽¹⁾, Fabrizio Rinalducci ⁽²⁾

⁽¹⁾ **Chief Engineer & Technical Manager**

*Angelantoni Test Technologies S.r.l., loc. Cimacolle 464,
06056 Massa Martana (PG) – Italy*

Email: leonardo.alemanno@angelantoni.it

⁽²⁾ **Aerospace Products Application Engineer**

*Angelantoni Test Technologies S.r.l., loc. Cimacolle 464,
06056 Massa Martana (PG) – Italy*

Email: fabrizio.rinalducci@angelantoni.it

ABSTRACT

This paper presents engineering approaches to realize Thermal Vacuum Chambers (TVC) for different R&D applications in the field of antenna systems: (1) increasing of the DUT (device under test) surface temperature up to +550°C inside the Thermal Vacuum Chamber (TVC), (2) near field testing of large antenna systems with dimensions up to 4 m x 1.5 m in extreme temperature conditions from -100°C to +100°C.

1. INTRODUCTION

In order to analyze and develop antenna systems it is often essential to reproduce and simulate the behavior of the system itself, or of parts of it, as by creating certain necessary operating condition. In the past years we have developed, manufactured and tested special equipment, capable to handle different challenges during thermo-vacuum or combined thermal and near field antenna tests. This paper presents engineering approaches for two different applications in particular.

2. TESTING FOR NEXT VOYAGE EXPLORATION TO MERCURY

The system is designed to simulate environmental conditions of a space vehicle during the next exploration voyage to Mercury (BEPI Colombo Mission), in order to verify the behavior of antenna receiver materials. The particular requirement towards the testing system is to increase and maintain the surface temperature of a specific device under test (DUT) up to +550°C under high vacuum conditions.

The requested conditions have been reached by heating the target through infrared (IR) ceramic emitters. The IR emitters are mounted on six reflective panels placed all around the target specimen corresponding to the six faces of a parallelepiped. Each face is fixed independently to an external cylindrical structure and can be adjusted or opened in order to allow the user to access inside the test volume, as it is shown in Fig. 1. The specimen is suspended in the center of this parallelepiped.

The cylindrical structure is made by a double layer of stainless steel reflective screens, closed on the rear side and with a removable double layer panel on the front side for the access during the test preparation. The scope of the above double layer envelope around the IR emitters parallelepiped, is to keep inside the test volume the most of the radiation produced by the IR emitters, in order to maximize the energy transferred to the target placed in the center and minimize the loss of heat in the external environment.

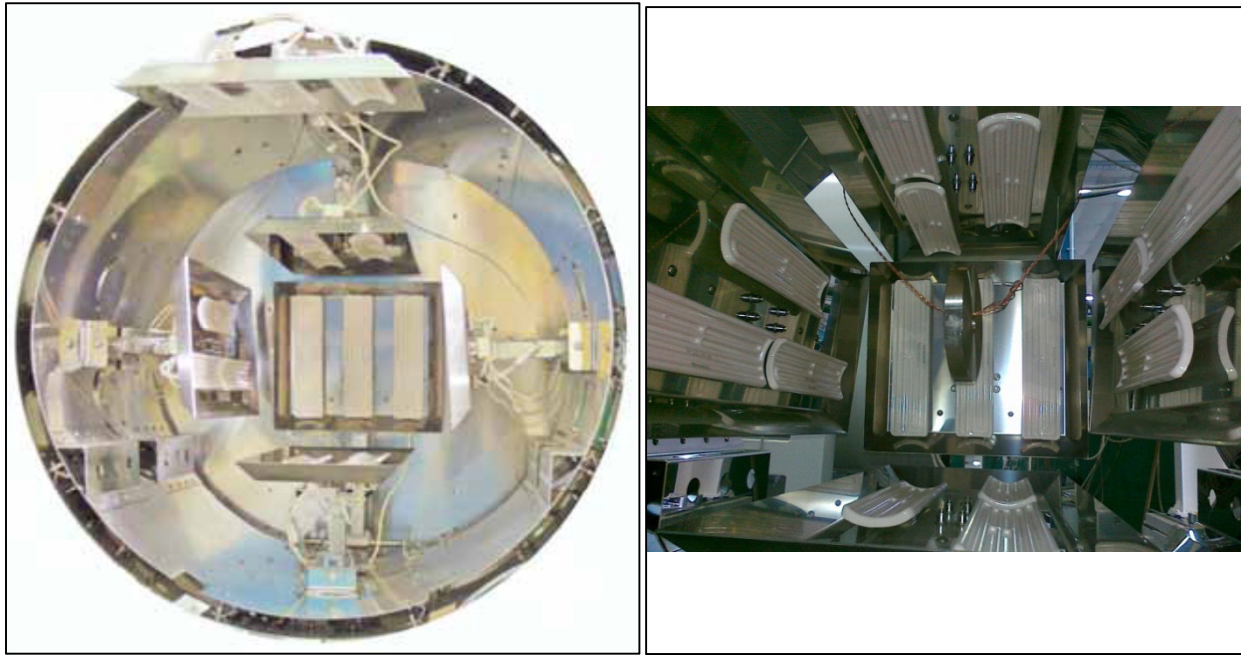


Fig. 1. Left: view of the internal test volume; right: specimen suspended inside the test volume

The above described equipment is placed inside a thermal vacuum chamber (TVC), in order to operate at the same pressure conditions of the real object (Fig. 2), that corresponds to vacuum on the order of 10^{-6} mbar.

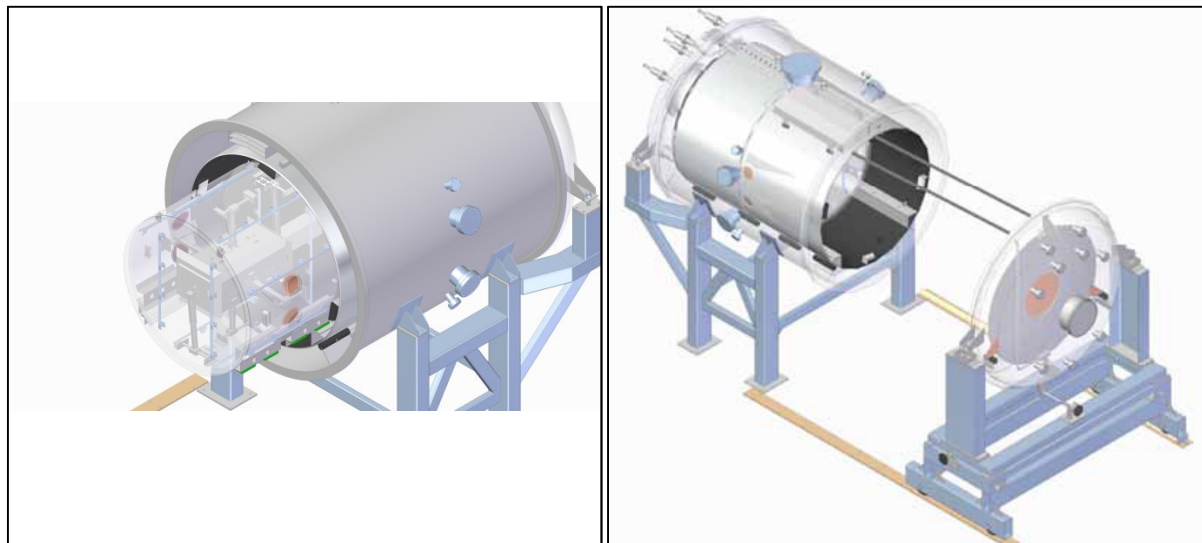


Fig. 2. Left: equipment admission into the TVC; right: overall view of the TVC

During the test, with the device placed inside the thermal vacuum chamber and with its IR heating enabled, the thermal shroud of the TVC is cooled by a heat transfer fluid in order to dissipate the heat irradiated outside by the high temperature equipment notwithstanding a low emissivity coefficient of the external surface. This approach allows to avoid temperature increase on the black painted shroud over values not compatible with the paint characteristics and it permits to limit the outgassing below unsuitable values for the requested vacuum level of 5×10^{-6} mbar.

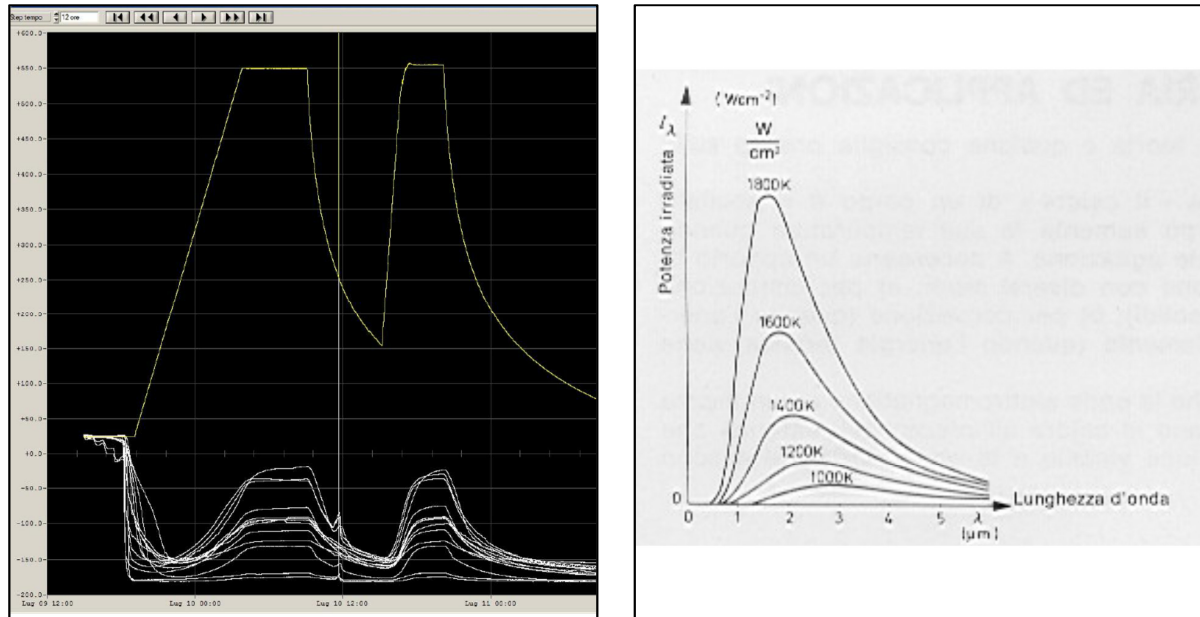


Fig. 3. Left: temperatures plot; right: radiated power vs wave length

In the Fig. 3 the white lines represent the temperature plot of the thermal shroud temperature sensors, while the DUT temperature reaches +550°C (yellow curve).

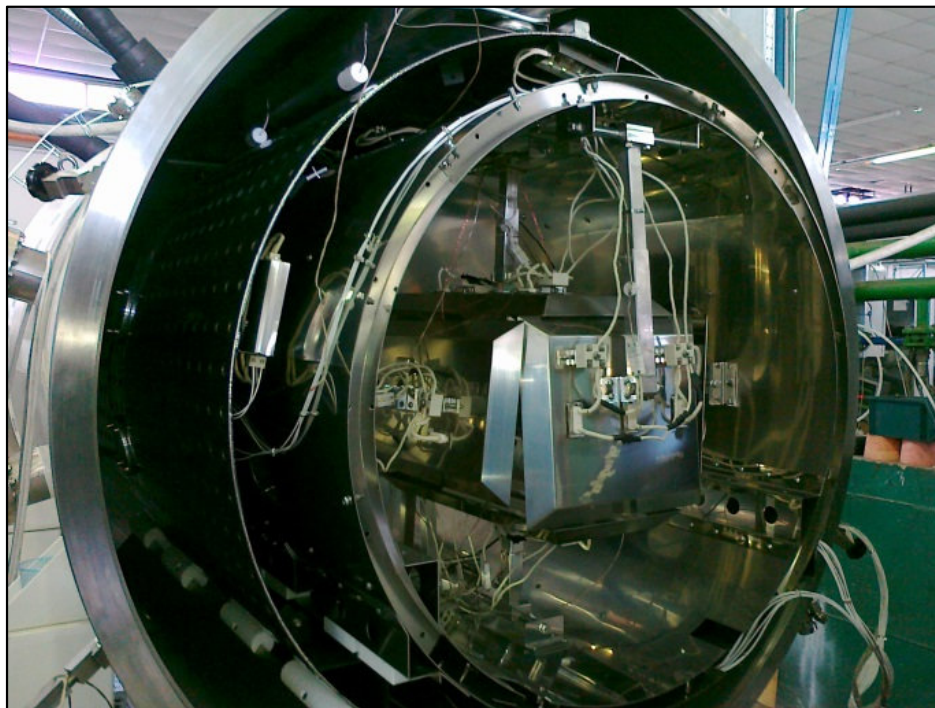


Fig. 4. Equipment cabling

The power for the IR emitters, the temperature sensors requested for the emitters surface temperature monitoring and the sensors for the DUT temperature control are brought inside the vacuum environment by dedicated feedthroughs placed on the chamber body portholes(Fig. 4).

The IR ceramic emitters can reach a surface temperature close to 1000K, which corresponds to maximum power λ_{\max} and a power emissivity of 6 Wcm⁻² (Fig. 3).

3. THERMAL TRANSPARENT CHAMBER FOR NEARFIELD TEST

The system is designed to perform near field measurements at critical working conditions of the antenna. The testing equipment consists of a thermal “transparent” with an internal volume of 22.5 m³ which is situated inside an anechoic chamber together with the wave scanner. The thermoregulation is realized with liquid and gaseous nitrogen by means of a remotely installed machine unit, connected to the test cell by rigid and flexible pipes, as it shown in Fig. 5 and 6.

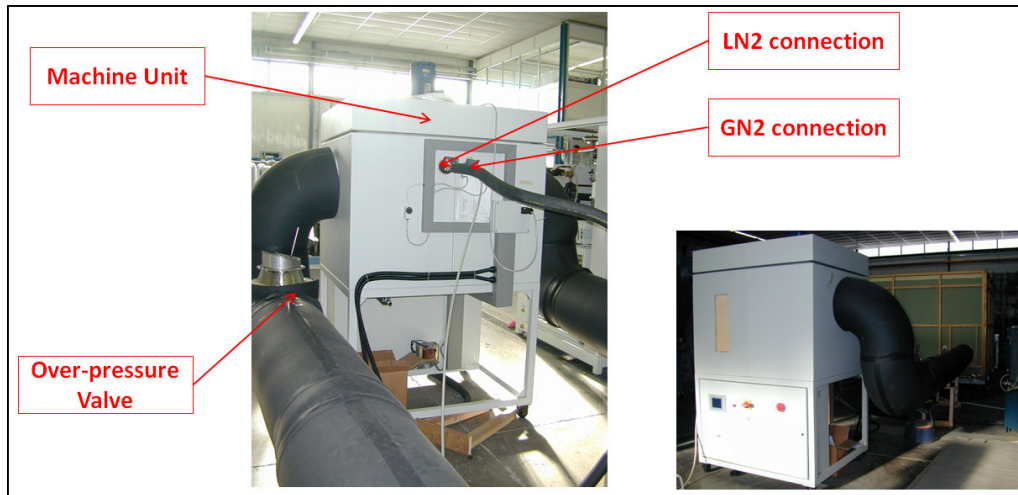


Fig. 5. Machine unit configuration

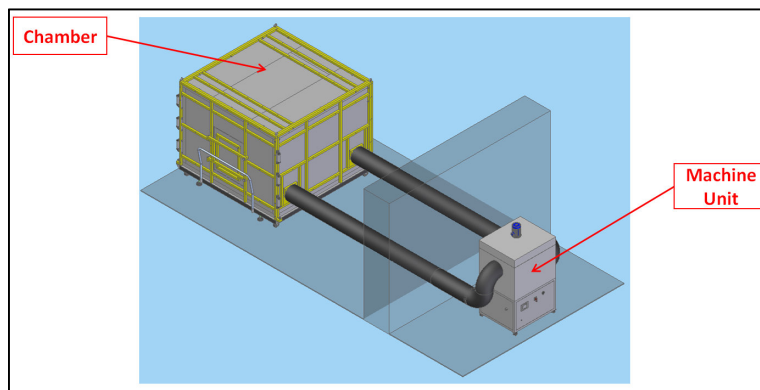


Fig. 6. External system configuration

The combination of thermal test and near field measurement raise especially for the test chamber construction a great challenge of choosing the right test cell material so as to provide following necessary characteristics:

- maximum transmission of the radiation
- good thermal insulation characteristics with the necessary tightness in order to avoid condensation
- avoidance of any antenna radiation signal disturbances

To resolve these problems Angelantoni Test Technologies has designed a construction without any metallic parts, choosing wood as the test cell frame material. The cell walls, made of special polymethan foam panels connected by nylon screws, feature good thermal insulation characteristics and at the same time allow a maximal radiation transmission. The test cell ceiling, which interfaces the scanner, is realized as a removable panel made of polymethacrylimide foam. This material was specially developed for antenna applications and has extremely low dielectric constants and particularly good transmission properties in the high frequency range up to 26.5 GHz.

The test cell incl. all internal systems is placed on movable support plate provided with wheels, as it is shown in Fig. 7.

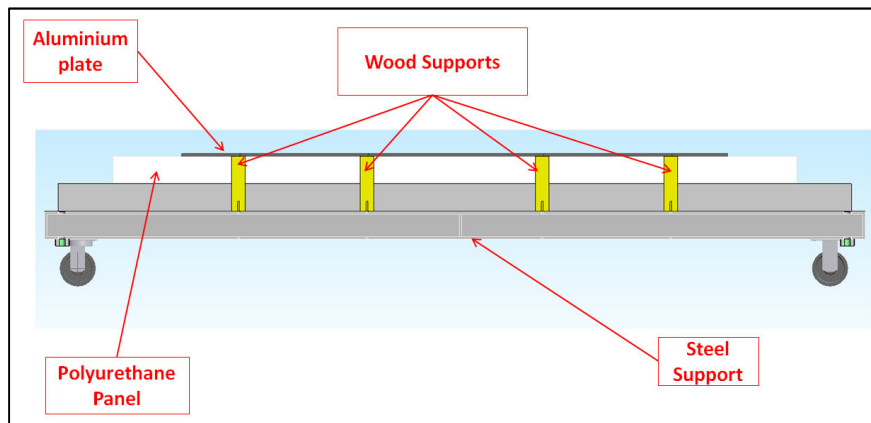


Fig. 7. Chamber basement section

The design of the thermoregulation system allows to reproduce critical working conditions by maintaining a set temperature in a range from -100°C to $+100^{\circ}\text{C}$, while compensating the thermal dissipation of the antenna system. The cooling is performed with by vaporization of liquid nitrogen and electrical heaters ensure high temperatures working conditions up to $+100^{\circ}\text{C}$. In order to obtain the thermal compensation Angelantoni Test Technologies has foreseen a special air circulation system inside the test cell, which provides a direct cooling of the horizontally installed antenna with preconditioned air. Fig. 8 shows the described cooling configuration of the antenna.

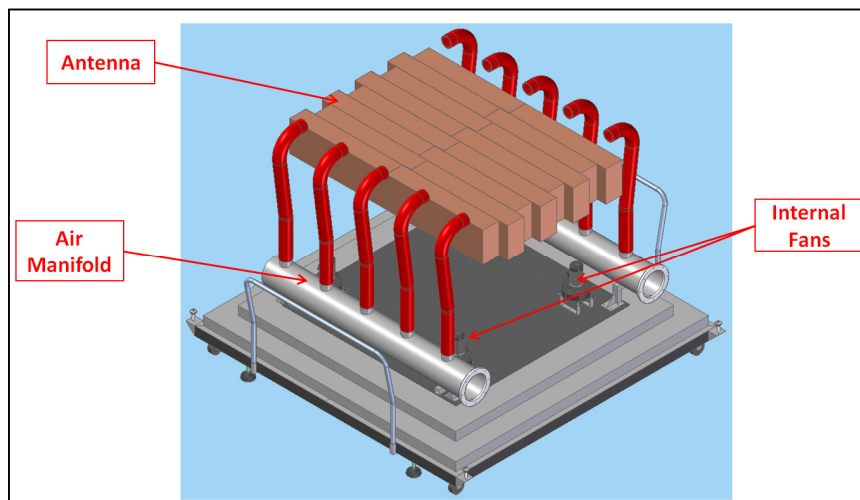


Fig. 8. Antenna cooling system inside the test cell

4. ABBREVIATIONS AND ACRONYMS

DUT – Device Under Test

TVC – Thermal Vacuum Chamber

Variation of Reference Strategy - A novel approach for generating optimized cutting patterns of membrane structures

Kai-Uwe Bletzinger, Armin Widhammer, Falko Dieringer

Lehrstuhl für Statik, Technische Universität München

Arcisstr. 21, D-80333 München, Germany

Email: {kub, armin.widhammer}@tum.de

ABSTRACT

Finding the plane shape of the double curved surfaces is a well-known challenge for every design engineer dealing with either fiber reinforced plastics lightweight designs or textile architectural membranes. A novel approach for generating optimized cutting patterns including nonlinear isotropic and anisotropic material behavior is presented. The so-called Variation of Reference Strategy can be seen as an inverse approach, defining the nodal positions in the material configuration as design variables holding the spatial configuration fixed. Thereby, the stress-free state of the cutting pattern which is an important characteristic of the manufacturing process is preserved. In order to demonstrate the abilities and robustness of the Variation of Reference Strategy several numerical examples considering different kind of materials are presented.

1. INTRODUCTION

In various fields of engineering a significant rise of lightweight design concepts can be observed, e.g. membrane antennas, stringers and ribs of fabric reinforced materials (aeronautic/aerospace engineering), frame components and car body panels (automotive engineering), membrane rooftops and pneumatic structures (architectural membranes). The basic idea of lightweight design is an increasing load carrying behavior due to a combination of curvature, i.e. anticlastic or synclastic surfaces, and high-tensile materials, like high-performance alloys, carbon fiber reinforced plastics (CFRPs) or coated textiles. Since the wrought material is mostly a plane textile, the shape of the blank, the so-called cutting pattern, is very important in the sense of manufacturing. Cutting patterns are determined by an inverse process starting from the intended final shape of the erected structure. The manufacturing process bringing the plane wrought material into its final shape is known as drape process or short draping. The optimal cutting pattern is found if – considering draping – the shape deviation of the real erected structure from the intended one is minimal. As a matter of fact the standard situation of continuum mechanics is inverted as the shape of the deformed structure (erected structure) is known but that of the undeformed one (the reference configuration or cutting pattern) is unknown. Consequently, theory and numerical simulation methods have to deal with the variation of the reference geometry to find the optimal pattern which explains the name of the method presented here. It will be shown that the thoroughly discussion of all aspects needs considerable modifications of standard theory and methods but pays off in most robust and precise techniques of unknown quality so far.

Considering the non-developable characteristics of a double curved surface, it is not possible to find an unique corresponding blank. Hence, getting a solution of the mentioned problem means achieving a compromise w.r.t. some predefined criteria, i.e. an optimization problem has to be solved. Gründig et al. [1] came up with the idea of using an affine map between the plane configuration (2D) and the spatial configuration (3D) defining the element edges as design variables. Other kinematics based approaches are summarized in Topping and Iványi [2]. The major drawback of these approaches is the disregard of the material behavior. In order to avoid this, Maurin and Motro [3] developed the so-called Stress Compensation Method. In a first step, an orthogonal projection of the spatial configuration (3D) into a plane leads to a non-stress-free intermediate configuration (2D). Followed by a second step, a least squares approach minimizes the difference between these residual stresses and a predefined stress state by varying the contour of the intermediate configuration. The approach published by Kim and Lee [4] is based on the stress compensation method. But in contrast to Maurin and Motro [3], not only the displacements of the contour of the intermediate configuration but also the internal displacements are defined as design variables. The methodology for optimized cutting patterns published by Haug et al. [5], [6] is based on solving a standard structural mechanics problem. In a first step, the desired material characteristics are assigned to a not necessarily pre-stressed structure by means of the so-called metric retrieval method. In a second step, the structure is divided into different subdomains defined by geodesic boundaries, also called geodesic gores. In a next step, each gore is separately forced into an appropriate plane. Finally, the optimized cutting patterns are found by finding the equilibrium state of the statically determinant supported flat gores allowing only in-plane motions of the nodes. Linhard et al. [7], [8] introduced two also mechanically motivated approaches for solving

the optimization problem. According to Maurin and Motro, Linhard et al. also minimize the difference between a predefined stress state and the residual stresses. But instead of using an intermediate configuration, Linhard et al. directly used the spatial configuration for computing the residual and predefined stresses. Additionally, Bletzinger et al. [9] and Bletzinger and Linhard [10] incorporated their approaches into an overall design strategy for architectural membranes. Further enhancements on the design of membrane structures considering cutting patterns has been published by Dieringer et al. [11].

A more general approach finding the stress-free (unloaded) configuration for a given set of boundary conditions (displacements and tractions) was published by Govindee and Mihalic [12] and Govindee and Mihalic [13]. According to the theory of finite deformations, the mapping of a point in the material configuration to the corresponding point in the spatial configuration is defined by a so-called motion. Govindee and Mihalic came up with the idea defining the inverse motion of a point as primary unknown.

Similar questions are arising in biomechanical applications. Gee et al. [14] addressed the problem of finding the unloaded configuration when patient-specific geometries are directly reconstructed out of in vivo imaging data.

In this contribution a novel approach for generating optimized cutting pattern will be presented. The key idea of the presented method, so-called Variation of Reference Strategy (VaReS), is to consider the elastic potential of the membrane arising due to the residual stresses. The paper is organized as follows. Section 2 shortly presents the important equations of nonlinear continuum mechanics. Section 3 will introduce and explain the fore-mentioned Variation of Reference Strategy in the very detail. Section 4 will draw the link between the Variation of Reference Strategy and a nonlinear kinematic description of plane structures within the context of finite elements. A general interface to hyperelastic material models will be introduced in section 5. The convergence behavior and the robustness of the presented approach is investigated in Section 6. Section 7 will show the good convergence of the presented method followed by other examples. Finally, a summary of the achieved results can be found in section 8.

2. NONLINEAR CONTINUUM MECHANICS FOR THIN MEMBRANE STRUCTURES

Thin structures are characterized by the in-plane dimensions (l_1 and l_2) being significantly larger than their dimension in normal direction l_3 , i.e. $l_1; l_2 \gg l_3$. Assuming a constant distribution of the normal stresses over the thickness, the kinematic of the membrane can be reduced to its mid-surface. Since dry or coated fabrics exhibit almost no resistance against bending, only the in-plane actions, so-called membrane actions, are responsible for load carrying. Plane stress conditions are applied. For the cutting pattern and draping simulation large deformations have to be considered. The position vectors for a surface point $P(\theta^1; \theta^2)$ are denoted as $\mathbf{X}(\theta^1; \theta^2)$ and $\mathbf{x}(\theta^1, \theta^2)$ in the undeformed and deformed configuration, respectively. As well, \mathbf{G}_i and \mathbf{g}_i denote the tangential and normal vectors in either configuration, Fig. 1. Generally, capital letters are used for material quantities and small letters are used for spatial quantities. The basic quantities to determine strain are the deformation gradient \mathbf{F} , the right Cauchy-Green tensor \mathbf{C} , and the Green-Lagrange strain tensor \mathbf{E} . The second Piola-Kirchhoff stress tensor \mathbf{S} is used as stress measure. Refer to e.g. Holzapfel [15] for further details.

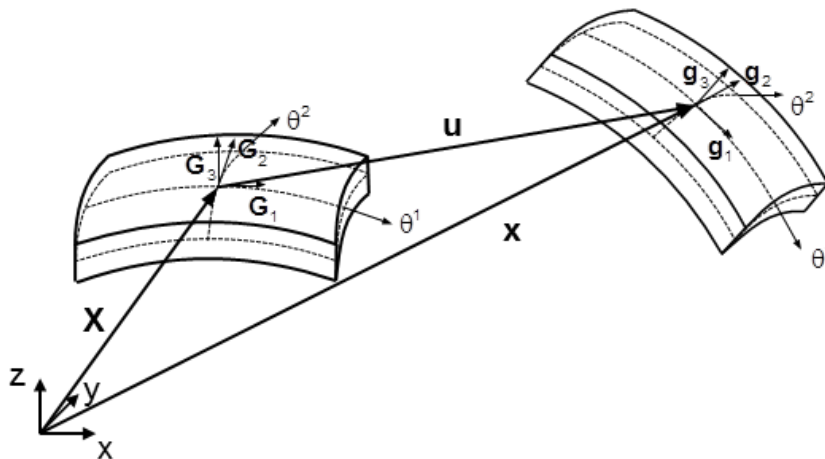


Fig. 1. Nonlinear kinematics of thin membrane structures

2.1. Anisotropic hyperelasticity for fabrics

Hyperelastic, anisotropic material behaviour with a certain elastic potential Ψ is assumed. It are defined in terms of invariants I_1 , I_2 , and I_3 of the right Cauchy Green tensor \mathbf{C} and further invariants $I_{4+2(i-1)}$ which represent the anisotropic fiber orientations Φ^i of anisotropic fabric material where \mathbf{M}^i being the corresponding structural tensors $\mathbf{M}^i = \Phi^i \otimes \Phi^i$:

$$\begin{aligned} I_{4+2(i-1)}(\mathbf{C}, \mathbf{M}) &= \Phi^i \cdot \mathbf{C} \Phi^i = \text{tr} \mathbf{C} \mathbf{M}^i \\ I_{5+2(i-1)}(\mathbf{C}, \mathbf{M}) &= \Phi^i \cdot \mathbf{C}^2 \Phi^i = \text{tr} \mathbf{C}^2 \mathbf{M}^i \end{aligned} \quad (1)$$

Various anisotropic material laws have been published which are suitable for fabrics, see Vidal-Sallé et al. [16] and Y. Aimène et al. [17], Balzani et al. [18], Schröder and Neff [19], Bonet and Burton [20], Reese et al. [21], etc.

3. VARIATION OF REFERENCE STRATEGY (VARES)

Consider a given non-developable surface \mathcal{S} which defines the intended shape of the structure. Every point $P \in \mathcal{S}$ is described by its spatial position vector \mathbf{x} . To every 3D spatial position \mathbf{x} an unique 2D material position \mathbf{X} is assigned representing the point on the 2D cutting pattern plane to be determined.

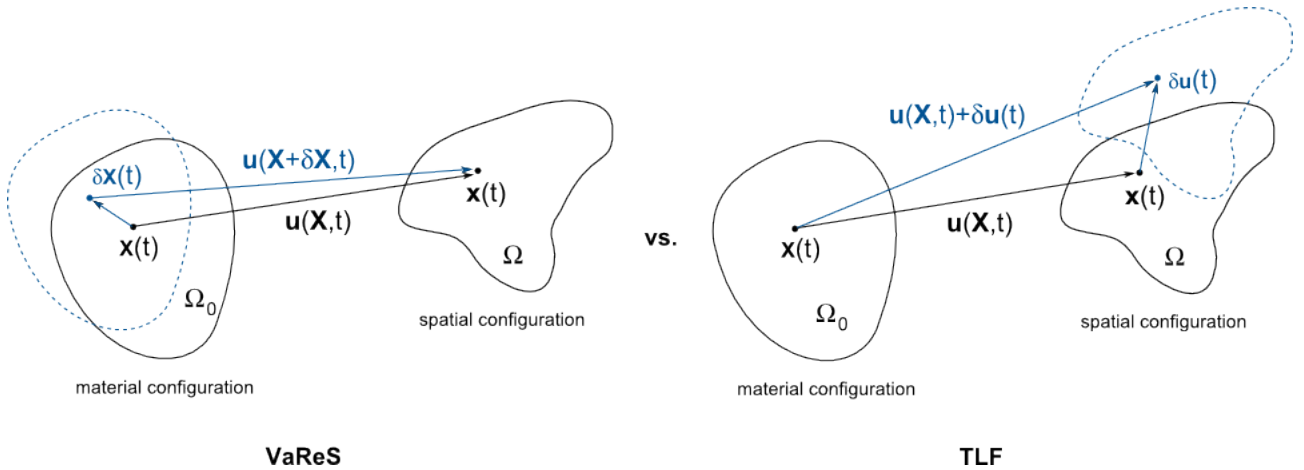


Fig. 2. Comparison: VaReS (left) vs. Total Lagrange Formulation (TLF) (right)

3.1. The shape-optimization problem to find the optimal cutting pattern

The aim of the following optimization problem is to find that material composition \mathbf{X} of the cutting pattern such that the deformation $\mathbf{X} \rightarrow \mathbf{x}$ generates the least potential energy $\Pi_{2D \rightarrow 3D}(\mathbf{X})$ for a given spatial composition \mathbf{x} . This can be seen as a reinterpretation of the Stress Compensation Method published by Maurin and Motro [3]. But instead of minimizing the difference of residual stresses and predefined stresses, the elastic potential Π due to these stresses is now considered. Opposite to standard continuum mechanics, now, the coordinates \mathbf{X} of reference shape are the unknowns instead of the spatial coordinates \mathbf{x} as usually. Thus, the optimization problem is formulated in terms of \mathbf{X} and will be called *Variation of Reference Strategy* or short VaReS. Additionally, a prestress field may act on the intended structure (as it is the case e.g. for tent like structures or fabric roofs):

$$\min_{\mathbf{X} \in \Omega_0} \rightarrow \Pi_{total}(\mathbf{X}) = \Pi_{2D \rightarrow 3D}(\mathbf{X}) - \Pi_{prestress}(\mathbf{X}) \quad (2)$$

3.2. Stationary point: variational formulation

The optimal cutting pattern \mathbf{X} is defined by the first variation of equation (2) which has to vanish:

$$\delta \Pi_{total}(\mathbf{X}) = D_{\delta \mathbf{X}} \Pi_{total}(\mathbf{X}) = 0 \quad (3)$$

Assuming hyperelastic material behavior in terms of the energy density function Ψ , the Green-Lagrange strains \mathbf{E} and 2nd Piola Kirchhoff stresses \mathbf{S} and applying the chain rule gives as governing equation equations:

$$\begin{aligned} \delta \Pi_{total}(\mathbf{X}) = & \int_{\Omega^{2D}} (\mathbf{S}_{2S \rightarrow 3D} - \mathbf{S}_{prestess}) : D_{\delta \mathbf{X}} \mathbf{E}(\mathbf{X}) d\Omega^{2D} \\ & + \int_{\Omega^{2D}} (\Psi_{2S \rightarrow 3D} - \Psi_{prestess}) : D_{\delta \mathbf{X}} d\Omega^{2D} = 0 \end{aligned} \quad (4)$$

Note, that the variation of the integration domain has to be considered as well. In contrast to other methods e.g. by Linhard VaReS ensures the objectivity of the material by considering the “forward” erection procedure to determine deformation whilst the “inverse” cutting pattern problem is solved.

4. FINITE ELEMENT FORMULATION

Standard finite element discretization techniques can be applied for the solution of the nonlinear equations (4). However, additional terms for residual force vector and stiffness matrix appear because of using the discrete material coordinates X_a defining the shape of the cutting pattern as unknowns and by the variation of the integral domain.

Straight forward the components R_a of the residual force vector \mathbf{R} are:

$$\begin{aligned} R_a = & l_3 \int_0^1 \int_0^1 \det J (\mathbf{S}_{2D \rightarrow 3D} - \mathbf{S}_{prestess}) : \frac{\partial \mathbf{E}}{\partial X_a} d\xi d\eta \\ & + l_3 \int_0^1 \int_0^1 \frac{\partial \det J}{\partial X_a} (\Psi_{2D \rightarrow 3D} - \Psi_{prestess}) d\xi d\eta = 0 \end{aligned} \quad (5)$$

with l_3 being the thickness and $\det \mathbf{J}$ defining the mapping of the material domain into the parametric space ξ, η . Further linearization of the residual force vector \mathbf{R} gives the nonlinear tangential stiffness matrix \mathbf{K} . Finally, a highly nonlinear system of equations has to be solved. As a consequence, standard pseudo-time stepping techniques (path following methods, numerical continuation), as known from other nonlinear structural problems, can successfully be applied together with Newton-Raphson schemes for the iterative solution within each time step.

5. EXAMPLES

The following 3 examples will show the capabilities of the presented Variation of Reference Strategy. A section of a cylinder (see section 5.1) will serve as a benchmark problem comparing both damping and pseudo-time stepping. Additionally, different material models (isotropic and anisotropic) were applied in order to outline the generality of the presented Variation of Reference Strategy, see section 5.2.

5.1. Section of a cylinder

As reference to an analytical solution of the cutting pattern problem, a 160° cylindrical segment is used as a benchmark. The applied material model is based on a Neo-Hooke strain-energy function. An orthogonal projection onto the x-y-plane serves as an initial guess, see figure 3 (left). Due to the projection method, the elements on both ends of the strip are heavily distorted. Hence, at least 3 pseudo-time steps were necessary. As expected, the final shape of the optimized cutting pattern is a rectangle of area equal to the 160° segment, see figure 3 (right). VaReS can be proved to be stable and robust. As a consequence of the consistent linearization the convergence properties are proved as intended by the chosen discretization and trial functions.

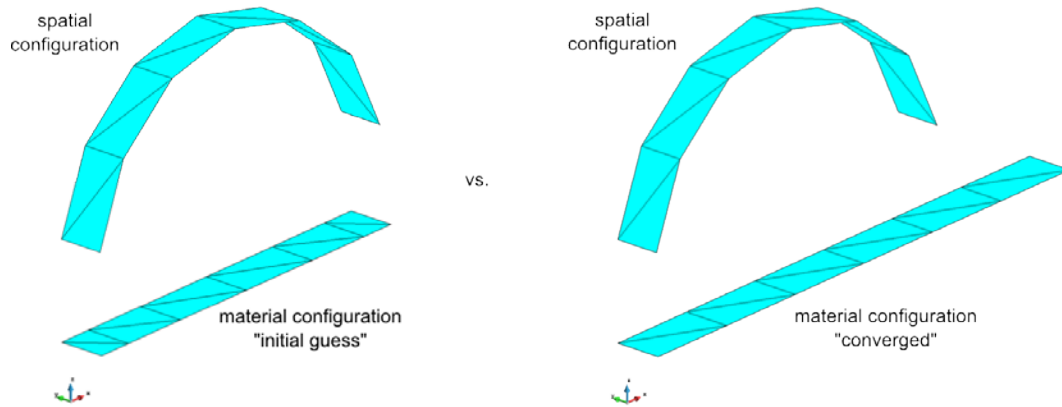


Fig. 3. Figure 12 160° segment: initial guess (left) and converged solution (right)

5.2. 30deg rib

The following examples deal with the cutting pattern generation of a generic rib segment (30° arc) of fiber composite structure. Figure 4 shows the plane initial guess and the corresponding determinant of the deformation gradients ($J = \det(\mathbf{F})$) as a measure for the resulting displacement field.

Two different material models were used, the Neo-Hooke model (see section 5.2.1) and the NCF model introduced by Vidal-Sallé et al. [16] and Y. Aimène et al. [17] (see section 5.2.2).

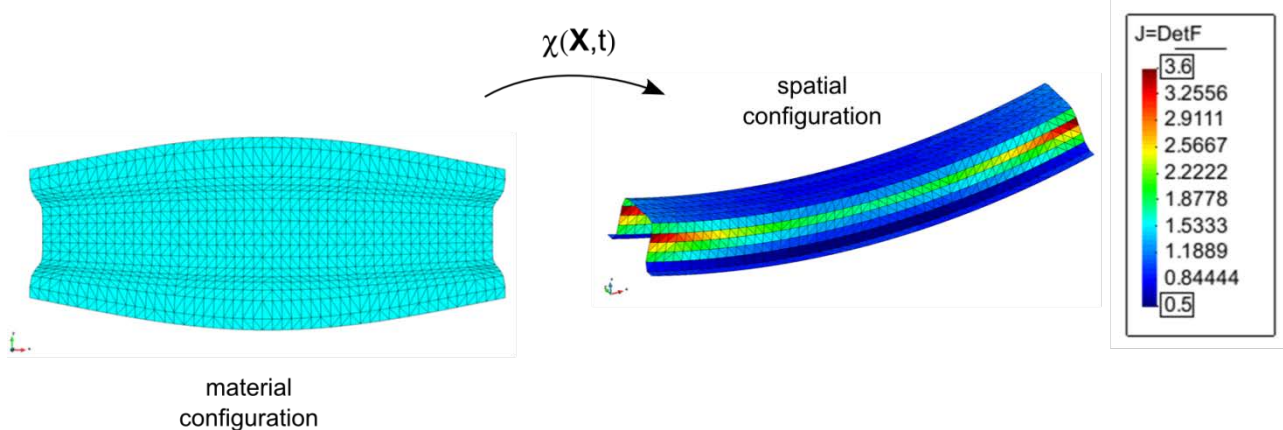


Fig. 4. Figure 17 30° rib: plane initial guess (left) and corresponding deformation gradients (right)

5.2.1. Neo-Hooke

The challenge is to controlling the large element distortions. Consequently, 5 pseudo-time steps have been taken. Figure 5 shows the determinant of the deformation gradients corresponding to each initial guess. The initial guess of the first pseudo-time step and the converged solution of the last pseudo-time step are shown in figure 6. Again, the method converges optimally.

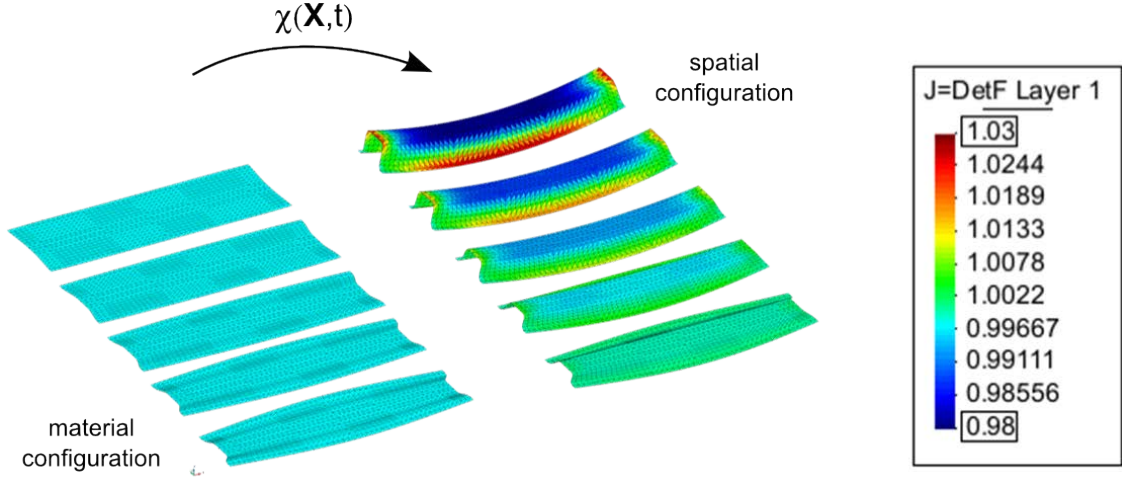


Fig. 5. Figure 18 30° rib: det(F) at the beginning of each pseudo-time step

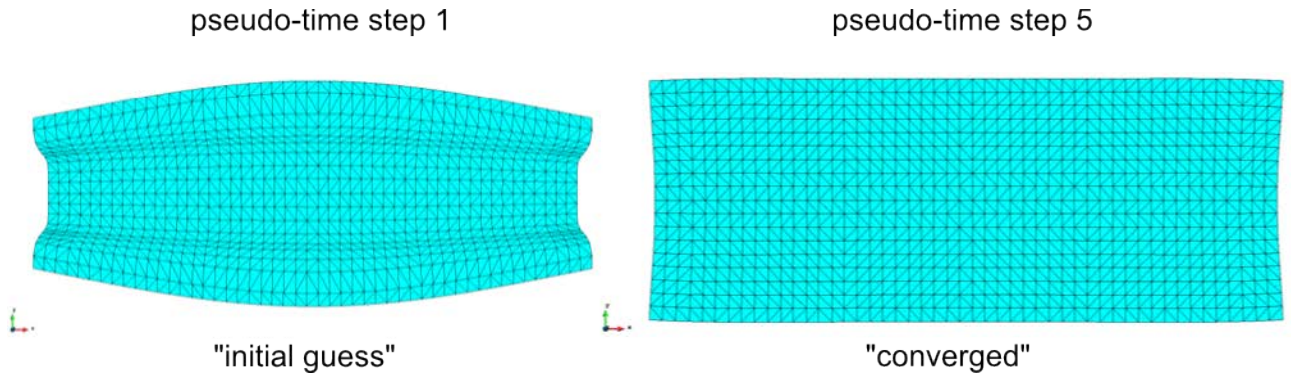


Fig. 6. Figure 19 30° rib: Initial guess (left) vs. optimized cutting pattern (right)

5.2.2. Strain-energy function for Non-Crimped Fabrics

Considering an anisotropic material behavior, the shape of the optimal cutting pattern strongly depends on the material orientation. In order to investigate these effects, a strain-energy function for non-crimped fabrics (see Y. Aimène et al. [17]) is used

$$\Psi(\mathbf{C}) = \sum_{i=0}^r \frac{1}{i+1} A_i (I_4^{i+1} - 1) + \sum_{j=0}^s \frac{1}{j+1} B_j (I_6^{j+1} - 1) + \sum_{k=1}^t \frac{1}{k} C_k \left(\frac{1}{I_4 I_6} \text{tr}(\mathbf{C} \mathbf{M} \mathbf{C} \mathbf{M}^2) \right)^k \quad (6)$$

The coefficients of the polynomials for a glass plane weave are listed in table 1 and table 2 published in Y. Aimène et al. [17]). Both, 0°/90° and 45°/-45° fiber orientations have been under investigation. Figures 7 and 8 show the

corresponding optimized cutting patterns and the resulting fiber distortions. Comparing both cutting patterns clearly shows the influence of the fiber direction. Furthermore, an analysis of the stresses in warp and weft direction provides a deeper understanding of potential areas where wrinkles are more likely to be expected. Figures 9 and 10 show the corresponding fiber stresses for the achieved cutting patterns.

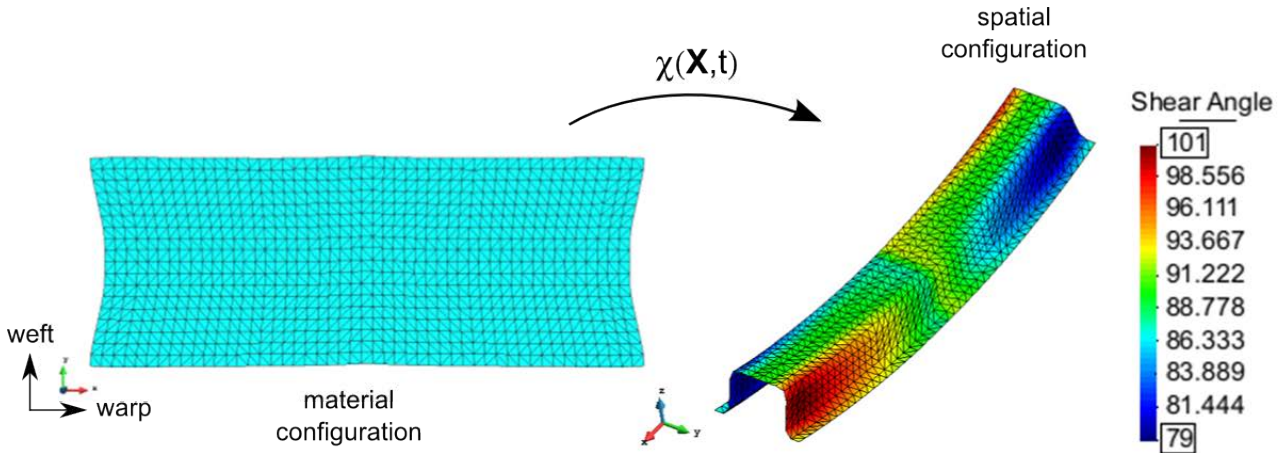


Fig. 7. Figure 21 30° rib: NCF 0°/90° - optimized cutting pattern (left) and fiber distortions (right)

Finally, figure 11 shows the dilemma every design engineer has to deal with, if a so-called stack of different plies has to be designed. For example, the application of the shape of the 45°/-45° configuration for a 0°/90° ply leads to areas with unprofitable compressive stresses in warp direction at the upper part of the rib, Fig. 11.

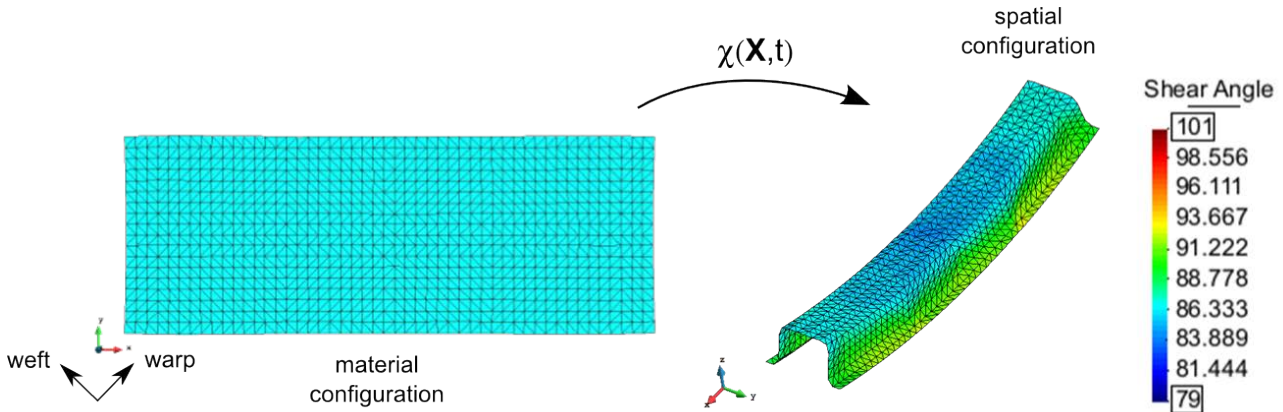


Fig. 8. Figure 22: 30° rib: NCF 45°/-45° - optimized cutting pattern (left) and fiber distortions (right)

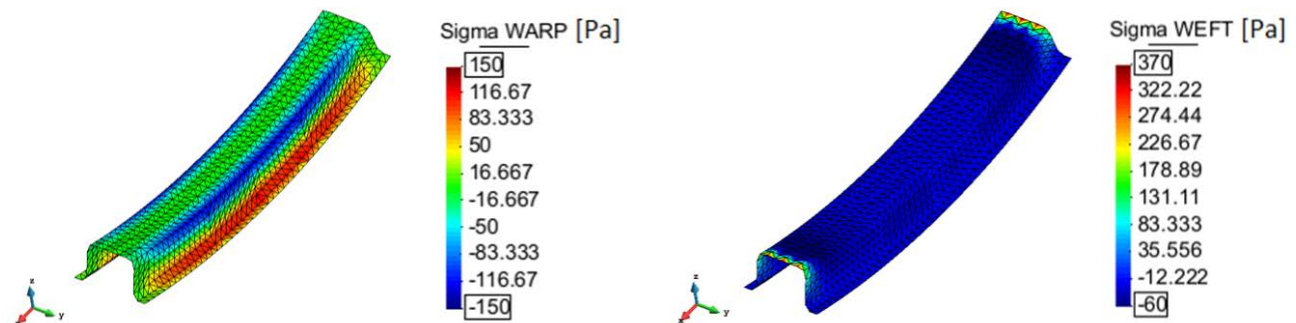


Fig. 9. Figure 23: 30° rib: 0°/90° ply - warp-stress (left) and weft-stress(right)

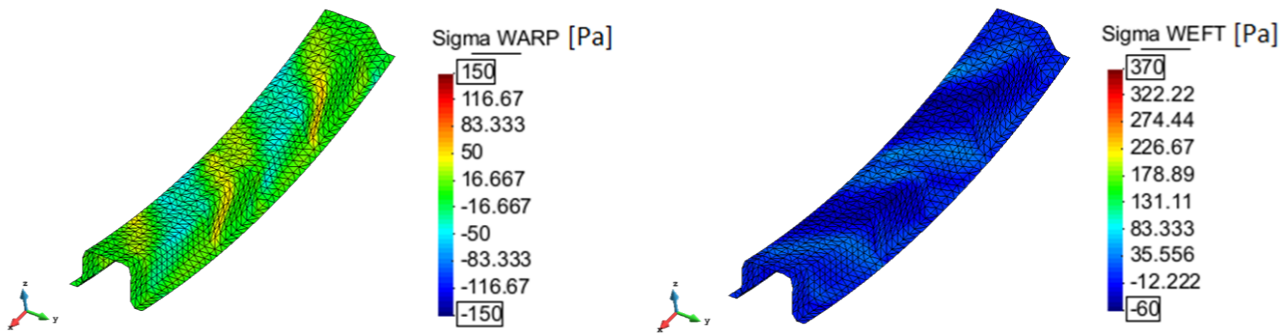


Fig. 10. Figure 24: 30° rib: 45°/-45° ply - warp-stress (left) and weft-stress(right)

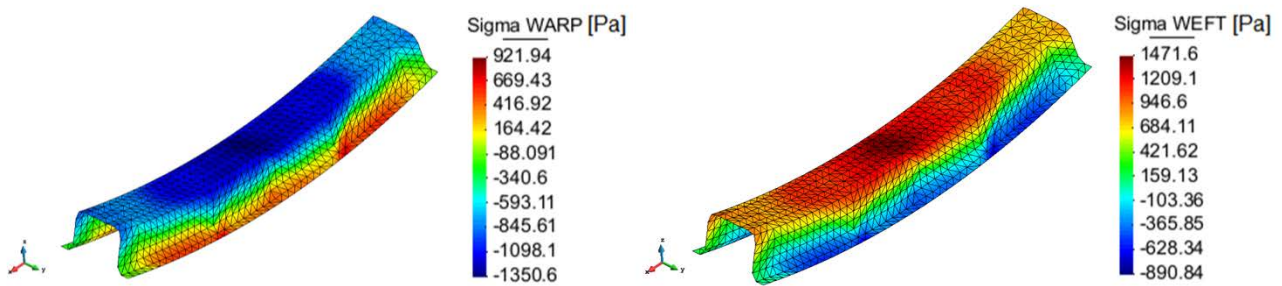


Fig. 11. Figure 25: 30° rib: Unprofitable cutting pattern - warp-stresses (left) and weft stresses (right)

6. CONCLUSIONS

The presented Variation of Reference Strategy deals with the challenge of finding the optimized plane shape for a given double-curved structure. The novel numerical approach is based on an unconstrained optimization problem, namely minimizing the stationary potential energy of the structure. At a first glance, the problem looks very similar to a Total Lagrange Formulation used for standard structural analysis. A direct comparison between both Variation of Reference Strategy and Total Lagrange Formulation clearly shows their similarities and differences. Both approaches are using the same conjugated work pair, namely Green-Lagrange strains in combination with 2nd Piola-Kirchhoff stresses. I.e. all integrals are established and evaluated with respect to the material configuration. Within a Total Lagrange Formulation the material configuration of a structure is known where the spatial configuration of the structure under loading conditions is of interest. The primary variables are the displacements of each node. However, when dealing with the Variation of Reference Strategy the spatial configuration of a double-curved structure is fixed in space (and therefore known) and the material configuration of the structure (cutting pattern) needs to be found. Hence, the primary variables are the nodal positions in the material configuration.

A major property of the presented method is the high nonlinearity of the governing equations and their sensitivity with respect to the initialization of the Newton-Raphson scheme. The pseudo-time stepping turns out to be a very powerful remedy coming along with small number of iterations within each pseudo time step. Finally, VaReS can be easily applied to all kind of isotropic and anisotropic hyperelastic material models allowing for the cutting pattern and draping simulation of fabric structures of one or more layers.

The problem of intra-ply shear locking arising due to highly anisotropic materials such as CFRPs is addressed to further ongoing research by the chair of structural analysis.

REFERENCES

- [1] L. Gründig, E. Moncrieff, P. Singer, D. Ströbel, High performance cutting pattern generation of architectural textile structures, in: Fourth International Colloquium on Computation of Shell and Spatial Structures, Chania-Crete, Greece, 2000, pp. 1–15.

- [2] B. Topping, P. Iványi, Computer Aided Design of Cable Membrane Structures, Saxe-Coburg Publications, Kippen, Stirlingshire, 2007.
- [3] B. Maurin, R. Motro, Cutting pattern of fabric membranes with the stress compensation method, International Journal of Spatial Structures 14 (2) (1999) 121–129.
- [4] J.-Y. Kim, J.-B. Lee, A new technique for optimum cutting pattern generation of membrane structures, Engineering Structures 24 (2002) 745–756.
- [5] E. Haug, P. D. Kermel, B. Gawenat, A. Michalski, Industrial design and analysis of structural membranes, in: International Conference on Textile Composites and Inflatable Structures - STRUCTURAL MEMBRANES, 2007.
- [6] E. Haug, P. D. Kermel, B. Gawenat, A. Michalski, Industrial design and analysis of structural membranes, International Journal of Space Structures 24 (4) (2009) 191–204.
- [7] J. Linhard, R. Wüchner, K.-U. Bletzinger, Introducing cutting patterns in form finding and structural analysis, Computational Methods in Applied Sciences 8 (2008) 69–84.
- [8] J. Linhard, Numerisch-mechanische Betrachtung des Entwurfsprozesses von Membrantragwerken, Ph.D. thesis, Lehrstuhl für Statik, Technische Universität München (2010).
- [9] K.-U. Bletzinger, J. Linhard, R. Wüchner, Extended and integrated numerical form finding and cutting patterning for membrane structures, Journal of the International Association for Shell and Spatial Structures 50 (3) (2009) 35–49.
- [10] K.-U. Bletzinger, J. Linhard, Tracing the equilibrium - recent advances in numerical form finding, International Journal of Space Structures 25 (2) (2010) 107–116.
- [11] F. Dieringer, R. Wüchner, K.-U. Bletzinger, Practical advances in numerical form finding and cutting pattern generation for membrane structures, Journal of the International Association for Shell and Spatial Structures 53 (3) (2012) 147–156.
- [12] S. Govindjee, P. Mihalic, Computational methods for inverse finite elastostatics, Comp. Methods Appl. Mech. Engrg. 136 (1996) 47–57.
- [13] S. Govindjee, P. Mihalic, Computational methods for inverse deformations in quasi-incompressible finite elasticity, Int. J. Numer. Meth. Engrg. 43 (1998) 821–838.
- [14] M. Gee, C. Reeps, E. Eckstein, W. Wall, Prestressing in finite deformation abdominal aortic aneurysm simulation, Journal of Biomechanics 42 (2009) 1732–1739. doi:10.1016/j.jbiomech.2009.04.016.
- [15] G. Holzapfel, Nonlinear Solid Mechanics - A continuum approach for engineering, John Wiley & Sons LTD, Chichester, Weinheim, New York, Brisbane, Singapore, Toronto, 2000.
- [16] E. Vidal-Sallé, Y. Aimène, P. Boisse, Use of a hyperelastic constitutive law for dry woven forming simulations, in: The 14th International Conference on Material Forming: ESAFORM 2011 Proceedings, 2011, pp. 883–888.
- [17] Y. Aimène, E. Vidal-Sallé, B. Hagège, F. Sidoroff, P. Boisse, A hyperelastic approach for composite reinforced large deformation analysis, Journal of Composite Materials 44 (1) (2010) 5–26.
- [18] D. Balzani, F. Gruttmann, J. Schröder, Analysis of thin shells using anisotropic polyconvex energy densities, Comput. Methods Appl. Mech. Engrg. 197 (2008) 1015–1032. doi:10.1016/j.cma.2007.10.005.
- [19] J. Schröder, P. Neff, Invariant formulation of hyperelastic transverse isotropy based on polyconvex free energy functions, International Journal of Solids and Structures 40 (2003) 401–445.
- [20] J. Bonet, A. Burton, A simple orthotropic, transversely isotropic hyperelastic constitutive equation for large strain computations, Comp. Methods Appl. Mech. Engrg. 162 (1998) 151–164.
- [21] S. Reese, T. Raible, P. Wriggers, Finite element modelling of orthotropic material behaviour in pneumatic membranes, International Journal of Solids and Structures 38 (2001) 9525–9544.
- [22] T. Belytschko, W. Liu, B. Moran, Nonlinear Finite Elements for Continua and Structures, John Wiley & Sons LTD, Chichester, Weinheim, New York, Brisbane, Singapore, Toronto, 2000.
- [23] P. Badel, S. Gauthier, E. Vidal-Sallé, P. Boisse, Rate constitutive equations for computational analyses for textile composite reinforced mechanical behaviour during forming, Composites: Part A 40 (2009) 997–1007. doi:10.1016/j.compositesa.2008.04.015.
- [24] S. Klinkel, S. Govindjee, Using finite strain 3d-material models in beam and shell elements, Engineering Computations 19 (3) (2003) 254–271.

- [25] S. Klinkel, F. Gruttmann, W. Wagner, A continuum based three-dimensional shell element for laminated structures, *Computers & Structures* 71 (1999) 43–62.
- [26] T. Hughes, *The Finite Element Method - Linear Static and Dynamic Finite Element Analysis*, Dover Publication Inc., Mineola, 2000.

ACKNOWLEDGEMENTS

The authors gratefully acknowledge the support of Deutsche Forschungsgemeinschaft as well as the very fruitful cooperation with BMW AG, München.

Efficient Automated Resizing of a Deployable Membrane SAR Antenna

Marco Straubel⁽¹⁾, Christian Hühne⁽¹⁾, Michael Sinapius⁽²⁾

⁽¹⁾Affiliation

DLR - Institute of Composite Structures and Adaptive Systems, Composite Design Department,
Lilienthalplatz 7, 38108 Braunschweig, Germany
Email: Marco.Straubel@dlr.de; Christian.Huehne@dlr.de

⁽²⁾Affiliation

Institute of Adaptronics and Function Integration – IAF, Technische Universität Braunschweig,
Langer Kamp 6, 38106 Braunschweig, Germany
Email: M.Sinapius@tu-braunschweig.de

ABSTRACT

The design and sizing of structural components for space antenna structures is by default strongly dominated by the RF-design of the antenna. As the regarding RF requirements are varying from mission to mission and relatively often also during an ongoing projects, a method has been developed that allows the automated resizing of a deployable membrane antenna in relation to RF and mechanical requirements.

The paper therefore introduces the basic design of a scalable deployable membrane antenna that was originally developed as a 40m² L-band SAR antenna. Moreover, the deployment method and the scaling approach are described. An automated resizing tool is presented that combines the capabilities of MATLAB, ANSYS and MS Excel to adapt the design of the antenna with respect to modified requirements within less than 30 minutes.

Some exemplary results for different requirement sets are presented and evaluated. Finally, an optimized parameter setup is presented that fulfils the defined requirements with less mass. It is a result of the gained understanding of this structure and the input of the various design parameters on the final configuration. This could mainly be achieved by reviewing the results of the previously performed calculations on the example parameter sets.

1. INTRODUCTION

For the optimization of SAR antenna performance the enlargement of the active antenna aperture is one possible way. Until today, huge antennas are usually designed using classical manifold structure concepts to pack them in a space saving manner for launch. However, the mass and packed size of such antennas is still relatively high and, therefore, the orbit transfer increases the mission costs markedly.

A reduction of mass and costs can be achieved using *gossamer structures*. The opportunity of saving volume and mass by using gossamer space structures leads to different but attractive opportunities:

- Larger structures can be used/deployed in space
- A smaller and, therefore, cheaper launcher can be used → decrease of mission costs
- A larger launcher system can carry more than one satellite → decrease of multi-satellite mission costs

During a four years lasting ESA-NPI* and DLR co-sponsored study, DLR investigates an alternative design for a 40m²-class membrane SAR antenna that will be presented hereunder by introducing a new *mechanical* gossamer antenna concept as well as a sizing strategy for a close-to-optimum structure.

* ESA Networking/Partnering Initiative (http://www.esa.int/Our_Activities/Technology/Networking_Partnering_Initiative)

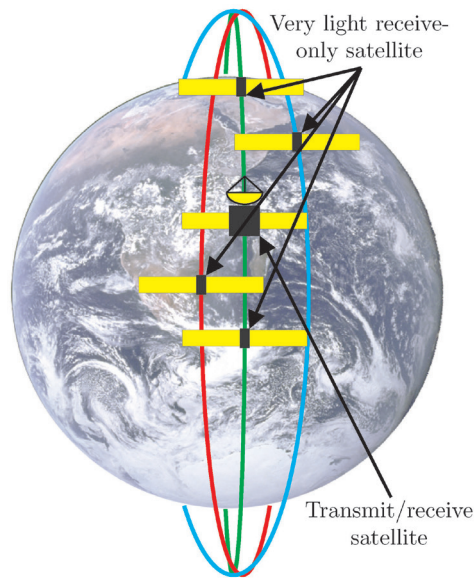


Fig. 1. Proposed mission design

Comparable antennas have been developed before [1, 2, 3]. The resulting concepts achieve specific masses of down to 1.6 kg/m^2 [4]. The objective of the study was to create a concepts with a lower specific mass.

1.1. Foreseen Mission Scenario

The envisaged mission of a satellite is the key information to define the overall design of the necessary SAR antenna. The mission profile for the here discussed antenna is the monitoring of *Global Change Indicators*. They can be defined as quantifiable natural physical occurrences that allow conclusions on global or local deviance of the climatic or the ecosystem. Exemplary indicators are vegetation distribution, soil moisture, polar caps, glaciers, ocean salinity, or ocean currents. For the defined mission profile radar frequencies in L- or P-band are preferred.

For the here given mission objective there is no need to have a high resolution but the radar signals have to partly penetrate the vegetation to monitor it or penetrate it completely for monitoring of soil properties without dependence to vegetation.

Aiming for an application for very light radar antennas, multi-satellite mission scenarios as previously described by Krieger and Moreira [5], Moreira et al. [6], and Zink et al. [7] are an attractive opportunity.

Thereby, Krieger and Moreira describe so called *Multistatic SAR Satellite Formations* [5], whereas Zink et al. name them *Cartwheel Constellations* [7]. Both use multiple receive antennae distributed over multiple satellite platforms in combination with one transmitting antenna. Using the transmitted radar signal and the received data of the entire formation in combination with the exact knowledge of the satellites spatial separation, enables the usage of interferometric SAR processing methods. Beside the higher resolution of the gathered data, the interferometric methods generate also 3-dimensional information on the observed object. Thus, highly detailed 3D mapping is possible.

In contrast Moreira et al. [6] present a formation flying of two almost identical SAR satellites. The TanDEM-X formation is an upgrade of the TerraSAR-X mission by a second similar satellite. Both platforms are orbiting each other and the Earth in a double helix like trajectory. In October 2010 [8] the first interferometric operation of both satellites was confirmed. The achieved results as well as the later collected data depict the huge potential of such formation flying SAR platforms.

However, contrary to the described TerraSAR-X/TanDEM-X concept, it is possible that future satellite formations will consist of highly differential platforms where the transceiver SAR satellite is much more complex than the receive-only ones.

Driven by the high power consuming SAR transmit functionality and the down link of the gathered data of the entire constellation, it is assessed that the transceiver satellite will have a considerably higher need for electric power than the receiver platforms. Thus, the demand for large solar arrays as well as batteries for backup is given at the transceiver which increases the weight of the power sub-system and, thereby, the mass of the entire satellite.

Contrary, the receive-only satellites do require less energy for their RF tasks and do not have to transfer the data to the ground by the transceiver satellite as relay station. This will decrease the mass of the satellite to a minimum. Bus architectures of *SmallSat* level are therefore realistic.

The proposed mission design is characterized by:

- Multi-satellite mission utilizing one transmit/receive- and multiple receive only satellites for interferometric SAR
 - Transmit option uses conventional parabolic antenna
 - Receive option requires only one extreme light and packing efficient antenna per satellite
- Antenna operating in L-band at 1.25 GHz
- Use in lower earth orbits
- Beam steering shall be possible

A visualization of this mission design is also given in Fig. 1 [9]. The here described antenna is consequently addressing the receive-only satellite out of the constellation.

1.2. Requirements

Resulting from the mission scenario defined before a set of mechanical requirements is defined here. The antenna is so far developed as equipment for an undefined satellite but exceeds the dimension that one would usually design according to *ECSS equipment loads*. Therefore, a reasonable set of generic requirements has been defined that is considered to be realistic.

Tab. 1 Loads and requirements for the stowed antenna configuration

Load Case	Value to track	Description
steady state acceleration	$a_{long} \leq 9,375 \text{ g}$ $a_{lat} \leq 9,375 \text{ g}$	expected steady state accelerations during launch
random vibration	$a_{3\sigma GRMS} \leq 33,36 \text{ g}$	the antenna shall be able to stand this random vibration equivalent load
first mode	$f_{1_SA} \geq 25 \text{ Hz}$	the first mode of the stowed antenna shall be above this value

The requirements for the stowed antenna configuration are given in Tab. 1. In addition, the antenna has to fulfill two requirements for the deployed configuration. The first deployed Eigen frequency shall not be less than the following limit: $f_{1_DA} \geq 0.4 \text{ Hz}$. Moreover, from a static view the deployed antenna structure needs to withstand the accumulated forces of the large amount of constant force springs that tension the membranes.

Moreover, basic requirements for the antenna design are listed hereunder and define the basis for all later developments:

1. Operation in *receive-only* mode,
2. Antenna operation frequency of 1.25 GHz (L-band),
3. Antenna aperture shape shall be rectangular
4. Antenna array size of $A_{AA}=40 \text{ m}^2$ with a length to width edge ratio k_{WL} between 1/4 and 1/6,
5. Maximum specific mass of 1.0 kg/m^2 ,
6. Stowed maximum volume of 0.8 m^3 ,
7. Operation in LEO (Lower Earth Orbit).

These values are reasonable assessments that result from expert interviews.

1.3. Motivation

During the study duration many requirements did change according to new findings or a modified mission scenario. As a consequence, the antenna structure needs to be resized manually each time to tune the mechanical behaviour to the updated requirements. This led to the insight that it might be very advantageous to have a FE antenna model that resizes automatically depending on a huge set of variable parameters. The development of this model and the regarding routines are described in the following section.

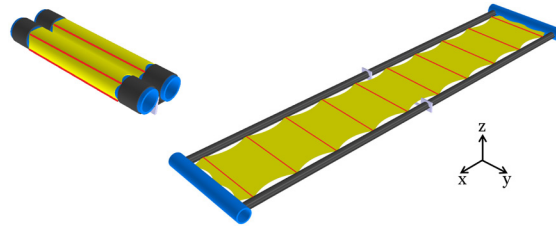


Fig. 2. Basic antenna concept in stowed (left) and deployed configuration (right), the antenna is composed of deployable booms (gray), rolling hubs (blue), membranes (yellow), and transversal stiffeners (red)

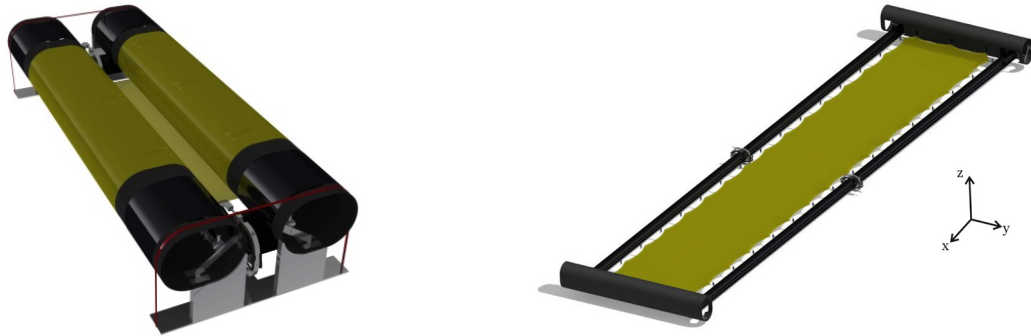


Fig. 3. Detailed antenna design in stowed (left) and deployed (right) configuration

2. CHOSEN ANTENNA DESIGN

Fig. 2 gives an impression on the basic design and deployment concept that is inspired by those of Fang et al.[10], Lopez et al.[3] and Huang[2]. A state of the art comparison of these previous concepts can be reviewed in [11].

It consists of a frame of two deployable booms, two rigid rolling hubs and some transversal frame stiffeners as well as four parallel membranes for the RF functionality. During packing each half antenna - including frame and membranes - is rolled on one hub. This rolling is performed with each hub from both sides and results in a compactly stowed antenna where the sensitive booms and membranes are safely wrapped around the rigid hub and are therefore protected from the static and dynamic launch loads.

The antenna functionality is provided by three membranes with applied antenna elements. As the RF design was not a task of the underlying study a membrane design is used that is in general identical to the one presented by Huang[2] (see Fig. 4). The presented antenna is designed for a radar operation frequency of 1.25 GHz (L-band). Therefore, this frequency will be also considered for the here discussed antenna.

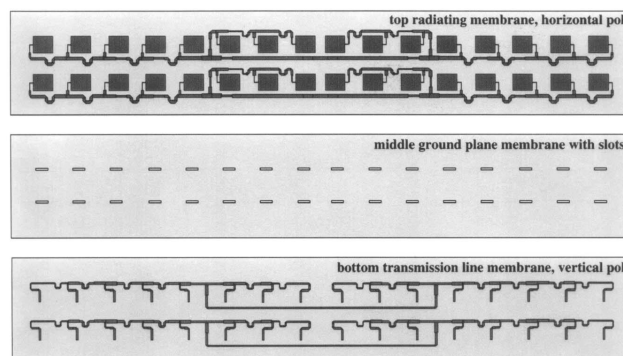


Fig. 4. Antenna membranes layout for dual-polarized micro-strip array as designed by Huang (image extracted from [2])

Huang describes the membrane setup as followed:

"The top layer has all the rectangular patches with a set of microstrip power divider lines for generating horizontal polarization. The middle layer is the ground plane with a set of aperture coupling slots. The bottom layer has only the power divider lines that excite the top-layer patches with vertical polarization through the coupling slots in the ground plane layer. [...] The three membrane layers are separated 1.27 cm between the top radiator layer and the middle ground-plane layer and 0.635 cm between the middle layer and the bottom transmission-line layer. [...] The membrane material used is a thin film of 5-micron-thick copper cladding on a 0.13-mm-thick Kapton dielectric material." [2]

A fourth membrane is added to carry the harness and amplifiers for feeding the antenna elements on the other three membranes. For this design approach each of the three antenna membranes weighs only 3.9 kg while the service membrane provides a mass of about 22.8 kg [12].

The used booms are rollable CFRP booms of the inflatable type that are further described in [13] and [14]. Due to the use of inflatable booms, the entire antenna can be deployed by applying pressure to the inner boom hose and does not require complex mechanisms.

The hubs are hollow cylinders of nearly circular cross section. The shell is made of a composite sandwich material of CFRP face sheets and aluminium honeycomb core material. Thereby, the minimum setup for the face sheets is a composite from two UD-CFRP layers in hub length direction and one layer in circumferential direction.

The transversal stiffeners are required to offload the booms from bending and shear loads evolving from the membrane tensioning forces introduced by the boom to membrane interfaces. These loads would otherwise deform the boom cross section which would degrade the boom integrity and lower its performance.

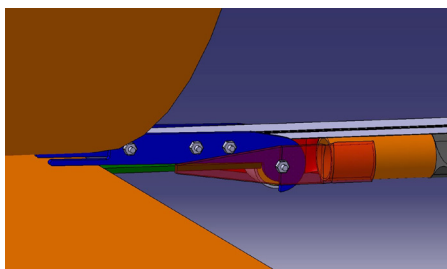
There are some frame-to-membrane interfaces which have their main task in establishing a mechanical connection between the antenna frame and the four membranes during all mission phases. As the frame consists of booms and hubs, two different interface types have been designed. The more complicated frame to membranes interface is shown in the Figures Fig. 5a and Fig. 5b.

The interface is designed according to the following requirements:

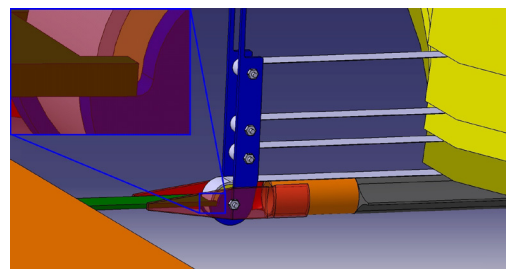
- The interface needs to compensate CTE related deformation differences between the CFRP frame and the polymer membrane without significant changes in membrane interface forces or membrane spacing.
- The interfaces need to support the membrane in stowed, deploying and deployed configuration.
- While in deployed configuration, the interfaces have to ensure that all membranes are in the defined parallel distance to each other.
- While in stowed configuration, the interfaces have to ensure that the distances between the membranes need to be close to zero to coil them on the same hub without risking in-plane travelling of the different layers due to different rolling radii.
- The transition of the interface from stowed to the deployed configuration is done automatically.
- The interface shall include interface points to the tips of the transversal stiffeners

The images of Fig. 5 display the interaction of the different interface and antenna components in stowed and deployed configuration:

1. Boom connection plate (green),
2. Fixed side plates (semi-transparent red),



(a) stowed configuration



(b) deployed configuration

Fig. 5. Boom to membrane interfaces

3. Movable side plates (blue),
4. CFSs(Constant Force Springs) (light grey),
5. Dry lubricated PTFE bearings for CFS support (not shown),
6. Screws and nuts (light grey)
7. Deploying boom (orange, on the left hand side),
8. Antenna (light yellow) and service (dark yellow) membranes,
9. Transversal stiffeners (orange rod) with membrane protective cover (dark grey).

Obviously, the interface consists of a fixed and a moveable part. The fixed part is connecting the boom flange with the service membrane CFS and the transversal stiffeners. The movable part carries the other three springs for the antenna membranes and is connected to the fixed part by a bolt.

The movable parts of the interfaces can be tilted by 90° for the antenna stowing process to decrease the distances between the membrane layers to zero. The flexibility of the CFS is thereby ensuring that only a minimal in-plane travelling of the membranes occurs.

To prevent an interface deployment in stowed antenna configuration, each movable part is equipped with a small extension that locks itself under the flange of the previous boom layer (see Fig. 5a).

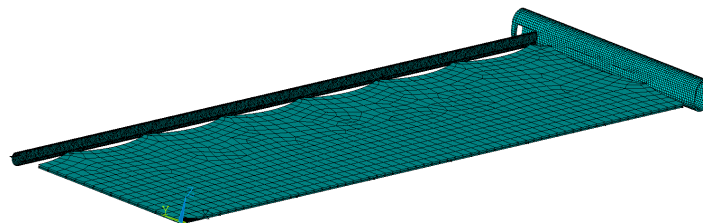
Once unlocked, the deployment of the interface is driven by the CFS. These forces are always aligned to the plane of the regarding membranes which is never on the same level as the rotation axis of the movable part (see again Fig. 5a for details). This offset between axis and forces generates a torque that is always acting such as the movable part tries to flip up to the upright position and lock into an end stop. This stop is established between the boom connection plate and the movable side plates. It is visible in the magnified part of Fig. 5b.

Caused by the small required distances between the membranes, the overall dimensions of this mechanism are very tiny. The movable side plates are only 45mm long, M1.0 screws and nuts are used for assembly and the overall mass of one interface is about 5.1 grams without margins. This value includes the first six components of the above given listing.

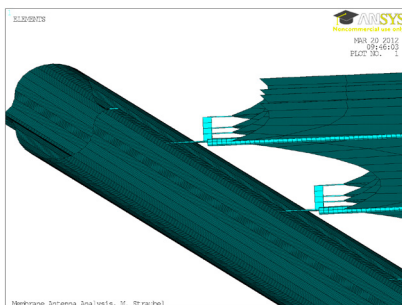
Earlier concept approaches for the antenna design can be reviewed in [15]. [4]

3. ANTENNA FINITE ELEMENT MODEL

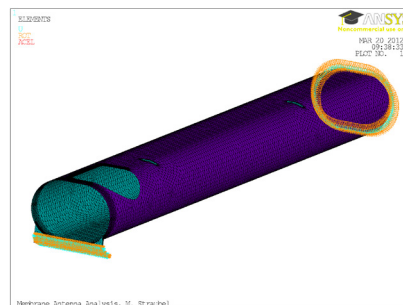
To size the different parts, a parameterised detailed FE model has been created using ANSYS script based input capabilities. This model allows calculating stowed and deployed antenna configurations due to selective meshing of the parts of interest.



(a) Antenna FE model for deployed antenna configuration (representative quarter)



(b) Detailed view on boom-to-membrane interface regions



(c) Antenna FE model for stowed configuration (representative half hub)

Fig. 6. Membrane antenna finite element model

Both stowed and deployed antenna configurations are modelled as quarter antennas to account for the obviously existing two symmetry axes and save computing time. Fig. 6a shows the deployed model while Fig. 6b shows a magnified section of the model with details on membrane interfaces and transversal stiffeners.

The boom, the hub and the membranes are modelled using shell elements. Thereby, the boom and membrane shells are modelled using single-layered shells. In contrast, the hub shell is modelled using a multi-layered shell to respect the sandwich layer setup and evaluate the strength criteria for each layer for the stowed configuration. The specific model made for the stowed configuration is shown in Fig. 6c. Although the image gives the impression that only the hub is taken into account, the coiled membranes, booms, stiffeners and interfaces are respected by locally increased density values of the hub core material. This method is valid because it is assumed that all this parts are wrapped around the hub firmly and relative movement of the layers is considered to be not possible.

4. CLOSED LOOP SIZING CHAIN

The detailed design and sizing of the antenna parts need to be performed in an appropriate order that starts with the element of highest mission interest and ends with the support structures that carries those mission relevant elements. Thus, the line-up specified in Fig. 7 has been chosen and implemented in a top-level MATLAB script bundle. This bundle is able to start ANSYS FE calculations with different sets of requirements and parameters and transfers the results of the FEAs back to MATLAB. The set of requirements and parameters that is transferred to ANSYS before the FEA contains more than 150 variables that specify requirements like launch loads levels but also user chosen parameters like boom cross section dimension or hub laminate setup or even material parameters. Moreover, a flag variable is defined that indicated the requested load case and therefore the kind of calculation that ANSYS is requested to run.

These software capabilities are used to build a combined software package that is able to perform all subtask of the strategy fully automated. Therefore, simple geometric calculation like the membrane shape calculation but also

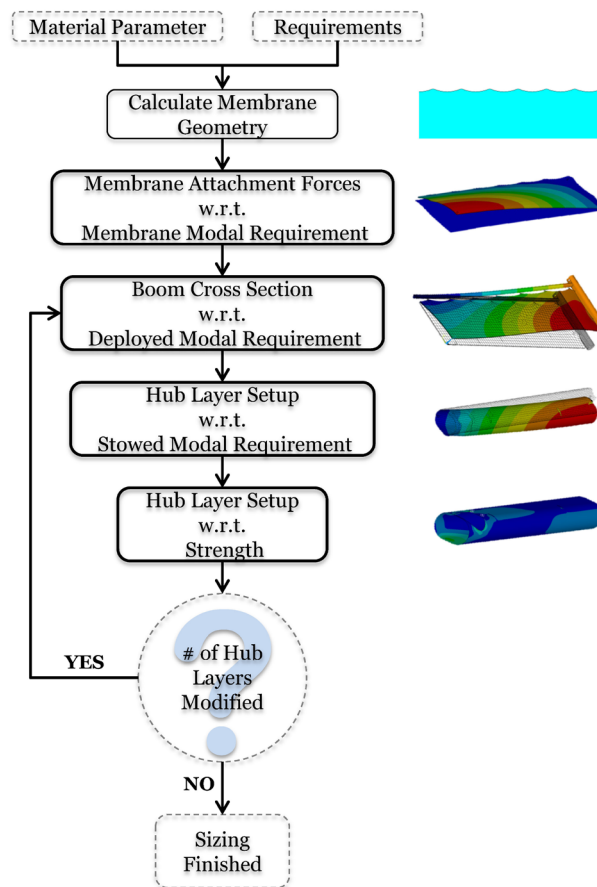


Fig. 7. Sizing Strategy

dedicated closed loop chain optimizations as required for the boom cross section sizing performed in the MATLAB script bundle.

To ease the understanding of the steps of the sizing strategy displayed in Fig. 7, some information on the particular bullets are given here:

4.1. Calculate Membrane Geometry

After defining material parameters and requirements, the geometry of the main function carrier - the membrane - is computed by Matlab using basic geometrical calculations.

4.2. Calculate Membrane Tensioning Forces according to Membrane Modal Requirement

Afterwards, the membrane attachment/tensioning forces, needed to fulfil the first mode frequency requirement of the pure membrane, are determined. This is realized in an automated process where Matlab is handling an iterative optimization routine. This routine is initiated with a start value for the membrane attachment forces that is numerically calculated from a hand book equation for the first mode frequency of an edge loaded membrane shell. Matlab starts an first FE run with this value and later on adjusts this force value until the resulting frequency equals the required one within a predefined accuracy. After this iteration, the forces that need to be provided by the CFSs is defined and thereby their subtype can be selected.

4.3. Calculate Boom Cross Section Geometry according to Global Modal Requirement

The next step is the sizing of the boom cross section according to the required first mode of the entire deployed antenna. Again, this sizing is done in an iterative routine that modifies the boom cross section until the first mode frequency fits the required 0.4Hz. Therefore, for each iteration run a three-step approach is used to respect the pre-stresses in the antenna structure introduced by the pulling forces of the before sized CFSs. The result of this iteration is a scaling parameter for the boom cross section dimension (except the shell thickness).

Step One – Static solution with CFS substituted by equivalent force pairs

At first, a static calculation is performed with a modified antenna model. Thereby, each CFS is substituted by a force pair. One single force is attached to the membrane attachment point of the CFS and pulling in an outwards direction. The other component of the force pair is acting in the opposite direction and is attached to the related connection point of the CFS at the antenna frame. This substitution is done for all CFS automatically by ANSYS. For an antenna configuration as shown in Fig. 6a, a number of $9 \cdot 4 = 36$ CFS is substituted. During this first static calculation, the membrane is stretched outwards and the frame parts are bended inwards as they would do under the load of all constant force springs. The deflections for each of the 72 force attachment points (each two points per CFS) are stored in a matrix.

Step Two – Static solution with CFS substituted by thermo-mechanical beams

The pairs of force attachment points are then connected by rod elements that are defined to be thermo-mechanical beams. Using the deflection data from the previous calculation as well as the material and cross section parameters of those beams, one can calculate a dedicated negative temperature difference value for each beam element that results in the same deflection of all force attachment points than previously achieved in step one. Please refer to section 9.8.2 of

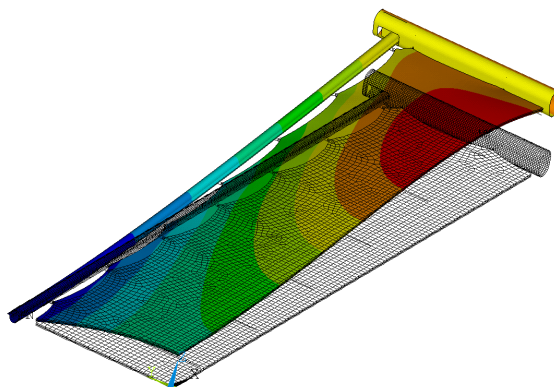


Fig. 8. First mode of antenna model vibrating at 0.4 Hz

reference [9] for more details on this analytical calculation.

Step Three – Modal solution of pre-stressed results obtained in previous step

The result of the last calculation in step one is now used as pre-stressed input structure for a classic modal analysis. Both membranes and frame are pre-stressed in a way as the CFSs would do. Moreover, frame and membrane are physically connected and can oscillate as one coupled structure (see Fig. 8). Thus, the result of this modal calculation is the first mode frequency of the antenna

4.4. Hub Sizing

With set boom geometry the hub geometry can be defined as well. As the boom is fed through a cut out in the hub and the boom needs to be coiled on the hub, a modified boom cross section results in a modified cut out geometry and the hub length needs to be adjusted in order to accommodate the stowed boom package that also changed its geometry.

With defined hub geometry, only the layer setup of the hub sandwich can be modified. Therefore, the layer setup is adjusted until the first mode frequency of the stowed antenna fulfils the launch requirements. This is realized by adding extra UD layers in hub length direction to both face sheet laminates.

Subsequently, the hub layers are investigated on potential strength failures when loaded with the random vibration equivalent $a_{3\sigma GRMS}$ static acceleration. If strength failures are detected, the layer setup is again modified until the strength behaviour is sufficient.

4.5. Block Interactions

The sizing of the hub layer setup and the boom cross section are influencing each other. For instance, a thicker hub laminate increases the mass of the hub and does require a stiffer boom to guarantee the deployed system stiffness. Contrary, an increased boom cross section does also increase the mass of the boom and thereby the additional mass applied to the hub for the modal and strength failure determination. Moreover, a larger boom cross section requires a larger boom feed through cut out in the hub which increases the hub length.

This interaction is the reason for the optional loop in Fig. 7. If the hub sizing requires a change in the hub laminate, the sizing of the booms needs to be redone to account for the heavier hubs. The hubs sizing is done again to account then for the heavier booms.

Fortunately, this *cross-tailoring* does not involve the optimisation of two real numbers. Such an optimisation would require a lot of iterative calculation or a more sophisticated optimisation with two unknowns.

Instead, here a *real* boom cross section scaling factor and the *integer* number of additional hub face sheet layers are tuned. The integer number is therefore stabilising the entire optimisation and is thus enabling this sequence of two optimisations with each one unknown.

4.6. Conclusion

So, except of the *Calculate Membrane Geometry* task all other sizing tasks shown in the chain of Fig. 7 are defined by an internal closed loop sizing that is able to tune an input sizing parameter in order to achieve the required output performance parameter.

Other previously performed calculations like buckling or thermo-mechanical analyses are not part of the closed loop sizing chain. This decision is made because in all performed calculations these load cases did not result in critical levels at all. However, it is understood that a final detailed design shall be checked against these failure modes.

5. EXEMPLARY RESULTS OF THE CLOSED LOOP SIZING CHAIN

The benefit of such a complex parameterised FE model in combination with the MATLAB script bundle is the possibility to run calculations of different configurations in an automated way. The software bundle is further enhanced adding Microsoft Excel to handle the high number of input and result variables for different configurations.

This option is of particular importance for the presented antenna design as the used set of requirements is no result of a detailed phase-A study but it is chosen by making reasonable assessments on mission design, launch loads and life environment. Consequently, a later defined mission and launch scenario will change a lot of boundary conditions which will generate the demand for an antenna resizing.

The first subsection shows the closed loop sizing chain results for different sets of requirements and discusses the findings. The examples orient to possible design changes that can result from modified mission objectives or a detailed RF-design for the membranes.

A second subsection shows a final configuration that is a consequence of the findings of the first part or simply other possible configurations that are not dedicated to the given antenna mission scenario but could be interesting for alternative applications.

Tab. 2 contains the combined results of the entire parameter study[†] with configurations from the first and the second subsection.

The table indicates the combined boom mass m_B , the combined mass of all three antenna membranes m_{3MA} , the mass of the service membrane m_{MS} , the combined hub mass m_H , the mass of the transversal stiffeners m_{St} , the over-all antenna mass m_A , the resulting specific mass per aperture area μ_A as well as the stowed antenna volume V_{AS} .

Values that have not changed with respect to the reference configuration are marked in grey font colour.

5.1. Example Configurations

The following reference and example configurations are listed in the table and provided with a unique identifier:

- RefConf: nominal reference configuration
- ExConf1: deployed first mode frequency reduced from 0.4 Hz to 0.3 Hz
- ExConf2: stowed first mode frequency reduced from 25 Hz to 20 Hz
- ExConf3: aperture area reduced from 40m² to 30m²
- ExConf4: specific additional mass on service membrane (represents amplifiers and harness) changed from 0.448 kg/m² to 0.1 kg/m²
- ExConf5: antenna functionality changed from *phased array* to *reflect array* (saves the heavy service membrane)
- ExConf6: aperture width-to-length ratio changed from 1/4 to 1/6

A dedicated evaluation for each configuration is given hereunder.

RefConf → *nominal reference configuration*

The reference configuration refers to the very basic and preliminary set of requirements, boundary conditions and a generic membrane design that defines masses for service and antenna membranes (see section 1 and 2).

The configuration requires a mass of 51.83kg to provide the required performance.

A look on the values of Tab. 2 motivates to examine the mass fracture of the different antenna parts with respect to the overall mass.

Tab. 2 Loads and requirements for the stowed antenna configuration

Result	RefConf	ExConf1	ExConf2	ExConf3	ExConf4	ExConf5	ExConf6	FiConf
m_B [kg]	1.87	1.66	1.87	1.42	1.74	1.66	2.58	2.28
m_{3MA} [kg]	9.61	9.61	9.61	7.23	9.61	9.61	9.65	9.65
m_{MS} [kg]	24.81	24.81	24.81	18.68	10.51	0.01	24.91	7.34
m_H [kg]	14.51	13.85	14.51	11.1	12.25	12.02	13.68	9.73
m_{St} [kg]	0.85	0.64	0.85	0.49	0.65	0.45	0.59	0.41
m_A [kg]	51.83	50.75	51.83	39.08	34.94	23.93	51.61	29.61
μ_A [kg/m ²]	1.296	1.269	1.296	1.303	0.874	0.598	1.29	0.74
V_{AS} [m ³]	0.608	0.569	0.608	0.504	0.584	0.568	0.563	0.523

[†] The automated sizing of each of the four configurations requires a calculation time of between 8 and 19 minutes on a notebook PC with 2.2GHz quad core processor and 8GB of RAM

For this reference configuration the following proportionate masses apply:

- Service membrane: 47.86%
- Hubs: 27.99%
- Antenna membranes: 18.54%
- Booms: 3.62%
- Transversal stiffeners: 1.65%

The function carrying combined membranes deliver a mass fraction of two third (66.4%). It is moreover obvious that the service membrane provides almost the half of the antenna mass whereas the hubs provide a quarter. Thus, it could be expected that changed requirements on the service membrane or the hubs will have the most significant impact on the antenna overall mass.

Unless the important role of the boom on the deployed system stiffness, the fraction of the boom mass in relation to the system mass is low. This can be explained with the relatively low stiffness requirements for the deployed boom in contrast to the hub that is designed to suit the launch loads.

ExConf1 → deployed first mode frequency reduced from 0.4 Hz to 0.3 Hz

The reduction of the deployed first mode frequency is directly affecting the boom cross section as it is the driven parameter for the deployed system stiffness. Moreover, the transversal stiffeners are modified due to change in the required first mode frequency of the pure membranes.

Interestingly, the downsized booms and stiffeners contribute each about 20% to the saved mass. But the hubs that are in general not significant for the deployed stiffness contribute 60%. This effect can be explained with the coupled geometries of the boom and the boom feed-through cut out in the hub. If the boom cross section is downsized, the cut out can be downsized, too. Such a smaller cut out does result in a reduced hub length. Due to the relative massive hub laminate each lost or gained centimetre in hub length has a strong impact on the antenna overall mass.

ExConf2 → stowed first mode frequency reduced from 25 Hz to 20 Hz

The grey numbers in the result column of this configuration in Tab. 2 show that a reduction of the stowed first frequency requirement has no effect on the overall design of the antenna. Fig. 7 indicates the reason for this effect: The stowed antenna is sized according to the here modified frequency *and* to strength criteria that are evaluated in the random vibration load case. Thereby, RefConf and ExConf2 do both require the same laminate setup to withstand the random vibration equivalent 33.3g. In both configurations the resulting hub has a first mode frequency of 28.6Hz which fulfils the requirements of both configurations. So as the random vibration load case is the sizing load case for the hub, a change in the frequency requirement has no effect on the structure.

ExConf3 → aperture area reduced from 40m² to 30m²

The results show how variations of one input parameter change the entire mass budget: Asking for a smaller antenna results in a lighter concept but the specific mass per aperture area is slightly increased. The saved mass is mainly generated by the saved area of the heavy service membrane. Moreover, the hub laminate in its basic minimum configuration is sufficient for all stowed load cases. Indeed, this basic hub laminate setup has no further downscaling capabilities which leads to an oversized hub and therefore to the increased specific mass of the antenna. This shows the limited parameter space of this model. For a design of smaller antennas of this dimension a light basic laminate should be defined by either choosing a lighter stacking or using thinner single layers to achieve an advanced granularity.

ExConf4 → specific additional mass on service membrane (represents amplifiers and harness) changed from 0.448 kg/m² to 0.1 kg/m²

ExConf5 → antenna functionality changed from phased array to reflect array (saves the heavy service membrane)

The most beneficial configurations are the forth and the fifth. They show that a reduction of the additional mass on the service membrane generates a much lighter and efficient structure. This additional mass is representing the harness and amplifiers for the antenna functionality and is an assessment based on literature reviews and expert interviews. Thus, the values used for configuration are not unrealistic assuming that RF-experts get involved in future detailed design studies.

ExConf6 → aperture width-to-length ratio changed from 1/4 to 1/6

Changing the width-to-length ratio of the antenna generates a longer antenna with decreased width. Hence, the booms are longer and require more mass while the hubs became shorter and therefore lighter. However, the overall mass and the specific mass remains the same so that the developer can choose the favourite configuration with respect to other

aspects. Here, one should prefer the 1/6 configuration because of the packed antenna volume. A higher width-to-length ratio generates shorter hubs which are resulting in a shorter stowed antenna package.

5.2. Resulting Final Configuration

The gained system understanding of the example configurations was used to compile a new set of requirements and boundary conditions in order to show the full potential of these concepts that can be exploited with modified geometry requirements and finer granularity of discrete optimization input variables.

Some significant numbers of the final configuration can be reviewed in the last column of Tab. 2.

The following modification with respect to the reference configuration RefConf has been made:

1. Change of aperture width-to-length ratio changed from 1/4 to 1/6
2. Reduction of specific additional mass on service membrane from 0.448 kg/m² to 0.1 kg/m²
3. Reduction of service membrane thickness from 100 µm to 50 µm
4. Reduction of the thickness of single UD-CFRP layers for the hub laminate from 0.1 mm to 0.05 mm

Thereby, the modifications 1 and 2 are direct results of the example configurations 6 and 4. Modification 3 is a logic consequence of modification 2 as a reduction of the additional mass on the service membrane should also allow a reduction of the membrane thickness.

Modification 4 is a result of the before mentioned limited downsizing capability of the hub.

The modifications result in a final mass of 29.6 kg and a specific mass of 0.74 kg/m² which more than fulfils the requirement defined in section 1.2.

6. CONCLUSION

The presented novel design for a deployable membrane space antenna is about 19 % lighter than the lightest state of the art gossamer system when considering the basic reference configuration (RefConf) but could not fulfil the set objective of 1 kg/m². A modified version with reduced RF-component mass is moreover able to further decrease the mass. However, these results need to be verified with tests on structural models to show the reliability of the used FEAs.

In addition, the presented automated sizing is able to optimize the shape and mass of the antenna according to changing requirement, materials or RF design.

This routines and the gained experience will enable DLR to react very fast on RF-design changes or requests for other membrane structures with a similar basic design. So, an adaption of the given concept for a passive reflector antenna or even a solar array with thin film solar cells could be performed easily.

A more detailed discussion of the here presented topic can be reviewed in the related doctoral thesis [9] which can be downloaded as full-text for free from the following website: <http://elib.dlr.de/81128/>.

ACKNOWLEDGEMENTS

We gratefully acknowledge DLR and ESA for funding the related NPI-Study on VERY LARGE STABLE MEMBRANE ANTENNA ARCHITECTURES.

REFERENCES

- [1] D. Cadogan and M. Grahne, "Deployment Control Mechanisms for Inflatable Space Structures," in *33rd Aerospace Mechanisms Conference*, May 1999.
- [2] J. Huang, "The Development of Inflatable Array Antennas," *Antennas and Propagation Magazine*, vol. 43, pp. 44–50, Aug 2001.
- [3] B. C. Lopez, M. C. Lou, J. Huang, and W. Edelstein, "Development of an Inflatable SAR Engineering Model," in *AIAA/ASME/ASCE/AHS/ASC Structures, Structural Dynamics, and Materials Conference and Exhibit*, vol. AIAA-2001-1618, Seattle, WA, USA, Apr. 16-19 2001.

- [4] M. Straubel, M. Hillebrandt, C. Hühne, and M. Sinapius, "Parameter Study Results on a Parameterised Deployable Membrane SAR Antenna Design Concept," in *ESA Workshop on Large Deployable Antennas*, ESA/ESTEC, Noordwijk, The Netherlands, Oct 2-3 2012.
- [5] G. Krieger and A. Moreira, "Multistatic SAR Satellite Formations: Potentials and Challenges," in *IEEE Geoscience and Remote Sensing Symposium*, Seoul, Korea, Jul 25-29 2005, pp. 2680–2684.
- [6] A. Moreira, G. Krieger, H. Fiedler, I. Hajnsek, M. Werner, M. Zink, and M. Younis, "TanDEM-X: A Satellite Formation for High Resolution Radar Interferometry," in *International Astronautical Congress (IAC)*, Oct 02-06 2006.
- [7] M. Zink, G. Krieger, and T. Amiot, "Interferometric Performance of a Cartwheel Constellation for TerrySAR-L," in *Fringe 2003 Workshop*, Frascati, Italy, Dec 1-5 2003.
- [8] M. Rodriguez-Cassola, P. Prats, D. Schulze, N. Tous-Ramon, U. Steinbrecher, L. Marotti, M. Nannini, M. Younis, P. Lopez-Dekker, M. Zink, A. Reigber, G. Krieger, and A. Moreira, "First Bistatic Spaceborne SAR Experiments With TanDEM-X," *Geoscience and Remote Sensing Letters, IEEE*, vol. 9, no. 1, pp. 33 –37, Jan 2012. [Online]. Available: <http://elib.dlr.de/70071/>
- [9] M. Straubel, "Design and Sizing Method for Deployable Space Antennas," Ph.D. dissertation, Otto-von-Guericke-Universität Magdeburg, GERMANY, Sep 2012. [Online]. Available: <http://elib.dlr.de/81128/>
- [10] H. Fang, M. Lou, and J. Huang, "Design and Development of an Inflatable Relectarry Antenna," JPL, Tech. Rep., May 15 2002, IPN Progress Report 42-149.
- [11] M. Straubel, C. Hühne, C. Arlt, S. Langlois, and M. Sinapius, "Design and Sizing of a 40m² Deployable Membrane SAR Space Antenna," in *European Conference on Spacecraft Structures, Materials and Environmental Testing*, Noordwijk, NL, Mar 2012.
- [12] M. Straubel, S. Langlois, M. Sinapius, and C. Hühne, "Simulation and Test on Mechanical Behavior of a Deployable Membrane Antenna," in *32th ESA Antenna Workshop*, Noordwijk, The Netherlands, Oct 5-8 2010.
- [13] M. Straubel, J. Block, M. Sinapius, and C. Hühne, "Deployable Composite Booms for Various Gossamer Space Structures," in *52nd AIAA/ASME/ASCE/AHS/ASC Structures, Structural Dynamics and Materials Conference*, no. 2023, Denver, Colorado, USA, Apr 4-7 2011.
- [14] M. Straubel, M. Sinapius, and S. Langlois, "On-Ground Rigidised, Deployable Masts for Large Gossamer Space Structures," in *European Conference on Spacecraft Structures, Materials & Mechanical Testing*, Toulouse, France, Sep 15-17 2009.
- [15] M. Straubel, C. Sickinger, and S. Langlois, "Trade-Off on Large Deployable Membrane Antennas," in *30th ESA Antenna Workshop*, Noordwijk, The Netherlands, May 27-30 2008.

STRUCTURAL CHARACTERIZATION AND MODELING OF METALLIC MESH MATERIAL FOR LARGE DEPLOYABLE REFLECTORS

G. L. Scialino ⁽¹⁾, P. Salvini ⁽²⁾, M. Migliorelli ⁽¹⁾, E. Pennestrì ⁽²⁾, P.P. Valentini ⁽²⁾, K. van't Klooster ⁽³⁾, J. Santiago Prowald ⁽³⁾, G. Rodrigues ⁽³⁾, Y. Gloy ⁽⁴⁾

⁽¹⁾ *Space Engineering S.p.A.*

Via dei Berio 91, 00155 Roma, Italy

Email: lorenzo.scialino@space.it, marzia.migliorelli@space.it

⁽²⁾ *University of Rome Tor Vergata, Department of Enterprise Engineering*

via del Politecnico 1, 00133 Rome, Italy

Email: salvini@uniroma2.it, pennestri@mec.uniroma2.it, valentini@ing.uniroma2.it

⁽³⁾ *ESA/ESTEC*

Keplerlaan 1, 2201 AZ Noordwijk, The Netherlands

Email: Kees.van.t.Klooster@esa.int, Julian.Santiago.Prowald@esa.int, Goncalo.Rodrigues@esa.int

⁽⁴⁾ *Institut fuer Textiltechnik (ITA) der RWTH Aachen University*

Otto-Blumenthalstraße 1, D-52074 Aachen, D

Email: yves.gloy@ita.rwth-aachen.de

ABSTRACT

Metallic mesh is a key component of Large Deployable Reflectors for telecommunication and Earth observation spacecraft antennas. Deep knowledge of mesh structural characteristics and the possibility to numerically simulate its behaviour are mandatory steps for its correct use in the reflectors. The mesh must be strongly compliant and is anisotropic; hence, a specific testing machine has been designed and built, able to stretch the specimen along two directions, with uncoupled motion laws, controlled both in force and displacement. The mechanical characterization is driven so that a numerical simulation of the mesh is derived requiring only common finite element formulations.

1. INTRODUCTION

Large Deployable Reflectors (LDR) are subsystems more and more used in high performance antennas embarked on spacecrafts for Telecommunication (Fig.1) and recently earth observation missions.

The Radio Frequency (RF) reflective surface is made by a metallic mesh, which is expanded after launch by a deployable structure and shaped by a tensioning system, either symmetrical nets (Fig. 2) or wires network (Fig.3).

The mesh is made of electrically conductive wire(s) arranged to provide an elastic surface, which can be stretched to achieve the prescribed surface profile once the reflector is deployed on orbit.

As it is demonstrated that the mesh shall be kept within a defined range of tension in order to provide the desired RF performances, it becomes of high importance to fully characterize its structural behaviour.

Currently the methods to characterize the mechanical behaviour of fabrics are driven by the textile industry for its requirements. None of the existing test set-up and machinery developed for the textile industry is suitable to characterize a very compliant, strongly non-linear and non-isotropic mesh material.

Hence, within the ESA study AO/1-7027/11/NL/MH, "Ultralight Reflector Mesh Material for Very Large Reflector Antennas", an innovative structural characterization method and a numerical simulation method have been developed for the mesh.

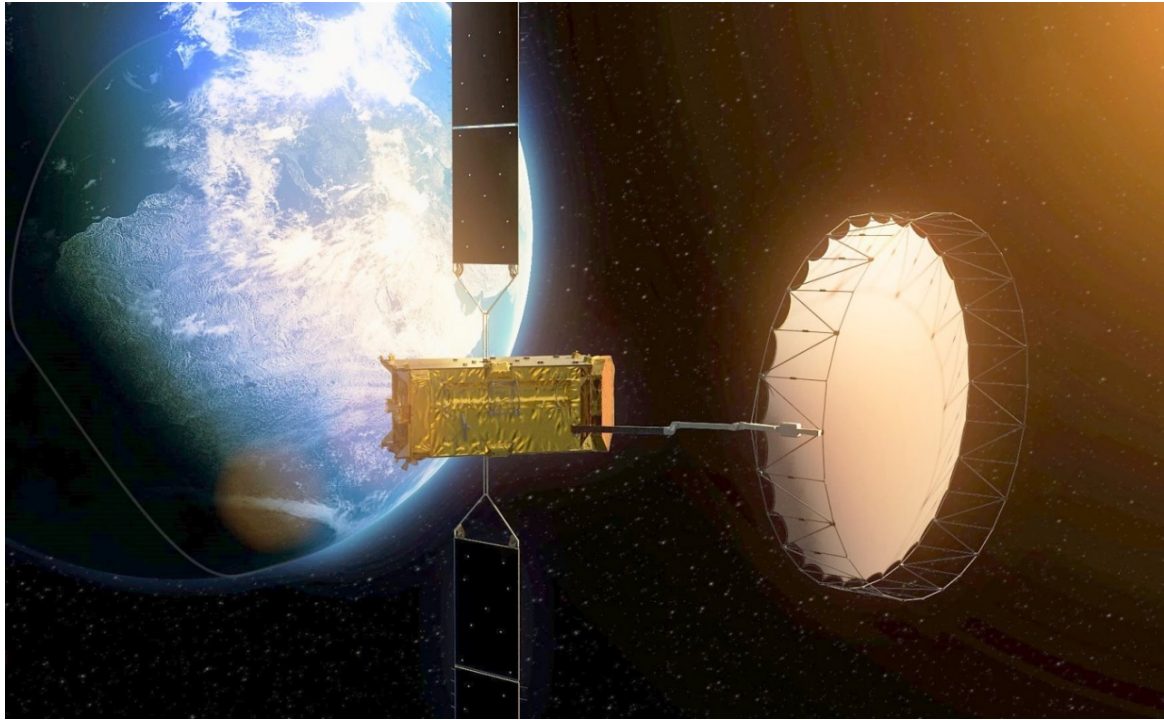


Fig. 1. LDR on board Alphasat – INMARSAT-XL with the Earth (ESA)

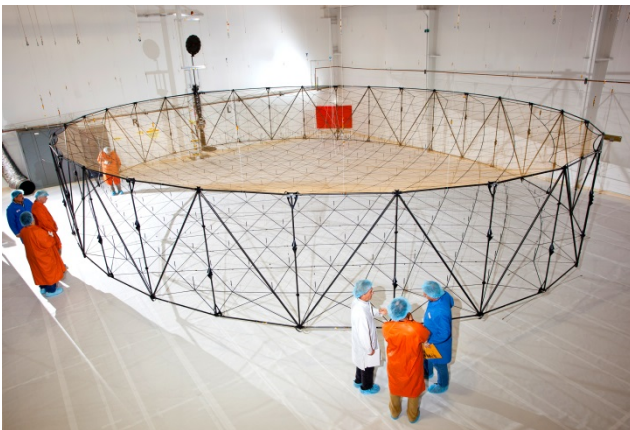


Fig. 2. LDR with symmetrical Mesh tensioning Nets (Northrop Grumman)

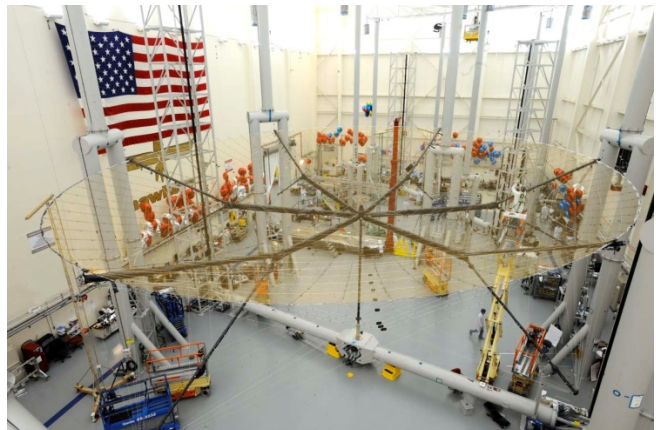


Fig. 3. LDR with Mesh tensioning by cable network (Harris Corporation)

2. LDR MESH

The mesh shall accomplish RF functions, after reflector deployment, through the orbital conditions for the entire life of the spacecraft.

The RF performances of the mesh are dependent on: the profile acquired by the mesh surface on the deployed reflector, the electrical conductivity of the basic material, the electrical resistivity of the wire to wire contact at each crossing, the size of the openings created by the wire(s) looping. These aspects are briefly discussed in the following subsections.

2.1. Orbital Conditions

The orbit used by the telecommunication satellites with LDR is generally the geostationary, while the orbits used by the Earth observation missions are generally low-medium altitude polar.

In both cases, the thermal range experienced by the LDR and the mesh is in the range from -190°C to $+140^{\circ}\text{C}$. Such wide thermal range affects the structural interaction of the mesh with the LDR structure and mesh profiling means.

The reflector structure is generally based on Carbon fibre reinforced plastic, hence with an expansion coefficient in the range of less than $5 \text{ ppm}/^{\circ}\text{C}$, the mesh generally has similar values, but the temperature distribution among the mesh, reflector structure, the mesh profiling system is strongly dependent on the thermo optical finishing and thermal inertia of the element. This is to say that across the orbital conditions temperature gradients are encountered among the various parts of the LDR. Temperature gradients induce deformation and redistribution of loads among the elements of the LDR.

The modification of the load distribution among the LDR elements can induce into the mesh either a relaxation or an increase of the stress level. The stress status shall not become lower than a defined limit to avoid the occurrence of Intermodulation of the RF signals, nor shall exceed the yield limit of the wires to avoid their permanent deformation with a consequent offsetting of the reference condition.

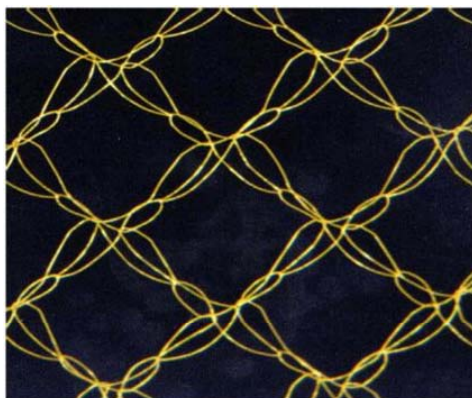
For these reasons, it is necessary that the mesh provides a limited stiffness, such that its loading status is slightly affected by the dimensional changes of the LDR structure and of the profiling means.

Furthermore, the mesh material shall not overcome the yield limit while exposed to the folding / deployment process of the LDR, neither during launch, nor across the orbital conditions. For this reason, a strong ultra-thin wire constituent is the preferable basic material for the mesh.

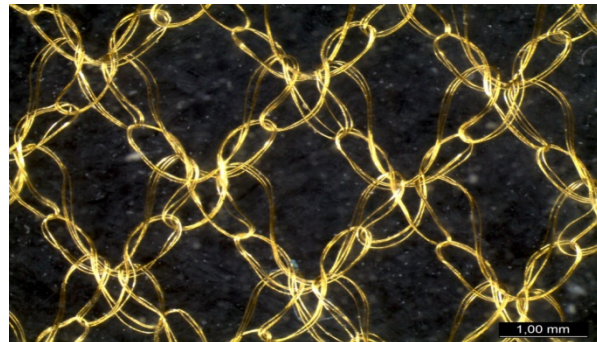
2.2. Mesh Alternative Configurations

Currently, the meshes of most of the flown LDR are made by single golden Molybdenum wire, but other alternative can be Tungsten either single or multiple wires either gold plated or bare. Tungsten exhibits higher tensile and yield limits than Molybdenum, smaller expansion coefficient and higher density; furthermore tungsten can be drawn at a thinner diameter than Molybdenum. The smaller diameter of the tungsten wire is beneficial in the mesh as the stress due to an imposed bending of the wire (due to mesh orbital loading) induces smaller stress level then in case of a larger wire diameter.

Another key factor of the mesh is the yarn configuration, to say if the mesh is made by the knitting of a single wire or by the knitting of multiple smaller wires, the latter provides a more efficient solution (see Fig.4).



Molybdenum single wire mesh



Tungsten three wire mesh

Fig. 4. Comparison between Mesh Yarn Configurations

The third key element of the mesh is the stitch type. As the goal is to have a mesh with similar (as far as possible) stiffness along and across the knitting direction the Warp type of stitches (multiple yarns processed in parallel across the knitting) is preferred to the Weft type (single wire processed back and forth across the width of the textile).

The candidate Warp knit alternatives are the Atlas-Atlas and the 1+1 (see Fig.5).

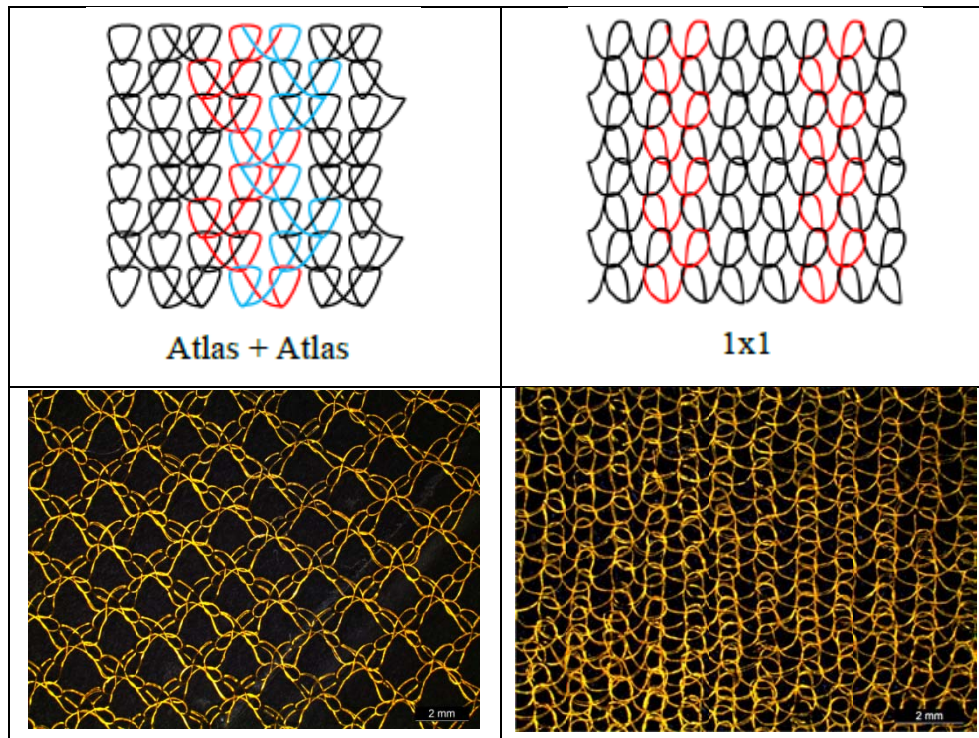


Fig. 5. Warp Knitted Mesh Alternatives: Atlas-Atlas & 1+1 (ITA)

The Atlas–Atlas is expected to be more compliant in all directions compared to the 1+1 due to the geometry with inclined leverages, but the 1+1 offers the advantage of smaller openings, which are of interest for the RF performances.

2.3. Mesh Structural Behaviour

The stiffness behaviour of the mesh is a function of several aspects acting together:

- the material of the basic wire (with its modulus),
- the diameter of the basic wire (smaller diameter provides a less stiff mesh),
- the routing of the yarn during the knitting process (rounded routing without exceeding the yield limit of the wire provides a “spring effect” at the level of each loop which is beneficial to the mesh),
- the stitch type (a stitch with inclined routing back and forth across the textile will be less rigid than a stitch with loops sequentially aligned along the knitting direction)

All these aspects are difficult to be evaluated a-priori to derive the structural behaviour of the mesh.

Furthermore the tension applied in one direction changes the shape of the stitch hence strongly modifying the stiffness of the mesh in the cross direction. To say that the response is strongly non-linear dependant from the cross coupling of the tension along orthogonal directions.

In practice the best approach is to actually measure the structural behaviour of the mesh in response of different loading conditions and then to derive a numerical modelling of such behaviour.

3. MESH STRUCTURAL PERFORMANCES MEASUREMENT APPROACH

The mesh is very compliant and anisotropic and for these reasons, the mechanical characterization cannot be achieved with standard one-dimensional approach (Chen, Matthews, 1993; Lecompte et al., 2007). For this purpose, a specific testing machine has been designed and built (see Fig. 6). The device includes a frame in which a portion of mesh can be mounted on. The mesh is grabbed using adjustable hooks and each edge can slide along very low-friction rolling guides. The equipment is able to apply an enforced and independent displacement along x and y directions and measure the corresponding reaction forces. The displacement is applied through a wire and pulleys system connected to two stepper motors. Loads are acquired by four load cell extensometers. With this architecture the equipment is capable to record independently the displacements and the forces along the two orthogonal directions.

The equipment includes a telecentric video camera capable to record high accuracy – undistorted pictures of the mesh under test to allow an accurate detection of the stitch deformation under each load condition.

The equipment is able to test different size of mesh (up to 400x400 mm) and produce very large displacements (up to 400 mm each direction). Five types of tests have been performed on the mesh. The first two measurements are the controlled stretching along x and y directions, keeping the opposite one fixed. The third and the fourth are the controlled stretching along x and y directions, keeping the opposite one free. The last measurement is the simultaneous controlled stretching along x and y directions, with equal and fixed-step increments. Both x and y reaction forces are acquired during the measurements. All the measurements start with an applied preload in both x and y directions able to reduce the vertical inflexion (sagging) to 1/50 of the length of the mesh.

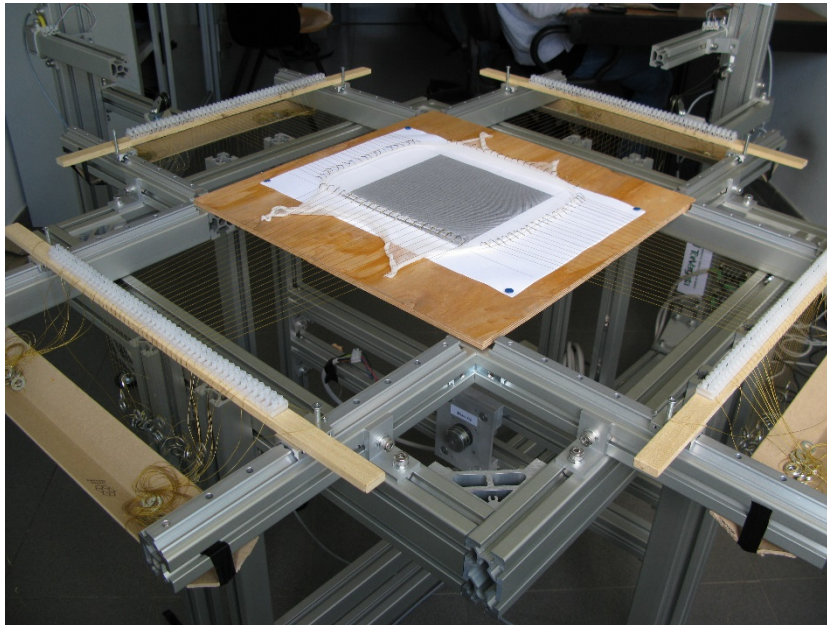


Fig. 6. A detailed view of the measurement device. A nylon mesh is mounted for preliminary assessment, calibration and verification.

4. MESH INITIAL PERFORMANCES MEASUREMENT

The initial tests have been performed on a quite large portion of metallic mesh. Fig. 7 reports the results for different measurements of the force/strain relationships. In the same plot, the curves related to the different boundary conditions explained in Section 3 are depicted.

It is clear to observe that the mesh has two different behaviours along the two testing directions and it has a global nonlinear trend of the force/strain relationships. For each load condition the larger stiffness is along the warp direction (along the direction of mesh production) and the smaller is in the weft direction (across the width of the mesh production).

Moreover, the mesh has revealed to be very compliant and a strain of 40% has been reached in two measurement configurations.

The stretching along one direction, keeping the other free, is counteracted by the lowest stiffness of the mesh. The stretching along one direction, keeping the other constrained, is counteracted by an intermediate stiffness of the mesh. The simultaneous stretching along both directions is counteracted by the highest stiffness.

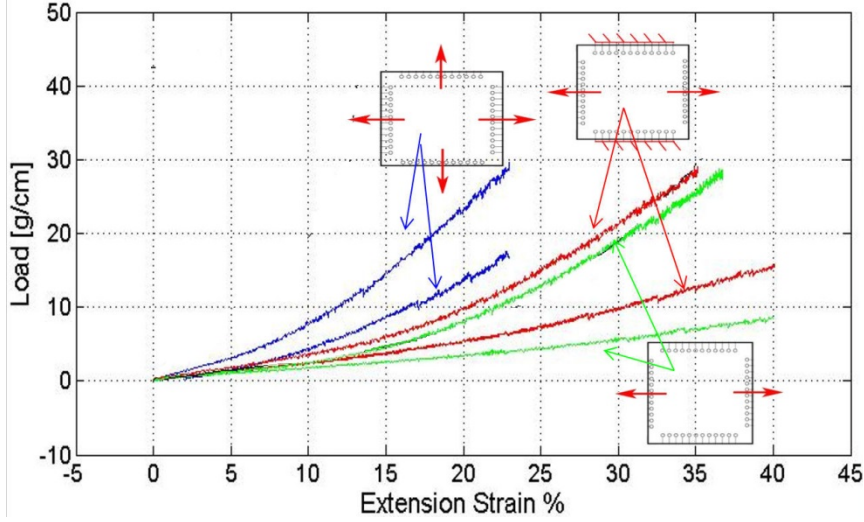


Fig. 7. Force/displacement relationships for different boundary conditions.

During each measurement, the mesh has been monitored using a CCD camera with a telecentric lens. The subsequent image processing has been useful to have an independent check on the deformation patterns. Images coming from the acquisitions have been automatically analysed by the computation of 2D Discrete Fourier Transform (DFT), in order to assess the frequency of the repetition of the loops. It can be considered an indirect measure of the mesh deformation $\{\mathcal{E}_x, \mathcal{E}_y\}$ by using the following formulas:

$$\mathcal{E}_x = \frac{l_{fx}}{l_{0x}} - 1 = \frac{\nu_x}{\nu_x - \Delta\nu_x} - 1 \quad (1)$$

$$\mathcal{E}_y = \frac{l_{fy}}{l_{0y}} - 1 = \frac{\nu_y}{\nu_y - \Delta\nu_y} - 1 \quad (2)$$

Where:

$l_{fx} = \frac{w}{\nu_x - \Delta\nu_x};$	w is the width of the image;
$l_{fy} = \frac{h}{\nu_y - \Delta\nu_y};$	h is the height of the image;
$l_{0x} = \frac{w}{\nu_x};$	ν_x and ν_y are the frequencies of the main peaks at the beginning of the test (after the application of the preload) along x and y directions, respectively;
$l_{0y} = \frac{h}{\nu_y};$	$\Delta\nu_x$ and $\Delta\nu_y$ are the frequency shifts between the initial condition and the full load condition along x and y directions, respectively;

Fig. 8 shows the acquisition hardware and an example of the taken picture and the corresponding Discrete Fourier Transform with a consistent peak.

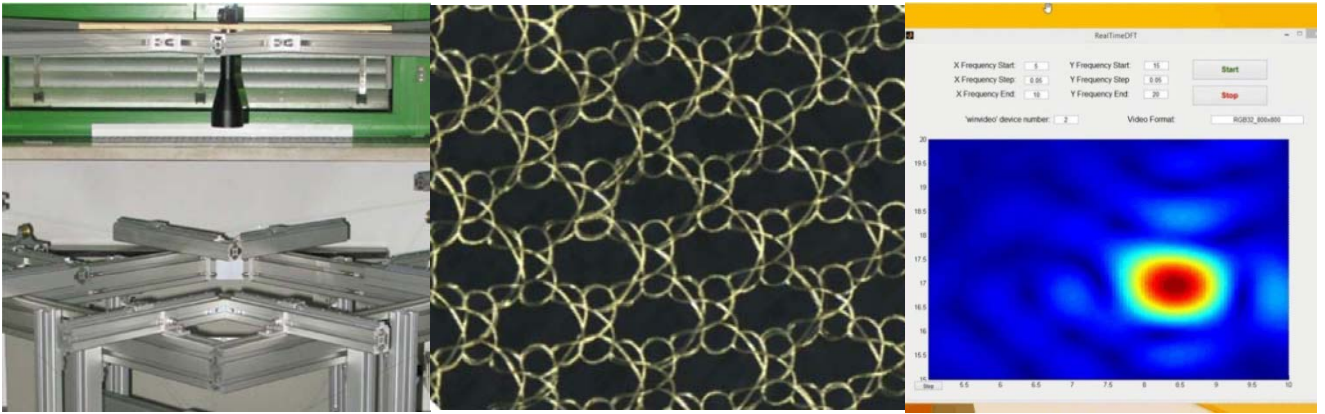


Fig. 8. Image processing of the metallic mesh

5. MESH STRUCTURAL MODELING BY CONDENSED MODEL

Starting from the interpretation of the behaviour of the metallic mesh during the experimental test, a numerical model of the structural behaviour of the mesh has been also developed by the University of Rome Tor Vergata, Department of Enterprise Engineering. The objective is to have a model suitable for the implementation of simulative scenarios using a Finite Element-like approach, but using condensed parameters in order to avoid the micro-scale description of the knitting pattern. In fact, the description of mesh details comes up with a very complex modelling approach very related to the specific knitting pattern, as testified by several authors (Kaldor et al. 2008; Taibei et al., 1999; Taibei et al. 2002).

The proposed model of the mesh is depicted in Fig. 9. It includes four boundary nodes (5, 6, 7 and 8), four mid-side nodes (1, 2, 3 and 4), which are connected by several spring elements. Ten springs describe the compliance along the main x and y directions (five springs for each direction). Four other springs are located transversally and their contribution to the horizontal and vertical stiffness depends on their attitude angle. This arrangement is able to include both generic compliance and non-linear geometrical behaviour due to the alignment of the fibres during the deformation.

It is easy to verify that this approach can be suitable for describing a variety of possible solutions and geometrical configurations after the identification of all the elastic parameters.

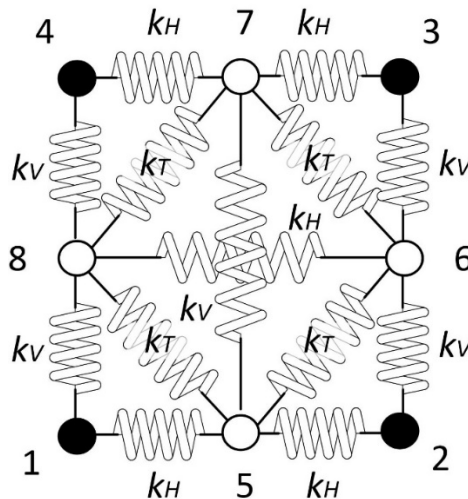


Fig. 9. The proposed basic element for the description of the knitted mesh

The element is symmetric and the independent stiffness parameters to be identified are three:

$k_H \rightarrow$ the stiffness parameter of the elements along the horizontal direction (5 elements);

$k_V \rightarrow$ the stiffness parameter of the elements along the vertical direction (5 elements);

$k_T \rightarrow$ the stiffness parameter of the elements along the diagonal direction (4 elements);

The deformation of the element can be described using four quantities:

$\varepsilon_H = \frac{l_H - l_{H0}}{l_{H0}}$ is the deformation in the horizontal direction (l_H is the horizontal length of the element after the deformation and l_{H0} is the horizontal length when undeformed);

$\varepsilon_V = \frac{l_V - l_{V0}}{l_{V0}}$ is the deformation in the vertical direction (l_V is the horizontal length of the element after the deformation and l_{V0} is the horizontal length when undeformed);

$\varepsilon_T = \frac{l_T - l_{T0}}{l_{T0}}$ is the deformation in the horizontal direction (l_V is the horizontal length of the element after the deformation and l_{V0} is the horizontal length when undeformed);

$\alpha = \arctan 2(l_H(1 + \varepsilon_H), l_V(1 + \varepsilon_V))$ is the internal angle (attitude of the transverse springs) measured from the horizontal direction.

The identification of the parameters k_H , k_V and k_T can be performed by the manipulation of the results coming from the experimental tests by using the equipment described in Section 3.

The measurement includes the increments of reaction forces (ΔF_H and ΔF_V) of the mesh along the two main directions when incremental displacements (ΔD_H and ΔD_V) are applied. Due to the symmetry of the mesh knitting, the incremental forces (Δf_H and Δf_V) and displacements (Δd_H and Δd_V) applied to the element can be computed as:

$\Delta f_H = \Delta F_H \frac{l_{H0}}{L_{H0}} \quad (3)$	$\Delta f_V = \Delta F_V \frac{l_{V0}}{L_{V0}} \quad (4)$	$\Delta d_H = \Delta D_H \frac{l_{H0}}{L_{H0}} \quad (5)$	$\Delta d_V = \Delta D_V \frac{l_{V0}}{L_{V0}} \quad (6)$
---	---	---	---

where L_{H0} and L_{V0} are the global horizontal and vertical lengths of the entire mesh, respectively.

In the same way, the stiffness coefficients of a single element are related to the stiffness coefficients of the global meshes by the same constant ratio l / L of the corresponding direction.

Considering and displacement increment Δd_H along the horizontal direction, we can write the balance of the forces in the element as:

$$\Delta d_H \rightarrow \begin{cases} \Delta f_H = -2(k_H \Delta d_H) - 2k_T \cos^2 \alpha \frac{\Delta d_H}{2} \\ \Delta f_V = -2k_T \sin \alpha \cos \alpha \frac{\Delta d_H}{2} \end{cases} \quad (7)$$

and for a displacement increment Δd_V along the vertical direction, we can write:

$$\Delta d_V \rightarrow \begin{cases} \Delta f_H = -2k_T \sin \alpha \cos \alpha \frac{\Delta d_V}{2} \\ \Delta f_V = -2(k_V \Delta d_H) - 2k_T \sin^2 \alpha \frac{\Delta d_V}{2} \end{cases} \quad (8)$$

Considering that from the measurements, the experimental stiffness coefficients can be defined as:

$$\begin{aligned}
 \frac{\partial F_H}{\partial D_H} &= -K_{HH} \\
 \frac{\partial F_H}{\partial D_V} &= -K_{HV} \\
 \frac{\partial F_V}{\partial D_V} &= -K_{VV} \\
 \frac{\partial F_V}{\partial D_H} &= -K_{VH}
 \end{aligned} \tag{9}$$

Experimental tests performed on the initial mesh specimens showed that the relationships force/displacement can be approximated with a second order polynomial. For this reason, the coefficients in Eq. (9) can be described by linear functions depending on the applied loads.

Extracting the stiffness coefficients in both (7) and (8) and taking into account the Eqs. (9), we can write:

$$\begin{aligned}
 K_{HH} &= 2k_H + 2k_T \cos^2 \alpha \\
 K_{VV} &= 2k_V + 2k_T \sin^2 \alpha \\
 K_{HV} &= K_{VH} = k_T \cos \alpha \sin \alpha
 \end{aligned} \tag{10}$$

The Eq. (10) can be rearranged in a matrix form and then solved as:

$$\begin{Bmatrix} k_H \\ k_V \\ k_T \end{Bmatrix} = \begin{bmatrix} 2 & 0 & \cos^2 \alpha \\ 0 & 2 & \sin^2 \alpha \\ 0 & 0 & \cos \alpha \sin \alpha \end{bmatrix}^{-1} \begin{Bmatrix} K_{HH} \\ K_{VV} \\ K_{HV} \end{Bmatrix} \tag{11}$$

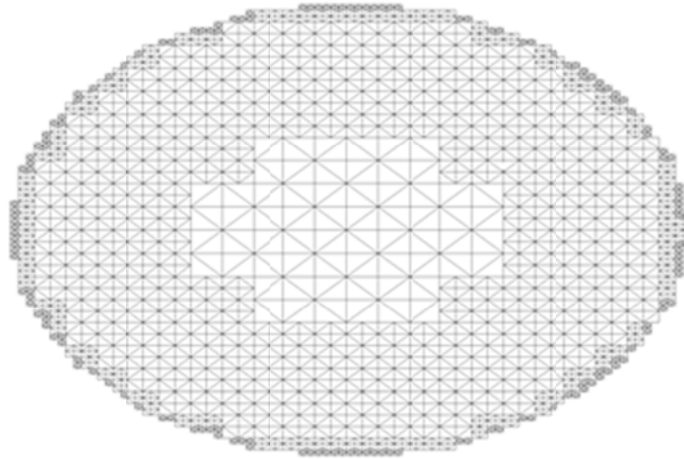


Fig. 10. Subdivision of an arbitrary region using mesh elements of different size

It is interesting to notice that the proposed approach in simulation using a condensed model is very suitable for subdivision and sub-structuring. This is the advantage to have defined the elements independent from the actual knitting pattern. For this reason, even if the basic element is rectangular, an arbitrary region can be approximated using a set of basic elements of different dimensions, connected together. Fig. 10 shows an example of this subdivision in which an elliptical region is approximated using rectangular elements of four different dimensions. In order to cope with such a configuration, the displacement of coincident nodes among the elements has to be properly constrained.

6. MESH STRUCTURAL MODELING BY WIRES SIMULATION

The metallic wire knitted mesh has been subject of a modelling exercise in the facilities of the Mechanical Department of ESA-ESTEC using non-linear finite element analysis methods. The purpose of the exercise is to support the testing and simplified modelling activities. The method has been applied to the Atlas-Atlas knit of a single wire that is equivalent to the behavior of a group of three Tungsten wires.

The procedure applied is as follows: the geometry of the mesh has been reproduced by beam elements taking into account the knot shape under pretension. This has been simulated by imposing an initial fictitious thermal load on a preform that follows the targeted knot deformation and acquires a determined tension level at the edges of a sample. The numerical implementation allows to detect and apply contact between wires automatically as it builds up during the load application. Although this is obviously an approximation to the real tensioning process, it can be observed that the acquired knot shape is not far from the reality and simulates the overall tension and geometry of the sample. It can be noticed that a certain level of anisotropy can be included in the model. Once the shape and tension are captured, due to the geometry and wire properties, the elastic behavior of the mesh represents a good approximation of the real mesh.

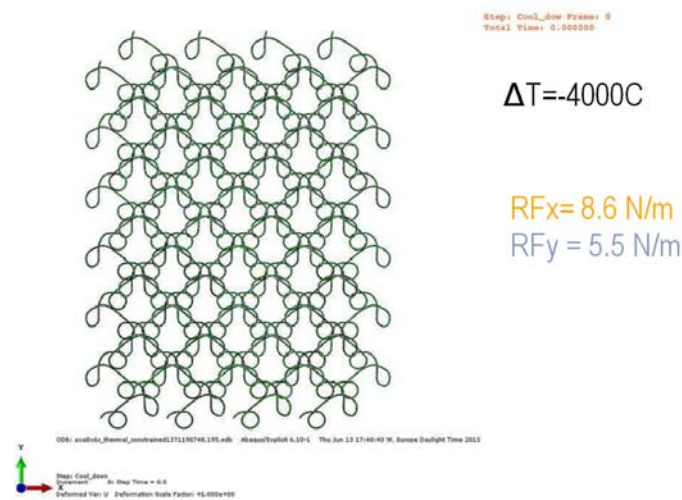


Fig. 11. Example of shape and tension level obtained under thermal fictitious load.

After the pretension and shape are captured, the next step is to apply elementary tension load cases in order to determine the overall sample properties. These load cases can follow the same ones defined for the test campaign. An example of this is shown in Fig. 12, for a given set of boundary conditions, which can be tuned to the test set-up.

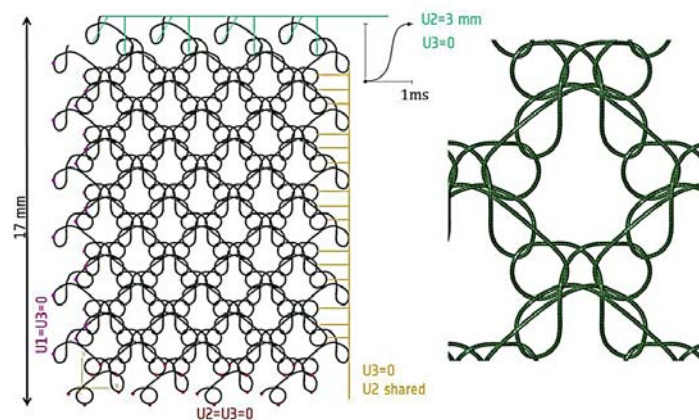


Fig. 12. Example of mesh analysis for a given sample, boundary conditions and load case.

The usefulness of the method is to provide more insight than the simplified analyses in the linear case, providing potentially a better physical understanding of the mechanical tests. This is expected especially if 3D effects play a role and in the case of large deformations. Furthermore, progressing into stress analysis, a by-product of the detailed simulation at wire level, could be the establishment of rules for limiting the tension and deformation of wires.

7. CONCLUSION

The development of Large Deployable Reflectors for telecommunication and Earth observation spacecraft antennas requires a very thorough understanding of the metallic mesh properties. This knowledge is mandatory for achieving an optimal design of the whole device, which can ensure high level of performances. In order to achieve this goal, the mesh has to be studied from different points of view.

The structural characteristics of the mesh are the preliminary features to be evaluated. The high compliance and anisotropy of the mesh require a dedicated experimental assessment, which is different from those used in fabric investigations or strong material tests. For this purpose, a specific machine has been designed. Experimental results, performed on a preliminary metallic mesh specimen, showed a nonlinear force/displacement relationship and a very relevant strain up to 40%.

In order to use the results coming from the experiments, a numerical model for simulating the structural behaviour of the mesh has been also proposed. The model is based on a condensed simplification of a mesh element by using springs and nodes. The nonlinearity of the model is also preserved thanks to the geometrical arrangement of the springs. The model is independent from the actual knitting pattern and the identification of its parameters can be easily performed from the results of the experimental tests by using the proposed procedure.

Further investigations will concern the direct comparison between different knitting patterns and the local investigation of the loop deformation useful for the electrical properties evaluation.

ACKNOWLEDGEMENTS

The Team of the “Ultralight Reflector Mesh Material for Very Large Reflector Antennas” wants to express its appreciation to the ESA that promoted and supported the study with high competence and enthusiasm.

REFERENCES

- A.S. Chen, F.L. Matthews, A review of multiaxial/biaxial loading tests for composite materials, *Composites*, Vol. 24(5), pp. 395-406, 1993.
- J. Kaldor, D.L. James, S. Marschner, Simulating Knitted Cloth at the Yarn Level, *Proceedings of SIGGRAPH 2008*, Los Angeles, California, August 2008.
- D. Lecompte, A. Smits, H. Sol, J. Vantomme, D. Van Hemelrijck, Mixed numerical–experimental technique for orthotropic parameter identification using biaxial tensile tests on cruciform specimens, *International Journal of Solids and Structures*, Vol. 44, pp. 1643–1656, 2007.
- A. Tabiei, W. Yi, Comparative study of predictive methods for woven fabric composite elastic properties, *Composite Structures*, Vol. 58, pp. 149-164, 2002.
- A. Tabiei, Y. Jiang, Woven fabric composite material model with material nonlinearity for nonlinear finite element simulation, *International Journal of Solids and Structures*, Vol. 36, pp. 1646-1660, 1999.

DESIGN AND CALCULATION OF THE SURFACE OF SPACE PARABOLIC ANTENNA ON THE BASIS OF DISCRETE CONCEPTION

E. MEDZMARIASHVILI ⁽¹⁾

Member of National Academy of Georgia, Prof., Dr.,

Georgian Technical University, Georgia

E mail: medzmariashvili@gtu.ge

D. PATARAIA ⁽²⁾

Prof., Dr., Senior researcher, G. Tsulukidze Mining Institute, Georgia

E mail: david.patarai@gmail.com

G. BALIASHVILI ⁽³⁾

Dr., Senior researcher G. Tsulukidze Mining Institute, Georgia

E mail: gbaliash@yahoo.com

E. TSOTSERIA ⁽⁴⁾

Dr., Georgian Technical University, Georgia

E mail: edishertso@gmail.com

G. NOZADZE ⁽⁵⁾

Dr., Senior researcher G. Tsulukidze Mining Institute, Georgia

E mail: g_nozadze@yahoo.com

ABSTRACT

Considered the problem of creating and calculating the space of a parabolic antenna . The reflective surface of the antenna is created by deploying after reaching orbit compact folded structure. Structural elements must be calculated and designed so that the material will be located on the reflective surface of the antenna with the exact precision after its the unfolding. The problem is solved by using the discrete representation of a rope - rod systems and standard software.

In this work the task of formation of the reflected surface of space antenna of parabolic shape by means of non-standard approach – modeling and calculation of solid deformable bodies on the basis of discrete conception is considered. This method initially was developed in G. Tsulukidze Mining Institute for complex cable -rod structures [1-4] the classic examples of which are cable ways and so called dumbbell systems of artificial objects connected by a cable of some tens kilometers in length [5]. The accuracy of the basic positions of this approach and obtained results has been checked parallel with implemented calculations by means of the set of computer programs “LIRA” and “SOLIDWORK” and also by the experiments carried out on the laboratory model of cable suspend bridge.

Description of the observable task. The sizes of parabolic space antenna are in work position, i.e. at being on orbit; they usually exceed the sizes of corresponding structure in process of transportation beginning from the start to putting into permanent orbit. The procedure of putting antenna from transportation position into work position can be compared with unfolding of umbrella. However, this analogy with unfolding of umbrella is not entirely just; really everything is rather complex as technologically as a result of unfolding of structure not only formation of antenna of definite shape-paraboloid is required but also very precise, of parts of millimeter disposition of units of the reflecting network on invisible surface of this parabolic antenna. The pointed out precision dislocation of units on the surface of paraboloid of antenna after unfolding must be provided with preliminary precise calculations, the finite result of which is a definition of the length of elements of the reflecting (active) surface and of the passive cup of antenna that also has a shape of paraboloid and pulling cable stays (see fig.1).

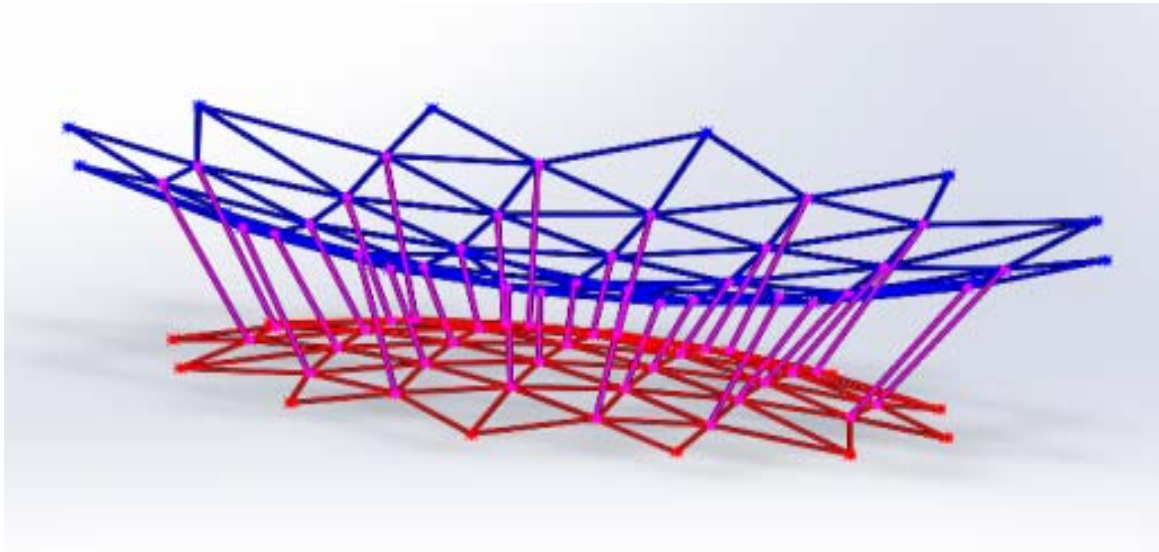


Fig. 1 The unfolded state of parabolic space antenna

At that for formation of a stable shape of antenna and provision of its normal functioning simultaneously with the above-mentioned basic condition of optimization-highly precise displacement of units on the surface of paraboloid a number of border conditions and additional limitations must be observed, for example, the structure elements as a rule must be subjected to stretching forces, provide workability at temperature and other disturbing influences.

Let's consider the set task more in details on the specific example (the structure of space parabolic antenna was developed by a team of scientists and designers of the Georgian Technical University under the leadership of Professor E.Medzmariashvili 15 years ago).

In Fig.2 are shown overall sizes of one of the versions of antenna in unfolded state.

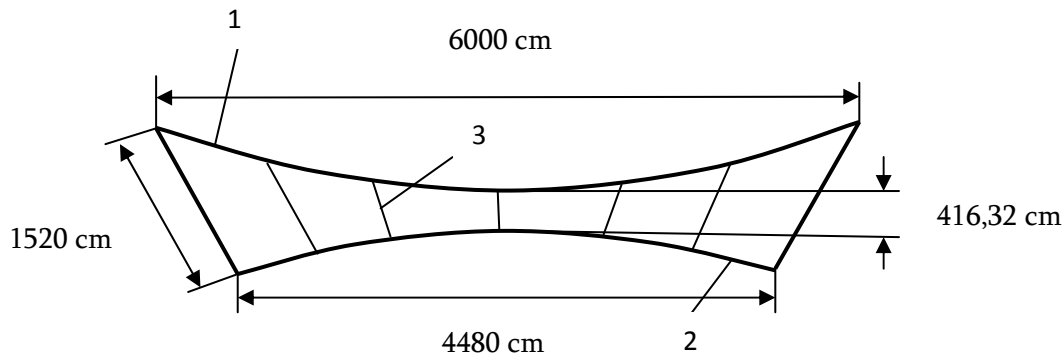


Fig.2. Overall sizes of antenna in unfolded state (1-reflecting surface, 2-secondary surface, 3-pulling cable stays; section area of elements is 2.44mm^2 , module of resilience is $5.88 \cdot 10^{10} \text{ N/m}^2$).

For explanation of the essence of applied approach during calculations it is sufficient to consider the plane task and removing a type element (see fig.3).

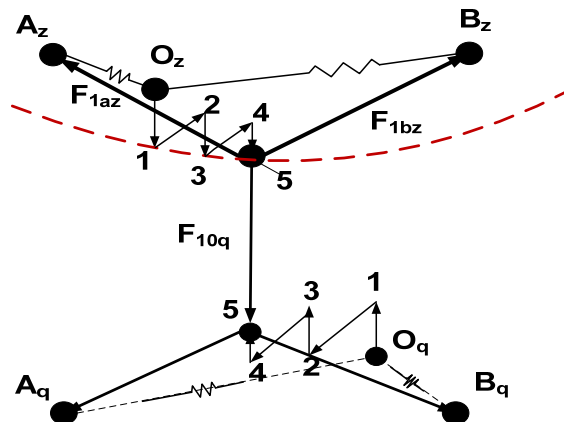


Fig.3. The bringing of unit of antenna to the target curve (reflecting surface is marked with dotted line) as a result of realization of algorithm of the minimization of resulting force.

First we will describe in general the developed algorithm to the considered task. Here the initial position of the unit of reflecting surface of antenna is marked with O_z and lower, secondary surface with O_q . The algorithm provides a travel of O_z unit in direction of the target line and its displacement on this line (in Fig. 3 position 1). Then for this state the algorithm moves the unit of secondary surface O_q in direction of the resulting force (see position 1 for this unit). In each cycle of displacement of units (there are 5 such in the figure) correction of force in linking unit (cable stay) takes place so that potential energy of the system takes a minimum meaning that means the stable balanced state. Finally in these iterations O_z unit will be displaced on the target line. Similarly will be processed the rest units of the surface of antenna. As a result for all the units of antenna the coordinates of units and forces in bracing members of the antenna cells and cable stays will be determined. The precision of obtained results practically depends only on the discretization degree of the antenna elements and the spent machine time.

Down is presented detailed description of the approach. The investigated cable-rod structure will be presented by the rings of discrete types linked with each other movingly (or rigidly) which from their part present the unity of

concentrated masses, resilient elements (springs) and dampers. Accuracy of such discrete model is not limited practically and depends on the degree of "discretization", in other words – on the obtained quantity of the elementary units.

The first step of modeling process will be "disintegration" of the research system into typical units and their presentation in a discrete form. Further, forces will be applied to the key points (these will be units capable of virtual displacement) taking into account the boundary conditions. Now, let's describe briefly the idea on the basis of which the tensed-deformed state of structure will be calculated. As an initial status we'll take any physical state and begin development of the system computer model sequentially with iterations (change of the cables system geometrical configuration) so that the system appears in equilibrium condition. For the purpose on each step of iteration the resulting force affecting the unit will be calculated and virtual displacement of this unit in this direction. As a result of such iterations the system approaches the equilibrium condition and, finally, will reach it with a certain preciseness (error depends only on the calculations preciseness). Inverse calculation from the geometrical configuration respective with the equilibrium condition of the cables system will enable to determine values of forces and respective deformations on any point of the cable-rod system. You can found more detailed information about the above described approach (method), and the corresponding demonstrative programs on the Internet at [6].

In the presented Project the imitation/modeling process of transfer of the aerial to be delivered to space from folded into working or unfolded (stationary) position. During solution to the mentioned task the basis of the proposal of this approach is given by the experience of its use in one Soviet Space Project which in its time was highly estimated. Particularly, here was discussed the imitation of expansion process of so-called dumbbell-like system from the stationary space station (the length of the linking cable after complete spreading was 120 km [5]).

For the purpose of getting more reliable results in the process of modeling the mechanical parameters of the parabolic antenna, similar calculations had been performed using a set of computer programs "LIRA" and "SOLIDWORK". Below is given a brief description of related parts of work.

While modeling the task by use of complex "LIRA-9.6" reflected surface was represented and considered by appropriate finite elements (see fig.4).

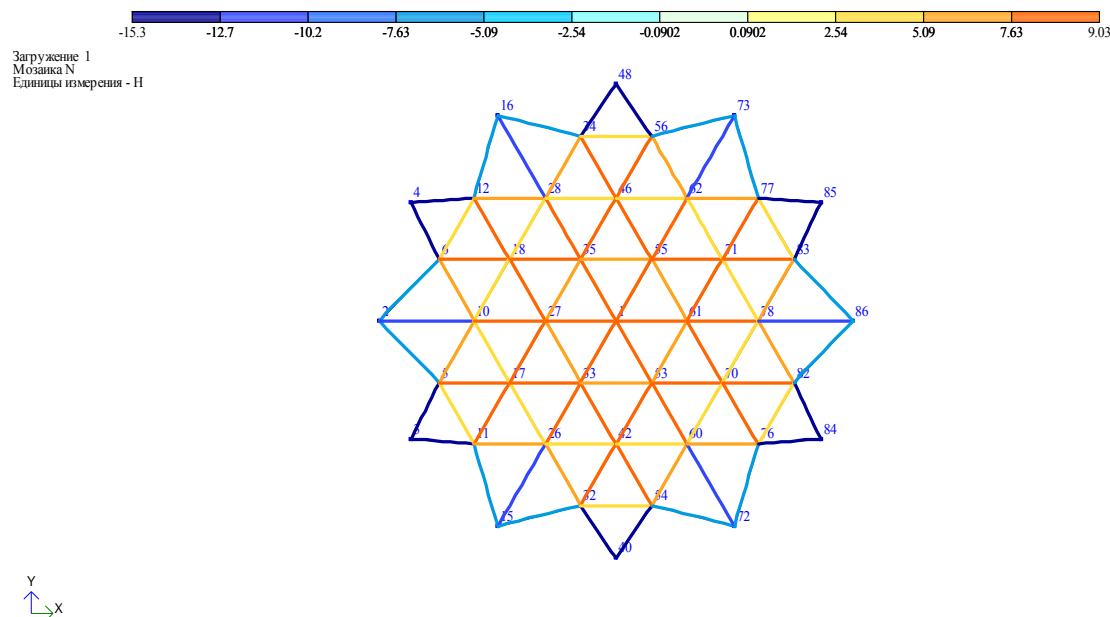
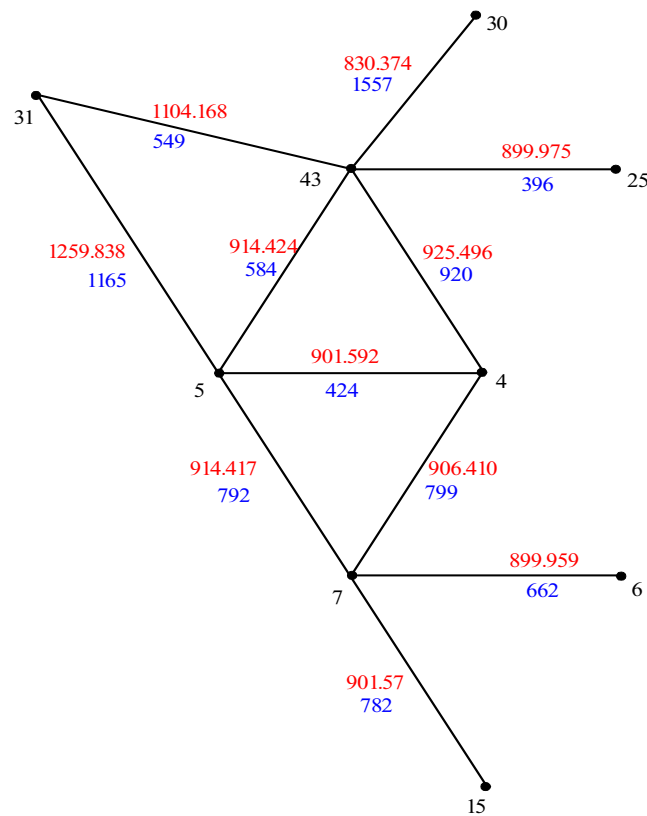


Fig. 4 Normal forces in finite elements of the reflecting surface of the antenna

In this case by phased modeling were determined optimal efforts for the elements at extreme (outer) nodes. In the model with desired geometry are applied the above mentioned forces along its axis. As a result we obtain a picture, which will be desired for all the systems; In such setting starting (initial) geometry of spatial structure will be determined. A fragment from the result of a particular variant of the calculations is shown on the fig.5.



15 – number of node

901.57– desirable (starting, not stretched) length of the element, mm

782 – effort, grf

Fig.5. The result of calculation of specific version, performed with the help of a set of program “LIRA 9.6” with the number of node, not stretched length of the element and effort.

The problem is posed and solved in the design software environment Solidwork 12.0. Necessary geometry is given as a two parabolic surfaces (see fig. 1). We consider two types of boundary value problem of linear elasticity.

Problem 1: The nodes which is placed on the perimeter of the reflecting surface of the antenna rigidly fixed. To provide design solutions of tensile surface of antenna, offers in a perimeter nodes of small parabolic antenna surface set radial forces 1 N as is shown in Fig. 6.

Problem 2: Nodes that are placed around the perimeter of the reflecting and the tensile surface of the parabolic antenna rigidly fixed. To provide design solutions for tensile surfaces of the antenna, it is proposed to specify a set of 6 N forces on the central nodes of the two parabolic surface, as shown in Fig. 7.

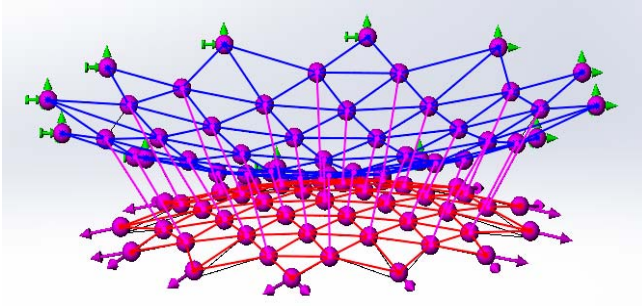


Fig. 6 The boundary value problem 1.

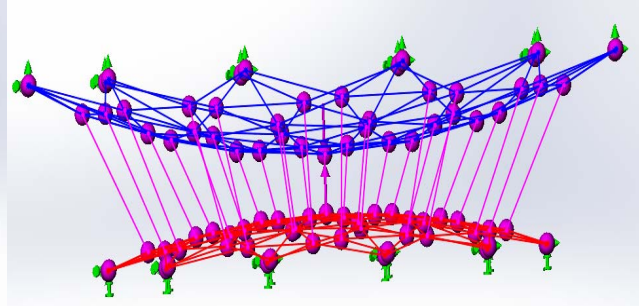


Fig. 7 The boundary value problem 2.

Solving Problems 1 and 2 are shown in Fig. 8-11.

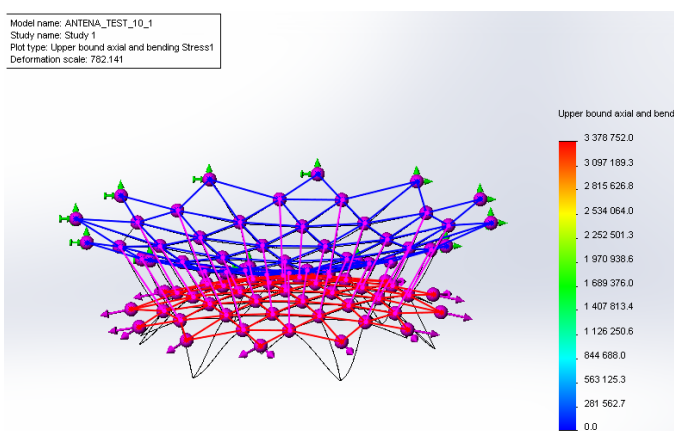


Fig. 8 Solving stress for problem 1

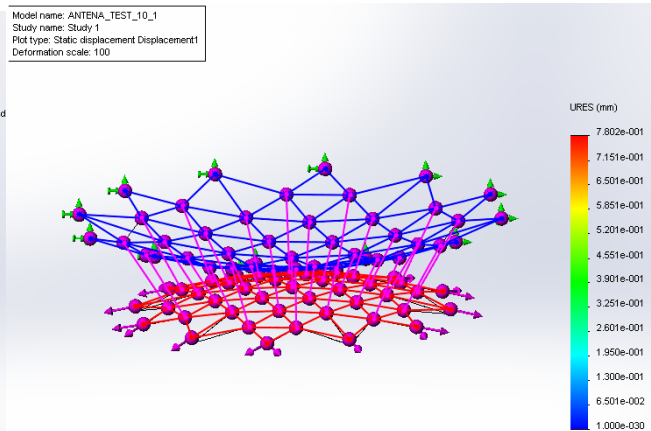


Fig.9 Solving displacement for problem 1

Fig. 8 - 9 given Solving of Problem 1. Stresses and displacements in structural elements of the antenna is in the range: The Stresses: $\sigma_{\min 1}=281\,562\text{ N/m}^2$, $\sigma_{\max 1}=3\,378\,752\text{ N/m}^2$, The Normal forces: $F_{\min 1}=0.68\text{ N}$, $F_{\max 1}=8.11\text{ N}$, The Displacements: $\Delta_{\min 1}=0,065\text{ mm}$ $\Delta_{\max 1}=0,7\text{ mm}$

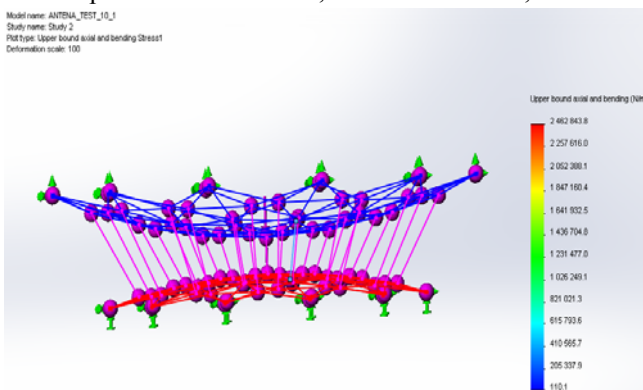


Fig. 10 Solving stress for problem 2

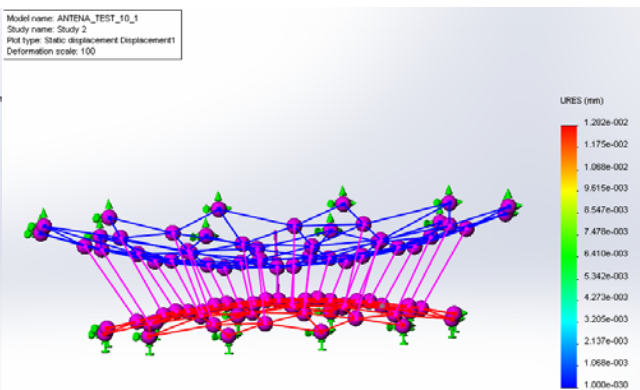


Fig.11 Solving displacement for problem 2

Fig. 10 - 11 given Solving of Problem 2. Stresses and displacements in structural elements of the antenna is in the range:

The Stresses: $\sigma_{\min 2}=205\,337\text{ N/m}^2$, $\sigma_{\max 2}=2\,462\,863\text{ N/m}^2$; The Normal forces: $F_{\min 2}=0.49\text{ N}$., $F_{\max 2}=5.91\text{ N}$.,

The Displacements: $\Delta_{\min 2}=0,0011\text{ mm}$, $\Delta_{\max 2}=0,13\text{ mm}$.

From this part of study we can do the following conclusions:

- Providing a predetermined stable form of parabolic antenna surface can be accomplished in two ways, as shown in the presented problems;
- If for reasons of implementation of these tasks could lead to practical problems can be addressed and resolved the corresponding a new boundary problems of elasticity.

The main result of this work is as follows: the performed research allows to conclude, that the method (approach) based on discrete representation of modeling and calculation of solid deformable bodies can be successfully applied in designing and expertise of such complex and important objects, as for example, parabolic antenna deployed in space.

Besides that applying the above given method accuracy of the results depends on degree of discretization of the object, in other words it depends on the number of elementary units, which is connected (linked) to increasing the computing time. The considered method – by its nature – refers to a discrete representation of the researched object, it gives an opportunity to easily solve problems of accuracy of the results by distribution of computation in computer network.

REFERENCE

- [1]. D. Patariaia Ein Beitrag zur diskreten Darstellung des Seiles. Wissenschaftliche Arbeiten des Instituts fuer Eisenbahnwesen, Verkehrswirtschaft und Seilbahnen, Technische Universitaet Wien, 1981
- [2]. Patariaia David The calculation of rope-rod structures of ropeways on the basis of the new approach , WORLD CONGRESS of O.I.T.A.F., RIO DE JANEIRO , BRAZIL , October, 2011, 24 – 27 , PAPERS OF THE CONGRESS, (<http://www.oitaf.org/Kongress%202011/Referate/Patariaia.pdf>)
- [3]. David Patariaia Calculation and design of cable systems for ropeways . Tbilisi: Metsniereba, 1991, -115 p. (in Russian).
- [4]. D.Patariaia. Discrete model and calculation method for rope – rod structures.//Problems of Mechanics. Tbilisi, N 2(31), pp.23
- [5]. D. Patariaia, G. Nozadze Modeling and calculation of big rarefied space structures on the basis of discrete model of the cable // International Scientific conference – Advanced Lightweight Structures and Reflector Antennas Proceedings //14 -16 October 2009. pp. 206 - 211, Tbilisi, Georgia
- [6]. <http://www.mining.org.ge/develop/patariaia-dmr/index.htm> .

Successful Starshade Petal Deployment Tolerance Verification in Support of NASA's Technology Development for Exoplanet Missions

M. Thomson², D. Webb², N. J. Kasdin¹, D. Lisman², S. Shaklan², E. Cady², G. W. Marks², A. Lo³

¹*Princeton University, Princeton, NJ, 08544 USA*

²*Jet Propulsion Laboratory, California Institute of Technology, Pasadena, CA, 91109 USA*

³*Northrop Grumman Aerospace Systems, Los Angeles, CA, USA*

ABSTRACT

A Starshade is a sunflower-shaped satellite with a large inner disk structure surrounded by petals. A Starshade flies in formation with a space-borne telescope, creating a deep shadow around the telescope over a broad spectral band to permit nearby exoplanets to be viewed. Removing extraneous starlight before it enters the observatory optics greatly loosens the tolerances on the telescope and instrument that comprise the optical system, but the nature of the Starshade dictates a large deployable structure capable of deploying to a very precise shape. These shape requirements break down into key mechanical requirements which include the rigid-body position and orientation of each of the petals that ring the periphery of the Starshade. To verify our capability to meet these requirements, we modified an existing flight-like AstroMesh reflector, provided by Northrup Grumman, as the base ring to which the petals attach. The integrated system, including 4 of the 30 flight-like subscale petals, truss, connecting spokes and central hub, was deployed tens of times in a flight-like manner using a gravity compensation system. After each deployment, discrete points in prescribed locations covering the petals and truss were measured using a highly-accurate laser tracker system. These measurements were then compared against the mechanical requirements, and the as-measured data shows deployment accuracy well within our milestone requirements and resulting in a contrast ratio consistent with exoplanet detection and characterization.

Keywords: External occulting, occulter, starshade, exoplanet, exo-Earth, high-contrast imaging, TDEM, habitable zone, large deployable structure

1. INTRODUCTION

This paper describes a recent technology demonstration toward a Starshade concept for imaging exoplanets that was performed under NASA's Technology Development for Exoplanet Missions (TDEM) funding. As a space based mission designed to image exoplanets, Starshade has several advantages including reduced requirements on the companion telescope and the ability to image nearby planets with reasonable apertures. However, Starshade has its own challenges including being a large structure with precision shapes. Previous work under this funding showed the ability to manufacture and verify flight-like occulter petals of the required shape for an external occulter design. In this test we demonstrated the capability to place those Starshade petals in the correct location and orientation such that we would have an as-deployed Starshade capable of aiding the imaging of exoplanets. It should be noted that our approach for designing the Starshade occulter uses optimization tools that result in a smaller occulter size while still obtaining the required starlight suppression over the desired spectral band, which translates into tighter mechanical tolerances. We took this approach because larger Starshades are increasingly difficult to manufacture, fit into a launch fairing, verify and test, despite the relaxed tolerances. The white paper for our TDEM describes in detail our technology milestone; however, the milestone statement is repeated below:

- Verify that the deviations of the petal base point from the design circle are repeatedly below the 3 sigma positioning requirement for a 10^{-9} contrast using a sufficient number of deployments to verify the requirements are met with 90% confidence.

Given the unprecedented nature of the development, we chose a milestone of 10^{-9} as it resulted in a relaxed requirement for the positional accuracy and repeatability of the petal root positions while still representing the ability to meet realistic size goals. Our hope was to do much better than this and/or discover through this TDEM how to greatly improve our mechanical design such that we could reach higher levels of contrast through tighter performance tolerances. The chosen contrast for our milestone resulted in a deployed petal root positional deployment accuracy requirement of ± 0.95 mm for each of the two petal roots at the base of each petal. We were able to achieve this accuracy at 90% confidence over 15 partial stow and deploy cycles.

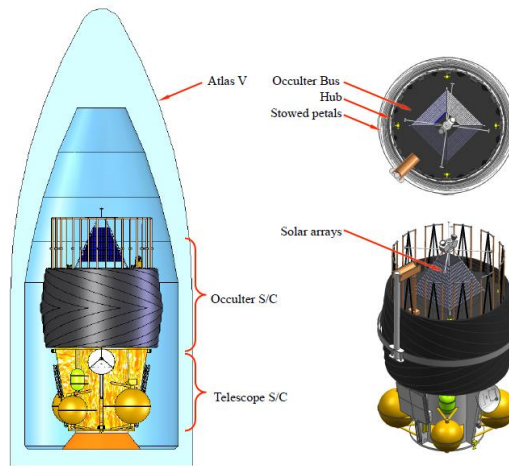


Figure 1. External occulter in fairing, launch configuration



Figure 2. Starshade petal unfurling sequence

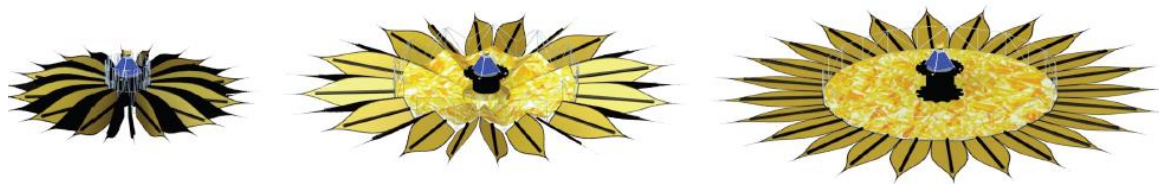


Figure 3. Starshade inner disk truss deployment sequence.

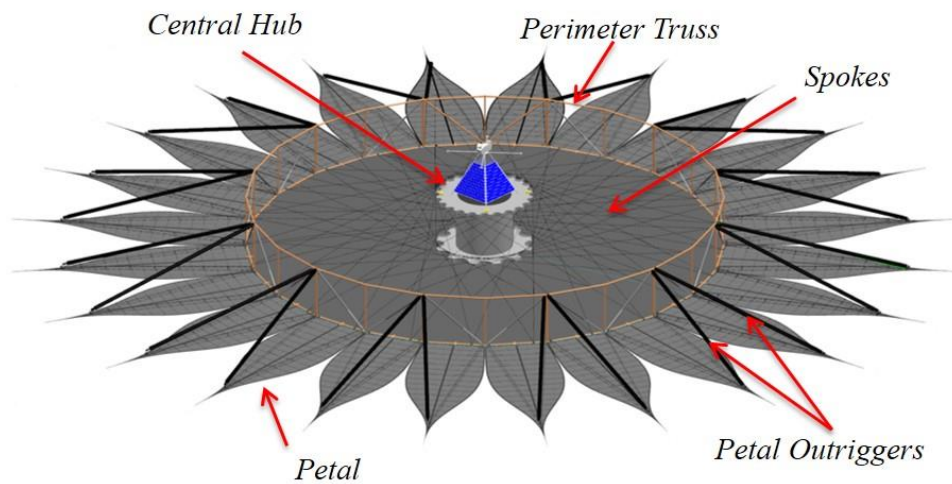


Figure 4. Starshade principle components.

2. EXPERIMENT DESIGN OVERVIEW

Given the intent of verifying petal root positional accuracy, our goal was to simulate the conditions most relevant to a flight-like system in order to validate our test. This meant our test Starshade needed to contain all the relevant components and assemblies from our Starshade baseline architecture in Figure 4. The architecture of the Starshade is similar to a bicycle wheel, with tensioned spokes connecting a central hub to the out rim, to which we attach petals. Because our petal roots are the component of interest and must be positioned accurately and repeatedly deployed, it makes sense that the petal root positions be very closely related to the most stable points on the truss, the truss nodes, to which the spokes attach and connect the truss stiffly back to the central hub. Additional out of plane stiffness is added to the petals by connecting the petal tips back to the truss via a component called an outrigger. This meant that our test setup needed to include petals, a truss, petal outriggers, spokes, a hub and gravity offloading system to allow the Starshade to deploy in a space like environment. The components and assemblies used in our test setup are shown in Figure 5 and described in the next section.

In order to validate our petal root deployment accuracy capability as well as capture the overall repeatability of deployment of the truss nodes, we needed a system to measure each of the petal roots' absolute position for each deployment as well as a number of other positions on the truss and nodes. . We chose to use a combination of photogrammetry and a laser tracker. We ended up primarily relying on the laser tracker due to the test environment. More detail of the data collection process and analysis are described later in this paper.

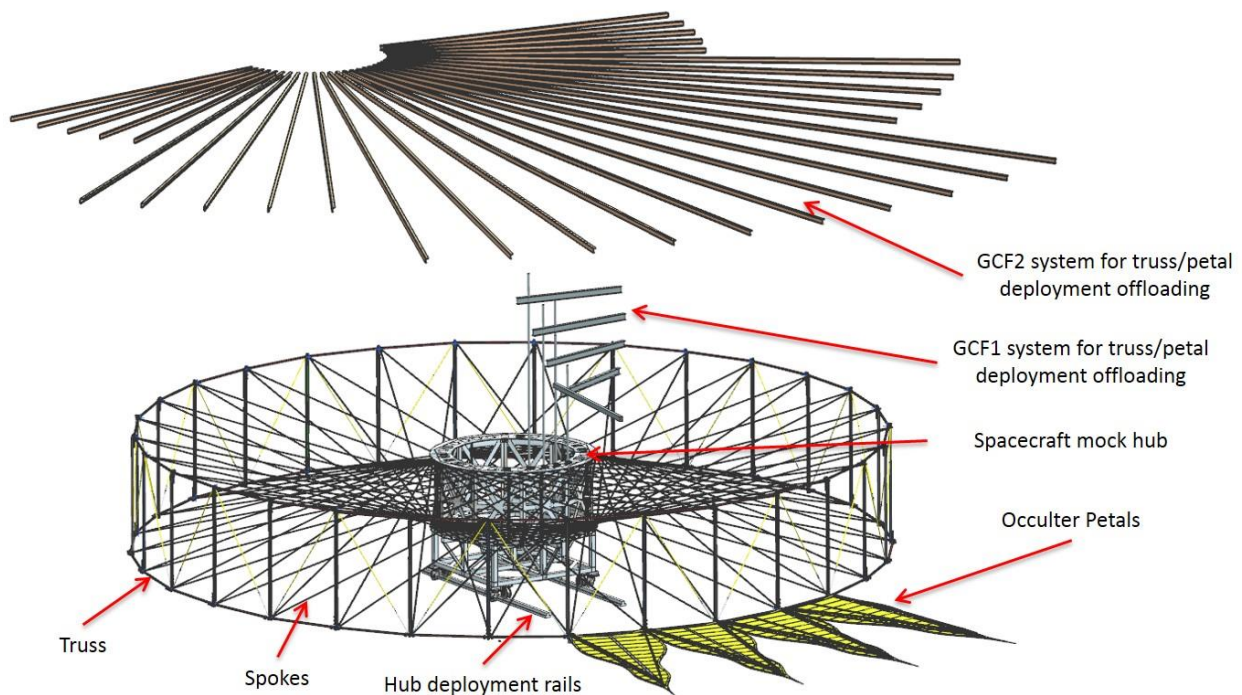


Figure 5. Starshade deployment tolerance test setup with gravity offloading systems.

3. EXPERIMENT MECHANICAL DESIGN

3.1 Hub Design and Manufacture

The central hub shown in Figures 5 & 6 provides a stiff body, emulative of the condition we will have in flight, from which to deploy the truss and petals. The hub was designed by Northrup Grumman Aerospace Systems (NGAS), Carpinteria, with high level requirements from JPL. The design allows 120 truss spokes to attach tangentially from the two parallel discs at the top and bottom of the hub to the individual nodes of the truss. This bicycle wheel spoke design,

from central hub to truss, creates a stiff structure to which we attached our Starshade petals. The hub was designed to have interfaces for features that allow the truss to collapse and stow around its outer perimeter. The petals then furl around the truss/hub system and mount against mounting hardware that protrudes from the hub and through the truss. Additional gravity compensation fixture hardware (GCF1) designed by JPL, offloaded the weight of the petals during the unfurling stage of the deployment. The central hub, hub deployment rails and petal attachment points were fabricated by NGAS.

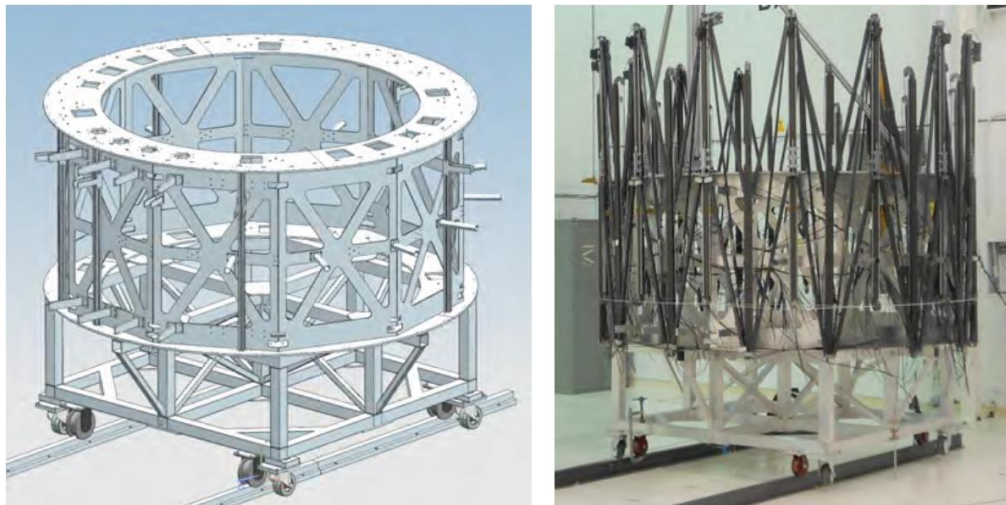


Figure 6. As-built hub with AstroMesh truss stowed around it.

3.2 Petal Design and Manufacture

A critical component of the deployment positioning and repeatability requirement, the Starshade petals were constructed in the summer of 2012 over a ten week period by two Princeton and two MIT undergraduate summer students. The Starshade petals consist of a center spine, or backbone, a base spine to interface to the truss, and structural edges to which the optical edges attach. The structural edges are tied back to the center spine via the battens and the whole structure is given shear stiffness from the longerons. A flexible material was used as the core of the petal center spine which allows the petal to be flexible enough to furl around a 3-meter spacecraft hub, and also passively become rigid as the petal unfurls and a pair of spring loaded ribs deploy and stiffen the petal. A schematic of the petal design (the same is in our first TDEM) is shown in Figure 7 and the completed as-built petals are shown in Figure 8 attached to the NGAS truss.

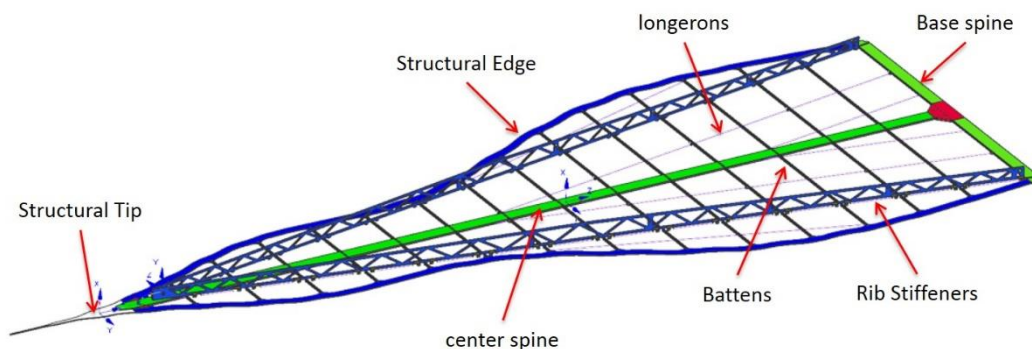


Figure 7. Petal main components.

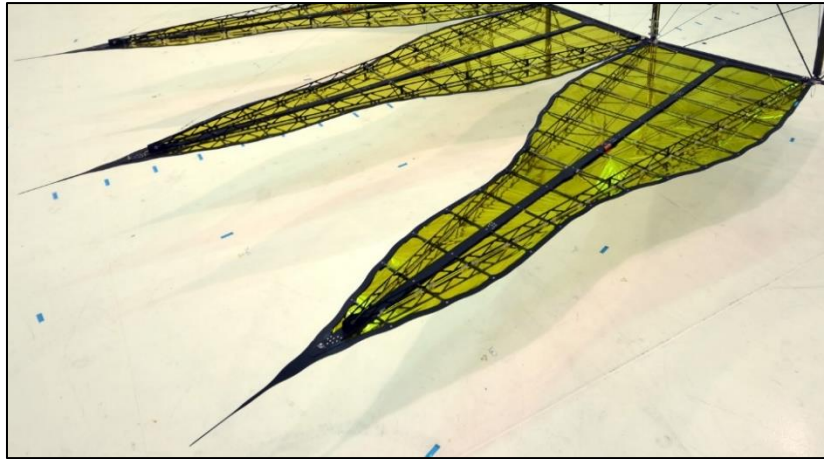
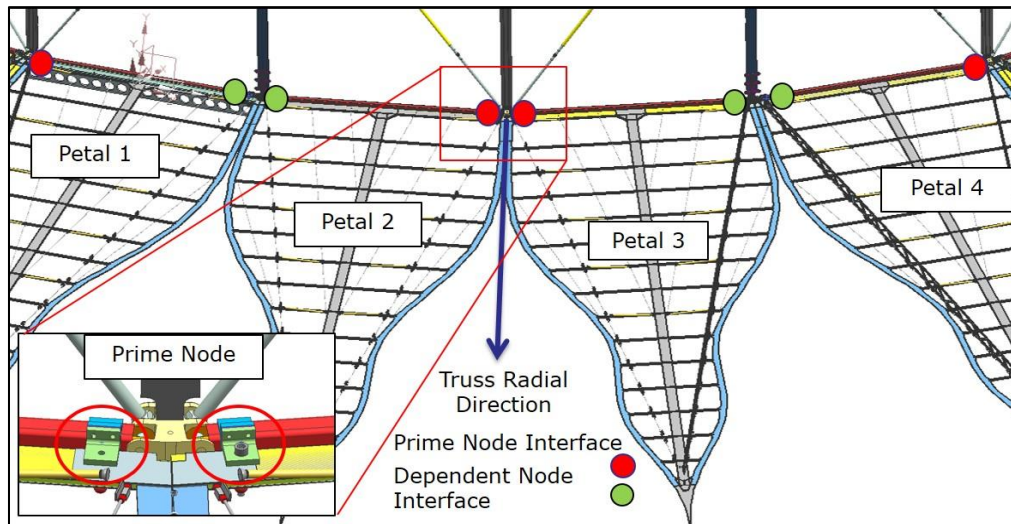


Figure 8. Petals as-built and installed on deployed truss.

3.3 Petal-Truss Interface Design and Manufacture

The petals mount to the truss longerons with precision pinned joints. The deployment tolerance milestone applies to the petal attachment points and more specifically, the center of each interface joint. This center point was precisely characterized relative to petal mounted targets using photogrammetry. Figure 9 shows the petal interfaces with respect to the truss nodes as well as prime and dependent truss nodes relative to the petal positions. The design of the Northrup Grumman truss was not commensurate with a petal-to-longeron interface that would allow furling of the petals around the truss in the stowed condition. For this reason, the fittings that were used to attach the petals to the truss were designed to meet the requirement of quick and repeatable detachment of the petal from the truss longerons via a quick release style fitting that was also designed to maintain the position of the petals with respect to the truss with great precision. Also designed into the petal-to-truss interface fitting is the ability to shim the petal in the truss radial direction, allowing us to correct for absolute radial position error of the petals after our first set of measurements. The interface fitting consists of two pieces: one that is permanently attached to the truss, and the other that is attached to the petal via the quick release mechanism already mentioned. Repeatability of the petal position pre- to post-shimming was maintained via registration features between the two parts of the fitting; this allowed repeatability over an order of magnitude better than our requirement.



**Figure 9. Petal interface points with respect to truss prime and dependent nodes.
Dots represent petal interfaces with color indicating type.**

Placing the petal interface fittings with the required precision to meet the milestone required a tool that would repeatedly place each petals interface fittings with respect to known locations on the truss. The tool that was used to place the petal-to-truss interface fittings was a single piece and was the same tool that was used for placing the petal interfaces into the petal base spine to which the petal-truss fitting connected. Placement of the petals with respect to known locations on the truss requires a truss that has known and repeated features at each bay of the truss to which the petal placement tool can be referenced. In our case this was a challenge as the truss was not designed with any known and repeated features to which we could reference and only every other node of the truss was identical. An additional challenge was that the truss model available to us was later found to vary from the as-built prototype. Because only every other node of the truss was identical, this created mirror image bay pairs to which we were only able to reliably place pairs of petals that were symmetric about the node that contained the reliable feature to which we could reference. This node that contained reliable features is referred to as the prime node, which in our case was centered on the inner two of the four petals. The node that was not referenced for tangential positioning of the petals is referred to as the dependent node. Because of this, the two outer petals referenced prime nodes that were the second node removed from the reference point of the two inner petals. This meant that the two outer petals could not be well related tangentially to the two inner petals. This relationship can be seen in Figure 9.

3.4 Truss Spokes

With the given position repeatability requirements for the petal root points, it was critical to create a very stiff connection from the petal roots back to the very stiff central hub structure. This was accomplished via a very stiff spoke that connected the nodes of the truss, to which the petal roots were very well coupled, and that was flexible when not tensioned so as to allow for easy stowing. The stiffness and thus repeatability of the system was achieved by choosing a material that was very low strain, thus reducing deflection and increasing repeatability. These spokes were also very thermally stable, which in our case was important not only for flight but also for testing, due to the very high precision required for the petal root positions. A challenge encountered in using these spokes was managing the long lengths of each of the 120 spokes during truss deployment such that the spokes would not catch on any of the truss or hub features and break. This was very important in that even one broken spoke could be responsible for changing the overall position of the petals. This required designing a spoke deployment method that controlled the spokes during deployment such that incremental lengths of the spokes were released as the truss deployed. This was accomplished with numerous small spring-like restraints that constrained the length of the spoke. Lower resistance restraint springs were used on the length of the spring near the truss connection and increasing resistance was used as the spoke approached the hub. This resulted in a very robust spoke deployment system that constrained determinant lengths of the spokes to release from their restraints only as the deploying truss tugged them out of their restraints.



Figure 10. Spokes uncontrolled on floor, before spoke restraint system.

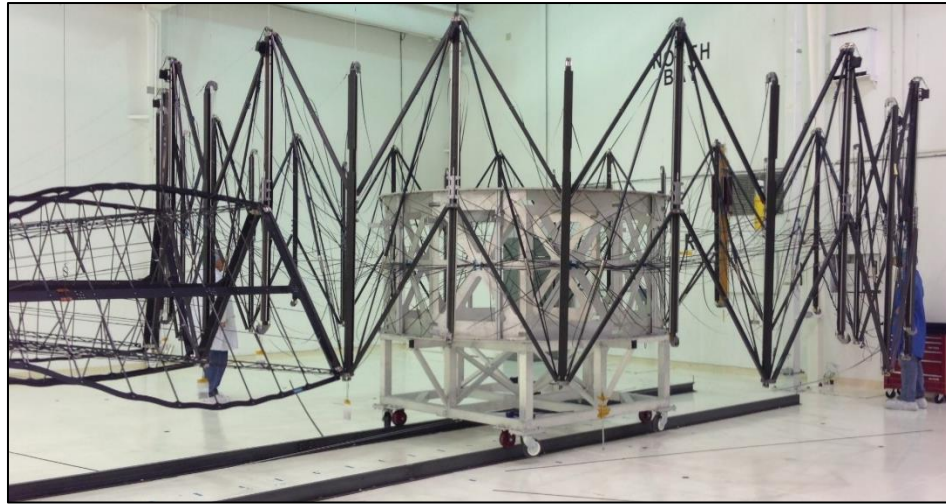


Figure 11. Spoke restraint system implemented, spokes remain taught and controlled throughout deployment.

4. DEPLOYMENTS AND METROLOGY

4.1 Initial Shimming and Metrology

The initial metrology plan called (described in our milestone whitepaper) for the use of photogrammetry to measure absolute positions at the roots of the petals as well as a number of points spread over each petal and the entire truss. With many points all over the truss and petals, this would give us many data points to determine the repeatability of the truss deployment. Additionally a laser tracker, referenced to a few points, was used for comparison, though the number of corner cubes applied was relatively small compared to the number of photogrammetry targets placed all over the truss, hub, and petals. We used both measurements for the initial estimates of the petal positioning before shimming. After completing pre-shim data analysis, however, it was found that the precision of the photogrammetry system was strongly dependent on target position on the occulter; a fact attributed to the geometry of the test facility used for the deployment. The pre-shim data analysis measurements showed that the laser was able to provide more accurate results for our specific location, as photogrammetry requires large angle triangulation, which was not available in our space constrained test area. Moreover, the precision of the laser tracker was uniformly better than the photogrammetry system

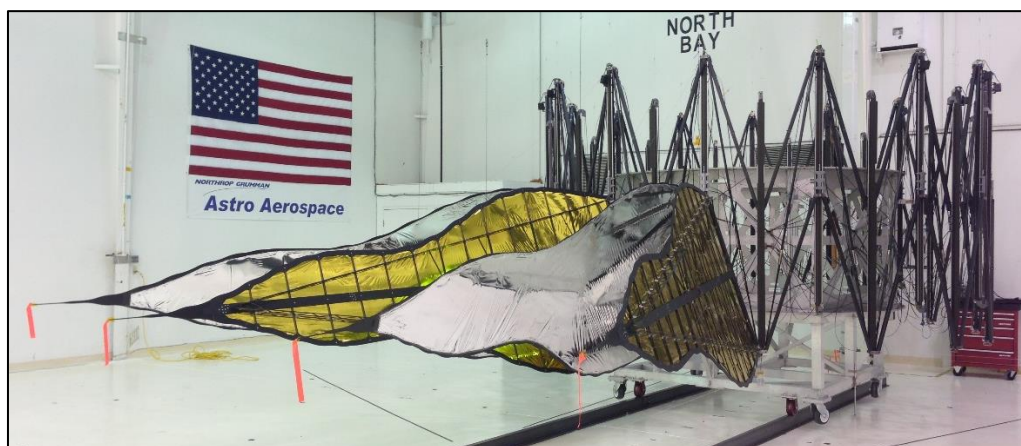


Figure 12. Petals on truss, ready to deploy.

Once it was determined that the laser tracker was more accurate, the laser tracker was used for the shim installation, post-shim data collection, and to measure the 8 petal root points as well as 42 other points on the truss nodes during deployment. Verification of the accuracy of each laser tracker measurement was performed by measuring each of the 50 points sequentially a total of three times and then comparing these measurements. If one measurement read an error, that measurement was compared to the other two measurements from the same deployment, and if those were in agreement and the initial erroneous, the erroneous measurement was removed. The laser tracker setup with respect to the Starshade system and the measured locations can be seen on the fully deployed system in Figure 13.

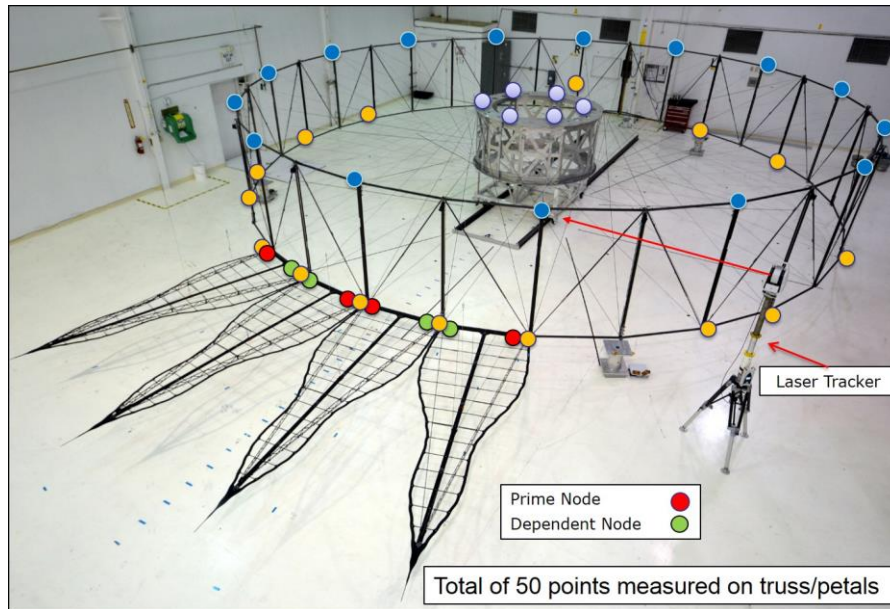


Figure 13. Metrology configuration, dots indicate location measured, color indicates type.

To shim the petals, a fit was performed to a set of model points using the procedures outlined later in Section 7.2. The differences, all less than 0.25 mm, were taken out manually in the radial direction with known shim increments at the petal-to-truss interface fitting (the architecture did not allow shimming in the tangential direction.) This proved effective: a post-shim measurement showed that the mean offset from the model in the radial direction decreased from 0.151 mm to 0.063 mm. The tangential direction remained virtually unaltered as expected, with a mean difference of 0.016 mm between before- and after-shim model offsets. Figure 14 shows both of these cases.

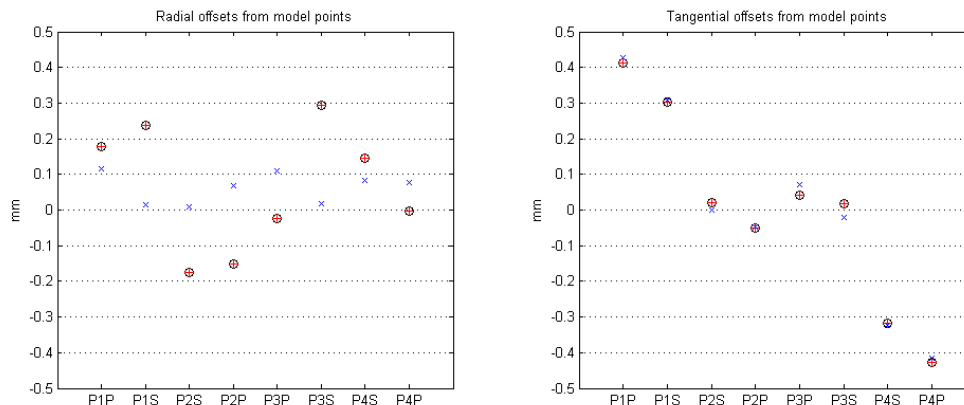


Figure 14. Offsets between data model points before and after shimming. Pre-shim points are designated with black circles with red crosses and post-shim points with blue X's. Left. Radial Direction (shimmed) Right. Tangential direction (not shimmed).

4.2 Partial Deployments

Initial plans called for furling the petals around the stowed truss between some of the deployments. However, because the gravity compensation system for furling the petals around the truss required a large structure mounted to the top of the hub that contained swinging rails that would rotate across the truss deployment path, it was determined that mounting this hardware to the hub before taking deployment data posed several risks. It was possible to damage the truss while mounting the hardware on top of the hub, a procedure that could only be performed after the hub was inside the truss structure. Additionally, there was a concern that detaching all the necessary truss gravity offloader lines would be extremely time consuming, posing a risk to achieving the number of deployments required to achieve 90% confidence. Upon reviewing the petal interface to the truss, it was also determined that petal furling would not contribute to any change in the petal root position points that were being measured, as the base spines were registered to stiff fittings that were firmly inserted into petal base spine and thus would not be affected by furling. Another reason for furling the petals would be to determine the effect of petal furling on the truss longerons. Because the existing truss design did not allow us to leave the petals attached to the truss longerons for stowing, but rather we had to detach the petals completely from the truss, the petals could not impart loads on the longerons during furling. For these reasons, no measurable gain would be realized in furling the petals between deployments. The petal unfurling gravity offloader hardware can be seen in Figure 15.



Figure 15. Petal unfurling sequence and unfurling GCF shown crossing stowed truss offloaders.

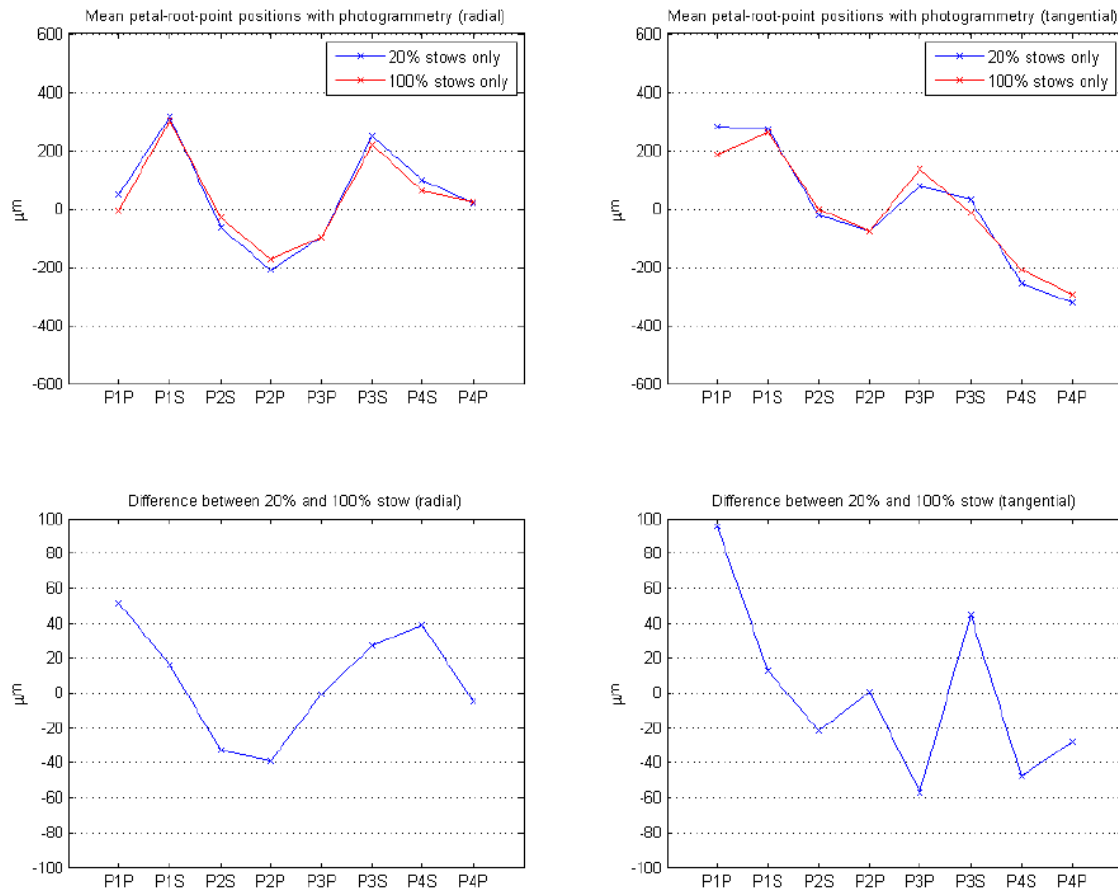


Figure 16. Top. Mean locations for the petal root points with partial stows (20% stowed) and full stows (100% stowed), in radial and tangential directions. Bottom. Differences between the partial- and full-stow cases. Unlike the data in the rest of the figures in this report, this data was taken with a photogrammetry system rather than a laser tracker. With the exception of the P1P point in the tangential direction, all differences are within the ± 75 micrometer error bars of the photogrammetry system.

5. PROCESSING AND ANALYSIS

The final tests occurred in October, 2013 at the Northrop Grumman Aerospace Systems (NGAS) AstroMesh production facility in Goleta, CA. Based on the 10 deployments with metrology performed in August 2013 to determine petal shimming amounts, 15 partial stow and deploy cycles were completed to verify the milestone in October to verify the milestone. Figure 13 shows a picture of the fully deployed truss with petals attached.

5.1 Data collection

The final set of data consists of 16 deployments: an initial re-deployment following the installation of the radial shims, and 15 stow-and-deploy cycles on the same day as the initial re-deployment and the two subsequent days. These cycles were a mixture of 10 10%-stows and 5 50%-stows, with the stow percentage representing roughly the fraction of the total radial motion of the truss which was exercised. During the initial photogrammetry tests, 7 20%-stows were taken along with 3 100%-stows. The mean locations of the petal root points were examined for both the partial and full-stow cases, and the residual differences in the locations of the resulting data points, shown in Figure 16, were found to be of comparable order to the 75 micrometer position-error specification for the V-STARS system. Given the longer periods of time required for the full stow (3 hours or more, compared to 30 minutes for a 50%-stow and 10 minutes for a 10%-stow), we decided to use a mixture of partial stows only in the post-shim testing. A listing of the data sets is given in Table 1.

5.2 Data processing

Each data set consists of three subsets which were taken in immediate succession without moving the deployed occulter. We expect, since the occulter was not moved between the three 45-second-long data collections, that these points should be identical except for the small random measurement error of the laser tracker, and for the most part this is true. However, there are occasionally strong outliers in a single data point from one of the three sets, which introduce nontrivial deviations in the locations of the measured points if the means of the three subsets are used. To avoid these deviations (which given the correspondence between the measured positions in the other two subsets, we believe to be nonphysical) we instead use the median of the three subsets as the canonical data value for that set. To co-fit the separate deployments, all 16 deployment datasets are placed into a single nonlinear least-square fit, which translates and rotates each of the 16 sets of data as a rigid body to co-align them. (As it is unreferenced to external fixed points, the resulting coordinate system is only unique up to a constant global translation and rotation, but this gauge transformation does not affect our analysis.) Not all of the data points are used for this fit, however. The rigid structure of the hub is not perfectly coupled to the truss, and neither are the petal tips. We exclude these points from the truss co-alignment fit, though we do apply the resulting coordinate transforms to look at the spreads of hub and petal-tip points.

Conversely, no other point (hub and petals included) was omitted from further analysis. Data quality was not used as a metric for excluding points; while some points appear suspect based on the data spread (e.g. HUB2, PTR8), we did not exclude them without a corresponding physical explanation for their excision. After the deployments are aligned to each other, we extract the points located at nodes at the root of each petal. These nodes are also present in a CAD model of the system, falling on a circle, and the locations of these nodes in the model were also extracted; the two were then fit against each other to determine the correspondence between measured and model points. The milestone specification called for a fit to a best-fit circle rather than points extracted from a structural model of the system. However, using explicit points in a model in the fit provides two primary advantages:

- (1) Using points derived from a model provides traceability between desired and measured locations for the nodes.
- (2) The coordinate system of the model is chosen such that the center of the model coincides with the origin, and so the vectors between the measured and model points may be projected into radial (directly outward from origin) and tangential (perpendicular to radial) directions. Given this, we can constrain the alignment of the petal root points in a tangential direction. With a best-fit circle, as originally suggested in our white paper, no such constraints can be placed. Figures 17 & 18 show the spread of the laser-tracker positions over the 16 deployments. As we have a set of coordinate transformations which take each of the 16 sets of data into a coordinate system with the model center of the truss at the origin, we have transformed them into radial and tangential coordinates as well. Note, these are deviations from each points mean only.

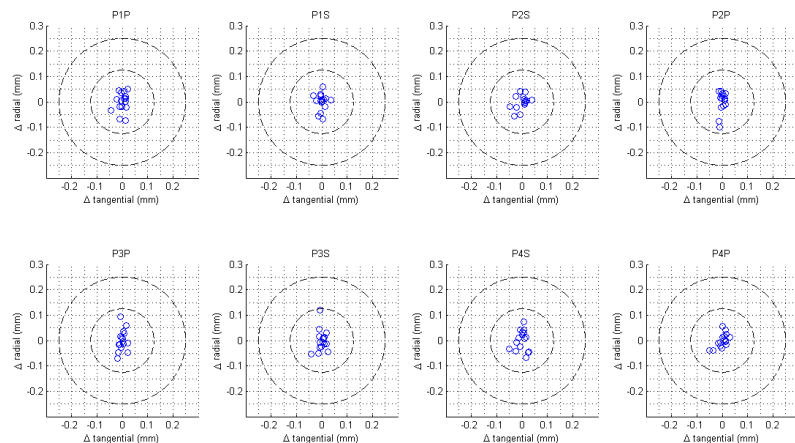


Figure 17. The spread of petal root points over the 16 deployments. Radial and tangential directions are the (r, θ) unit vectors in a polar coordinate system with the nominal occulter center at the origin. Blue circles represent individual deployments. Circles of radius 125 micrometers and 250 micrometers are shown for scale.

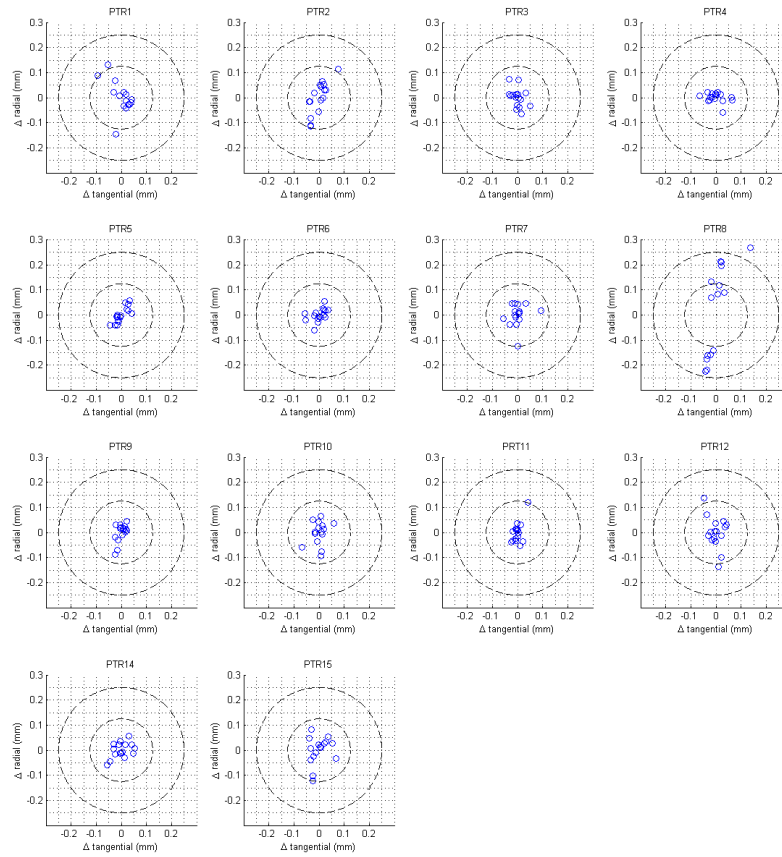


Figure 18. The spread of petal truss ring points over the 16 deployments. Radial and tangential directions are the (r, theta) unit vectors in a polar coordinate system with the nominal occulter center at the origin. Blue circles represent individual deployments. Circles of radius 125 micrometers and 250 micrometers are shown for scale.

6. ANALYSIS AND APPLICATION TO MILESTONE.

The statistic used to check if we met our milestone was a tolerance interval (2). Unlike a confidence interval, which provides confidence bounds on the value of a parameter, a tolerance interval provides confidence bounds on a range of data. For our milestone, we wished to create a tolerance interval such that we are 90% confident it contains 99.73% of the population of future data points. (For a normal distribution, 99.73% of the distribution falls in the mean ± 3 sigma). The equations and assumptions used to calculate our tolerance interval are further explained in our TDEM report. For brevity, I will not include it here. The resulting tolerance intervals are given graphically in Figure 19.

Figure 19 shows the mean deviation of the 8 petal root points after the 15 deployments with the resulting tolerance intervals, in both the radial and tangential directions. Radial errors show a residual bias that could be reduced with additional shimming. Tangential errors are minimal for the two inner petals and larger but still within the tolerance limit for the two outer petals. This behavior is an expected manifestation of using existing hardware. The petals need to be registered to truss nodes (junction between bays) as they are the only points with precision deployment repeatability. The existing AstroMesh antenna provides no registration features to precisely locate the nodal position. A retrofitted registration feature was possible for only the primary nodes, but not the alternating dependent nodes. A registration tool was installed to the primary node between petals 2 and 3 (attach points 4 and 5). A precision tool is used to locate attach points 3 and 6. Attach points on petals 1 and 2 (attach points 1, 2, 7 and 8) are positioned with further extrapolation and the errors start compounding. Future custom designs will include the necessary registration features at every node. Nevertheless, the 90% confidence is well within the milestone requirement of ± 0.95 mm.

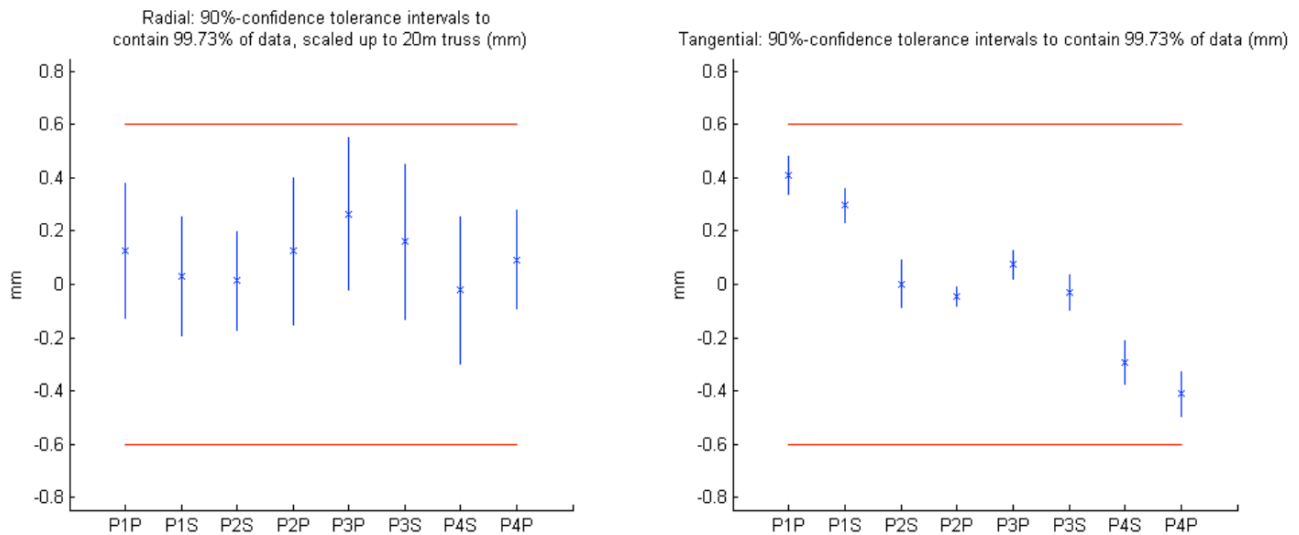


Figure 19. A set of tolerance intervals for the eight petal root points which contain 99.73% of deployments with 90% confidence. Left. In the radial direction Right. In the tangential direction

7. FINAL REMARKS

Most importantly, our technology demonstration retired a major technology element of Starshade manufacturability in showing that it is possible to achieve the required in-plane tolerance of the petal root positions for a 10^{-9} contrast Starshade. Focusing on the mechanical requirement, the milestone of ± 0.95 mm, being an absolute position accuracy requirement, is easily achievable to a very small residual mean offset, which was demonstrated by removing most of the radial offset from the theoretical model position with just one iteration of shimming. Future designs will allow for or eliminate the need for tangential shimming, which would reduce our residual tangential error to nearly zero, leaving absolute position error to be dominated by repeatability. This is very encouraging because our repeatability data, when looked at without its mean residual error component, was extremely good with most all deployment data in Figures 17 & 18 falling within circles of a diameter of 250 microns, or ± 0.125 mm. Future development work for a Starshade-specific inner disk truss will allow us to design a truss specifically suited for attaching, furling and deployment of the Starshade petals and will also focus on in-plane petal position and deployment repeatability. This will allow us to do further deployment positional accuracy and repeatability testing and hopefully demonstrate an even better Starshade contrast possibility.

8. ACKNOWLEDGEMENTS

This work was carried out at the Jet Propulsion Laboratory, California Institute of Technology, under contract to the National Aeronautics and Space Administration.

Copyright 2014. All rights reserved

9. REFERENCES

- [1] R. J. Vanderbei, E. J. Cady, and N. J. Kasdin. Optimal occulter design for finding extrasolar planets. *Astrophysical Journal*, 665:794-798, 2007.
- [2] G. J. Hahn and W. Q. Meeker. *Statistical Intervals: A Guide for Practitioners*. John Wiley and Sons, Inc., 1991.
- [3] W. A. Jensen. Approximations of tolerance intervals for normally distributed data. *Quality and Reliability Engineering International*, 25(5): 571-580 (2009).
- [4] E. Cady. Boundary diffraction wave integrals for diffraction modeling of external occulter. *Optics Express*, 20:15196-15208, July 2012.
- [5] Stuart B. Shaklan, M. Charley Noecker, Tiffany Glassman, Amy S. Lo, Philip J. Dumont, N. Jeremy Kasdin, Eric J. Cady, Robert Vanderbei, and Peter R. Lawson. "Error Budgeting and Tolerancing of Starshades for Exoplanet Detection," *Proc. SPIE 7731*, 77312G (2010).
- [6] Kasdin, N. Jeremy, et al. "Advancing Technology for Starlight Suppression via an External Occulter, Technology Milestone White Paper," JPL Document D-68672 (2011).
- [7] Kasdin, N. Jeremy, et al. "Advancing Technology for Starlight Suppression via an External Occulter, Technology Milestone Report," JPL Document D-74384 (2012).
- [8] Kasdin, N. Jeremy, et al. "Verifying Deployment Tolerances of an External Occulter for Starlight Suppression, Technology Milestone White Paper," JPL Document D-80947 (2013).
- [9] Kasdin, N. Jeremy, et al. "Verifying Deployment Tolerances of an External Occulter for Starlight Suppression, Technology Milestone Report," (2014).
- [10] Shaklan, Stuart, B., Marchen, Luis, Lisman, P. Douglas, Cady, Eric, Martin, Stefan, Thomson, Mark, Dumont, Philip, Kasdin, N. Jeremy. "A Starshade Petal Error Budget for Exo-Earth Detection and Characterization," *Proc. SPIE 8151*, 815113 (2011).

ULTRALIGHT DEFORMABLE MIRRORS FOR LARGE APERTURE SPACE TELESCOPES

S. Pellegrino

*Graduate Aerospace Laboratories
California Institute of Technology
1200 E. California Boulevard, Pasadena, CA 91125, USA
sergiop@caltech.edu*

ABSTRACT

This paper presents a novel active mirror concept based on carbon fiber reinforced polymers. A nanolaminate facesheet, active piezoelectric layer and printed electronics are implemented in order to provide the reflective surface, actuation capabilities and electrical wiring for the mirror. Mirrors of this design are very thin (on the order of 0.5 mm thick), lightweight (on the order of 2 kg/m²) and have large actuation capabilities (on the order of 100 micrometers peak-to-valley deformation per channel). Replication techniques along with simple bonding/transferring processes are implemented eliminating the need for grinding and polishing steps. An outline of the overall design, component materials and fabrication processes is presented. A method to size the active layer for a given mirror design, including simulation predictions on the correction capabilities of the mirror, is also outlined.

1. INTRODUCTION AND BACKGROUND

Large optical-quality mirrors are heavy, expensive and difficult to manufacture. Traditional telescope mirrors, such as that the mirror for the Hubble Space Telescope, were made by grinding and polishing a thick slab of near-zero coefficient of thermal expansion (CTE) glass down to nanometer-level precision. Not only is this method difficult and time consuming, but the areal density of such mirrors was also very high [1]. Advancements in lightweight mirrors such as those for the James Webb Space Telescope have lowered the areal density [2]. However, these mirrors must still be polished down to optical-quality tolerances, and hence their cost and manufacturing complexity are still considerable. Even lighter mirrors have been recently constructed using replication techniques [3,4], however they often suffer from a lack of figure accuracy and surface quality.

Several efforts have also been made to incorporate actuation into mirror structures. Actuation, coupled with wavefront sensing and control, allows mirrors to 1) correct for manufacturing figure errors, 2) correct for any errors introduced during operation (e.g. due to thermal variations) and 3) modify their figure in order to accommodate different optical prescriptions. Concepts incorporating a variety of materials and actuation schemes for both thick and thin-shell mirrors have been proposed. The most advanced of these is the Actuated Hybrid Mirror (AHM) from AOA Xinetics [5,6]. These structures are made from lightweighted silicon carbide with embedded piezoelectric stack actuators. Mirrors of this design have been demonstrated on large scales (>1 m) and optical-quality tolerances (< 10 nm RMS) have been achieved. However, they are expensive to produce and their full-scale actuation range is limited as they are relatively stiff structures. Highly-deformable shell mirrors are also under development [7,8], although they are currently limited in terms of aperture size.

In collaboration with the Jet Propulsion Laboratory and the Lawrence Livermore National Laboratory, we have proposed a novel method of constructing lightweight, highly active carbon shell mirrors (CSM) using simple, low-cost and scalable manufacturing processes. Mirrors of this design integrate passive and active materials in order to create an active laminate structure. Replication techniques along with subsequent bonding processes are implemented, eliminating the need for any grinding/polishing steps. Our mirror designs have the potential to be used as segments of a primary aperture for the next-generation of large aperture space telescopes. Such concepts include those for the Advanced Technology Large-Aperture Space Telescope [9] or the concept for on-orbit assembly envisioned by the Large Space Aperture study sponsored by the Keck Institute for Space Studies [10] and currently under development through a technology demonstration that uses nanosatellites [11,12]. Lightweight mirrors have been identified as a key technology for the realization of both of these concepts. Alternatively, this technology could also be used as a cost-effective solution for the emerging class of Earth-observing imagers based on small-scale platforms [13,14].

The paper is structured as follows. Section 2 provides an overview of the CSM design as well as details on the various layers within the structure. Section 3 outlines a method to size and shape the active layer of the mirror in order to maximize its actuation and its ability to correct figure errors. Section 4 presents a study to predict the corrective capabilities of a mirror through numerical simulations. Section 5 outlines a fabrication scheme to build CSM prototypes. Section 6 concludes the paper.

2. OVERVIEW OF MIRROR DESIGN

An exploded view of the various layers within the CSM is shown in Figure 1. The overall structure of the mirror is provided by a thin carbon fiber reinforced polymer (CFRP) substrate. A high-quality nanolaminate face-sheet is bonded to the front of the substrate in order to provide the reflective mirror surface. On the back, a layer of active material is bonded providing a surface-parallel actuation scheme. A common ground, as well as custom patterned electrodes are incorporated on either side of the active material providing spatial control over the imposed actuation. Finally, a thin electrode routing layer is incorporated on the back of the active material in order to access each actuator. Such a scheme allows the construction of very thin CSM's that are hence highly flexible.

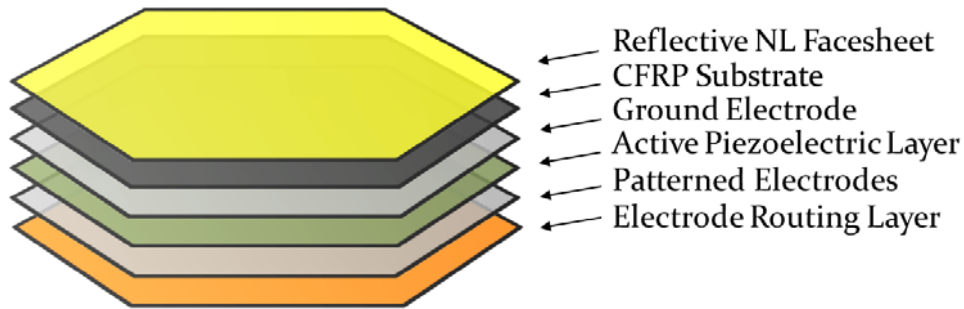


Figure 1: Exploded diagram of CSM displaying the various layers.

2.1 CFRP Substrate

The mirror substrate is a composite shell made from ultra-thin plies of pre-impregnated carbon fibers and epoxy resin. Each ply of the laminate is only $30\text{ }\mu\text{m}$ thick allowing quasi-isotropic laminates to be constructed while keeping the overall thickness to a minimum. For the current effort, two laminates have been considered consisting of either 8 or 16 plies. The laminate orientation is defined as $[0^\circ/45^\circ/-45^\circ/90^\circ]_{ns}$ where $n = 1$ for 8 plies and $n = 2$ for 16 plies ($[]_s$ denotes a symmetric laminate). These CFRP shells have a total thickness of $240\text{ }\mu\text{m}$ and $480\text{ }\mu\text{m}$ with an areal density of 0.45 kg/m^2 and 0.90 kg/m^2 for the 8- and 16-ply designs respectively.

Figure 2 is an example of a bare CFRP substrate. The as-manufactured front surface of the shell appears to be relatively smooth however, due to thermal contraction of the epoxy during curing, the underlying unidirectional fibers protrude through the top-surface of the laminate. This effect is known as fiber print-through and is common in replicated composite optics.

2.2 Reflective Layer

In order to obtain an optical-quality front surface, a reflective nanolaminate facesheet is bonded to the carbon substrate. Nanolaminates are multilayer metal foils formed by sputter deposition on a precision glass mandrel [15,16]. The overall thickness of the nanolaminate can be tuned by varying the number of layers within the structure. Process alterations have been made in order to ensure that the nanolaminates contain an extremely low amount of internal stress. The incorporation of the nanolaminate practically eliminates the presence of fiber print-through.

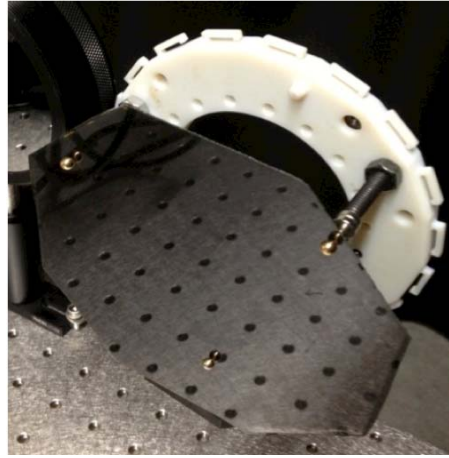


Figure 2: CFRP substrate displaying smooth front surface and desired mirror figure.

2.3 Active Layer

In order to provide the surface-parallel actuation scheme, a layer of piezoelectric material is bonded to the back of the CFRP substrate. The d_{31} piezoelectric coupling coefficient is utilized by applying an electric field through the thickness of the material resulting in a proportional in-plane strain. As the material is bonded to the CFRP substrate, this in turn produces an out-of-plane curvature change of the mirror.

Several candidate materials have been explored as options for the active layer. Due to the high actuation capabilities of Navy Type II Lead Zirconate Titanate (PZT-5A), thin plates of this material were selected. Table 1 presents a summary of the properties of this material.

Table 1: Material properties for PZT-5A [17].

Property	Value
Modulus, E (GPa)	66.0
Poisson's Ratio, ν	0.35
Piezoelectric Constant, d_{31} (pC/N)	-250
Maximum Electric Field, E_{max} (MV/m)	0.8

A continuous ground plane and patterned electrodes are printed on the top and bottom surfaces, respectively, of the piezoelectric layer using a silver nano-particle ink and a Dimatix 2800 Materials Printer [18]. The electrodes allow high electric fields to be applied across the mirror. The actuator pattern, shown in Figure 3, is a custom design optimized to correct for specific modes of figure error associated with the CSM. More details are provided in Section 3.

2.4 Electrode Routing Layer

Due to the relatively large number of actuation channels, active mirrors often contain cluttered, bulky connecting wires that can impart shape errors onto the mirror surface. In order to alleviate this problem for the CSMs, conductive electrode traces are printed on a thin Kapton routing layer as shown in Figure 4. Connections to the underlying electrode pads are then made using through-thickness vias and conductive epoxy. The pattern is designed to route the traces away from the active surface of the mirror to a flex-cable connector where connections to the control electronics can be made using more standard cabling techniques. The low modulus and thickness of the Kapton layer allows the CSM to remain highly flexible during actuation.



Figure 3: Patterned electrodes of 150 mm diameter CSM prototype containing four PZT-5A plates.

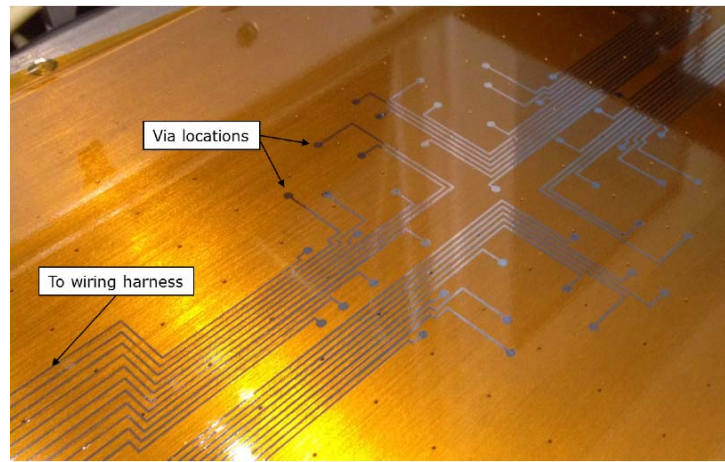


Figure 4: 25 μm thick Kapton routing layer with printed electrode traces.

3. ACTIVE LAYER DESIGN

Since the CSMs are very thin structures, the relative thickness of each layer has a significant effect on the overall mechanical behavior. The thickness of the active layer is of particular importance as small changes in this value can have a large impact on the mirror's actuation capabilities. If the active layer is too thick it will dominate the flexural stiffness of the mirror while if it is too thin there will not be enough actuation authority in order to correct for the expected deformations. In order to determine the optimal thickness of the active layer a linear analysis based on Classical Lamination Theory (CLT) was performed [19].

Table 2: CSM laminate design

Layer	Material	Thickness (μm)
1	Nanolaminate	50.0
2	CFRP	240.0 (8-ply) 480.0 (16-ply)
3	PZT-5A	Variable
4	Kapton	25.0

The maximum curvature change of an 8-ply and 16-ply laminate was calculated as a function of the active layer thickness. Table 2 describes the various layers within the two designs. The thickness of the nanolaminate and Kapton routing layer are set to 50 μm and 25 μm respectively as these are the current values used in a

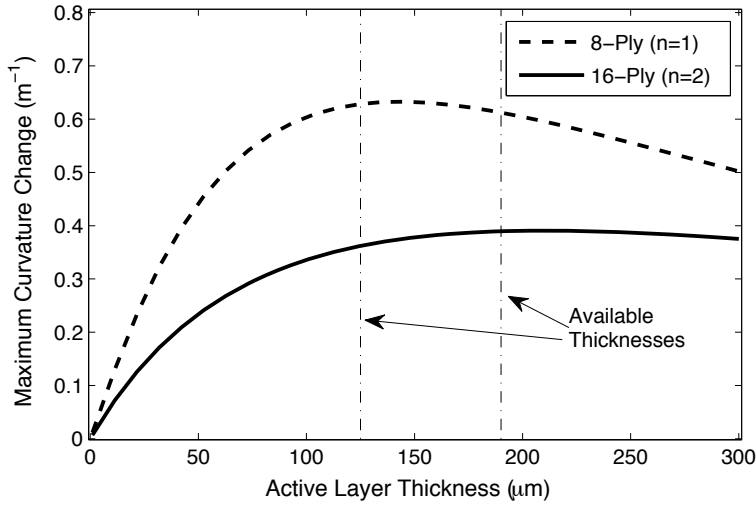


Figure 5: Maximum curvature change due to actuation as a function of active layer thickness.

practical setting. Figure 5 displays the results of this process. The first thing to note is that the maximum curvature change is significantly larger for the 8-ply laminate. This is as expected as the flexural stiffness of the 16-ply CFRP substrate is much higher. Next, it is evident that for both substrates and small active layer thicknesses there is approximately a linear increase in actuation capabilities with the active layer thickness. However, this linearity starts to diminish for active layer thicknesses over approximately $40 \mu\text{m}$. For the 8-ply substrate, an optimal active layer thickness of $150 \mu\text{m}$ is determined to maximize the actuation capabilities of the mirror. For the 16-ply substrate this point is shifted further to the right, having an optimal value of $240 \mu\text{m}$. However it can be seen that very minimal gains are realized after a certain point ($\sim 150 \mu\text{m}$). As the PZT material is the most dense component in the CSM, there is a trade between obtaining slightly higher actuation capabilities while significantly increasing the overall mass of the mirror. Therefore, taking into account practical constraints what is currently available, an active layer thickness of $125 \mu\text{m}$ was chosen for both the 8-ply and 16-ply designs.

4. SIMULATION OF CORRECTION CAPABILITIES

In order to make predictions on the correction capabilities of various designs, the CSM was modeled using Abaqus CAE/Standard 6.12 [20]. Details on this analysis can be found in Ref. [21]. Figure 6 displays the modeled actuation pattern as well as the influence functions associated with the unique electrode positions. It is apparent that the CSM design has significant actuation capabilities as each influence function has a full-scale peak-to-valley (PV) deformation range of $45\text{--}100 \mu\text{m}$ for a 16-ply, 150mm dia. design.

Using the calculated influence functions a variety of performance simulations can be conducted. A constrained least-squares algorithm taking into account voltage limitations of the piezoelectric material is used in order to determine the necessary voltage map required for correction; ref. [22] provides more details on this process. Figure 7 displays the result of one such case where the active elements are used to correct a 16-ply mirror with $50 \mu\text{m}$ of initial astigmatism-based error. It can be seen that with this magnitude of initial error, $0.76 \mu\text{m}$ of residual error is present after correction (considering 95% of the overall aperture). It can also be seen that 12 of the 49 actuators are saturated at their maximum voltage values ($\pm 100 \text{ V}$), while others are operating at much lower values. The saturated actuators are those located around the perimeter of the mirror as these have the greatest influence when performing astigmatism correction. This is also where the majority of residual error is present.

Figure 8 is a more comprehensive study detailing the performance of an 8-ply and 16-ply CSM by observing the amplitude of residual error after correction as a function of initial astigmatic error amplitude. Several observations can be made from this figure. The first is that for small initial errors ($< 45 \mu\text{m}$ RMS), both the 8-ply and 16-ply designs have correction factors of approximately 99%, demonstrating significant correctability. It

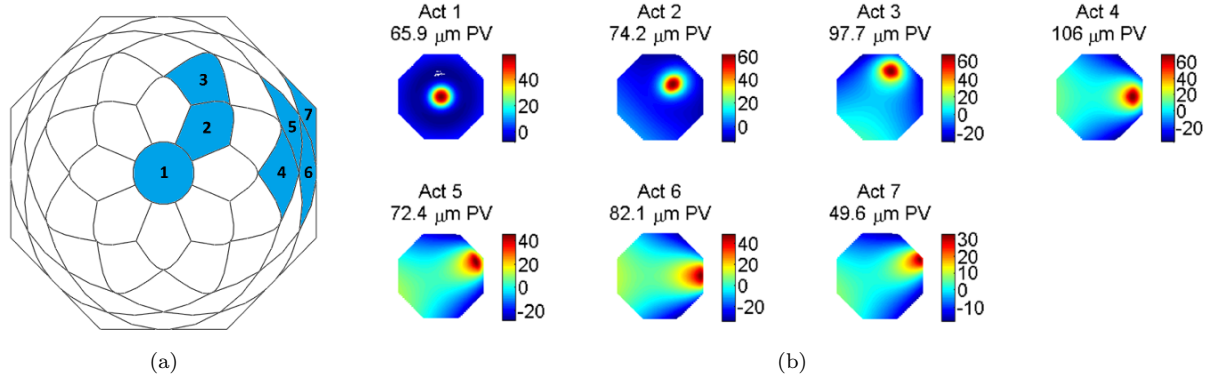


Figure 6: (a) Actuation pattern used for the CSM model showing unique actuator shapes. (b) Shape and magnitude of the corresponding influence functions for a 16-ply design.

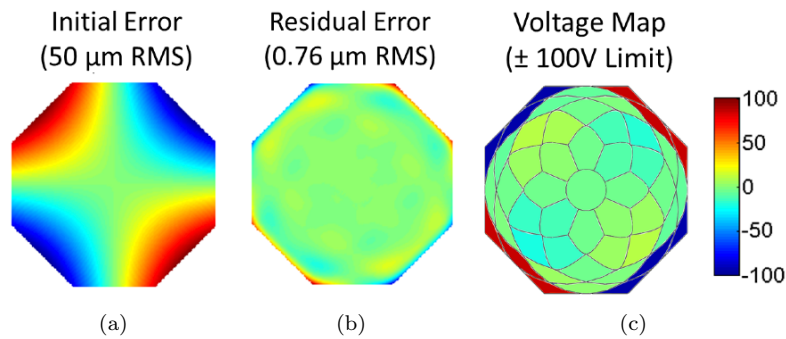


Figure 7: Simulation results for a 16-ply CSM model showing: (a) the 50 $\mu\text{m RMS}$ of initial astigmatic error, (b) the residual error of 0.76 $\mu\text{m RMS}$ after correction (considered over 95% of the pupil), and (c) the corresponding actuator voltages required for correction.

can also be seen that the 16-ply mirror slightly outperforms the 8-ply design over this range of initial errors. This is due to the fact that the influence functions of the stiffer 16-ply mirror have a slightly more global behavior in comparison to those of the 8-ply design. This essentially acts as an inherent low-pass spatial filter, thus reducing the magnitude of residual error. The next observation is related to the effect of actuator saturation. For the 16-ply mirror, as the magnitude of initial error is increased beyond 45 μm , the magnitude of residual error starts to increase drastically. This is due to the fact that several of the actuators have reached their voltage limit and can no longer support any further corrections. Since the 8-ply mirror is more compliant, and thus the influence functions have a higher full-scale deformation value, this effect is delayed and the mirror can correct for larger initial errors without saturation.

In previous efforts the actuators were shaped according to simple geometric patterns [7,8], but the performance of active mirrors can be significantly enhanced by choosing actuators designed according to an optimal topology [22].

The design of the electrodes shown in Figure 3 is based on the observation that the correction of a figure error that has two planes of mirror symmetry can be done optimally with twin actuators of identical shape but rotated through 90°. Applying a positive voltage to the first actuator and a negative voltage to the second one has the effect of removing the axis-symmetric component of the correction while also doubling the magnitude of the non-axisymmetric component. In this set of twin actuators, the basic actuator shape is obtained from the numerical optimization of an objective function that includes both the correctability of the mirror, defined as the ratio between the RMS wavefront error before and after correction, and the stroke, defined as the maximum error amplitude that can be corrected without saturating any actuators. The basic actuator system defined by this shape is made more versatile, i.e. able to correct wavefront error modes that are different from the

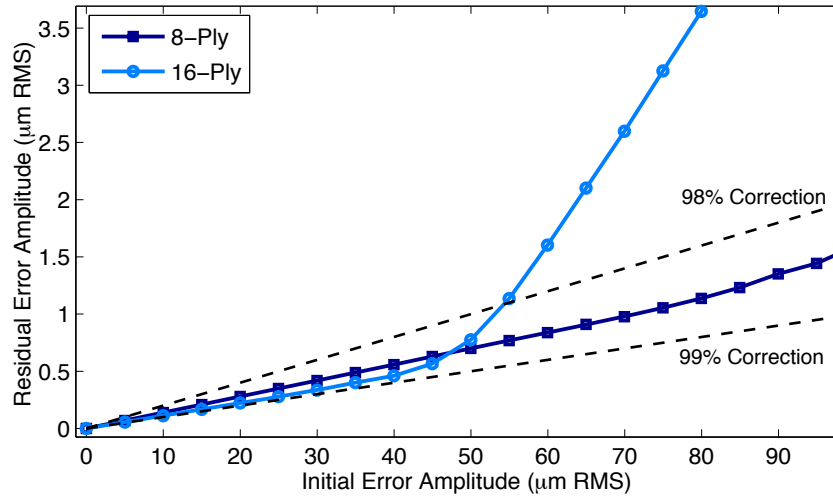


Figure 8: Comparison of correction capabilities for CSMs constructed from 8 and 16 plies.

modes for which the basic shape had been originally obtained, by independently controlling the voltage in each of the actuation zones defined by the intersection of the basic actuator shapes. Further improvements, particularly in the correctability of higher-order Zernike components of the error, are achieved by subdividing the central actuation zone into further sets of similarly defined twin-actuator systems. It has been shown that this approach leads to actuator systems that provide higher correctability than simple, geometrically-based actuators with twice as many actuators, for the first 25 Zernike modes.

The actuator pattern shown in Figure 3 was obtained by initially generating a pattern of 129 actuators, based on four nested sets of twin actuators, of the kind described above, augmented with an identical pattern rotated through 45° . This initial pattern was simplified by grouping some of the smaller actuators while ensuring that the performance of the active mirror was not severely impacted.

5. PROTOTYPE FABRICATION

Figure 9 is a schematic of the current fabrication process for the CSM prototypes. First, a lay-up of unidirectional carbon fiber prepreg is placed on top of a polished glass mandrel (Step 1). The laminate is vacuum bagged and autoclave cured at elevated temperature and pressure to provide consolidation of the plies. During this process the CFRP laminate replicates the surface of the underlying mandrel providing the overall figure of the mirror. Care must be taken during the lamination and curing process as slight deviations from a symmetric lay-up will cause significant figure errors. Next, the PZT plates are bonded to the back of the CFRP substrate with the mandrel underneath to provide support (Step 2). A common ground plane and patterned electrodes are printed onto either side of the plate before the bonding process takes place. A low viscosity, room-temperature cure epoxy is used for this bonding process in order to ensure even epoxy flow out and to avoid thermal distortions. Once cured, the assembly is removed from the underlying mandrel and bonded to a nanolaminate facesheet (Step 3). This nanolaminate has been deposited on a mandrel with the same figure as that used for the CFRP replication process, producing a matching part. Care must be taken in order to ensure a uniform thickness distribution of epoxy between the CFRP substrate and the nanolaminate during this bonding process. The Kapton electrode routing layer is then incorporated onto the backside of the mirror using conductive epoxy (Step 5) and lastly, the completed CSM is parted from the secondary mandrel and trimmed to size (Step 6).

Figure 10 displays the front and back surface of CSM prototypes constructed using these techniques. These prototypes range from 150-175 mm in diameter, 500-850 μm in total thickness and have an areal density of 1.5-2.7 kg/m^2 . They display good surface quality (2.2 nm Ra surface roughness) and have large actuation capabilities (up to 150 μm PV measured influence functions).

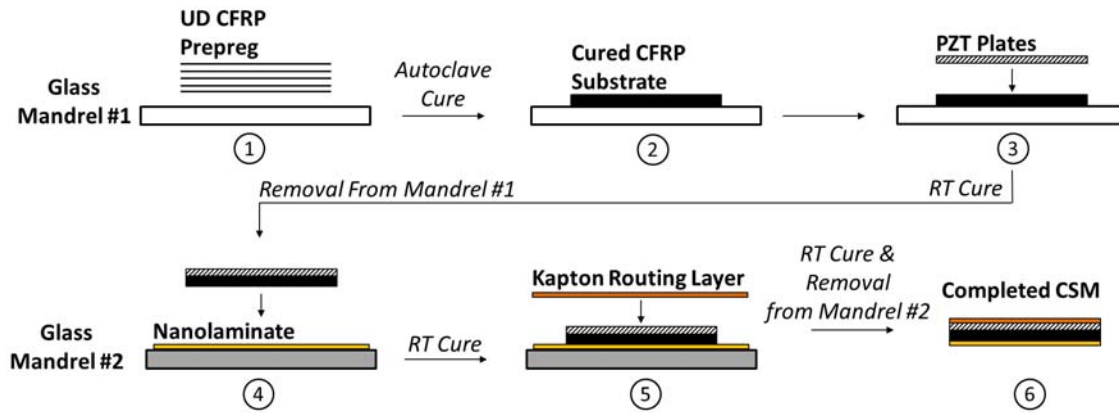


Figure 9: Fabrication schematic for CSM prototypes.

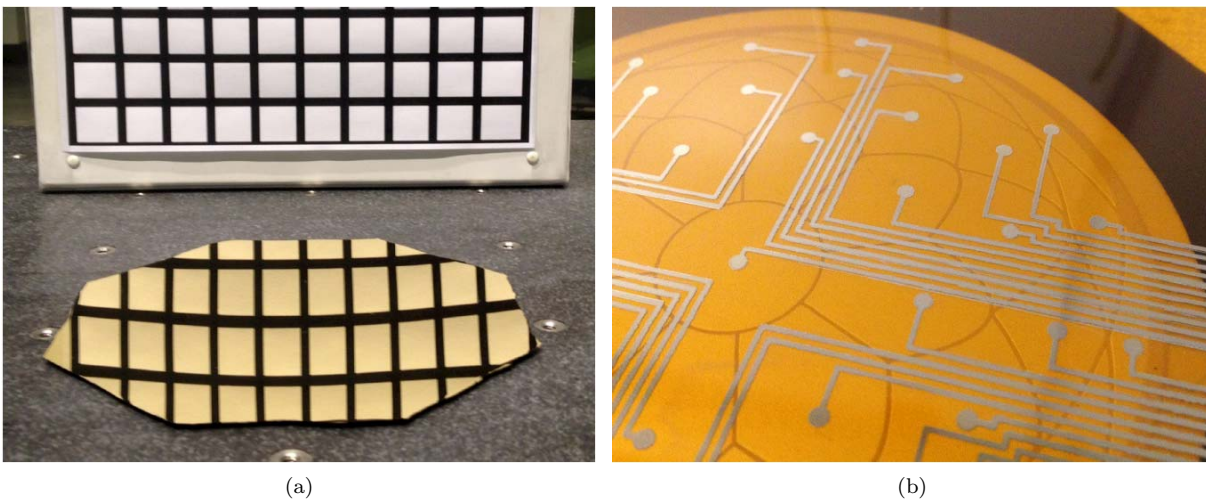


Figure 10: A CSM prototype displaying (a) the reflective front surface obtained through the nanolaminate integration and (b) the electrode pattern and Kapton routing layer.

6. DISCUSSION AND CONCLUSION

A novel method of constructing ultra-lightweight active carbon shell mirrors has been presented. These mirrors are laminates of active and passive materials providing the intended mirror figure, reflective front-surface, actuation capabilities, and electrode wiring. They are extremely thin, ranging from 500-850 μm in total thickness with an areal density of 1.5-2.7 kg/m^2 ; a drastic improvement over traditional mirrors.

A method to size the active layer thickness in order to maximize the actuation capabilities of two CSM designs was presented. With the desire to also minimize the overall mass of the structure and taking into account practical limitations, an active layer thickness of 125 μm was chosen as an optimal value both designs. The corrective capability of these two designs with 49 actuator channels was also modeled. It was shown that the 8-ply design had significantly more actuation stroke than the 16-ply design, however both displayed correction factors approaching 99% before actuator saturation, correcting initial shape errors of up to 50 μm down to < 1.0 μm . Therefore, the CSMs show great potential to correct for large shape errors originating from initial manufacturing errors or thermal deformations.

Fabrication methods have been developed in order to construct CSM prototypes. They display good surface quality (2.2 nm Ra surface roughness) and large actuation capabilities (150 μm PV measured influence functions).

Current efforts are focused on the construction of a fully-integrated 16-ply CSM with a post-correction figure error of $< 1.0 \mu\text{m}$ RMS. Additional efforts are underway in order to reduce the magnitude of the initial shape error, reduce the overall thickness of the designs and increase the correction capabilities.

ACKNOWLEDGMENTS

The research outlined in this paper was carried out together with a number of collaborators: Marie Laslandes and John Steeves (Caltech); Case Bradford, David Redding and Kent Wallace (JPL); and Troy Barbee (Lawrence Livermore National Laboratory). A part of this research was carried out at the Jet Propulsion Laboratory, California Institute of Technology under a contract with the National Aeronautics and Space Administration (NASA).

REFERENCES

- [1] H.P. Stahl, "Design study of 8 meter monolithic mirror UV/optical space telescope," *Society of Photo-Optical Instrumentation Engineers (SPIE) Conference Series*, 7010, 2008.
- [2] J.P. Gardner, J.C. Mather, M. Clampin, et al., "The James Webb space telescope," *Space Science Reviews*, 123.4: 485-606, 2006.
- [3] J.D. Hochhalter, "Replicated mirrors using carbon fiber reinforced polymers," Master's Thesis, University of New Mexico, 2005.
- [4] P.C. Chen, et al., "Advances in very lightweight composite mirror technology," *Optical Engineering*, 39(9), 2320-2329, 2000.
- [5] G. Hickey, T. Barbee, M. Ealey and D. Redding, "Actuated hybrid mirrors for space telescopes," *Society of Photo-Optical Instrumentation Engineers (SPIE) Conference Series*, 7731, 2010.
- [6] Northrop Grumman, AOA Xinetics, <http://www.northropgrumman.com/BusinessVentures/AOAXinetics> (2014).
- [7] J. Sinquin, J. Lurcon and C. Guillemard, "Deformable mirror technologies for astronomy at CILAS," *Society of Photo-Optical Instrumentation Engineers (SPIE) Conference Series*, 7015, 2008.
- [8] K. Patterson and S. Pellegrino "Ultralightweight deformable mirrors." *Applied Optics*, 52, pp. 5327-5341, 2013.
- [9] M. Postman et al., "The Advanced Technology Large Aperture Space Telescope (ATLAST): Science drivers and technology developments," *Optical Engineering*, 51(1), 011007, 2012.
- [10] Keck Institute for Space Studies, Large Space Structures, <http://kiss.caltech.edu/study/largeststructure/technology.html> , 2011.
- [11] K. Patterson and S. Pellegrino, "Shape correction of thin mirrors in a reconfigurable modular space telescope," *Society of Photo-Optical Instrumentation Engineers (SPIE) Conference Series*, 7731-72, 2010.
- [12] C. Underwood and S. Pellegrino, "Autonomous assembly of a reconfigurable space telescope (AAReST) for astronomy and earth observation." *8th IAA Symposium on Small Satellites for Earth Observation*, April 4-8, 2011 Berlin, 2011.
- [13] Planet Labs Inc., <http://www.planet.com/> , 2014.
- [14] Skybox Imaging Inc., <http://www.skyboximaging.com/> , 2014.
- [15] T.W. Barbee, "Nanolaminate thin-shell mirror structures," *Society of Photo-Optical Instrumentation Engineers (SPIE) Conference Series*, 5166, 2003.
- [16] T.W. Barbee, "Nano-structure Multilayer Materials", *State of the Laboratory*, Lawrence Livermore National Laboratory UCRL-5200-91-718, 1991.
- [17] Piezo Systems Inc., <http://piezo.com/> , 2014.
- [18] Fujifilm Inc. *Dimatix Materials Printer DMP-2831*. http://www.fujifilmusa.com/products/industrial_inkjet_printheads/deposition-products/dmp-2800/ , 2014.
- [19] R.M. Jones, "Mechanics of Composite Materials," 2nd ed., 1998.
- [20] SIMULIA, Abaqus Standard/CAE Version 6.12.
- [21] J. Steeves, M. Laslandes, S. Pellegrino, D. Redding, S.K. Bradford, J.K. Wallace and T. Barbee, "Design, fabrication and testing of active carbon shell mirrors for space telescope applications," *Astronomical Telescopes and Instrumentation 2014: Advances in Optical and Mechanical*

- Technologies for Telescopes and Instrumentation, Montreal, Quebec 22-27 June 2014, SPIE 9151-4.
- [22] M. Laslandes, J. Steeves, S. Pellegrino, and K. Patterson, "Optimization of electrode configuration in surface-parallel actuated deformable mirrors," *Society of Photo-Optical Instrumentation Engineers (SPIE) Conference Series*, 9148-151, 2014.

Deployable Structures in the CubeSat Program MOVE

M. Langer⁽¹⁾, C. Olthoff⁽¹⁾, L. Datashvili⁽²⁾, H. Baier⁽²⁾, N. Maghaldadze⁽²⁾, U. Walter⁽¹⁾

⁽¹⁾*Institute of Astronautics, Technische Universität München
Boltzmannstraße 15, 85748 Garching, Germany
Email: martin.langer@tum.de, c.olthoff@tum.de, walter@tum.de*

⁽²⁾*Institute of Lightweight Structures, Technische Universität München
Boltzmannstraße 15, 85748 Garching, Germany
Email: datashvili@llb.mw.tum.de, baier@llb.mw.tum.de, n.maghaldadze@tum.de*

ABSTRACT

This paper investigates the utilization of deployable and expandable structures for communication purposes and solar power generation on CubeSats. We present the design and on-orbit results of the flight-proven solar-panel release mechanism of the first satellite of Technische Universität München First-MOVE, as well as the preliminary design of a solar panel deployment mechanism based on smart memory alloys for the second satellite MOVE II. Preliminary studies on a CFRS (carbon fibre reinforced silicone) shell membrane antenna as well as two other possible payloads for MOVE II are briefly described.

1. INTRODUCTION

The CubeSat program MOVE (Munich Orbital Verification Experiment) was initiated in 2006 at the Institute of Astronautics (LRT) at the Technische Universität München (TUM) in Munich, Germany, with the objective of educating students and the validation of new technologies in space. After a successful launch of the programs' first CubeSat First-MOVE in late 2013, the second CubeSat MOVE II is currently under development.

CubeSats, a class of satellites established in 1999 by CalPoly and Stanford University, are defined by the CubeSat Standard [1], which among other constraints, limits the satellites volumes to multiples of a so-called Unit, a 10x10x10 cm cube. Although for the designers of such systems this standardization has many advantages, the inherent volume constraint presents a challenge, e.g. for payloads that require large solar power generators, or for missions with high communication data rates requiring either parabolic antennas or a low-interference environment far away from the satellite's main body. Deployable and expandable structures are a versatile option to overcome these restrictions and facilitate advanced payloads on CubeSats.

Current and past CubeSat missions are based on self-developed [2] or commercial off-the-shelf (COTS) [3], [4] deployable and/or expandable structures for solar power generation. Most of the mechanisms used for solar panel deployment rely on conventional techniques like the utilization of melting wires and springs for hold down and release. For some missions more complex systems for gravity gradient stabilization [5], communication purposes [6] or a combination of communication and solar power generation [7] have been proposed or already flown.

For the 1-Unit (1U) CubeSat First-MOVE a multi-purpose deployment mechanism for two solar panels, as well as the UHF and VHF antennas of the satellite were developed. The student-designed mechanism, based on two redundant melting wires and springs, deployed two extra "flap panels" for additional surface area to generate electrical power via solar cells. An iterative design process and the subsequent verification of the mechanism on the REXUS 4 (Rocket-borne Experiments for University Students) sounding rocket resulted in the successful deployment of both panels in space during the First-MOVE mission.

Based on the experience from the first satellite, an advanced solar panel deployment mechanism for the 2-Unit CubeSat MOVE II, called SMARD (Shape Memory Alloy Reusable Deployment mechanism) is currently under development at LRT. Rather than melting wires the new mechanism will use destructive shape memory alloy technology, enabling repeated deployment tests with the flight units. This repeatability will allow the team to perform more tests in less time and will therefore enhance the reliability of the deployment mechanism and the confidence in the overall system. SMARD has been selected by DLR (Deutsches Zentrum für Luft- und Raumfahrt) for the REXUS 17/18 launch campaign in early 2015.

Preliminary studies, started in 2013 and led by the Institute of Lightweight Structures (LLB) of TUM, highlighted the potential of expendable and deployable Carbon Fibre Reinforced Silicone (CFRS) structures for CubeSats. In particular the unfolding of a CFRS shell-membrane antenna reflector with parabolic shape and flexible Copper Indium Gallium Selenide (CIGS) solar cells on the back side was studied for C-Band or X-Band communication on CubeSats or small satellites.

This paper is structured as follows: In Section 2 the multi-purpose deployment mechanism of First-MOVE as well as its on-orbit deployment are presented. Section 3 deals with the shape memory alloy reusable deploy mechanism currently in development at LRT for the second satellite mission MOVE II. The proposed deployable CFRS structures for MOVE II are briefly discussed in Section 4.

2. FIRST-MOVE MULTI PURPOSE DEPLOYMENT MECHANISM (MPDM)

For First-MOVE, as for many other university satellites in the last decade, the CubeSat Standard from CalPoly [1] was chosen. Among others the geometrical requirements defined by this standard (see Fig. 1 for 1U) usually impose limits on power generation (i.e. the available surface area of the cube for solar cells) and communications (e.g. antenna length without deployment, usage of patch antennas). Since CubeSats use standardized commercially available launch adapters from various providers, there are no exceptions with regard to the geometric requirements. Deployable solar panels and/or deployable antennas can be used to overcome these constraints and enhance the capabilities of a CubeSat.

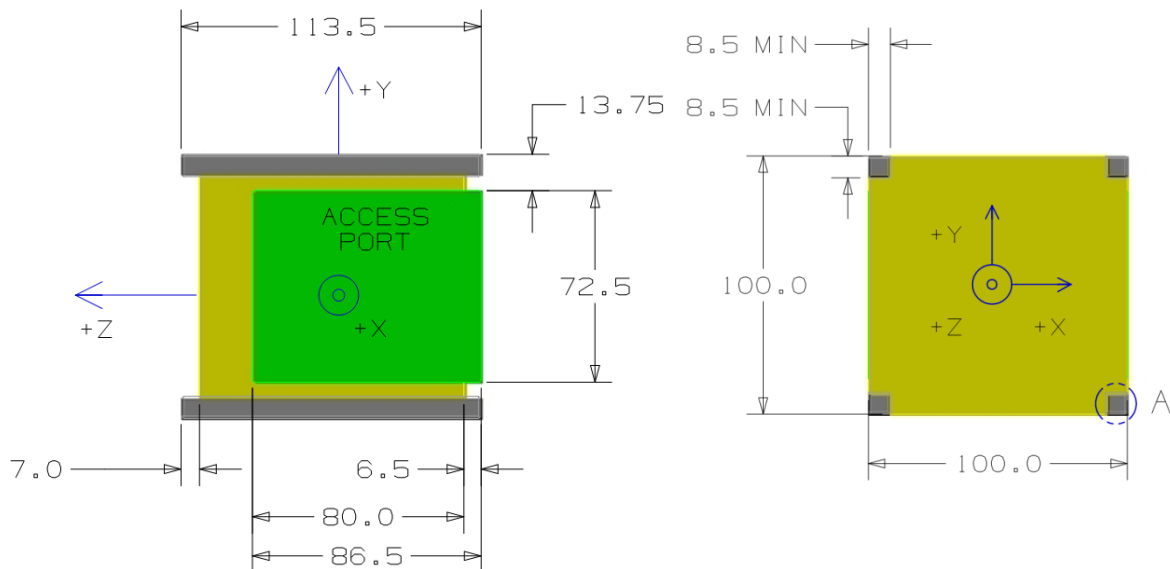


Fig. 1. Geometrical restrictions from the CubeSat Standard for 1 U [1].

Hence the design of First-MOVE includes two deployable solar panels, increasing the maximum power produced by 60%. For communication demands, half dipole antennas for UHF and VHF are attached to the upper and lower panel, respectively (see Fig. 2). To keep the panels in a locked position during launch and deploy them via a signal from the on-board data handling system (OBDH) of the satellite, a hold down and release mechanism (HDRM) was designed over several iterations [7]. Further requirements regarding acceleration, vibrations, temperature and shock were considered and resulted in a redundant melting wire concept with a rotational spring-articulated bracket (see Fig. 3).

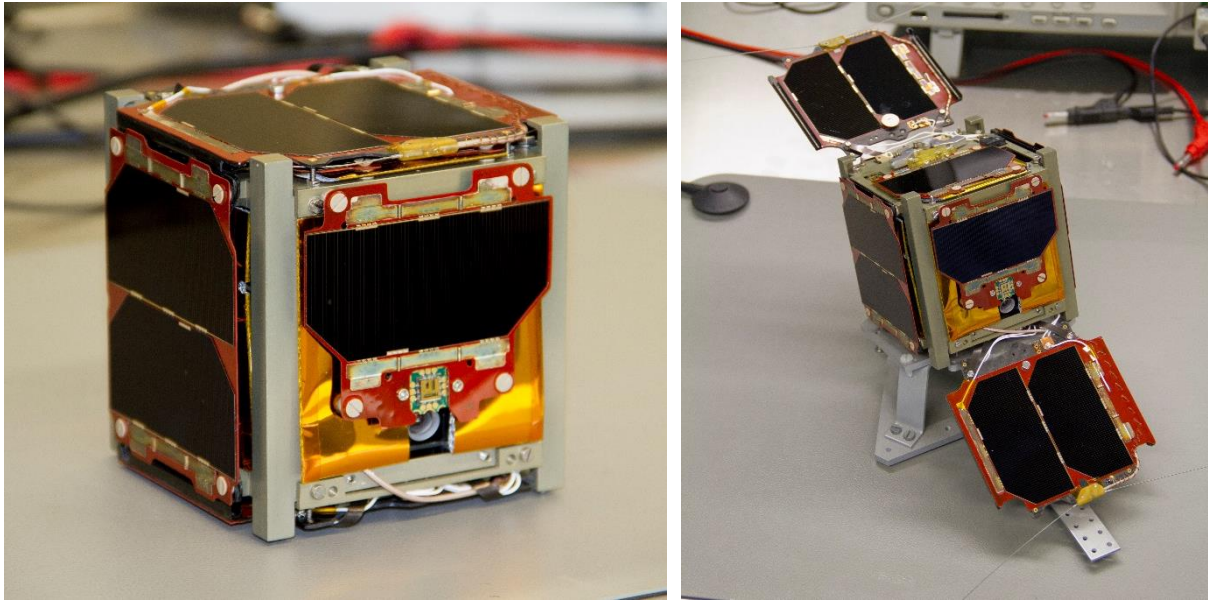


Fig. 2. First-MOVE in launch configuration (left) and deployed configuration (right).

The HDRM functions as follows: After the successful deployment from the launch adapter, redundant deployment switches sense the deployment and the boot sequence of the OBDH is started. After a predetermined time (8 minutes) both HDRMs are actuated sequentially by a signal from the OBDH. The signal switches a MOSFET transistor to allow a current of ~ 800 mA at 3.3V to pass through redundant Constantan wires, again in a sequential fashion. The dissipative heat produced by the Constantan wires melts a Dyneema string that holds two spring-loaded brackets together. Subsequently the rotation spring articulates both brackets, freeing a half cone attached to the flap panel. This way the panel can move freely and is rotated by the so-called C-Springs (the C-Springs are highlighted in Fig. 3). Along with the flap panels the two antennas are deployed. During launch the antennas are curled up between the side panels and the satellites' body.

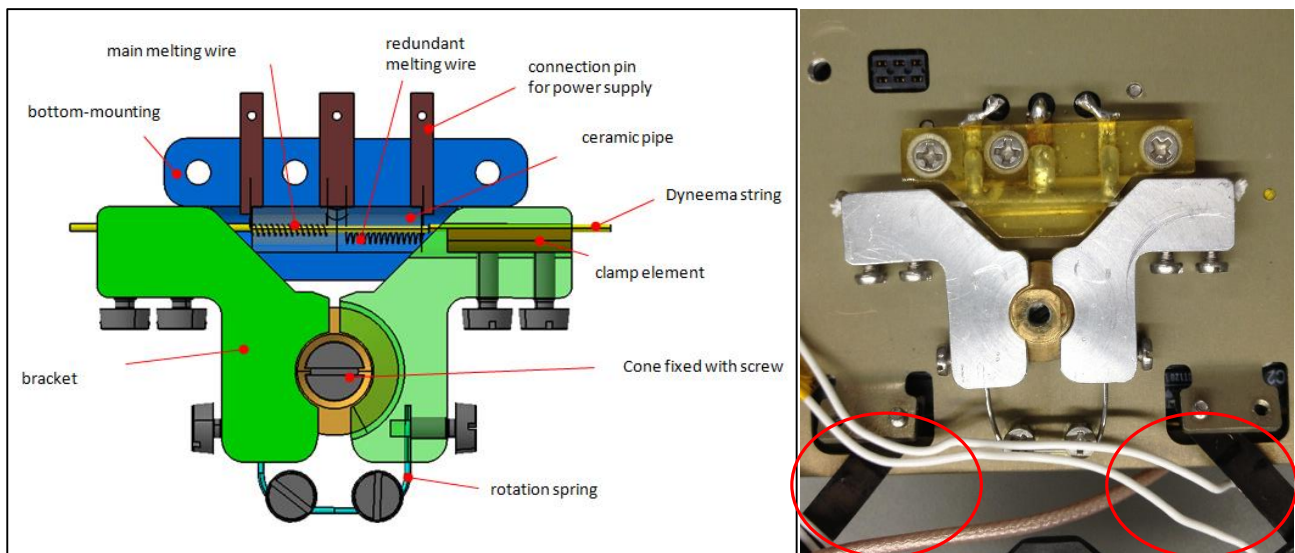


Fig. 3. HDRM mechanism design (left) [8] and final HDRM with highlighted C-springs (right).

Successful ground deployment tests were followed by vacuum chamber tests at LRT and vibration/acceleration tests at IABG GmbH in Ottobrunn, Germany. After each test the deployment of the panel was tested and the HDRM visually inspected. For verification purposes one HDRM was flown on the REXUS-4 mission. The sounding rocket hosted among others a verification experiment for critical pico-satellite components, called VERTICAL (Verification and Test of Initiation of CubeSats after Launch). Hosted inside the VERTICAL experiment, the HDRM showed nominal behaviour

and released the panel 1.48 seconds after activation of the melting wire. Flap Panel maximum velocities of 1.66 m/s were observed, which are in good agreement with the data obtained during ground tests [8]. On a second sounding rocket mission in 2009 the HDRM was used operationally in the FOCUS experiment to deploy an experimental structure that cured under UV lighting [9].

First-MOVE was launched on the 21st of November 2013 with the Dnepr Cluster Mission from Yasny, Russian Federation. 937 seconds into the flight, the deployment from the ISIPOD deployer number 2 occurred as expected, placing the satellite into a low earth orbit at 97.79° inclination. 8 minutes after ejection from the ISIPOD, both panels were deployed. Along with the first data beacons received from the satellite, the successful deployment of both panels was proven. The communication link established on launch day can be taken as the first evidence of deployment at least of the lower panel with the downlink VHF antenna attached. Additionally, temperature sensor data retrieved via automatic data beacons (see Fig. 4) during the commissioning phase showed a temperature variation of the flap panel between -88.8°C and +13.5°C. According to thermal simulations, we interpret the data as a deployed upper panel (not facing the satellites' body but outer space).

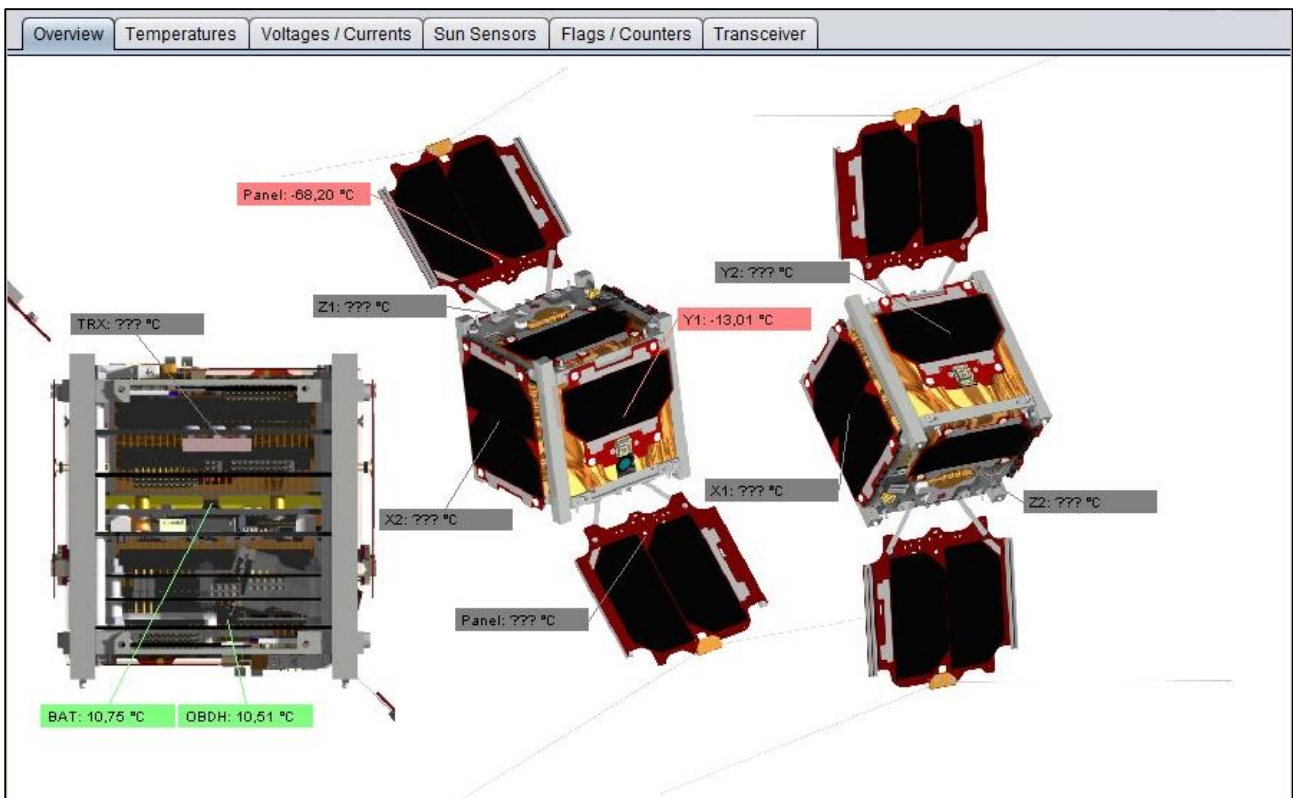


Fig. 4. Example of on-orbit data received from First-MOVE showing the satellites' temperature during eclipse.

Unfortunately it was not possible to retrieve data from the satellite after December 19th 2013, presumably due to a malfunction in the OBDH system, which left the satellite in a mode where it is only transmitting CW beacons. Although the short mission duration seems somewhat discouraging, the overall MOVE program with more than 70 students involved and major in-house technology development and validation outweighs the fact that several secondary mission goals were not achieved.

3. MOVE II SHAPE MEMORY ALLOY REUSABLE DEPLOYMENT MECHANISM

To follow up the educational and technological achievements of First-MOVE, MOVE II was initiated as the successive satellite project of LRT at the end of 2011. To enable the mission to include a scientific payload, the satellites' size was doubled to 2U, allocating the bus in 1U and the scientific payload in the other unit. Furthermore, as the potential payload enhances the demand for computational and electrical power, the successful solar-panel deployment concept of First-MOVE has been continued and the HDRM refined. Following the success of VERTICAL for verification of the first

mechanism, a new student project called SMARD was initiated in late 2013 [10]. The goal of SMARD is to develop a solar panel hold down and release mechanism for a 2U CubeSat using shape memory alloys. As with the previous HDRM mechanism the validation will take place on a REXUS sounding rocket, scheduled for launch early 2015. Since the project is currently ongoing, only the preliminary design of SMARD will be described.

The biggest incentive for a re-design of the flight-proven HDRM mechanism of First-MOVE was the testability with respect to multiple resets of the system. For the First-MOVE mechanism, the reset of the HDRM was accomplished by installing a new Dyneema string and melting wires each time, soldering the melting wires to the connection pins. Although the confidence in the system had been built up by numerous tests, every reset created a non-proven (i.e. prototype) assembly. With MOVE II our goal is to enable multiple successive tests without irreversibly destroying parts of the mechanism during test, thus leading to “true resetability” of the mechanism. In Fig. 5, a prototype design of the mechanism is depicted (preliminary design review (PDR)-level). It is based on the utilization of smart memory alloys (SMA) for articulation. An SMA-spring is used for the articulation of a slider. It is attached to a mount (“Springmount”) which also acts as the electrical interface. The slider itself holds the solar panel in place via the highlighted yellow hook. Therefore the panel with the attached hook is freed by the electro-thermally induced movement of the SMA-spring (see Fig. 6). The rotational opening movement of the panels is enforced by rotational springs mounted in the hinges of the panel (see Fig. 7).

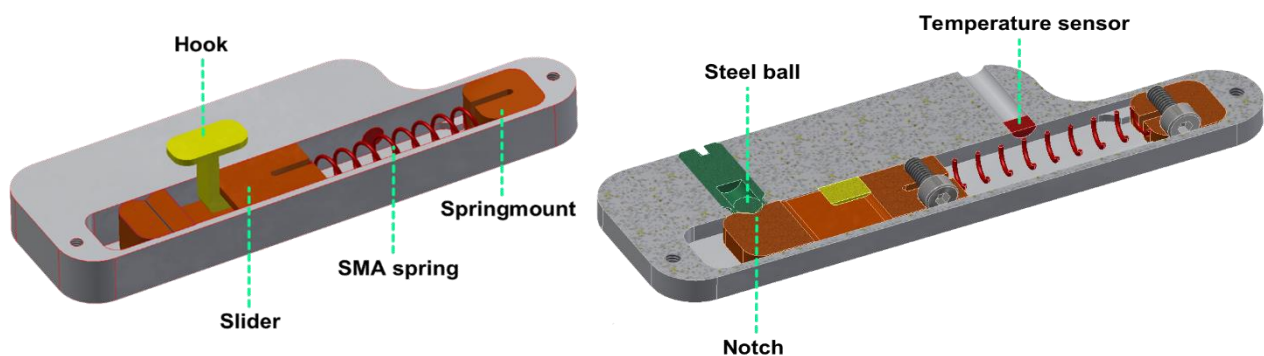


Fig. 5. Preliminary deployment mechanism of SMARD for REXUS 17/18 [10].

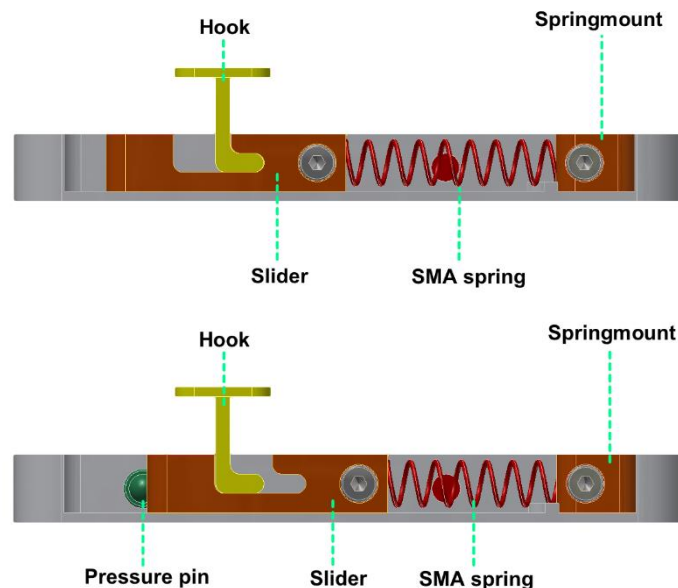


Fig. 6: SMARD in closed configuration (top) and deployment configuration (bottom)

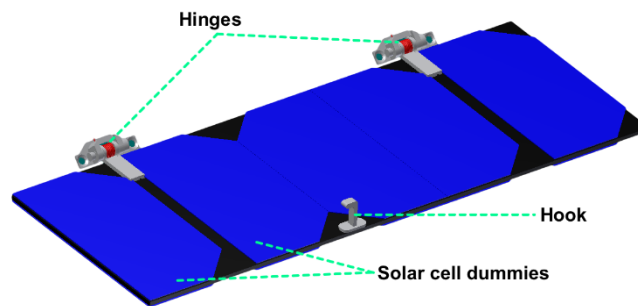


Fig. 7. Preliminary Solar Panel Assembly for REXUS 17/18 with hinges housing the rotational springs [10].

As its predecessor on REXUS 4, the mechanism of MOVE II is scheduled to be verified during the REXUS 17/18 launch campaign. For that purpose a measurement setup consisting of a camera, accelerometers and a magnetic rotation sensor will be integrated into the experiment module. The knowledge of not only the deployment in milli-gravity but also the response of the panel after articulation will be indispensable for the MOVE II mission. Ultimately assuming a moderate number of reset cycles is possible with the mechanism, repeated deployment tests with the flight units seem achievable for us, resulting in a flight-verified, non-destructively testable deployment mechanism.

4. MOVE II EXPANDABLE CARBON FIBRE REINFORCED SILICONE STRUCTURES

Preliminary studies, started in 2013 and led by the Institute of Lightweight Structures (LLB) of TUM, highlighted the potential of expendable and deployable Carbon Fiber Reinforced Silicone (CFRS) structures on CubeSats. Communication systems have been identified by others [11], [12] as a possible bottleneck for future CubeSats, especially when higher data rates than achievable with traditional patch or dipole-antennas are required for scientific or commercial applications [13]. Work published in [14] through [28] shows the high potential of foldable shell-membrane reflectors, even for SmallSat applications. Utilizing a CFRS shell membrane antenna reflector (see Fig. 8) for enhancement of the communication link on CubeSats has therefore been identified as a one possible scientific goal for MOVE II.

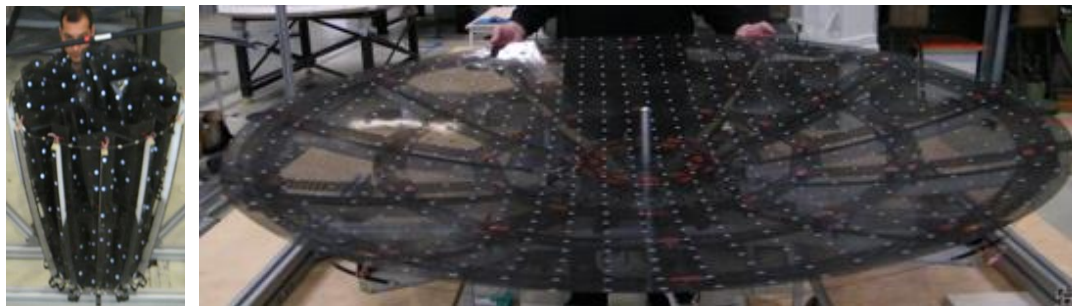


Fig. 8. Deployment of a CFRS shell-membrane reflector.

As a preliminary design goal, the storage and unfolding of a 0.6 m – 1.0 m shell-membrane reflector from a 1U (10x10x10cm) CubeSat shall be investigated. For folding a shell-membrane, there are several ways to follow: umbrella type folding, rolled umbrella type, folded and rolled as in Fig. 9, Miura-ori folding pattern and combined four fold pattern as depicted in Fig. 10 among others. Some other simple patterns of CFRS shell-membrane folding are shown in Fig. 9. A capability of a piece of the membrane material to be freely folded thanks to its low bending stiffness is demonstrated in the figure.

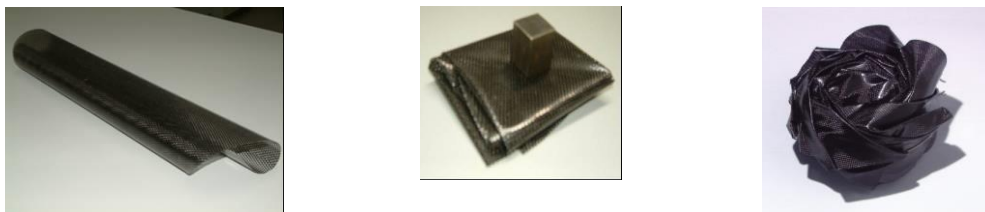


Fig. 9. Schemes of folding of a CFRS shell-membrane: rolled, folded, folded and rolled.

As for more regular and denser folding of a CFRS shell-membrane surfaces into a small volume of a CubeSat, one may need to apply a rigid origami folding geometry. Following the Miura-ori pattern for rigid origami folding, one can derive a folding pattern for CFRS shell-membrane surfaces shown in Fig. 10. The synthesized folding pattern shown in the figure gives a proof of the fitting the package into the given volume. Further investigations will be related to the surfaces made by a hybrid composite CFRS/P material of LLB development [25]. Carbon fibers reinforce both the stiff and the soft matrices. The stiff matrix areas define a shell stiffness, while the soft matrix areas between them act as hinges [25], [29].

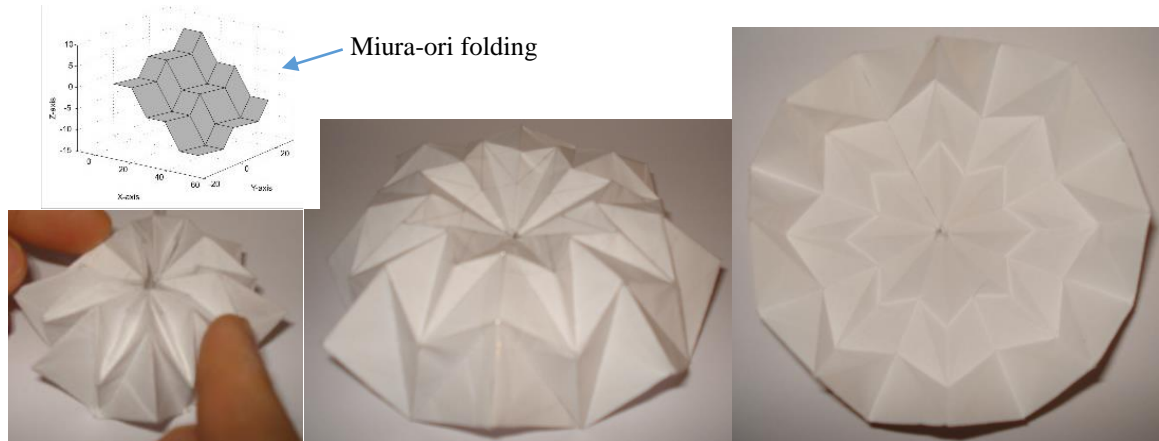


Fig. 10. Miura-ori folding (top) and synthesized rigid origami folding pattern for reflecting CFRS surfaces.

Besides the CFRS shell-membrane investigations further work in the direction of a CubeSat deployable mast is planned. A starting concept of the deployable unit (Fig. 12) of the mast, which shall deploy and tension a membrane is adapted from the membrane direct radiating array (DRA) concept discussed in [30] and demonstrated in the figure.

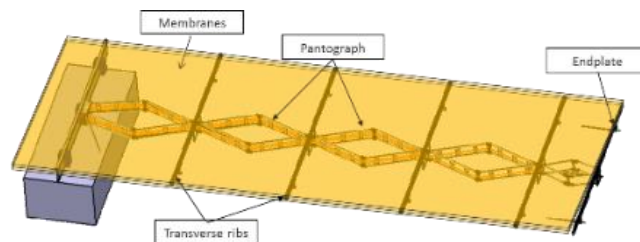


Fig. 11. Membrane DRA half model attached to the satellite, deployed 10.0 m [30].

Several diverse cross sections of the mast, as shown in Fig. 12, can be accommodated into the CubeSat but only few of them allow membrane and CFRS surface accommodation into the same cube volume.

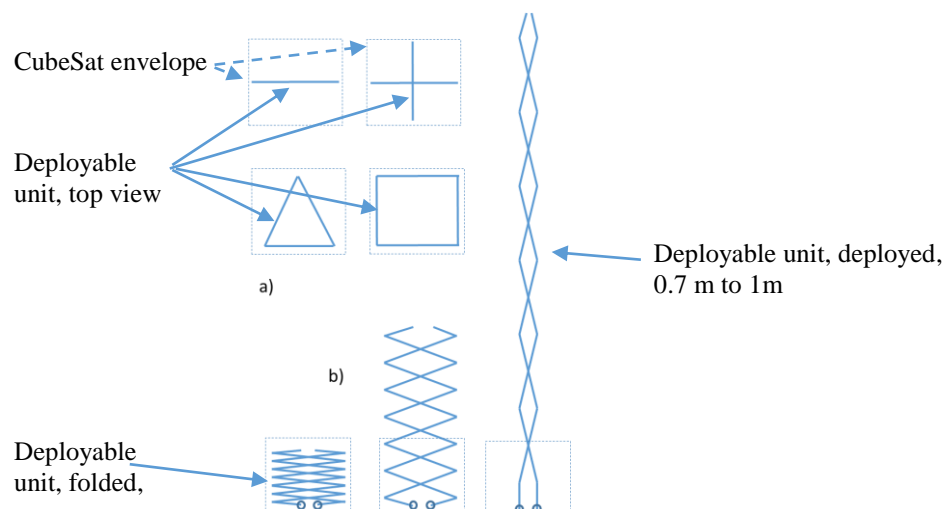


Fig. 12. A concept of a deployable CubeSat mast: cross-section examples.

Three different concepts of the MOVE II payload are shown in Fig. 13: a CFRS reflector, a mast tensioning the membranes and both concepts combined. As can be seen in the left rendering, the parabolic CFRS shell-membrane antenna reflector shall be precisely unfolded during the mission, proving the feasibility of the small deployable reflector concept. In addition, this could be visually verified in orbit by a small video-camera system, mounted on an expandable mast. In future verification missions, this reflector-camera system could be modified to a reflector-feed system, thus enabling C-Band or X-Band communication tests, depending on the reflector's size. Flexible Copper Indium Gallium Selenide (CIGS) solar-cells could be applied on the reverse side of the membrane reflector, and/or around the deployable mast, further enhancing the electrical power produced on the satellite.

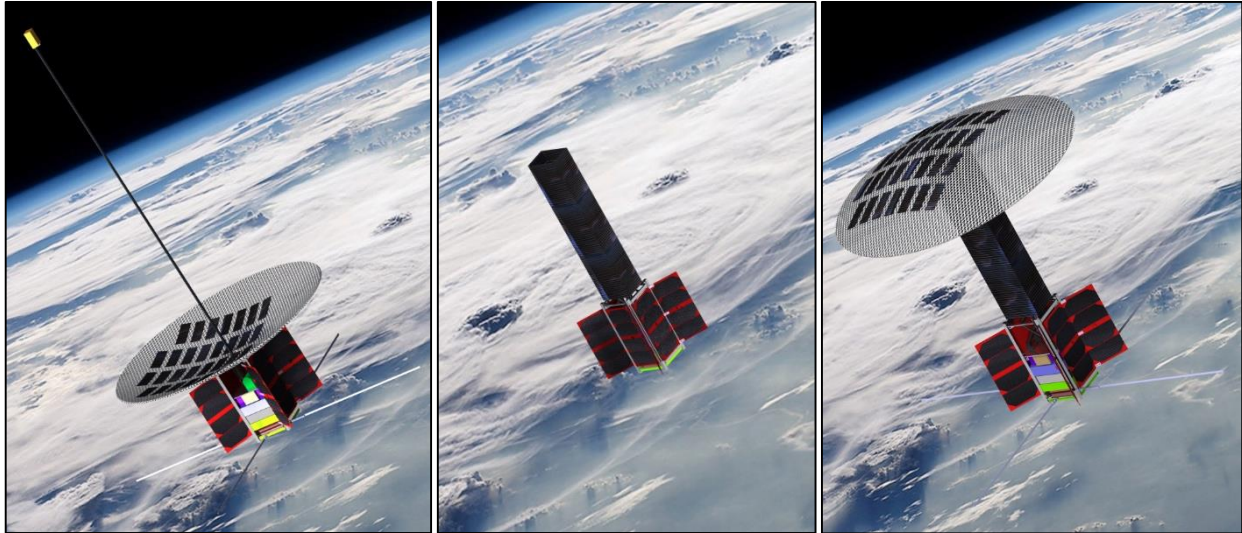


Fig. 13. Preliminary Studies of possible payloads for MOVE II. A parabolically shaped, deployable CFRS-reflector carrying flexible solar cells and a camera for optical verification (left). A CFRS gravity-gradient mast with flexible solar cells on tensioned membrane (middle), a combination of both (right).

5. SUMMARY

Preliminary studies for the upcoming CubeSat mission MOVE II show the potential of expandable reflectors or masts on CubeSats. They may overcome the current CubeSat limitations in available power or downlink data rate. Due to their large area-to-mass ratio they furthermore significantly increase drag and hence reduce orbit lifetime, thus assisting with space debris mitigation in LEO. Utilizing novel folding techniques for parabolic CFRS antennas, MOVE II may pave the way for C-Band or X-Band communication systems on CubeSats or for small satellites.

REFERENCES

- [1]. The CubeSat Program: CubeSat Standard CubeSat Design Specification Rev. 13, <http://www.cubesat.org/index.php/documents/developers>, Cal Poly, Saint Louis Obispo, USA, retrieved 21.07.2014.
- [2]. M. Czech, A. Fleischner and U. Walter: "A First-MOVE in Satellite Development at the TU-München", in: *Small Satellite Missions for Earth Observation*, R. Sandau, H.-P. Roeser und A. Valenzuela, Springer Berlin Heidelberg, pp. 235-245, 2010. http://dx.doi.org/10.1007/978-3-642-03501-2_22.
- [3]. ClydeSpace: CubeSat Solar Panels, www.clyde-space.com/documents/2625, Clyde Space Limited, Glasgow, United Kingdom, retrieved 21.07.2014.
- [4]. Pumpkin Inc.: Pumpkin Price List, <http://www.pumpkininc.com/content/doc/forms/pricelist.pdf>, Pumpkin Incorporated, San Francisco, USA, retrieved 21.07.2014.
- [5]. J. Weaver, "ExoCube and a Gravity Gradient ADCS," *Proceedings of the AIAA/USU Conference on Small Satellites*, CubeSat Developers' Workshop, SSC13-WK-20. <http://digitalcommons.usu.edu/smallsat/2013/all2013/13/>, 2013.
- [6]. Costantine, J.; Tawk, Y.; Christodoulou, C.G.; Banik, J.; Lane, S., "CubeSat Deployable Antenna Using Bistable Composite Tape-Springs," *Antennas and Wireless Propagation Letters*, IEEE, vol.11, no., pp.285,288, 2012. doi: 10.1109/LAWP.2012.2189544

- [7]. R. Hodgins, B. Shah, D. Muthulingham and T. Freeman, "ISARA – Integrated Solar Array and Reflectarray Mission Overview," *Proceedings of the AIAA/USU Conference on Small Satellites*, CubeSatDevelopers' Workshop, SSC13-WK-19. <http://digitalcommons.usu.edu/smallsat/2013/all2013/12/>, 2013.
- [8]. W. Rackl, *Multi Purpose Deployment Mechanism for the MOVE Satellite*, Semester Thesis, Technische Universität München, RT SA 2009/1, 2009.
- [9]. P. Reiss, E. Breunig, P. Zimmerhagl, N. Newie and A. Zeiner, "Investigating new space structures with the FOCUS experiment", *Proceedings of the 20th ESA Symposium on European Rocket and Balloon Programmes (PAC Symposium)*, ESA, 2011.
- [10]. SMARD Student Rocket Experiment: <http://smard-rexus.de/>, Technische Universität München, retrieved 21.07.2014.
- [11]. M. Bille, P. Kolodziejski and T. Hunsaker, "Distant Horizons: Smallsat Evolution in the Mid-to-Far Term", *Proceedings of the AIAA/USU Conference on Small Satellites*, Technical Session IV: On the Horizon, SSC11-IV-1. <http://digitalcommons.usu.edu/smallsat/2011/all2011/29/>.
- [12]. A. Babuscia, B. Corbin, M. Knapp, R. Jensen-Clem, M. Van de Loo and S. Seager: "Inflatable antenna for cubesats: Motivation for development and antenna design", in *Acta Astronautica* 91 (0), S. 322–332, 2013. DOI: 10.1016/j.actaastro.2013.06.005.
- [13]. B. Klofas, K. Leveque, "The Future of CubeSat Communications: Transitioning Away from Amateur Radio Frequencies for High-speed Downlinks", in *Proceedings of the 2012 AMSAT-NA Space Symposium and Annual Meeting*, Orlando, Florida. Retrieved on 21.07.2014 from www.klofas.com/papers/.
- [14]. L. Datashvili, H. Baier, E. Wehrle, T. Kuhn and J. Hoffmann, "Large Shell-Membrane Space Reflectors", In *proc.: 51st AIAA/ASME/ASCE/AHS/ASC Structures, Structural Dynamics, and Materials Conference*, 2010. DOI: 10.2514/6.2010-2504.
- [15]. H. Baier, L. Datashvili, Z. Gogava, E. Medzmariashvili, V. Montuori: *Building blocks of large deployable precision membrane reflectors*, In: *Proceedings of the 42nd AIAA/ASME structures, structural dynamics and materials conference*, AIAA paper no. 2001-1478, April 2001, Seattle. DOI: 10.2514/6.2001-1478.
- [16]. L. Datashvili, H. Baier, „Derivation of Different Types of Antenna Reflectors from the Principle of Highly Flexible Structures", *Proceedings of the EuCAP 2014 - The 8th European Conference on Antennas and Propagation, The Hague*, The Netherlands, 6 – 11 April, 2014
- [17]. Leri Datashvili, Nikoloz Maghaldadze, Stephan Endler, Julian Pauw, Peng He, Horst Baier, Alexander Ihle, Julian Santiago Prowald, "Advances in Mechanical Architectures of Large Precision Space Apertures", *Proceedings of the European Conference on Spacecraft Structures, Materials & Environmental Testing*, 01 – 04 April, 2014, Braunschweig, Germany
- [18]. Leri Datashvili, "Foldability of Hinged-Rod Systems Applicable to the Deployable Space Structures", *CEAS Space J* (2013) 5:157-168
- [19]. L. Datashvili, H. Baier, "Flexible Fiber Composites for Space Structures", chapter in the book *"Fiber-Reinforced Composites"*, Edited by G. Chang, pp. 605-640, ISBN: 978-1-61470-303-7 (hardcover), 2012, Nova Science Publishers, NY, USA
- [20]. L. Datashvili, H. Baier, L. da Rocha-Schmidt, "Multi-scale Analysis of Structures made of Triaxially Woven Fabric Composites with Stiff and Flexible Matrix Materials", *proceedings of the 52th AIAA/ASME/ASCE/AHS/ASC Structures, Structural Dynamics, and Materials Conference* 2011, Denver
- [21]. L. Datashvili, H. Baier, T. Kuhn, J. Hoffmann "Large Shell-Membrane Space Reflectors", *proceedings of the 51st AIAA/ASME/ASCE/AHS/ASC Structures, Structural Dynamics, and Materials Conference*, 12 - 15 Apr 2010, Orlando, Florida
- [22]. L. Datashvili, "Review and Evaluation of the Existing Designs/Technologies for Space Large Deployable Apertures", *proceedings of the International Scientific Conference "Advanced Lightweight Structures and Reflector Antennas"*, 14-16 October, 2009 Tbilisi, Georgia
- [23]. L. Datashvili, H. Baier, "Large Membrane Reflectors" *Proceedings of the 3rd European Conference on Antennas and Propagation - EuCAP 2009*, 23-27 March 2009, Berlin, Germany
- [24]. L. Datashvili, H. Baier, "Precision Deployable Shell-Membrane Antenna Reflector for Space Applications", *Proceedings of the 59th International Astronautical Congress 2008*, Glasgow, Scotland
- [25]. L. Datashvili, "Multifunctional and Dimensionally Stable Flexible Fibre Composites for Space Applications", *Journal of the International Academy of Astronautics "Acta Astronautica"*, 2009 (special issue: Glasgow)

- [26]. L. Datashvili, H. Baier, "Shell-Membrane Reflecting Surface Material for Deployable and Transformable Space Reflectors", *Proc. ESA Conf. on Antennas*, Noordwijk, Mai 2008
- [27]. L. Datashvili, H. Baier, J. Schimitschek, M. Lang, and M. Huber, "High Precision Large Deployable Space Reflector Based On Pillow-Effect-Free Technology"; AIAA-2007-2186 *Proceedings of the 48th AIAA/ASME/ASCE/AHS/ASC Structures, Structural Dynamics, and Materials Conference*, 23 - 26 Apr 2007, Honolulu, Hawaii
- [28]. L. Datashvili, M. Lang, M. Huber, H. Baier, "Accuracy Study of a Space Deployable Antenna Reflecting Surface Under 0g and 1g Conditions"; *Deutscher Luft- und Raumfahrtkongress 2006*, 06.-10.11.2006, Braunschweig, Deutschland, published in the proceedings of 2007, band III-IV
- [29]. Lin Tze Tan "Stored Strain Energy Deployable Hybrid CFRP-CFRS Reflector Antennas", *proceedings of the International Scientific Conference "Advanced Lightweight Structures and Reflector Antennas"*, 14-16 October, 2009 Tbilisi, Georgia
- [30]. Kuhn, T.; Langer, H.; Apenberg, S.; Wei, B.; Datashvili, L.: A Very Large Deployable Space Antenna Structure Based on Pantograph Tensioned Membranes. International Conference on Textile Composites and Inflatable Structures, Structural Membranes, CIMNE 2011, Barcelona, 2011

ACKNOWLEDGEMENTS

The authors acknowledge the funding of First-MOVE by the Federal Ministry of Economics and Technology, following a decision of the German Bundestag, via the German Aerospace Center (DLR) with funding grant number 50 RU 0801 and the funding of SMARD by the DLR Mobile Rocket Base (MORABA).

PRE-MANUFACTURING ESTIMATION AND POST-MANUFACTURING COMPENSATION OF INDUCED SHAPE ERRORS OF FIBER COMPOSITE STRUCTURES

Horst Baier

*Institute of Lightweight Structures (LLB), Technische Universität München, 85747 Garching,
Germany; E-mail: baier@tum.de*

ABSTRACT

High precision satellite and instrument structures inherently deviate from their nominal ideal shape during manufacturing and integration. So techniques are to be applied to compensate such deviations. Apart from metrology and actuation devices, also formal techniques to determine proper actuation strokes are discussed. Generic applications and considerations are presented for different types of instrument structures for communication as well as visible and X-ray observation.

1. INTRODUCTION AND OVERVIEW

Satellite instrument structures for opto-mechanical systems such as mirrors, lenses and optical benches as well as those for communication reflectors have to achieve and maintain precise geometrical shape. There are many reasons for possible shape and pointing deviations already on ground. In order to minimize these, appropriate error compensation techniques are to be applied after manufacturing and during integration, in addition to, proper design concepts. Even if such deviations might be anticipated e.g. via “false” mold shapes, certain scattering in properties and processes still leads to results which are difficult to anticipate. So in the following related compensation techniques are discussed based on different possible steps. A formalization of such steps leads to certain optimization problems to determine proper compensation strokes. Related approaches are discussed for generic parts as well as for different dimensionally stable components to operate from mm down to nm wavelengths. Though the basic ideas for such different types of applications are similar, the actual implementation often significantly differs e.g. for shape measurement techniques and even more so for compensation devices. In case the structure will be assembled including a series of geometrically nominally identical parts, the assembly process can be made such that it results into minimal overall geometrical errors.

Most investigations presented in this paper are taken from running technology studies for future projects, the results of which then should be considered as preliminary from work in progress.

2. THE BASIC SHAPE ERROR COMPENSATION AND SHAPE ADJUSTMENT PROCESS

2.1 Basic steps

Irrespective of the actual application, the basic principle is that as outlined in Fig. 1. From this figure the main elements of a typical adjustment process can be identified:

- a metrological system to determine the actual shape and its deviation from the nominal or goal shape
- techniques to determine proper actuation positioning and strokes which induce forced rigid and elastic body deformations which cause a minimization of residual shape errors
- actuation methods and devices to compensate for such errors in the best possible way
- introducing these compensation measures
- verification of proper compensation

2.2. Application scenarios

Typical current and future application scenarios are those outlined in Fig. 2. The smaller the wavelength, the higher the shape accuracy requirements and the smaller the expected compensation strokes.

For communication reflectors in Ka-band or higher (wavelength in the order of several mm) typically composed of CFRP sandwich and plate structures, reflecting surface shape can be measured by photo- or videogrammetry.

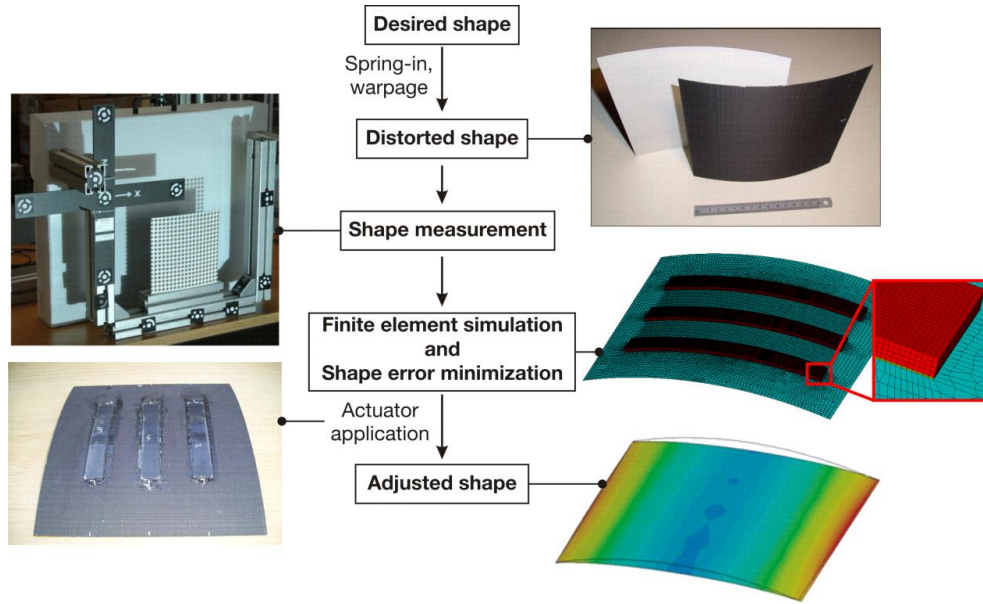


Fig. 1: the basic steps in shape adjustment

Small fine adjustment screws e.g. made out of Invar can be integrated as compensation actuators into areas outlined in Fig. 2 (a). Smooth actuation load introduction into the structure is relevant, and gets even more important for applications for still smaller wavelength and surface accuracy. This holds for future large telescope for visible or IR wavelength (μm range) based on the principle of photon sieves or Fresnel lenses generated in membrane foils of diameters of 10m and higher. Future X-ray satellites shall have effective mirror surfaces of several m^2 , to be composed of thousands of parabolic and hyperbolic mirrors of sizes typically of 200mm x 300mm x 0.5mm. These have to be highly precisely aligned into mirror carrier structures by proper bonding and adjustment techniques, with compensation strokes in the sub- μm range.

2.3 Determination of compensation strokes

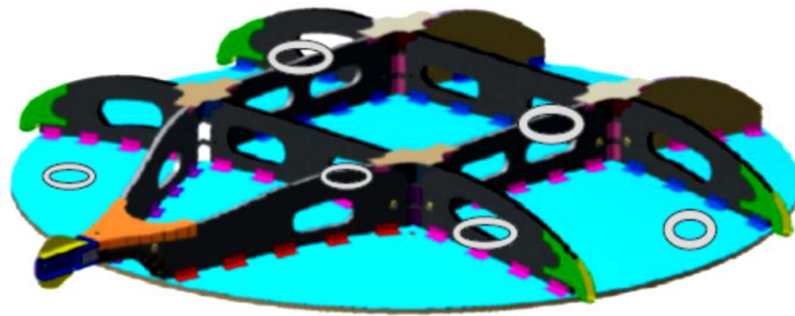
The required compensation actuation strokes can be obtained from the least squares problem

$$\text{minimize } f = \sum_i (d_i - \sum_j u_{ij} x_j)^2, i = 1, \dots, m, j = 1, \dots, n \quad (1)$$

where d_i is the shape error at reference point number i of in total m reference points. The actuation influence matrix $[U]$ with its coefficients u_{ij} is the deformation at this reference point number i out of a number m of such points due to a unit stroke at an actuator position j of in total n actuators. So the quadratic error between actual shape deviation and that induced by actuating compensations x_j is minimized. The solutions x_j then are the actual actuator or error compensation strokes to be applied. The technical meaning of x_j depends on the type of compensation device j , which can be induced displacements, forces or any other quantity. In case linear behaviour of the system under consideration, problem (1) results into a linear least squares problem which can be solved in a single step. In case of nonlinear behaviour, the influence matrix will have to be updated stepwise. The matrix $[U]$ usually is to be determined via a finite element model, and in addition or alternatively also experimentally once hardware is available. The latter is reasonable only in case of a relatively small number of actuation devices.

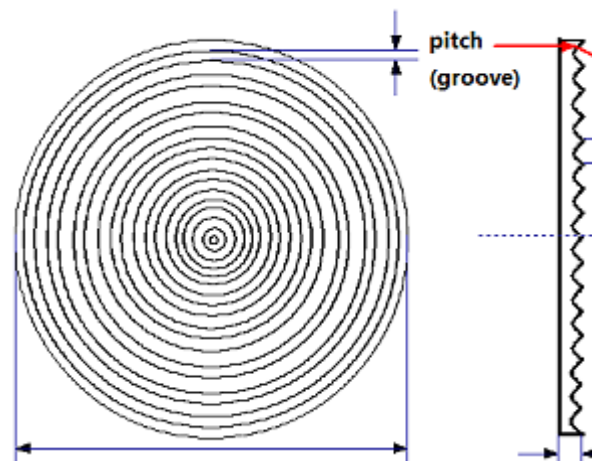
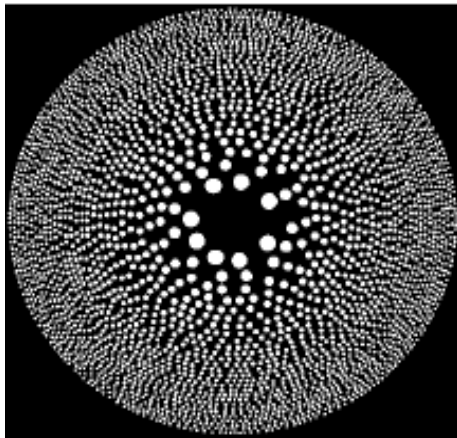
In many cases further constraints are to be considered and added to problem statement (1). For example, additional mass or volume of the compensation devices might be constrained. There might be also lower bounds x_{jl} and upper bounds x_{ju} for the allowable strokes of actuator j

$$x_{jl} < x_j < x_{ju} \quad (2)$$

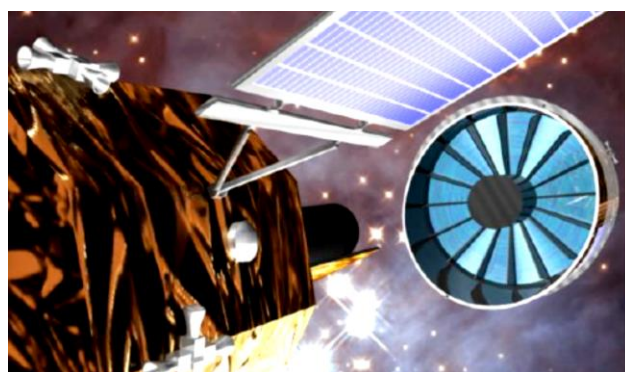
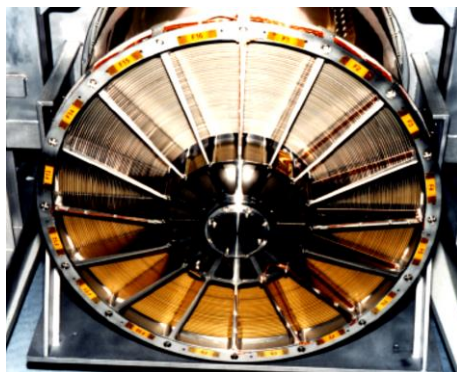


some possible compensation
actuation positions

(a) Backside of a communication reflector with possible positions for shape error compensators; operational wavelengths in the order of mm



(b) Photon sieve (left) and Fresnel membranes (right) for visible and IR wavelength (sub- μm and μm range); anticipated membrane diameter around 10-20 m



(c) X-ray mirror module (left) and formation flying focal image satellite (right), (sub)-nm wavelengths, with thousands of mirror shells

Fig. 2: Typical (future) applications for shape and alignment adjustment

Moreover, rigid body displacements of the reflector or opto-mechanical parts should be either part of the full set of displacements u_{ij} , or they can be handled separately via standard rigid body least squares problems with rigid body displacements to be determined. This results into shifts of mirror rigid body focal point. Apart from constraining, these quantities could be optimized in an alternative objective function in (1).

In case of linear behaviour with constant influence matrix u_{ij} or when updating the influence matrix in the nonlinear case, the condition values of the matrix $[U]^T[U]$ of the least squares problem gives an indication of proper or improper selection of actuator positions. Low condition number with (nearly) linear relation between columns number i and j indicate redundant actuators in these positions i and j , which generate very similar deformation shapes. So one of the related actuators could be discarded.

While for on-ground adjustment and alignment the deviation vector $\{D\}$ is that caused by manufacturing and integration errors, it could be considered to also include errors caused by disturbances in space. Then the compensation strokes are those which kind of falsely produce shapes or pointing errors which by superposition of in-orbit deviations cause an overall minimum deviation.

Determination of proper actuation position

In many practical cases possible actuating positions are determined by the applicability and availability of proper positions of such means in this specific design, as will become more obvious in the different case studies discussed further below. Besides such considerations and engineering insight, selection of proper actuation positions can be supported by applying controllability criteria as those used for shape control. Such criteria mean to check the level of parallelism of the shape deviation vector $\{D\}$ with the vector of displacements $\{U\}_j$ generated by actuator j . The more parallel these vectors are, the more efficient actuator j is to compensate $\{D\}$. So the cosine between these can be taken as a quantitative measure, where then actuators having a small cosine (say less than 0.5) could be disregarded.

2.4 Possible error sources in the compensation process

The process basically requires precisely determined (measured) deviation data and precise actuation strokes. The latter also depends on the accuracy of the influence matrix $[U]$, i.e. on the accuracy of the finite element model of the system under consideration. So the set of possible error types is

- measurement errors for $\{D\}$, which includes errors induced by the test set up (effects in boundary conditions, non-observed gravity load effects) and those arising from measurement sensors
- modeling and simulation errors, which are especially related to the determination of the influence matrix $[U]$
- compensation actuation errors and scattering caused by the actuation devices
- deviations induced in space. Within the context here this is understood as degradations primarily from the compensation devices (e.g. stress relaxation, creep)

It some cases it has been observed that the overall compensation process takes many iterations especially when the sensitivity matrix $[U]$ determined not sufficiently precise. Taking all these effects together means that in addition to the aspects discussed above, also a certain robustness in the overall process should be included in the optimization problem statement and the whole process.

2.5 Optimal allocation of parts

Often the satellite and instrument structures are composed of nominally identical elements. For example, a typical communication antenna reflector such as that of Fig. 2 (a) consists of several nominally identical elements. So it makes sense to allocate and integrate these elements in an optimal way. This could be such that the overall effective thermally induced distortion or shape derivation under critical temperature loads is minimized.

Assuming identical parts to be measured w.r.t. their individual CTE (and possibly also modulus), such parts allocation problems can be formulated as an optimal assignment problem. Due to the inherent combinatorial nature of such problems, they are difficult to solve especially under a limited number of function evaluations. Integer variables could provide a straightforward way of mathematical modelling of practical optimization problems. Though evolutionary or genetic algorithms could be applied for those type of problems, they become prohibitively computationally expensive especially for a larger number of variables or parts to be properly allocated. Several improved integer and mixed continuous-discrete variables optimization problems have been reported within the context of optimal structure design problems [11].

3. SOME SHAPE MEASUREMENT TECHNIQUES

In order to attain the relevant measurement data, optical methods have become unavoidable due to their non-intrusive approach, their high spatial resolution, their high sensitivity. Measurement accuracy including sufficient spatial and data resolution is a fundamental requirement. Apart from the measurement principle and its sensors, this also depends on the measurement setup, including parameters like properties of the surface to be measured, and also sensitivity against external disturbances like temperature variations.

Holographic interferometry is a surface measurement method with imaging. It is as sensitive as interferometry. It does not require auxiliary optics. Recent developments show that both reflective and diffuse surfaces can be measured [7]. As for interferometry, this method requires a high mechanical stability.

Videogrammetry or photogrammetry is based on triangulation and uses digital photographs as the recording medium for metrology. By taking images from at least two different locations, the so-called "lines of sight" can be developed from each camera to points on the object. These lines of sight are mathematically intersected to produce the 3-dimensional coordinates of the points of interest. Knowing the camera parameters, a linear position on the detector is translated into an angular position of the point.

In case precise (digital) cameras together with dimensional stable reference frames are used, the resolution can be in the order of $10\text{ }\mu\text{m}$ for a surface area of $1\text{m} \times 1\text{m}$. While reasonable cost of equipment and relatively straightforward handling are an advantage, the need for reflective markers to be applied at the points to be measured could be cumbersome and might be a drawback,

Deflectometry measures the detection angle of a test beam reflected by a surface. Considering a mirror or lens, this can be implemented in two ways. Either by using a single light source and a spatially extended detector or vice versa, namely an extended light source and a singular imaging detector, which is called Deflectometry.

Physical implementation of deflectometry systems uses a screen to display a sinusoidal grating pattern and an imaging camera to capture the reflection image from the surface under test. Using several phase shifted test patterns allows to precisely determine which camera pixel, and therefore line of sight, corresponds to which position on the screen. This correspondence enables the determination of the slope angle of the surface under test at which the specific camera ray is reflected, as is depicted in Fig. 3.

It is often of interest for many measurement campaigns to convert the surface slope data into spatial surface information. In general this is possible by integration of the slope data, where it is necessary to supply additional boundary conditions to the problem. This can be achieved among others by taking measurements from different known camera positions and performing a data fusion on the free integration parameters.

More details of this technique can be found e.g. in [1], with applications for X-ray mirrors discussed in [9].

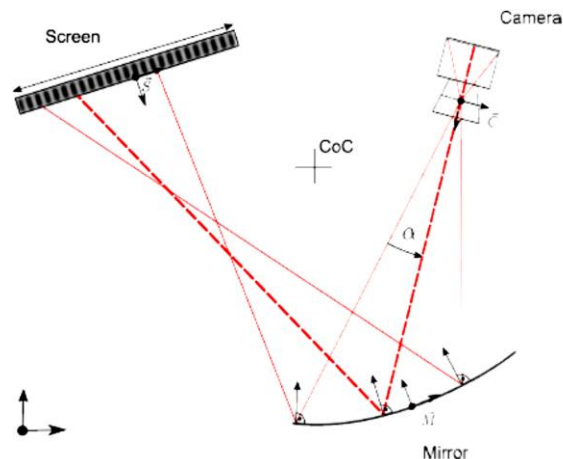


Fig. 3: A measurement setup for deflectometry

4. COMPENSATION ACTUATORS

4.1 General remarks

As mentioned above, the physical type of compensation devices very much depends on the type of application. Relevant criteria primarily are actuation precision and resolution, volume and mass, proper in-orbit behavior including compatibility with the opto-mechanical components etc. In addition, proper and smooth introduction of the actuator stroke into the opto-mechanical component is important.

For space communication reflectors, mechanical fine positioning screws might be appropriate, but sometimes also special means like shimming might be sufficient. Since also the number of strokes to be executed is relatively small and ideally is one, actuation techniques based on shape memory could be an option as well. Since shape memory polymers show a certain compatibility to high precision opto-mechanical systems, which is discussed in more detail in the following.

4.2 Shape memory polymers (SMP) as adjustment actuators

SMPs usually show a *one-way*-shape memory effect. Heating the material above its transition temperature T_{Trans} , the Young's modulus E drops down and it can be easily mechanically deformed. Cooling down the material in this mechanically constrained state, the deformation freezes in. This process is called *programming* and ends up with the programmed, temporary shape. Tension strains in the order of 50% and higher, and compression strains in the order of 30% can be easily achieved. Heating up the material above the transition temperature again, the shape recovery starts and the material returns to its original, permanent shape, see also Fig. 4, see also [2]. The physical-chemical background and further data are described by Leng and Du [4]. Trigger mechanisms other than mostly used heat are under investigation, such as the use of light of certain wavelength.

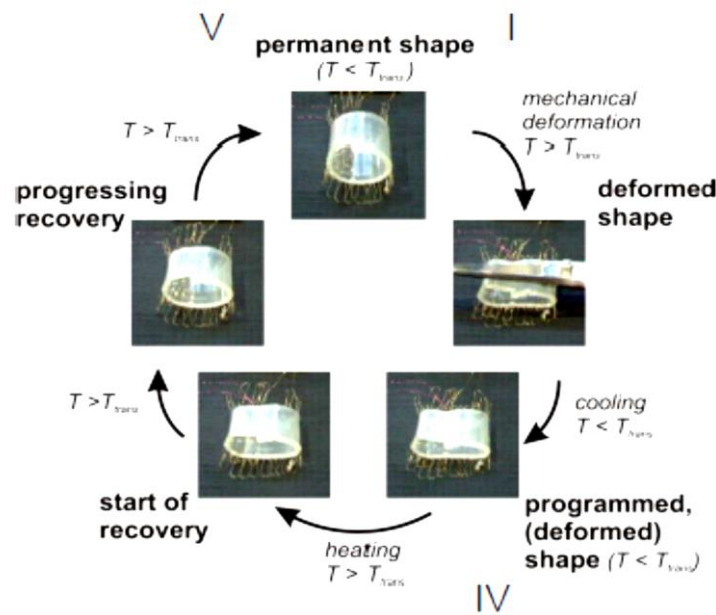


Fig. 4: Working principle of shape memory polymers (SMP)

When such SMP are attached to a component and the shape recovery mechanism I triggered, the SMP exerts forces onto this component. These forces can be used as actuation strokes, such as outlined in Fig. 5: two strips of SMP attached to a plate with an initial shape error rms of 0.46 mm can reduce this error to around 0.03 mm in that case.

The actuation force or stress induced by the SMPs is composed of the part generated when it is fully blocked together with the part considering the thermal expansion effect

$$\sigma_{act} = \sigma_{block} + \alpha * E(T) * \Delta T$$

with α being the coefficient of thermal expansion, $E(T)$ a temperature-dependent Young's modulus and ΔT being the temperature change. While the blocking stress is only based on the shape memory effect and the programming history, the actuation stress shows a relevant additional due to possibly further thermal stress [4].

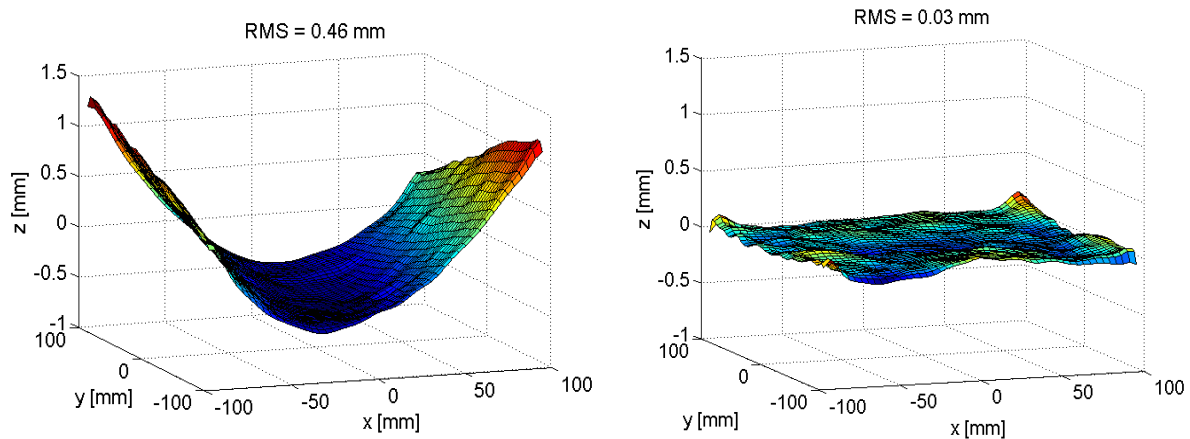


Fig. 5: Effect of two SMP shape correction actuators attached to a flat plate [3]

Some possible drawbacks or limits of SMP are:

- Though strain strokes with 50% or higher are large, force strokes are relatively low because of their low stiffness modulus
- Trigger mechanisms and especially temperatures have to fit to the application
- As for many polymers and even more so due to the special chemical composition of SMP, undesirable creep and stress/force relaxation effects are to be taken into account. This also limits possible applications to those with well controlled temperature environment around RT or lower.

5. CONSIDERATIONS FOR FUTURE APPLICATION SCENARIOS

5.1 Communication reflectors

Application of shape error compensation techniques to space communication reflectors is quite straightforward, and lends itself quite naturally to (large) mesh reflectors. The antenna reflector is composed of flexible mesh surface, cable networks, and support structures. Length adjustment mechanisms are attached to the suspension wire between the surface cable and the backup network, and the shape of the mesh surface is controlled by the adjustment mechanisms. For the purpose of effective adjustment, the matrix of influence coefficients (sensitivity matrix) of the adjustment length to the surface displacements is needed, and the matrix is usually calculated by analytical model. But some modeling errors, such as prediction error of material properties or error due to model simplification, are unavoidable in the preliminary analysis. Besides, the sensitivity matrix may change during the process of adjustment because of nonlinearity of the structure in some cases. The effectiveness of the algorithm is confirmed by numerical simulations and an experiment using a model of a large antenna reflector. Since this algorithm allows the change or modeling error of structural sensitivity, it shall also be useful for the on-board shape control of flexible reflectors.

Since compensation techniques become even more relevant and at the same time their technical implementation even more challenging for highly precise instrument structures, considerations for possible applications in future large mirror systems are briefly outlined in the following

5.2 Large telescope structures for visible wavelengths

Design drivers for future large telescopes for visible and IR wavelengths are apertures in the order of 10 to 20 m, the observation of wavelength preferably $< 10 \mu$, and the achievement of a total aerial density of $< 3 \text{ kg/m}^2$.

Since up-scaling of classical structural telescope and mirror designs is no realistic option due to high mass and difficult to achieve stowage and deployment, alternative optical together with new structural concepts are required. Some of these are so called photon sieves and Fresnel Zone Plates (FZP), which do not need those very stringent shape accuracy requirements as reflective mirrors do. On the other side, optical bandwidth is limited, and focal lengths might become quite large.

Whereas FZPs consist of concentric rings, see also Fig. 2 (b), photon sieves consist of small holes that may be just a few microns in diameter. In the order of millions and higher of these concentrically or otherwise arranged pinholes focus the image usually with quite large focal lengths. This then requires a related detector sub-satellite in quite far distance from the photon sieve, which then results into formation flying.

In *photon sieves*, global out-of-plane shape deviations for such holes can be in the order of even some mm, which also eases efforts for shape control. More stringent in-plane deviation limits especially relate to the sizes and positioning of the very high number of holes. So deviations of hole diameters should be below 10% or lower, while positioning accuracy should be better than some μm . Deviations in membrane thickness should be also very small and below the order of μm . It is obvious that a photon sieve in the 10 m range or larger with a tremendous number of different holes will pose some challenges not only for manufacturing but also in membrane behavior such as proper pre-tensioning of such extremely perforated membranes.

Manufacturing trials with laser drilling of Kapton membrane foils have shown the need of further improvement in rim geometry of the holes [5]. This could be achieved by further optimizing the required power of the laser, the hole drilling sequence, and also adjusting the thickness of the foil. The very high number and dense packaging of these holes might also cause difficulties in providing smooth and constant pre-tensioning over the whole area of the membrane. This is also shown by the analysis results given in Fig. 6: due to the massive perforation quite irregular displacement and pretension fields are generated even under nominally smooth pretension loads at the rim. Very local wrinkling due to such stress variations including generation of very local shear has to be avoided as well. Moreover, in case of quite irregular topology of the holes with no or little lines of symmetry, finite element modeling also gets quite ambitious.

Further Improvements could be obtained by modified hole drilling, and possibly also by using thicker membranes with higher in-plane stiffness, possibly together with a “carrier” membrane composed of C-fiber reinforces silicone CFRS [6]

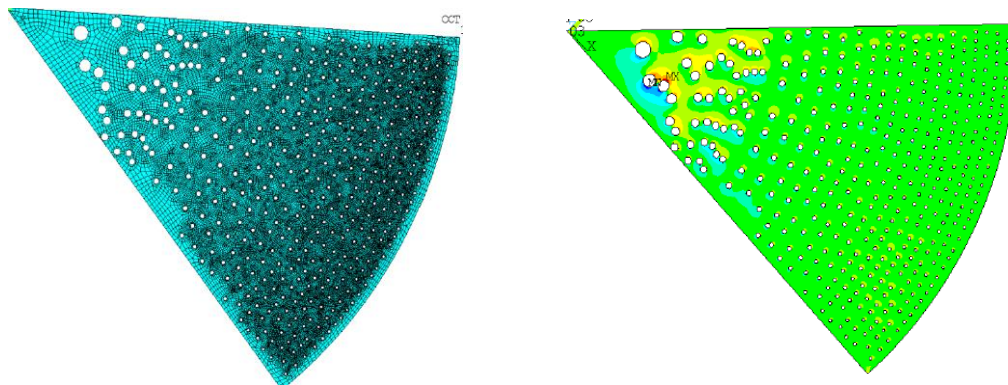


Fig. 6: Uneven strain under even pretension for photon sieve membrane with holes [5]

Fresnel membrane-plates under investigation in the MOIRE studies [7] are etched with circular concentric grooves hundreds of microns across at the center down to only 4 microns at the outside edge. The membranes are integrated into thin metal “petals” that would launch in a tightly packed configuration roughly 20 feet in diameter. Upon reaching its destination orbit, a satellite would then unfold the petals to create the full-size multi-lens optics with a diameter in the range of 20m. From GEO, it is believed, a satellite using MOIRE optics could see approximately 40 percent of the earth’s surface at once. The satellite would be able to focus on a 10 km-by-10 km area at 1-meter resolution, and provide real-time video at 1 frame per second.

To improve manufacturing accuracy, effort is under way to quantify and anticipate membrane behavior. For instance, that the photoresist-coating process consistently causes the material to stretch and sag. Understanding this effect will allow to compensate for it in the master pattern or correct for it through adaptive optics—in effect, to create a corrective lens for the telescope.

Proper tensioning of the membrane is also non-trivial, since unacceptable shape changes of the grooves are to be avoided. A thin optically transparent carrier structure with high in-plane modulus and because of low thickness low bending stiffness would allow sufficient pretension loads. The optical membrane then could be attached as a kind of coating to the tensioned carrier structure. Optically transparent glass fibers and polymers still under investigation are expected to reach a transparency of standard glass. It has to be seen whether and how much this can be further improved in order not to get too much optical losses.

5.3 Future X-Ray space mirrors

Many stellar systems omit radiation in X-ray bandwidth. Since the earth’s atmosphere absorbs these rays, several X-ray telescopes have been brought to space in the last 20-30 years. They are usually based on the principle of grazing incidence reflection by the so called Wolter optics. It consists of confocal paraboloid and hyperboloid surfaces forming a drum-like closed shell with a grazing angle of the order of 1 degree. The mirror systems will

be composed of tens of thousands of single mirror shells, as outlined in Fig. 7. Several hundreds of such mirror segments typically of the size of 20cm x 30cm x 0.05cm are integrated into a mounting structure forming a single mirror module. Up to more than hundred such modules are then mounted into an optical bench structure that supports them in correct position and alignment with respect to each other.

The shells housing structure will be made from TI because of its CTE compatible with that of the mirrors, while these housings then are to be integrated into an overall mirror structure with low effective CTE and a framework topology. Nevertheless, thermal control shall keep the temperature variation within of the whole mirror system below 1 °C and around RT.

It is obvious that alignment and integration plays a crucial role within this design not only because of the stringent precision requirements. For the mirror shells pointing accuracies in the range of arcsec and shape deviations in fractions of μm have to be reached. It is also their sheer number which generates a high challenge.

Shape accuracy deviations again have a number of different sources such as:

- gravity sag of the mirror segment during integration
- viscous forces during adhesive application
- shrinkage of the adhesive used for integration
- CTE mismatch between mirror segment, module structure and adhesive
- aging effects

Analysis has shown the adhesive itself that is used for the mirror segment integration to be a dominant error source. Typically epoxy based adhesives are used for this kind of mechanical interface because of their superior strength and good adhesion. Epoxies however exhibit cure shrinkage from a few percent down to about 0.1% for optimized low shrinkage formulations with UV-curing. Even with such a relatively low shrinkage, the glue is able to deform the mirror considerably. Fig. 8 (left) shows a deflectometry measurement result that clearly reveals increased mirror distortion in the edge region where the mirror has been bonded to the support structure. While epoxy type adhesives have about a factor of 10 higher strength than those of silicone type, shrinkage of the latter is one order of magnitude smaller. Since there has not been much systematic investigation on this effects w.r.t modular x-ray mirrors it is a central subject of the current investigations. Requirements w.r.t to the launch loads as well as the deformation during optical ground testing will probably lead to a mounting configuration with estimated 5-8 interface points.

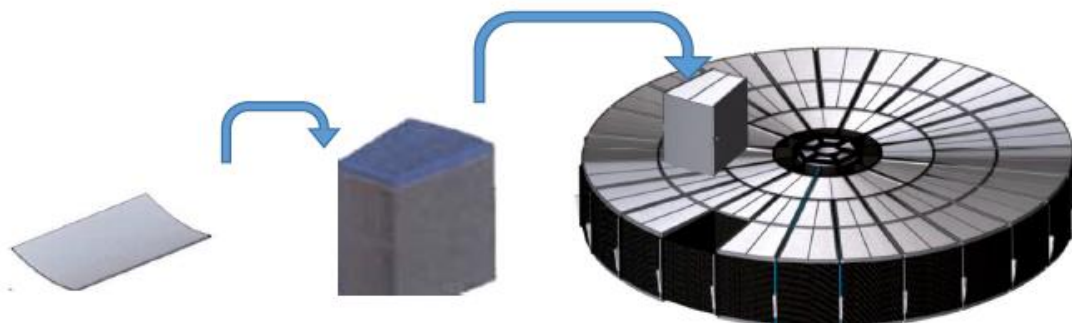


Fig. 7: Integration sequence X-ray-instrument: single mirror shell, shell housing, mirror system

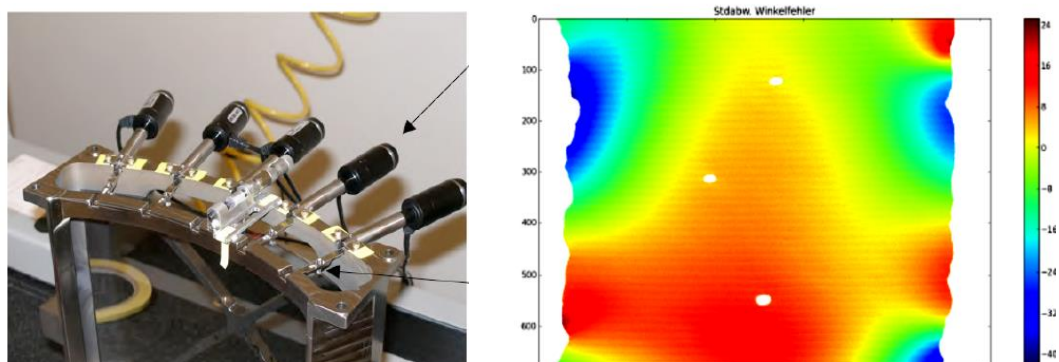


Fig. 8: Precise bonding tests (left) of mirror shell with precision adjustment actuators [10] and effects of glue shrinkage (right) with red and blue colors indicating areas of pointing errors above allowable limits

There are several possibilities to reach sufficient precision and alignment accuracy for mounting the individual mirror shells. Apart from precision slumping, most relevant is proper handling the adhesive curing, bonding and mirror integration process. So properties of the adhesives especially w.r.t. shrinkage but also possible creep and long term behavior have to be known. Small misalignment in fractions of μm to cover shrinkage effects is one option. There are passive and different levels of active means which can be considered in the gluing, joining and integration process steps. For example, high precision actuators fix the mirrors to their supporting frame until the adhesive is glued. Further compensation of shrinkage errors by (additional) compensation actuation can be considered, such as micro-devices inducing forces or forced distortion. These devices could be composed of MEMS type micro-actuators based e.g. on shape memory materials / polymers, which could possibly be triggered by light.

The mirrors might be also stiffened by ribs, which allows for integration of shape modification and control devices. Irrespective which means are chosen and possibly combined, the gluing and integration process itself will be quite complex and will have to be automated to reach good repeatability of results for that many parts to glue.

Optimal parts allocation

The optimal parts allocation problem briefly discussed above could be also considered here to improve the overall integration process. This especially holds for the truss type mirror module carrier structure a preliminary design of which is outlined in the right hand side of Fig. 7. Struts belonging to the same geometry group could be allocated into the overall topology such that thermo-elastic or other accuracy deviation effects are minimized. In addition, this process could be also applied in principle to the allocation of parabolic together with hyperbolic mirrors in the mirror segments, as well as the integration of the many mirror segments into the whole mirror system.

CONCLUSION

Adjusting shape and alignment is highly challenging part in development of high precision space structures and instruments, which requires special measurement and actuation techniques. The processes should be robust, and possible disturbance effects in space shall be kept to a minimum. Irrespective of this, proper design concepts and manufacturing processes shall keep possible deviations small from the beginning.

REFERENCES

- [1] C. Faber, E. Olesch, R. Krobot, and G. Hausler., Deflectometry challenges interferometry - the competition gets tougher. In Interferometry XVI: Techniques and Analysis. SPIE, 2012.
- [2] S. Rapp, and H. Baier, "Shape memory polymer actuator patches for shape adjustment of fiber composite parts", Proc. 19th AIAA/ASME/AHS Adaptive Structures Conference, Denver, USA, (2011)
- [3] S. Rapp, Shape Memory Polymers in Fiber Composite Structures for Shape Adjustment, Dissertation TU München, 2011
- [4] Leng, J., and Du, S., [Shape Memory Polymers and Multifunctional Composites], CRC Press, (2010)
- [5] H. Baier, L. Datashvili, S. Endler, S. Roose, Y. Stockman, G. Rodriguez, Large deployable telescopes – also for μm wavelengths ?, CEAS Space Journal, 2013
- [6] Datashvili, L. and Baier, H., Flexible fiber composites for space structures, in: George Chang (ed.), *Fiber Composite Structures*, Nova Science Publishers, Inc., USA (2011)
- [7] "First folding space telescope." Phys.Org. 6, Dec 2013.
- [8] ATHENA – Advanced Telescope for High Energy Astrophysics, SRE-PA/2011/117, Mission Review Report, ESA Publication, 28th Feb., 2012
- [9] E. Breunig, P. Friedrich, L. Proserpio, A. Winter and H. Baier, Characterization of shape accuracy during alignment and integration of thin shell mirrors for large modular X-ray optics
- [10] M. Civitani et.al., IXO X-Ray mirrors based on slumped glass segments with reinforcing ribs: optical and mechanical design, image error budget and optics unit integration process; Proc. of SPIE Vol. 7732 773242-19, 2010
- [11] Y. Zhang, H. Baier, "Optimal Parts Allocation for Structural Systems via Improved Initial Solution Generation", VII. ALIO / EURO-Workshop on Applied Combinatorial Optimization 2011, Porto, Portugal

OVERVIEW OF 3D AND PLANAR BAR LINKAGES FOR SPACE DEPLOYABLE STRUCTURES

Julian Santiago-Prowald, Rafael Bureo Dacal, Torben Henriksen

European Space Agency –ESTEC- Mechanical Department

Keplerlaan 1, 2200AG, Noordwijk, The Netherlands

Email: Julian.Santiago.Prowald@esa.int

ABSTRACT

Space deployable structures constructed with closed nR bar linkages have served as a basis for developments of deployable structures such as masts, antennas and shields. The fact that they employ in principle only revolute joints to connect the structural components, provides certain advantages as compared to other deployable structures with linear joints. The main advantages are in terms of mass, control of friction and accuracy, which can be critical for space applications. Basic building blocks that employ this concept can be classified in terms of 2D and 3D movement, as well as their number of degrees of freedom and mobility. In particular, it can be noted that many of these bar linkages are overconstrained according to Grübler-Kutzbach criterion, but still exhibit mobility one.

A non-exhaustive review of known overconstrained spatial nR linkage mechanisms is performed, starting with the first mechanism of this type identified by Sarrus in 1853 and Bennett's skew isogram. Several of these constructions are presented succinctly, in particular Sarrus and Bennett linkages, Goldberg 5R, Myard and Bricard loops, as well as examples of realisation. The common characteristic of being overconstrained offers interesting benefit in terms of stiffness, load capacity and synchronisation, although for space applications this is not always a plus. Considering thermo-elastic stability and mass and volume limits, overconstraining can represent loss of mass optimisation, excessive envelope and risk of failure due to jamming during deployment. Other 3D deployable structures such as foldable tetrahedra and hexahedra are shown and discussed.

Planar families of linkages are presented and compared to well-known ones, mainly the pantographic elements. These have been employed in existing hardware of space antennas, including recent developments within ESA activities. Their characteristics in terms of degrees of freedom and complexity are summarised for the application. Some of them are pre-selected for the possible construction of scalable and modular deployable structures, mainly antenna reflectors and deployable booms.

1. INTRODUCTION

The classification of bar-linkage mechanisms employed for the construction of large deployable space structures can be established in terms of several criteria: the types of joints between bars, the topology of the chain (open or closed), radial and peripheral architecture, the kinematic nature (i.e. number of degrees of freedom and possible trajectories), the actuation and control principle, and many other. These classifications are found in academic works as predominant aspects, giving often secondary relevance to other aspects that are more important from the point of view of the users. It is hence not the purpose of this paper to establish a thorough classification of structural mechanisms, but to address characteristics that determine the behaviour of a deployable structure during deployment and in the deployed state, i.e. stiffness, mass, stowage volume and reliability of deployment. Obviously the fundamental concepts have to be understood prior to designing and selecting an architecture, as well as specific details concerning actuation (based on springs or integrated elastic actuation, electrical motors, inflatable devices), especially when there is influence in the mentioned performances.

In section 2 closed chains of three-dimensional bar linkages with revolute joints are studied. Three-dimensional is understood in this context as the non-planarity of the trajectories of all members in a unit cell. The fact that the members are connected in closed chain poses additional considerations in terms of kinematical compatibility, stiffness and accuracy. Open chains are not discussed in this paper as they are well known and do not introduce conceptual difficulty. In section 3 planar linkages are briefly presented and two particular configurations are compared in terms of their kinematical behaviour, mobility and implementation in recent deployable antenna developments.

The conclusions of this paper are necessarily an open question since developments are still ongoing and each of the presented options may have application in different cases.

2. OVERVIEW OF 3-D BAR-LINKAGES FOR SPACE DEPLOYABLE STRUCTURES

Closed-chain linkages represent a particular group of deployable structures with interesting characteristics and applications such as space antennas and masts. In this section the 3 dimensional case is treated. One of the characteristics is their kinematic nature, due to the periodicities and the closure constraint. Within this family, overconstrained spatial nR bar-linkage mechanisms (closed chains linked exclusively by revolute joints with $n \geq 4$) represent a particular type of closed-chain mechanisms. These linkages have deserved special attention since the identification of the first mechanism of this type by Sarrus in 1853 [1], a single-mobility $6R$ bar-linkage with rectilinear movement. See Fig. 1.



Fig. 1. Sarrus $6R$ bar linkage, schematic (left) and wooden model built by Bennett in Cambridge (right).

An example of space application of the Sarrus loop within a longitudinal deployable structure can be identified in the Foldable Articulated Square Truss (FAST) mast, used for the deployment of the solar arrays on the International Space Station [2]. The actuation is provided by flexible glass-fibre bows that deploy each bay and tension the diagonal cables.

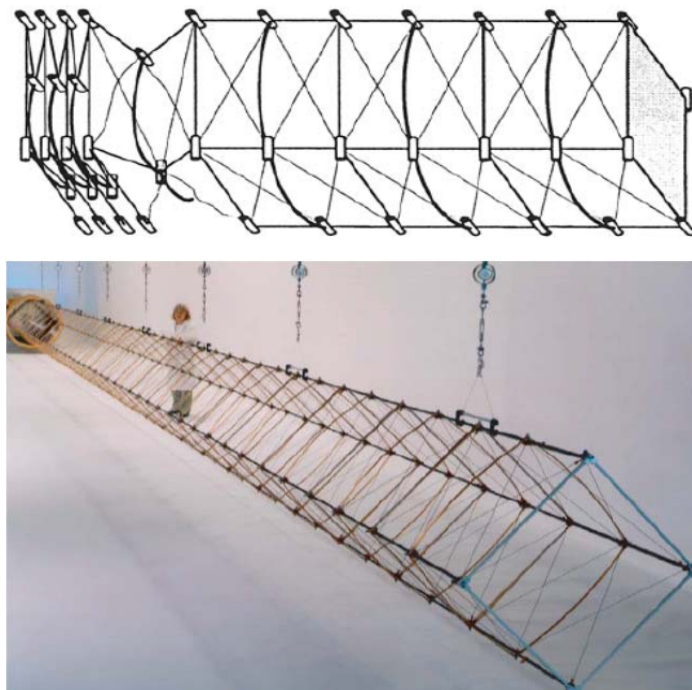


Fig. 2. FAST mast sketch and photo (from ref. [2]).

Recent developments in deployable antenna structures based on overconstrained 3D linkages have been carried out using the Sarrus loop as a building block [3]. The alternative constructions explored by the authors include a Sarrus 6-bar linkage as the facets of a peripheral ring, although the final design is a hybrid Sarrus loop in which one of the linkages is replaced by a pantograph scissor pair, therefore no longer based on revolute joints only. This architecture is also overconstrained, even more than the pure Sarrus. A fixed-angle conical ring is considered for exploiting the stiffening effect provided as compared to a cylindrical ring. Given this kinematical design, the packaging ratio is somewhat constrained by the fixed angles. Nevertheless, the concept has been developed and demonstrated on ground showing reliable deployment performances. More work would be needed to increase the stiffness and tension-bearing capacity of the ring.

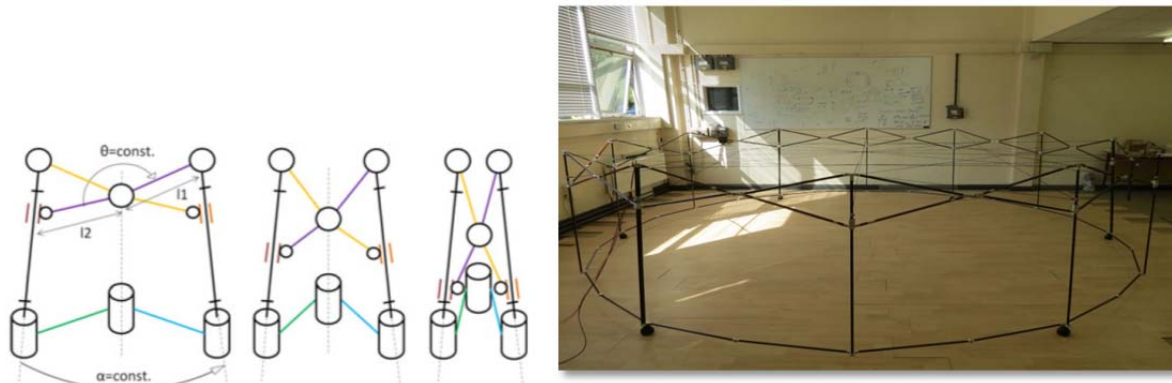


Fig. 3. Hybrid Sarrus-pantograph cell employed in a circular ring (courtesy of ABSL and OSS).

The overconstrained nature of Sarrus' and other linkage mechanisms with respect to Grübler-Kutzbach's criterion can be considered a consequence of particular geometries in the kinematic chains comprising a number of links, reflecting redundancy of some of the constraints. Otherwise said, the mobility criterion is not a necessary condition for a desmodromic mechanism. According to the mobility criterion applied to 3D bar-linkages with revolute joints, the minimum number of bars for single mobility is seven. This can be easily derived by counting degrees of freedom of the links and discounting the single constraints imposed by the rotational pairs. For open chains of n links and p revolute joints, the mobility is simply $m = 6(n-1) - 5p$. In the case of closed chains $p = n$ and hence $m = n - 6$. In the planar case the equation reduces to $m = n - 3$, which means that the minimum number of bars for single mobility is 4, i.e. the hinged planar quadrilateral has single mobility, as known. If a planar linkage is analysed as 3D, the discrepancy between the planar and the spatial mobility results is due to the redundancy of some restrictions, in particular the parallelism of the rotation axes. In the case an external perturbation would alter the alignment of any of the axes, the mobility would be lost. This is the risk implicit in overconstrained mechanisms. In addition, the discrepancy between the planar and the spatial behaviour does not happen in open chains.

Bennett published in his paper of 1903 his skew isogram [4], four bars joined by revolute joints (4R) in a non-planar linkage, as sketched in Fig. 4. This mechanism has been subject of a large number of studies since then, focussing mainly in his interesting kinematical properties. Very specific conditions apply to the geometrical relations of lengths and angles that result in single mobility in the non-planar mechanism [4,5]. In the case any of these constraints ceases to hold due to external perturbations the mechanism would block. Among many properties, it has been proven that the Bennett linkage is the only 4R spatial linkage with revolute joints, exhibiting mobility one.

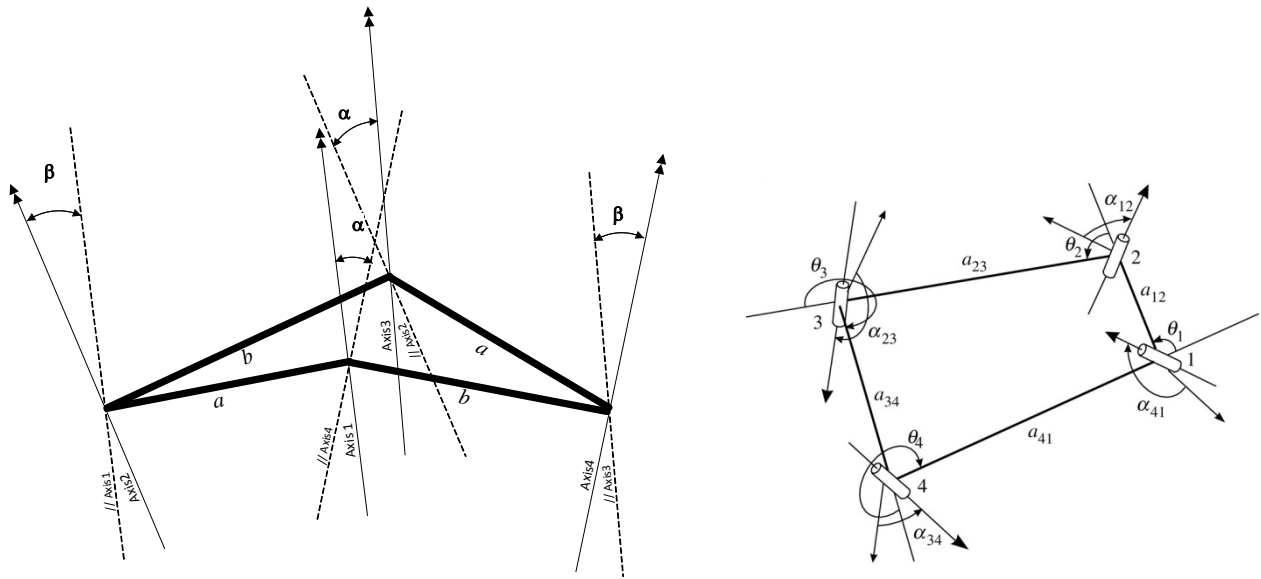


Fig. 4. Bennett's skew isogram, showing some of the relations between angles and lengths necessary for achieving mobility in the case of rectangular deployed shape (left). General notation (right, from ref. [5]).

The apparent conundrum between mobility and degree-of-freedom count has spurred the discovery of complex linkages with single mobility. A systematic review of spatial overconstrained linkages with historical background has been published by Chen and You [6], following the publications of Baker [7]. It has been noted that there is a limited number of known possibilities for spatial 4R, 5R and 6R linkages. So far, Bennett's loop is the only spatial 4R mechanism known and in addition, it serves as basis for higher order chains.

Spatial five-bar linkages with revolute joints are mainly the Goldberg 5R and Myard linkages. Goldberg 5R linkages can be in fact obtained by combining Bennett linkages either by summation or subtraction.

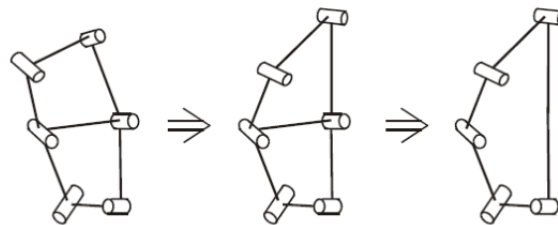


Fig. 5. Sketch for summation of Bennett's linkages generating a Goldberg 5R linkage (from ref. [5]).

Alternatively, Bennett linkages can be assembled forming a network, as shown by Chen and You [6]. The usefulness of these constructions for space structures is however unclear, since they rely on very specific kinematical constraints that result in non-optimal deployed trusses in terms of mass, stiffness, in addition to the mentioned packaging ratio and deployment reliability concerns. The packaging ratio concern is a consequence of the large number of revolute joints required, which are located in non-optimal positions for the stowed package.

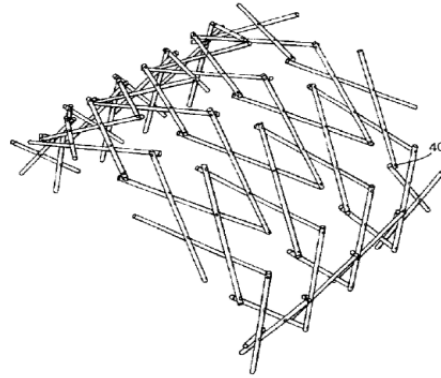


Fig. 6. Network of Bennett's linkages forming a curved deployed surface (from ref. [8]).

Myard [9] produced the first known overconstrained 5R linkage, which exhibits plane-symmetry. A particular combination of Myard linkages has been recently integrated into a deployable antenna structure [10], showing that a spatial network can be obtained starting with the combination of three Myard loops in a cell. The overall structure made of such cells has single mobility. Other combinations of Myard linkages allow building hexagonal constructions among other possibilities. The concept has been subject to optimisation of mass and stiffness, resulting in a more attractive solution than the combination of Bennett's linkages.

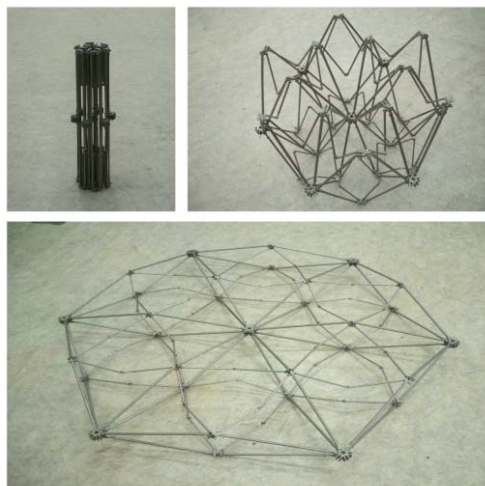


Fig. 7. Prototype of the large deployable mechanism based on Myard linkages (from ref. [10]).

In general, 6R linkages are more common and hence several types have been synthesised over the years, starting with Sarrus'. Among the 6R linkages are the well-known Bricard loops, which can be classified in six variants. One of them results in a planar regular hexagon when deployed [5,7,11]. It should be noted that in some cases these linkages are subject to bifurcations in their trajectories and may then experience blockage.

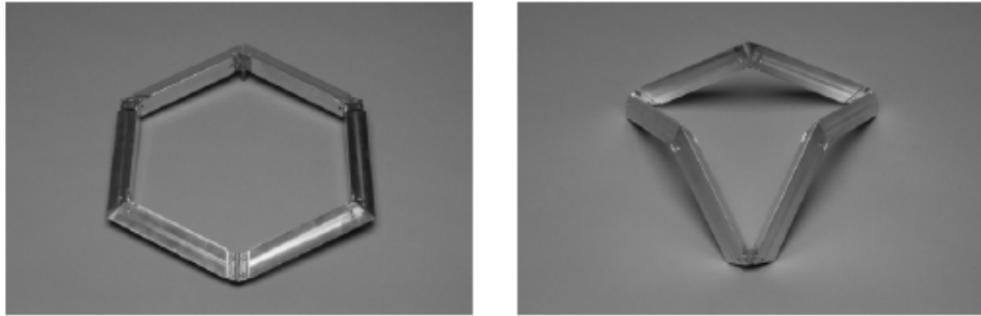


Fig. 8. Model of Bricard loop (from ref. [5]).

There are more 6R overconstrained bar-linkages identified, although despite their mathematical elegance, they rarely result in useful deployable structures for space applications. In general it can be concluded that the Bennett and Bricard loops are the basic building blocks for most of the practical solutions and higher-order overconstrained linkages.

The number of linkages can be increased while keeping the condition of mobility one, for the construction of peripheral rings of deployable structures, arms or modules. A nice example of this can be traced back to the work of Hedgepeth and others in the 70s, materialised in several known antenna structures, such as the hoop-column. Nevertheless, the principle of choosing specific geometrical relations to achieve single mobility while overconstraining has not been always kept. An example of this is Harris Corporation hoop truss construction [12]. As a consequence of the large number of members and potential effect of their compliance and misalignment of rotation axes, overconstraining by introducing the concepts previously summarised, may result in a large complexity. Therefore, the movement has to be produced and controlled by several actuators wisely located or by propagation of the movement with synchronisation devices. In the case of the hoop truss structure, the ring does not obey the rules of nR overconstrained linkages, and hence the synchronisation has been implemented by other methods.

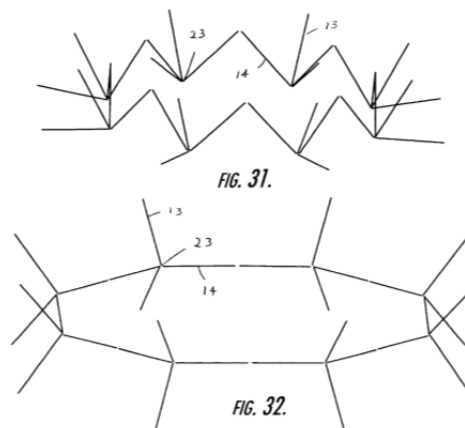


Fig. 9. Deployment of Hoop truss antenna (from ref. [12]).

The positive feature offered by overconstrained structural mechanisms is that, if well controlled, provides self-synchronisation, additional load paths and sometimes improved stiffness. These are important benefits. However, these features have to be well controlled in applications where mass, thermo-elastic stability and reliability are the design drivers. Overconstraining could lead to blockage during the deployment process or to unwanted thermo-elastic distortions when deployed in a space environment. For those reasons desmodromic mechanisms and isostatic structures are typically preferred by designers.

Looking back, the spatial mechanisms with single mobility discussed so far are different from most of the modular structures made by combination of deployable tetrahedra, prisms or hexahedra employed in space deployable antennas.

Several examples of these are well known, such as the 5 m deployable truss, consisting of tetrahedra linked in an hexagonal assembly, developed by Surrey University [13,14] with the support of British Aerospace. This particular arrangement of tetrahedra does not result in an efficient stowed assembly, but alternative configurations of tetrahedral have been found which solve this problem.

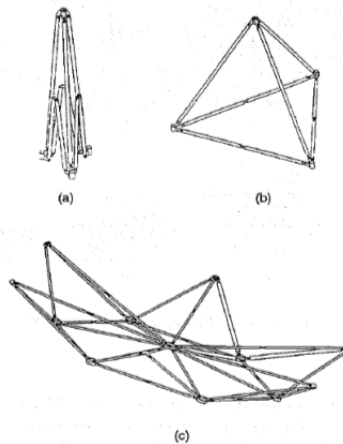


Fig. 10. Deployable tetrahedra truss [13,14].

There are however other issues that appear with the tetrahedra themselves and their combinations. The mobility depends largely on the way the struts are linked by revolute or other joints. If only revolute joints are considered, the system is overconstrained according to the mobility criterion, although it can be shown that a deployable tetrahedron is possible as shown in Fig 10 by implementing sufficient connecting elements. In this case, synchronization devices are necessary if mobility one is the target.

Another example of 3D truss is the ERA 9 m antenna (Fig. 11) developed by Aerospatiale in the 80s, now Airbus DS. It is based on a truss of deployable triangular prism cells. It was flown in 1988 on the MIR station. The deployment of each cell involves the transformation of facets of 12 articulated links (6 struts in a V-folding parallelogram and another 6 articulated rods in the diagonals). Even if the truss was tested and flown on-board the MIR station, the flexibility of the concept for adapting to mission parameters and requirements of large antennas was questioned.

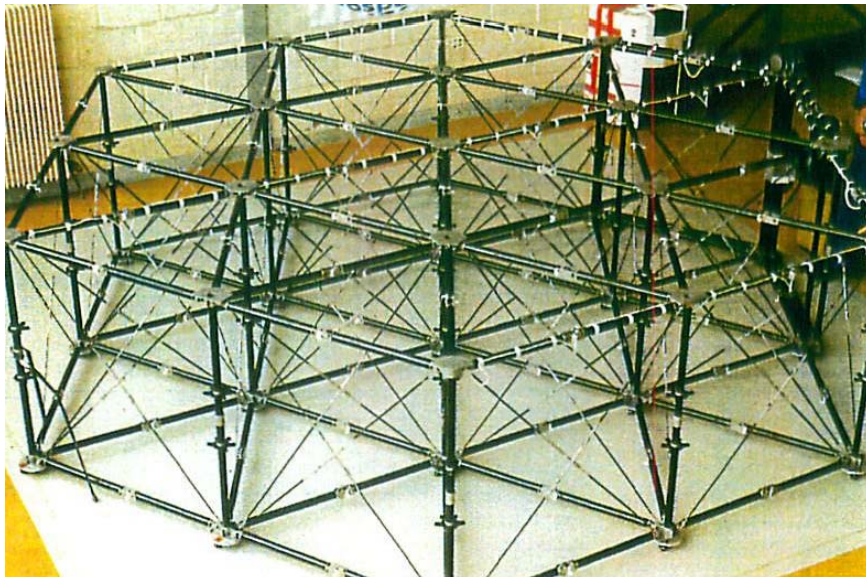


Fig. 11. Structure deployment test of ERA 9 m antenna (Courtesy of Airbus DS).

All the spatial constructions shown require a careful analysis of the degrees of freedom and trajectories for understanding their kinematics during deployment. Very often actuation during deployment and stability in deployed configuration are constrained by the design. This can lead to possible singularities, loss of control or excessive thermal distortions when deployed. These analyses can be particularly complex considering the actuation principle, the number of members and the complexity of the joints. It is in any case clear that the possible loss of alignment of joints (and hence fulfilment of geometrical relationships) can lead to deployment failure.

3. PLANAR BAR-LINKAGES FOR SPACE DEPLOYABLE STRUCTURES

Planar bar linkages have been the work-horse of most large deployable structures, inserted as elements of radial arms, peripheral rings or in modules. Due to the large number of developments it is not the intention to review all of them in this paper. The reader is referred to the classic book of E. Medzmariashvili [15] and the recent review paper [16]. In this chapter the main objective is to compare the behaviour of the single pantograph and the V-folding quadrilateral (in particular the trapezoidal shape).

The unit cells presented in Fig. 12 are the pantograph concept (a variant of four-bar linkage) and the 6-bar linkage with folding bars, showing the different types of joints. The pantograph has cylindrical pairs in addition to revolute joints. By applying Grübler's criterion, the pantograph has mobility -2 in 3D, while it has obviously mobility 1 as a 2D shape. This is a consequence of the parallelism of the rotational axes of the revolute joints, which could be used to reduce constraints by replacing revolute joints by less restrictive ones such as spherical joints. This is however not the case in practice [17].

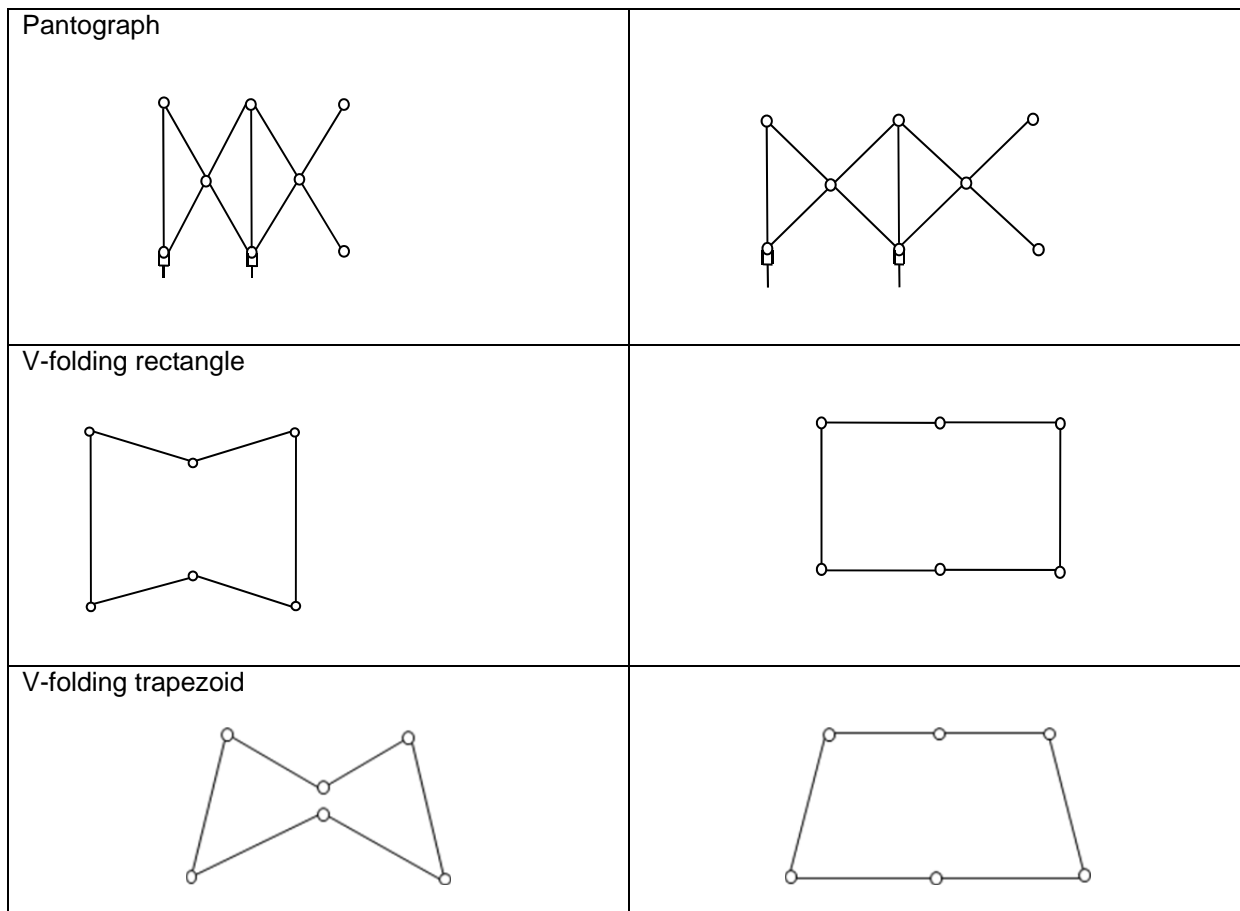


Fig. 12. Sketches representing the unit cells of ring lateral facets.

The V-folding 6-bar linkage has mobility 0 in 3D and mobility 3 in 2D. This higher degree of mobility as compared to the pantograph means that, in order to control the movement during transformation from folded to deployed state, two additional constraints need to be applied if mobility 1 is sought for the planar linkage. This can be achieved by implementing two conditions: 1. Fixation of the angles of the non-folding struts as a first step after release and 2. Synchronisation of neighboring cells in the ring [18]. This methodology has been implemented in the demonstrator constructed by GTU for the development of ESA Patent 568. In particular, the movement of each of the two rings of V-folding bars is synchronized from cell to cell, independently in the two rings. Therefore, there is not a full restriction of the degrees of freedom leading to mobility 1, although very close to it. In the absence of gravity, the synchronization of the rings individually would be sufficient, but not on ground during deployment testing. It has been necessary to introduce a controlled release of the V-folds with an additional release cable. This would not be necessary if electric actuators were used in the folds.

Fig. 13 shows the two 6-m rings constructed in the TALDES study, one for the double pantograph and the other one for the conical ring with folding bars. Both exhibit similar performances in terms of mass and stiffness, although different kinematical behavior, despite having single mobility.



Fig. 13. Deployment test of the 6 m double pantograph ring demonstrator of TUM (Photo ESA/A. Le Floch) and the 6 m conical ring of GTU (photo GTU). Both developed under ESA contract.

4. CONCLUSIONS

Spatial and planar deployable structures have been presented and analysed focusing on the kinematical properties. The overconstrained nature of some of the mechanisms while retaining single mobility can be seen as an inherent advantage from the point of view of stiffness and self-synchronisation. However, given the specific nature of the constraints that maintain the subtle balance of kinematical degrees of freedom, this could result in blockage during deployment or loss of stability under thermal environment. It has been postulated that a relaxation of the mobility 1 condition could provide an increased robustness during deployment in the presence of disturbances. This has been demonstrated with on-ground deployments of a V-folding 6-bar linkage integrated into a peripheral conical ring structure.

5. REFERENCES

- [1] Sarrus, P.F.: Note sur la transformation des mouvements rectilignes alternatifs, en mouvements circulaires et reciproquements. Acad. Sci. **36**, 1036–1038 (1853).
- [2] Pellegrino, S. (ed.). Deployable Structures in Engineering, in Deployable Structures, CISM Courses and Lectures N. 412, International Center for Mechanical Sciences, Springer, 2001.
- [3] V. Fraux, M. Lawton, J. R. Reveles and Z. You, Novel Large Deployable Antenna Backing Structure Concepts for Foldable Reflectors, CEAS Space Journal (2013) Vol. 5, issue 3-4, pages 195-201.
- [4] Bennett, G.T.: A New Mechanism. Engineering 76, 777–778 (1903).
- [5] Chen, Y., Design of Structural Mechanisms, Ph. D. Thesis dissertation, University of Oxford, 2003.

- [6] Chen Y. & You, Z., Spatial Overconstrained Linkages – The Lost Jade, in Explorations in the History of Machines and Mechanisms, Proceedings of HMM2012 History of Mechanism and Machine Science, Koetsier, Teun; Ceccarelli, Marco (Eds.), Springer Verlag, Volume 15, 2012, pp 535-550.
- [7] Baker, E. J. (1979), The Bennett, Goldberg and Myard Linkages – In Perspective, Mechanism and Machine Theory, Vol. 14, 239-253.
- [8] Chen Y., and You Z., US Patent US6941704B2, Deployable Structure, Sept. 2005.
- [9] Myard, F.E.: Contribution à la géométrie des systèmes articulés. Société Mathématique de France 59, 183–210 (1931).
- [10] Qi, X., Li, B., Deng, Z., Liu, R., Guo, H.: Design and optimization of large deployable mechanism constructed by Myard Linkages. CEAS Space Journal (2013) Vol. 5, issue 3-4.
- [11] Gan, W and Pellegrino, S (2003), Closed-loop deployable structures, AIAA 2003-1450
- [12] Harless, R., Lightweight compactly Deployable Support Structure, US Patent US6313811B1, Nov. 2001.
- [13] Fanning, P. and Hollaway, L., The Modal Analysis of a Unit Building Block for a 5 metre Deployable Antenna for Space Applications, in Proceedings of the 4th International Conference on Space structures, Vol. 1, pp. 432-441, 1993. Space Structures 4, Surrey, UK.
- [14] You, Z., Deployable Structures for Masts and Reflector Antennas, Ph. D. Thesis dissertation, University of Cambridge, 1994.
- [15] Medzmariashvili, E.: Transformable Space and Ground Constructions. Valemar S&T Ltd–Gregory & Co., Georgia (1995). (in Russian).
- [16] Santiago-Prowald, J. and Baier, H., Advances in Deployable Structures and Surfaces for Large Apertures in Space. CEAS Space Journal (2013) Vol. 5, issue 3-4, pp. 89-115.
- [17] Datashvili, L., Endler, S., Baier, H., Langer, H., Friemel, M. Tsignadze, N., Santiago-Prowald, J., Study of Mechanical Architectures of Large Deployable Space Antenna Apertures: From Design to Tests, Large Deployable Antenna Workshop, 2-3 October 2012, ESA-ESTEC, Noordwijk, The Netherlands.
- [18] Medzmariashvili, N., Medzmariashvili, E., Tsignadze, N., Tusishvili, O., Santiago-Prowald, J., Mangenot, C., Baier, H., Scialino, L., Philipenko, L., Possible Options for Jointly Deploying a Ring Provided with V-Fold Bars and a Flexible Pre-Stressed Center, Large Deployable Antenna Workshop, 2-3 October 2012, ESA-ESTEC, Noordwijk, The Netherlands.

ACKNOWLEDGEMENTS

The authors wish to thank L. Datashvili, E. Mezmarishvili, N. Tsignadze, S. Tserodze (and both teams at TUM and GTU), M. Lawton (and all the team in ABSL) as well as L. Scialino, M. Such and G. Rodrigues for their major contributions in the developments of the pantograph and conical ring structures.

CONCEPTUAL DESIGN OF DEPLOYABLE COMPOSITE REFLECTOR OF AN X-BAND SATELLITE PAYLOAD

Omer Soykasap⁽¹⁾, Sukru Karakaya⁽²⁾, Ahmet Gayretli⁽³⁾, Yelda Akcin⁽⁴⁾

⁽¹⁾*Afyon Kocatepe University, Department of Material Science and Engineering,
ANS Campus, 03200, Afyonkarahisar, Turkey,
Email: soykasap@aku.edu.tr*

⁽²⁾*Afyon Kocatepe University, Department of Mechanical Engineering,
ANS Campus, 03200, Afyonkarahisar, Turkey,
Email: skarakaya@aku.edu.tr*

⁽³⁾*Afyon Kocatepe University, Department of Mechatronics Engineering,
ANS Campus, 03200, Afyonkarahisar, Turkey,
Email: agayretli@aku.edu.tr*

⁽⁴⁾*Afyon Kocatepe University, Department of Metallurgical and Materials Engineering,
ANS Campus, 03200, Afyonkarahisar, Turkey,
Email: yeldaakcin@aku.edu.tr*

ABSTRACT

Conceptual design of a deployable composite reflector which will be used as an X-band payload is being developed Afyon Kocatepe University (AKU). For this purpose, deployable composite reflectors which are either already developed or being developed for different missions in the literature, including solid surface reflectors, flexible shell reflectors, membrane reflectors are considered as potential candidates. The reflectors are evaluated using several aspects of design as follows: geometry, mechanical and RF performance, manufacturing, technological maturity, surface precision, cost etc. The winning concepts in each group are selected for further study as follows (i) Solid Surface Deployable Reflector, ACERAD, CTD, (ii) Membrane surface reflector, CTD, (iii) Shell surface reflector of AKU. The reflectors are scaled, and redesigned for a baseline reflector of diameter of $D=3\text{m}$, and $F/D=0.6$ to be used for SAR mission. Finite element analyses show that the membrane surface and shell surface reflectors has the most potential with lower areal mass and sufficient stiffness.

1. INTRODUCTION

Deployable composite reflectors have been developed for spaceborne antennas due to their light weight, high thermal stability, and high surface accuracy [1]. In order to reduce launch cost and structural mass, compactly folding and self-deployment of the reflector is preferred. Conceptual design of a deployable composite reflector of an X-band payload is being developed at AKU. For this purpose, deployable composite reflectors including solid surface reflectors, flexible shell reflectors, membrane reflectors are considered as potential candidates. Deployable composite reflectors studied in this paper can be divided into three major groups: solid surface reflectors, flexible shell reflectors, membrane reflectors. There are several designs in each group, which are either already developed or being developed for different missions in the literature. The several concepts of the past and recent reflectors are evaluated for SAR mission in this paper. First, the concepts of solid surface reflectors are considered as follows: (i) large aperture, solid surface deployable reflector by CTD [2], (ii) sunflower reflector TRW [3], (iii) Daisy, MEA, MEA, DASA-Dornier (now Astrium) [4], (iv) Solid surface deployable antenna SSDA, DSL [5], (v) Solid surface reflector XM1 XM2, Hughes [6], and (vi) Foldable tips reflector, Alenia Spacio [7]. Next, the concepts of membrane surface reflectors are considered as follows: (i) Large SAR membrane antennas with lightweight deployable booms [8], (ii) Large and precision deployable membrane reflector, SMART [9], (iii) Huge Deployable Antenna Structure for space mission [10], (iv) Precipitation radar antenna [11], (v) Ultra rapid deployable antenna (URDA) [12], (vi) CRTS, ESTEC/Cambridge University [13], (vii) Deployable

reflector for small satellite, CTD [14]. Finally, flexible shell surface concepts are considered as follows (i) shell surface reflector of CTD [15], (ii) Springback reflector of Cambridge University [16], (iii) Parabolic cylindrical SAR reflector of Cambridge University [17], (iv) Thin shell slit reflector [18], (v) Astrium's thin shell reflector [19], (vi) Large tape spring reflector [20], (vii) Springback reflector of Afyon Kocatepe University (AKU) [21].

The reflectors are evaluated using several aspects of design as follows: geometry, mechanical and RF performance, manufacturing, technological maturity, surface precision, cost etc. The winning concepts in each group are selected for further study. They are scaled, and redesigned for a baseline reflector of diameter of 3m, and F/D=0.6 to be used for SAR mission.

2. REFLECTOR CONCEPTS AND EVALUATION

2.1. Thermal, Structural and Environmental Requirements

Although there are several requirements of the reflector for thermal, structural and environmental aspects, which should be considered in three groups: prelaunch, launch, and orbit. For a conceptual and preliminary study, the main requirements of the reflector being developed are summarized for X-band mission as given Table 1.

Table 1. Thermal, structural and environmental requirements.

Reflector Diameter	2-3 m
Packaged volume	1m diameter and 3 m long
Mass	≤ 12 kg
Ability of folding and deployment	available
Natural frequency during launch in folded reflector	≥ 25 Hz
Vibration and acoustic loads during launch (sine loading with varying frequency and 144 dB)	No material failure
Absolute temperature in orbit (-180°C; +110°C) and a gradient of 100°C along aperture.	RMS error ≤ 0.600 mm
High deployed stiffness/mass ratio	Areal density ≤ 1.5 kg/m ² and natural frequency ≥ 1 Hz

2.2. Concept Evaluations

Main concept evaluation criteria include several aspects of design as follows: geometry, surface accuracy, mechanical and RF performance, technological maturity, cost. On the other hand, secondary aspects of design such as satellite interface, launch and orbital loadings, interference during deployment and operation are not considered at this stage, which could be considered in a later design phase. The geometry criteria include the diameter, type of the reflector (central or offset), reflector rim (circular or elliptical), packaged volume (diameter and length). The reflector must meet all geometrical criteria. Offset type, larger diameter is preferred for electromagnetic performance. The diameter is the most critical one that should be determined first: 2-3 m diameter is considered in this study. Packaged volume depends on the launch vehicle to be used, but smaller volume is preferred in order to reduce the launch cost. Hence the cylindrical volume of a diameter of 1m and a length of 3 m is considered. The surface RMS error must be coherent with the frequency band used. The RMS error is about $\lambda/50$, where λ is the wavelength. Therefore 0.6 mm RMS accuracy for an X-band ($\lambda=0.31$ mm and 9.65 GHz) is required.

The mechanical design criteria include areal density, number of parts, deployment robustness under environmental conditions, design flexibility, strength against micrometeoroids. Areal density and the number of parts should be less as much as possible in order to reduce the manufacturing cost. A maximum of 1.5 kg/m² is chosen for the areal density, which limits the use of most solid surface reflectors. Reflector is folded during launch, but it must be ensured that it reliably deploys in space. Design flexibility to a larger size of the concept can be adapted if possible for different applications and it is important that it has the development potential. The material resistance against micrometeoroids in space limits the use of membrane-surface reflectors. On the other hand, rigidity and strength against dynamic as well as acoustic loads during launch and dynamic load of orbit must be provided. These criteria must be satisfied for all the reflectors, hence are not assessed.

In terms of RF performance, PIM (passive intermodulation) and losses are taken into account. Reflecting losses do not create problems for solid surface and shell surfaces, although losses in the membrane surface can be significant and the surface must be coated with a thin metal layer such as aluminium vapour deposition method. PIM causes losses and unwanted frequencies by interference with a mixture of two or more of the signals. Surface cracks, oxidation, pollution, ferromagnetic materials along RF path or near may change the electrical and magnetic properties of the material that causes PIM. Hence they should be avoided. A certain gap between the neighbouring panels should be created or isolation must be provided between the panels if the reflector surface is not monolithic.

In terms of technological maturity of the concept, there are various technology readiness levels from conceptual design and analysis, detail design, prototype produced to prove the concept on earth, and space mission as the final stage. The concepts served in the space are preferred; however, new concepts being developed need technological maturity. Cost is one of the most important criteria. For this reason, lifetime cycle costs (raw materials, manufacturing, assembly, testing, launching, operating, etc) should be considered.

Foldable reflector concepts derived from the literature are evaluated in terms of geometry, surface accuracy, mechanical design, RF, technological maturity and cost. Reflectors are scored according to these criteria as good (10 points), medium (3 points) and low (0 points). Good, medium and low mean that the relevant criterion is provided exactly, partially, or not met, respectively.

Solid surface, membrane surface and shell surface reflectors are compared in Table 2, 3 and 4. A total score of each reflector is obtained according to the criteria. Among the solid surface reflectors, foldable solid surface reflector of ACERAD (128 points) and the Alenia's reflector with foldable ends (121 points) are found to be more advantageous according to the results. Both show similar characteristics in terms of geometry RF evaluation criteria. ACERAD concept could have circular geometry with design changes, even if the original one does not have. In terms of mechanical evaluation criteria, it has higher design flexibility, provides better synchronization and deployment control because of shape memory elements. However, it is a concept that needs to be improved in terms of technological maturity.

Comparison of the membrane surface reflectors shows that foldable antenna reflector designed by CTD Company and the SMART reflector developed by Datashvili and et al. has the highest points of 159 and 155. The structure with membrane surface provides advantages such as lightweight, less folded volume and deployment ease. Both reflectors fold like an umbrella, providing smaller diameter, but the height remains unchanged. The surface accuracy is also good. However, the areal density of the CTD reflector is higher due to the need of rigid support members of the membrane surface. When compared to the solid surface and shell surface reflectors, the membrane surface is less resistance to micrometeoroids. Although the number of parts of the CTD is higher, it is evaluated that the deployment is controlled by the parts produced from the shape memory elements that also provide synchronization, hence is more reliable.

Last but not least, the shell surface reflector concepts are evaluated. The shell surface reflector of AKU (152 points) and EDU reflector of CTD (149 points) are scored the highest. Among the advantages of this concepts compared to other concepts, the reflective surface is monolithic; there are a small number of parts that will cause the complexity and the cost is low. Continues surface is important that will make a positive contribution to RMS error as well as the reliability of deployment. For AKU reflector, the elastic energy gained during the folding provides deployment after cutting a cable that holds the reflector in folded configuration. The deployment control of the AKU reflector is limited whereas it is a more controlled way for the EDU reflector by using shape memory elements. However the number of parts and areal density of the EDU reflector is more than that of AKU reflector.

When the solid surface, the membrane surface and the shell surface concepts are compared together, the solid surface ECERAD reflector (128 points), the membrane surface EDU reflector (159 points) and the shell surface AKU's reflector (152 points) have the highest scores. Among the winning concepts, solid surface ACERAD reflector was developed by Composite Technology Development (CTD). ACERAD was designed for Dragonian antenna with main with a size of 2.5 m by 5 m and sub reflector. The ends of the main reflector and the sub reflector are folded by 90° and 45°, respectively. The preliminary analysis showed the feasibility of the concept, but new designs must be developed for the rigid sections and the elastic memory components to meet the surface accuracy requirements for W-band [2]. CTD also developed a membrane surface reflector EDU made of graphite composite for Ku-band. It is made of a furlable composite surface with elastic memory stiffener around its rim, and a deployable backing structure. The deployed reflector has a diameter of 4 m, and $F/D=0.6$. There is a rigid centre section, and deployable outer section [14]. AKU has developed all composite springback reflector made of carbon/epoxy for Ku-band. The reflector has a shell surface reinforced by flat skirt. 1/3 scaled model was manufactured, and tested. It has a fundamental frequency of 6.8 Hz, and 0.42 mm RMS surface accuracy. The reflector can be folded by rolling up two opposite ends toward the centre, and deploys itself using stored elastic energy during folding [21].

Table 2. Solid surface reflectors.

<div>Criteria</div> <div>Concepts</div>			ACERAD CTD Reflector	Sunflower Reflector TRW	Daisy, MEA, DASA-Dornier	SSDA, DSL Cambridge University	XM1, XM2 Hughes	Foldable Tips, Alenia
Diameter \ Dimensions			5 m × 2.5 m	5.5 m	4.7 m	3 m	5 m	3.7 m
Geometry	Reflector type	Central	good	good	good	good	good	good
		Offset	good	medium	good	medium	good	good
	Rim	Circular	good	good	good	good	good	good
		Elliptical	good	low	good	good	good	good
	Package volume	Diameter	medium	good	medium	medium	medium	medium
		Height	low	low	low	low	low	low
Accuracy	RMS error ≤ 0.6 mm		good	good	good	good	good	good
Mechanical	Areal density		low	low	low	low	low	low
	Number of parts		medium	medium	low	low	medium	medium
	Deployment robustness	Reliability	medium	medium	medium	medium	medium	medium
		Control	good	good	good	good	medium	medium
		Repeatability	medium	medium	medium	medium	medium	good
		Synchronization	good	good	good	good	medium	medium
	Design flexibility		good	medium	low	medium	medium	medium
	Resistance to micrometeorites		good	good	good	good	good	good
RF	PIM		good	good	good	good	good	good
	Losses		good	good	good	good	good	good
Technological maturity	Orbit		low	low	low	low	low	low
	Ground		medium	good	medium	good	good	good
Cost			medium	medium	medium	medium	medium	medium
Total			128	118	115	118	114	121

3. CONCEPT ANALYSES

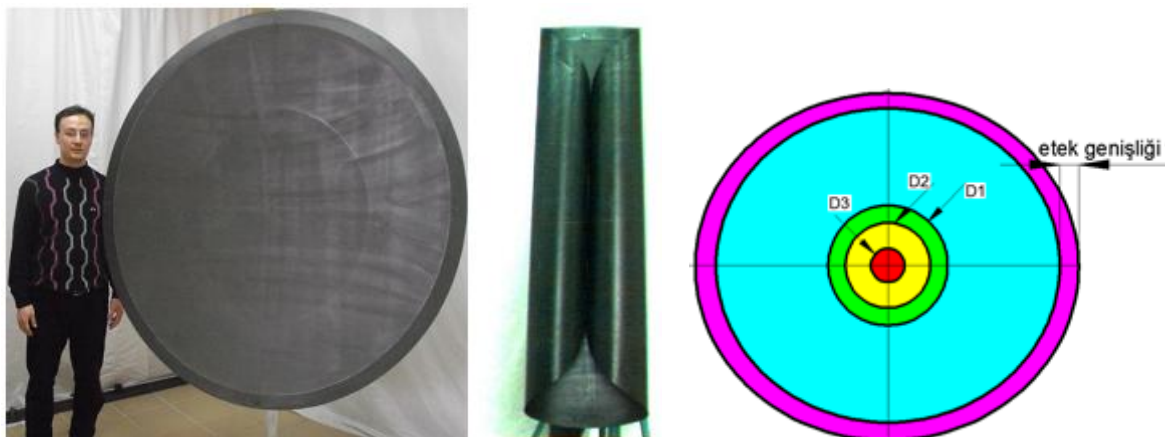
The winning concepts in each group are selected for further preliminary design study as follows (i) solid surface reflector ACERAD, (ii) membrane surface reflector EDU (iii) shell surface reflector AKU. In order to compare the concepts, a diameter of $D=3\text{m}$, $F/D=0.6$ and central reflector is chosen, and the concepts are scaled accordingly. The concepts are modelled in Abaqus 6.13 finite element program. Mass and natural frequencies are obtained in free-free boundary conditions.

3.1 Analysis of Shell Surface Reflector

The reflector is made of thin CFRP shell surface and skirt, as seen in Fig.1. The shell surface is reinforced at central region and along the rim. The thickness of the shell surface varies along the radial direction: eight layers $[0/45]_{2s}$ within diameter of D_3 , five layers $[0/45_3/0]$ between D_2 and D_3 , three layers between D_1 and D_2 , and two layers $[0/45]$ for the rest, where $D_3=300\text{ mm}$, $D_2=600\text{ mm}$, $D_1=900\text{ mm}$. The skirt has a width of 0.1m and three layers $[0/45/0]$. Plain wave CFRP with a ply thickness of 0.11 mm is use. The material properties are as follows: $E_1=E_2=53.7\text{ GPa}$, $G_{12}=2.85\text{ GPa}$, $\nu_{12}=\nu_{21}=0.15$. The model is then meshed using 28086 shell elements (*S4R*). The first mode of the model is given in Fig.2, showing a rigid central region and symmetrical bending mode.

Table 3. Membrane Surface Reflectors.

Criteria \ Concepts			CTD Reflector	Xidian University's Reflector	Precipitation Radar Antenna ILC Dover	Smart Reflector	CRTS, ESTEC, Cambridge University
Diameter \ Dimensions			4 m	60 m	5m×5m	4 m	1.5 m
Geometry	Reflector type	Central	good	good	low	good	good
		Offset	good	medium	low	good	good
	Rim	Circular	good	good	low	good	good
		Elliptical	good	good	low	medium	good
	Package volume	Diameter	good	good	good	good	good
		Height	low	low	low	low	medium
Accuracy	RMS error ≤ 0.6 mm		good	low	good	good	low
Mechanical	Areal density		medium	good	good	good	good
	Number of parts		medium	low	good	medium	medium
	Deployment robustness	Reliability	good	medium	good	medium	good
		Control	good	low	good	good	low
		Repeatability	good	medium	good	good	good
		Synchronization	good	medium	medium	medium	low
	Design flexibility		good	good	low	good	medium
	Resistance to micrometeorites		medium	low	low	medium	low
RF	PIM		good	good	good	good	good
	Losses		good	good	good	good	good
Technological maturity	Orbit		low	low	low	low	low
	Ground		good	low	good	good	good
Cost			good	good	good	good	good
Total			159	102	113	155	129

**Fig.1. AKU reflector (left) and finite element model (right).**

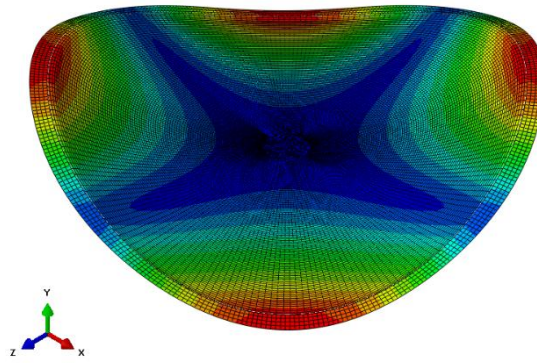


Fig.2. First mode of shell surface reflector (Mod I=4.56 Hz)

Table 4. Shell surface reflectors.

Criteria \ Concepts			Astrum Thin Shell Panel Reflector	Cambridge University's Springback Reflector	Cambridge University's SAR Reflector	Tibbald's Reflector	EDU Reflector	AKU's Springback Reflector	Large Tape Spring Reflector
Diameter \ Dimensions			3 m	6 m	3.6 × 8 m	1 m	4 m × 2.5 m	6 m	17.3 × 2.8m
Geometry	Reflector type	Central	good	good	good	good	good	good	good
		Offset	good	good	good	good	good	good	good
	Rim	Circular	good	good	low	good	good	good	medium
		Elliptical	good	good	low	low	good	good	good
	Package volume	Diameter	good	medium	good	good	good	good	good
		Height	low	low	good	low	low	low	low
Accuracy	RMS error ≤ 0.6 mm		medium	good	medium	medium	good	good	good
Mechanical	Areal density		medium	good	medium	medium	medium	good	good
	Number of parts		medium	good	good	medium	medium	good	medium
	Deployment robustness	Reliability	medium	good	good	medium	good	good	good
		Control	good	medium	medium	medium	good	medium	medium
		Repeatability	good	good	good	medium	good	good	good
		Sync.	good	medium	medium	good	medium	medium	medium
	Design flexibility		medium	medium	medium	medium	good	good	good
	Resistance to micrometeorites		medium	medium	medium	medium	medium	medium	medium
RF	PIM		good	good	good	good	good	good	good
	Losses		good	good	good	good	good	good	good
Technological maturity	Orbit		good	low	low	low	low	low	low
	Ground		good	good	good	medium	good	good	good
Cost			medium	good	good	medium	good	good	good
Total			141	145	128	100	152	159	145

3.2 Analysis of solid surface reflector

Some simplifications of the reinforcing elements of the original ACERAD concept are made for modelling ease as given in Fig. 3. The reflector has a CFRP surface attached to three solid sections: central and side sections. The two sides are connected to the central part by the hinges that enable for folding of the reflector. A sandwich structure with aluminium core and three layered (0/45/0) CFRP surface is considered for the structure. The ply thickness of the CFRP is 0.12 mm and a total thickness of the sandwich is 12 mm. The reflective surface and the hinges are made of CFRP material with three layers (0/45/0) for the reflective surface and eight layers (0/45)_{2s} for the hinges. The material properties are $E_1 = E_2 = 53.7$ GPa, $\nu_{12} = 0.15$, $G_{12} = 2.85$ GPa, $G_{13} = G_{23} = 2.85$ GPa for the CFRP, and $E_1 = 0.376$ GPa, $E_2 = 0.216$ GPa, $\nu_{12} = 0.3$, $G_{12} = 0.186$ GPa, $G_{13} = G_{23} = 0.0965$ GPa for of the honeycomb. The model is meshed 17568 shell elements. The first mode of the model is given in Fig.4, showing a rigid central region. Bending modes occur at the fold region of the reflector where the sides are connected to the central part.

3.3 Analysis of membrane surface reflector

The reflector based on EDU concept is modelled and as shown in Fig.5. The reflector can be folded like an umbrella. The furlable membrane surface is reinforced with six equally spaced radial struts, two rings at the rim and at the centre. There is a hole at the centre with diameter of 0.5 m. The outer ring support is 30 mm wide and 0.3 mm thick. The struts connected to the outer and inner rings are modelled as box beam (40 mm wide, 60 mm high, 0.3 mm thick). The inner ring has a cross section of box beam (40 mm wide, 80 mm high, 0.3 mm thick), outer diameter of 400 mm, and inner diameter of 320 mm. All supports are assumed to be made of quasi isotropic CFRP material. The reflective surface is also made of 0.3 mm thick composite material. The material properties are $E = 45$ GPa, $\nu = 0.3$, density = 1480 kg/m^3 for the CFRP, and $E = 1$ GPa, $\nu = 0.3$, density = 1480 kg/m^3 for the membrane. The model is meshed using *S4R* shell elements: 7869 elements for reflective surface, 162 elements for struts, 660 elements for inner ring and 187 elements for outer ring. The mode shape is given in Fig.6, showing rigid central region, and bending along the rim between the struts.

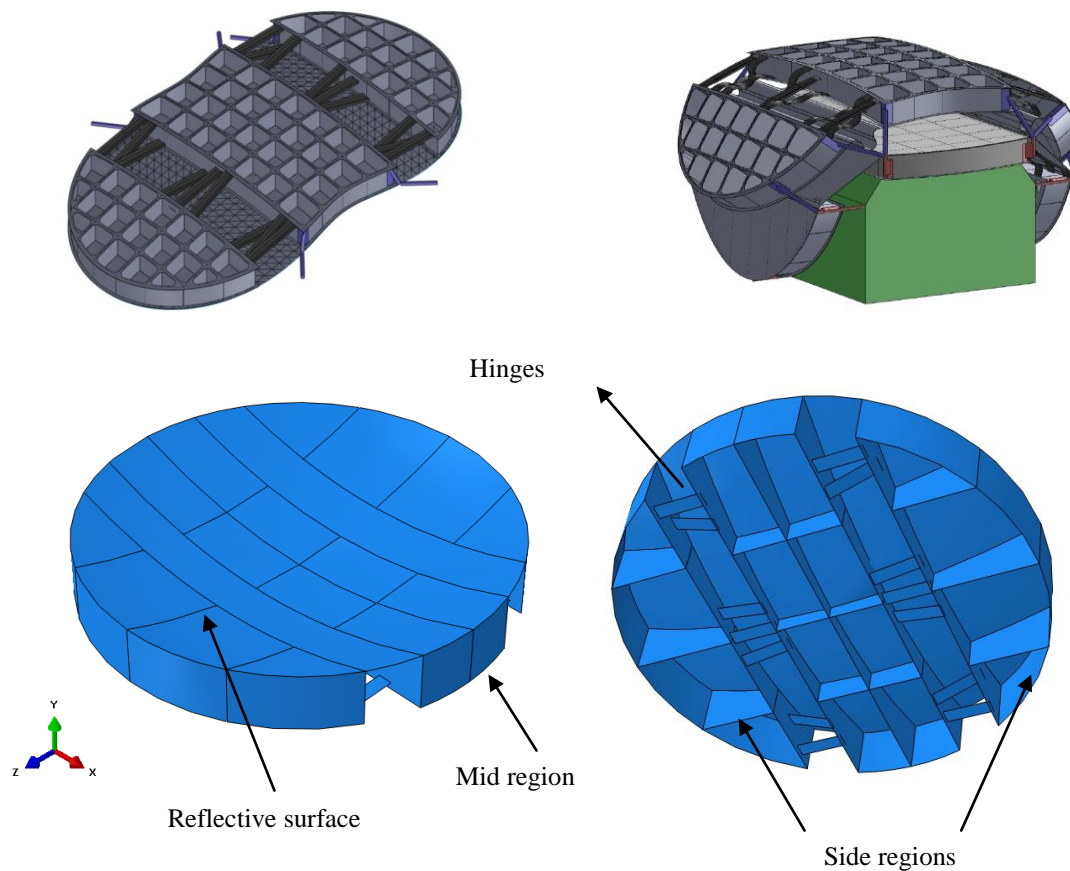


Fig. 1. Solid surface reflector, original concept ACERAD (top) [2] and simplified model (bottom).

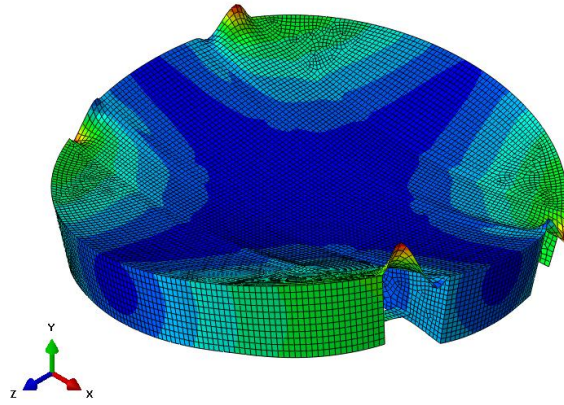


Fig. 4. First mode of solid surface reflector (Mod I=16.4 Hz)

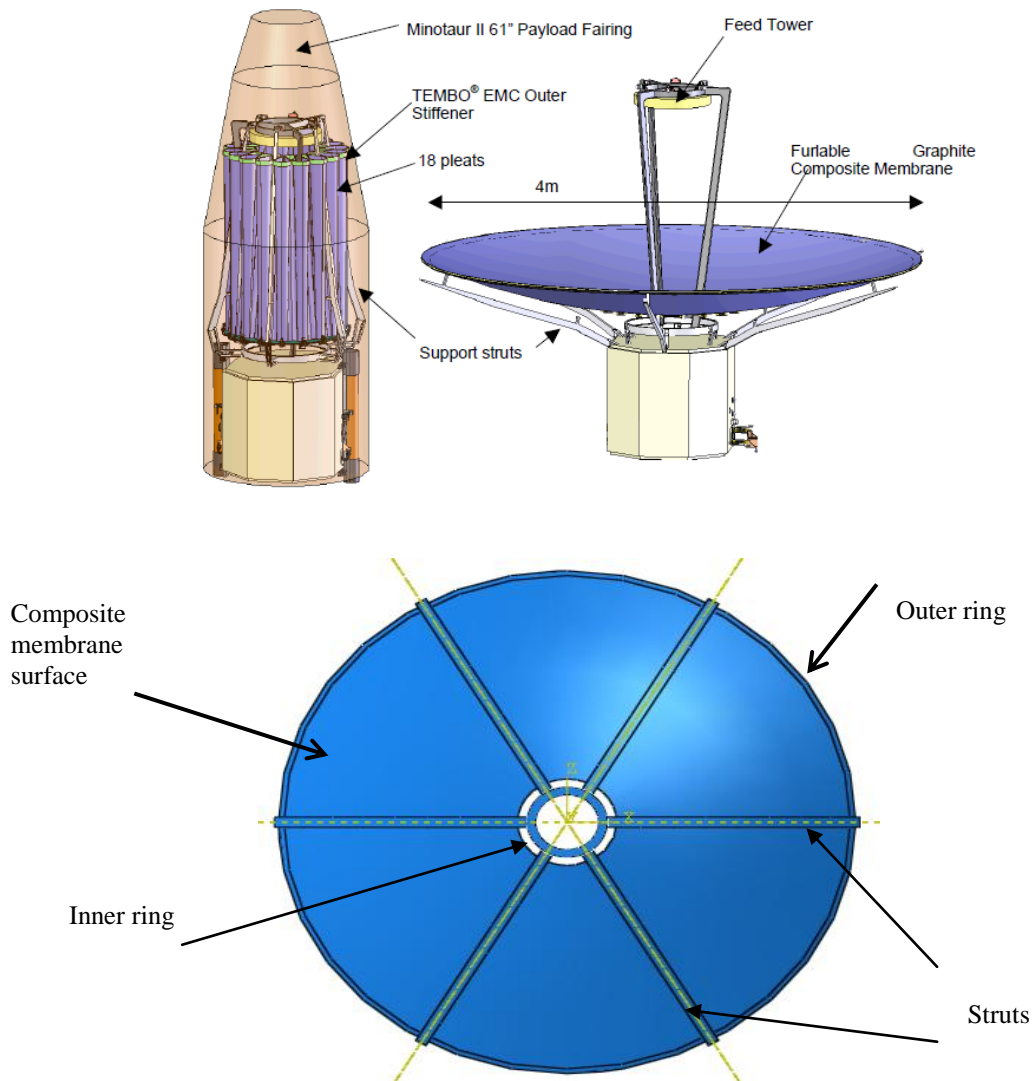


Fig. 5. Membrane surface reflector, original concept (top) [14], finite element model (bottom)

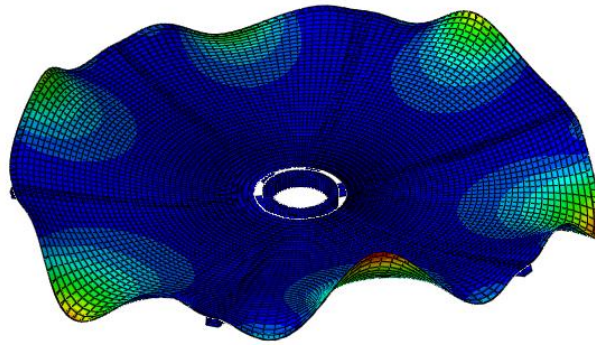


Fig.6. First mode of membrane surface reflector (Mod I= 2.08 Hz)

4. CONCLUSIONS

In the study, solid surface, shell surface and membrane surface reflectors available in the literature are evaluated using concept selection criteria. Winning concepts in each group are further evaluated for a preliminary design study of a reflector to be used an X-band payload. The results are compared for mass, areal density natural frequency in Table 5. It is required that the fundamental frequency of the reflector ≥ 1 Hz, and areal density ≤ 1.5 kg/m². It is found that the solid surface reflector has high rigidity but does not meet the requirement of the areal density. The both membrane and shell surface reflectors are met the fundamental frequency and areal density, hence they are applicable. The shell surface reflector is the best for being higher rigidity and lightweight. It should be noted that the designs have not been optimized, and other requirements have not meet yet. Both concepts are selected for a more detailed study, the final decision will be made after further analyses.

Table 5. Comparison of the reflector concepts.

Concept	Mass (kg)	Areal density (kg/m ²)	Natural frequency (Hz)	Applicability
Solid surface	15.6	2.21	16.41	not applicable
Shell surface	3.1	0.44	4.56	applicable
Membrane surface	4.15	0.59	2.08	applicable

REFERENCES

- [1]. Mikulas, M. M., and Thomson, M., "State of The Art and Technology Needs for Large Space Structures," Vol. 1: New and Projected Aeronautical and Space Systems, Design Concepts, and Loads of Flight-Vehicle Materials, Structures, and Dynamics—Assessment and Future Directions. ASME, New York, 1994, ch. 3, pp. 173–238.
- [2]. Taylor, R and Turse, D., "Large Aperture, Solid Surface Deployable Reflector," ESTF Conference, Research Report, 2011.
- [3]. Hachkowski, M. R., and Peterson, L. D. "A Comparative Study Of The Precision Of Deployable Spacecraft Structures," Tech. Rep. CU-CAS-95-22, Center for Aerospace Structures, University of Colorado, Boulder, CO, USA, December, 1995.
- [4]. H. Baier, L. Datashvili, N. Nathrath, S. Pellegrino, "Technical Assessment Of High Accuracy Large Space Borne Reflector Antenna", Final Technical Report, Reference No.: LLB-R-03/03/03-03, ESTEC/Contract, No: 16757/02/NL/LvH/bj, Technical University of Munich, Germany, 2003.
- [5]. Guest S. D. and Pellegrino S., "A New Concept for Solid Surface Deployable Antennas", Acta Astronautica, Volume 38, No:2, pp 103-113, 1996.
- [6]. Boeing Satellite Systems, <http://www.hughespace.com> (28 November 2001), 191 BIBLIOGRAPHY.

- [7]. Badessi S., Fei E., Grimaldi F., Tempesta G., Bruno C. Rosati G., Bruschetta F., “20/30 GHz ASTP Multibeam Antenna,” Executive Summary, ESA Report Reference: ESA CR (X) 3107, Alenia Spacio, Roma, Italy, 1990.
- [8]. Leipold, M., Runge, H., Sickinger, C., “Large Sar Membrane Antennas With Lightweight Deployable Booms,” 28th ESA Antenna Workshop on Space Antenna Systems and Technologies, ESA/ESTEC, May 31 - June 03, 2005.
- [9]. Datashvili, L., Baier, H., Lang M., Baier, H. and Sixt, T., “Membranes for Large and Precision Deployable Reflectors,” Proceedings of the European Conference on Spacecraft Structures, Materials and Mechanical Testing (ESA SP-581), Noordwijk, The Netherlands, 10-12 May 2005.
- [10]. Zheng, F., Chen, M., Yang, W.L. and Yang, P., “Conceptual Design of a New Huge Deployable Antenna Structure for Space Application,” IEEEAC, paper 1221, Version 7, Updated January 13, 2008.
- [11]. ILC Dover Firması, <http://www.ilcdover.com/Precipitation-Radar-Antenna/>, Access date: 12.03.14.
- [12]. Ultra Rapid Deployable Antenna (URDA), European Space Agency, HPS(High Performance Space Structure Systems GmbH), INVENT, ND SATCOM, COBHAM, <http://telecom.esa.int/telecom/www/object/index.cfm?fobjectid=32450>, Access date: 12.03.2014.
- [13]. Pellegrino, S. “Deployable membrane reflectors,” The 2nd World Engineering Congress, 2002.
- [14]. Barret, R, et al, “Deployable Reflector for Small Satellites,” 21. Annual Conference on Small Satellites, Logan, UT, August 13-16, 2007.
- [15]. TEMBO_Large Aperture, Solid Surface Deployable Reflector Composite Technology Development (CTD), 2013.
- [16]. Soykasap, Ö. and Tan L.T. "High Precision Offset Stiffened Spring-Back Composite Reflectors," AIAA Journal, 49(10), 2144-2151, 2011.
- [17]. Soykasap, Ö., Watt. A.M. and Pellegrino, S., “New Concept for Ultra-Thin Deployable Structures,” Journal of the International Association for Shell and Spatial Structures: IASS., 46(147), pp.3-8, 2005.
- [18]. Tibbalds, B., Guest, S. and Pellegrino, S.D., “Inextensional Packaging of Thin Shell Slit Reflectors,” Technische Mechanik, Band 24, Heft 3-4, pp 211–220, 4 April 2004.
- [19]. Schmid, M. and Barho, R., “Development Summary and Test Results of a 3 Meter Unfurlable CFRP Skin Antenna Reflector,” Proceedings of the 10th European Space Mechanisms and Tribology Symposium, San Sebastian, Spain. Compiled by R. A. Harris. ESA SP-524, Noordwijk, Netherlands, ISBN 92-9092-834-4, pp. 145 – 151, 24-26 September 2003.
- [20]. Soykasap, Ö., Pellegrino, S., Howard, P., Notter, M. “Folding Large Antenna Tape Spring,” Journal of Spacecraft and Rockets, Vol.45(3), pp. 560-567, 2008.
- [21]. Soykasap, Ö. Karakaya S., Turkmen D., “Manufacturing of Thin-Shell Offset Demonstrator Reflector”, Advanced Material Research, 445, 514-519, 2012.

ACKNOWLEDGEMENTS

This study is supported by ASELSAN.

ACTIVE SHAPE CONTROL OF RECONFIGURABLE ANTENNA REFLECTORS

Gonçalo Rodrigues, Jean-Christophe Angevain, Julian Santiago Prowald

*ESTEC, European Space Agency,
Keplerlaan 1, 2200AG Noordwijk Zh, The Netherlands
Email: goncalo.rodrigues@esa.int*

ABSTRACT

Mechanically reshapeable reflectors have the potential for enabling satellite antenna reconfiguration with lower cost, mass, power consumption and thermal dissipation than beam-forming active antenna arrays. This paper addresses two key challenges for the successful implementation of this technology which are the shape definition of the reflector and its on-orbit shape control.

A method of shape optimization which simultaneously guarantees performances in terms of the Radio-Frequency pattern on-ground and structural strength and stability is presented. The actuator commands for reshaping the reflector is determined by global optimization with Simulated Annealing, seeking to minimize strain arising in the reflector, while respecting the Directivity and Cross-Polar Discrimination constraints imposed on the ground service-area. This process managed to reduce maximum strains in the reflector down to 22% of what would result from a shape best-fit to an ideal surface produced by a pure RF optimization.

For the shape-control system of the reflector, an Open-Loop implementation would be preferred, requiring a single-calibration of the system on-ground. However, the time-invariance of the properties of the reflector might be difficult to ensure throughout several years of exposure to the space environment. In such a case, the Closed-Loop operation will have to be envisaged and the system identification will have to be performed periodically on-orbit with a dedicated sensing system

1. INTRODUCTION

The on-orbit reconfiguration of satellite antennas has the potential to make Telecommunication and Earth Observation missions more versatile [1,2,3,4]:

- Service areas and satellite orbits can be modified in order to follow the market evolution.
- The radiation pattern can be adapted to varying meteorological conditions, mitigating absorption losses by rain and snow[5,6].
- And also manufacturing and stability tolerances of deployable main reflectors can be made looser by compensating their shape errors at the sub-reflector level [7,8].

Antenna reflectors reshaped by electro-mechanical actuators have the potential to enable mission reconfiguration with a lower-mass, lower-cost and lower power dissipation than the Active Array antenna technology.

This paper addresses in detail to which shapes a flexible thin-shell based reflector must be conformed and discusses how the nature of the electro-mechanical reflector will drive the type of shape control that needs to be implemented on-orbit.

A new strategy for the shape optimization of an antenna reflector was developed, which produces the required contour beam over different service areas on ground, but which at the same time results in a lightly stressed reflector in order to

- Mitigate the occurrence of creep.
- Allow a high number of reconfigurations, by promoting a long fatigue life.
- Ultimately preventing the occurrence of structural failure.

The shape optimization approach developed took the maximum strains in the reflector as the cost-function and managed to reduce them by almost a factor of five when compared to the classical approach followed for shaping antenna reflectors. In the meanwhile, the actuation requirements (stroke and force) and the RF performance requirements (Directivity and Cross-Polar-Discrimination) were kept as constraints. Simulated Annealing was selected as the search algorithm since, as a global method, it prevents the premature convergence to the first optimum that is encountered and also allows the natural incorporation of constraints.

The bench-mark used is the design being considered in the ESA ARTES5.1 activity Reconfigurable Antenna Optics – RAO, which consists of a Gregorian dual-reflector Earth Deck antenna for telecommunications in Ku-band employing a single feed, Fig. 1.

The shape control system for this application can be considered as quasi-static, due to the foreseen slow reconfiguration transitions, and assuming a sufficiently stable environment of the antenna. Its implementation on-orbit is mostly an open point, but clearly it will be driven by the electro-mechanical nature of the reshaping reflector.

The most convenient situation will be to control the shape of the reflector in Open-Loop, where a Look-up table, constructed with the optimization approach described above, will contain sets of commands to the actuators that can be applied in Feed-Forward to produce a switch between service areas. This would require a single calibration of the reflector and actuators while still on-ground. A reflector which responds linearly to the actuator commands will make this task mostly trivial, while different degrees of non-linearity will call for more complex models with a larger number of parameters to fit. However, Open-Loop control will only be feasible if the reshaping reflector exhibits very stable electro-mechanical properties during the full operational life.

If this time-invariance cannot be ensured throughout years of exposure to the space environment, then Closed-Loop operation will have to be envisaged and the system identification will have to be performed periodically on-orbit with a dedicated sensing system. A penalty will then have to be paid in terms of lower operational time and larger telemetry effort, and embarked power and computational resources.

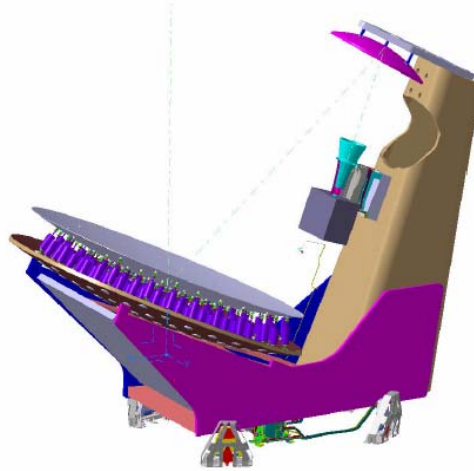


Fig. 1. Reconfigurable Gregorian antenna (Courtesy of Thales Alenia Space France and Technical University of Munich/LLB [9]).

2. SHAPE OPTIMIZATION

Codes which can optimize the shape of a reflector for RF performance already exist. For instance, in POS from TICRA [10], a desirable coverage can be assigned for a set of stations on ground, for example in terms of Directivity and Cross-Polar discrimination. The output of this optimization is an ideal reflector surface that minimizes the error to this coverage and which is typically expressed in terms of splines.

However, the definition of such an ideal surface does not shed any light on how well the hardware of the reflector can be deformed to approximate such splines when it is actuated or, even if a good approximation can be achieved, issues on strength and stability (creep).

In this paper, the problem of the shape optimization is posed in terms of searching for the set of actuator displacements which will minimize the value of the strain arising in the reflector. The actuator displacements are therefore the optimization variables, which are bounded by their stroke, and the force limits of the actuators as well as the RF requirements of Directivity and XPD within all the stations of the coverage are imposed as constraints.

$$F_{max} < 20 \text{ N} \quad (1)$$

$$D_{min} > 29 \text{ dB}_i \quad (2)$$

$$XPD_{min} > 30 \text{ dB} \quad (3)$$

The optimization process is as depicted in Fig. 2. It starts indeed with the a reflector shape which is a Least-Squares fit to the ideal splines computed by POS, and then, it carries out multiple iterations of the actuator displacements, which are evaluated both in Mechanical and Radio Frequency terms. Finally, at the end of each iteration, an optimizer code checks both the convergence of strains, and if the constraints are being respected, and devises the next iteration of actuator displacements.

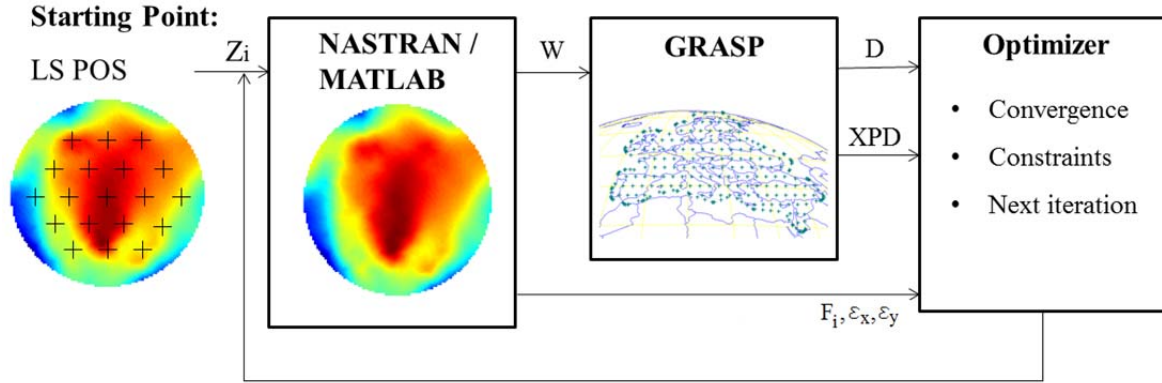


Fig. 2. Flowchart of coupled mechanical–RF optimization [11].

2.1. Mechanical Model

The mechanical modelling in the optimization is based on a finite element model of a Carbon-Fibre Reinforced Silicon (CFRS) reflector. CFRS is a very promising composite developed by the Technical University of Munich very flexible but very stable. Under actuation, the most likely mode of failure of a CFRS reflector is the micro-buckling of the carbon fibres, [12].

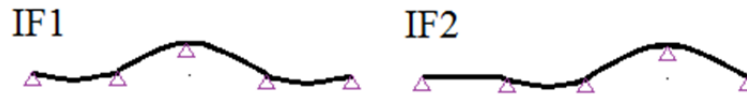


Fig. 3. Generation of Influence Functions [11].

Using NASTRAN [13], it was possible to determine the independent influence of each actuator alone when all the other actuators are set to zero displacement. The computation of these Influence Functions of these actuators was done both in terms of overall shape, of normal strains and of forces in the actuators. The mechanical model used for the optimization then, consisted of superimposing these influence functions weighed by the actuator displacements to obtain the deformed shape, and doing the same with the strains and forces, according to equations 1, 2 and 3.

$$\{W\} = [IF_w]\{Z_i\} \quad (4)$$

$$\varepsilon_{x,y,max} = \max(|[IF_{\varepsilon_{x,y}}]\{Z_i\}|) \quad (5)$$

$$F_{max} = \max(|[IF_F]\{Z_i\}|) \quad (6)$$

2.2. RF Model

The RF model represented a Gregorian dual-reflector Earth Deck antenna operating in Ku-band, and iteratively GRASP [14] was consecutively launched for analysing the RF propagation from each iterated mechanical shape and determining Directivity and Cross-Polar Discrimination in all the stations of an European coverage.

2.3. Simulated Annealing

In this case, the derivatives of the cost function and the constraints were not directly available, and so the optimization had to rely on methods of direct search which evaluate the performance at every new iteration of the actuator displacements. This can be done with the Hill descent method.

In each new iteration, the current location of the search is perturbed. If the perturbed location yields a lower cost function, the search moves there. Otherwise, the candidate is discarded and a new candidate is generated by perturbing the current location. The process continues and eventually it converges to the first minimum it encounters.

In general, however, such a local minimum will be of very limited interest. One way to circumvent this, is by launching the local search from many different points. But it is more effective to use nature-inspired methods such as Genetic Algorithms or Simulated Annealing [15].

Simulated Annealing mimics the minimization of energy that occurs during the cooling of molten metal from a high temperature in which atoms have a permanent random motion. If this cooling is done slowly, the atoms have time to try out multiple configurations and they will settle themselves in the state of minimum energy forming a large single crystal. However, quickly cooling prevents the crystal formation and the result is an amorphous solid in a higher than minimum energy state.

The algorithm of Simulated Annealing can be seen as the introduction of a random exploratory character to the Hill Descent. Again, a survey of the vicinity of each current iteration is performed by perturbing the current point of search and setting a new candidate. If the candidate has a lower cost than the current location then, immediately it is accepted as the new step in the search for a minimum, just like in Hill Descent, Eq. 7. However, even if the new candidate has a higher cost there is still a probability that we accept it and continue our search, now in the vicinity of this less good point, Eq. 8. This probability is driven by a parameter T called temperature which is scheduled throughout the search. In the first iterations the algorithm shall freely roam in the variable space to identify regions which are globally lower, and this is achieved by starting the algorithm with a high temperature. Eventually the algorithm shall converge, which will be achieved by applying a totally deterministic Hill Descent by setting the temperature to 0.

$$\text{If } f(\{Z_i\}_c) < f(\{Z_i\}_k), \{Z_i\}_{k+1} = \{Z_i\}_c \quad (7)$$

$$\text{elseif } r < e^{\frac{f(\{Z_i\}_k) - f(\{Z_i\}_c)}{T}}, \{Z_i\}_{k+1} = \{Z_i\}_c \quad (8)$$

$r \in [0,1] \text{random}$

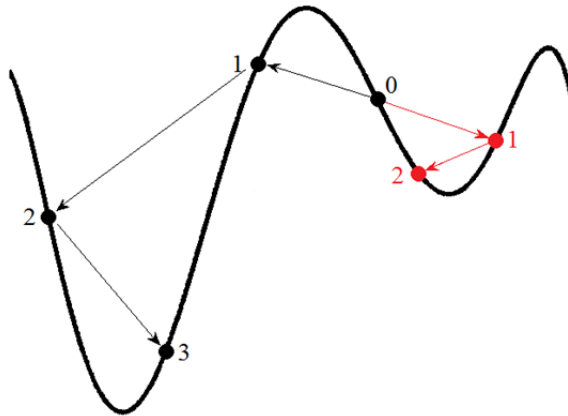


Fig. 4. Search of variable space with Simulated Annealing [15].

The convergence of our search for low compressive strains with Simulated Annealing, is shown in Fig. 5. Starting with the Least Squares fit to the splines determined by POS, it was possible to reduce the normal compressive strains to almost 1/5 of those of the best fit to the ideal RF optimum. This resulted in an increase of the Margin-of-Safety with relation to micro-buckling from a marginal 0.25 to 4.6 at the end of the optimization (assuming $FoS=1.25$ and $\epsilon_{limit}=0.25\%$). This reduction of strains in the reflector can be seen as an “unwrapping” of the surface, in which a smoothing the shape of the reflector is achieved at the cost of a larger displacement Peak-To-Valley.

The constraints of equations 1 to 3 were implemented by simply excluding all the unfeasible points from the search. It was observed that the minimum Directivity within the coverage became an active constraint right in the first steps of but

a large margin of XPD was preserved throughout the entire search. The actuator requirements of force and displacement never became active during the optimization.

Clearly, Hill Descent converged to a less interesting solution.

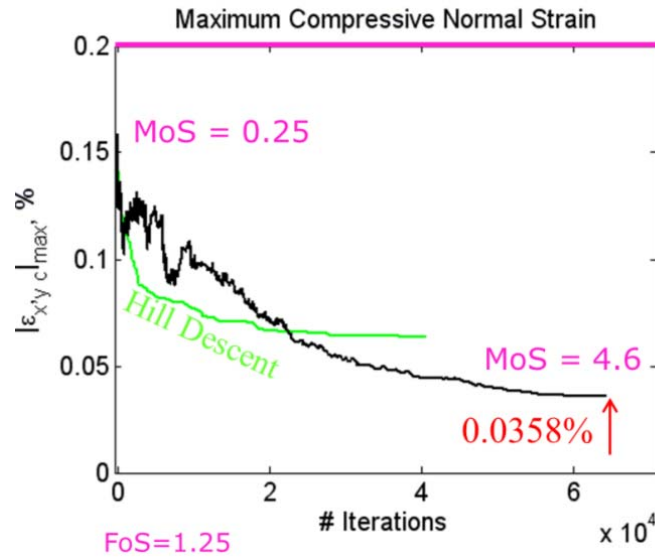


Fig. 5. Minimization of the maximum compressive strain in a reshapable reflector with Simulated Annealing.

Table 1. Optimization Results [16]

	#iters.	$ \epsilon_{comp} $, %	D, dBi	XPD, dB	F, N
LS fit to POS	-	0.160	30.3	33	3.1
Hill Descent	40754	0.064	29.0	32.6	2.4
Simulated Annealing	64510	0.036	29.0	32.1	2.0

3. SHAPE CONTROL SYSTEM

The shape control of an antenna reflector faces a Multi-Input-Multi-Output (MIMO) system. The surface of the reflector responds to the independent commands given to the actuators, and the output can be considered as a discretization of the coverage on ground, which is its ultimate purpose of this application, or a discretization of the shape of the reflector itself. Taking into account the low number of reconfigurations to be performed during the mission life-time and assuming a sufficiently stable environment of the antenna, the control problem can be considered as quasi-static. The real challenge in controlling the reflector will be to ensure the long-term stability and predictability of its response or otherwise periodically perform its system identification on-orbit.

3.1. Open-Loop Shape Control

Ideally, simply applying to the actuators the commands derived by the optimization procedure described above would provide acceptable performance.

Even, if this would require that the behavior of the full system does not change during 15 years in space, the models used in the optimization need to be quite accurate. In particular, the model of the reshapable reflector will have to be calibrated on-ground.

If the shape of the reflector shows a linear dependence on the commands applied to the actuators, this on-ground calibration will simply consist of measuring the Influence Function of each actuator alone and building the interaction matrix for the reflector.

Otherwise, a non-linear FE model will have to be considered, in which the material properties, the geometry, the layup definition and the boundary conditions can be tuned from correlation with tests.

Finally, it might be observed that the FE non-linear prediction will not exhibit sufficient accuracy, and in such a case other non-linear models with a much higher number of parameters, such as Neural Networks or Surface Response Functions, will have to be calibrated.

3.2. Closed-Loop Shape Control

If the time-invariance of the system cannot be ensured throughout 15 years in operation, in particular for the stiffness of the reflector under radiation or for creep under actuation, then the means for closing the loop while on operation will have to be provided.

Monitoring the coverage directly on-ground would bring no added mass neither complexity to the spacecraft but it would require the maintenance of a distributed infrastructure on ground.

Alternatively, taking on-board measurements of the RF pattern would allow a characterization of the reflector and diffraction systems, but at the cost of added embarked mass and complexity. A trade-off will have to be made between taking multiple RF measurements on-board or using a lower number of ground-beacons and steering the antenna or the platform throughout the calibration.

The direct measurement of the reflector surface for performing the system identification is directly suited to the shape optimization strategy described above and avoids the need for inferring the reflector shape from the RF measurements. The sensing of the shape of the reflector requires the integration of a dedicated sensing system on the spacecraft such as photogrammetry or a 3D laser scanning systems or linear position sensors in the reflector, which will allow to periodically identify the behavior of the reflector on-orbit.

Again, the electro-mechanical nature of the reflector will affect the system identification in the same way as discussed for the on-ground calibration.

If the degree of non-linearity is not very high, the modelling of the reflector can even be considered through multiple linearizations to be performed inside the optimization process itself.

In any case, for on-orbit system identification, a more complex behavior of the reflector will become more penalizing with costs in terms of service availability, telemetry and embarked complexity and weight.

4. CONCLUSIONS

This paper addressed two key aspects for the shape control of antenna reflectors: the shape optimization of the antenna reflector for RF and mechanical performances and the definition of the shape control system for operation on-orbit.

First, it was shown that by taking the maximum compressive strains in the reflector as the cost-function and driving the search with the algorithm of Simulated Annealing it was possible to optimize the shape of an antenna reflector for a desired coverage in Ku-band while reducing strains by almost a factor of five. This yielded comfortable margins-of-safety for micro-buckling, which is the dominant mode of failure for selected material for the reflector (CFRS) under actuation. By being a global method, Simulated Annealing prevented the premature convergence to the first local optimum encountered throughout the search and allowed the natural incorporation of the RF and actuation requirements as constraints.

In terms of implementation of the shape control system, it is recognized that the preferred operation mode would be in Open-Loop, with the actuator commands determined by optimization being applied in Feed-Forward to produce a switch between service-areas. Such an approach would require a single calibration of the reflector while still on-ground, with different levels of complexity depending on the degree of non-linear behaviour exhibited by the reflector in response to the commands to the actuators. However such Open-Loop operation will only be feasible if the reflector and the actuators exhibit very stable electro-mechanical properties. If this time-invariance cannot be ensured, then Closed-Loop operation will have to be envisaged and system identification will have to be performed periodically on-orbit with a dedicated sensing system. This will incur in a penalty in terms of operational time, telemetry effort, and embarked power and computational resources.

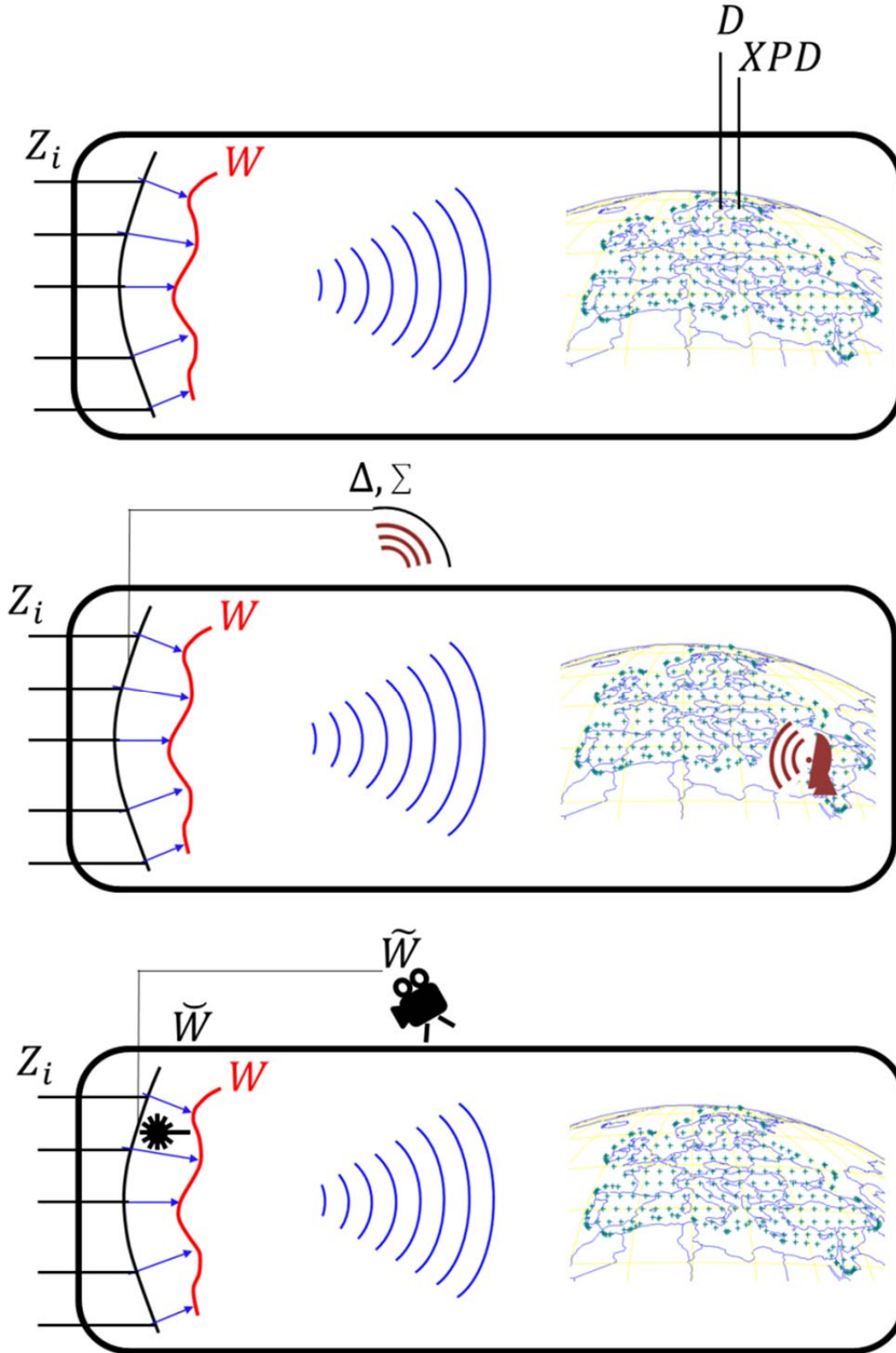


Fig. 6. Closing the Loop in a Reshapable Antenna Reflector. From top to bottom: Direct sampling of coverage, on-board measurement of the pattern from a ground-beacon, and direct reflector shape measurement, [16].

REFERENCES

- [1]. P.J.B. Clarricoats, Z. Hai, R.C. Brown, G.T. Poulton, G.A.E Crone, "A Reconfigurable Mesh Reflector Antenna", 6th International Conference on Antennas and Propagation 1989 (ICAP89), 4-7 April 1989, Volume 1, pp. 112-116.
- [2]. H. Viskum, K. Pontopiddan, P.J.B. Clarricoats, G.A.E Crone, "Coverage Flexibility by means of a reconformable subreflector", IEEE APS International Symposium, 13-18 July 1997, Volume 2, pp. 1378-1381.
- [3]. G.N. Washington, M. Angelino, H.T. Yoon, and W.H. Theunissen, "Design, Modeling, and Optimization of Mechanically Reconfigurable Aperture Antennas", IEEE Transactions on Antennas and Propagation, 50, No. 5, May 2002, pp. 628-637.
- [4]. C. Cappellin and K. Pontoppidan, "Feasibility Study and Sensitivity Analysis for a Reconfigurable Dual Reflector Antenna". In Proc. of EuCAP2009, March 2009, Berlin, Germany
- [5]. P. Gabellini, A. Paraboni, A. Martellucci, P. Rinous, S. Nakazawa, N. Gatti, F. Maggio, C. Capsoni, L. Resteghini and R. Nebuloni, "The RF Design of a Ka-Band Reconfigurable Broadcast Antenna for Atmospheric Fade Mitigation", Proc. 33rd ESA Antenna Workshop, Noordwijk (The Netherlands), October 2011.
- [6]. P. Gabellini, N. Gatti, C. Capsoni, L. Resteghini, A. Martellucci, P. Rinous, "An On-Board Reconfigurable Antenna System for Ka-Band Broadcasting Satellite Services", 6th European Conference on Antennas and Propagation (EUCAP 2012), 26-30 March 2012, pp. 2636-2640.
- [7]. W.A. Imbriale "Distortion Compensation Techniques for Large Reflector Antennas", Aerospace Conference 2001 IEEE Proceedings, Volume 2, pp. 799-805.
- [8]. R.A. Hoferer, Y. Rahmat-Samii, "Subreflector Shaping for Antenna Distortion Compensation: An Efficient Fourier-Jacobi Expansion With GO/PO Analysis", IEEE Transactions on Antennas and Propagation, December 2002, Volume 50, Issue 12, pp. 1676-1687.
- [9]. S. Depeyre, V. Belloeil, P. Lepeltier, L. Schreider, L. Datashvili, H. Baier, J. Hoffman, B. Wie, "Potential membrane technologies for in orbit reconfigurable reflector". In: Proceedings of the ESA antenna workshop, Noordwijk, October 2010.
- [10]. The POS software. [Online] <http://www.ticra.com/products/software/pos/> (as of August 20124).
- [11]. G. Rodrigues, J.-C. Angevain, and J. Santiago-Prowald. "Shape optimization of reconfigurable antenna reflectors." CEAS Space Journal: 1-12.
- [12]. L. Datashvili, H. Baier, B. Wei, S. Endler, and L. Schreider, "Design of a Morphing Skin Using Flexible Fiber Composites for Space-Reconfigurable Reflectors". In: Proceedings of the 54TH AIAA/ASME/ASCE/AHS/ASC Structures, Structural Dynamics and Materials Conference, Boston, April 2013.
- [13]. The NASTRAN software. [Online] <http://www.mscsoftware.com/products/cae-tools/msc-nastran.aspx> (as of August 2012).
- [14]. The GRASP software. [Online] <http://www.ticra.com/products/software/grasp/> (as of August 2014).
- [15]. S. Kirkpatrick, C.D. Gelatt, M.P. Vecchi: "Optimization by Simulated Annealing". Science 220(4598), 671-680 (1983).
- [16]. G. Rodrigues, J.-C. Angevain, and J. Santiago-Prowald. "Shape Control of Reconfigurable Antenna Reflector: Concepts and Strategies", EuCAP 2014 - The 8th European Conference on Antennas and Propagation, The Hague, The Netherlands, April 2014.

ACKNOWLEDGEMENTS

The authors wish to thank L. Schreider, S. Depeyre, and I. Faro, from Thales Alenia Space - France and L. Datashvili and H. Baier from the Laboratory of Lightweight Structures of the Technical University of Munich, for the fruitful exchanges and technical discussions in the frame of the ESA ARTES 5.1 study "Reconfigurable Antenna Optics".

MODELLING OF MECHANICAL SHOCK INDUCED BY DEPLOYMENT OF APPENDAGES

J. R. Reveles⁽¹⁾, V. Fraux⁽²⁾, M. Lawton⁽³⁾

^(1,2,3) *Oxford Space Systems Ltd, Harwell, OX11 0QX, UK*

⁽¹⁾ juan.reveles@oxfordspacesystems.com

⁽²⁾ vincent.fraux@oxfordspacesystems.com

⁽³⁾ mike.lawton@oxfordspacesystems.com

ABSTRACT

All mechanical and electronic, electrical and electromechanical (EEE) spacecraft components are subjected to shock events during their life and thus predicting and testing the response of the dynamic system to transient mechanical loading is imperative. Shock events have their origin in a variety of sources, namely: launcher staging, separation pyrotechnics and deployment of appendages. It is the latter which we wish to address in the current paper. The case study we present here pertains to a multi-element boom which is deployed using stored energy elements. We are interested in predicting the mechanical shock induced at the mechanical interface and our aim is to obtain Shock Response Spectrum (SRS) levels which could be used by the platform integrator to conduct shock test at platform level. The avenue we pursue to predict deployment-induced shock is addressed in two stages. Firstly, we develop the dynamic model of the deployable structure using Lagrangian mechanics. In this model the external forces can be tailored according to the characteristics of the stored energy elements. The numerical method and recursive algorithm of solution of the full set of coupled, non-linear ordinary differential equations are also presented. Following the definition of the dynamic model the SRS of the acceleration time histories is obtained using the Smallwood method. Results and conclusions from our case study are presented in the closing sections of the paper.

1. INTRODUCTION

Spacecraft mechanical and EEE components are subjected to severe mechanical loading during their lifetime. Transient dynamic loading such as sinusoidal and random excitation must be taken into account during the development process to ensure survivability of the system during launch. Equally important is mechanical shock generated by rocket staging, pyrotechnics separation devices and deployment of appendages. Shock is often characterised by high intensity and high amplitude transient loading which excites many natural frequencies in a complex structure. This excitation can produce four basic types of failure in electronics and mechanical systems. The root cause for these failures can be summarised as follows:

- 1) high stresses, which can cause fracture or permanent deformations in the structure
- 2) high acceleration levels, which can cause relays to chatter, potentiometers to slip and bolts to loosen
- 3) high displacements which can cause impact between adjacent boards –cracking components and solder joints, breaking cables and harnesses, and fracturing castings
- 4) electrical malfunctions that occur during the shock but disappear when the shock energy dissipates, an effect which can occur in relays, oscillators and capacitors for example.

1.1 Problem definition

In the current paper an analytical method to assess the intensity of shock generated as a result of deployment of a multi-element antenna is addressed. The analysis presented in this paper pertains to a multi-element boom which is deployed using stored energy springs. We are interested in predicting the mechanical shock induced at the mechanical interface and our aim is to obtain Shock Response Spectrum (SRS) levels. This frequency dependant transient mechanical loading levels can in turn be used by the platform integrator to conduct shock test at platform level. The avenue we pursue to predict deployment-induced shock is addressed in two stages. In the first stage we develop the dynamic model of the

deployable structure using Lagrangian mechanics. Then we obtain acceleration time histories at the mechanical interface with the spacecraft and employ the Smallwood method to obtain the system SRS as a result of deployment.



Fig. 1. Multi-element antenna in its stowed (L) and deployed configurations

2. DERIVATION OF THE DYNAMIC EQUATIONS OF MOTION

The dynamic equations of the system can be obtained through classical methods such as the Newtonian or the Lagrangian approach. We choose to apply the Lagrangian approach to our problem. In the Lagrangian formulation, the Lagrangian function can be written in terms of the kinetic energy T and potential energy V of the system; this takes the following form:

$$L = T - V \quad (1)$$

Upon identification of the generalised coordinates and generalised forces acting on the dynamic system, the equations of motion can be obtained by direct substitution of the Lagrangian function into the Euler-Lagrange equations:

$$\frac{d}{dt} \left(\frac{\partial L}{\partial \dot{q}_i} \right) - \frac{\partial L}{\partial q_i} = f_i \quad (2)$$

Where q_i and \dot{q}_i represent the generalised coordinate i and its derivative with respect to time.

It can be said that in general the Lagrangian formulation yields a function which has the following form:

$$L(q_1, q_2, q_3, \dots, q_n, \dot{q}_1, \dot{q}_2, \dot{q}_3, \dots, \dot{q}_n, t) \quad (3)$$

For our specific case, assuming no gravitational effects and some degree of viscous damping between any two adjacent bodies, the Lagrangian function of the system under consideration can be expressed as follows:

$$L = T_1 + T_2 + T_3 \quad (4)$$

The subscripts in the expression above refer to specific bodies comprising the dynamic system.

In expanded form, the kinetic energy of the system can be expressed as follows:

$$T_1 = \frac{1}{2} m_1 \left[(l_1 \dot{\theta}_1 \cos \theta_1)^2 + (l_1 \dot{\theta}_1 \sin \theta_1)^2 \right] + \frac{1}{2} I_1 \dot{\theta}_1^2 \quad (5)$$

$$T_2 = \frac{1}{2} m_2 \left[(L_1 \dot{\theta}_1 \cos \theta_1 + l_2 \dot{\theta}_2 \cos \theta_2)^2 + (L_1 \dot{\theta}_1 \sin \theta_1 + l_2 \dot{\theta}_2 \sin \theta_2)^2 \right] + \frac{1}{2} I_2 \dot{\theta}_2^2 \quad (6)$$

$$T_3 = \frac{1}{2} m_3 \left[(L_1 \dot{\theta}_1 \cos \theta_1 + L_2 \dot{\theta}_2 \cos \theta_2 + l_3 \dot{\theta}_3 \cos \theta_3)^2 + (L_1 \dot{\theta}_1 \sin \theta_1 + L_2 \dot{\theta}_2 \sin \theta_2 + l_3 \dot{\theta}_3 \sin \theta_3)^2 \right] + \frac{1}{2} I_3 \dot{\theta}_3^2 \quad (7)$$

where T_i represent the kinetic energy of body i , m_i its mass, l_i is the distance from body $i-1$ to the centre of mass of body i in body coordinates, L_i is the main geometric parameter that defines body i (e.g. length), I_i are the moments of inertia and θ_i are the generalised coordinates. In these definitions the inertial frame of reference shown in Figure 2 applies.

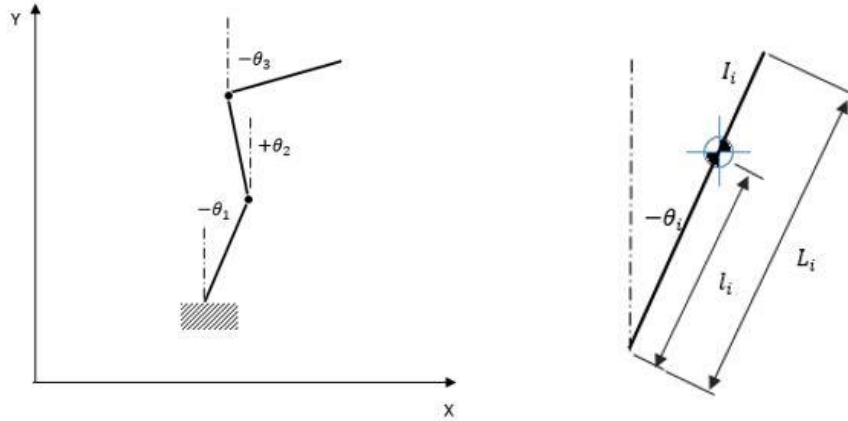


Fig. 2. Definition of the inertial co-ordinate system (L) and geometric definitions

Rearranging terms in the above expression the following equations are arrived at:

$$T_1 = \frac{1}{2} \dot{\theta}_1^2 (m_1 l_1 + I_1) \quad (8)$$

$$T_2 = \frac{1}{2} m_2 (L_1^2 \dot{\theta}_1^2 + 2L_1 l_2 \dot{\theta}_1 \dot{\theta}_2 \cos(\theta_1 - \theta_2) + l_2^2 \dot{\theta}_2^2) + \frac{1}{2} I_2 \dot{\theta}_2^2 \quad (9)$$

$$T_3 = \frac{1}{2} m_3 (L_1^2 \dot{\theta}_1^2 + 2L_1 L_2 \dot{\theta}_1 \dot{\theta}_2 \cos(\theta_1 - \theta_2) + 2L_1 l_3 \dot{\theta}_1 \dot{\theta}_3 \cos(\theta_1 - \theta_3) + L_2^2 \dot{\theta}_2^2 + 2L_2 l_3 \dot{\theta}_2 \dot{\theta}_3 \cos(\theta_2 - \theta_3) + l_3^2 \dot{\theta}_3^2) + \frac{1}{2} I_3 \dot{\theta}_3^2 \quad (10)$$

The equations of motion of the system can be obtained by deriving the Lagrangian function with respect to the generalised coordinates and their derivatives and with respect to time. The Euler-Lagrange equations can be written as follows:

$$\frac{d}{dt} \left(\frac{\partial L}{\partial \dot{\theta}_1} \right) - \frac{\partial L}{\partial \theta_1} = \tau_1(\theta_1(t)) \quad (11)$$

$$\frac{d}{dt} \left(\frac{\partial L}{\partial \dot{\theta}_2} \right) - \frac{\partial L}{\partial \theta_2} = \tau_2(\theta_2(t)) \quad (12)$$

$$\frac{d}{dt} \left(\frac{\partial L}{\partial \dot{\theta}_3} \right) - \frac{\partial L}{\partial \theta_3} = \tau_3(\theta_3(t)) \quad (13)$$

In compact notation, the resulting equations of motion will have the following form:

$$\mathbf{M}(\theta_i) \ddot{\boldsymbol{\theta}} + \mathbf{C}(\theta_i, \dot{\boldsymbol{\theta}}) \dot{\boldsymbol{\theta}} + \mathbf{K}(\theta_i) = \mathbf{U}(\theta_i) \quad (14)$$

Where \mathbf{M} , \mathbf{C} , \mathbf{K} and \mathbf{U} are the matrices associated with the inertia, damping, stiffness and generalised forces of the system. In the equation above bold letters represent vector quantities.

The properties of these matrices are as follows: \mathbf{M} and \mathbf{K} are symmetric and non-singular whereas \mathbf{C} is skew-symmetric.

For the dynamic system under consideration, the following equations are obtained:

$$M_{11} \ddot{\theta}_1 + M_{12} \ddot{\theta}_2 + M_{13} \ddot{\theta}_3 + C_{11} \dot{\theta}_1 + C_{12} \dot{\theta}_2 + C_{13} \dot{\theta}_3 = \tau_1 \quad (15)$$

$$M_{21} \ddot{\theta}_1 + M_{22} \ddot{\theta}_2 + M_{23} \ddot{\theta}_3 + C_{21} \dot{\theta}_1 + C_{22} \dot{\theta}_2 + C_{23} \dot{\theta}_3 = \tau_2 \quad (16)$$

$$M_{31} \ddot{\theta}_1 + M_{32} \ddot{\theta}_2 + M_{33} \ddot{\theta}_3 + C_{31} \dot{\theta}_1 + C_{32} \dot{\theta}_2 + C_{33} \dot{\theta}_3 = \tau_3 \quad (17)$$

where:

$$M_{11} = m_2 L_1^2 + m_3 L_1^2 + m_1 l_1^2 + I_1 \quad (18)$$

$$M_{12} = L_1 L_2 m_3 \cos(\theta_1 - \theta_2) + L_1 l_2 m_2 \cos(\theta_1 - \theta_2) \quad (19)$$

$$M_{13} = L_1 l_3 m_3 \cos(\theta_1 - \theta_3) \quad (20)$$

$$M_{21} = M_{12} \quad (21)$$

$$M_{22} = m_3 L_2^2 + m_2 l_2^2 + I_2 \quad (22)$$

$$M_{23} = L_2 l_3 m_3 \cos(\theta_2 - \theta_3) \quad (23)$$

$$M_{31} = M_{13} \quad (24)$$

$$M_{32} = M_{23} \quad (25)$$

$$M_{33} = l_3^2 m_3 + I_3 \quad (26)$$

$$C_{11} = \delta_1 \quad (27)$$

$$C_{12} = L_1 L_2 m_3 \dot{\theta}_2 \sin(\theta_1 - \theta_2) + L_1 l_2 m_2 \dot{\theta}_2 \sin(\theta_1 - \theta_2) \quad (28)$$

$$C_{13} = L_1 l_3 m_3 \dot{\theta}_3 \sin(\theta_1 - \theta_3) \quad (29)$$

$$C_{21} = -L_1 L_2 m_3 \dot{\theta}_1 \sin(\theta_1 - \theta_2) - L_1 l_2 m_2 \dot{\theta}_1 \sin(\theta_1 - \theta_2) \quad (30)$$

$$C_{22} = \delta_2 \quad (31)$$

$$C_{23} = L_2 l_3 m_3 \dot{\theta}_3 \sin(\theta_2 - \theta_3) \quad (32)$$

$$C_{31} = -L_1 l_3 m_3 \dot{\theta}_1 \sin(\theta_1 - \theta_2) \quad (33)$$

$$C_{32} = -L_2 l_3 m_3 \dot{\theta}_2 \sin(\theta_1 - \theta_2) \quad (34)$$

$$C_{33} = \delta_3 \quad (35)$$

The solution process of this systems is described next.

3. SOLUTION PROCESS OF THE DYNAMIC MATHEMATICAL MODEL

A change of variable is introduced as follows:

$$\omega_1 = \dot{\theta}_1 \quad (36)$$

$$\omega_2 = \dot{\theta}_2 \quad (37)$$

$$\omega_3 = \dot{\theta}_3 \quad (38)$$

This change of variable yields a modified system of equations which is amiable to numerical implementation:

$$[M_{ij}]\{\dot{\omega}_i\} + [C_{ij}]\{\omega_i\} = \{\tau_i\} \quad (39)$$

Pre-multiplying by $[M_{ij}]^{-1}$ yields:

$$\{\dot{\omega}_i\} = [M_{ij}]^{-1}\{\tau_i\} - [M_{ij}]^{-1}[C_{ij}]\{\omega_i\} \quad (40)$$

In the above equation the angular velocity is defined at the previous time step:

$$\{\omega_i\} = \begin{Bmatrix} \omega_1^{t-1} \\ \omega_2^{t-1} \\ \omega_3^{t-1} \end{Bmatrix} \quad (41)$$

The solution for the angular acceleration vector is advanced in time using a standard backward finite difference scheme as follows:

$$\{\dot{\omega}_i\} = \begin{Bmatrix} \frac{\omega_1^t - \omega_1^{t-1}}{\Delta t} \\ \frac{\omega_2^t - \omega_2^{t-1}}{\Delta t} \\ \frac{\omega_3^t - \omega_3^{t-1}}{\Delta t} \end{Bmatrix} \quad (42)$$

The recurring algorithm is applied until convergence (e.g. the equilibrium state of the dynamic system) is achieved.

Once the dynamic model is solved, acceleration time history at the mechanical platform interface can be obtained. These time histories are then used to estimate the expected shock response spectrum (SRS) resulting from deployment. The in-plane acceleration at the mechanical interface is estimated by computing the linear momentum of a system of particles and then using Newton's second law to estimate the acceleration of the centre of mass of the multi-body arrangement. By definition:

$$\vec{P}_{cm} = M\vec{v}_{cm} \quad (43)$$

where M is the total mass of the system, and P and v are vector quantities that refer to the momentum and velocity of the system, the sub-index cm indicates the centre of mass of the system. The right hand side of the equation can also be written as follows:

$$M\vec{v}_{cm} = \sum_{i=1}^n m_i\vec{v}_i \quad (44)$$

Therefore, the reaction forces at the mechanical interface of the antenna as a result of inertial effects can be expressed as follows:

$$F_{res} = \frac{d\vec{P}_{cm}}{dt} \quad (45)$$

Thus the acceleration at the mechanical interface can be estimated if the accelerations of the centre of mass of every member of the antenna are known, mathematically:

$$\vec{a}_{cm} = \frac{1}{M} \sum_{i=1}^n m_i\vec{a}_i \quad (46)$$

Once accelerations time histories have been computed, the time history response has to be converted into a frequency response format which can then be used in platform level shock test.

4. THE SHOCK RESPONSE SPECTRUM (SRS)

The shock energy released by shock events generally presents a complex waveform which tends to oscillate in a somewhat symmetric manner about a zero baseline. Its overall envelope has an exponential decay although lingering reverberation is also present. In most cases the resulting shock pulse is too complex to represent via a mathematical function in the time domain thus attempting to replicate a time dependant pulse during a test campaign would be a futile effort. Instead, the Shock Response Spectrum plot and analysis methodology is employed. In the SRS method the time history of the transient shock signal is spectrally decomposed into a signal depicting load (e.g. acceleration) as a function of natural frequencies which are logarithmically spaced at integer fractions of an octave. A typical scheme is based on a proportional bandwidth, such as 1/6 octave which means that each successive natural frequency is $2^{1/6}$ times the previous natural frequency. The SRS model captures the effect of a time history signal on a system comprising an infinite number of single-degree-of-freedom (SDOF) systems, each one with its unique natural frequency and typically with the same amplification factor Q . The SRS plot provides designers with a concise indication of the maximum dynamic loads various parts of the system will experience depending on their frequency and it provides test engineers with a way of ensuring repeatability during test. The SRS approach is unique in that rather than describing the response of dynamic systems to a given input pulse, the main goal is to capture the effects of the shock pulse on the system. SRS can thus be defined as a plot of peak responses of an infinite number of SDOF systems to an input transient. These SDOF systems can be regarded as "massless" in that they do not load the input. It is important to emphasize that the SRS is not a picture of the input pulse nor of any responses, neither does it provide the frequency content of the input; it simply bounds the peak response of all possible SDOF systems to a particular transient signal. The resulting SRS plots can thus be employed as a test specification which is not dependent on how the shock pulse is generated. In our specific case, the SRS plot resulting from deployment has been obtained using the Smallwood method details of which are provided in the referenced documents. Smallwood's is the most widely used algorithm for SRS calculation. His ramp invariant digital recursive filtering relation requires impulse

response functions, Laplace and Z transforms and its rigorous mathematical treatment it outside the scope of this paper. However, its application to the acceleration time history resulting from deployment is presented in the following section.

5. RESULTS

Damped dynamic deployment results and resulting SRS are presented in this section for the case of non-linear tape springs. The configuration and initial conditions of the problem are summarised in the following table.

Table 1: Main parameters of boom deployment problem

	Body 1	Body 2	Body 3
Initial conditions, Θ_i [rad]	-2.35	0.785	-2.35
Mass, m_i [kg]	0.25	0.25	0.25
Length, L_i [m]	0.308	0.308	0.321
Centre of mass, l_i [m]	0.106	0.154	0.249
Moment of Inertia, I_i [kgm ²]	1.42E-03	8.23E-04	1.05E-03
Damping coefficient, C [Nms/rad]	8.00E-03	8.00E-03	8.00E-03

The simulation time was 50 s.

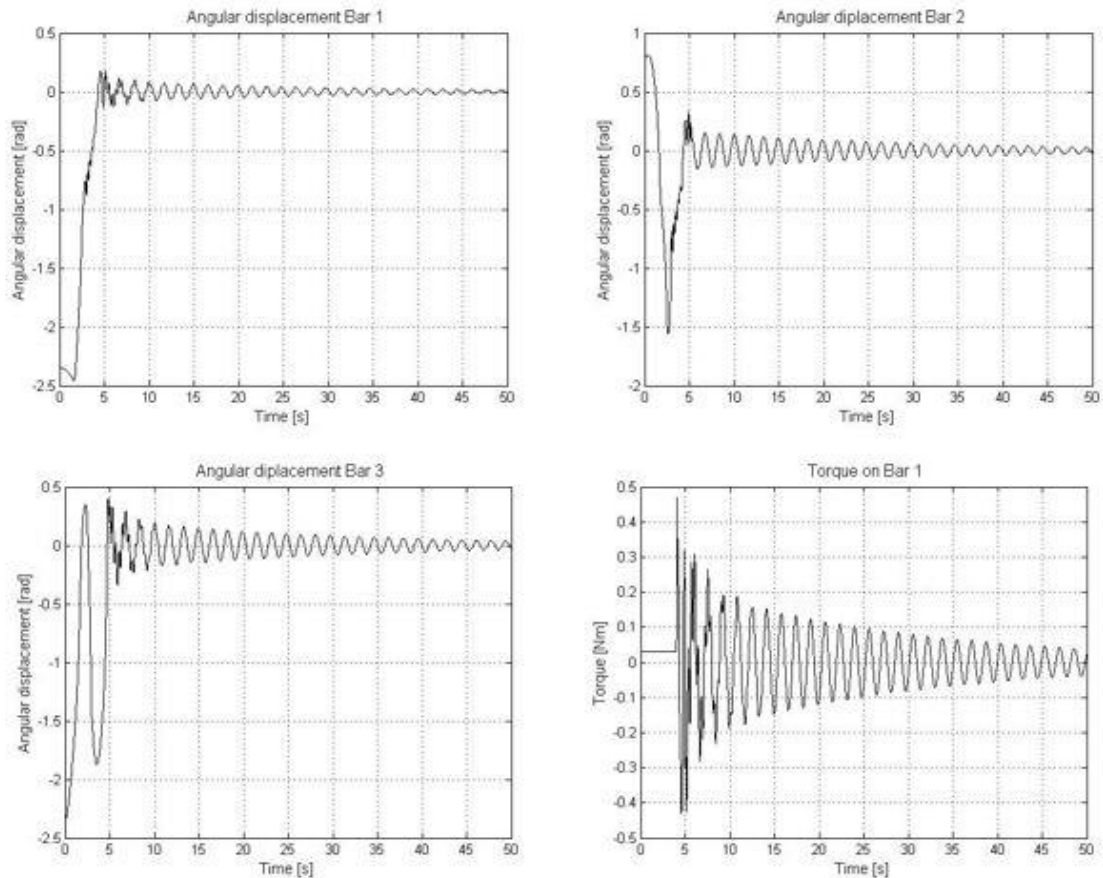


Fig. 3. Angular displacements and non-linear spring torque during deployment

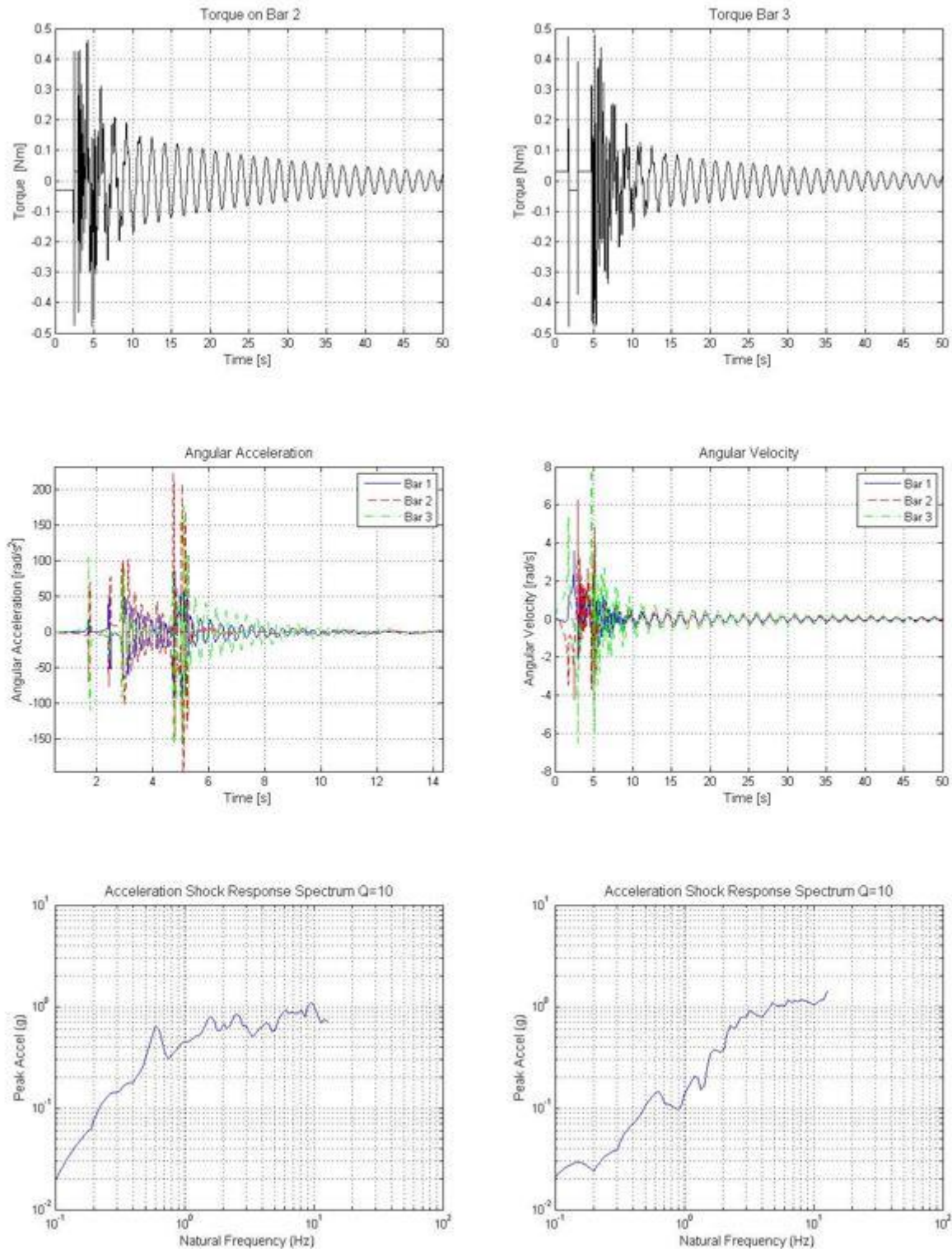


Fig. 4 Angular velocities, accelerations and resulting deployment-induced in-plane SRS, x(L) and y axis.

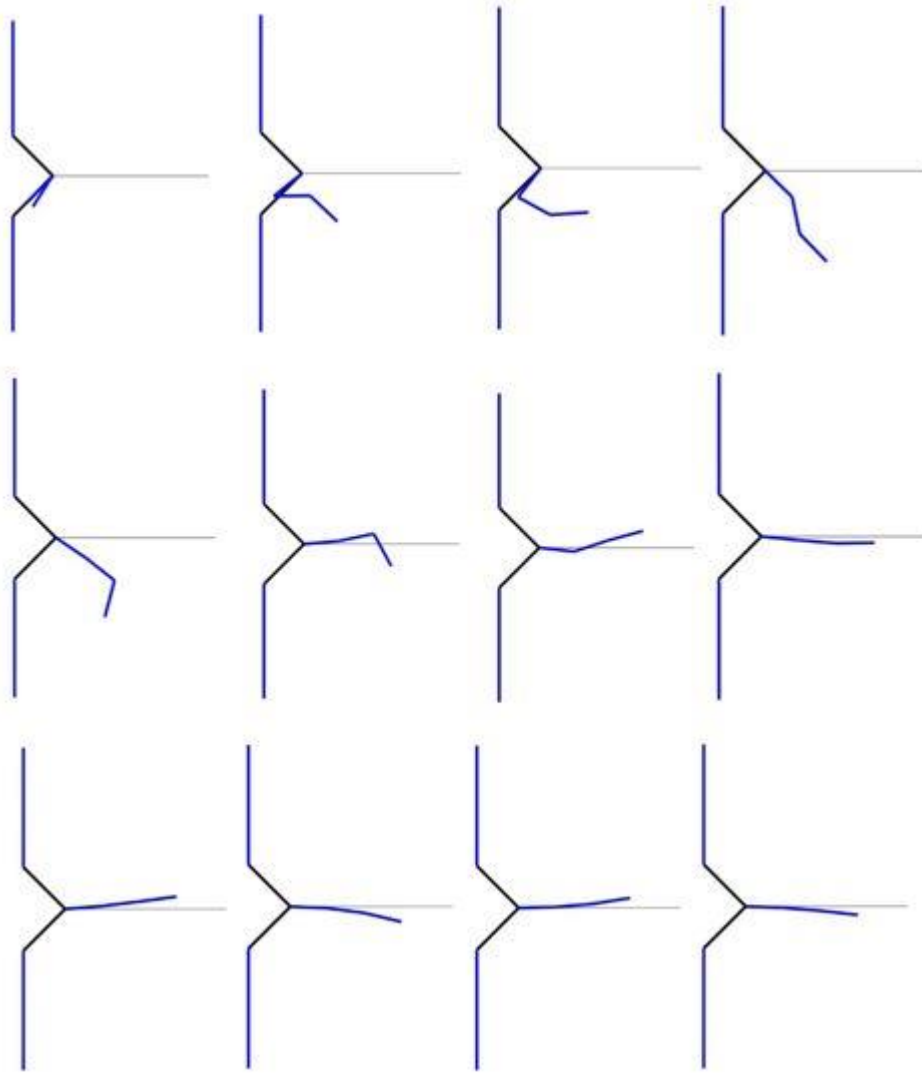


Fig. 5. Simulation visualisation. The first 10 seconds of deployment have been captured in this figure. Time vector runs from left to right and top to bottom.

6 CONCLUSIONS

An analytical approach to model shock impulse as a result of deployment of a multi element boom has been presented. The dynamic model to simulate the deployment of the boom by means of stored energy elements has been developed using Lagrangian mechanics. A recursive algorithm for the numerical solution of the governing equations was also provided. The SRS has been computed using Smallwood's recursive formula to calculate shock response. The combination of dynamic modelling and the SRS analysis provide an analytical avenue to ascertain whether a system will survive shock loading as a result of deployment of appendages. The approach presented can be particularly useful to the design engineer during early phases of product development as it provides a concise indication of the maximum loading his system will be exposed to during shock events. In addition it provides the test engineer with a test specification that is easily repeatable in laboratory conditions.

7 REFERENCES

- [1] D. Steinberg, *Vibration analysis for electronic equipment*, Wiley Inter-Science, ISBN 0-471-37685-X.
- [2] *Electronic component susceptibility to shock*, <http://www.congrex.nl/08c08/presentations/DAY2/S4-2.pdf>
- [3] *Shock handbook part 3: Shock damage risk assessment*, <http://www.congrex.nl/08c08/>.
- [4] A. Bogdanov, *Optimal control of a double inverted pendulum on a cart*, Technical Report CSE-04-006, December 2004
- [5] T. Irvine, *An introduction to the Shock Response Spectrum*, revision R, July 2010
- [6] W. Tustin and G. Hieber, *Understanding and measuring the shock response spectrum*, Spectral Dynamics Corporation, San Diego CA, Technical Publication No SSA-3 4-73
- [7] D. O. Smallwood, *An improved recursive formula for calculating shock response spectra*, Sandia National Laboratories, Shock and Vibration Bulletin, No. 51, May 1981
- [8] T. Irvine, *Derivation of the Filter Coefficients for Ramp Invariant Methods as Applied to Base Excitation of a Single Degree of Freedom System*, Revision B, April 2013

DUAL GRIDDED REFLECTORS - TECHNOLOGY DEVELOPEMENTS OVER 30 YEARS

N. Nathrath,

NTP, Neubiberg, Germany, ntp.nathrath@gmx.com

ABSTRACT

Dual gridded reflectors are widely used for Ku band antennas for satellite communication with linearly polarized signals. Gridding of the reflecting surface is introduced to reduce the inherent crosspolarization of single offset antennas. The concept requires two reflector shells arranged one behind the other in a special configuration.

The early development in the eighties started with a typical dielectrical reflector shell and a reflecting grid applied on its surface. This front shell then was put in front of a second reflector shell (rear shell), which can be fully reflective. Application of the front shell grid was a complicated process partly realized by hand. In the nineties the gridding process was further developed by introducing laser technology. The principal built up - dielectric shell with RF grid in front of it - has not been changed.

As the reflector is an RF& structural component which has to meet RF- and structural requirements (e.g. stiffness and eigenfrequencies) RF requirements limit the thickness of the shell to typically a quarter wavelength of the RF. This then limits the diameter of a free standing shell in Ku - band to about 1,2 m. Larger reflectors need additional structural elements inside, disturbing the RF performance.

New and ongoing developments initiated by ESA/ESTEC and realized within RUAG (Sweden) and HPS (Germany) in recent years have changed the concept fundamentally. The dielectric reflector shell is totally skipped and a free standing grid made of CFRP blades or rods has been realized. Of course also this new concepts cause technical problems which have to be overcome in the development.

1. INTRODUCTION

Offset reflector antennas suffer from field distortions by the oblique projection of feed fields into the reflectors aperture. The distortion increases with decreasing focal length (F/D -ratio). It causes two or four crosspolar lobes close to the main copolar beam direction – in case of linear polarization. For circular polarization a slight change in the main beam direction would result (so called beam squint).

Linearly polarized fields in the reflector aperture can be cleaned by making the reflector polarization sensitive in a sense, that only one polarization is reflected, while the orthogonal component is then fully transmitted. To allow for frequency reuse (i.e. both orthogonal field components have to be used for communication signals) a second system – feeds plus reflector shell - has to be arranged in a suitable configuration.

There are different geometrical solutions possible, but the preferred arrangement is such, to position two antenna systems – reflector shells with feeds in the related focal points - one behind the other, sharing the same aperture, but rotating the systems against each other by some degrees around a common geometrical axis (not necessarily the boresight axis). Typical rotation angles are in the range of ± 10 to 12 deg., depending on antenna geometry and coverage zones. These rotations have the effect to separate the two linear feedsystems geometrically. Feedsystems then have to be rerotated around their feed axes by the same angle, not to lose the polarization orthogonality .

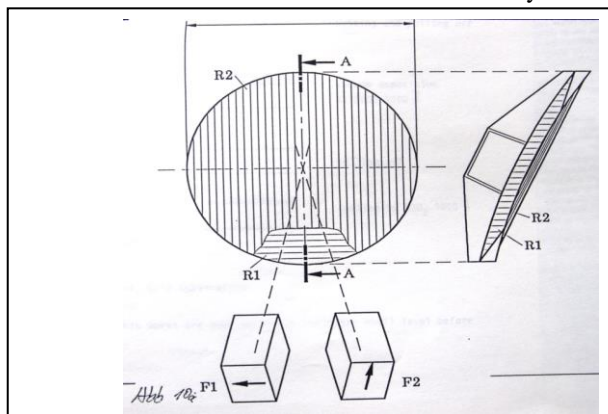
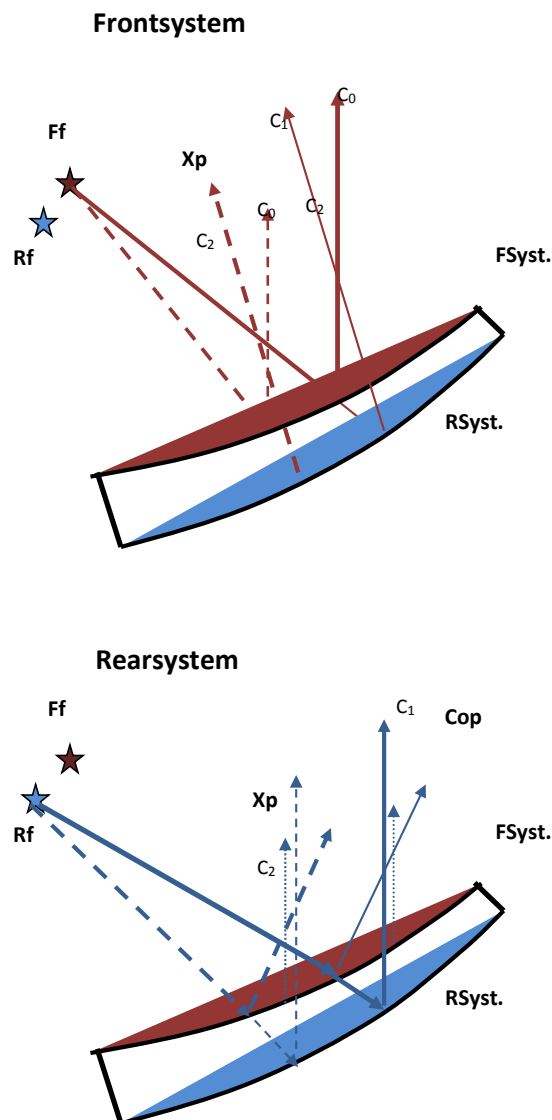


Fig.1: Principal Configuration of DGR Antenna System

. The RF effect of this arrangement is as each feed is defocussed wrt. the other reflector, that field components reflected by it will fall outside the copolar coverage. This then is the crosspolar cleaning effect wanted. Fig.1 shows a principle sketch of such a system and Fig. 2 contains the main ray paths. Fig. 3 and Fig.4 show the crosspolar reduction achieved by DGR system.

There are some general advantages of such dual polarization systems compared to a dual pol. feed illuminating a single solid reflector or a crosspolar compensated double reflector configuration:

- Short focal length (F/D about 0,7) is possible, resulting in compact potentially top deck antenna systems,
- single linearly polarized feeds are much simpler to build and allow high power to be transmitted
- Tx/Rx separation can easily be achieved
- Different coverages can be realized for each polarization



The RF analysis of the two grid configuration is not standard. It has to include three scattering contributions, i.e.

- that from the front grid (c_0),
- that from the rear grid (c_1),
- and a new scattering coming from the rear grid and hitting the front grid from the back side (c_2).

The various contributions are shown in Fig.2.

Main pattern contributions are depicted as thick lines –fully for Copol, broken for Xpol rays, minor contributions as thin lines,

Frontsystem radiation in red,
Rear system in blue colours.

The RF design then has to be such, that the main Xpol components are sufficiently far outside the copolar coverages –see Fig.5- and the minor Xpol contributions (falling into the main beam direction) are made sufficiently small. This is a requirement for scattering by dielectrics and their design (if present) and the Xpol reflection coefficients of the grids.

Fig.2: Main Ray Paths of Copol. and Crosspol. Pattern Contributions for Front and Rear System

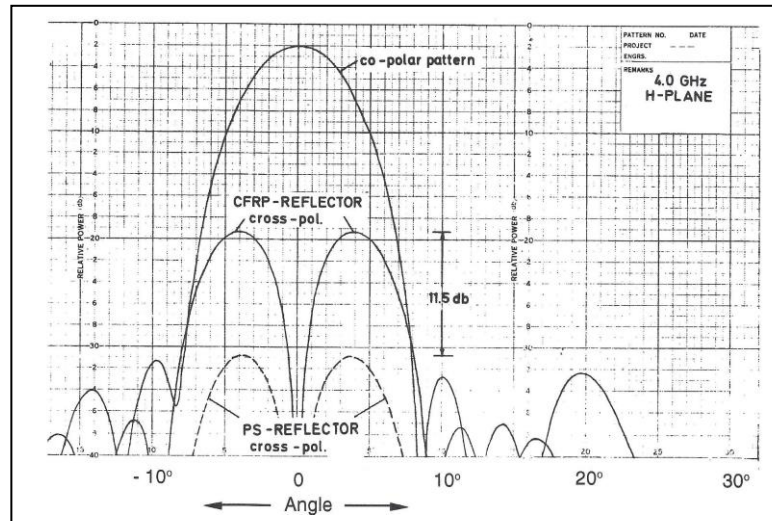


Fig.3: Typical Pattern of a Single Offset Antenna with CFRP- And Gridded Reflector (PSR)

2. GENERAL SOLUTIONS

The reflector shells have to be polarization sensitive – how is this achieved? “Normal” solid reflectors are isotropic conductive being made of fully electrically conductive material e.g. CFRP material or metallized surfaces. Reflectors used here have nonisotropic electrical conductivity, e.g. by applying metallic stripes or wires on a dielectric shell surface, thus forming a grid with parallel grid lines, parallel in their projection into the reflector aperture. For the RF performance it is sufficient to grid only the front reflector of a dual shell system. Then the copolar component of the front system is reflected in the right direction. The crosspolar fields being transmitted hit the rear reflector and are reflected defocused out of the coverage. The copolar fields of the rear system being transmitted by the front grid are then reflected by the second reflector into the right direction, while their crosspolar fields are deflected by the front grid, Fig.2. Therefore there are two general solutions of a so called DGR (dual gridded reflector) system possible:

- Both reflector shells gridded, orthogonally wrt. polarization arranged,
- Only one front grid in front of a solid rear shell.

3. RF-REQUIREMENTS TO BE REALIZED

All components used in realizing a DGR shell basically have to meet RF requirements and in addition of course structural and thermal requirements.

- Grid dimensions have to be defined such to give sufficiently high/low copolar/crosspolar reflectivity and low transmission losses. This results into typical dimensions strip-/wire distances of ca. $\lambda/10$ and strip/wire width of about $\lambda/30$.
- Shell dimensioning: if the grid is applied on top of a dielectric shell, this shell then will be by stiffness reasons a honeycomb with two face sheets. RF – components are on a reduced level being reflected by the face skins of the honeycomb. To minimize RF-reflections by the face skins the two reflected signals shall be out of phase - best by 180 deg.- to fully cancel these reflections. For this reason the two skins of the honeycomb have to be spaced by $\lambda/4$ of the RF wavelength. For C-band frequencies this is about 15mm, for Ku- band it is about 6 mm. Such thin reflector shells need some structural support to meet eigenfrequency requirements if their aperture size is more than e.g. 1,2 to 1,5 m. Such so called intercostals (Fig.5) can disturb the RF performance by some scattered fields. This then needs a careful RF-driven intercostal design.

- **Reflector shape**
Depending on the coverages required for each polarization the reflector surface can be a paraboloid or have a shaped contour. Shape and coverage may be different for each polarization. This also is an advantage compared to a single feed antenna system.
- **Configuration**
The arrangement of the two systems-feeds plus reflector shells is also driven by RF requirements. The defocussed Xpol Pattern for each polarization has to be deflected out of the related copolar coverage. The rotation angle between the systems needed then depends on the shape of the coverage and the focal length selected. The main pattern contributions for front and rear system as indicated in Fig. 2. can lead to pattern as in Fig.4.

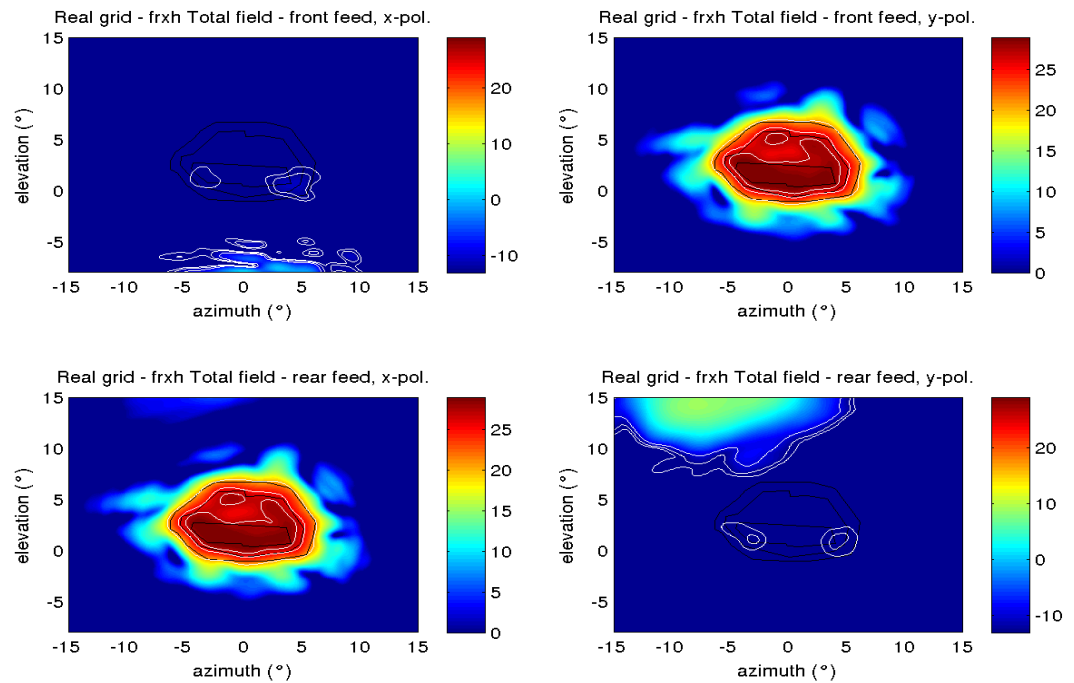


Fig 4: Examples of Crosspolar Cleaning By DGR: Co- and Crosspolar Pattern of Front – and Rear Shell of a Shaped DGR

4. STRUCTURAL AND THERMAL REQUIREMENTS

Structural and thermal requirements are standard as for all space antennas. Especially thermal distortion requirements may hardly be met for reflector shells made of non CFRP - dielectric materials, like Kevlar. Also moisture absorption effects have to be dealt with.

5. TECHNICAL SOLUTIONS –STANDARD CONCEPTS

Problems to overcome in realizing such a reflector system are manifold. The standard design of a DGR is to apply a metallic grid on a dielectric reflector shell. A fully new solution is to avoid dielectric material at all and to use CFRP material also for building the grid(s).

Changes and optimizations in the past concentrated then for many years in optimizing the process of gridding and the layout of struts between the shells (intercostals).

5.1. The gridding Process

Two fundamentally different methods have been applied:

- Create the grid on the completely manufactured sandwich shell by metallic vapor deposition, – as a last step
- create the grid on a foil, which then has to be glued onto the reflector surface,

5.1.1. Gridding of the dielectric sandwich shell

The problem here is, that a wet treatment of the sandwich has to be avoided. Thus photo etching processes are not allowed. This led to rather complex procedures:

One early approach introduced by MBB (later EADS Astrium) was to apply a layer of a special lacquer on the reflector surface, then cut by hand and a suited cutting tool parallel stripes, pull off each second lacquer stripe, and then apply a metallic Aluminum layer (about 1 micron thick) onto the surface. By pulling off the remaining lacquer stripes the final grid is created. This process (Fig.6) worked very well – a Ku band reflector has been developed as technical demonstrator-but of course was really laborious with a lot of hand work.

A big improvement was achieved by replacing the whole lacquer/cutting/pulling process by introducing a Laser to burn grooves into the Al layer again being created by vapor deposition. The reflector was moved on a numerically controlled machine and the fixed laser beam burned off the metal between the grid stripes. By selecting and optimizing the Laser parameters it was possible to achieve a good overall process (evaporation of the metal without violating the dielectric material below in an acceptable process time). This process being developed by MBB and Batelle institute has been patented and successfully been applied for a large C-band reflector within the flight program of the chinese telecommunication satellite DFH-3/1/.

The general advantage of both solutions was the possibility to easily create a grid with straight and parallel lines in the aperture of the reflector. On the reflector surface – depending the surface shape – this leads to slightly bended lines being non strictly straight and parallel.

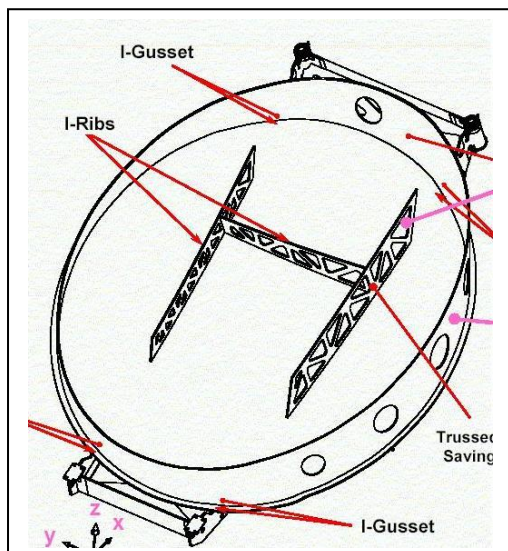


Fig. 5: Typical Configuration of Intercoastal Components

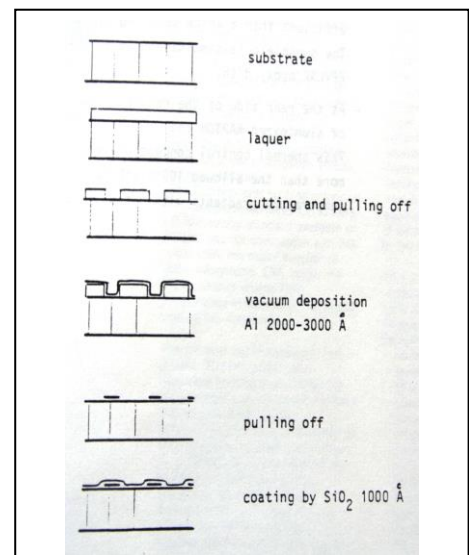


Fig.6: Grid Manufacturing by Al Vapor Deposition and Cutting Process

5.1.2. Gridding of a dielectric foil – e.g. Kapton

The grid can be created by a photo etching procedure in which the metal not needed - between the stripes - is removed in an etching bath after applying a grid mask by photo techniques. This process is standard, but the problem here is, that the total grid foil cannot be made as one piece, because the reflector surface is not flat but bent in three dimensions. Using non flexible material – like Kapton- the grid has to be composed by foil segments (stripes) being cut in a suited manner. The grid then is split in various parts, where the grid strips are aligned with the foil stripes. Each stripe is broader in its center and smaller at the ends and also the strip distance varies a little, so that in the aperture a straight strictly parallel grid pattern is achieved.

Even if this process is quite complex it nevertheless was the preferred one by reflector manufacturers e.g. COI (US) and AS (Les Muraux, France).

5.1.3. Further processes

There have been some ideas for new gridding processes being studied and also being patented:

- Apply the grid as CFRP rovings being placed by a 5 axes numerically controlled placing machine. This type of CFRP lay-up was intended to be used for manufacturing high precision optical mirrors. This process has been patented by MBB – Germany/2/, but in fact has never been applied.
- CO I(US) proposed to realize the grid by including thin Cu wires into the Kevlar weave, which finally builds the face skin of the reflector /3/. Although this process had been patented – to my knowledge it has not been applied. At least one of the problems associated with this process is an exact control of the grid lines position.

6. SHELL DESIGN

6.1. Standard design

The typical shell is made as a three element sandwich of Kevlar face skins and Nomex or Kevlar core. Its dimensions – thickness is determined to achieve minimum RF reflectivity. Main RF reflection stem from the face skins. As there are two contributions – front skin, rear skin – the skin distance ,i.e. core thickness can be selected such, that these two contributions will cancel at least for midband frequencies and typical incidence angles fully and get substantial reduction over the full frequency range (Fig. 7). This is a lambda-quart design with some 6mm/15 mm thickness for Ku/C-band antennas. Single face skin reflection can be in the order of some -20 dB. The combined signal then goes down substantially. This cancelation of course will be the less effective the wider the frequency bands are. For larger reflector apertures the sandwich with lambda-quart design gives not sufficient stiffness to meet eigenfrequency-requirements. Therefore additional structural elements – so called intercostals – have been put between the reflector shells (Fig.5). This is the standard process, whereby the intercostal design has to be made carefully to minimize RF scattering effects enhancing the crosspolarization.

6.2. Alternative concepts

Some concepts have been investigated to overcome some of the problems addressed:

- Multiple sandwiches
The shell then is built up of three or four face skins and two or three core layers. The core thicknesses are selected such, that the skin reflections cancel at two frequencies (Tx – as well as Rx- center frequency). The design is similar to a two pole filter. There are two advantages of such a design: the better RF performance and the total thickness and consequently stiffness of the shell is also higher. It is at least a little more than 2x lambda quart for the upper frequency, some 10 mm/25mm for Ku/C-band frequencies. Depending on the reflector size intercostals may not be needed then. Draw back of course is increased manufacturing complexity and higher mass. Typical reflection curve is shown in Fig. 8.

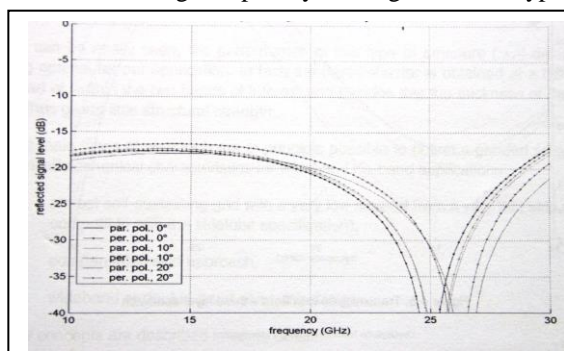


Fig.7: Typical Reflection Curve of a Threelayer Layer Sandwich ($\lambda/4$ Design)

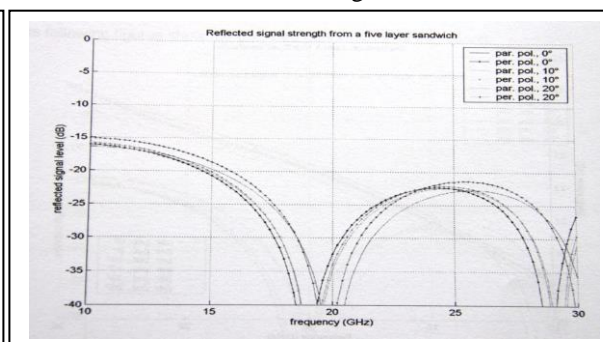


Fig.8: Typical Reflection Curve of a Five Sandwich, Dual Band Design

- Wedge concept

A second design approach was to increase the stiffness by filling the distance between front and rear shell of the two reflector system fully with core material. This then would give up RF – cancelation and also lead to a very unsymmetrical structural design associated with high mass. This concept then has been discarded.

- Double grid design

From the RF point of view the main aspect in shell design is to reduce its crosspol. reflections. As the field components reflected by a dielectric sheet and a metallic layer are opposite in phase, there is also the possibility of some cancelation. This then requires a double grid, one on the front and one on top the rear face skin. The grid design (strip width and distance) then has to be selected such as to compensate the reflection of the dielectric face skin. This concept has the big advantage, that the shell design especially the core height can be selected solely by structural requirements. Of course it adds some more complexity by the second grid and also mass by the thicker core, but thus could avoid intercostal struts. Multiple sandwich plus double grid design had got a Patent for EADS Casa (Spain), /4/.

7. EXAMPLES OF DGR SYSTEMS

The standard concept selected for space antennas is a gridded dielectric shell in front of a CFRP rearshell. Beam shaping – if required – is realized by a multifeedsystem illuminating parabolic reflectors or single feeds and shaped reflector shells.

7.1.1. DFH-3 – C-Band, /1/.

This is an example of a C-band Tx-/Rx- system with contoured beams over China. Beam contouring has been achieved with two multifeedsystems and large (2,1m) C-band Kevlar reflectors, both gridded. The antenna was successfully developed by MBB in the early nineties and finally flown on a Chinese satellite, Figs. 9,10.

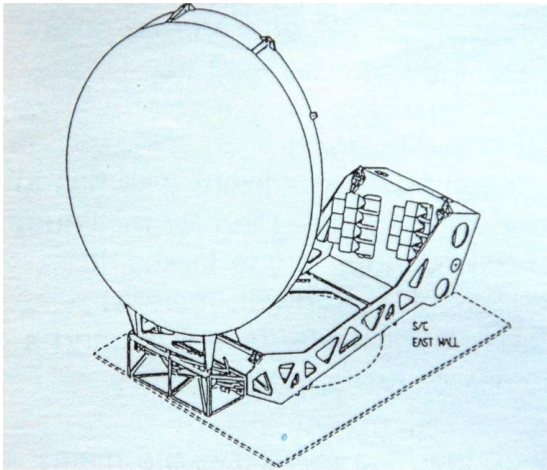


Fig.9: CAD Modell of DFH3 Antenna System

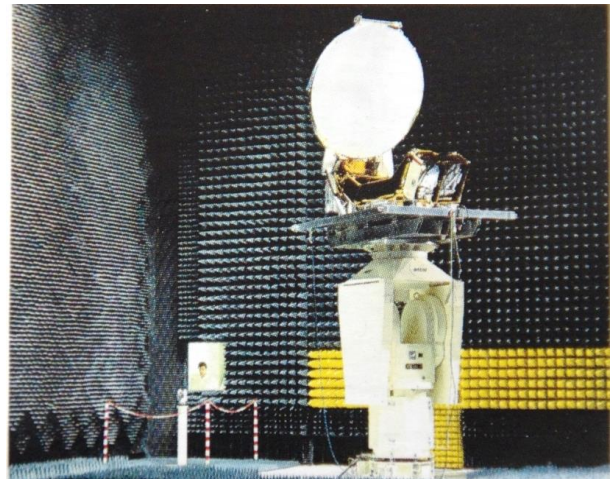


Fig. 10: DFH3 Antenna During CCR Test Campaign

7.2. Nahuel Ku-Band

Nahuel Ku- antenna illuminating the south American continent with 5 contoured beams was realized by shaped gridded reflectors and special dual band single feed systems, Fig.11. A further example of a shaped gridded reflector is shown in Fig.12.

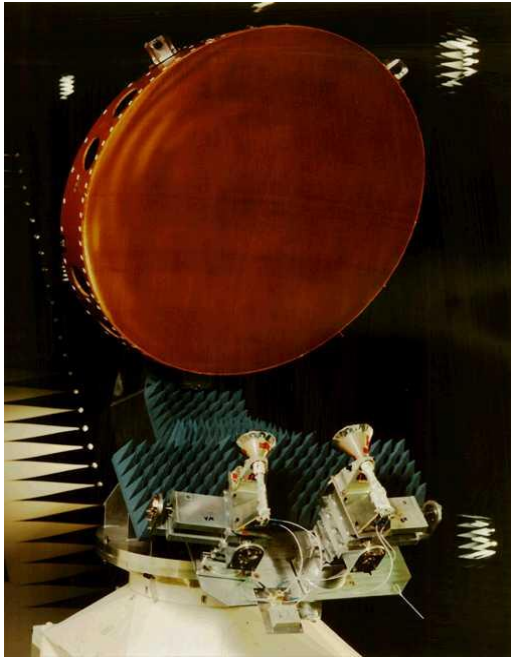


Fig.11: Nahuel Antenna Subsystem With Shaped DGR Illuminated by Single Two Band Feeds During CCR Tests



Fig.12: Example of a Shaped DGR (Front Shell), for the Program Express AM1 (EADS, Astrium)

8. TECHNICAL SOLUTIONS – NEW CONCEPTS

In recent time new concepts of a DGR antenna is being developed by RUAG/Sweden and HPS Munich under contract with ESTEC, /5,6/. Both concepts follow a completely new front shell design avoiding a dielectric shell supporting a grid. The grid is a freestanding structure made of CFRP vanes (RUAG) or CFRP wires (HPS), Fig13,14. Electrically the two types behave different: while the CFRP wire grid is a normal grid with same design parameters as wire grids on dielectric shells, the CFRP vane (or blade) grid behaves like a stack of parallel plate waveguides. Its b – dimension have to be under cut off for the RF frequencies, i.e. smaller than $\lambda/2$ for the upper frequency e.g. 14/5mm for Ku/Ka band.

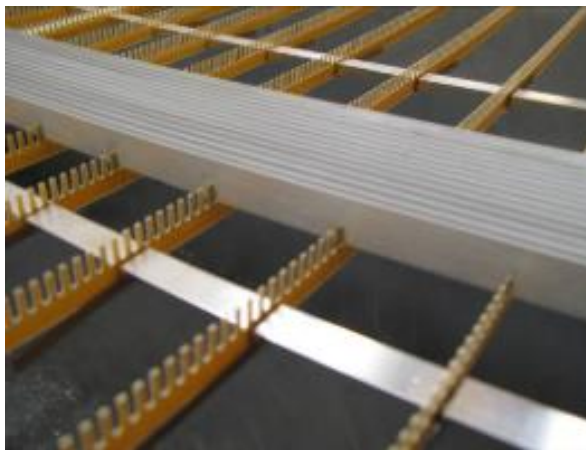


Fig.13: CFRP Grid Formed by Conducting Vanes (RUAG)

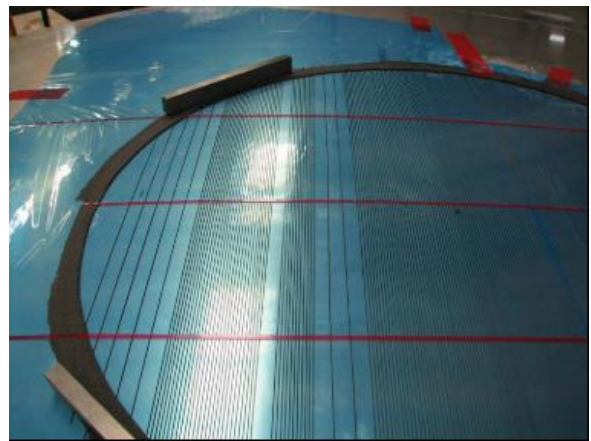


Fig. 14: Grid Formed by CFRP Wires (HPS)

In both designs the single grid elements (blades, wires) are not sufficiently stiff to form a reflector surface – potentially a shaped one. They need interconnections. The blades get a pectinate structure made of Kevlar and the CFRP wires are interconnected by some few CFRP cross wires. Their RF influence – although visible in the pattern is acceptable small and can be tolerated.

Rear shells in both cases were full CFRP solids.

EM reflectors for Ka frequencies of both concepts have been manufactured and partly been tested, Figs.15, 16,18.



Fig. 15: EQM Reflector for Ka Frequencies (RUAG) (HPS)

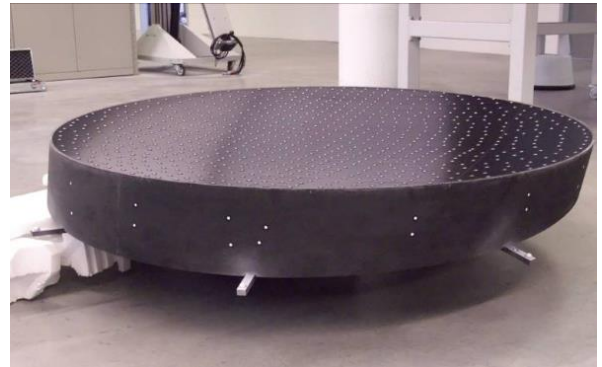


Fig. 16: EQM Reflector for Ka Frequencies

An ongoing follow on project with HPS now realizes the CFRP wire concept for KU band frequencies, /7/. The grid surface is shaped for an European three zone coverage as indicated in Fig.5. There are some improvements introduced compared to the first Ka design: to be even more lightweight there are two grid reflectors : front and rear grid. This then requires a new structural design. The stiff structural element is a so-called Omega ring (Fig. 19) supporting both grids, which also will provide the interface to the satellite platform.

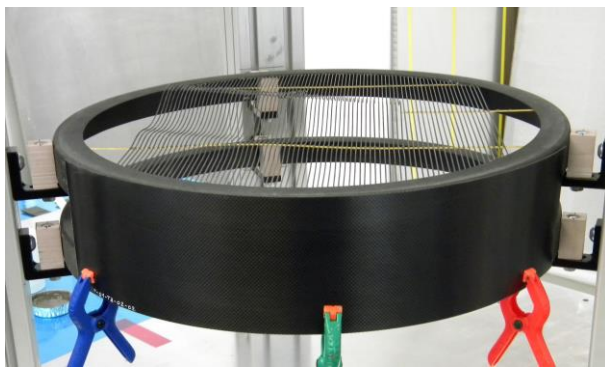


Fig. 17: Technical Demonstrator for a Shaped Grid (HPS)

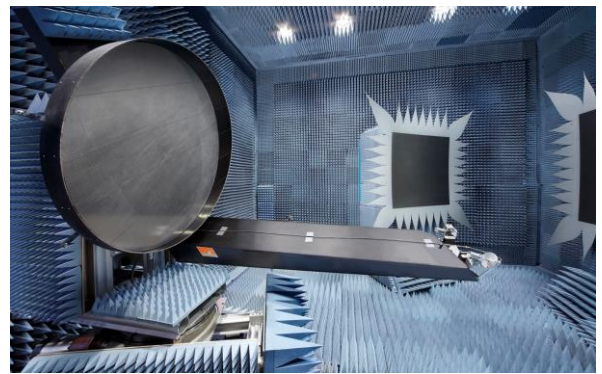


Fig. 18: Ka Reflector (HPS) During RF Test Campaign in CCR Of HM

For the shaped grids – a demonstrator is shown in Fig. 17 – each grid wire is manufactured in a separate flat mold in its required shape by INEGI (Portugal) and the whole grid then is composed within an integration mold. The grid itself is changed by replacing the CFRP cross wires by Quartzel wires. As being non conductive they do not disturb the RF performance. Their thermal expansion coefficient is sufficiently small – not too far from that of CFRP -. Thus the overall thermal stability is excellent.

The full CFRP concept has a lot of advantages compared to the Kevlar shell concepts: it is

- more lightweight, has
- better thermal stability and has less
- RF copolar transmission losses.

The grids for this new Ku-band reflector have already been manufactured and the integration is in progress.

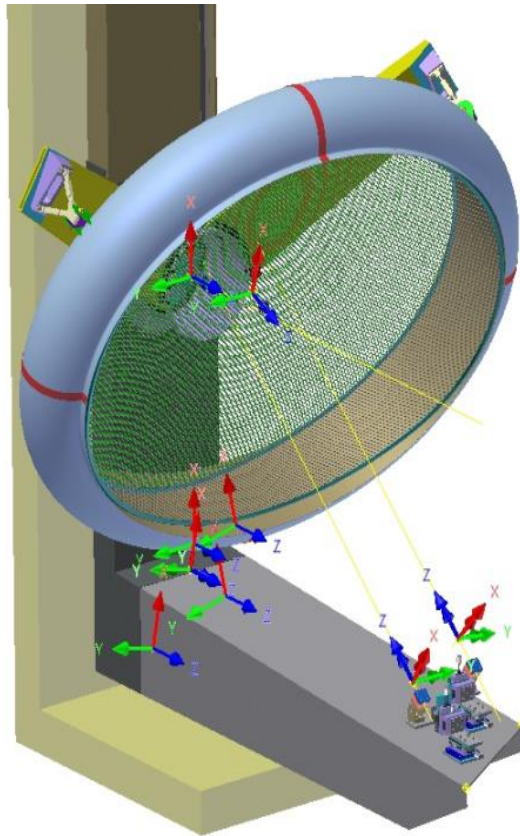


Fig. 19: CAD Model with Structural Element (Omega Ring) for The Dualgridded Ku Band Reflector of HPS

REFERENCES

- /1/. W. Schäfer, N.Nathrath, E. Golusda, G.A.E.Crone, R.Garcia Prieto; "Dual Gridded Reflector Technology", ESA Technology Programme Quarterly, Vol.2, No 4, December 1992.
- /2/. B.Abt, Th. Kutscheid, N.Nathrath, "Verfahren zur Herstellung Polarisationsselektiver Reflektoren", DE 197 13 735.0-35, Feb.2004.
- /3/. J.Marks, G.Pynchon, "Composite Antenna", US Pat. 5771027, June 1998
- /4/. C.E. Montesano Benito, E. Ozores Monge, " Process for Improving the Reflectivity of Reflective Surface Antennas" US Pat. 8, 317,960,B2, Nov. 2012
- /5/. RUAG Space AG, P-DGR-REP-00010-RSE, 23.10.2009.
- /6/ HPS GmbH, KaDGR-HPS-RP-010,7.12.2009.
- /7/ ESA, SOW " Dual Gridded Carbon Fibre Reinforced Plastic Reflector", Item 5B.087 , 9.6.2010.

ACKNOWLEDGEMENTS

Many thanks to my old friends from the Antenna community, who supported this work by providing pictures from various programmes: H. Wolf from EADS, now Airbus Defence and Space, D. Fasold from Hochschule München and C.Mangenot from ESA/ESTEC

MANUFACTURING PROCESS SIMULATION FOR A HIGH PRECISION COMPOSITE REFLECTOR

Liangyu Liu, Houfei Fang, Yang Zhou, Yongbin Wu, Xiaobin Mang, Yangqing Hou

Shanghai YS Information Technology Co., Ltd., Shanghai 200240, China

Email: 492449405@qq.com

ABSTRACT

A typical high precision Graphite Fiber Reinforced Composite (GFRC) reflector consists of three major parts: front panel; rib network; and back panel. The reflector manufacturing procedure includes curing the front panel on a mold in an autoclave; assembling composite ribs to form the rib network; incorporating the back panel to form the whole reflector; and removing the reflect from the mold. Unfortunately, high residual stress unavoidably occurs in the front panel during the curing process due to Coefficient of Thermal Expansion (CTE) mismatch between the mold and front panel. Residual stress in the front panel will seriously deform the reflector after the reflector is removed from the mold and degrade its surface precision. To minimize the fabrication introduced geometry error, this study tried to simulate the whole fabrication process. Based on the surface quality of the mold and the quality/quantity of the release agent being applied, the front panel may or may not slide on the mold during the curing process. These two scenarios require two different mold geometries and associate with two different simulation approaches. This study has developed two modeling techniques to accommodate these two scenarios. With the help of these simulation procedures, the design of the reflector can be optimized; the mold compensation can be precisely implemented.

1. INTRODUCTION

Carbon fiber composite materials increasingly show potential promise in aerospace structures due to superior performance, such as ultra-light weight, high specific elastic modulus and strength, low thermal expansion coefficient and high design flexibility in mechanical properties and configurations [1-5]. In recent years, it has had wide applications in the manufacturing of spacecraft antennas working in space environment of high vacuum, strong ultraviolet and charged particles radiation, intense alternating high and low temperature conditions. Lightweight carbon fiber composite material is gradually replacing the metal materials for fabricating the antennas. Fig.1 illustrates one example of the composite reflector made by COI [6].



Fig. 1. Lightweight and thermally stable composite reflector

The curing process of carbon fiber composite materials is the state change of resin from liquid to solid, which is a complex and drastic transformation process of thermal, chemical, and mechanical properties. High residual stress unavoidably occurs during the curing process. There are many factors that cause residual stress, but the major factor is the mismatch of Coefficient of Thermal Expansion (CTE) between the mold and front panel. This article focuses on the fabrication error introduced by the CTE mismatch.

During the curing process, composite materials are tightly pressed on the mold under the pressure of vacuum bags. Generally, the coefficient of thermal expansion of mold is greater than composite's. After curing, the residual stress left in the front panel will seriously deform the reflector after it is removed from the mold and degrade its surface precision. Figure 2 illustrate the interaction between mold and front panel [7].

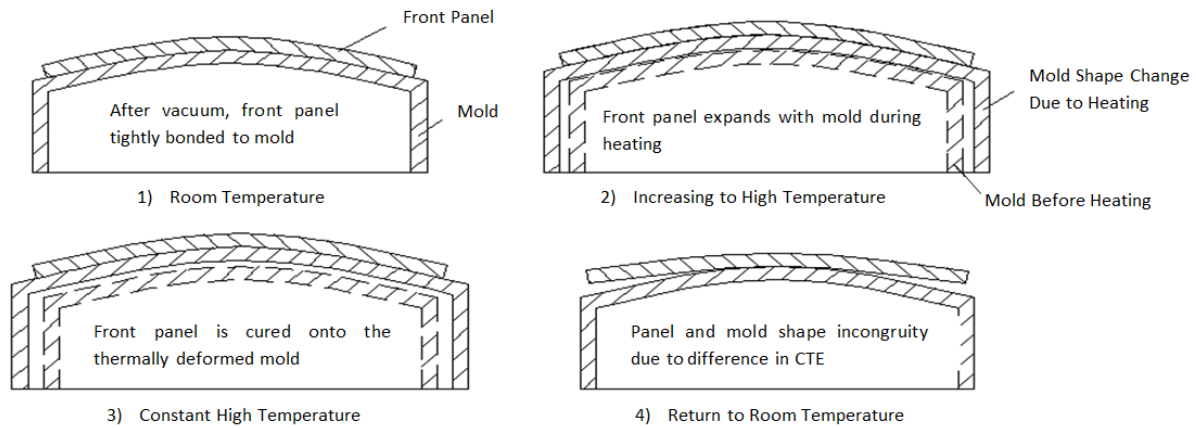


Fig. 2. The interaction between mold and product

2. SIMULATION OF REFLECTOR MANUFACTURING PROCESS

2.1. Introduction of Composite Reflector and Mold

We will simulate the manufacturing process for a 2 m diameter GFRC reflector. The GFRC reflector consists of three major parts: offset parabolic front panel, rib network and back panels. The supporting rib network is fabricated by assembling composite panels in three directions (i.e. 0° , 60° and 120°). 25 composite back panels connect to the rib network as illustrated in Fig. 3. The composite is formed by 8 layers $(0/45/-45/90)_s$ of unidirectional tapes and its Coefficient of Thermal Expansion (CTE) is almost equal to zero. Table 1 is the material parameters of unidirectional tape with thickness of 0.075mm.

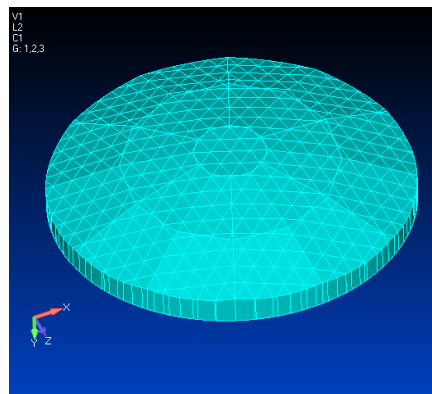


Fig. 3. Back panels of the 2-m diameter offset GFRC reflector

Table 1. Material parameters of unidirectional tape

$E_{11} (Pa)$	$E_{22} (Pa)$	ν_{12}	$G_{12} (Pa)$	$\rho (kg/m^3)$	$\alpha_{11} (/^\circ C)$	$\alpha_{22} (/^\circ C)$	Thickness (mm)
2.8e11	1.1e10	0.25	5.08e9	1500	5e-7	20e-6	0.075

The reflector is made on a mold. The mold has a quadrangular grids supporting structure, as illustrated in figure 4, and made of carbon fiber woven cloth. Table 2 gives parameters of the woven cloth.

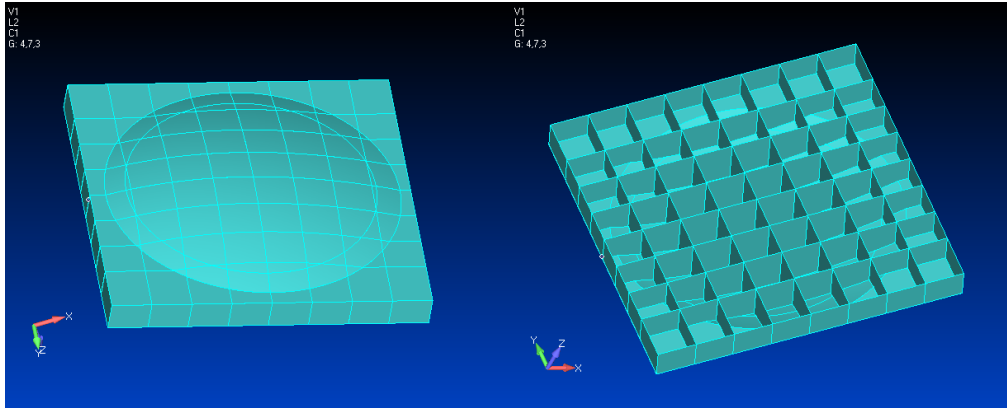


Fig. 4. Geometry of the composite mold

Table 2. Material parameters of carbon fiber woven cloth for the mold

$E_{11} (Pa)$	$E_{22} (Pa)$	ν_{12}	$G_{12} (Pa)$	$\rho (kg/m^3)$	$\alpha_{11} (/^{\circ}C)$	$\alpha_{22} (/^{\circ}C)$
6.81e10	6.81e10	0.05	3.2e9	1230	3e-6	3e-6

2.2. Introduction of Manufacturing Process Analysis

In general, the reflector manufacturing process has following steps: 1) pre-pregnant composites are laid up on the mold to form the front panel; 2) the front panel is cured in an autoclave with a given pressure, temperature and curing time; 3) the pressure and temperature are decreased to the ambient environment, curing process complete and residual stress occurs at this time; 4) composite ribs and back panels are assembled to form the whole reflector; 5) the reflector is separated from the mold, the reflector deforms from the mold geometry at this moment. Based on the surface quality of the mold and the quality/quantity of the release agent being applied, the front panel may or may not slide on the mold during the curing process. According to the above described, there are two different analysis methods: glue method and contact method.

The first simulation procedure assumes the front panel doesn't slide on the mold. Numerical simulation of the manufacturing process is conducted using finite element method, which takes into consideration of the CTE differences between the mold and the front panel. The behavior of the front panel under thermal load is represented by nodal positions and stress distribution. The interface between the front panel and the mold is modeled as rigidly connected. For the second scenario, simulation assumes the front panel does slide on the mold, and a nonlinear contact approach (i.e. permitting tangential displacement) is employed.

The first step of both analysis procedures is to calculate the stress distribution in the front panel that is introduced by high temperature curing as well as the CTE mismatch between the front panel and the mold. The second step of both analysis processes is to update the nodal locations of the front panel based on the results from the first step. Elements of rib network and back panels are created and assembled to the front panel to form the whole reflector model. The third step is to remove the elements of the mold and apply the residual stress distribution obtained from step one to the front panel. The as-built geometry of the reflector can thus be obtained, which includes the deformations introduced during the fabrication. Results of the aforementioned analyses are used to calculate the Root Mean Square (RMS) error of the reflector surface. These analysis procedures are further used to conduct the mold compensation analyses.

2.2.1. Glue Method

This method assumes the front panel does not slide on the mold during the curing process. The commercial software FEMAP is used to create and modify the Finite Element (FE) models, the NASTRAN is used for the analysis. Fig. 5 shows the analysis flow chart.

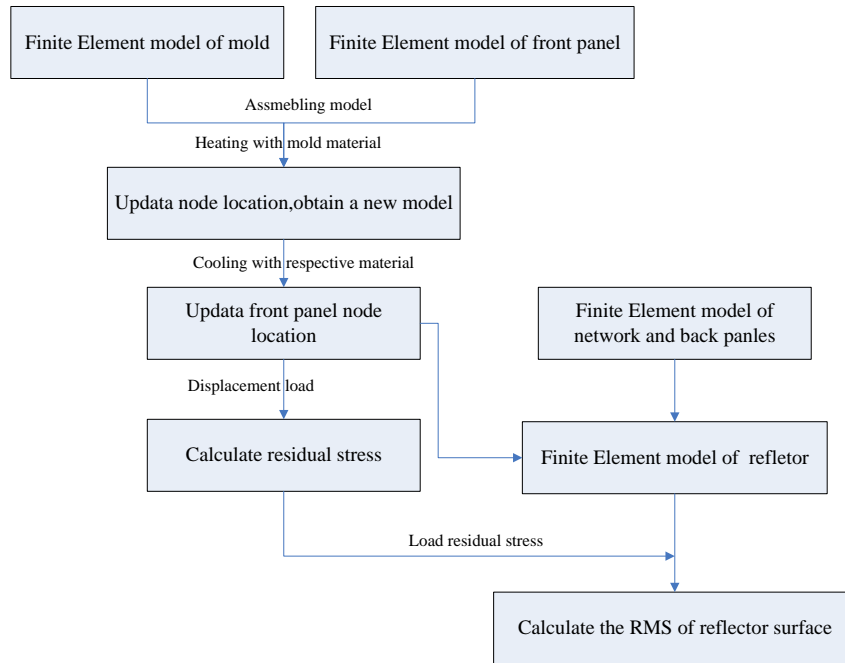


Fig. 5. Analysis flow chart of glue method

Figures 6-9 are results of the first approach:

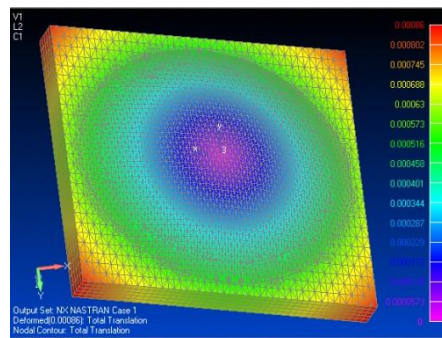


Fig. 6. Displacement of mold and front panel at curing temperature

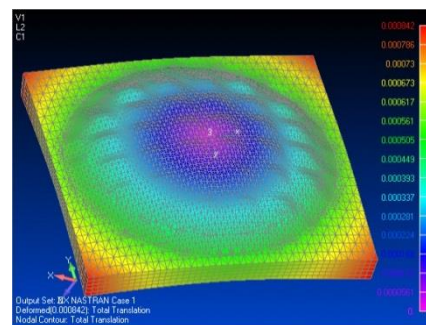


Fig. 7. Displacement (magnified 10 times) of mold and front panel after it is decreased to room temperature

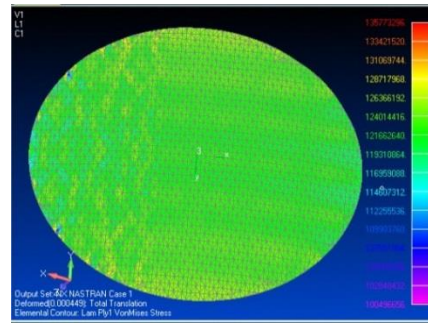


Fig. 8. Residual stress of the front panel after curing

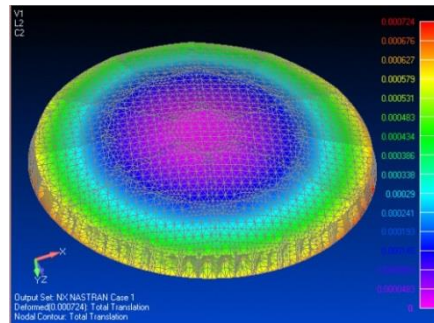


Fig. 9. Displacement (magnified 2 times) of GFRC reflector under residual stress

One can see that the displacement distributions in Fig. 6 and 7 are not exactly the same, even though the temperature changings are of the same magnitude. Displacement in Fig.6 is slightly greater than that of Fig. 7, this is because material properties of the front panel are different between pre-curing and post-curing. Print through is also observed in Fig. 7, this is mainly caused by CTE mismatch between the mold and front panel. Fig. 8 illustrates the residual stress. The residual stress is introduced during the curing process and its magnitude is significant, which seriously deforms the reflector after it is removed from the mold (see Fig. 9).

2.2.2. Contact Method

During curing process, due to the pressure of vacuum bags, there is no vertical displacement between front panel and mold. However, depends on the surface hardness and smoothness of the mold as well as the lubrication of release agent, the front panel sometimes can slide on the mold. Compared with glue method, the contact method considers tangential displacement between the mold and front panel, which will lead to much smaller residual stress and better surface precision.

Because of the powerful nonlinear calculation capability of MARC, we selected MARC for the simulation. In contact analysis, contact is defined by contact pairs, which consists of contact body and target body. Contact body is a deformed body while the target can be a deformed or rigid body. Generally, the body with much higher stiffness is defined as a rigid. We defined the front panel as a contact body and the surface of mold as a deformable target body. In order to ensure the calculation precision, the element density of front panel is greater than that of the mold surface. Figure 10 is the finite element model of the whole system. The model is formed by shell elements.

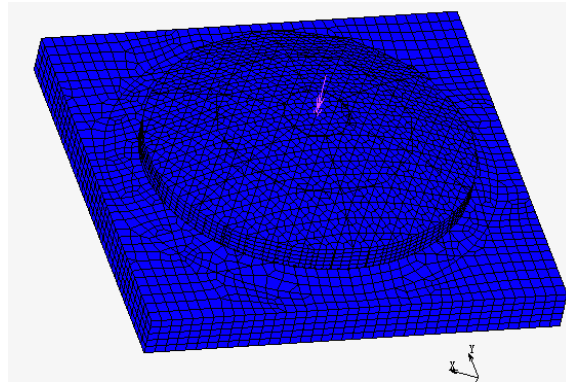


Fig. 10. Finite element model of the reflector and mold

Special attention should be paid to the offset parameter and direction (pointing to the contact bodies) of a shell element. Contact type, boundary type and contact area are the three key points for the definition of a contact pair. Meanwhile, contact parameters, load parameters, iterative parameters and output parameters need to be defined in the solution module. Contact parameters and iterative parameters are critical to the convergence of the nonlinear analysis. The contact parameters consist of contact control method, tolerance, friction model and contact table. Convergence method and parameters setting is the most important part in the iterative process. By introducing the nonlinear contact, the time spent to calculate greatly increases. Figure 11 is the analysis flow chart of contact method.

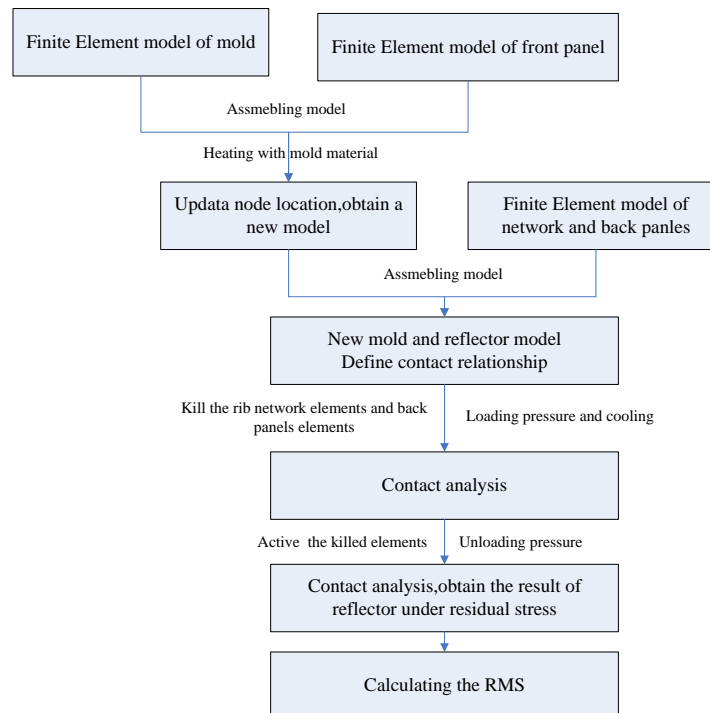


Fig. 11. Analysis flow chart of contact method

Figs. 12 and 13 are the temperature and pressure changing with time of the autoclave.

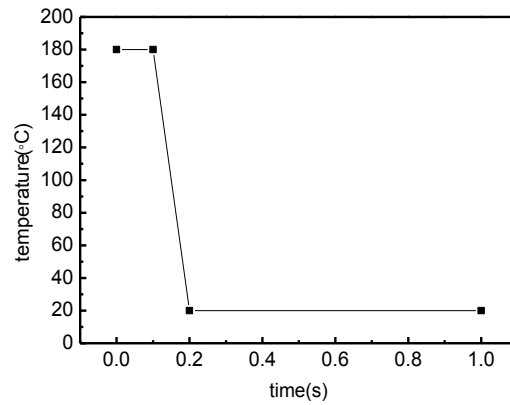


Fig. 12. Temperature-time curve

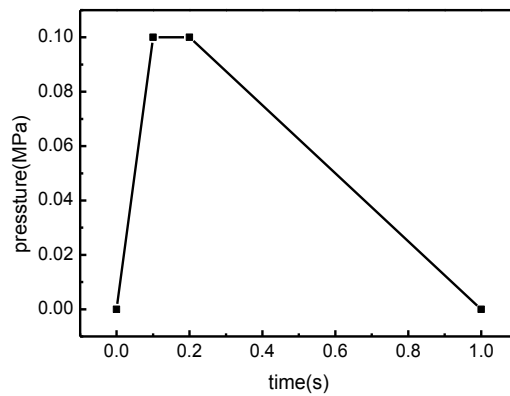


Fig. 13. Pressure-time curve

As illustrated in Fig. 14, the vacuum bag is simulated by applying pressure on both mold surface and front panel. The pressure is equal in magnitude and opposite in direction.

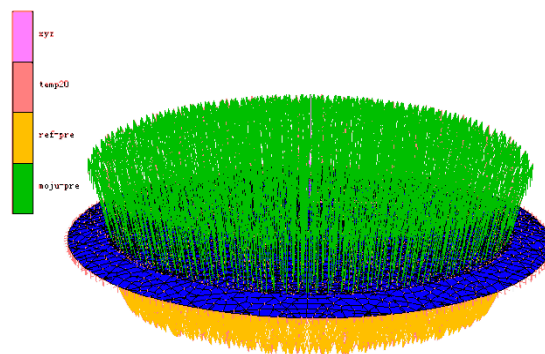


Fig. 14. Simulation of vacuum bags by pressure

Figs. 15-16 are the results of contact analysis:

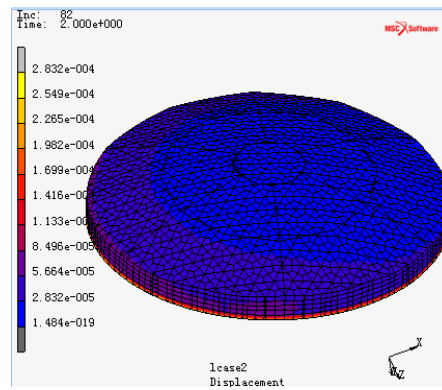


Fig. 15. Deformation of the reflector after the contact analysis

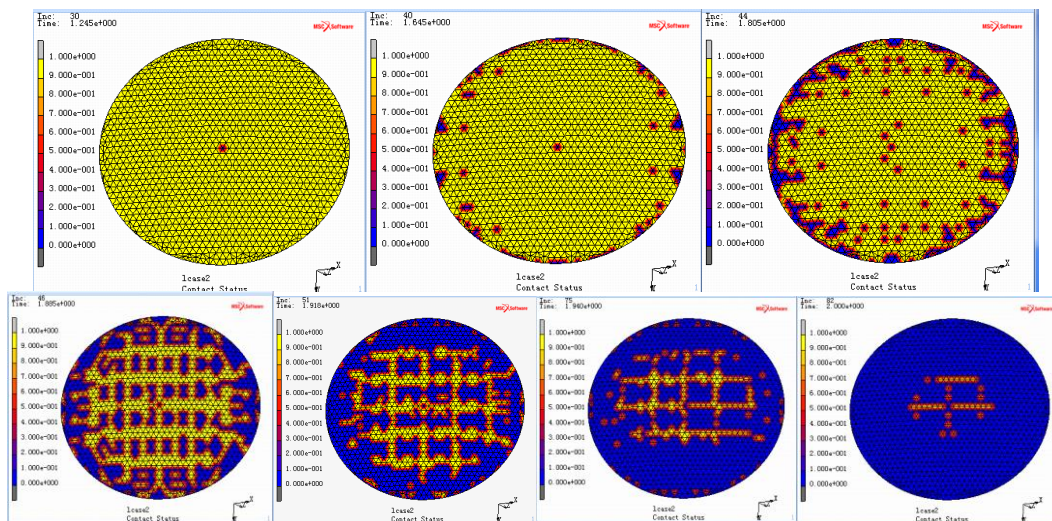


Fig. 16. Contact states at different time

Since the first step between glue method and contact method are the same, therefore the deformation introduced by temperature increasing from room to curing temperature is identical to what is given in Fig. 6. Fig.15 gives the deformation of the reflector, which is with respect to the status when the mold and front panel is in the curing temperature (Fig. 6). Results from Fig. 6 and Fig.15 are then used to conduct the RMS analysis. Figure 16 gives contact status change of the reflector during depressurization and separation between mold and front panel, yellow represents full contact and blue represents separate.

2.3. Surface Precision

Compared to ideal parabolic, the RMS results of both deformed reflectors are given in table 3.

Table 3. RMS results obtained from different analysis methods

	Contact method	Glue method
RMS (m)	1.2195e-5	1.6251e-5

It can be observed from 3, allowing front panel to slide on the mold offers a better surface accuracy than that of rigidly connected.

3. MOLD COMPENSATION

In order to improve the RMS of reflector surface, it is necessary to make a numerical compensation for the mold. Table 4 gives the compensation results by employing glue method. Total three iterations were conducted to have sufficient

precision.

Table 4. Results of mold compensation

	Original	Compensation 1	Compensation 2	Compensation 3
RMS	1.6251e-5	7.0554e-7	2.356e-7	1.8606e-7

Mold compensation can greatly improve the accuracy of reflector surface.

4. CONCLUSIONS

Two analytic methods for simulating the reflector fabrication process have been developed. Print through on the front panel and back panel has been observed by this study. Considering the residual stress introduced by CTE mismatch between the mold and front panel, the rigid connection method gives much higher stress level than that of slide contact method, so is the RMS results. After three iterations of the mold compensation analysis, the accuracy of reflector surface has been significantly improved. Since the front panel can or cannot slide on the mold during the curing stage has a great impact to the surface precision of the reflector, how to fabricate a mold with very smooth and hard surface is extremely important. In conclusion, analysis procedures presented by this paper can provide constructive advice for the manufacturing of a high precision composite reflector.

REFERENCES:

- [1]. Soykasap O., Lin Tze Tan, "High-precision Offset Stiffened Springback Composite Reflectors," *AIAA Journal*, vol. 49, pp. 2144-51, Oct. 2011.
- [2]. Tremblay Gary A., and Eddy A. Derby, "Design and Manufacture of an Ultra-Lightweight Solid Deployable Reflector," *SPIE Proceedings*, vol. 1532, pp. 114-23, December 1991.
- [3]. Changling Hao, Xianbin Zhou, Xiaoqiang Li, "Solution to Boundary-value Problems in Fabrication of High-precision Reflector Panels," *Chinese Journal of Aeronautics*, vol. 22, pp. 97-104, February 2009.
- [4]. Lang, Michael, Baier, Horst, Ernst, and Thomas, "Surface accuracy prediction and optimization of a high precision Q/V-Band reflector," *AIAA/ASME/ASCE/AHS/ASC Structures, Structural Dynamics and Materials Conference*, vol. 10, pp 7413-7426, 2006.
- [5]. Valsecchi, G., Franchini, C., Prieto, R.C., and Van't Klooster, K., "Nickel sandwich technology for high precision reflector antennas," *IEEE Antennas and Propagation Society International Symposium*, vol. 3, pp. 2170-3, 1999.
- [6]. S. J. Connell, and A. Abusafieh, "Lightweight Space Mirrors from Carbon Fiber Composites," *SAMPE Journal*, vol. 38, pp. 46-55, July/August 2002.
- [7]. H. Fang, P. Huang, Y. Zhou, L. Liu, Y. Liang, W. Jiang, S. Zhang, "Analytical Investigation of a High Precision Reflector," *AIAA Science and Technology Forum and Exposition (SciTech 2014)*, National Harbor, Maryland, pp. 13-17, January 2014

A novel press-bending forming shell structure for parabolic cylinder reflectors

Huifeng Tan⁽¹⁾, Liuyi Yang⁽¹⁾, Rongrong Xu⁽²⁾, Xilin Luo⁽¹⁾, Hao Liu⁽²⁾

⁽¹⁾Affiliation

Center for Composite Materials and Structures, Harbin Institute of Technology, China

Email: tanhf@hit.edu.cn, yangliuyi439@163.com

⁽²⁾Affiliation

Tianhe Navigation Communication Technology Co., Ltd., China

Email: arron_xu@126.com

ABSTRACT

A novel shell architecture for large parabolic cylinder reflectors based on press-bending forming technology is proposed. The innovative PBF technology for flexible shell structures is presented according to Euler-Bernoulli beams theory. Then the boundary conditions for parabolic profile are analyzed and the calculate method of surface RMS is improved. A 1400mm×1000mm test model was fabricated with overall surface RMS of 4.68 mm and centre one third RMS of 1.53mm before tuning. Results indicate that the creep effects should be addressed to meet the required accuracy in a follow-on program.

1. INTRODUCTION

As the Tropical Rainfall Measuring Mission (TRMM) has successfully demonstrated the feasibility of measuring rainfall using spaceborne antenna, to enhance the performance of the precipitation radar and realize lightweight, a parabolic cylinder reflector has been researched for the next generation of precipitation radar. The new reflector is designed to be rolled up around a rigid mandrel when stowed, and the cylindrical bundle are desired with a launch volume no greater than a square cross section of 1.3m×1.3m and 5.3m in length. Once in space, the thin film reflector can be deployed in the space propelled by elasticity energy or inflatable booms [1][2]. Several system level concepts have been developed, including “Hybrid Chain Link with Inflatable Rigidizable Boom and Rib”, “Precision Formed U-shaped Boom with Compressive Membrane Supports” and “Precision Chain System”. A half-size (2.65m×2.65m) antenna prototype model was built, which can be only able to achieve a 2-mm RMS accuracy [3]. To investigate the influence of the gravity, a 1-m-scale model of the parabolic antenna fixed on the high precision mandrel through turning screw has been tested for surface accuracy in both 0-and 1-g [4]. The test results indicate that the tension of the thin film has great influence on the membrane wrinkling, which is the reason for degradation of the surface accuracy. The thin film can't be wrinkle free in 0-g case, and the configuration can't meet the RMS accuracy levels desired [5].

Since the thin film panels supported in tension are prone to out-of-plane rippling, two efforts should be done to overcome this problem. The first one is to reduce the effective Poisson's ratio of the thin film material, which has been studied in [6]. The second is to increase the compressive resistance of the surface material. High flexible ultra-thin shell structures made of CFRP or CFRS may be reasonable replacers. Thin shell antenna enjoyed the advantages of high surface accuracy, and had been researched widely. A flexible reflecting surface material composed of CFRS had been developed in [7], which can be used in large space deployable reflectors. The stowage and deployment strength of thin CFRP shell reflectors had been studied and the ways to reduce the creep effects had been researched in [8]. A ultra-thin shell structure demonstrator for offset parabolic reflector had been designed and tested in [9].

In a preliminary study, a novel shell architecture for parabolic cylinder reflectors basing on the press-bending forming

(PBF) technology is proposed. The boundary conditions for parabolic cylinder are analyzed. A $1400\text{mm} \times 1000\text{mm}$ test model was fabricated and a loading device which can be used to load compression and bending load was developed. The test model was loaded depending on the analytical angles and displacement, then the surface accuracy testing of the model was conducted.

2. PBF TECHNOLOGY FOR FLEXIBLE SHELL STRUCTURES

Once subjected to press-bending load, shell structures with certain rigidity will changed in different shapes. As to the unidirectional curvature of parabolic cylinder reflectors, a desired curvature surface can be developed by enforcing the shell structures with certain displacements and rotation.

A PBF method is proposed to realize the wanted surface in Fig.1. The flexible shell structure is connected to the gripping jaws on the two ends. The gripping jaws are hinged to the fixed ends. One of the fixed ends can be fixed on the satellite bus, while the other one could be extended away from the satellite. The displacement between the two fixed ends can be controlled through ropes or inflatable rigidizable booms. Some gears and hinges can be designed to rotate the gripping jaws to a certain angles. Once the displacements and the angles are loaded, a related curvature surface can be obtained.

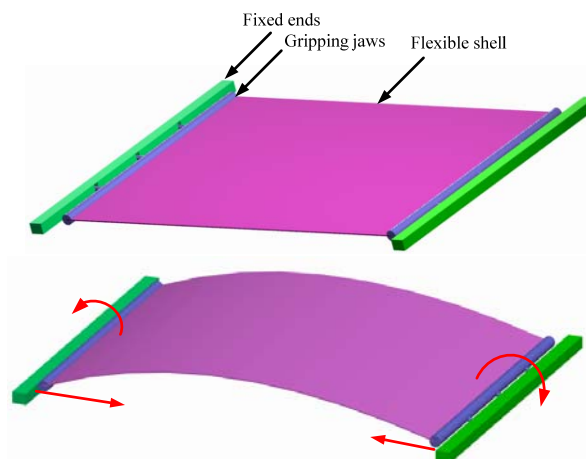


Fig. 1. Press-bending forming architecture

Cross section rigidity of the shell structure will affect the surface configuration. Assuming no warping effect, the flexible shell structures can be simplified as flexible beams subjected to tip point loads. Then the Euler-Bernoulli beams theory can be used to study the surface configuration. Fig.2 depicts a schematic view of a cantilever beam subjected to a combined tip point loading [10]. M_0 , P and Q are, respectively, general moment, horizontal force and vertical force. a and b are, respectively, the x and y coordinates of the flexible beam after deformation.

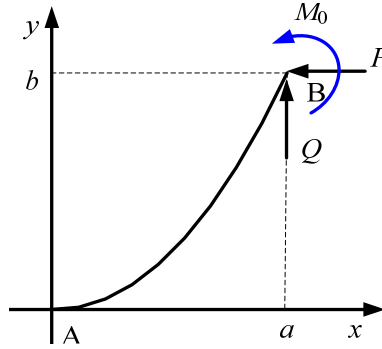


Fig. 2. A schematic view of a cantilever beam subject to concentrated loads

Depending on the Euler-Bernoulli beams theory, there is the curvature-moment relation as shown in Equation(1).

$$EI \frac{\ddot{y}}{(1 + \dot{y}^2)^{3/2}} = Q(a - x) + P(b - y) + M_0 \quad (1)$$

Where, E is the Young's modulus, and I is the inertia moment of the cross section. The choice of the material E, the cross section inertia moment I, and the values of M_0 , P and Q play crucial roles in the configuration of the flexible beam. Different configurations can be obtained under different load cases through solving (1).

As one of differential equations, (1) can be solved using elliptic integrals. Since an elliptic integral ultimately relies on numerical values, a numerical method for the differential equation has been developed basing on the Runge-Kutta method.

3. BOUNDARY CONDITIONS OF PARABOLIC PROFILE

Theoretic boundary conditions for parabolic profile are given as shown in Fig.3.

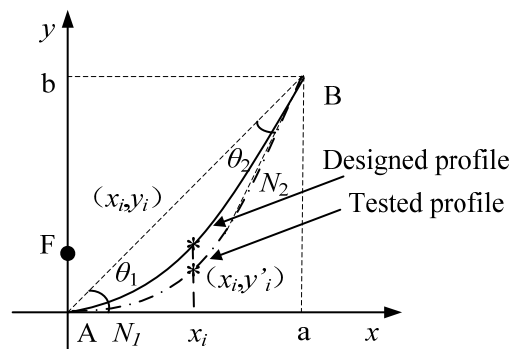


Fig. 3. Boundary conditions for parabolic cylinder

The profile of the parabolic cylinder can be described as:

$$y = \frac{x^2}{4F} \quad (2)$$

Where, F is the focal length.

The chord length l can be calculated as:

$$l = a \sqrt{1 + \left(\frac{a}{4F} \right)^2} \quad (3)$$

The values of θ_1 and θ_2 can be obtained by Equation (4).

$$\begin{cases} \theta_1 = \arctan \frac{a}{4F} \\ \theta_2 = \arctan \frac{a}{2F} - \arctan \frac{a}{4F} \end{cases} \quad (4)$$

For a parabolic cylinder reflector, the parabolic profile can be found analytically once the focal length, aperture distance, and offset distance of the reflector are made certain.

The theoretical parabolic profile is defined in XY coordinate system as in(2).The root mean square error(RMS) for y direction can be calculated considering the designed profile and tested profile as follows:

$$\varepsilon_{\text{rms}} = \sqrt{\frac{\sum_{i=1}^n (y_i - y_i')^2}{n}} \quad (5)$$

Where ε_{rms} is the RMS, n is the number of tested points, y_i' is the coordinate of a tested points on the tested profile and y_i is the corresponding coordinate of a point on the theoretical parabolic profile as shown in Fig.3.

4. MODEL ACCURACY TEST AND ANALYSIS

A plain-woven carbon/epoxy composite flexible plate with 1400mm length and 1000mm width was fabricated for test. The test model has a surface thickness of 0.12mm and an areal density of 184g/m². The material properties of the reflective surface are obtained as: $E_1 = E_2 = 60\text{GPa}$, $\nu = 0.34$ and $\rho = 1533\text{kg/m}^3$.

The genetic algorithm has been used to determine the best values of the loads through solving(1),and the overall accuracy RMS is 0.33mm, as shown in Fig.4.The optimization loads are obtained as $M_0 = 0.009\text{N}\cdot\text{m}$, $P = 0.004\text{N}$, and $Q = 0.005\text{N}$.

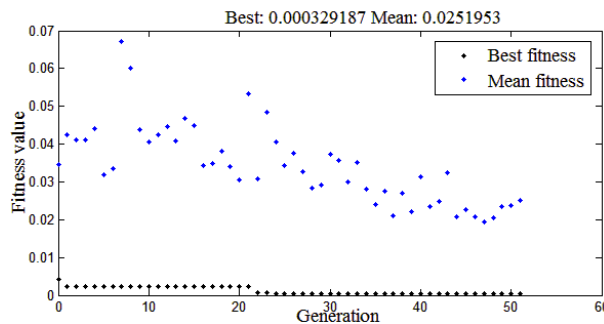


Fig. 4. Fitness value vs generation

A loading device which can be used to load compression and bending load was developed as shown in Fig.4. The test

model was loaded depending on the analytical boundary conditions. Video-Simultaneous Triangulation and Resection System(V-STARS) was used to test the surface accuracy of the model with 477 targets and 13 code targets as shown in Fig.5. There is an interval of about 50mm between two near targets and the test system with test RMS of 0.04mm.

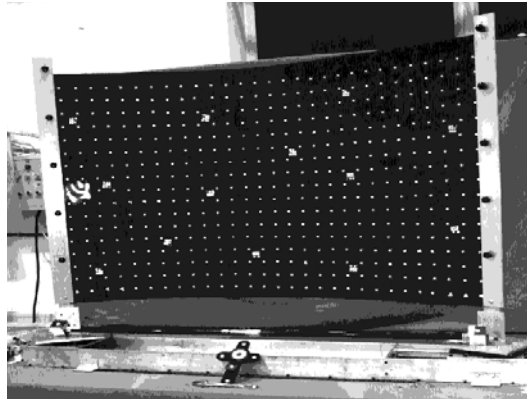


Fig. 5. Test model(1400×1000) with targets and Auto bar

The test model with an overall RMS of 4.6mm and the centre one third showed an RMS of 1.53mm as shown in Fig.6. The results indicate that the centre one third profile is fairly accurate, but due to the residual deformation of the two ends of the flexible shell surface, the overall RMS value is poor. Once the flexible shell was rolled out, tip curl occurred with nearly 5mm height parallel to the bending axis. Creep effects must be addressed when flexible shell fabricated in the following study.

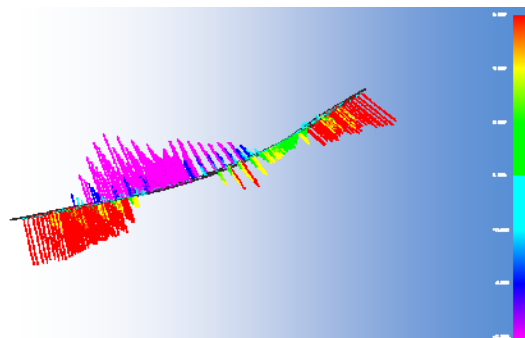


Fig. 6. Initial accuracy test result of the model, side view

5. CONCLUSION

A novel shell architecture for large parabolic cylinder reflectors based on PBF technology is proposed. This type of shell structure can provide a highly compact stowage volume, high accuracy and low mass.

A scaled model is fabricated, which has an overall RMS of 4.60mm and centre one third RMS of 1.53mm under analytical loads, while the analytical accuracy RMS of 0.33mm. The creep effects contribute to the bad precision.

Test results demonstrated the feasibility of PBF to achieving the reflector shape accuracy requirements, and determined the path forward to meet the required accuracy in a follow-on program. Besides, to enable the reflector to have high structural stiffness and stability in deployed configuration without having to prestress the structure as required by thin films, stiffened backside supports are designed to consolidate to the flexible shell backside in the future.

REFERENCES

- [1]. E. Im, S.L. Durden, G. Sadowy, A. Berkun, J. Huang, M. Lou, et al, "System concept for the Next-Generation Spaceborne precipitation radars", in *Aerospace Conference Proceedings, 2000 IEEE proceedings*, Vol.5, pp.151-1823, Big Sky,MT,2000.
- [2]. G. Sadowy, A. Berkun, S. Durden, J. Huang, E. Im, M. Lou, et al, "Technologies for the next generation of spaceborne precipitation radars", in *Aerospace Conference Proceedings, 2001 IEEE proceedings*, Vol.4, pp.1811-158, Big Sky,MT,2001.
- [3]. J.K. Lin, G.H. Sapna III, S.E. Scarborough, B.C. Lopez, "Advanced precipitation radar antenna singly curved parabolic antenna reflector development", in *44th AIAA/ASME/AHS Structures, Structural Dynamics, and Materials Conference*, AIAA-2003-1651, Virginia,2003.
- [4]. C.G. Meyer, J. Leifer, B.C. Lopez, D.C. Jones, B.C. Caddell, "Zero-and One-g comparison of surface profile in Single-Curved parabolic membrane", *Journal of Spacecraft and Rockets*, Vol.42, No.6, pp.1101-1108, 2005.
- [5]. J. Leifer, D.C. Jones, A.M. Cook, "Gravity induced wrinkling in subscale singly curved parabolic gossamer membrane", *Journal of Spacecraft and Rockets*, Vol.47, No.1, pp.214-219, 2010.
- [6]. H.F Fang, M. Lou, "Isogrid Membranes for precise singly curved reflectors", NASA NPO-40035, 2005.
- [7]. L. Datashvili, "Multifunctional and dimensionally stable flexible fibre composite for space applications", *Acta Astronautica*, vol.66, pp.1081-1086, 2010.
- [8]. T.J. Keil, J.A. Banik, "Storage and deployment strength of a rollable composite shell reflector", in *52nd AIAA/ASME/ASCE/AHS/ASC Structures, Structural Dynamics and Materials Conference*, AIAA-2011-2103, Colorado, 2011.
- [9]. O. Soykasap, S. Karakaya, "Design and testing of a ultra-thin composites shell reflectors demonstrator", in *53rd AIAA/ASME/ASCE/AHS/ASC Structures, Structural Dynamics and Materials Conference*, AIAA-2012-1839, Hawaii,2012.
- [10]. H. Tari, "On the parametric large deflection study of Euler-Bernoulli cantilever beams subjected to combined tip point loading", *International Journal of Non-Linear Mechanics*, vol.49, pp.90-99,2013.

ACKNOWLEDGEMENTS

The research work herein has been funded by Tianhe Navigation Communication Technology Co., Ltd. The support is gratefully appreciated.

HYBRID FIBER REINFORCED POLYMER COMPOSITES FOR LIGHTWEIGHT STRUCTURES

N.M. Chikhradze, G.S. Abashidze, G.I. Baliashvili, G.B. Pkhaladze, D.T. Tsverava

*G.Tsulukidze Mining Institute of Georgia, 7, E. Mindeli St., 0186, Tbilisi, Georgia
Email: Chikhradze@mining.ogr.ge*

ABSTRACT

Fiber-reinforced polymers are characterized with high-specific durability, corrosion resistance, high exploitation-technological properties, and are successfully used in construction, space, aviation, auto, marine, chemical manufacturing, etc. Hybrid fiber reinforced materials has high potential application in renewable energy industry (for production of wind turbine blades). Accordingly, the demand on new polymeric composites reinforced by fibers is rapidly increasing. One of the perspective direction in development of polymeric materials is production of composites reinforced by different combination of fibers (carbon, glass, basalt, etc). It enables to give materials the necessary mechanical properties and optimize cost of products. The results of investigations new composites prepared on the base of polymeric matrix and hybrid carbon, basalt, glass fibers are discussed in the paper.

1. INTRODUCTION

Polymeric reinforced materials are characterized by a number of advantages over traditional structural materials since they offer such unique properties as high specific strength in some cases, in combination with light transmission, radio transparency, high electrical insulating characteristics, non-magnetic properties, corrosion resistance.

The possibility of the preparation of new materials with predetermined characteristics is one of the main advantages of reinforced plastics. In Table 1 the standard mechanical characteristics of the most abundant structural materials as well as averaged standard characteristics, for example, of oriented and randomly reinforced glass-plastics are given. In recent years an information on new type of polymeric composite-basalt plastic (BP), in which the basalt fiber is used instead of glass reinforcing one [1,2], is of frequent occurrence. Basalt fibers are practically highly competitive with glass ones by main mechanical characteristics and surpasses them by some of them, in particular, by water-resistance and chemical stability. But in the form of twisted and non-twisted threads, rovings, roving cloth and discrete fibers, basalt ones represent an alternative and promising reinforcing element for composites. In addition, at solving of a series of specific problems, for example, for preparation of materials with predetermined strength and deformation characteristics in different directions of load application, the combination of glass, high-strength basalt, high-strength and high-modulus carbon fibers were used, that is to say, the production of composites, reinforced by hybrid fibers (HFRC) was organized [3-8].

Here we don't detail the properties of these and other types of reinforcing fibers. We have restricted ourselves to the comparison of glass, basalt and carbon fibers (Table 2).

Table 1. Mechanical properties of structural materials

Material	Density Kg.m ⁻³	Tensile strength, MPa	Tensile modulus, GPa	Specific strength km	Specific rigidity km
<u>Metals</u>					
Steel	7800	400	200	5.1	2560
Aluminum alloy	2800	300	72	10.7	2580
Titanium	4500	350	115	17.8	2560
<u>Wood</u>					
Oak	720	130	15	15.2	1750

<u>Plastics</u>					
Polyethylene	960	20	0.5	2.1	52
Vinyl plastic	1400	60	3	4.3	210
<u>Glass reinforced plastics</u>					
Unidirectional	2000	1600	56	80.0	2800
Glass-cloth-base laminate	1900	500	30	26.2	1570
Randomly oriented	1400	100	8	6.7	530

Table 2. Properties of reinforcing fibers

Fiber	Density gr.cm ⁻³	Failure stress, GPa	Extension at failure, %	Elasticity modulus GPa
Glass	2.4-2.5	2.8-3.0	4.7-5.6	74-95
Basalt	2.6-2.8	1.9-2.6	3.5-4.5	70-90
Carbon	1.9-2.1	2.2-7.2	0.5-2.4	200-785

Remark: Indexes are given for the production of the firms of various countries.

2. GENERAL METHODOLOGY OF INVESTIGATION

At designing of structures and items from composite materials, primarily the values of their calculated resistances are necessary. By long-term calculated resistance (R_{cl}) of the material in normal conditions the product of normative resistance of the material by coefficient of long-term resistance and by coefficient of the uniformity of its mechanical characteristics is meant:

$$R_{cl} = R_{nor} K_{l-t} K_u$$

Normative resistance (R_{nor}) was determined a strength limit of the materials under study by the results of short-term testing of small samples, carried out in accordance with acting standards. Coefficient of long-term resistance (K_{l-t}) was determined by testing to failure of the series of the samples of the materials at long-term loading at the stresses comprising a definite part from a strength limit of the material. Uniformity coefficient (K_u) was determined by well-known three sigma rule by calculation of arithmetic mean and by root-mean-square deviation of the strength, which are defined on the basis of statistical analysis of the results of mass testing of strength properties of BP and HFRC. Calculated resistances of the materials, operating at the joint action of static load and regimes, different from normal ones (elevated temperature, high humidity, corrosive medium and etc.) were determined by multiplying the long-term calculated resistances into corresponding coefficients of operating conditions:

$$R_{cl}^T = R_{cl} \cdot K_T, \quad R_{cl}^w = R_{cl} \cdot K_w, \quad R_{cl}^{cor} = R_{cl} \cdot K_{cor}, \quad R_{cl}^{atm} = R_{cl} \cdot K_{atm}$$

where K_T , K_w , K_{cor} , K_{atm} - coefficients of operating conditions of composites, service of which is provided, respectively, at elevated temperature, in water or at high humidity at the action of corrosive media, in atmospheric conditions, as well as at synchronous long-term action of load as well as of external factors. In some cases the

coefficients of operating conditions were determined at the joint action of various factors, for example, of temperature, water /humidity ($K_{T,w}$).

The objects of investigations were:

2.1. Basalt Reinforced Plastics

BP-1. Sheet basalt plastic. Thickness (δ)-1.5-2.5mm; density (ρ)-1360-1380 kg.m⁻³; Matrix – unsaturated polyester resin of Turkish production (65 mass%). Reinforcing element – chopped fiber, obtained by cutting of basalt roving of Georgian production with following characteristics: rectilinear density 600-4800 tex; elemental fiber diameter 10-16 μ ; specific tenacity 350-450 mN/tex.

The mode of preparation: contact moulding (without pressure and temperature).

Expected field of application: light-transparent guarding building structure.

BP-2. Basalt cloth – based laminate. $\delta = 0.7$ -5.0 mm; $\rho = 1530$ -1560 kg.m⁻³. Matrix-phenol-formaldehyde resin of Ukrainian production (25-35 mass%). Reinforcing element – cloth from twisted threads of Georgian production with following characteristics: thickness 0.25-0.35 mm; surface density 150-450 g/m²; density in warp 4-8 th/cm; density in weft 6-12 th/cm, or cloth from basalt roving with the indexes: thickness 0.4-0.9 mm; surface density 300-700 g/m²; density in warp – 1.7-3.5 th/cm; density in weft 2.9-4.0 th/cm;

The mode of preparation: direct pressing, pressure 45-55 kgf/cm², pressing temperature 413-443K, holding time on 1 mm-5-12 min.

Expected field of application: shells of three-layered building panels (among them for corrosive media).

BP-3. Oriented basalt plastic. $\delta = 1.0$ -7.0 mm; $\rho = 1520$ -1540 kg.m⁻³. Matrix-epoxy-phenol resin of Ukrainian production (25-32 mass%). Reinforcing element-permanently oriented basalt fiber in the form of roving (data see in BP-1).

The mode of preparation: production of veneer, its impregnation by a binder, direct pressing of semifinished item.

Expected field of application- auxiliary structural elements and details.

BP-4. Pressed basalt plastic. $\delta = 2.0$ -8.0 mm; $\rho = 1850$ -1950 kg.m⁻³. Matrix – modified phenol-formaldehyde resin of Ukrainian production (25-35 mass%). Reinforcing element-chopped or permanently oriented basalt fiber (data see in BP-1, BP-2).

The mode of preparation: preliminary impregnation of reinforcing element, direct pressing at the temperatures of 140-160°C; pressure 250-350 kgf/cm², holding time 2-5 min on 1 mm of material.

2.2. Composites on the Basis of Hybrid Fibers

HFRC-1 . Oriented bi-directional composite. $\delta = 1.5$ -2.5 mm; $\rho = 1450$ -1550 kg.m⁻³. Matrix – epoxy resin of Ukrainian production (70-75 mass%). Reinforcing elements – glass and carbon fibers (GF, CF), located in the composite by the scheme, presented in Fig.1. Glass fibers of alkalineless composition are presented in the form of roving of Ukrainian production. Polyacrylonitrile carbon rovings of Russian production offer the strength 2.3 GPa and elasticity modulus 220 GPa. Ratio GF: CF = 0.3÷0.7 (by mass).

The mode of preparation: production of prepreg, its direct pressing.

Expected field of application: shell of wind turbine blade.

HFRC-2. The same, but 20% of carbon fiber is replaced by basalt one in the form of roving.

HFRC-3. Oriented composite. $\delta = 2$ -3 mm, $\rho = 1450$ -1550 kg.m⁻³. Matrix – the same as in the case of HFRC-1 and HFRC-2; Reinforcing elements – the same as in the case of HFRC-1 and HFRC-2 . They are located by the scheme, shown in fig. 2.

The mode of preparation: the same as in the case of HFRC-1 and HFRC-2.

Expected field of application: the spar of wind turbine blade.

HFRC-4. The material similar to the composite HFRC-3, but 20% of carbon fiber is replaced by basalt one in the form of roving.

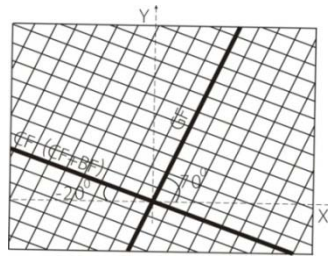


Fig .1

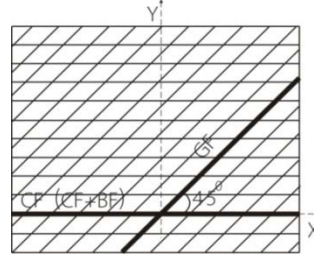


Fig .2

Remark: GF-Glass fiber; BF-Basalt fiber; CF-Carbon fiber

The results of determination of normative resistances at various types of stressed state (tension, bending, compressing, shear - R_{nor}^t , R_{nor}^b , R_{nor}^c , R_{nor}^{sh} , as well as of short-term elasticity modulus at tension, bending and compressing (E_{s-t}^t , E_{s-t}^b , E_{s-t}^c) and coefficients of uniformity of strength properties of the materials under study are given in Table 3.

Table 3. Normative resistances, short-term elasticity modulus and uniformity coefficients for BP and HFRC

Material	R_{nor}^t MPa	R_{nor}^b MPa	R_{nor}^c MPa	R_{nor}^{sh} MPa	E_{s-t}^t GPa	E_{s-t}^b GPa	E_{s-t}^c GPa	K_u
BP - 1	69.0	145.0	105.6	55.0	6.0	-	-	0.65
BP - 2	250.8	130.0	105.5	75.0	26.0	-	-	0.78
BP - 3	480.6	750.8	410.2	190.0	31.5	-	-	0.75
BP - 4	$\frac{85.0}{560.0}$	$\frac{130.0}{260.0}$	$\frac{110.0}{210.5}$	-	$\frac{19.3}{19.5}$	-	-	0.75
HFRC-1	$\frac{195.6}{163.1}$	$\frac{480.2}{270.3}$	$\frac{261.1}{219.1}$	$\frac{10.2}{8.1}$	$\frac{9.4}{3.9}$	$\frac{14.5}{3.4}$	$\frac{10.6}{4.2}$	0.72
HFRC-2	$\frac{292.5}{228.2}$	$\frac{567.2}{351.4}$	$\frac{410.2}{319.9}$	$\frac{12.2}{10.2}$	$\frac{15.0}{5.4}$	$\frac{23.4}{5.4}$	$\frac{14.6}{5.8}$	0.68
HFRC-3	$\frac{455.4}{6.9}$	$\frac{718.1}{19.9}$	$\frac{420.8}{8.0}$	$\frac{24.8}{1.2}$	$\frac{96.9}{5.8}$	$\frac{78.6}{5.2}$	$\frac{78.1}{4.1}$	0.74
HFRC-4	$\frac{132.2}{85.6}$	$\frac{415.7}{95.9}$	$\frac{160.2}{107.7}$	$\frac{8.8}{2.4}$	$\frac{49.7}{19.8}$	$\frac{58.8}{16.4}$	$\frac{51.0}{16.7}$	0.70

Remark: 1 BP-1. Resistances at shear are given in the direction, perpendicular to sheet plane.

2. BP-2. For efforts acting in the direction of the base of basalt cloth ($\delta=7\text{mm}$).

3. BP-3. At the ratio between longitudinal and transverse fibers, equal to 1:1 for efforts, acting in the direction of fibers.

4. BP-4. In numerator and denominator at reinforcing by chopped and oriented fibers, respectively.

5. HFRC-1, HFRC-2, HFRC-3, HFRC-4. In numerator and denominator the values along and transversely to X axis, respectively (Fig. 1,2).

Under prolonged (long-term) strength of the solid the dependence of time duration up to its failure on the stress and temperature is meant. The coefficient of long-term resistance is a value, determined by testing of a series of the materials samples under prolonged loading to failure at the stresses, constituent a definite part from material strength limit. Thus, in the terms “long-term resistance” and “durability” an equal meaning is assigned.

The equation of temperature-time dependence of the solids, as it well known, relates durability (τ), stress (σ) and temperature (T) to each other [9,10]:

$$\tau = \tau_0 \exp\left(\frac{U_0 - \gamma\sigma}{kT}\right) \quad (1)$$

where τ_0 - is a constant, approximately equal to 10^{-13} sec, which in order of a value is near to the period of thermal oscillations of atoms; U_0 – initial activation energy of the process of material destruction; k – Boltzmann’s constant; γ - average coefficient of over stresses.

Physical meaning of the formula (1) may be explained by means of thermal fluctuation theory of strength. According to this theory, destruction is kinetic, thermally fluctuating process of permanent accumulation of damages, developed in the body since the load application to its destruction. Breaking of interatomic bonds, activated by applied stress, is an elementary act of destruction process.

In the course of experiments it has been established that BP and HFRC under our study are, mainly, obey the temperature-time dependence. Along with it, it should be noted, that in relation to BP and HFRC, which are bi or more component composites, physical meaning of the values τ_0 , U_0 and γ is not reasonably evident. But it should be taken into account that the main goal of our investigations is to obtain the empirical relationships between long-term resistance (durability) of new types of structural materials and the conditions of their operation. In this case the question about physical meaning of above-mentioned values does not need to be posed.

From (1) the following is obtained:

$$\sigma = \frac{U_0 - \frac{kT}{\lg e} \lg \frac{\tau}{\tau_0}}{\gamma} \quad (2)$$

If in formula (2) it is granted that $\tau = \tau_i = \text{const}$, we obtain

$$\sigma = \frac{U_0}{\gamma} - BT \quad (3)$$

Where: $B = \frac{K \lg \frac{\tau_i}{\tau_0}}{\gamma \lg e}$

3. MECHANICAL PROPERTIES OF BP AND HFRC

3.1. Effect of Duration of Static Loading and Temperature on Strength

Dependence of breaking stress of BP and HFRC on temperature was estimated by the coefficients of operating conditions $K_T = \sigma_T / \sigma_{s-t}$, where σ_T and σ_{s-t} are breaking stresses for the samples after temperature action and at short-term testing, respectively. The values of K_T are presented in Table 4.

If in formula (1) it is granted that

$$T = T_i = \text{const}, \text{ then } \sigma = \frac{U_0}{\gamma} - A \lg \frac{\tau}{\tau_0} \quad (4)$$

$$\text{where } A_i = \frac{kT_i}{\gamma \lg e}.$$

Table 4. Coefficients of operating condition K_T in the structures, operating at elevated temperatures

Material	Temperature, K					
	313			333		
	Tension, Compression	Bending	Shearing	Tension, Compression	Bending	Shearing
BP-1	0.65	0.85	0.67	0.60	0.79	0.63
BP-2, BP-3	0.88	0.79	0.78	0.77	0.72	0.72
BP-4	0.70	0.88	0.72	0.63	0.78	0.66
HFRC-1	0.72	0.88	0.77	0.70	0.85	0.72
HFRC-2	0.72	0.82	0.82	0.70	0.79	0.77
HFRC-3	0.74	0.86	0.88	0.71	0.81	0.80
HFRC-4	0.75	0.85	0.79	0.74	0.78	0.75

Remark: 1. Coefficients of operating conditions of materials in the structures at temperature 273 K are taken to be unity; 2. At intermediate temperatures K_T may be determined by interpolation.

To estimate a time dependence of the strength, the coefficients of operating conditions of the material were used: $K_\tau = \sigma_\tau / \sigma_{s-t}$, where σ_τ breaking stress after the time interval, corresponding to service life of the structure or item. The values K_τ for BP and HFRC are given in Table 5.

Table 5. The values of the coefficient K_τ at various types of stressed state

Material	Tension			Compression			Bending		
	10^3h	10^4h	10^5h	10^3h	10^4h	10^5h	10^3h	10^4h	10^5h
BP-1	0.71	0.65	0.60	0.71	0.68	0.58	0.68	0.56	0.45
BP-2	0.86	0.75	0.68	0.81	0.67	0.59	0.83	0.72	0.55
BP-3	-	0.68	0.56	0.88	0.77	0.61	0.87	0.74	0.59
BP-4	0.81	0.77	0.70	0.89	0.78	0.51	0.78	0.72	0.63
HFRC - 1	0.91	0.79	0.69	0.85	0.76	0.62	0.78	0.69	0.55
HFRC - 2	0.88	0.73	0.66	0.82	0.71	0.59	0.80	0.63	0.51
HFRC - 3	0.90	0.76	0.71	0.88	0.77	0.68	0.82	0.66	0.59
HFRC - 4	0.81	0.72	0.62	0.79	0.70	0.62	0.80	0.63	0.49

Direct experimental determination of σ_τ is fraught with great difficulties: the maintenance of constant external conditions and predetermined stress over a long period of time is necessary. Therefore the values σ_τ were determined for three values: 1, 10^2 , 10^3 hours by extrapolating on the basis of equation (1), obtained curve and by assuming that external factors don't distort a linear character of temporal dependence of the strength.

Hence, we have, separately, the coefficients of operating conditions providing the temperature influence as well as considering the loading duration. Over many years the method of multiplying of these coefficients has been used to account the joint effect of these factors on long-term resistance. But as it was shown in [11], this method leads to considerable overstating of calculated resistances of glass plastics, especially at the temperatures close to glass

transition temperature of a binder. To check this fact, a materials under study were subjected to the joint action of loading and temperature (313 K, 333 K), correlating the data, obtained in this case with the values of the coefficients of operating conditions K_τ and K_T (Table 6).

Table 6. Values of coefficients of operating conditions of BP at bending

Coefficient	Temperature, K	BP - 1	BP - 2	BP - 3	BP - 4
K_T	313 333	0.84 0.65	0.88 0.72	0.90 0.85	0.85 0.79
K_τ ($\tau = 5$ years)		0.52	0.82	0.89	0.83
$K_T \cdot K_\tau$	313 333	0.44 0.34	0.72 0.59	0.80 0.76	0.71 0.66
K_τ^T ($\tau = 5$ years)	313 333	0.41 0.28	0.69 0.49	0.75 0.69	0.65 0.59
$\frac{K_\tau^T}{K_T \cdot K_\tau}$	313 333	0.93 0.82	0.95 0.83	0.94 0.91	0.91 0.89

The analysis of the data of Table 6 confirms the fact that the method of coefficients multiplying really leads to enhanced values of the coefficients of operating conditions and consequently to overstating of calculated resistances of BP. Thus, it was decided to determine the coefficients of operating conditions for the joint action of external factors and loading.

3.2. Effect of the Time of Loading Action and Temperature on Deformation Characteristics

Deformability of the materials under study, caused by force action, was estimated by short-term and long-term elasticity and shear modulus (E_{s-t} , E_{l-t} , G_{s-t} , G_{l-t}) were determined by short-term static testing of small standard samples as a ratio between the increment of stress and the increment of relative deformation of a sample. E_{l-t} , G_{l-t} were obtained by long-term static testing of the samples at stresses equal to calculated long-term resistance of materials as a ratio between the stress and maximum relative deformation of the sample at damping of creeping. It should be noted that the term “long-term elasticity modulus” is conventional in this case, since deformations of polymeric composites at long-term loading, in reality, aren't elastic.

At the temperatures, no greater than the temperature of beginning of binder destruction, reinforcing fibers act as linear-elastic materials. Binders are characterized by visco-elastic properties. Therefore, deformations of BP and HFRC, generally, depend significantly on duration and temperature of operation.

As might be expected, in uni-directional or orthogonally-reinforced BP and HFRC, the creep is formed at the action of constant loading applied to the direction of reinforcement. But after a time, this process is practically terminated. This fact is quite clear since at first an effort is distributed between fibers and binder, but stresses in binder relax and all stresses are progressively imparted to fibers.

At loading of BP and HFRC, randomly reinforced and oriented at angle to loading direction, creep isn't damped and is continued up to material destruction. Creep anisotropy of these materials is expressed to a considerable more extent than an anisotropy of elastic properties and sharply enhances with temperature elevation.

In Table 7, 8 the values of the coefficients of operating conditions are given, considering the variation of deformation characteristics of BP and HFRC depending on duration of loading action and on temperature variation.

Table 7. The values of the coefficients of operating conditions K_T by deformation properties

Material	Index	K_T after hours		
		10^3	10^4	10^5
BP-1	E ^t	0.72	0.61	0.52
	G	0.69	0.59	0.50
BP-2	E ^t	0.91	0.82	0.78
	G	0.89	0.85	0.79
BP-3	E ^t	0.95	0.89	0.82
	G	0.72	0.68	0.62
BP-4	E ^t	0.91	0.86	0.82
	G	0.85	0.79	0.71
HFRC - 1	E ^t	0.92	0.87	0.85
	G	0.85	0.76	0.69
HFRC - 2	E ^t	0.88	0.82	0.79
	G	0.79	0.71	0.62
HFRC - 3	E ^t	0.95	0.89	0.85
	G	0.91	0.86	0.78
HFRC - 4	E ^t	0.89	0.82	0.75
	G	0.81	0.72	0.69

Table 8. The values of the coefficients of operating conditions K_T by deformation properties

Material	Index	K_T at temperatures		Material	Index	K_T at temperatures	
		313K	333K			313K	333K
BP-1	E ^t	0.53	0.42	HFRC-1	E ^t	0.85	0.79
	G	0.51	0.39		G	0.82	0.75
BP-2	E ^t	0.71	0.64	HFRC-2	E ^t	0.82	0.72
	G	0.81	0.74		G	0.79	0.71
BP-3	E ^t	0.88	0.76	HFRC-3	E ^t	0.89	0.82
	G	0.83	0.74		G	0.85	0.79
BP-4	E ^t	0.78	0.61	HFRC-4	E ^t	0.82	0.85
	G	0.77	0.85		G	0.80	0.72

The sphere of BP and HFRC application:

- Small scale energy (renewable energy sources, namely, production of wind turbine blades working on the low speed of air flow). The research jointly conducted with the special design-constructive bureau “Yuzhnoe” (Dnepropetrovsk) confirmed that for production of blade shell and spar which are adapted to different velocity of air flow, is optimal the positions of carbon, basalt and glass fibers to the axis as it is shown on Fig. 1 and 2. The task is to substitute partially 20-30 times cheaper basalt fiber for expensive and deficit carbon fiber avoiding a negative influence on material exploitation characteristics.
- Construction of industrial, dwelling, public and agricultural buildings, namely, production of bounding constructions (panels, ceilings, walls, among them optical constructions). Constructions and details produced by proposed composites are effective when is essential: to reduce the mass of a building (e.g. while working on subsident ground and undermining territories); to reduce transportation and construction-installation volume and accordingly, construction periods (e.g. distant and hard-to-rich mountainy regions); to insure corrosion and resistance of constructions operating in aggressive environment; to increase reliability of their exploitation in high seismic regions; to prevent revealing of magnetic properties of building constructions and to decrease possibility of spark formation. Possible schemes of construction elements used in building are shown in Fig. 3, Fig. 4, Fig. 5.

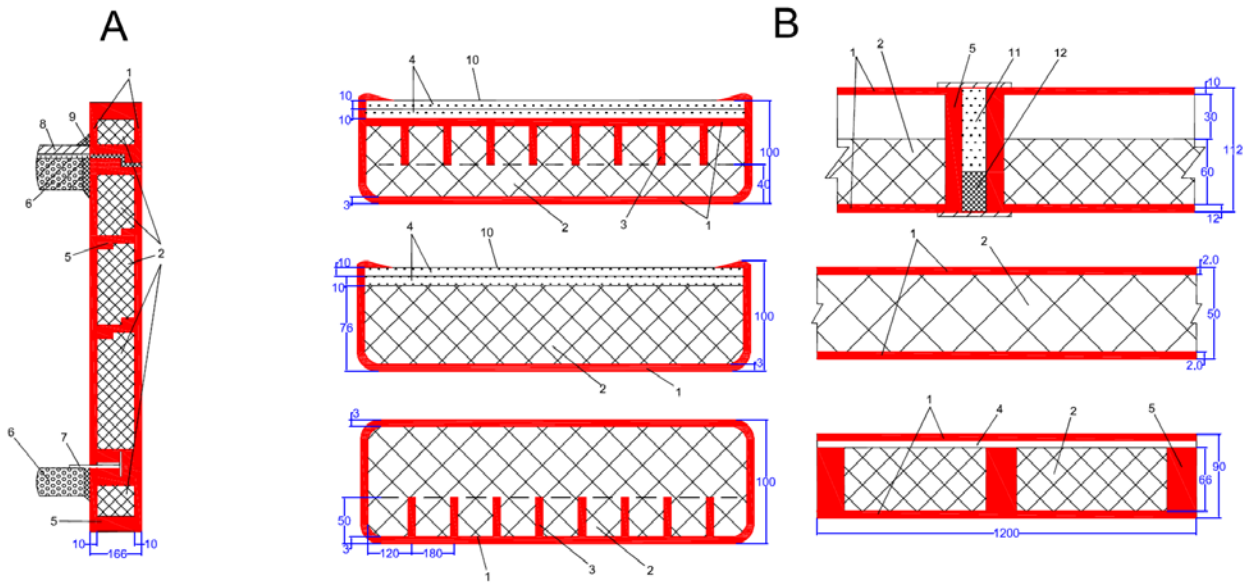


Fig. 3. Curtain Wall.

A-wall B-panel.

1-plating (BP or HFRC); 2-insulation; 3-the rib, BP ($\delta=50\text{mm}$); 4-sheet drywall; 5-the bar, BP; 6-overlap; 7-item for fixing; 8-cement slab; 9-skirting; 10-fabric, BP; 11-mineral wool; 12- vapor barrier.

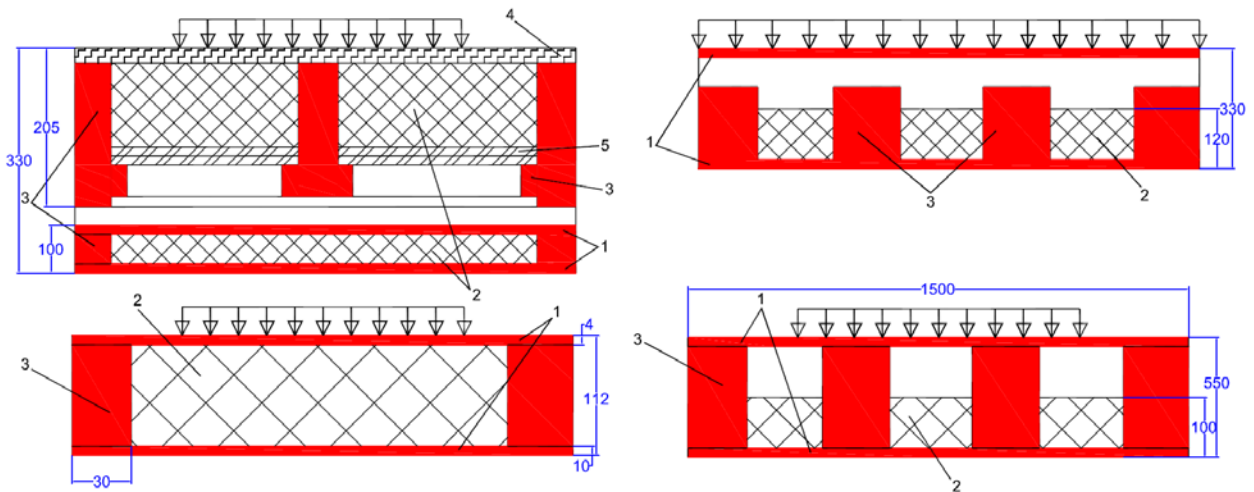


Fig. 4. Overlap, Floor.

1-plating (BP or HFRC); 2-insulation; 3-the bar, BP; 4-wooden flooring ($\delta=30\text{mm}$); 5-sheet, BP ($\delta=4\text{mm}$).

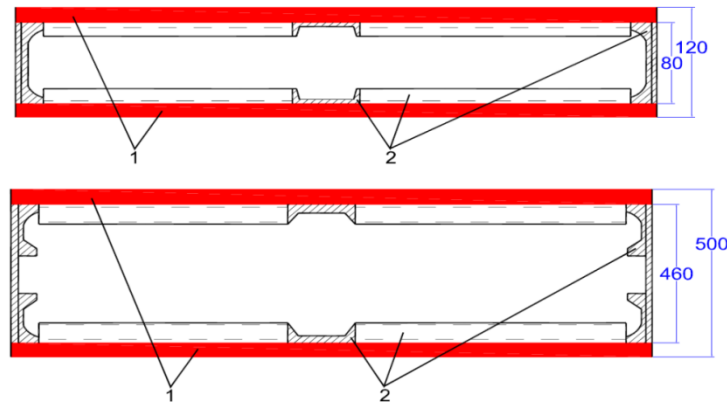


Fig. 5. Partition
1-plating, BP ($\delta=10\text{mm}$); 2-u-profile metal.

4. CONCLUSION

At present a sufficient experience is accumulated in world practice in the field of the technology of preparation of basalt plastics and composite materials with reinforcing structures from hybrid fibers. Development of the works along this line is determined by possibility of preparation of new generation of materials with a wide spectrum of properties. Along with it, a diversity of the requirements, imposed to structural materials, tended to the fact that none of newly elaborated materials can occupy the dominant place at current stage of technology development, at least, in the immediate future. Each type of materials may be optimal in certain specific cases. A wide spectrum of needed materials, apart from considered here, may be prepared by the use of a number of reinforcing fibers with various elastic and strength characteristics and combined with carbides and oxides of the binders, as well as of reinforcing schemes which permit a purposeful control of strength, rigidity and other properties of materials.

In parallel with it, it should be noted that at present the data for physical-mechanical properties of basalt plastics and composites on the basis of hybrid fibers as well as for variation of these properties in expected operating conditions are extremely limited, which retards their use as structural materials.

5. REFERENCES

- [1]. J. M. Park, W. G. Shin, D.J. Yoon *Composites Science and Technology*, vol. 59, 1.3: 355-370, 1999.
- [2]. K.E. Perepelkin Polymer fibrous composites, their main types, production principles and properties. *Chemical fibers*. №1: 41-50 (in Rus.), 2006.
- [3]. P. Bronds, H. Lilhopt, A. Lystrup *Composite Materials for wind power turbine blades*. Annual Review of Materials research, vol. 35: 505-538, 2005.
- [4]. D.A. Griffin SAND 2002-1879, vol. I, Albuquerque, NM: *Sandia National Laboratories*, 2002.
- [5]. D.A. Griffin, T.D. Aswill *Proceedings of the 48 International SAMPE Symposium and Exhibition*. Long Beach, CA, 2003.
- [6]. D.A. Griffin SAND 2004-0073, vol. II, *Sandia National Laboratories*, 2004.
- [7]. E.S. Zelenski Reinforced plastics-modern structural materials. *Russian Chemical journal*. v.XIV, №2: 56-74 (in Rus.), 2001.
- [8]. Carbon/glass hybrids used in composite wind turbine rotor blade design. By Karen Fisher Mason, *Contributing Writer Composites Technology*, 2004.
- [9]. S.N. Zhurkov, E.E. Tomashevski In: Some problems of the strength of the solid. M., *Publishing House of Academy of Sciences of USSR*, p.61-66 (in Rus.), 1959.
- [10]. V.R. Regel. Kinetic nature of the strength of the solid. M., "*Nauka*" (in Rus.), 1974.
- [11]. V.I. Alperin– In: Hand book on plastic masses. v. II, M. "*Khimia*", pp. 442-512 (in Rus.), 1975.

ENHANCEMENT OF THE ELECTRO-MAGNETIC BEHAVIOUR OF FLEXIBLE FIBER COMPOSITE MATERIALS BY SURFACE COATING

Endler, S. ⁽¹⁾, Datashvili, L. ⁽¹⁾, Baier, H. ⁽¹⁾, Roose, S. ⁽²⁾

⁽¹⁾*Institute of Lightweight Structures, TU München,
Boltzmannstraße 15, 85747 Garching (Germany)
Phone: 089.28916110, Fax: 089.28916104
Email: endler@lwb.mw.tum.de,*

⁽²⁾*Centre Spatial de Liège,
Av du Prè Aily, 4031 Angleur Liège (Belgium)
Email: sroose@ulg.ac.be*

ABSTRACT

Many space applications require materials with specific mechanical and thermo - elastic properties combined with a sufficient electromagnetic behavior. One example requiring such combinations of different material properties are large deployable reflecting surfaces. A candidate material for such surfaces is carbon fiber reinforced silicone (CFRS), which is flexible enough to allow foldability but sufficiently stiff to achieve a certain (e.g. parabolic) shape after deployment in space. In addition, a very low coefficient of thermal expansion (CTE) can be achieved. To enhance the electro - magnetic behavior of the CFRS a metal coating of the reflecting surface has been investigated to increase the surface reflectivity up to optical requirements in the range of sub μm wavelengths. Due to the properties of the silicone matrix and the limited dimensions of available coating facilities, a reliable process for direct optical coating of a large CFRS surface is still not state of the art. Especially the very poor bonding strength of metallic coatings on silicone requires some further investigations in the direction of suitable coating methods. A so called transfer coating process was developed showing promising results after the determination of proper process parameters. The developed coating process together with the influence of the different process parameters on the surface quality are presented in the paper. In addition to optical and mechanical tests different FEM analysis on material level have been performed to investigate the influence of the coating layer on the overall mechanical and thermo - elastic material properties of CFRS.

1. INTRODUCTION

Fibre composite materials with an elastomer matrix like carbon fibre reinforced silicone (CFRS) are promising materials for deployable space reflector surfaces achieving demanding requirements on shape accuracy after deployment and thermo - elastic stability over a wide range of temperatures [1]. One possible future application is the generation of large optical reflective surfaces like telescopes being deployed in space [2]. Although CFRS can fulfil many requirements concerning the electro - magnetic reflectivity in the range of radio frequencies similar to carbon fiber reinforced plastics (CFRP), a non - coated surfaces show practically no optical reflectivity for wavelengths in the range of sub μm . This creates the need of an additional surface coating layer to enhance the electromagnetic reflectivity of CFRS also for non - imaging optical applications. Investigations performed to overcome different challenges arising in optical coating on a silicone matrix composite for large diameters have been performed and are presented in the paper. In addition the influence of the coating layer on important material properties of CFRS like its stiffness and thermo - elastic stability have been investigated by using different micromechanical modelling techniques.

2. TYPICAL SURFACE COATING PROCESSES

A well-known surface coating process widely used for CFRP reflectors and telescopes is the physical vapor deposition (PVD) method. It generally describes a variety of different coating methods depositing thin films by the condensation of a vaporized form of the desired film material onto the substrate. A second candidate coating process investigated is the so called sputtering method. Sputtering is a process where the atoms of the coating material are ejected from a solid target material due to bombardment of the target by energetic particles (e.g. atoms or molecules of the inert gas). This energetic particles are usually generated using an inert gas in the chamber and a high voltage applied between the substrate and the coating material block. Typical materials used for optical coatings are aluminum and silver depending on the optical surface requirements. To increase the bonding of the coating layer to the substrate several methods like a plasma treatment of the substrate's surface can be incorporated in the coating process.

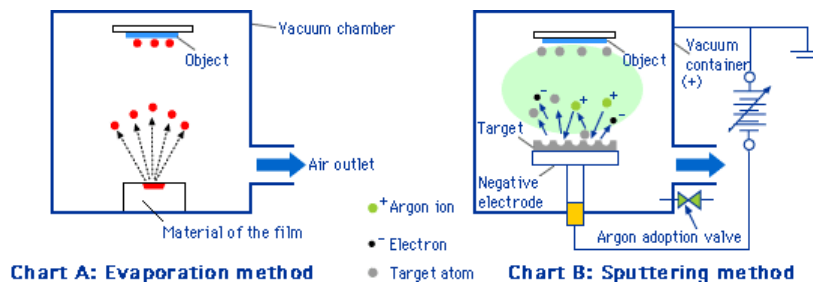


Fig. 1. Principle sketch of PVD and sputtering processes. [3]

The quality of coating layer deposited in a VDA process is mainly driven by the vacuum reached in the chamber. The higher vacuum reached (about 2×10^{-4} mbar) the less particles in the coating chamber are able to disturb the coating process. Remaining particles can either block the vapor to reach the substrates surface or make some chemical reactions with the gaseous coating material. Both effects will reduce the optical quality and the bonding strength of the coating layer to the substrate. The maximally achievable layer thickness with a high optical quality is about 300nm. For thicknesses of more than 300nm more material has to be vaporized increasing the danger of condensation of the coating material and forming drops of the coating material on the substrate. The coating in multiple steps to achieve higher layer thicknesses is also not recommended. The bonding strength between each of the multiple coating layers is extremely low.

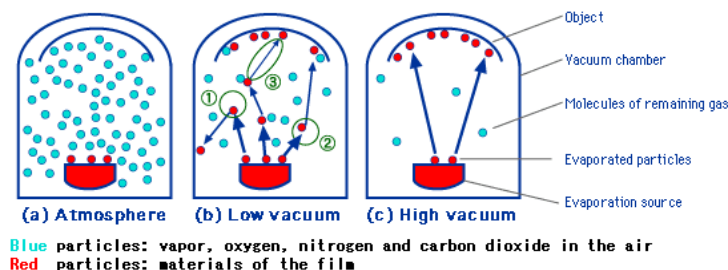


Fig. 2. Principle sketch of vacuum influence on coating process and quality. [3]

2.1. Material properties of vapour deposited metal films

As given in literature the material properties of thin deposited metal films are quite different compared to bulk material properties. Especially the E-modulus and the CTE of thin films are much lower as compared to the bulk materials. In contrast to that, the strength of thin deposited metal films is higher. As testing of such thin metal films is quite challenging and complex values found in literature show quite a broad distribution. In Table 1 some mean values of material properties found in literature are shown.[4],[5],[6]

Table 1. Average material properties of vapor deposited aluminum

E [GPa]	R _{p0.2} [MPa]	α [10 ⁻⁶ /°C]
35	400	18,23

3. CHALLENGES IN CFRS COATING

Due to the properties of silicone, a reliable process for direct optical coating of a CFRS surface is still not state of the art. Especially the very poor bonding strength of metallic coatings on the silicone requires some further investigations. The main reason for the poor bonding behavior on cured silicone are unchained silicone molecules on the silicone's surface which remain there even after the curing of the silicone is finished. The effect of this molecule layer is similar to a release agent applied to the surface. With a simple peel – off test using an adhesive tape the poor bonding strength of directly coated CFRS can be seen in Fig. 3

Due to the low stiffness of the silicone matrix, any temperature induced stresses during the coating process create a so-called print through effect of the first fiber layer on the coating. This can be seen in Fig. 3 showing the fiber print - through of a 0°/90° fabric CFRS layer. Usually temperatures of about 50°C occur on the substrate during a standard PVD process. In addition, available PVD coating facilities are limited in size to typically 2.0m in diameter limiting the target size of the reflecting surface. Keeping in mind diameters of up to 10m and the low bending stiffness of the CFRS a direct surface coating would also require a compensation of the gravity induced deformations of the surface during the coating process to avoid any pre – stress induced deformations of the surface in 0g environment.



Fig. 3. VDA coated CFRS specimens with print – through effect (left) and poor bonding to silicone matrix (right)

4. TRANSFER SURFACE COATING PROCESS

The principle idea behind this process is the coating of the mould before lamination instead of coating the cured CFRS laminate afterwards. In this process, first, the surface of a highly precise mould is treated with a release agent and then PVD coated with aluminum. Because of the release agent the adhesion of the coating layer to the mould surface is minimized. After that, a suitable primer is applied on the coating layer to provide a good bonding strength between the coating and the silicone matrix. The primer can only increase the bonding strength if the silicone is cured on the applied primer. Several investigations have been performed in applying the primer on an already cured CFRS laminate and a subsequent PVD coating. Due to the already cured silicone matrix the primer cannot increase the bonding strength anymore but will even degrade the optical quality of the coating layer. Finally, the lamination process of the actual CFRS laminate can happen. After the curing of the CFRS is finished the de – moulding of the laminate together with the aluminium surface layer follows.

The basic process steps of the transfer coating process are presented in Fig. 4.

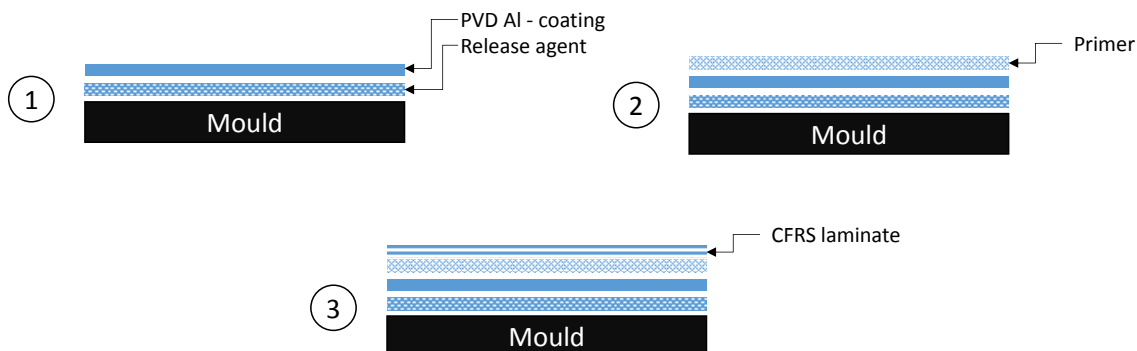


Fig. 4: Basic steps of the “transfer coating process”

A large variety of different combinations of process parameters have been investigated and tested on sample level. The most important results of the investigations are discussed in the following chapters. The influence of the different process steps on the resulting properties of the coating layers are summarized in Table 2.

Table 2. Process Parameters and their influence on the coating quality

Process Steps / Parameters	Influence on:
Type and application of the release agent	<ul style="list-style-type: none"> • Brightness of the coating • De-moulding behavior • Cracks in the coating layer
PVD coating thickness	<ul style="list-style-type: none"> • Print through of primer and fibers
Application method of the primer	<ul style="list-style-type: none"> • Cracking of coating layer due to shrinkage of primer • Bonding behavior
Lamination of the CFRS laminate	<ul style="list-style-type: none"> • Fiber print - through • Bonding behavior • Presence of voids, air bubbles

4.1. Type and application of the release agent

Mainly the type of release agent and its application is deciding the optical quality of the coated surface. A variety of different release agents from standard CFRP manufacturing has been investigated. Especially their ability to be polished is influencing the surface brightness and so reflectivity of the coating layer. In addition the release agent selected must not degrade under the temperatures arising during the PVD coating process. Finally wax based release agents show best results compared to others. A second important requirement to the release agent is the de - moulding behavior. That means it has to provide as little bonding of the coating to the mould as possible. This behavior has been investigated with a modified peel – off test. Adhesive tape with a very low bonding strength has been used trying to remove the coating from the mould treated with different release agents. In Fig. 5 two results of different release agents can be seen. On the left, no removal of the coating was possible whereas on the right a full removal can be achieved.

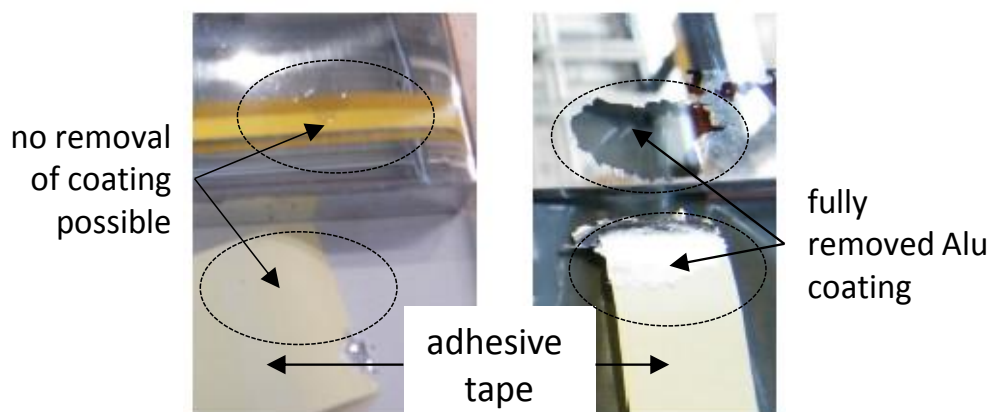


Fig. 5: Modified peel of test to derive different release agents' behaviors

4.2. Coating layer thickness

Coating layer thicknesses from 150nm to 450nm have been investigated. Especially layers below 300nm show a high tendency of cracking after the application of the primer. This can be explained by the shrinkage of the primer while curing and the missing adhesion of the coating layer to the mould surface due to the release agent. In Fig. 6 one can see two typical cracking patterns due to a too thin coating layer.



Fig. 6: Micro cracking of a too thin aluminum coating layer after primer application

With increasing thickness of the aluminum coating layer the intensity of the fiber print - through effect can be minimized due to the increasing stiffness of the aluminum layer. Layer thicknesses of more than 450nm could not be achieved in the used PVD coating process. A consecutive coating of several layers to increase the total thickness showed very poor adhesion between the aluminum layers itself. In order to minimize the impact of the coating layer on the initial CFRS properties it should be kept as thin as possible.

4.3. Application of the primer

The application method of the primer must ensure an equal distribution on the coating layer without damaging it. Furthermore, the right amount of primer to be applied must be controlled. A too high amount of primer is increasing the risk of cracks due to its shrinkage (see above). An uneven distribution of the primer is resulting in locally poor or no bonding of the coating to the CFRS laminate. Spots with poor or no bonding to the CFRS remain uncoated after de-moulding. Best results have been achieved with an application by a foam roll and a slight thinning of the primer with white spirit.



Fig. 7: Primer application on the coated mould (left) and effect of uneven distributed primer (right)

4.4. Lamination of the CFRS laminate

During the lamination, especially of the first layer, special care has to be taken to avoid any inclusion of air bubbles between the coating and the CFRS laminate. Every air bubble is a location of poor or no bonding between the laminate and the coating layer. Also a direct contact between the fibers and the coating layer shall be avoided in order to minimize the print-through effect. For that reason, an additional silicone "buffer" layer has been applied on the coating before the first CFRS layer of about 0.2mm. This thickness is a compromise between a low fiber print-through and a still low CTE of the Al-CFRS composite.

5. OPTICAL TEST RESULTS

The reflectivity of the surface coating was tested on coupon level showing satisfying results of 85% reflectivity in the visible and 95% in infrared wavelength. In Fig. 8 the reflectivity over wavelength for different combinations of process parameters is shown. Above 850nm wavelength only a very little difference in the reflectivity between the different specimens is present whereas below 850nm two specimens show clearly better reflectivity compared to the rest. This difference can be related to the type of release agent applied and its way of application respectively polishing.

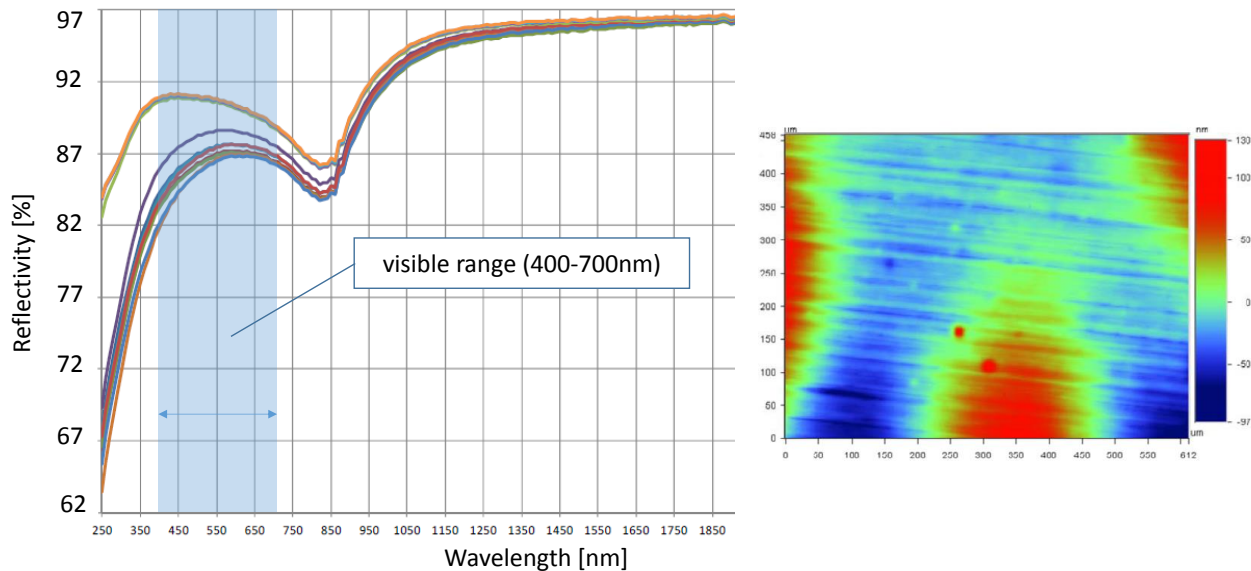


Fig. 8. Optical surface test results: Reflectivity test results (left), surface roughness measurement (right)

On the right picture in Fig. 8 a so called interferometric profilometer measurement of the coating surface is shown. The measurements have been made on different areas of the samples covering 0.5mm x 0.5mm. A typical fiber – like pattern with a periodicity of 20 μm can be noticed. If it would be a fiber pattern then, it should show a periodicity of $\sim 7 \mu\text{m}$ (the diameter of the filament). Therefore the fiber pattern was related to remainders and traces from the application and polishing of the release agent. Another aspect confirming that is the changing direction of the pattern for different places measured. A fiber print - through would show a constant pattern direction all over the specimen.

6. TECHNOLOGY DEMONSTRATOR MODEL

Because of the promising results of the investigations described above a demonstrator model of a flexible thin shell reflector with an aluminum coated surface has been manufactured and tested in the frame of an ESA study *Large deployable telescopes (LDT)*. The main objective of the project was to investigate reasonable concepts for large deployable telescopes carried out together the Universite Libre Bruxelles (ULB) under the lead of Centre Spatial de Liège (CSL). The demonstrator shown in Fig. 7 represents a spherical surface shape with a diameter of 700mm.

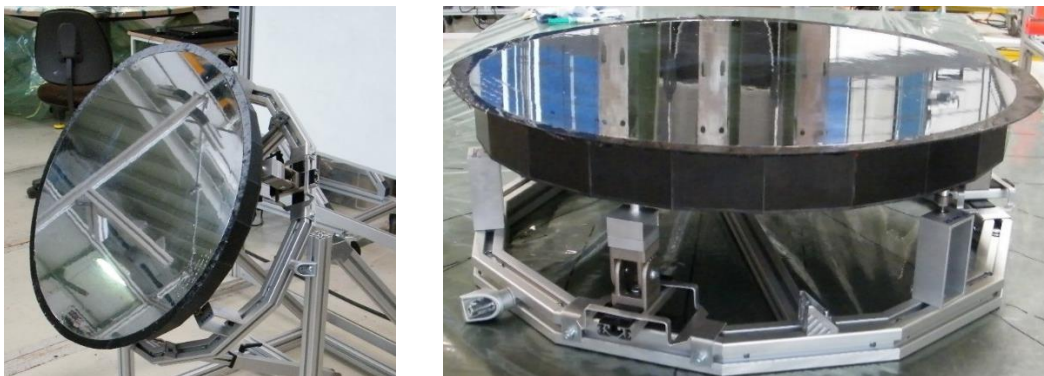


Fig. 9. Flexible thin shell demonstrator model made of surface coated CFRS

7. MICROMECHANICAL INVESTIGATIONS ON COATED CFRS PROPERTIES

In order to predict the influence of the metallic surface coating layer on the material properties of the CFRS laminate micromechanical models with different modelling approaches have been built. With these models several parametric studies have been performed to quantify the influence of different coating layer and silicone buffer – layer thicknesses on the material behaviour of CFRS. Especially properties like the young's moduli and coefficients of thermal expansion have been investigated. Additional parametric studies on the thickness of the silicone buffer and coating layer have been performed to investigate their influence on the material properties of the Al – CFRS compound.

7.1. Classical laminate theory (CLT)

As a first approach, a comparison of the laminate properties of coated and uncoated CFRS has been performed by using the Classical Laminate Theory (CLT). The properties of the carbon fibres, the silicone matrix and a single unidirectional CFRS layer and are given in Table 3 and Table 4. Due to the large difference in stiffness between the carbon fibre and the silicone matrix only the values for E_1 , ν_{12} and ν_{13} have been derived with the rule of mixture. For all other properties the Halpin – Tsai equations have been used being much more appropriate for a large difference in fiber and matrix stiffness.

Table 3. Material properties of silicone and fiber material

E_{Fiber} [MPa]	230.000
E_{Silicone} [MPa]	1.2
α_{Fiber} [$10^{-6}/\text{K}$]	$-0,41 \cdot 10^{-6}$
α_{Silicone} [$10^{-6}/\text{K}$]	$290 \cdot 10^{-6}$
ν_{Silicone}	0,495

Table 4. Unidirectional CFRS layer properties

E_1 [MPa]	92000
E_2 [MPa]	3,59
E_3 [MPa]	3,59
G_{12} [MPa]	0.93
G_{13} [MPa]	0.93
G_{23} [MPa]	0.91
ν_{12}	0.37
ν_{13}	0.37
ν_{23}	0.96
α_1 [$10^{-6}/\text{K}$]	-0,408
α_2 [$10^{-6}/\text{K}$]	266,251
α_3 [$10^{-6}/\text{K}$]	266,251

With the material properties mentioned above the properties of an aluminium - coated quasi – isotropic CFRS laminate derived with the CLT are given in Table 5. The laminate consists an 8 layer quasi – isotropic layup with an additional 0.1mm silicone buffer layer and 100 μm aluminium coating.

Table 5. Coated CFRS laminate properties

E_1 [MPa]	26560
E_2 [MPa]	24216
α_1 [$10^{-6}/^\circ\text{C}$]	-0.386
α_2 [$10^{-6}/^\circ\text{C}$]	-0.372

It can be seen, that according to the CLT the coated laminate is becoming slightly orthotropic although the layup is quasi – isotropic. Due to the additional aluminium coating layer on one side of the laminate the laminate's geometrical symmetry plane is slightly shifted in thickness direction. Due to this shift of the symmetry plane, components in the [B] section in the [ABD] – matrix occur. This indicates a tensile – bending coupling. A comparison of two [ABD] matrices for a quasi – isotropic CFRS with and without a coating layer is presented below. The [ABD] matrix of a coated and un – coated CFRS laminate can be seen in Fig. 10 and Fig. 11.

$$[ABD]_{\text{CFRS quasi-isotropic}} = \begin{bmatrix} A & B \\ B & D \end{bmatrix} = \begin{bmatrix} 27601.1 & 9200.4 & 0 & 0 & 0 & 0 \\ 9200.4 & 27601.1 & 0 & 0 & 0 & 0 \\ 0 & 0 & 9200.4 & 0 & 0 & 0 \\ 0 & 0 & 0 & 2576 & 306 & 276 \\ 0 & 0 & 0 & 306.7 & 736.1 & 276 \\ 0 & 0 & 0 & 276 & 276 & 306.7 \end{bmatrix}$$

Fig. 10. [ABD] matrix of the pure quasi – isotropic CFRS laminate

$$[ABD]_{\text{coated CFRS}} = \begin{bmatrix} 27605.2 & 9201.8 & 0 & \mathbf{1379.6} & \mathbf{459.9} & \mathbf{0} \\ 9201.8 & 27605.2 & 0 & \mathbf{459.9} & \mathbf{1379.6} & \mathbf{0} \\ 0 & 0 & 9201.7 & \mathbf{0} & \mathbf{0} & \mathbf{459.9} \\ \mathbf{1379.6} & \mathbf{459.9} & \mathbf{0} & 2646 & 330 & 275 \\ \mathbf{459.9} & \mathbf{1379.6} & \mathbf{0} & 330 & 806 & 275 \\ \mathbf{0} & \mathbf{0} & \mathbf{459.9} & 275 & 275 & 330 \end{bmatrix}$$

Fig. 11. [ABD] matrix of the coated quasi – isotropic CFRS laminate

As the results of several parametric studies show, the factor of orthotropy (E_1/E_2) of the coated CFRS laminate is increasing with the thickness of the aluminium layer and the silicone buffer layer.

7.2. Layered shell elements approach

A very common method for modelling thin walled structures like the coated CFRS surface with finite element tools is the use of shell elements. Especially the use of so called “layered shell elements” is a common technique when analysing structures made of layered composite materials. As the FE – software tools derive the effective element stiffness matrices for the elements from the layers’ material properties and orientations with the use of the CLT results matching the ones derived with analytical CLT models. Several micro – mechanical models with layered shell elements have been built for the coated CFRS laminate and it can be concluded that the derived stiffness properties and [ABD] matrices are almost coincident with the ones from analytical CLT calculations. Some FE tools allow to account for the transverse shear in the shell elements. The results of this method are much closer to the shell – solid approach mentioned in 7.3 but still not fully coincident.

7.3. Shell - Solid element approach

The other approach is the use of solid and shell elements for the unit cell model. In particular, the unidirectional CFRS layers have been modelled as solid elements with several elements over the layer thickness. The aluminium coating is represented by shell elements. For the CFRS layers the homogenized properties of the UD layers have been used to avoid the modelling of fibres and matrix separately. In Table 6 the derived material properties from the shell – solid unit cell model are listed.

Table 6. Coated CFRS laminate properties from shell /solid unit cell model

E_1 [MPa]	30577
E_2 [MPa]	30585
α_1 [$10^{-6}/^{\circ}\text{C}$]	-0.411
α_2 [$10^{-6}/^{\circ}\text{C}$]	-0.410

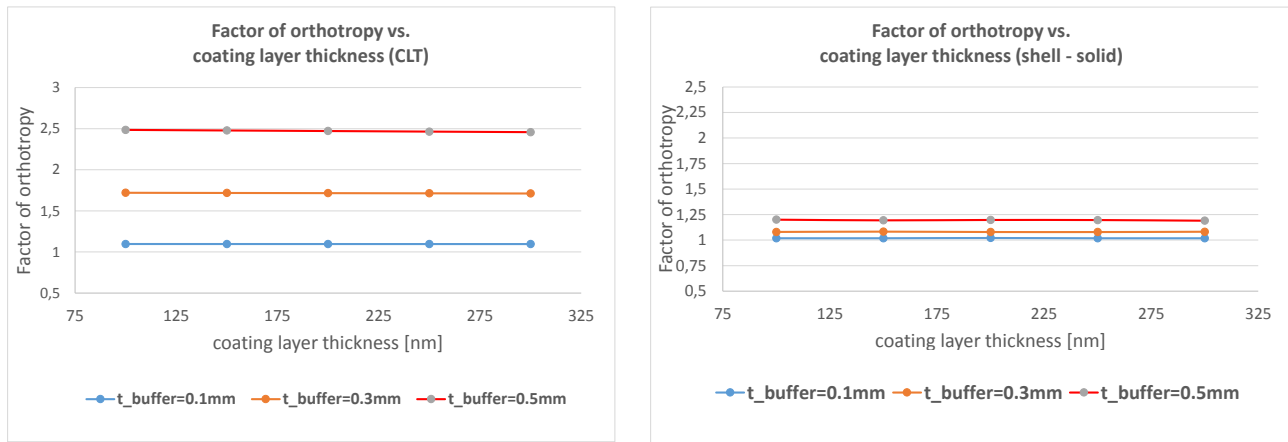
It can be seen, that the factor of orthotropy is close to 1. The same can be found for the CTE values. The reason for the changed behaviour concerning the orthotropic behaviour is the ability of the solid model to take the transvers shear stiffness of the laminate into account. In the CLT calculations, stiffness properties in thickness direction are not taken into account. Because of the very low shear modulus of the silicone matrix compared to an epoxy matrix the effects of the matrix shear stiffness especially in thickness direction play a more important role and have to be taken into account when deriving the laminate’s material properties.

7.4. Comparison and discussion of the micromechanical investigations

As it can be seen from the results discussed in the chapters above the CLT and respectively the shell elements are predicting a different material behaviour of the surface coated CFRS compared to the detailed shell – solid modelling approach. Especially the orthotropy of the E –moduli and CTE values is much higher in the results obtained by CLT and shell element models. This can explained by the missing influence of the transverse shear stiffness in the CLT and shell elements which has a quiet high influence for composite materials like CFRS with a very soft silicone matrix material. In Fig. 12 the factor of orthotropy over the coating layer thickness is presented for different silicone buffer layer thicknesses. In the left graph the results according to CLT are given, in the right one according to the shell – solid model. From this two graphs it can be concluded, that the coating layer thickness has a negligible influence on the orthotropic behaviour of the laminate for both modelling approaches. However the CLT results show higher factors of orthotropy compared to the shell – solid model especially for higher buffer layer thicknesses. This can be explained by the increasing

shift of the laminates symmetry plane with thicker buffer layers. The influence of different coating thicknesses is comparably small due to its small stiffness compared to the in - plane stiffness of the CFRS laminate. For the absolute values of the E – modulus a similar behaviour can be seen with the buffer layer thickness having the major influence.

Fig. 12: Factor of orthotropy vs. coating thickness according to CLT and shell – solid model



In order to analyse a full-scale model of a large coated CFRS structure like a deployable telescope or reflector the use of solid elements is not applicable due to its tremendous amount of computational effort. On the other hand, also layered shell elements seem to predict a not fully correct material behaviour. A proposed way to model the correct material behaviour with a reasonable amount of computational effort is the use of shell elements with their stiffness values defined by the [ABD] matrix obtained from a shell – solid unit cell model instead of defining layer material properties and orientation angles of the laminate.

8. CONCLUSION AND OUTLOOK

Within that paper, a possible method for enhancing the electromagnetic behaviour of a flexible fiber composite material (CFRS) has been presented. The optical surface coating of CFRS describes a functionalization method of flexible fibre composite material achieving surface qualities up to optical applications. The development of a suitable coating process has been demonstrated being applicable for the optical coating of large flexible CFRS surfaces. Different process steps and parameters together with their influence on the coating properties and their influence on the surface quality have been presented and discussed. Micro – mechanical investigations on the material behaviour of coated CFRS have been performed based on different modelling approaches from CLT to shell – solid FE – models. Concerning the micromechanical investigation, future micro mechanical models should include the nonlinear behaviour of the silicone over a wide range of temperatures like -220° - $+150^{\circ}$. Especially the significant change of the silicone stiffness and CTE at its glass transition temperature (about -110°) can have an influence on the laminates properties above and below that temperature. Verification of the results obtained through the mechanical and thermo – elastic tests will be another aspect of future investigations.

ACKNOWLEDGEMENTS

Parts of the work has be done under ESA contract No. 22378/09/N//RA. Special thanks to the technical officer form ESTEC, Dr. Eric Wille.

REFERENCES

- [1]. Datashvili, L.; Baier, H.: Flexible Fiber Composites for Space Structures. In: Fibre Composite Structures. Nova Science Publishers, Inc., 2011, USA, 2011
- [2]. Baier, H.; Datashvili, L.; Endler, S.; Stockman, Y.; Rodrigues, G.: Large deployable telescopes - also for μm -wavelengths?; CEAS Space Journal 2013
- [3]. Mechanism of the vacuum thin film coating system (o. J.),
http://www.shinmaywa.co.jp/vac/vac_e/vacuum/vacuum_2.html (Stand: 05.06.2014)
- [4]. H. Huang, F. Spaepen, "Tensile testing of free-standing Cu, Ag and Al thin films and Ag/Cu multilayers", Harvard University, Cambridge, Massachusetts, USA, 2000
- [5]. Dr. U. Brand, "Untersuchung eines Messverfahrens der mechanischen Eigenschaften dünner Schichten auf der Grundlage von SPM und MEMS", Physikalisch-Technische Bundesanstalt, Braunschweig, 2010
- [6]. W. Fang, C.-Y. Lo, "On the thermal expansion coefficients of thin films", National Tsing Hua University, Taiwan, 1999

A hybrid inflatable boom/rigid hinge membrane cylindrical reflector

*Lin Guo Chang^a, Luo Xi Lin^a, Du Juan^a, Tan Hui Feng^a

Center for Composite Materials, Harbin Institute of Technology, Hei Long Jiang, China

*Corresponding author: lingc@163.com, Tel: +86-451-86402317, Fax: +86-451-86402317

Address: No.2, YiKuang Str. Nan Gang region, Harbin, Hei Long Jiang Province, China

Abstract: Inflatable structures have advantages of lightweight and small folding volume, yet its drawback is the low structural stiffness compared with mechanical structures. This paper present design and accuracy test of a singly parabolic membrane cylindrical reflector combined the inflatable and mechanical structures. The deployable structure of the reflector consists of a pair inflatable booms and rigid hinge, which has the advantages of inflatable structures and rigid structures. The membrane reflector is supported by suspension cables connected to the rigid hinge, and the reflector could be folded before launching to the space. When the cylindrical reflector is launched into orbit, the reflector will be deployed by airing the inflatable booms. The rigid hinge with multiple joints will self-locking after deployed completely and high structural stiffness will provide for membrane cylindrical reflector. To validate the effectiveness of the reflector concept, a 2.6×2.6 m membrane cylindrical reflector model is manufacture. The membrane reflector is made of 25 μ m thickness Kapton[®] film and its two edges are reinforced by flexible carbon sheets, which will keep the membrane reflector in the designed parabolic shape. The surface accuracy of the reflector is performed by photogrammetry, and its accuracy error is analyzed. It is observed from the test results that the wrinkle on the membrane has great influence on the surface accuracy, and wrinkle must be eliminated to improve the surface accuracy.

Keywords: membrane cylindrical reflector; inflatable boom; rigid hinge, photogrammetry.

1. Introduction

High-performance thin-film material has advantages of light weight, easy to fold and excellent mechanical properties. During the past twenty years, more and more high-performance thin-film materials are used in large space structure design, especially Gossamer structures, such as inflatable parabolic antennas, planar films antenna, solar sail, inflatable booms, the second-generation precipitation radar antenna and so on^[1-5]. Although Gossamer structures made of flexible film material has advantages of light weight and small folded size, the whole structure will also show low strength and stiffness, low-frequency characteristics.

In order to improve the Gossamer structure's strength, rigidity and the low frequency, many kinds of rigidable materials, which is a kind of soft materials and can become rigid by some method, are developed. But these materials is far away from its practical application in space structures. At present, combining the mature rigid mechanism and Gossamer structures to fully use their advantages is a good choice.

In this paper, a hybrid parabolic cylindrical membrane reflector design is proposed. This paper first introduces the design concept of the reflector and its components, then a full-size reflector is manufactured according to the design. Finally, the reflector

surface precision is measured analyzed by photogrammetry.

2. Concept of a cylindrical reflector

Fig.1 shows the hybrid parabolic cylindrical membrane reflector design sketch. The whole structure consists of membrane reflector, rigid hinges, inflatable booms, mandrels and suspension systems. Among them, the inflatable booms are the structure's deployment power source. The shape of the membrane reflector is a parabolic cylinder, and the equation of the parabola is $y = x^2/4F$, the focal length $F=0.928\text{m}$.

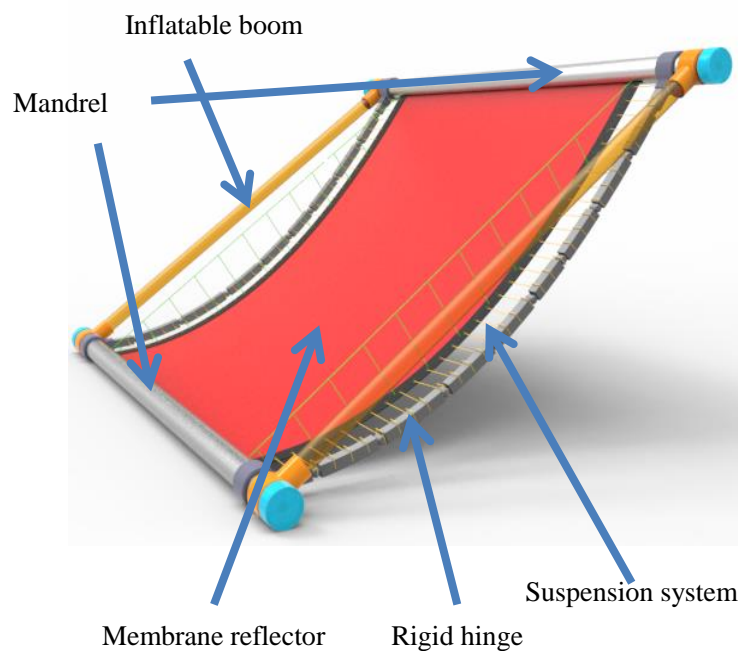


Fig.1 Parabolic cylindrical membrane reflector design sketch

2.1 Reflector and shape guides

Large-scale membrane reflector is usually made of aluminized polyimide membrane materials with several mils thickness. The Membrane reflector is connected to rigid hinges via suspension systems that is made of Vectran® fibers with low creep, due to the compressive stiffness of thin membrane materials is almost zero, there will be many structure wrinkles on the connection sides. Therefore, the membrane connection sides are reinforced by flexible carbon fiber composite plates. Besides, these composite plates are used as shape guides for the membrane reflector to improve and maintain the reflector accuracy. In order to ensure the shape guides accuracy, a wire systems are used to make fine adjustment of the shape guide's curve (Fig.2).



Fig.2 Composite edge reinforcement shape guides

2.2 Mandrel

Two mandrels are made of rigid hollow tube, one is connected to satellite, the other is used as the crimp-folding axis of the membrane reflector. Mandrels are one of the supporting parts of the whole structure; rigid hinges, inflatable booms and thin-film reflector are connected to them directly. Therefore, the mandrels should have high strength, light weight and better straightness, and carbon fiber composites are ideal materials for mandrels.

2.3 Inflatable boom

Inflatable booms are curly collapsed on the mandrel initially, the antenna will deploy on orbit by gassing the two inflatable booms. After the deployment of the antenna, the gas in the inflatable booms do not be kept. Fig.3 shows a inflatable boom made of thin-walled aluminum laminated materials that are manufactured by polyimide film and aluminum film (Polyimid/Al/ Polyimid). To prevent gas losing, a liner made of Kapton® film is put in each inflatable boom's interior. In order to improve stiffness of inflatable boom, it enhanced by four flexible carbon fiber composite ribs. Velcro straps are stucked on the outside of inflatable boom, that will give a deployment damping to make the inflatable boom deploy steadily.



Fig.3 Inflatable boom made of aluminum laminated materials

2.4 Rigid hinge mechanism

An articulated rigid hinge mechanism is designed to enhance the overall stiffness and strength of the antenna. The hinge has ten joints and each has different sizes and tilt angle. Fig.4 shows the expanded and folding state of the hinge mechanism. Adjacent joints are equipped with a self-locking mechanism, when the hinge is expanded, the self-locking will lock the joints tightly, as shown in Fig.5.



(a)

(b)

Fig.4 Rigid hinge mechanism (a) expanded state, (b) folding state



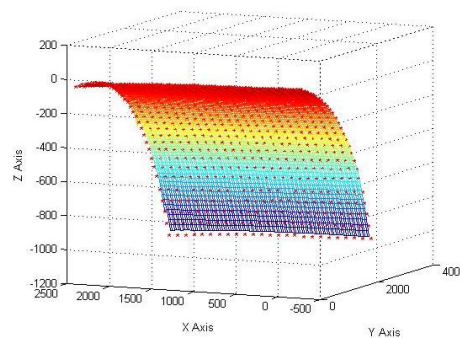
Fig.5 Self-locking mechanism

3. Accuracy test of the reflector

According to the above antenna design, a reflector model is manufactured and its surface precision is test by digital photography technology. Digital photogrammetric system used in the test is V-STARS digital photogrammetric system and its measuring accuracy is up to $5\mu\text{m}+5\mu\text{m}/\text{m}$. About 900 retro reflective targets with 3mm diameter and twenty code targets are pasted on the reflector surface (Fig.7(a)). A 130.018mm length carbon baseline ruler is put near the reflector. The test results show that the overall surface precision is 3.6mmRMS and the middle one-third of the reflector is 2.2mmRMS. It was found that errors are mainly from two aspects, one is the low accuracy shape guide plates and the other is the wrinkle on the reflector surface.



(a)



(b)

Fig.6 Accuracy test of the reflector (a)test setup, (b)test result

4. Conclusions

In this paper, a parabolic cylindrical reflector is proposed by combination of inflatable booms and rigid hinge mechanism. The reflector can be folded before launch and deployed on orbit by gassing inflatable booms. After complete deployment of the reflector, the rigid hinge will be self-locked and provide enough stiffness and strength for the reflector. According to design, a reflector model is manufactured and its surface precision is test by photogrammetry. The result of the test shows that the overall surface precision is 3.6mmRMS and the middle one-third of the reflector is 2.2mmRMS.

Reference 参考文献

- [1] John K. Lin, George H. Sapna, Stephen E. Scarborough, Bernardo C. Lopez. Advanced precipitation radar antenna singly curved parabolic antenna reflector development. 44th AIAA,

- 2003.
- [2] Yahya Rahmat-Samii, John Huang, Bernardo Lopez, Michael Lou, et. Advanced Precipitation Radar Antenna: Array-Fed Offset Membrane Cylindrical Reflector Antenna. IEEE TRANSACTIONS ON ANTENNAS AND PROPAGATION, VOL. 53, NO. 8, AUGUST 2005
 - [3] Christopher G. Meyer, Jack Leifer, Bernardo C. Lopez, David C. Jones, Boyd C. Caddell. Zero- and One-g Comparison of Ripple Amplitude in Single Curved Parabolic Membranes using Photogrammetry. 45th AIAA/ASME/ASCE/AHS/ASC Structures, Structural Dynamics & Materials Conference, 19 - 22 April 2004, Palm Springs, California
 - [4] Eastwood Im, Stephen L. Durden. Next-generation Spaceborne Precipitation Radar Instrument Concepts and Technologies. 45th AIAA Aerospace Sciences Meeting and Exhibit, 8-11 January 2007, Reno, Nevada.
 - [5] Jack Leifer. Gravity-Induced Wrinkling in subscale, Singly Curved Parabolic Gossamer Membrane. Journal of Spacecraft and Rockets, Vol. 47, No.1, January-February 2010

**LIGHTWEIGHT INFLATABLE STRUCTURES
for THERMAL PROTECTION DURING RE-ENTRY.
State of the art and future perspectives for their development.**

Marco Adami⁽¹⁾, Lorenzo Fiore⁽¹⁾, Luciano Battocchio⁽¹⁾

⁽¹⁾*Sekur Space & Technology*

Via Bianco di Barbania 16, I-10072 Caselle Torinese (TO) - Italy

Email: adami@sekur.it, fiore@sekur.it, battocchio@sekur.it

ABSTRACT

The paper describes the activities performed by Aero Sekur (mother Company of Sekur Space & Technology) in order to develop adequate thermal protection for re-entry phase based on flexible, foldable and inflatable structures.

The activities performed included analytical approaches as well as design and manufacturing of models for testing purpose. Three models have been tested in CIRA Plasma Wind Tunnel "Scirocco", while other samples of materials have been tested with less representative, but much cheaper, test facilities. Development of a new test facility that is useful for a first screening of solutions for thermal protection materials is also described.

1. BACKGROUND

Aero Sekur S.p.A. is a Company which mission is to provide products and services aimed to support life and survival of people and security forces, as well as operation of aerospace, maritime and land vehicles, on the basis of proven and best mechanical, software, textile and advanced material technologies

Aero Sekur was formed in 1993 – as Irvin Aerospace – by the merger of the former Irvin company founded in 1968 and the Sekur division of Pirelli, bringing together 40 years of experience in parachutes, CBRN equipment, aircraft fuel tanks and complex flexible structures. Since July 2007, Aero Sekur SpA is part of the English group Aero Sekur Ltd.

In the Space market, Aero Sekur SpA was the only European firm capable of designing and producing inflatable modular habitats, planetary landing systems, pneumatically activated mechanisms and flexible heat shields suitable for a very wide range of applications.

In 2012, in the frame of a general Company restructuring, Aero Sekur reorganized the Space and Innovation Division, moving its central location to Caselle Torinese (Torino, Italy) and giving to this site the mission of developing all the relevant activities. Since years the company's newest unit has been the European leader in inflatable systems for space applications in parallel all the related activities were transferred from Aero Sekur Headquarters, located in Aprilia (40 Km south-east of Rome), to Caselle Torinese.

More recently Aero Sekur established in Caselle Torinese a new Company (fully owned subsidiary of Aero Sekur SpA) named Sekur Space & Technology S.R.L. (SST) aimed to gradually incorporate all activities (including personnel and resources) related to the Space and Innovation Division and the related Projects.

Therefore Sekur Space & Technology is presently developing all the space activities of Aero Sekur group, based on Aero Sekur heritage.

2. INTRODUCTION

Atmospheric re-entry represents an important challenge in the space programs. Atmospheric re-entry firstly applies to the return to Earth surface of humans or payloads processed on board the International Space Station.

Atmospheric re-entry applies also to the space exploration missions, either if it is a return mission from an outer space body (planet, asteroid, comet...), or if it is the entry in an atmosphere of an outer planet (e.g. Mars).

Therefore the protection of the re-entry (or entry) space vehicle against the overheating due to the friction with the atmosphere and the very high velocity is a real problem. The typical solution to this problem is the implementation of a rigid TPS (Thermal Protection System).

In the past years Aero Sekur performed several activities in order to develop adequate thermal protection for re-entry phase based on flexible, foldable and inflatable structures. These activities were funded by an ESA sponsored Program (IRT - Inflatable Re-entry Technologies) or an Italian DoD sponsored Program (SPEM - SPacecrew Emergency Module), as well as internally funded activities.

The activities performed by Aero Sekur included analytical approaches as well as design and manufacturing of models for testing purpose. Three models have been tested in CIRA Plasma Wind Tunnel (PWT) "Scirocco", while other samples of materials have been tested with less representative, but much cheaper, test facilities. In particular, Aero Sekur contributed to the development of a test facility that is useful for a first screening of solutions for thermal protection materials.

The tests in PWT "Scirocco" were extremely interesting since the test simulated a re-entry from a terrestrial orbit, with the full thermal load; the temperatures obtained externally to the structure were similar to those experienced during re-entry, while internal side of the structure reached temperatures that would not cause damages to the equipment. Inflated structure, obviously, did not present failures.

Finally, in 2013 Aero Sekur developed, with the support of Italian Air Force, a thermometric facility to test specimens of thermal protection materials immersed inside an high speed hot gas flux ejected by aircraft turbine.

3. PAST EXPERIENCES

Many inflatable structure programs have resulted in conceptual designs and limited testing of the manufacturing and materials choices. In the late 1960's NASA studied a re-entry vehicle using an Attached Inflated Decelerator (AID). The studies concentrated on a ram-air inflated decelerator system for entry of the Mars atmosphere. An AID is a low-mass inflatable canopy directly attached to a payload. The AID was designed as an efficient deceleration system at high supersonic speeds in low-density planetary atmospheres. Canopy construction utilized Viton coated Nomex fabric. This type of canopy decelerator system would not be suitable for Earth return missions.

In the late eighties was developed an Inflatable Recovery Vehicle (IRV) concept. A truncated cone was designed with a small torus linked by inflatable cylindrical elements to a larger torus. Materials suggested for this concept include a canopy made of Nextel or Kevlar fabric and coated with a suitable insulation such as silicone. The payload would be located at the top of the truncated cone to insure that the IRV stabilizes in the preferred flight orientation.

Finally, having International Space Station in operation, inflatable reentry vehicles (capsules) have been under study in Europe and the US for several years in particular because of the cost savings associated with de-orbiting payloads from the ISS via a passive means rather than using the Shuttle or Progress/Soyuz spacecraft vehicles.

IRDT

The first important European experience was IRDT (Inflatable Reentry Descent Technology)

The IRDT program was an outgrowth of technology developed for the Mars 96 spacecraft - a flexible inflatable shield for the entry and descent of a penetrator into Mars' atmosphere. After several preliminary studies and a feasibility assessment performed between December 1998 and March 1999, the IRDT program was officially initiated on 1 May 1999.

The first IRDT mission contained two separate inflatable reentry modules. The smaller capsule referred to as the IRDT Demonstrator deployed an inflatable envelope able to withstand the extreme hypersonic flight environment before re-entry. The Demonstrator deceleration system consisted of a small ablative nose and a flexible envelope inflated in two stages (see Figure 1). The nose assembly used a nose radius of 0.61 m and a cone half angle of 45° to assure adequate stability during all phases of re-entry. The flexible entry shield first stage increased the capsule diameter from 80 cm to 2.8 m. The second stage of the flexible entry shield for the IRDT Demonstrator replaced a conventional parachute system. Second stage inflation causes the diameter of the vehicle to increase to 3.8 m.

Launch of the IRDT-1 mission took place on 9 February 2000. Formal flight-evaluation review then took place at ESTEC on 4 and 5 April 2000

The flight data showed the Demonstrator's stability during the beginning of the re-entry phase and that the inflatable structure survived intact the peak heat-flux (350 kW/m^2) and g-load (15 g) conditions; however, the structure appeared to have partially collapsed later in the flight, resulting in unstable conditions and in a local temperature increase.

The second cascade opened nominally (close to Mach 0.8), but did not inflate. The final descent was therefore faster than nominal, leading to a touch-down velocity of around 60 m/s (the free fall velocity of the rigid core body), instead of the 13 m/s design value. When the spacecraft hit the ground, its lower section containing sub-systems and a radio beacon was damaged. All experiments in the sensor package worked perfectly.

The second test of the IRDT system was scheduled to occur in tandem with a solar sail experiment named Cosmos-1 and sponsored by the Planetary Society in the US. This experiment was launched into a sub-orbital flight on Friday 12 July 2002 by a ballistic missile from a submerged nuclear submarine stationed in the Barents Sea. Upon release, the IDU was to be deployed, increasing the diameter of the re-entry vehicle to 2.5 m. The second IDU to be deployed at about 25 km altitude was to provide further aero braking by increasing the diameter to 4.1 m. The return capsule was not found and Russian authorities searched extensively for the Demonstrator-2 vehicle or identifiable remains; however no material definitely belonging to this spacecraft has been recovered. The most likely cause of the failure is non-separation between third stage of the missile and the payload. No confirmed pieces of this spacecraft have been located during several searches of the impact range

The objective of the IRDT-3 test flight was to verify an enhanced IRDT system concept under representative orbital flight conditions. This enhanced concept resulted from recommendations of the IRDT-1 flight evaluation. Improvements include the shield design, the internal pressure control and monitoring, a telemetry system for the landing phase and an enriched sensor package providing the flight evaluation data.

The spacecraft, designated as "Demonstrator 2" was a 80-cm diameter sphere in the folded position that weighs 146 kg. Once released in a sub-orbital trajectory, two separate thermal shields, 2.3-m and 3.8-m in diameter were to be inflated for control of aero-braking descent and re-entry.

The IRDT-3 mission was launched into a sub-orbital flight by a submarine launched ballistic missile. Although sub-orbital, the entry conditions of 7000 m/s entry velocity and -6° entry angle were representative for an orbital entry with around 7800 m/s and -2° in terms of heat flux and g-loads which mainly determine the design of the heat shield. The Demonstrator was launched on 7 October 2005 and was scheduled to land in Kamchatka approximately 30 minutes later. Received telemetry data confirmed the initial phases of the mission to be nominal. Shortly after the re-entry phase radio contact with the Demonstrator disappeared. Search and recovery activities were initiated, but the IRDT has not been retrieved.

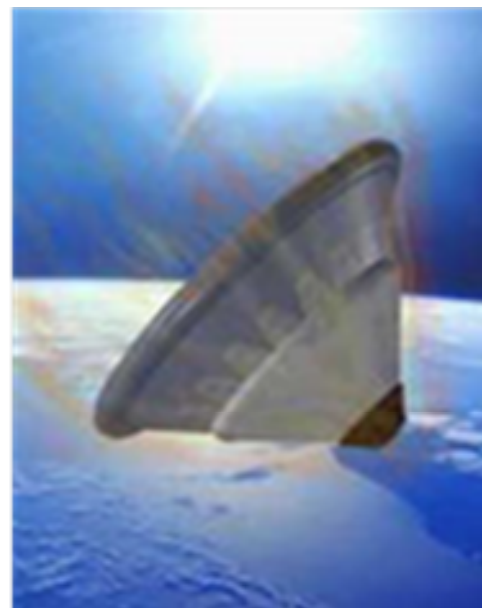


Figure 1 Pictorial view of IRDT-1 Demonstrator with 2nd stage deployed

4. AERO SEKUR EXPERIENCE: IRT

The first study on inflatable structures for thermal protection during re-entry on which Aero Sekur was involved was IRT: Inflatable Reentry Technology, a Program sponsored by the European Space Agency in which Aero Sekur was Prime Contractor with Alenia Spazio (now Thales Alenia Space – Italia), CIRA and GCE as subcontractors.

The responsibilities were subdivided between the Companies as follows:

- ✓ Aero Sekur was in charge of materials selection, System Design, Manufacturing of samples, full scale model and scaled model for PWT and functional tests
- ✓ Alenia Spazio was in charge of Structural Analysis
- ✓ CIRA was in charge of Aerothermodynamic Analysis and Testing
- ✓ GCE was in charge of Review of requirements and support for Materials selection.

The primary objective of the IRT program was to identify leading candidate materials that would be suitable for use in the design and testing of a new generation prototype inflatable reentry capsule.

A second objective was to design and manufacture a full scale model in order to develop manufacturing technologies.

A third objective, finally, was to test in PWT a scaled model of the manufactured model (in particular with respect to Thermal Protection System – TPS) in order to verify the capability of the selected design to approach the hot phase of an orbital reentry.

MATERIALS

Materials selection for the inflatable reentry capsule clearly depends both on mission requirements and on the chosen manufacturing methods, since different materials are necessary to meet the requirements for different vehicle construction techniques and different mission profiles.

Therefore several materials have been identified and tested in order to verify their potential utilization for reentry vehicles.

However, since the purpose of the program was to manufacture and test a ground model, finally some materials have been selected even if they were not space qualified.

The materials utilized have been evaluated considering in principle that purpose of the program was to also that the inflatable structure would have three principal layers: the restraint for structural resistance, the bladder for pneumatic retention and the thermal protection.

Material considered and tested were:

<i>Structural Materials</i>	<i>Pneumatic Retention Materials</i>	<i>Thermal Protection Materials</i>
<ul style="list-style-type: none"> ○ Coated polyester fabrics <ul style="list-style-type: none"> ▪ Aertex 90930 ▪ Aertex 91320 ○ Coated Kevlar fabrics 	<ul style="list-style-type: none"> ○ Kapton 100HN ○ Polyester breather 	<ul style="list-style-type: none"> ○ Ablative rubbers <ul style="list-style-type: none"> ▪ Silicone ▪ Fluorosilicone ○ Nextel 312 A10 ○ Saffil

The materials samples have been tested after exposure of the Test Articles to environment simulating space conditions:

Vacuum, Infra-Red (IR), Ultra-Violet (UV), Atomic Oxygen (AO)

The tests performed on the samples were essentially (but not only) oriented to characterize the materials from mechanical point of view:

Tensile strength, Permeability, Mass loss, Folding capability, Packaging efficiency

FULL SCALE MODEL

The full scale model was a cone with an angle of 60° and an external diameter of 3 meters, and it was made by a truss structure supporting the TPS.

Considering that it was not a flight hardware, the full scale model was manufactured with some simplifications with respect to a space qualified re-entry vehicle architecture.

In particular, the design was done in a way that the same layer was in the same time restraint for structural resistance and bladder for pneumatic retention; this layer was in Aertex, a coated polyester fabric that is largely utilized in Aero Sekur for the manufacturing of emergency floating devices for helicopters.

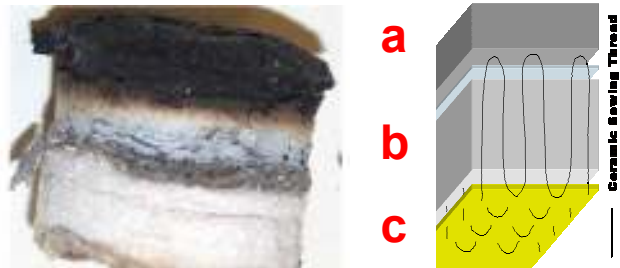
The IRT truss structure therefore was made by pneumatic beams supporting all the mechanical loads foreseen; no test was clearly performed, but the structural resistance was verified by means of analytical tools. The truss structure in the conical part was covered by a Kevlar layer which function was to mechanically support the TPS in the structure free spaces.



Figure 2 IRT Full scale model

Figure 3 TPS after PWT and TPS architecture

- a:** Ablative Silicon
- b:** Thermal Protection (Nextel and Saffil)
- c:** Structural layer



Finally the TPS was made by three layers; the two internal layers were made in Nextel and Saffil, while the external layer was in Ablative Silicon which preparation was based on an Aero Sekur specification. The function of the Ablative Silicon was clearly to absorb the heat due to atmospheric re-entry in order to protect internal structure.

SCALED MODEL FOR PWT TEST

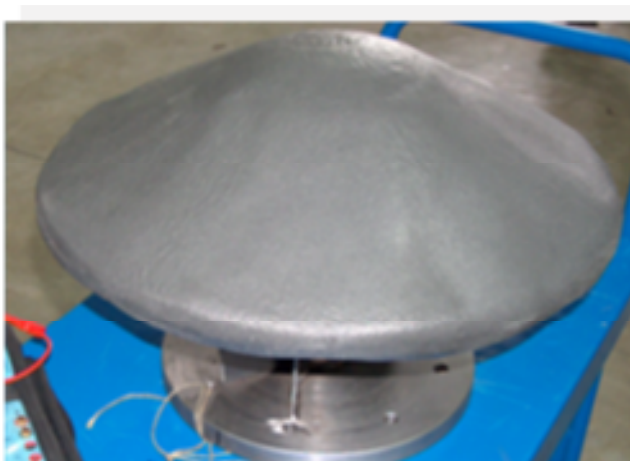


Figure 4 IRT scaled model for PWT test

The last step of the study activities was the performance of the test in the CIRA Plasma Wind Tunnel “Scirocco”.

In order to fit with the dimensions of the PWT, a scaled model of IRT was prepared.

In this scaled model only the Thermal Protection System, including also Kevlar support, was represented.

Before the performance of the test on the scaled model, thermal properties of the TPS have been tested in a smaller PWT.



The model was supported by a metallic structure interfacing with PWT. The diameter of the scaled model was 600 mm.

Two test articles have been prepared and tested.

The tests were performed on Jan 30th, 2004 and April 7th, 2004 with a peak heat flux of 700 KW/m² and the total heat load was 60 MJ/m²

The test results were positive: the ablative material protected the internal layers and no damage occurred to the TPS internal layers.

Figure 5 IRT scaled model during PWT test

5. AERO SEKUR EXPERIENCE: SPEM

The acronym SPEM stands for “SPacecrew Emergency Module”. As a matter of fact, the idea behind this acronym was to develop a flexible, inflatable and foldable module for emergency re-entry from orbiting Spaceships, such as Space Shuttle or International Space Station. Clearly the way to develop and qualify this Emergency Module is very long, but one of the first steps is certainly the development and the orbital re-entry test of a small flexible, inflatable and foldable capsule.

Based on the IRT experience Aero Sekur developed a capsule to test the IRT Thermal Protection approach in real re-entry from orbit conditions in the frame of Roberto Vittori “ENEIDE” mission to the ISS. A contract was given to Aero Sekur by Italian DoD. Due to several problems it was not possible to fly the capsule in ENEIDE mission or in other flight missions; therefore a scaled model was tested in the CIRA PWT “Scirocco” in order to obtain at least some significative indications.

The capsule was made of the following subsystems:

- Inflatable structure, including TPS
- Inflation Subsystem
- Avionics
- Parachute
- Capsule support structure

The inflatable structure was made of one Kevlar structure containing 16 chambers in Kapton pressurized at 1.5 barg; the Kevlar structure would provide mechanical support to the Kapton chambers that would provide pneumatic retention. The reason of 16 chambers was to eventually guarantee a good (even if degraded) support to TPS in case of a depressurization of one chamber.

The diameter of the inflated structure was 1 m, with a cone of 60°.

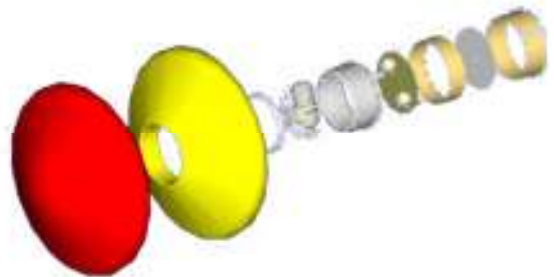


Figure 6 SPEM Configuration

The TPS was made (according to the IRT experience) with two layers of Nextel and Saffil, covered by a layer of ablative silicon.

The inflation subsystem was made of a GN2 bottle with a volume of 1.1 liters and a pressure of 100 bar, and plumbing to pressurize the Kapton chambers. Each chamber had a specific line for pressurization, in order to avoid that a failure in a chamber would propagate in the other chambers.

Figure 7 Inflation Subsystem

Purpose of the avionic subsystem was very simple:

- Provide energy to the SPEM electrical equipment
- Command of the inflation valve
- Handling of data from sensors (Pressure, temperature and accelerometers)
- Arm command to open the parachute
- Download data to Ground Station

The Parachute was a ringsail type parachute with a diameter of 2 m activated at 10 Km altitude through a barometric command. Final velocity of the SPEM capsule was 10m/sec.

Finally, the Capsule support structure was an Aluminum cylinder containing all the interfaces with the other subsystems. The design was such that the structure (420 mm diameter, 380 mm high) was containing all the subsystems, including the inflatable subsystem in folded configuration and the folded parachute.

The total mass of the capsule was 15 Kg.

The capsule for cost reasons was manufactured utilizing COTS avionic components, while TPS was identical to the one tested in the PWT "Scirocco" in the frame of IRT study. During the design and assembly phase several potential re-entry missions were analysed. The most important possibility evaluated was the re-entry with a Progress vehicle: SPEM would be separated from Progress just before the destructive Progress re-entry. As said, unfortunately, no real return mission was possible.

SPEM PWT TEST

Since it was not possible to perform a real return mission from orbit, it was decided to perform a PWT test in order to simulate the reentry heat load on a scaled capsule.

Therefore, in order to validate the SPEM concept, it was decided to perform a test in "Scirocco" PWT with a scaled model of 600 mm diameter.

A scaled model was designed and manufactured. In this model there was an inflatable structure protected by the TPS. TPS was made, according to IRT experience, by the Nextel and Saffil layers covered by ablative Silicon developed according to an improved Aero Sekur specification, while the inflatable structure was made by a single Kapton chamber protected by an external structural Kevlar layer. For safety reasons it has not been possible to perform the inflation in the PWT, but the test article was inflated before the installation in the PWT. In this way it has been possible to verify that no damage would occur to the inflated structure. Finally, there was a metallic structure interfacing the test facility.



Figure 8 SPEM scaled model before (left) during (centre) and after (right) PWT test

The test was performed on September 26th, 2008. Test data are: Heat flux: 1240 KW/m² and time of exposition 108 sec. The maximum Temperature reached on the external layer (ablative Silicone) was 1250°C, while the internal temperature of the inflated chamber was lower than 40°C.

As it is possible to see from Figure 8, no damage occurred to the inflated structure.

6. AERO SEKUR EXPERIENCE: SPEM GSE

The IRT and SPEM programs have been extremely important not only from a technology development point of view; their development has also demonstrated that the activities necessary require a very high level of economical effort.

As a matter of facts, the study and the experimental evaluation of aerospace materials is actually one of the most challenging and money demanding issues in the aerospace science.

This applies in particular to the thermal tests of new materials for TPS application and for ablative materials development.

Based on this experience, Aero Sekur studied the possibility of performing tests, at least in the preliminary stages of development, with more economical facilities.

For this reason in 2010, with Italian Air Force, Aero Sekur developed a thermometric facility to test specimens of thermal protection materials immersed inside an high speed hot gas flux ejected by aircraft turbine. This Italian Air Force facility has been successfully tested with the support of Experimental Flight Test Center of Italian Air Force located in Pratica di Mare near Rome. The facility is able to evaluate flux enthalpy by measuring gas speed, stagnation point and free stream temperatures as well as front and back temperatures in the specimen in order to evaluate the evolution of the thermal flux versus the time.

The facility (improperly called as SPEM GSE - Ground Support Equipment) is basically a High speed gas turbine exhaust facility for TPS materials testing; it has been firstly designed to test ablative materials, nevertheless it can be used also for testing different thermal protections materials as those used for hot structures (combustion chambers, nozzles, thermo-structural protections for hypersonic flight).

The expected main advantages of this experimental method are:

- To be able to compare ablative and thermal materials performances before deep tests are performed in a dedicated facility (arc jet and plasma tunnels); this allows a reduction of costs, enhancing the effectiveness of the qualification test program, introducing, where necessary, a pre-qualification screening phase;
- To be quick to use, flexible and adaptable to several applications with negligible impact in the test set up configuration.
- Adaptability to different specimens sizes.
- Capability of achieving test durations of several minutes.

The drawbacks are mainly concerning:

- The representativeness of the environment mainly for what the ablative materials are concerning, even if the enthalpies which can be achieved are sufficient to activate pyrolysis and to start ablation, therefore the method is considered effective whenever a comparison in performance of different materials is needed. In particular the environment is characterized by an high gas mass rate at lower speed and temperature compared to the plasma chamber.
- Additional heat flux due to molecular recombination cannot be reproduced.

Therefore the method is considered cooperative/complementary to the standard facilities able to represent the re-entry environment, being effective whenever a comparison in performance of different materials is needed

The SPEM GSE is composed by:

- Calorimeter:
 - Pitot tube;
 - Thermocouples with exposed junction and grounded junction
 - Specimen of ablative material insulated with mullite tube
- Calorimeter support;
- Thermistor for temperature control of the acquisition electronics;
- Acquisition electronics;



Figure 9 SPEM GSE test configuration

The test was concerning specimens of Silicone elastomer ablative material with a diameter of 100 mm and a thickness of 50 mm, and have been placed at 4.5 meters from the aircraft engine nozzle at 2 meters height. They were inside mullite tubes to avoid heat dispersion.

The aircraft provided at least three steps of increasing power before the achieving of the operating environment (this in order to reduce the transients); full power test was about 80 secs long (it could be increased if necessary)

The max front temperature achieved on the specimens was 1100 °C in a gas flux having speeds up to Mach number around 0,6. Reference Enthalpy achieved in the working point was 1,9 MJ/kg with a reference heat flux of 0,5 MW/m² and a flow rate of 120 kg/m²s

The specimen started the ablation process which extended to about 2 mm of its exposed surface. This is confirmed by the fact that the weight before the test was 0,62735 kg, while the weight after the test was 0,61785 kg, with a Delta Weight of 9,5 grams

The most significant conclusions of this development activities are:

- The thermometric facility (SPEM GSE) designed is able to test specimens of thermal protection materials immersed inside an high speed hot gas flux ejected by aircraft turbine.
- Values of temperature, speed, enthalpy and heat flux reached during the test are sufficient for comparison in performance of different materials.
- Screening of different materials is useful and costs saving before deep tests in dedicated facility.
- The facility could be improved and easily adapted for different needs and configurations (materials tests, full scale and scaled models/systems tests, aircraft engine heat flux characterization,...).
- The facility is conceived to be used for dual uses applications, covering either institutional aeronautical and also specific space applications.
- The GSE could potentially be used also to assess other materials performance used for aircraft support/protectons



Figure 10 SPEM GSE before (left) during (centre) and after (right) test

7. PERSPECTIVES

The problems associated with the reentry in the Earth atmosphere of vehicles returning from space, or the landing on the surface of a planet with atmosphere, are becoming more and more important.

In particular there is no return vehicle from ISS (with the obvious exception of the Soyuz capsule), and therefore it is not possible to download Payloads or samples resulting from orbital experiments in order to perform post-process in the PI facilities.

In a similar way, there will be severe problems in landing large modules on the surface of an outer planet (e.g. Mars) utilizing traditional rigid thermal protection. However these large modules are necessary to land on a planet large payloads, such as rovers or modules for a human base or directly humans.

The limits for this second case are essentially due to the limits that launchers pose to payloads in terms of mass and dimensions.

The TPS based on flexible, foldable and inflatable structures could provide a solution to this problem, since an inflatable structure is less constrained by the dimensions imposed by launcher fairings. Therefore large inflatable TPS will have lower launch volume and lower launch mass with respect to a rigid one.

Having larger surfaces, they could reduce the thermal load and therefore they could deliver to the surface larger or heavier modules.

Therefore the future of exploration (including human exploration) will be based on the availability of flexible, foldable and inflatable TPS.

Considering the achieved state of the art it will be possible to restart a development program that will provide in few years on-orbit demonstration of the flexible, foldable and inflatable TPS; a second step will be the qualification of capsules for payload return from the ISS, in order to arrive to a final step that will be the qualification from terrestrial orbit of a large flexible, foldable and inflatable structure with TPS.

8. CONCLUSIONS

The future of exploration (including human exploration) will be based on the availability of flexible, foldable and inflatable TPS.

The state of the art will permit in a very short time period the availability of this technology fully qualified for two main applications, the return of payloads to terrestrial surface and the delivery of large modules on the surface of outer planets, such as Mars.

The state of the art has demonstrated that flexible, foldable and inflatable TPS could sustain thermal loads that will occur during orbit entry phase.

Facility cost for materials development could be reduced by means of solutions that will permit the first selection of candidates materials.

Finally, IRT and SPEM programs have been extremely important not only from a technology development point of view, since they demonstrated also the capability of Aero Sekur in dealing with primary level technological challenges.

This paper presents the heritage that Aero Sekur gives to Sekur Space & Technology; Sekur Space & Technology is ready to accept the challenge and to proceed with further developments on re-entry lightweight inflatable structures for thermal protection.

Design Analysis of an Inflatable Satellite Communication Reflector

He HUANG¹, Fu-ling GUAN¹, Houfei FANG²

1. College of Civil Engineering and Architecture, Zhejiang University, Hangzhou 310058, China

hehuang0623@hotmail.com

ciegfl@zju.edu.cn

2. Jet Propulsion Laboratory, CA 91109, the USA

houfei_fang@yahoo.com

ABSTRACT

Due to its lightweight and high package efficiency, the inflatable antennas have been used on the ground for satellite communications. How to precisely make and maintain the geometry of the reflective membrane brings great challenges to the design of this inflatable antenna. This study has introduced a set of equations and an analysis process for form finding analysis with orthotropic membrane materials. Determining the shape of each piece of flat membrane is the second introduction of the design analysis. Then based on the results from the design analyses, a detailed finite element model of the whole antenna can be established to verify the design. The surface shape as well as the RMS error of the reflector at the determined inflation pressure can thus be calculated. The geometry deviations introduced by the wind loads can also be determined by using this finite element model (FEM). An example will be given by the paper to discuss all these analysis results.

Keywords: Inflatable antenna, Form finding, Cutting design, FEM analysis

1. Introduction

Due to its lightweight and high package efficiency, the inflatable antennas have been used on the ground for satellite communications. Fig. 1 is one of these antennas made by GATR Technologies [1]. This inflatable antenna has two half-sphere chambers—the front chamber and the back chamber. These two half-sphere chambers are separated by a piece of reflective membrane. The pressure difference between the front chamber and back chamber forms the reflective membrane to be a parabolic shape.



Fig. 1. Inflatable Antenna Made by GATR Technologies

This inflatable antenna has been employed as the quickly deployable high-bandwidth communications in areas that the infrastructure has been wiped out and also utilized for search/rescue operations, infrastructure repair efforts, and medical support [1]. However, the design methodology and structural analyses have been seldom particularly introduced in the public [2].

The general inflatable antenna in space [3-5] consists of one close convex chamber and circumferentially supporting structure. One side of the chamber is used as the reflector and the other side is made to be an integrate chamber with the reflector. The supporting structure around the equator

of the chamber can supply the edge with counterforce so as to prevent it from becoming spherical after inflated [6]. Compared with the general inflatable antenna, this terrestrially spherical inflatable antenna has many different points in the structural respect. In the first place, the profile of the reflector is kept by the difference of the pressure between the two half chambers while there is one chamber in general antenna. Secondly, the reflector of this antenna is supported on the equator of the inflated sphere while general antenna needs independent supporting system outside to keep the reflector profile. Finally, the mechanic circumstance is totally different between the terrestrial and the spacial such as gravity, atmospheric pressure and other loads.

As there are these differences, a series of analyses and technologies for terrestrially spherical inflatable antenna should be reconsidered when referring to the general inflatable antennas. The first analysis is form finding analysis for inflatable membrane antenna that has been studied by many researchers [7-9]. It should be conducted at the beginning of the design for the reflector. Then, the second task is determining the shape of each piece of flat membrane to be seamed together to form a parabola. Many methods [10, 11] have been researched to find the cutting lines. In contrast, the load analysis for finite model and the parameters of this antenna are more important because few references can be consulted.

This paper introduces the whole process of design and analyses for this terrestrially spherical inflatable antenna. In Section 2, the design analyses are stated to mainly talk about form finding analysis and piece cutting design. In Section 3, the FEM analyses are established in detail to study the design parameters and an example is given to discuss all these analysis results. And the conclusions are summarized in the end.

2. Design Analyses

The design analyses are mainly about the form finding analysis and piece cutting design. It is important to process these design analyses so that the accurate initial profile of the reflective membrane and the cutting pieces can be got to carry on the manufacture and the subsequent analyses.

2.1 Form Finding Analysis

It is essential that the so-called form finding analysis is conducted to find the fabricated shape of the membrane without pressurization from the desired inflated parabolic shape, since the reflective membrane becomes to have tensions after the antenna is inflated by the pressure that causes the shape deviation between the inflated and deflated membrane.

Form finding analysis starts from deformed shape to calculate the original shape as well as the inflation pressure, which can't be readily performed by using commercial finite element software. Besides that, orthotropic material property of the membrane makes this analysis even more complicated. This study introduces a set of equations and an analysis process for form finding analysis with orthotropic membrane materials on the base of Ref. [11].

Considering the symmetry, the cylinder coordinate system $r\theta z$ is built as shown in Fig.2. The arbitrary point on the reflective membrane changes its coordinate from (r_1^0, z_1^0) before inflating to (r_1, z_1) after inflated and the local coordinate systems are built as $\xi\eta\zeta$ and $\xi'\eta'\zeta'$ respectively, defining the longitude and the latitude as the orientations of ζ and η respectively.

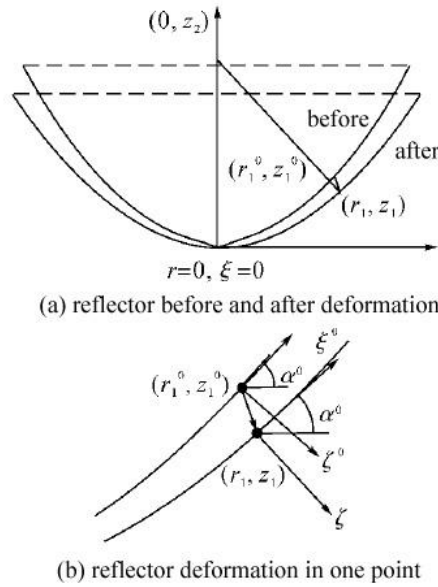


Fig. 2. Reflector's Deformation

The strains and forces of the arbitrary point on the longitude and the latitude can be

$$\varepsilon_{\xi} = \frac{d\xi - d\xi^0}{d\xi^0}, \quad \varepsilon_{\eta} = \frac{d\eta - d\eta^0}{d\eta^0} \quad (1)$$

$$N_{\xi}^0 = N_{\xi}(1 + \varepsilon_{\xi}), \quad N_{\eta}^0 = N_{\eta}(1 + \varepsilon_{\eta}) \quad (2)$$

where N_{ξ}^0 and N_{η}^0 are tension forces in the unit arc $d\eta^0$ and $d\xi^0$ respectively while N_{ξ} and N_{η} are tension forces in the unit arc $d\eta$ and $d\xi$ respectively.

The equations based on the membrane theory [12] are

$$\kappa_1 N_{\xi} + \kappa_2 N_{\eta} = p \quad (3)$$

where curvatures on longitude and latitude are $\kappa_1 = 4F^2(4F^2 + r_1^2)^{-3/2}$ and $\kappa_2 = 1/r_2$ respectively, which r_1 and r_2 the radiuses on longitude and latitude. F is the focus of reflector. The tension forces are drawn from (2) and (3) as

$$N_{\xi} = \frac{pR_2}{2}, \quad N_{\eta} = \frac{pR_2}{2} \left(2 - \frac{R_2}{R_1} \right) \quad (4)$$

The constitutive equations can be given by taking the orthotropic of the material into account as shown

$$\begin{bmatrix} N_{\xi}^0 \\ N_{\eta}^0 \\ 0 \end{bmatrix} = t \begin{bmatrix} d_{11} & d_{12} & 0 \\ d_{21} & d_{22} & 0 \\ 0 & 0 & d_{33} \end{bmatrix} \begin{bmatrix} \varepsilon_{\xi} \\ \varepsilon_{\eta} \\ 0 \end{bmatrix} \quad (5)$$

where the parameters of material are $d_{11}=E_x/v$, $d_{22}=E_y/v$, $d_{12}=E_y v_{yx}/v$, $d_{21}=E_x v_{xy}/v$, $d_{33}=G$ and $v=1-v_{yx} v_{xy}$, which E_x , E_y and v_{xy} , v_{yx} are the elastic modulus and Poisson's ratios on the longitude and

the latitude, G is shear modulus and t is the thickness of reflective membrane.

Plug (2) to (5) to get

$$\begin{cases} N_{\xi}(1 + \varepsilon_{\eta}) = (d_{11}\varepsilon_{\xi} + d_{12}\varepsilon_{\eta})t \\ N_{\eta}(1 + \varepsilon_{\xi}) = (d_{21}\varepsilon_{\xi} + d_{22}\varepsilon_{\eta})t \end{cases} \quad (6)$$

So the solutions of strains are

$$\begin{cases} \varepsilon_{\xi} = \frac{N_{\xi}d_{22}t - N_{\eta}(d_{12}t - N_{\xi})}{d_{11}d_{22}t - (d_{12}t - N_{\xi})(d_{21}t - N_{\eta})} \\ \varepsilon_{\eta} = \frac{N_{\eta}d_{22}t - N_{\xi}(d_{21}t - N_{\eta})}{d_{11}d_{22}t - (d_{12}t - N_{\xi})(d_{21}t - N_{\eta})} \end{cases} \quad (7)$$

and the solutions of the initial profile are shown as

$$\begin{cases} r_1^0 = \frac{r_1}{1 + \varepsilon_{\eta}} \\ z_1^0 = \int_0^{\xi} \sqrt{1 - ((1 + \varepsilon_{\xi}) \frac{dr_1^0}{d\xi})^2} \frac{d\xi}{1 + \varepsilon_{\xi}} \end{cases} \quad (8)$$

The equations stated above are the theoretical solutions of parabolic reflective membrane made of orthotropic materials. By this form finding analysis, the mould for the reflector can be designed and manufactured with the parameters of the material and the difference between the chamber pressures.

2.2 Piece Cutting Design

The processes of piece cutting design usually are the cutting line design and piece deploying analysis. Since the reflective membrane is parabolic surface that cannot be completely deployed into flat membrane for cutting, the cutting design should be conducted to get suitable cutting pieces so as to approximate the profile and keep the error acceptable.

It is widely known that the geodesic methodology is generally utilized in the cutting line design for the curved surface. Specifically, the meridian is a kind of geodesic line for the axisymmetric parabolic reflector. Thus this reflector can be divided into some identical curved pieces by meridians as cutting lines, as shown in Fig.3.

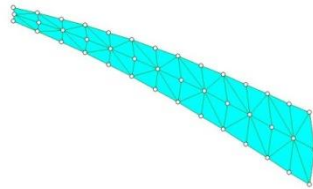


Fig. 3. Reflector piece by meridians as cutting lines

The curved piece can be analyzed with a kind of method, namely “spring-mass system”[11], to approximately get the flat form for cutting. The basic idea is to make the membrane stresses of each element equal to the spring forces. Then, it can cause internal forces in equivalent springs to keep the

nodes of all the elements on the reflector membrane into the plane along one vector. The nodes on one plane will move by the action of these internal forces in springs and the final form of the piece in the flat membrane can be gotten when all the nodal forces are balanced.

The reflective membrane stresses of elements can be equally expressed by the internal forces of equivalent springs as

$$\mathbf{T} = \{T_1 \quad T_2 \quad T_3\}^T = \mathbf{V}\mathbf{B}^T\boldsymbol{\sigma} = \mathbf{V}\mathbf{B}^T\mathbf{D}\mathbf{B}\boldsymbol{\delta} = \mathbf{K}\boldsymbol{\delta} \quad (13)$$

where \mathbf{V} is the volume matrix of elements, \mathbf{B} is compatibility matrix, \mathbf{D} is material matrix, $\boldsymbol{\sigma}$ is stress vector and $\boldsymbol{\delta}$ is strain vector of springs. The spring-mass system can be expressed by the Lagrange Equations and solved by the Euler Method.

The pieces of the reflector for a kind of engineering prototype are cut as shown in Fig.4 and these pieces are pasted along the cutting line as the butt-joint with the gluing band on the pasting mould that is designed by the aforementioned method of form finding analysis. The pasted reflector shown in Fig.5 indicates that these design analyses stated above are feasible.



Fig. 4. Cutting pieces of the reflector

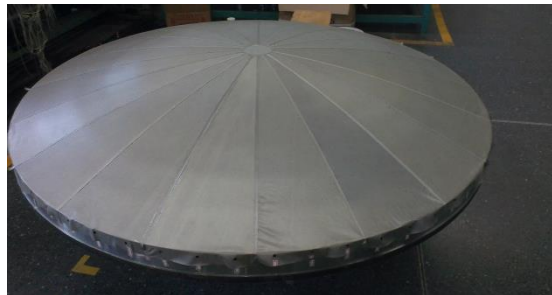


Fig. 5. Pasted reflector

3. FEM Analyses

The FEM analyses can be helpful for the processing and tests of the inflatable antenna. These mainly include the FEM analyses by the internal pressure and the wind load. Then the parameters for the antenna can be obtained.

3.1 FEM analyses by internal pressure

The state when the spherical antenna is already inflated with internal pressure but without other loads, namely initial state, will be analyzed in this section. It is essential and clear to conduct the mechanic analysis in this state to get the effect of the internal pressure on the RMS of the reflector.

The FE model of this antenna shown in Fig.6 contains the reflector and the sphere. The reflector inside is connected with the sphere outside by the belt on the equator of the sphere. In order to make the model more accurate, the belt and gluing bands are also taken into consideration.

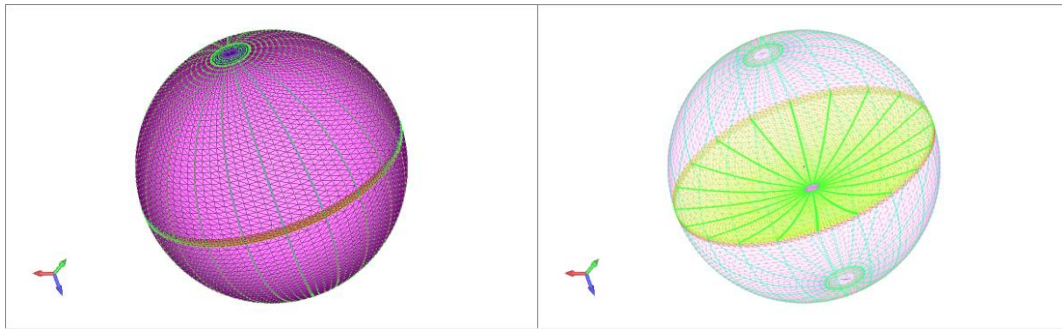


Fig. 6. Solid drawing and perspective drawing of antenna FE model

The diameter of this sphere is 1800 mm while the desired focus of the reflector is 1170 mm. The element thickness of the reflector, the band of reflector, the sphere, the band of sphere and the belt is 0.14 mm, 0.28 mm, 0.48 mm, 0.96 mm and 1.28 mm respectively.

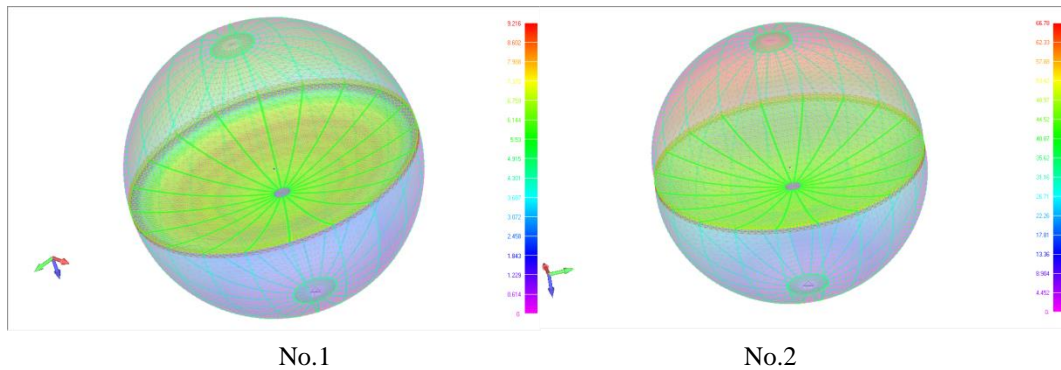
The material of the reflector is orthotropic, of which the elastic modulus on longitude and latitude is 180 MPa and 160 MPa respectively, the shear modulus is 60 MPa and Poisson's ratios on both direction are 0.3. Both the sphere and the belt are the isotropic materials. The elastic modulus and the Poisson ratio of the sphere is 100 MPa and 0.3 respectively while these of the belt is 45.6 GPa and 0.278 respectively.

The boundary condition is to fix three translational degrees of freedom of the node on the bottom of the sphere. The internal pressures of front and back chambers (PF and PB) are listed in Tab.1 as different operation while the difference of pressure between two chambers (DP) is settled as 100 Pa. And the focuses (FD), RMSs and the maximum stress (MS) as the FEM solutions are also listed in Tab.1.

Table 1. FEM solutions for each operation

No.	DP	PF	PB	FD	RMS	MS in reflector	MS in sphere
	Pa	Pa	Pa	mm	mm	MPa	MPa
1	100	1100	1000	1136.01	2.08	0.928	2.304
2	100	10100	10000	1147.47	1.91	1.038	38.46
3	100	21100	21000	1171.19	1.58	1.118	110.4
4	100	100100	100000	1618.48	1.03	3.682	914.4

The displacement diagrams for each FE model listed in Tab.1 are illustrated as following.



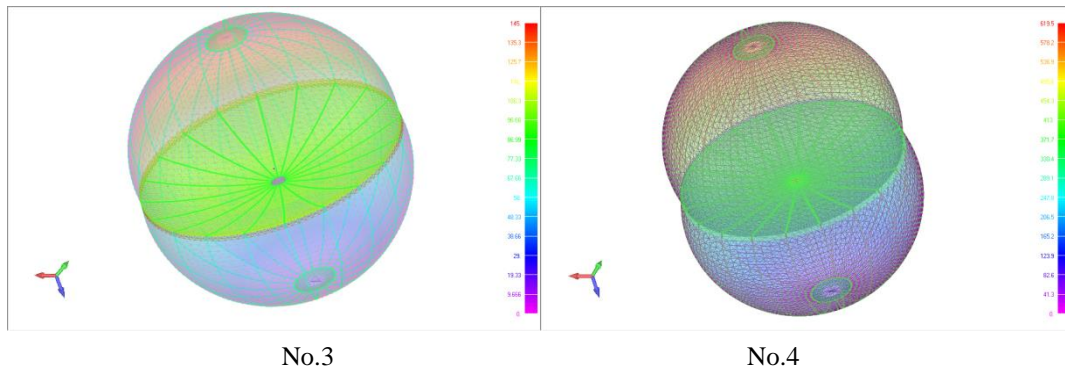


Fig. 7. Displacement diagrams for each FE model

According to the solutions in Tab.1 and Fig.7, it is indicated that the profile precision, the focus and the stress become larger with the increase of the internal pressure. The solutions of Model No.4 are much larger than others while the internal pressure is raised one order of magnitude. The focus of Model No.3 fit the desired reflector best, of which the error is 0.10%. Thus, it is concluded that there is the fittest internal pressure to make the reflector of inflated antenna matching the function requirement. The smaller pressure cannot inflate the antenna to match the profile precision while the larger pressure may lead to high strain and large displacement. From the FEM analyses, the maximum stress locates in the belt, which means that the belt as the boundary is important to support the reflector and the strength and the modulus of its material are required to be large.

3.2 FEM analyses by wind load

With regard to the working state of antenna shown in Fig.1, the antenna is pulled by ropes to fix on the ground as the analysis model in Fig.8. The parameters that influence the profile precision of reflector are the prestress in ropes and the fixed endpoint position of the rope. Other parameters of the sphere are same as the model No.3 (pressure in front and back chamber is 21100 MPa and 21000 MPa respectively and difference of pressure on reflector is 100 Pa).

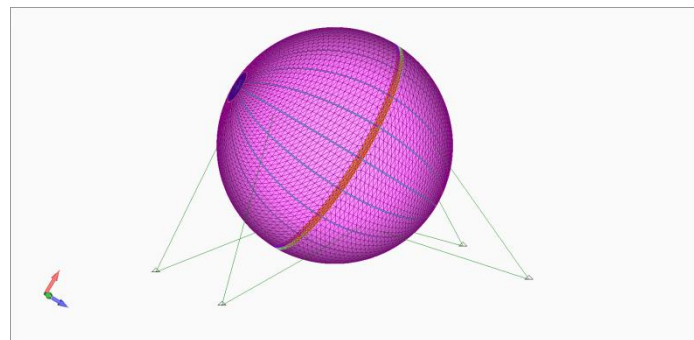


Fig. 8. FE model pulled by ropes

The prestress in ropes (PR) are chosen as 50 MPa and 100 MPa. There are four fixed endpoints of the rope forming a square on the ground. The lengths of this square side (L) are chosen as 1000 mm and 1200 mm. The speed of the wind load is set as 15 m/s, and the pressure of the wind load can be got as 150 Pa. The orientation of the wind load (OW) is axis Y+, axis Z+ and axis Z- in each operation (the axis X, axis Y and axis Z are stood by green, red and blue axis shown in Fig.7, respectively). The groups of the parameters and the analyses solutions as the focuses, errors of focus (EF), RMSs with the wind load and the translational displacements (TD) are listed in Tab.2.

Table 2. FEM solutions with wind load for each operation

No.	PR	L	OW	FD	EF	RMS	TD in axis X	TD in axis Y	TD in axis Z
	MPa	mm		mm	mm	mm	mm	mm	mm
1	50	1000	Y+	1171.10	1.0997	0.3267	1.7404	93.3557	2.2933
2	100	1000	Y+	1170.00	1.0794	0.3236	1.6593	92.4677	2.3141
3	200	1000	Y+	1171.10	1.0852	0.3254	1.5362	92.4743	2.3809
4	400	1000	Y+	1171.10	1.0852	0.3254	1.5362	92.4743	2.3809
5	50	1000	Z+	1170.00	-0.0011	0.0289	0.5726	-5.80E-04	2.1121
6	100	1000	Z+	1170.00	-0.0014	0.0283	0.5498	-0.0021	2.0835
7	50	1000	Z-	1170.00	0.0480	0.041	-1.3191	-0.0012	-2.4737
8	100	1000	Z-	1170.00	0.0480	0.0412	-1.3390	-0.0021	-2.4676
9	50	1200	Y+	1170.00	0.8920	0.2708	0.9040	70.9436	2.0804
10	100	1200	Y+	1170.00	0.8881	0.2706	0.8131	70.6699	2.1344
11	50	1200	Z+	1170.00	0.0028	0.0309	0.5368	-0.0405	3.5852
12	100	1200	Z+	1170.00	0.0023	0.0304	0.5099	-0.0386	3.5630
13	50	1200	Z-	1170.00	0.0529	0.0447	-1.5564	0.0040	-3.4474
14	100	1200	Z-	1170.00	0.0532	0.0451	-1.5925	0.0032	-3.4437

Overall, all the error of focus by the wind load are very small and below 1 % of the focus. The RMSs of reflector by the wind load are below 0.33. These results indicate that the internal pressure at the level as 21000 MPa in the back chamber can keep the profile of reflector by the wind load.

Comparing operation No.2 with No.1, 3 and 4, the only variable is PR that is 50, 100, 200 and 400 MPa respectively. It is obtained that the FD, EF and RMS are most suitable when the prestress is 50 MPa. With the level of the prestress raising after 200 MPa, these solutions keep constant.

Then, comparing operation No.2 with No.6 and 8, the each OW makes the solutions very different. Especially in orientation Y+, the lateral wind load makes this inflated structure mechanically adverse.

Moreover, considering the only variable L, the groups of which L is 1200 mm have better effect on resisting the lateral wind load, compared with those of which L is 1000 mm accordingly.

Finally, based on analyses of different parameters, the parameters of the operation No.10, 12 and 14, specifically PR is 100 MPa and L is 1200 mm, have the best effect on resisting the wind load.

It is concluded that the prestress in ropes can develop the control of the reflector precision and the resistant stiffness to wind loads. And the prestress can avoid the stress relaxation in ropes by the wind. There is a best prestress level and there is no contribution to the resistant stiffness above this level. Secondly, the position of the fixed endpoints of ropes has much influence on resistance to wind loads, especially to the lateral wind. Moreover, the position can be expressed by the angle between the rope and the ground. The force in ropes delivering the horizontal wind load to the ground can become little with the decrease of the angle. Thus, the position that L is 1200 can be a better choice respecting to the mechanic and the construction.

4. Conclusions

This paper introduces the form finding analysis and piece cutting design for the design of the terrestrially spherical inflatable antenna. And it mainly conducts the FEM analyses for the states by the initial pressure and by the wind loads. The example is employed to illustrate these processes and some

conclusions are got as following.

It is proved that the methods for the design, namely form finding analysis and piece cutting design, are feasible by the example analyses.

There is a best internal pressure in chamber to supply the inflated antenna with the suitably initial membrane stress. The belt of antenna is the boundary of the reflector and it is suggested to have high strength and modulus.

The parameters of the antenna model containing the ropes are analyzed by the wind loads. The reflector precision can be stable and the stiffness of the model can be developed with the improving of the prestress in ropes.

The position of the ropes, specifically the length of the square side formed by four fixed endpoint of ropes, are contrasted and a better choice is selected to develop the function of the mechanic and the construction for the antenna.

The following research can be the more accurate model and analyses for the design parameters of spherically inflatable antenna. The dynamic analysis also should be taken into consideration to develop the solution.

REFERENCE

- [1]. Inflatable deployable satellite communication systems [EB/OL]. [2008-06-12]. www.gatr.com
- [2]. Guan F. and Qian L., "Structural analysis and test of an inflatable ground antenna," *Journal of Zhejiang University: Engineering science*, 2012(02): 257-262. (in Chinese)
- [3]. Lin John K.H, Candogan David P. "A hybrid inflatable disk antenna system for spacecraft," *42nd AIAA/ASME/ASCE/AHS Structure, Structural Dynamics and materials Conference & Exhibit AIAA Gossamer Spacecraft Forum*. April 16-19, 2001
- [4]. Yahya R S and Hoferer R A. "Arise a challenging 25-m space antenna design," *Department of Electrical Engineering*, University of California
- [5]. Freeland, R. E., Bilyeu, G.. "IN-STEP Inflatable Antenna Experiment," presented at *the 43rd Congress of the International Astronautical Federation*, IAF-92-0301, 1992, Washington, D.C.:1-12
- [6]. Ma X., Song Y., Wei J., et al. "Summary in inflatable deployable structure for spatial antenna," *Space Electronic Technology*, 2006(03): 10-15. (in Chinese)
- [7]. Jenkins, C.H. and D.K. Marker, "Surface precision of inflatable membrane reflectors," *Journal of Solar Energy Engineering, Transactions of the ASME*, 1998, 120(4): p. 298-305.
- [8]. Greschik, G., et al. "Approximating paraboloids with axisymmetric pressurized membranes," in *Proceedings of the 39th AIAA/ASME/ASCE/AHS/ASC Structures, Structural Dynamics, and Materials Conference and Exhibit*, 1998.
- [9]. Greschik, G., M.M. Mikulas and A. Palisoc, "Torus-less inflated membrane reflector with an exact parabolic center," *AIAA journal*, 2004, 42(12): p. 2579-2584.
- [10]. Yao X. and Xu Y., "Application of discrete differential geometry to the design of membrane structure," *Low Temperature Architecture Technology*, 2006(05): 74-77. (in Chinese)
- [11]. Xu Y., "Precision and deployment analysis researches for membrane inflatable antenna," 2009, *Zhejiang University* (in Chinese).
- [12]. Yang Y. Q., "Theory of Thin Shell", 1981, *Chinese Railway Press*, page33 (in Chinese).

IMPROVING THE INFLATABLE PARABOLIC REFLECTOR

Geuskens F.⁽¹⁾, Vermij G.⁽²⁾, Ording B.⁽³⁾

⁽¹⁾ **Dr. MSc. François Geuskens**
P.O. Box 32070 – 2303 DB Leiden (the Netherlands)
Email: f.geuskens@dutchspace.nl

⁽²⁾ **Ir. Guus Vermij & MSc. Barend Ording**
P.O. Box 32070 – 2303 DB Leiden (the Netherlands)
Email: g.vermij@dutchspace.nl & b.ording@dutchspace.nl

ABSTRACT

This project focusses on the development of inflatable parabolic reflectors for micro-and nano-satellites since the stowage volume is too small for other type of high-gain-reflectors. The surface tolerance of current state-of-the-art inflatable parabolic reflectors is however disappointing. This paper explains how to change the design in order to make significant improvements in the surface tolerance without the aid of active control. Geometrical changes are presented to reduce edge support errors and to eliminate the need for pressure control. It is shown that using near-zero-CTE-materials and implementing a stiffness distribution that mimics the membrane stress distribution improves the surface tolerance of the reflector. Furthermore, fabrication errors can be reduced by minimizing the assembly steps in the manufacturing.

1. INTRODUCTION

The optimization of the antenna performances is a key issue in the design of satellite systems. Even if current trends are toward miniaturisation of all RF equipment and platforms, antenna size is expected to grow for higher sensitivity instruments and access to the end user with small terminal [1]. There are multiple alternative concepts that offer solutions in case the desired size of the antenna is larger than the available volume (e.g. the *Astromesh* of *Alphasat*) but all alternative concepts:

- have a higher stowage volume and are heavier than the inflatable concept
- are intrinsically not able to offer a smooth continuous parabolic surface

The inflatable reflector is an old concept and has already been developed by *L'Garde* (Fig. 1) and *Contraves* (Fig. 2) a few decades ago. *Contraves* developed an offset antenna while the concept of *L'Garde* was a simpler axi-symmetric inflatable reflector.

The overall objective in this study is to develop an inflatable parabolic reflector that has better dimensional stability than former inflatable concepts. The 3m diameter LDP inflatable antenna of *L'Garde* had for example an accuracy of about 1.4mm rms [2]. The current target is to achieve an RMS-value of less than 0,5mm. Achieving this surface tolerance makes the inflatable reflector more competitive than any other type of deployable reflector with respect to this requirement.

The risks and investment costs for the development of large reflectors ($\varnothing > 10\text{m}$) are high. Consequently it was decided to reduce the risks and the development costs by developing inflatable antennae for nano- (range 1-10kg) and micro-satellites (range 10-100kg). The goals for these spacecraft are becoming more ambitious in terms of physical distance (moving from Low Earth Orbit (LEO) to Geostationary Earth Orbit (GEO) or further), and of the amount of data to relay back to Earth (from Kbits to Mbits). The communication systems currently implemented (mostly dipole, monopole or patch antennae) are not able to fully support these missions. There are two possible strategies to solve these issues [3]:

1. Increase the time available to communicate to the ground by using existing satellite networks as communication relays.
2. Equip the satellite with a more powerful antenna compatible with the volume and mass constraints imposed by CubeSats and small satellites.

Both options are currently investigated at the Massachusetts Institute of Technology (MIT) under the name *CommCube 1* and *CommCube 2*, of which the *CommCube 2* is shown in Fig. 3.

ISIS (one of Europe's leaders in the nano-satellite domain) acknowledged that:

- The market for miniature satellites is booming and up until now exceeding every prognosis. The latest prognosis made by *SpaceWorks Enterprise* is added in Fig. 4.
- The professionalization in the nano- and micro-satellite domain demands for better communication capabilities.



Fig. 1. Inflatable antenna of L'Garde

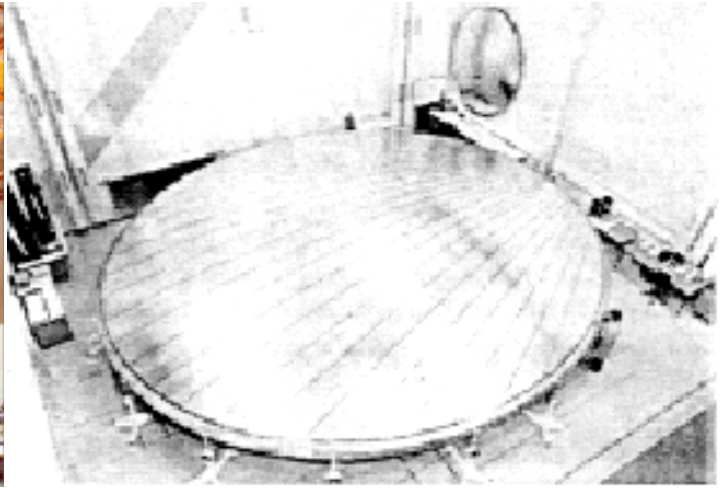


Fig. 2. Inflatable antenna of Contraves

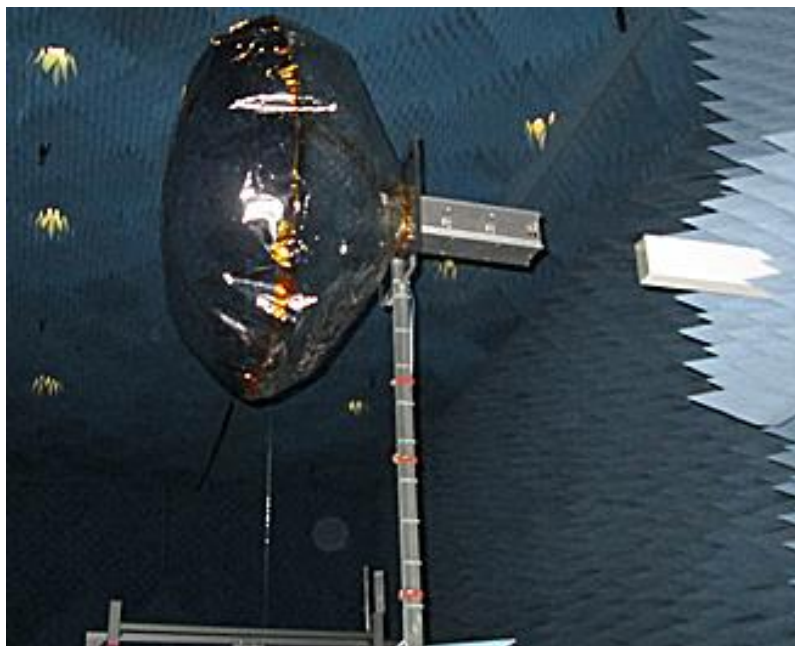


Fig. 3. Test set-up of the CommCube 2

Nano/Microsatellite Launch History and Projections

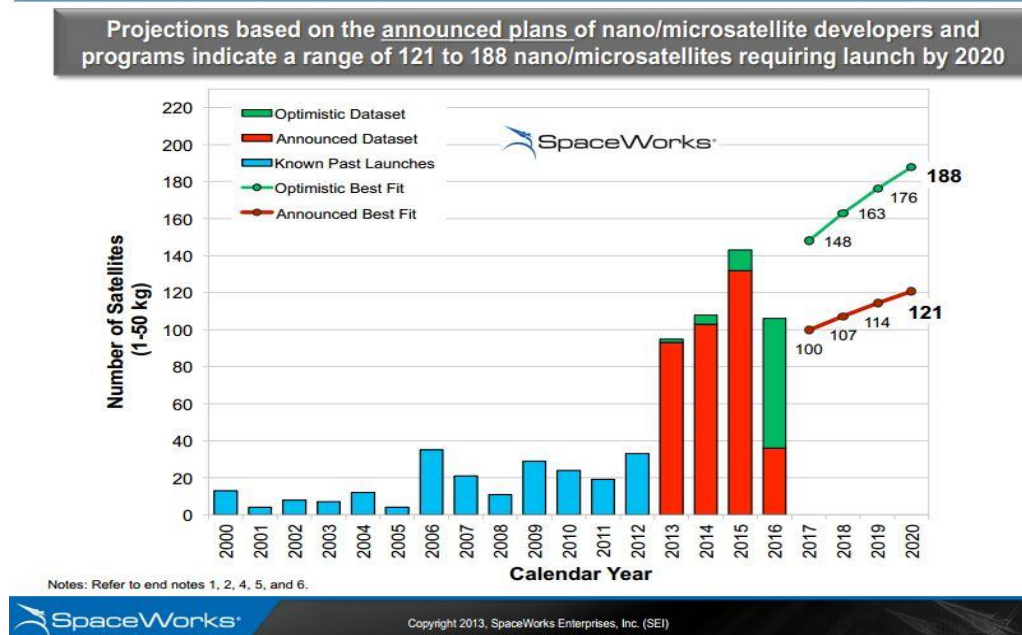


Fig. 4. Nano/Microsatellite Launch History and Projections (Source: SpaceWorks Enterprises Inc., 2013)

2. CURRENT STATE-OF-THE-ART

The concept of *L'Garde* is explained in Fig. 5. The red arrows in this figure represent the membrane forces as a result of pressurization. When taking the vertical and horizontal components of these membrane forces, it shows that the vertical forces of the parabolic-and the arbitrary membrane cancel each other out and the horizontal forces of the parabolic-and the arbitrary membrane are cancelled out by the equal and opposite force of the inflated torus, resulting in an inflatable which is in equilibrium. Omitting the inflatable torus in this concept would result in compressive hoop stresses at the intersection.

The development of the inflatable concept stagnated because the required surface tolerance of the reflector could not be attained. The surface tolerance was even more of a problem for *Contraves* compared to the axi-symmetric concept of *L'Garde*. The axi-symmetric concept is straight-forward and predictable because the membrane forces around the perimeter are constant, which is not the case for an offset antenna. Using a simple parabolic reflector in combination with a multi-beam feed for multiple data relays and beam steering is therefore favourable. This multi-beam feed is a new development and this technology was not accessible in the previous century. The primary error sources in inflatables are found in (Table 1):

Table 1. Membrane error sources in inflatable space structures

<ul style="list-style-type: none"> • Variations in membrane stiffness • Creep • Moisture effects • Thermal distortions • Wrinkling or creasing due to packaging 	<ul style="list-style-type: none"> • Fabrication • Analytical shape predictions • Edge support conditions • Different pressure levels • Gravitational effects in earth testing
--	---

Today's research is concentrating on the development of different correction mechanisms to maintain the parabolic shape of the reflector. These correction mechanisms are based on using piezoelectric [4 and 5], shape memory alloy (SMA) [6 and 7] actuators and shape memory polymers [8].

These active control mechanisms are still in development. It has not yet been demonstrated (experimentally) that the implementation of these actuators on existing inflatable concepts are adequate to provide highly accurate parabolic reflectors. The development of active control mechanisms is complex. It involves complicated control algorithms and

continuous shape monitoring, making it high risk and expensive. The philosophy in this study is to omit complex control mechanisms and to design and manufacture a parabolic inflatable that is and remains highly accurate, regardless the environmental conditions it is exposed to. Active control mechanisms could be considered in the future as an additional add-on for miniscule corrections.

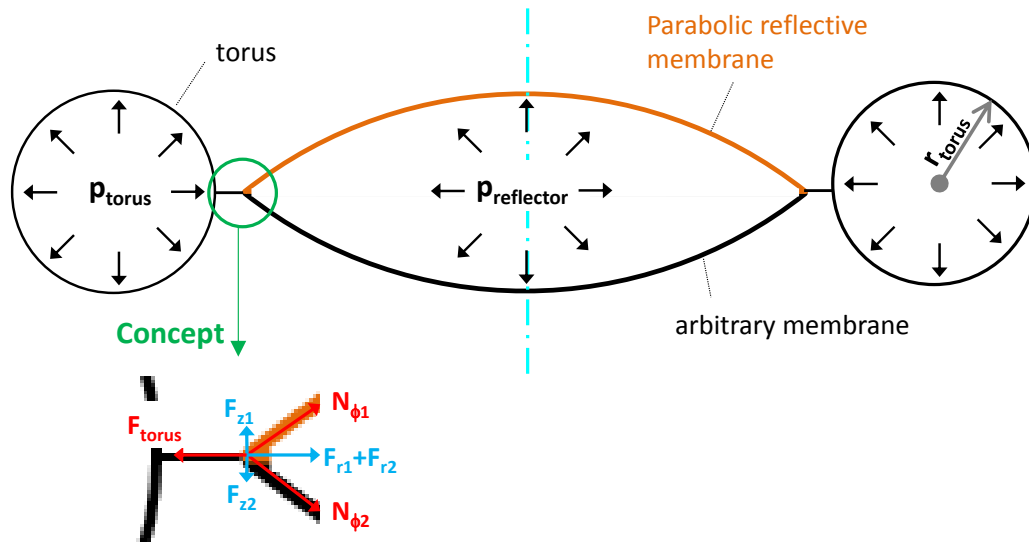


Fig. 5. Conceptual idea behind the inflatable reflector of L'Garde

3. DESIGN OF THE PARABOLIC INFLATABLE REFLECTOR

The parabolic reflector developed in this project relies on the same principles as the inflatable reflector of L'Garde. This chapter first explains the analysis of membrane forces of the L'Garde concept (section 3.1) in order to support the understanding of new design considerations (section 3.2). Section 3.3 describes the effect on the surface tolerance of these new design changes. Finally, the technical challenges that still need to be resolved for these new concepts are presented in section 3.4.

3.1 Analysis of the L'Garde Reflector

3.1.1. Analysis of the Parabolic Reflector

The equation of a parabola with focal length F , can be written as [9]:

$$z = \frac{R^2}{4F} - F, |R| \leq \frac{D}{2} \quad (1)$$

An illustration of the parabola is given in Fig. 6.

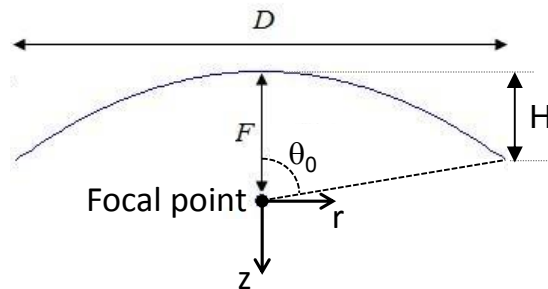


Fig. 6. Illustration of parabola with defining parameters [9]

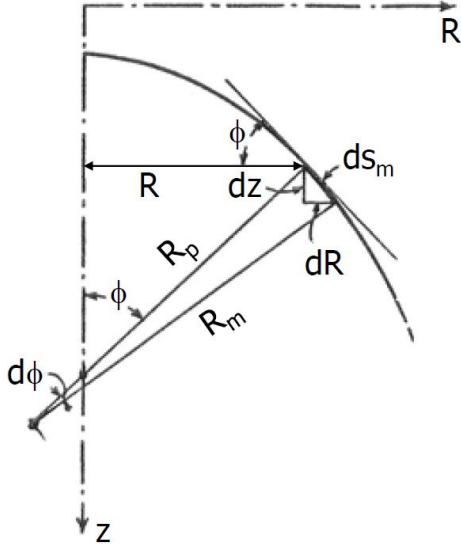


Fig. 7. Meridian of a shell of revolution [10]

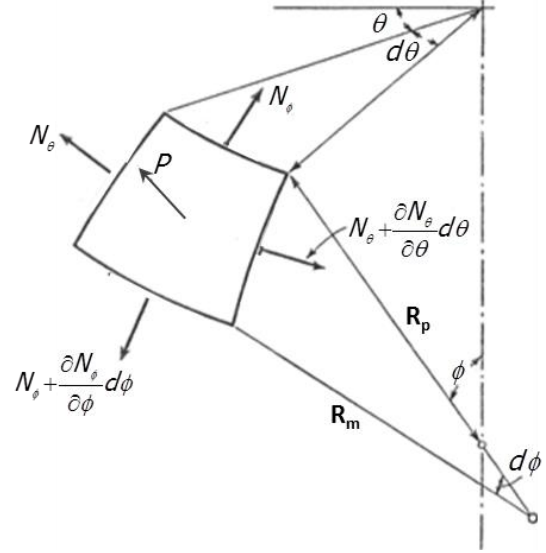


Fig. 8. Forces and loads on a membrane element [10]

The membrane forces as a result of pressurization are dependent on the radii of curvature. The analysis of the mechanical response of the membrane is enabled by describing the geometry of the membrane elements in geodetic coordinates [10].

An illustration of a meridian with its defining parameters is given in Fig. 7, showing:

- the axis of rotation (*Z-axis*)
- the radius of curvature of the meridian (R_m)
- the angle of the meridian (ϕ)
- the radius of the parallel (R_p)

The pressurization induces a meridional force N_ϕ and a the hoop force N_θ illustrated in Fig. 8. The forces, defined per unit length are defined as [10]:

$$N_\phi = \frac{1}{2} p R_p \quad (2)$$

$$N_\theta = p R_p \frac{2R_m - R_p}{2R_m} \quad (3)$$

Dividing the force by the membrane thickness gives the membrane stress.

The radii of curvature in (2) and (3) are defined as:

$$R_m = \frac{\left[1 + \left(\frac{dz}{dx}\right)^2\right]^{3/2}}{\left|\frac{d^2z}{dx^2}\right|} = \frac{\left[1 + \frac{x^2}{4F^2}\right]^{3/2}}{\frac{1}{2F}} \quad (4)$$

$$R_p = \frac{r}{\sin \phi} \quad (5)$$

For which

$$\phi = \arctan\left(\frac{dz}{dr}\right) = \arctan\left(\frac{r}{2F}\right) \quad (6)$$

The non-dimensional membrane forces are defined as:

$$n_\phi = \frac{N_\phi}{p \cdot D \cdot \left(\frac{F}{D}\right)} \quad (7)$$

and

$$n_\theta = \frac{N_\theta}{p \cdot D \cdot \left(\frac{F}{D}\right)} \quad (8)$$

The non-dimensional forces as a function of the meridional angle ϕ are shown in Fig. 9. The actual membrane force is obtained by multiplying the non-dimensional force with the pressure (p), the diameter (D) and the focal ratio (F/D). Equations (7) and (8) show that membrane forces increase for increasing focal ratios. Fig. 10 shows the meridional angle at the perimeter for different focal ratios. For example, for a focal ratio of 1, the angle ϕ at the perimeter is $\pm 14.04^\circ$, meaning that the maximum non-dimensional membrane forces n_ϕ and n_θ are respectively 1.03 and 1.09.

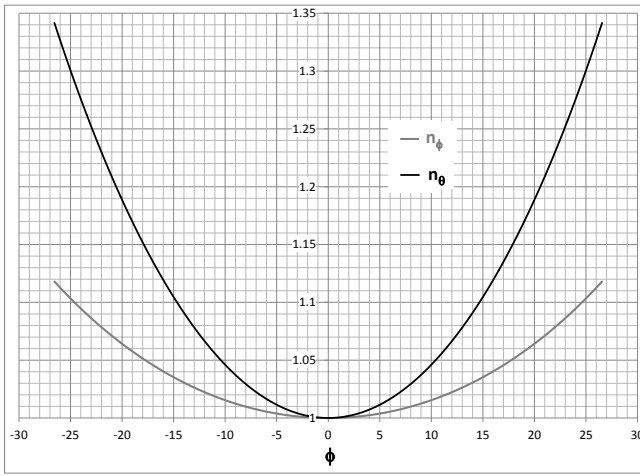


Fig. 9. Non-dimensional membrane forces for the inflatable parabolic reflector

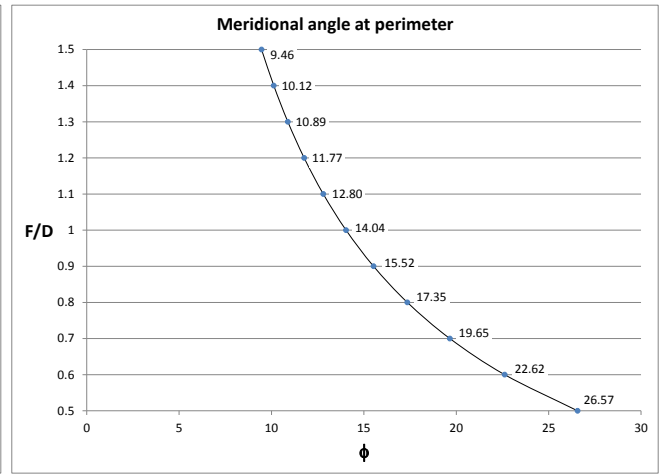


Fig. 10. Meridional angle at the perimeter for the inflatable parabolic reflector

3.1.2 Analysis of the Inflatable Torus

The horizontal force, generated by one parabolic membrane, which needs to be cancelled out by the inflatable torus is defined as (see Fig. 5):

$$F_{r1} = N_\phi \cos \phi \quad (9)$$

Where ϕ is the meridional angle at the perimeter. This angle can be obtained in Fig. 10.

The torus needs to cancel out two horizontal forces ($F_{r1} + F_{r2}$), as shown in Fig. 5. In order to assure that the torus is capable of generating an equal and opposite force, the following condition needs to be fulfilled:

$$\pi r_{\text{torus}}^2 p_{\text{torus}} - (F_{r1} + F_{r2}) \frac{D}{2} \geq 0 \quad (10)$$

, where r_{torus} is indicated in Fig. 5. An active pressure control system could be omitted in case the pressure in the torus is identical to the pressure in the reflector. This has serious implications however to the feasibility of the design of the inflatable. The radius r_{torus} needs to be more than $0.4D_{\text{reflector}}$ and $0.565D_{\text{reflector}}$ for a focal ratio of respectively 0.5 and 1 with the assumption that F_{r1} and F_{r2} are equal. An equal pressure in all membrane elements leads therefore to an

inflatable of which the reflector is a fraction of the total surface of the entire inflatable. A smaller torus is possible in case the pressure is increased. The pressure needs to be increased respectively 10 and 82 times for a focal ratio of 0.5 and 1 in case it is decided to have $H_{\text{reflector}} = r_{\text{torus}}$. The parameter $H_{\text{reflector}}$ is defined in Fig. 6. It is clear that the design envelop is small for a high focal ratio because high pressures imply thick membranes and this complicates the foldability. Furthermore it shows that the torus needs to be oversized when focal ratios increase.

3.2. Design Considerations concerning the Parabolic Reflector

The design of a structure involves an interdisciplinary process where the geometrical design, material selection, definition of mechanical and physical properties and fabrication are intertwined. All these processes are examined to see where improvements can be made regarding surface tolerance. Geometrical considerations are discussed in section 3.2.1. Section 3.2.2 explains how the surface tolerance is improved by changing the material properties and the membrane stiffness. Finally, section 3.2.3 describes what improvement can be made regarding the fabrication of the inflatable.

3.2.1 Geometry

Two possible alternatives are identified in order to bypass the difficulties that are experienced with the *L'Garde* concept:

1. A torus with a small r_{torus} is inflated and rigidized prior to the inflation of the reflector. Studies are already performed to stabilize inflatables by filling them with foams [11]. This technology could for example be combined with the rigidization of a fibre reinforced torus by means of UV curable resins [12]. In this case, concepts with simpler intersections as shown in Fig. 11 could be considered. The advantage of this concept is that the size increase related to increasing focal ratios (see previous section) can be limited. This concept however still requires a pressure control system.

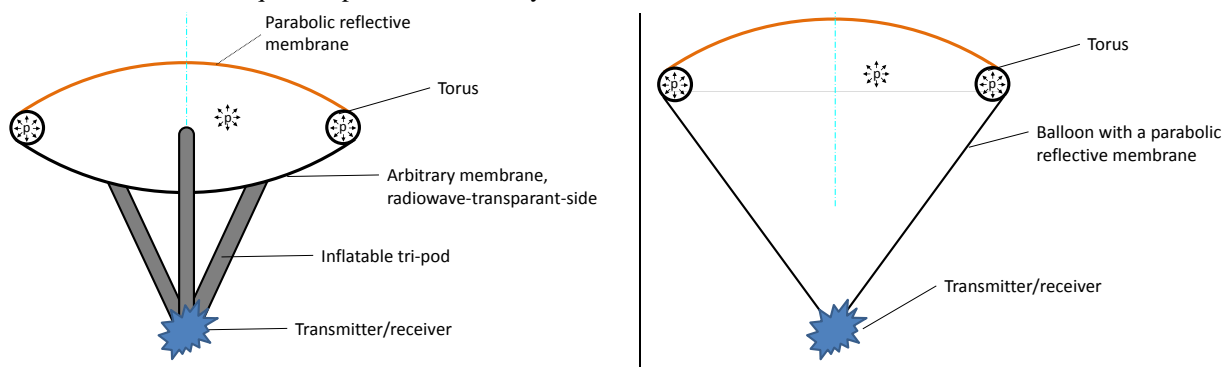


Fig. 11. A lenticular inflatable reflector with internal torus supported a) with, and b) without inflatable tri-pod

2. There is also the opportunity to bypass the torus. Fig. 12a and b show the smallest inflatable for a focal ratio of 0.5 and 1 respectively. The focal point is located at the cross-section of the axes. Making the inflatable more compact will introduce compressive hoop forces. This is illustrated in Fig. 13b, showing the force distribution of the oblate spheroid in Fig. 13a.

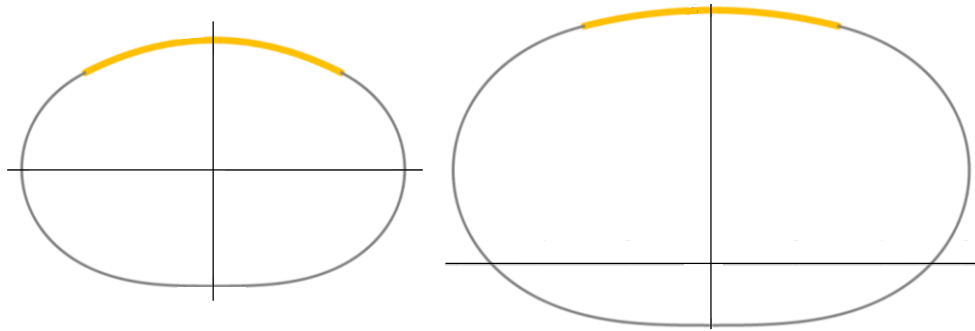


Fig. 12. Illustration of the smallest balloon for a reflector of equal diameter with a) a focal ratio of 0.5 and b) a focal ratio of 1. The parabolic reflector is highlighted on top of the balloon.

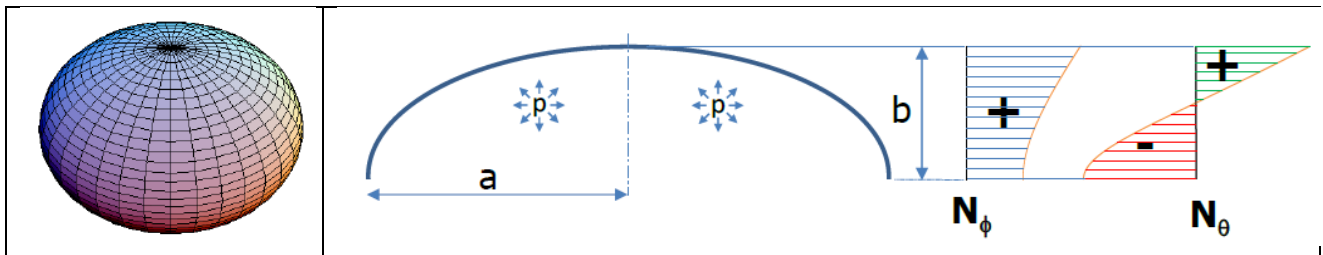


Fig. 13. a) Illustration of the oblate spheroid b) Illustration of the force distribution in the oblate spheroid

Figs 12a and b show that the size of the inflatable increases with increasing focal ratio, similar as the *L'Garde*-concept. It needs to be noted that this concept is considerably more compact than the *L'Garde*-concept for which the pressure in the torus is identical to the pressure in the reflector. Moreover, the two membrane elements are simpler to join due to the tangential connection. Lastly, pressure control can be omitted, which is explained in section 3.2.2.2.

3.2.2 Improving the Surface Tolerance

The surface tolerance will be improved when the primary error sources, as listed in Table 1, are reduced or eliminated in the new design concept. The surface tolerance improvement is achieved when the concepts as shown in Fig. 11 and Fig. 12 are equipped with:

- A membrane that has a CTE which is close to zero
- A membrane of which the stiffness distribution is such that an equal and uniform strain is assured in all directions.

A surface tolerance improvement can also be found in the reduction of fabrication errors. The current state-of-the-art involves a lot of manual dexterity and reducing the human factor gives the opportunity to improve the RMS-value of the reflector. New state-of-the-art processes provide the opportunity to reduce human factor and therefore consequently provide the opportunity to reduce fabrication errors.

More information concerning the improvement techniques are given in sections 3.2.2.1, 3.2.2.2 and 3.2.2.3.

3.2.2.1 Near-Zero-CTE-Materials

Analysis in [13] shows that the thermo-elastic distortions are the most dominant error-source concerning reflector surface distortions. The best (passive) way to reduce these errors is by using materials which have a CTE which is close to zero. Two options have been identified:

- Fibre Reinforced Membranes

An example is shown in Fig. 14, showing a membrane that consists of fibers with a negative CTE, embedded in a polymer film. The concept is that the fiber architecture and the polymer thickness is chosen such that the global membrane properties exhibit a CTE that is close to 0.

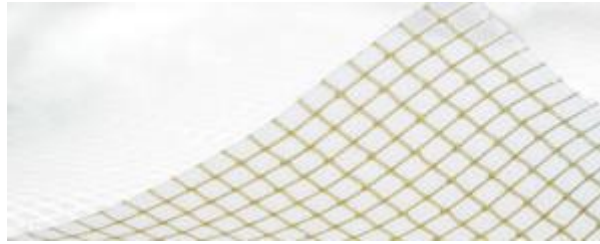


Fig. 14: Example of aramid reinforced mylar

- Zero-CTE-materials

Another option is to make a reflector of a material that has a CTE that is close to zero. Alternatives are for example ultra-thin *Invar* foils or *Novastrat 905* (a poly-imide with a CTE that is close to 0). The drawback of ultra-thin *Invar* foils is that these are only available as rolls with limited width, implying that reflectors can only be made by joining multiple gores.

3.2.2.2 Uniform Equal Strain Distribution

The current state-of-the-art consists of multiple gores of 'isotropic' films with constant thickness. These multiple gores are seamed into a three dimensional paraboloid. The paraboloid is approximated because these reflectors are an assembly of single-curved gores, similar as an umbrella. More gores approximate the doubly-curved shape better but additional errors appear due to the increase of the assembly-effort.

The isotropic films with constant thickness result in a stiffness distribution that deviates from the stress distribution (see Fig. 9). The strains are for that reason not constant all over the membrane surface. This means that the paraboloid changes shape in the process of deformation. A paraboloid can for this concept only be achieved at a dedicated pressure and the deflated shape has to deviate from the required inflated shape at design pressure. The current state-of-the-art therefore requires pressure control for an optimal antenna performance.

The paraboloid will however remain a paraboloid when the stiffness distribution is identical to the stress distribution. This stiffness distribution results in deformations that are everywhere the same in every direction, which means that:

- the shape of the reflector will not change, only the size (aperture) of the parabola will differ and consequently be a function of the pressure. The deformed geometry is easily assessed once the strain ε is known. The deformed shape is a scale factor $(1+\varepsilon)$ larger than the original shape
- the focal point will not move position
- Linear membrane theory is valid which simplifies the analysis of forces and deformations.

Each material-concept, as mentioned in section 3.2.2.1, has a different method to obtain the desired stiffness distribution:

- A uniform equal strain distribution is obtained by changing the fiber orientation and the thickness of the fiber-bundles for the fibre reinforced membrane option.
- A uniform equal strain distribution is obtained by implementing thickness variations when isotropic membrane materials are used.



It would be nice from a processing point of view to create a flat membrane that results in a paraboloid after inflation. This is however not in line with the philosophy of the proposed concept, for which the manufactured shape is identical to the inflated shape.

3.2.2.3 New Processing Techniques

Multiple alternatives are currently investigated for the manufacturing of inflatable reflectors from fibre reinforced materials or zero-cte-materials. The objective is to fabricate the reflector by means of one-shot-manufacturing, in contrast to the current state-of-the-art which consists of assemblies of multiple gores. The investigation is ongoing and the corresponding findings are documented in future publications.

3.3 Reduction of Geometric Errors

An overview of the error sources that will be reduced or eliminated are listed and justified underneath:

1. Variations in membrane stiffness

As mentioned in section 3.2.2.2, the membrane stiffness is tuned such that the process of deformation does not deteriorate the antenna performance. There will still be variations in membrane stiffness on a microscopic level but this does not affect the reflector performance.

2. Creep

Performance reduction due to creep will be reduced due to the fact that the membrane has the optimal stiffness distribution. Creep as a result of pressurization does not change the reflector performance. Only creep as a result of temperature differences remains an issue. The creep sensitivity of the materials in mind is however very low.

3. Thermal distortions

The selected materials will drastically reduce (one order of magnitude) the thermal-elastic distortion.

4. Fabrication

Aiming for one-shot manufacturing provides the opportunity to: a) create a true paraboloid (instead of an approximated one) and b) reduce fabrication errors

5. Analytical shape predictions

The inflated shape is very predictable assuming that the desired stiffness distribution is feasible.

6. Edge support conditions

The geometric concepts presented in Fig. 11 Fig. 12 simplify the edge supports and make the deformation of the parabolic reflector more predictable.

7. Different pressure levels

Surface errors are already reduced by implementing the desired stiffness distribution. Surface errors as a result of different pressure levels are eliminated when the concept presented in Fig. 12 is equipped with the optimal membrane stiffness.

3.4 Challenges

There are many technical challenges with this new concept. The success of this concept relies on the manufacturability of an affordable doubly curved zero-cte-membrane with optimal stiffness. Furthermore, methods:

- how to rigidize the inflatable
- how to apply a conductive coating on a doubly curved surface
- how to integrate the inflatable reflector with the surrounding structure

need to be explored for all potential concepts.

The project is currently investigating which concept provides the best surface tolerance while taking costs and manufacturability into account. The next step is to obtain funding for the co-development of a demonstrator with other European partners.

4. REFERENCES

- [1]. Large Reflector Antenna Working group (ESA), Final Report, 8 September 2010
- [2]. <http://www.lgarde.com/deployable-antennas.php>, (August 2014)
- [3]. A. Babuscia et al. , "CommCube 1 and 2: A CubeSat Series of Missions to Enhance Communication Capabilities for CubeSat, Aerospace Conference, 2013 IEEE, doi: 10.1109/AERO.2013.6497128
- [4]. T. Voß and J. M. Scherpen, "Stabilization and shape control of a 1D piezoelectric Timoshenko beam," *Automatica*, vol. 47, no. 12, pp. 2780-2785, 2011.
- [5]. A. Maji, P. Montemerlo and T. Ng, "Shape correction of inflatable membranes by rigidization and actuation," *Journal of Spacecraft and Rockets*, vol. 41, no. 4, pp. 558-563, 2004.
- [6]. F. Peng, X. Jiang, Y. Hu and A. Ng, "Actuation precision control of SMA actuators used for shape control of inflatable SAR antenna," *Acta Astronautica*, vol. 63, no. 5-6, pp. 578-585, 2008.
- [7]. J. Roh and I. Lee, "Configuration maintenance of inflated membrane structures using SMA film actuators," *Computer Modeling in Engineering and Sciences*, vol. 26, no. 1, pp. 13-30, 2008.
- [8]. D. P. Cadogan, S. E. Scarbrough, J. K. Lin and S. H. George, "Shape Memory Composite Development for Use in Gossamer Space Inflatable Structures," in AIAA, Denver, 2002.
- [9]. <http://www.antenna-theory.com/antennas/reflectors/dish.php>, (August 2014)
- [10]. F. Geuskens, "Conformable Pressurized Structures: Design and Analysis", ISBN 9789088915017, Published by: Uitgeverij BOXPress, 's-Hertogenbosch
- [11]. J-M. Gosau, J. Barlow, T. Wesley and R. E. Allred, "Polyurethane chemistry in space" Proc. Intl. SAMPE 09 Symp. and Exhib.
- [12]. O. Le Couls, Inflatable boom rigidized in space – Synthesis Report – TRP Ultra-Light Structures, ESTEC / Contract n° No.18738/05/NL/PM, 2011
- [13]. J.C. Pearson, J.D. Moore and H. Fang, "Large and High Precision Inflatable Membrane Reflector", conference proceeding, AIAA 2010-2500

SATELLITE INFLATABLE DEORBETING EQUIPMENT FOR LEO SPACECRAFTS

B.RASSE⁽¹⁾, P.DAMILANO⁽²⁾, C.DUPUY⁽³⁾

⁽¹⁾*Affiliation*

*Airbus Defence and Space, rue du Général Niox B.P 20011
33165 St Médard en Jalles France
Email: benjamin.rasse@astrium.eads.net*

⁽²⁾*Affiliation*

*Airbus Defence and Space, 31 rue des Cosmonautes
31402 Toulouse Cedex 4 France
Email: patrice.damilano@astrium.eads.net*

⁽³⁾*Affiliation*

*CNES, 18 avenue Edouard Belin
31401 Toulouse Cedex 9 France
Email: christian.dupuy@cnes.fr*

ABSTRACT

Debris remediation and mitigation is one of the biggest challenges space engineering has to face today. Debris removal is taken into account as early as during the design phase of a space system by selecting the right materials, including the need for demise in the design and introducing de-orbiting strategies and corresponding subsystems. Today Airbus Defence and Space dedicates part of its activity to the development of a passive de-orbiting subsystem embedded in LEO satellites (altitude ~ 750 km). Based on the IDEAS in-flight prototype (currently in phase D with a qualification campaign completed mid 2014) developed in the framework of the CNES MICROSCOPE project, the subsystem consists in the deployment of aero-braking membranes by an inflatable boom made of aluminium laminate at the end of the spacecraft's operational life. On this basis, the system optimization - with different geometries of the deorbiting subsystem - is carried out to ensure re-entry in less than 25 years with a minimum impact on architectural design of the vehicle. Airbus Defence and Space's final objective is to address the market with "off-the-shelf" flight-ready deorbiting equipment meeting the requirements of the forthcoming Space Debris French legislation.

1. INTRODUCTION

Debris remediation and mitigation is one of the biggest challenges space engineering has to face today. Debris removal is taken into account as early as during the design phase of a space system by selecting the right materials, including the need for demise in the design and introducing de-orbiting strategies and corresponding subsystems. An increasing number of spacecraft are now on low earth orbit (LEO). As a consequence of spacecraft fragmentation, a growing population of orbital debris has been induced. Therefore spacecraft shall be de-orbited at the end of their operational lives to lower the amount of orbital debris and new legislation like the French Space Act require or will require spacecraft to de-orbit within a 25 year timeframe. Today Airbus Defence and Space dedicates part of its activity to the development of a passive de-orbiting subsystem embedded in LEO satellites (altitude ~ 750 km) and compliant with the French legislation.

This paper will first present the inflatable passive deorbiting equipment IDEAS which has been developed in the framework of the MICROSCOPE mission (300-kg, circular orbit 700-km). The programme is in phase D and the flight model is to be delivered by the end of 2014. The subsystem will be operational and flight-proven by the end of 2017. It consists of two inflatable 4.70 m booms, each deploying two aero-braking membranes. An extensive qualification campaign of the material and subsystem has been carried out following ESA-CNES regulations and TRL7/8 is now considered achieved.

Based on IDEAS, mass reduction and new architectures have then been investigated in order to improve re-entry performances. The modularity and scalability of the technology enables the system's adaptation onto various panel geometries and satellite classes. In this framework, performance assessment has been done to cover Myriades and Myriades Evolution spacecraft classes (100-500 kg) at a typical SSO orbit between 700 and 800 km.

Hereinafter, a review of the functional and design assets provided by passive de-orbiting equipment is done with the aim to provide the satellite system engineer with a clear overview during the early phase of design (phase A). In the following, the satellite inflatable de-orbiting equipment will be called SIDE (Satellite Inflatable Deorbiting Equipment).

2. IDEAS DEORBING SYSTEM

The IDEAS aero-braking system is a GOSSAMER structure designed to be deployed as post mission disposal in order to increase the ballistic coefficient (ratio mass/ surface) of the MICROSCOPE satellite (CNES) and to allow re-entry within 25 years. The IDEAS development has been carried out jointly with Air Liquide for the inflating subsystem, Airbus Defence and Space for the deployable assembly and with the CNES as system and project coordinator. The MICROSCOPE launch is scheduled for the first semester 2016 and the post mission disposal should take place at the end of 2017.

2.1. IDEAS Architecture

The IDEAS system is made of three subsystems: the inflating subsystem and two booms/sails subsystems (see Fig. 1). Each boom/sails subsystem weighs 6.7 kg and the common inflating subsystem 3.1 kg for an total mass of 16.5 kg.

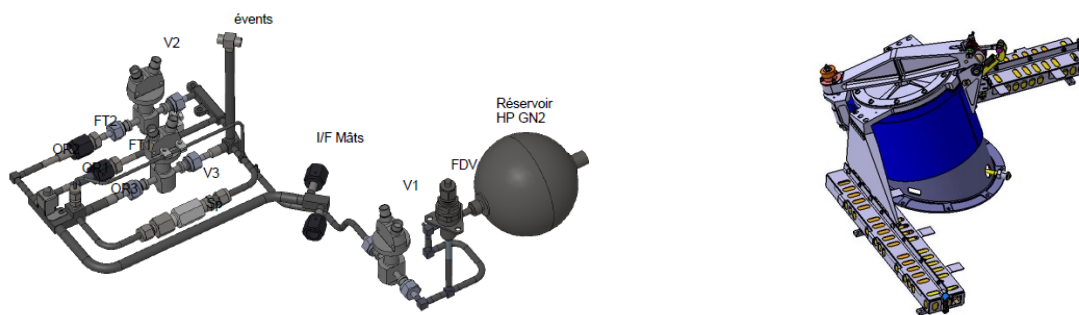


Fig. 1. Inflating subsystem (left) and stowed boom-sail subsystem (right)

The inflating subsystem's main component is a titanium tank containing 133 g of N_2 at 190 bars in order to inflate the two booms (193 litres) up to 300 mbars pressure. Three pyro-valves complete the subsystem to first deploy at 50 mbars and then rigidify the booms at 300 mbars. A constant leakage in the subsystem allows a full flushing-out of the booms after 24 hours.

The boom-sails subsystem is made of a 4.7 m boom (diameter: 0.16 m), two 1.85-m² sails each and a Hold-Down Release Mechanism (HDRM). The boom material is polyimide-aluminium laminate (130 μ m thick) with a thin SiOx coating to protect the polyimide against ATOX corrosion. Its mass is 248 g/m². By inflating the boom with a 300 mbars pressure, the strain in the boom material is beyond its yielding point. After release of the pressure, the deployed assembly keeps a residual stiffness exactly like a soda can.

The sails are also made of a polyimide-aluminium laminate but only 50 μ m thick. Each face is coated with SiOx and its mass is around 100 g/m². Once deployed, the membranes interact with the thin upper atmosphere and create a drag force which accelerates the re-entry. The thermo-optical properties of the polyimide shall limit the membrane temperature under solar exposure.

In the stowed configuration, the boom is maintained by the HDRM (see Fig.2), which consists of a low-shock pyro-bolt called Pyrosoft. Before the inflating phase, the Pyrosoft is fired and the strap is opened, enabling boom deployment. The deployment dynamic is controlled and guided through a subsystem called TADECS (Tetragonal Accordion Deployment Control System), inserted in the folded boom, which releases the folds one-by-one (see Fig.2). TADECS is a patent-filed by Airbus Defence and Space.

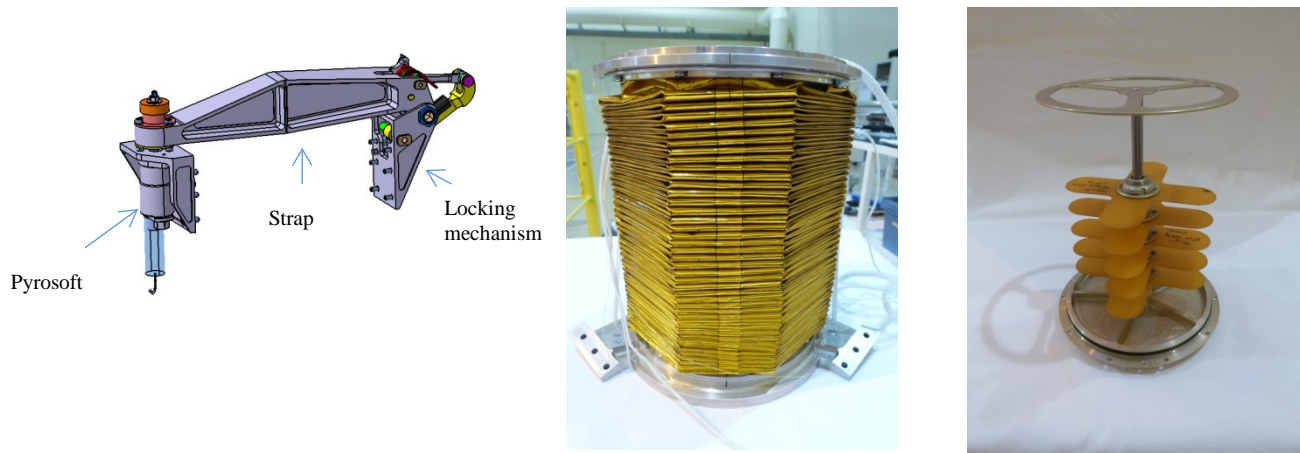


Fig. 2. HDRM (left), folded boom (center) and TADECS (right)

As shown in Fig.3, the IDEAS system is set-up on +X MICROSCOPE's panel. The booms are deployed with a 21° angle w.r.t vertical. This configuration ensures an average aerodynamic surface of 5 m^2 in tumbling dynamics for the MICROSCOPE satellite. The introduced angle minimizes the variation around this mean value.

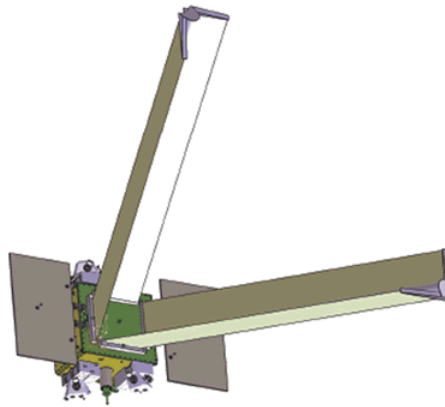


Fig. 3. Microscope satellite after IDEAS deployment

2.2. Materials testing

Sustaining LEO space environment during 25 years is the main driver behind the new materials introduced by IDEAS. Therefore, an extensive Airbus-CNES joint characterization and qualification campaign has been performed on the sail membrane and the boom materials. The tests included:

- Outgassing tests done w.r.t E-ECSS-Q-70-02-A. The table below summarizes the results

Table 1 : Outgassing test results

Material	Test Results	Test	Status
Boom laminate	TML = 1,3 %, RML = 0,20 % CVCM = 0,02 %	ECSS-Q-ST-70-02C	OK
Sail membrane	TML = 0,22 %, RML = 0,09 % CVCM = 0,00 %	ECSS-Q-ST-70-02C	OK

- Ageing tests including humidity and thermal cycling tests. No damage was noted on the membrane and the boom laminate. The ageing tests did not degrade the material's mechanical performances.
- Radiation tests with 41 Mrad-82 Mrad doses w.r.t ECSS-Q-ST-70-06C. No damages were observed on the material or the bonding joints.

- Micrometeoroid impact to assess rip risk. The micro-meteoroid campaign demonstrated that impacts in the aluminium are ductile (see Fig. 4) and that there is no risk of rip propagation. Based on the MASTER-2005 tool, the space debris cumulative flux (particles $> 1 \mu\text{m}$) seen by the membranes is estimated at $1.36 \cdot 10^4/\text{m}^2/\text{year}$ leading to a surface loss smaller than 0.1 % over a 25 year period.
- ATOX resistance tests. The protection provided by the SiOx coating appears to be efficient. No significant mass loss was noted after ATOX exposition.
- Folding tests. Superficial cracks and fragments of the SiOx coating were observed after the folding and compacting process (see Fig.4). The laminate polyimide-aluminium foil was also partially disrupted at bends. These defaults are not deemed critical to the membrane's integrity.
- Thermal expansion coefficient evaluation.
- Thermo-optical properties.

Table 2 : Thermo-optical properties

Material	Absorptance α	Emissivity ϵ_N	Test
Sail membrane	0.362	0.685	ECSS-Q-ST-70-09C

All these tests have demonstrated the ability of the IDEAS materials to sustain space environment during 25 years without creating debris or fragments.

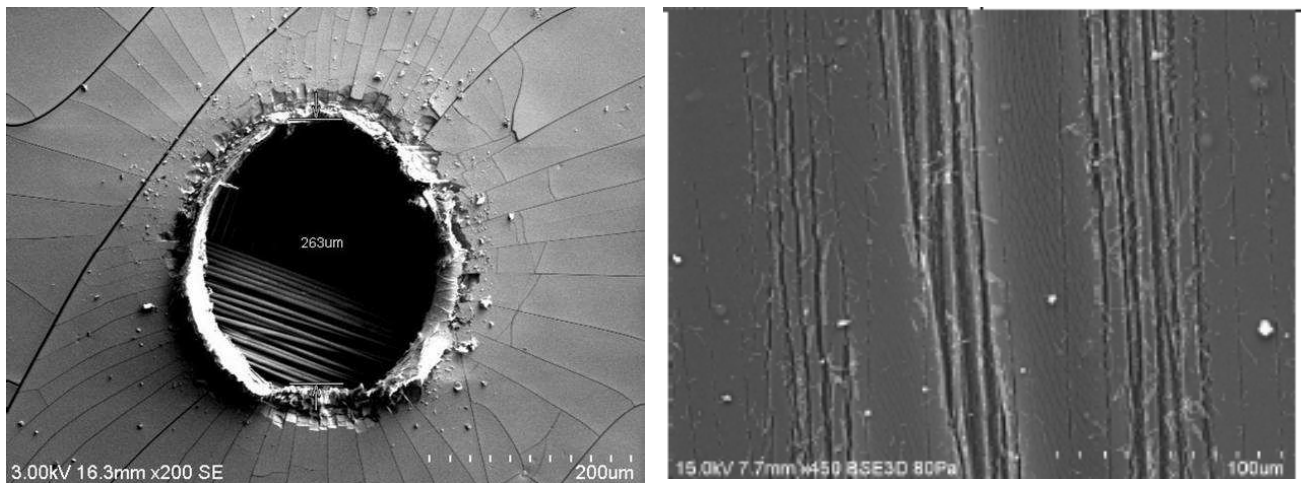


Fig. 4. Micrometeoroid impact (left) and SiOx coating cracks after folding (right)

2.3. Subsystem testing

The IDEAS qualification was performed on a flight representative EQM model in compliance with the ECSS-E-10-03A rules. The test campaign consisted of:

- Sinus and random vibration (see Fig. 5)
- Shock test
- Thermal vacuum cycling
- Leak test
- Functional deployment and rigidization test
- Mechanical performances of the deployed boom

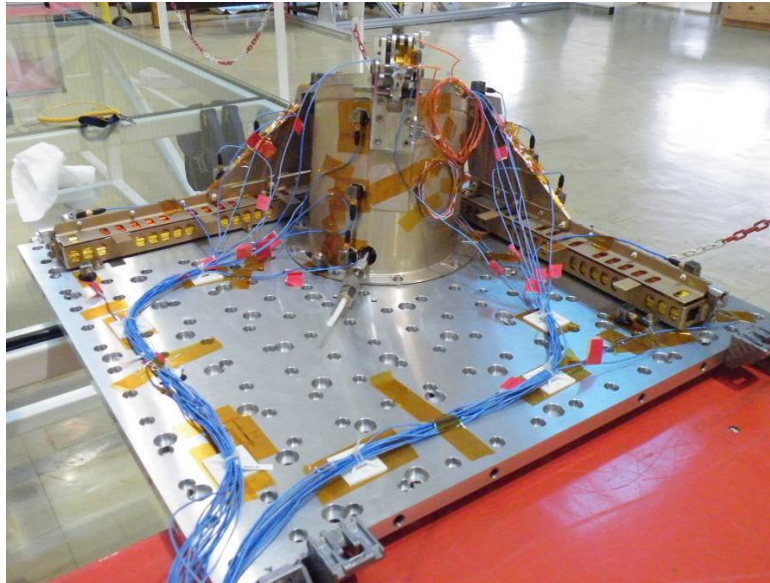


Fig. 5. Instrumented EQM model before vibration campaign and MLI integration

The environment testing demonstrated the robustness of the IDEAS mechanical design and results were in line with test predictions.

The HDRM opening test (see Fig. 6) validated the strap motorization, the strap locking mechanism after opening and the Multi Layers Insulation (MLI) design. Subsequently the deployment was nominally performed in 323 seconds without any blocking point or deviation of the boom axis. Rigidization was correctly achieved with a 300 mbar pressure: external aspect of the boom was smooth with no folding. (see Fig. 6)

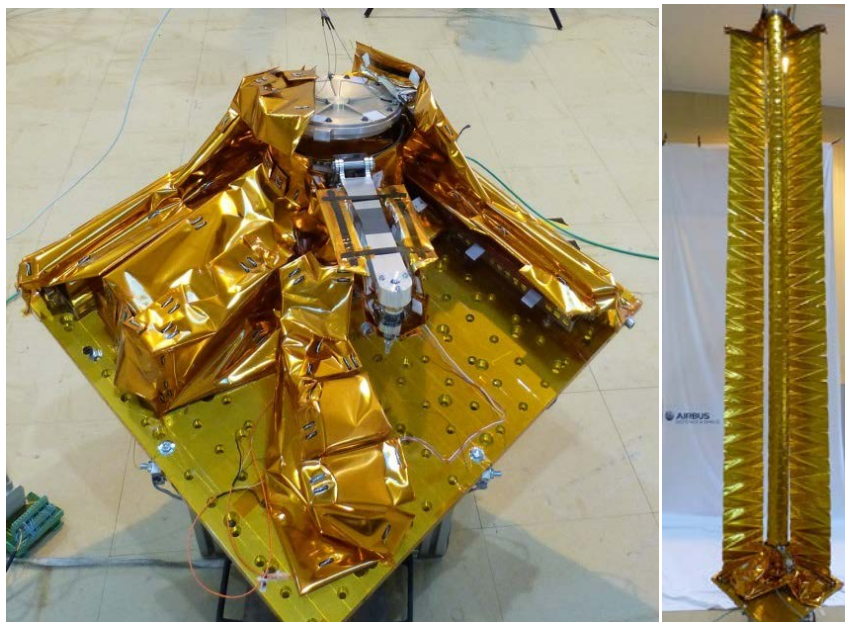


Fig. 6. EQM model after HDRM release (left) and after full deployment (right)

The last step of the test campaign consisted in evaluating the boom's mechanical properties. The maximal compression load before buckling was 22.5 N. The bending test was performed by applying a transverse effort to the boom's top extremity. The maximal bending moment before buckling was 8 N.m.

This mechanical stiffness and resistance are deemed sufficient to withstand in-orbit loads after the deployment due to aerodynamic pressure and spacecraft spin.



Fig. 7. Plastic deformation upon maximal bending stress

3. NEW ARCHITECTURES PROPOSALS

Thanks to the achievements done during the IDEAS project, several optimizations of the system have been identified. Based on the IDEAS building blocks, a study was performed in order to reach a better ballistic ratio ($S_{\text{deployed}} / M_{\text{system}}$) for SIDE and to integrate panel accommodation constraints.

One of the main aspects of the SIDE mechanical design is the modularity (see Fig. 8) and scalability of its main components so as to be easily accommodated on all types of spacecraft:

- The length of the boom can be extended up to 10 m in order to increase the deployed sail area if needed
- The number of sails attached to the boom can be increased (see Fig.8)
- The attachment angle of each sail to the boom can be adapted to the spacecraft panel's specificities
- The width of the sail can be extended up to 1.20 m. Its length is not limited.
- The boom's angle of deployment can vary from 0° up to 50° w.r.t panel normal by changing the base's structural piece

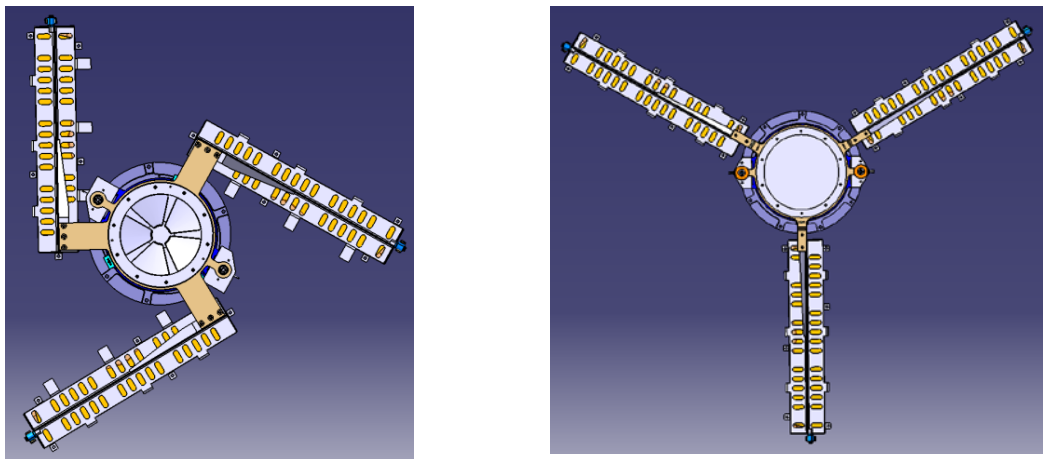


Fig. 8. SIDE modularity examples

Typically implemented on the +X panel, the stowed equipment height is around 300 mm. An accommodation on Y or Z panel can be easily envisaged.

With the feedback from the IDEAS design, possibilities of mass savings have been investigated:

- Simplification of the inflating subsystem by merging the inflating and the rigidization fluidic lines. The boom deployment and rigidization will be done in a single phase.
- HDRM re-design by introducing a second pyro-bolt and suppressing the strap and its locking mechanism.
- Review of heavy mechanical parts which can be optimized

From these mass optimizations two architectures have been defined which cover the mini-satellite category (100 kg - 500 kg):

- A mono-boom architecture, called SIDE-1, with an 8-metre boom which provides an extra aerodynamic surface of 5.35 m² for a mass around 8 kg. This configuration is compatible with satellites up to 250 kg
- A bi-booms architecture, called SIDE-2, with two 6.5-metre booms which provide an extra aerodynamic surface of 7 m² for a mass around 12 kg.

4. RE-ENTRY PERFORMANCES

Passive re-entry performances were assessed by Airbus Defence and Space for satellites on circular SSO orbits (typical inclination of 98.8°) between 700 and 800 km. The study was also limited to mini-satellites (100-500 kg) which likely do not exceed the specified limit of human casualties of 0.01% per uncontrolled re-entry. In this case, an uncontrolled de-orbit is permissible.

The performance evaluation was performed with the STELA software which is the reference tool used by CNES for re-entry duration. (See [2]). The used atmosphere model was the NRLMSISE-00. The main assumption used in the simulation was a constant mean solar activity (Flux F10.7 = 140). This assumption allowed to study cases of re-entry which were de-correlated from the solar activity and independent from the starting date.

The spacecraft model was identical to the MICROSCOPE spacecraft (see Fig.1) with a minimal surface of 0.6 m², a maximal surface of 2.2 m² and a mean surface in tumbling configuration of 1.65 m². Relative attitude of the spacecraft re-entry was computed independently and re-injected in the STELA tool by hybridizing the drag coefficient file.

The Fig.9 shows the typical re-entry of a 250-kg spacecraft with SIDE-1. De-orbiting is done in 26 years instead of 126 years without SIDE system.

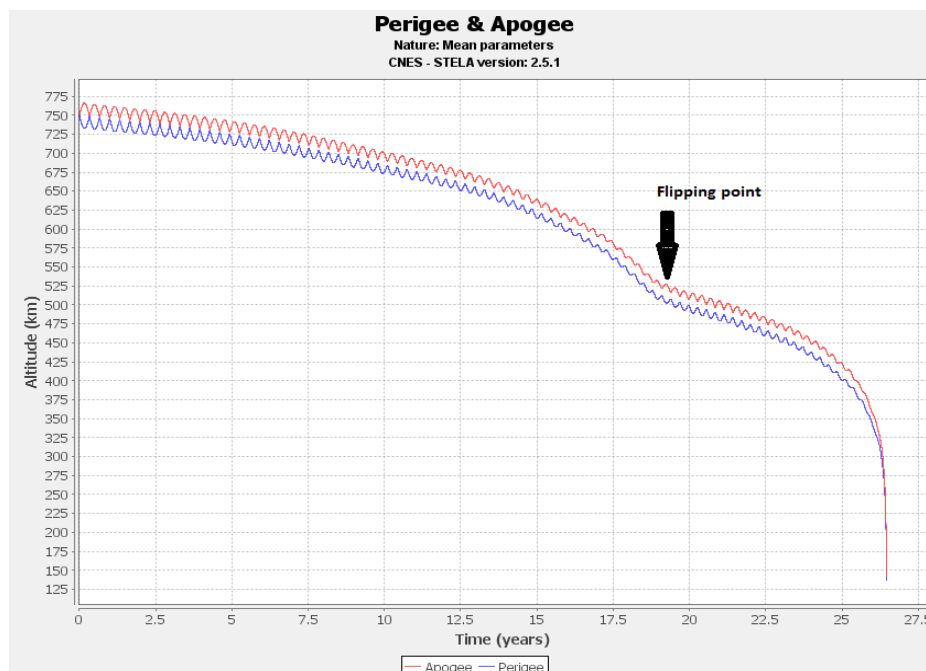


Fig. 9. 250 kg-Satellite, Initial altitude 750 km, SIDE-1

Both architectures were benchmarked with IDEAS and de-orbiting strategy using a high-thrust impulsive Hohmann-type manoeuvre that sent the spacecraft onto an elliptic orbit with a 25-year remaining lifetime. According to [1], this solution leads to a minimal ΔV requirement for satellites where an uncontrolled re-entry is admissible. [1] has also demonstrated that monopropellant thrusters seem to be the best trade-off taking into account availability, maturity level and performances.

Fig.10 shows the domains for SIDE-1 (resp. SIDE-2) respecting the 25 years re-entry criterion. Two abacuses representing the de-orbiting performances of 7 kg (resp. 12 kg) have been added so as to compare the performances of SIDE to an equivalent mass of hydrazine.

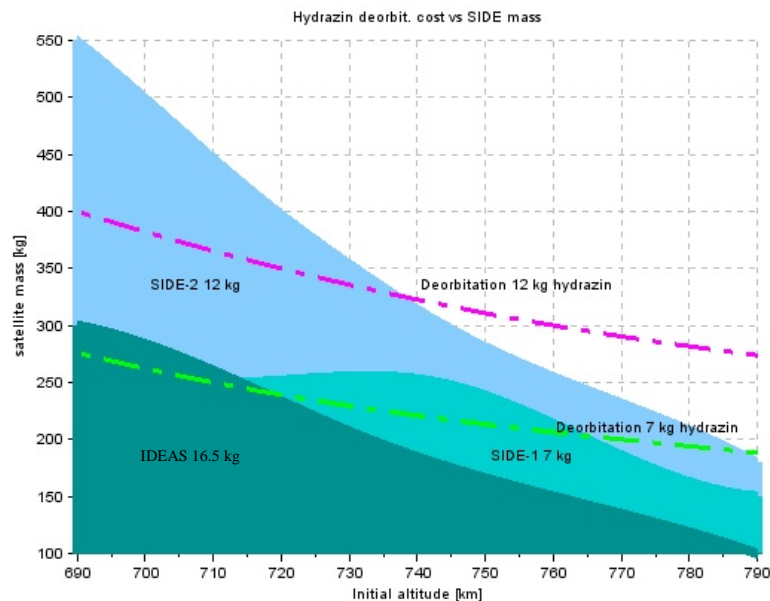


Fig. 10. 25 years re-entry criterion domains

Up to 750 km altitude, there is no real mass penalty to embark a SIDE-1 or SIDE-2 on a satellite with a mono-propellant propulsion subsystem. Beyond this altitude, SIDE loses its efficiency in comparison to thrusters.

5. INFLATABLE DE-ORBITING SYSTEM ASSETS

In order to be compliant with the coming legislations imposing a re-entry in less than 25 years, most of the spacecraft will likely propose to use the chemical propulsion subsystem for the post mission disposal (see [1]). The SIDE equipment offers anyway specific advantages which worth to be taken into consideration in the spacecraft design and mission.

5.1. Fail-Safe Deorbiting Subsystem

One major asset of the proposed de-orbiting subsystem in comparison with propulsion subsystems is the ability to perform post mission disposal on loss of the satellite. The SIDE can be linked to Hardware Watchdog (WD) which triggers the boom release and its inflation in case of a major failure (battery failure, OBC failure). No energy (except the pyro signals) is required to perform sail-boom deployment.

The subsystem is also efficient in case of attitude control loss (propulsion subsystem major failure, AOC equipment failure) and is more reliable than a braking thrust which requires full operability and is hazardous at EOL.

The boom can also act as de-tumbling device by modifying the spacecraft inertia and can enable attitude stabilization (Earth communication, Sun direction) even if this will cause the re-entry to start earlier than expected.

Finally SIDE provides a functional redundancy to the de-orbiting function done typically by the propulsion subsystem and improves re-entry reliability.

5.2. Hydrazine tank threshold effect and Mission life extension

As mentioned in §4, there is no mass penalty to embark a specific inflatable de-orbiting equipment aside a monopropellant propulsion subsystem.

On one hand, by suppressing this hydrazine mass (around 30 % of the volume), it could be possible to change the propellant tank to a smaller one (hence the so called “tank threshold effect”). The consequences are the following:

- Cost reduction

- Mass gain beyond the hydrazine mass
- Internal accommodation volume gain, opening new scale factor gains.

By taking into account the SIDE equipment at the very beginning of the design, a more compact satellite can be defined with unexpected mass gain.

On the other hand, SIDE is also a good solution to extend the spacecraft's lifetime without changing its design (added hydrazine, tank size). The spared hydrazine is then dedicated to the operational life of the satellite instead of the re-entry. Typically 30% of the embedded hydrazine is used for reentry operation. This roughly corresponds to a 30% increase of lifetime.

5.3. Mixed re-entry strategies

At iso-architecture (hydrazine mass, satellite mass), the SIDE equipment opens the flight domain of the satellite to higher altitudes. A mixed reentry strategy consists of a first lowering of the perigee to an altitude where the SIDE system is efficient and then to deploy SIDE. The reentry will proceed nominally with the passive re-entry. Mixed re-entry strategies are consistent with a global optimization including hydrazine tank threshold effect.

As an example, a 250-kg satellite at 715 km needs 7 kg hydrazine to perform an uncontrolled reentry within 25 years by lowering its perigee to 496 km. By combining a braking manoeuvre to lower the perigee and then the deployment of a mono-boom SIDE-1, the satellite can start at 870 km:

- First decrease the perigee to 660 km with 7 kg of hydrazine
- Then deploy the aero-braking sail to finish the uncontrolled re-entry within less than 25 years

If the satellite performs reentry using thrusters only, it needs 14 kg of hydrazine to decrease the perigee down to 450 km.

5.4. Re-entry Operations Costs

A major advantage of SIDE in comparison with thrusters braking manoeuvre is the simplicity of the operations to be carried out.

The deployment sequence of SIDE can be triggered on a single TC "Fire & Forget" without parameter and its completion lasts less than 10 minutes, meaning that the whole process will be completed during a single ground station visibility window. Only a reduced OPS team is necessary to perform the re-entry.

On the contrary, transferring a spacecraft to an elliptical orbit with thrusters requires a lot of preparation, a complete OPS team and several ground stations visibilities. After the braking boost, the final orbit shall still be assessed with ground infrastructures. Finally the de-orbiting cost of the spacecraft with thrusters could exceed the cost of a SIDE system itself.

6. CONCLUSION

The technology of passive aero-braking re-entry developed by Airbus Defence & Space in the frame of IDEAS project funded by CNES has reached today a high level of maturity (TRL7/8) and shall be "mission proven" in 2017. By developing new architectures based on these building blocks, Airbus Defence & Space proposes lightweight, low cost deorbiting equipment for mini-satellites (100kg-500 kg), filling the requirements of space legislation which comes into effect in 2021.

Satellite inflatable deorbiting equipment seems to be a competitive alternative to thrusters for all mini-satellites up to 750 km altitude. The addition of a de-orbit function on a spacecraft has in most cases a significant effect on satellite design; SIDE appears to be a low cost, reliable and lightweight solution. Embarking SIDE aside a monopropellant propulsion subsystem can also be envisaged as it provides potential spacecraft design optimization such as tank size reduction and operation cost savings.

This study was intended to highlight also the functional advantages of SIDE and to provide a global overview of its performances (mass, re-entry duration) to the satellite architect in the early phase of spacecraft design. However the selection of SIDE will have to be made in case by case taking into account the spacecraft mass, its altitude and the space availability on external panels.

7. REFERENCES

REFERENCES

- [1]. R.Janovsky et al, "End-Of-Life De-orbiting Strategies for Satellites", OHB System : ESA-contract 15316/01/NL/CK in press
- [2]. STELA User's Guide version 2.5 October 2013 CNES

ACKNOWLEDGEMENTS

The work presented in this paper was performed by Airbus Defence and Space and CNES in the frame of the IDEAS programme.

ERECTION CYCLE OF DEPLOYABLE SPACE REFLECTORS USING THE FUNCTIONAL AND TECHNOLOGICAL SCREEN MESH

**M. Sanikidze⁽¹⁾, E. Medzmariashvili⁽²⁾, G. Gratiashvili⁽³⁾,
O. Tusishvili⁽⁴⁾, N. Medzmariashvili⁽⁵⁾, M. Janikashvili⁽⁶⁾**

⁽¹⁾ The Institute of Structures, Special Systems and Engineering Maintenance
of Georgian Technical University
77, M. Kostava str., 0175, Tbilisi, Georgia.
E-mail: sanikidze@gtu.ge

⁽²⁾ The Institute of Structures, Special Systems and Engineering Maintenance
of Georgian Technical University
77, M. Kostava str., 0175, Tbilisi, Georgia
E-mail: medzmariashvili@gtu.ge

⁽³⁾ The Institute of Structures, Special Systems and Engineering Maintenance
of Georgian Technical University
77, M. Kostava str., 0175, Tbilisi, Georgia.
E-mail: george_gratiashvili@yahoo.com

⁽⁴⁾ The Institute of Structures, Special Systems and Engineering Maintenance
of Georgian Technical University
77, M. Kostava str., 0175, Tbilisi, Georgia.
E-mail: tusishvili@gtu.ge

⁽⁵⁾ The Institute of Structures, Special Systems and Engineering Maintenance
of Georgian Technical University
77, M. Kostava str., 0175, Tbilisi, Georgia.
E-mail: nika-medzmariashvili@mail.com

⁽⁶⁾ The Institute of Structures, Special Systems and Engineering Maintenance
of Georgian Technical University
77, M. Kostava str., 0175, Tbilisi, Georgia.
E-mail: mikheiljanikashvili@gmail.com

ABSTRACT

Paper is dedicated to the one of the newest methods to create reflecting surface in antenna reflectors. The advantage of such method is the high range of more approximated accuracy of the surface that is gained in case of its application. The work is intended to reduce elasticity, arrangement of tensioners and to experimental research of its tensioning force. Here is determined average meaning of mesh reduce elasticity, also the dependence nature among tensioning force and tangency points of displacement of tensioners on mesh.

On the bases of results received from experimental researches we can conclude that elasticity modulus of reflecting mesh is similar for longitudinal and lateral directions of knitted structure. The mesh elasticity coefficient is established. Within the particular loads they are constant magnitude. Increment dynamic of fixed motion magnitude in tensioners joints are nonlinear. Tensioning force was determined. In case of load influencing in tensioning points arises so called convexities.

1. INTRODUCTION

In the reflecting antennas special responsibility task represents issue of its reflecting surface - screen arrangement technology. This task is even more complicated when it is related to large-sized deployable space reflecting antenna. In the Earth's environment as well as in space the reflecting antennas screens are characterized by very high precision design geometry. If the conventional building structures variation of the elastic limits for designs makes range up to

1/100 - 1/1000 of span, in the reflecting antenna its reaches up to 1/10000 and sometimes 1/100000 of overall dimensions. The solution of such tasks require the development of current technologies [1, 2, 3, 4, 5, 6].

2. A DEPLOYABLE SPACE OFFSET REFLECTOR ANTENNA CONSTRUCTION FOR THE AREA OF $4 \div 25$ M

Construction has (Fig. 1): an upper functional mesh 1 and screen (not shown in the figure), that are fixed in a contour element (2); a lower technological mesh (3) with rarefied cells in the units of which a technological knitted fabric type mesh (not shown in the figure), also having contour elements (2), are attached; the contour elements are mounted on a deploying oval load-bearing ring having posts (4), upper and lower pantograph elements (5), elastic cross rods (6) for attaining accuracy; shaping of the system is ensured by means of tensioners (7) engaged in respective units of the functional mesh and technological mesh and provided with length compensators (8), as well as tensioners (9) disposed in the units of the technological mesh and respective functional mesh, that in turn are passed through the screen mesh cells.

The folded construction transport package size is always fallen within cylindrical dimensions having the sizes of $D = 800$ mm, $H = 4000$ mm (Fig. 1 b).

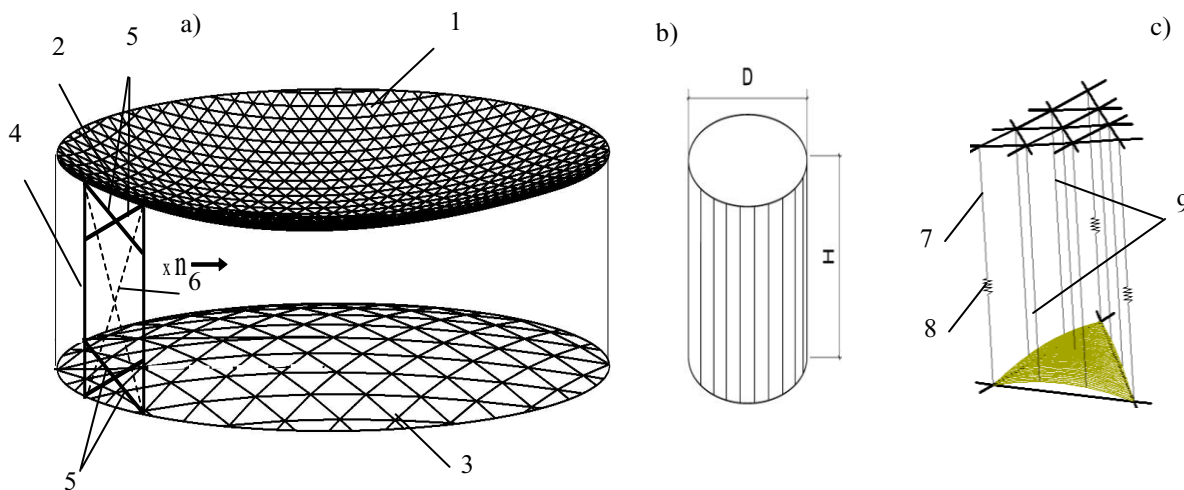


Fig. 1. a, b – The construction in deployed and folded states; c – fragment of coupling the functional and technological meshes

3. NEW TECHNOLOGICAL METHOD OF REFLECTING ANTENNA SCREEN

Reflecting surface of the reflector is carried out by various methods. The advantage of stated, new method consists in this method application case would be reached higher design precision.

On the I stage is carried out deployment of reflector's ring up to design position and ring arrangement on the zero-weight stand by fixing of upper points in one plane (Fig. 2).

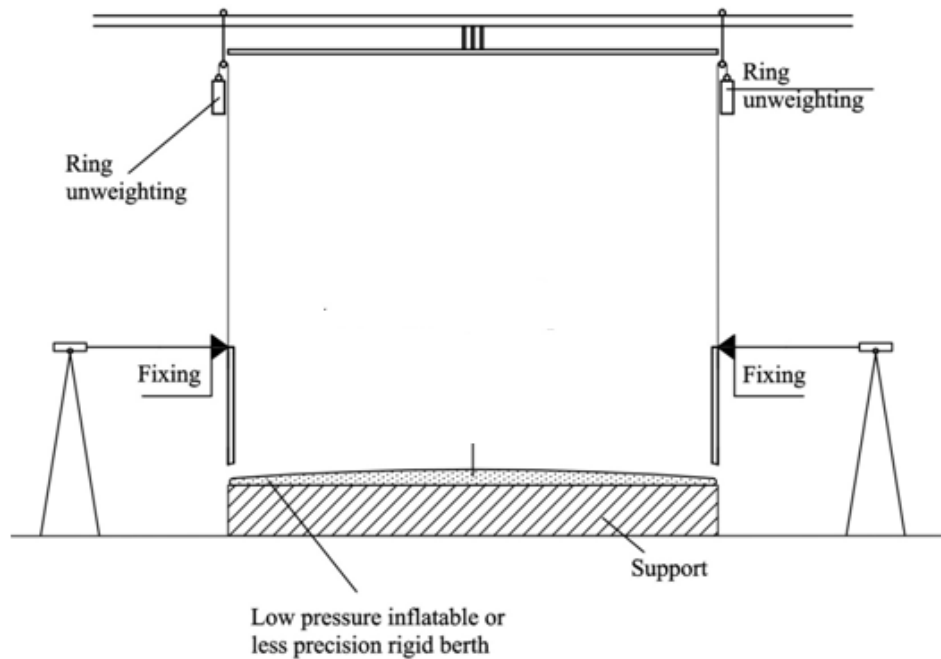


Fig. 2. The deployment of reflector ring up to design position and hanging on zero-weight stand with fixing in one plane

On the II stage is carried out inflation of arranged on special support low pressure inflatable berth that in inflated condition reproduce the technological mesh surface. It is possible to apply the rigid hard berth with less precision. On the berth is arranged the technological mesh. Thus, the lower technological mesh has some temporary curvature, after shaping up to design curvature of which the lower technological mesh by edges will be attached to the deployment ring lower surface (Fig. 3).

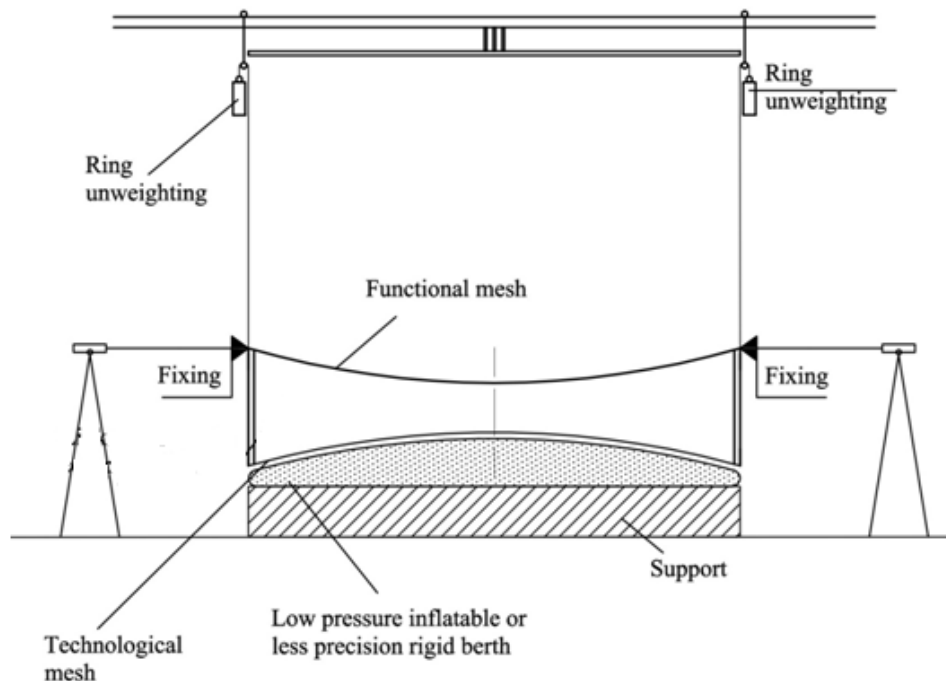


Fig. 3. Attaching of functional and technological meshes in reflector ring deployed almost in design position

At attaching of upper technological mesh due the influence of Earth's gravity force mesh itself makes the shape, but it's still not the final shape, and it still requires the tension by certain forces.

On the III stage is carried out the installation of hosiery technological mesh from upper (inner) side and under the upper functional mesh installation of reflecting mesh and attachment with ring (Fig. 4).

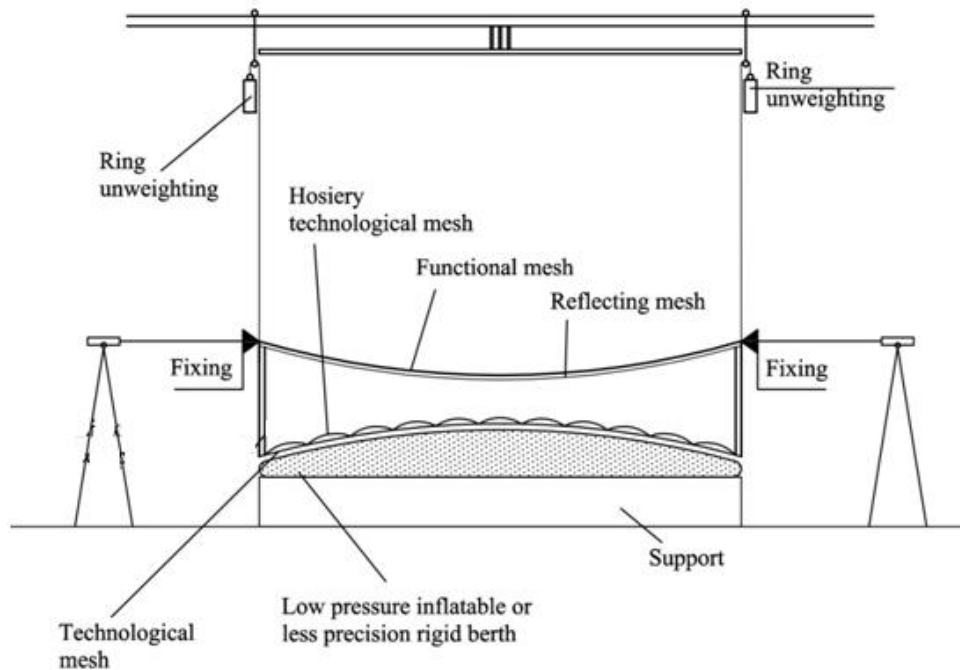


Fig. 4. Attachment of hosiery technological and functional meshes

On the Stage IV is carried out installation (gluing) of the length compensating tensions in the technological mesh nodes that also represents the hosiery technological mesh fixing points with technological mesh. At the same time the tensions attachment occurs only in the lower nodes, on the upper nodes they are not attaching – their passing is executed in the similar to functional mesh (symmetric) nodes, and continues up to hanging on guide pulleys and will be tensioned by weights with preliminary calculated masses (Fig. 5).

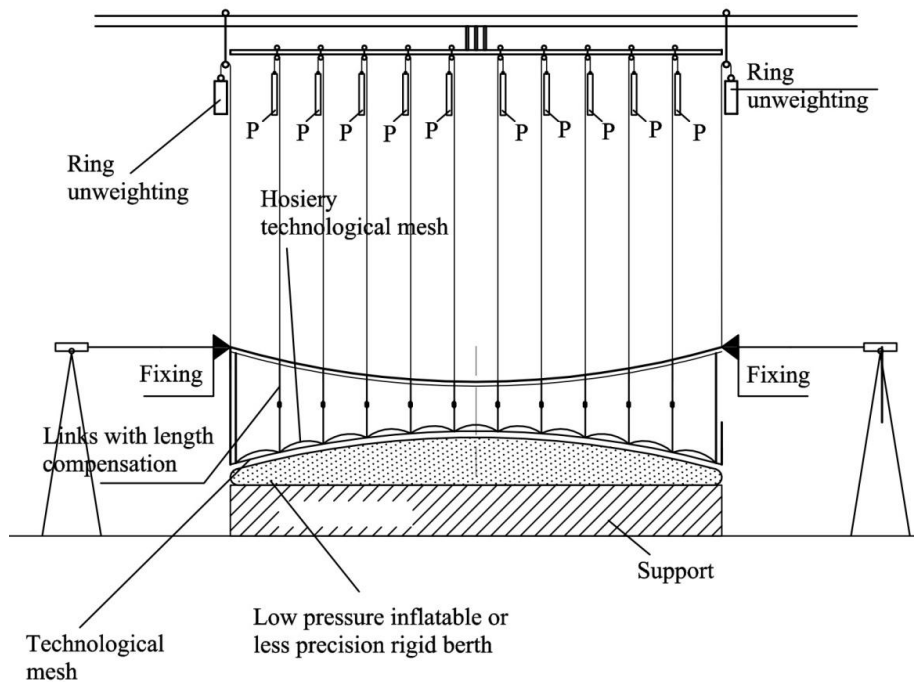


Fig. 5. The tension of lower technological mesh

On the V stage is carried out is the upper functionality mesh tension. The upper mesh tension is carried out as follows: the attached in the technological mesh nodes compensating tension that, in turn, are freely passed through symmetrical nodes of functional mesh, upward on the tensions are attaching cutting with one side weights, whose mass is similar to the hanging on arranged on guide pulleys the lower technological mesh tension P weight. Thus, the upper and lower symmetrical points under the influence of gravity force were tensioned by same value (Fig. 6).

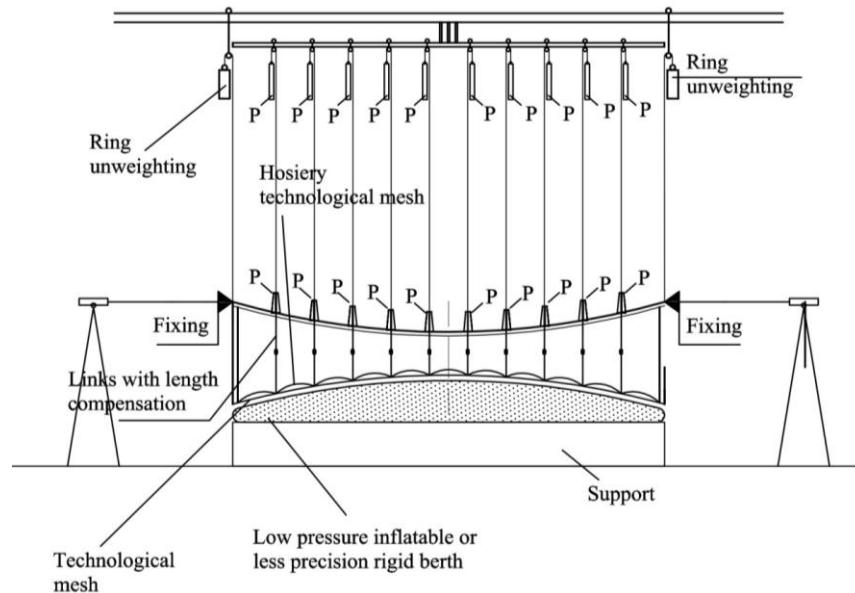


Fig. 6. Shaping of technological and functional meshes by symmetrical loadings

On the VI stage is carried out tensions attachment in the hosiery technological mesh nodes and straining also by similar to length compensating tensions weights, but, in contrary to the attached in technological mesh nodes tensions, the attached in hosiery technological mesh tensions are not installed length compensating springs. Further, similarly to the above considered V stage, is executed the functional mesh tension with removable weights (Fig. 7).

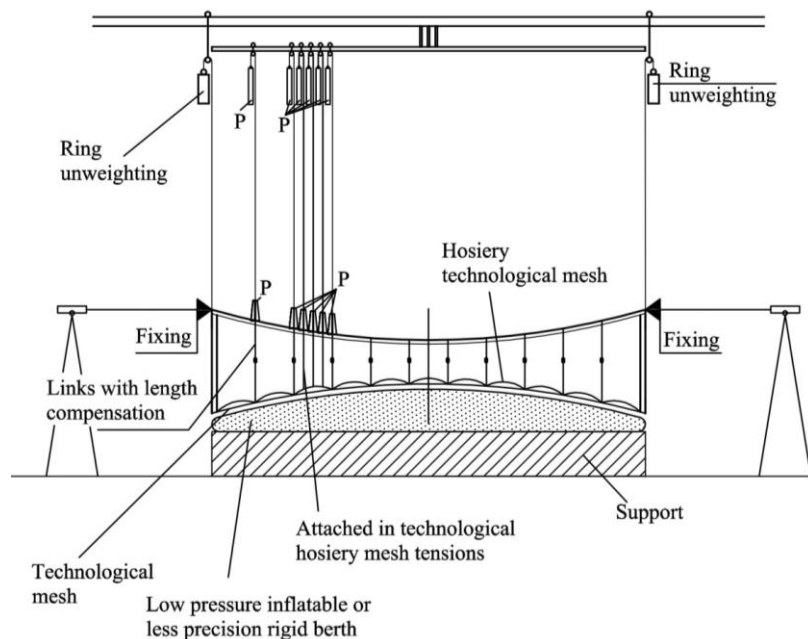


Fig. 7. tension of hosiery technological mesh an its symmetrical points

On the VII stage is carried out fixing of tensions with functional mesh by glue and after this is possible to cut off excess part of tensions (Fig. 8).

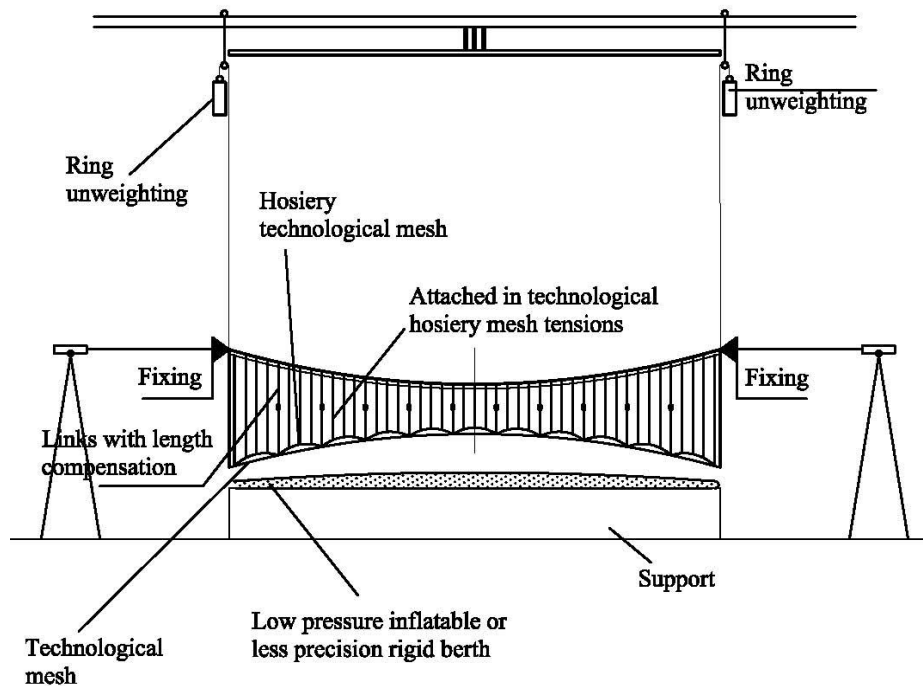


Fig. 8. Tensions cutting and berth deflating

As a result of the technological cycle's completion the received reflecting surface is characterized by high level of approximation precision.

4. EXPERIMENTAL RESEARCH REFLECTING MESH OF REFLECTOR

The meaning of reflecting mesh is to reflect different radio waves. The highest meaning is given to the reflecting mesh, that's why we carried out experimental researches on mesh, to determine: reduce elasticity of mesh for different meaning of tensioning force; and dependence between motions of joints fastening tensioners on mesh and tensioning force [7, 8].

4.1. EXPERIMENTAL DETERMINATION OF REDUCED ELASTICITY MODULE OF THE REFLECTING MESH

The test bench manufactured for experimental study of the elasticity module of the reflecting mesh is a frame consisting of upper and lower fixed bars (1) and posts (2) (Fig. 9). A special reflecting mesh (3) knitted with metal wire of the diameter of 0.05 mm and having the size of 100×100 cm (1m² mesh weight is 80 g) was prepared for testing (Fig. 9, 10) that is fixed on the test bench upper bar by its upper end, and, with its lower end, – on a vertically movable bar (4) whereon loads (5) are hanged.

The mesh was tested on static vertical evenly distributed load in longitudinal and transversal directions of the knitted structure. The initial load was 0.25kg. The load was increased gradually, namely by 0.2kg up to 2.05kg (see table 1 and 2). At each step of increasing the load, vertical displacement l was recorded on a centimeter scale mounted on the post by the delay of 2-3 minutes. As can be seen from the tables, at different steps of the load, increase in the displacement of the mesh structure Δl in longitudinal and transversal directions varies within the range of 4-6 cm. At the final, 11th step of the loading ($P=2.05\text{kg}$), vertical displacements of the mesh structure in longitudinal and transversal directions were 66cm and 64.2cm respectively (difference – 1.8cm). Maximal and minimal differences between the longitudinal

and transversal directions were notice at the loads of $P=0.25\text{kg}$ and $P=1.65\text{kg}$ and were 3.8sm and 0.3sm respectively. It can be noted that there is small difference between the displacements in longitudinal and transversal directions.

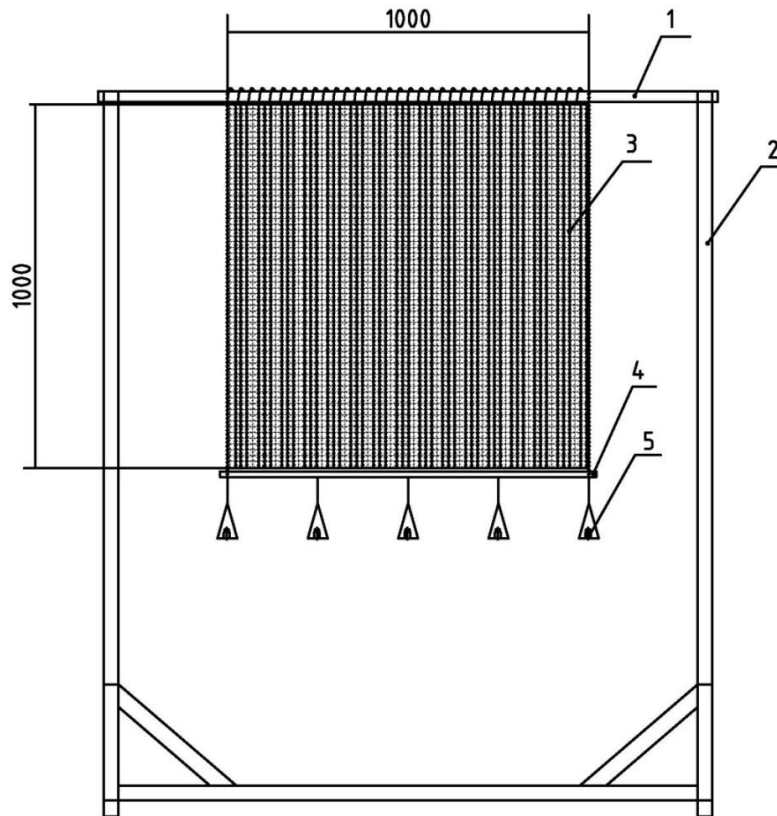


Fig. 9. Testing bench

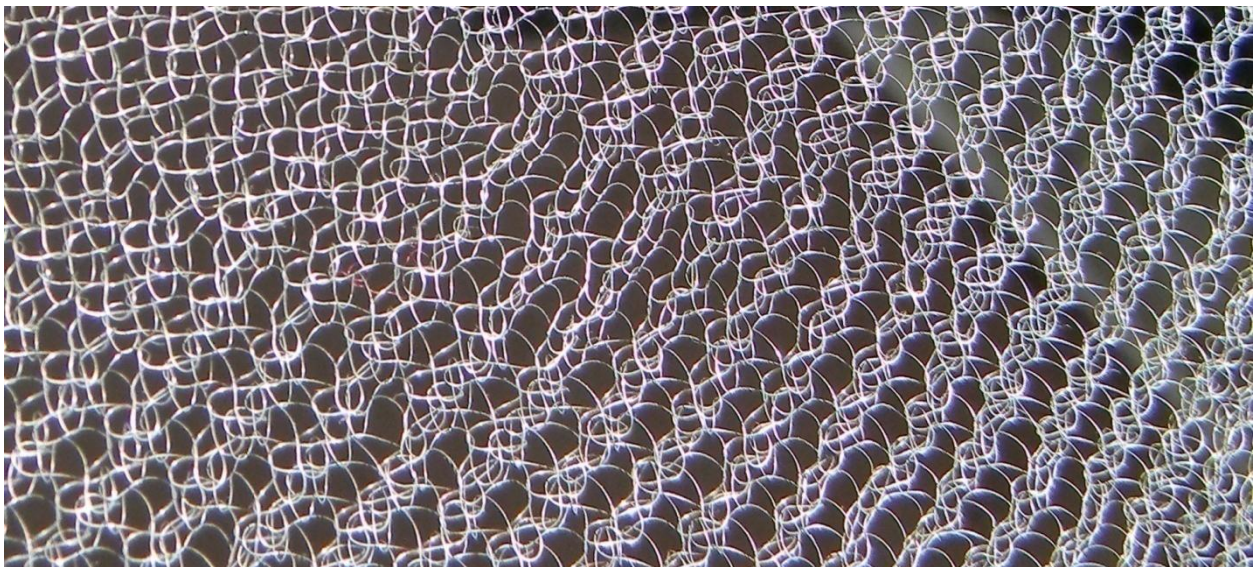


Fig. 10. Tested reflecting mesh (fragment)

In Fig. 11, the mesh structure stretched by 2.05 kg is shown. As can be seen from the figure, the stretched mesh structures in longitudinal and transversal directions slightly differ from each other.

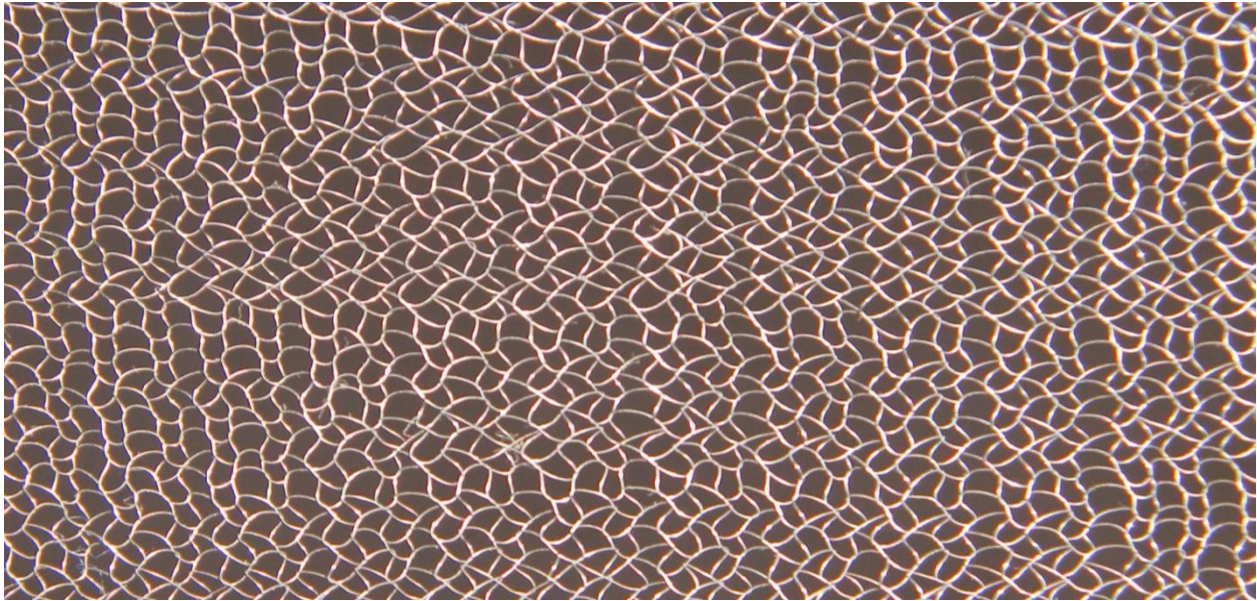


Fig. 11. The reflecting mesh in stretched state (fragment)

The mesh elasticity module is calculated by the formula:

$$E = \frac{Pl}{A\Delta l}, \quad (1)$$

where: E is elasticity module, kg/cm^2 ; P – force applied to the mesh, kg ; A – surface area where the force is distributed, cm^2 ; l – length or width of the mesh, cm ; Δl – gain of the length or width of the mesh, cm .

In our case, cross section of the mesh of the length or width of $l=100$ cm , where the force P is distributed, $A=0.0266$ cm^2 , then from the formula (1) we assume:

$$E = 3760 \frac{P}{\Delta l}. \quad (2)$$

Based on the conducted tests, the elasticity module values calculated by the formula (2) for longitudinal and transversal directions of the mesh structure at different loads are given in tables 1 and 2. The elasticity module values at the initial load $P=0.25\text{kg}$ were $E=41.4\text{kg}/\text{cm}^2$ and $E=50.0\text{kg}/\text{cm}^2$ respectively, and at the final step load $P=2.05\text{kg}$ - $E=116.7\text{kg}/\text{cm}^2$ and $E=120.0\text{kg}/\text{cm}^2$.

Table 1. Elasticity module E in the longitudinal direction of the fabric

№	P , kg	l , cm	Δl , cm	E , kg/cm^2	EF , kg
1	0	100.0	0	–	–
2	0.25	122.7	22.7	41.4	1.101
3	0.45	124.8	24.8	68.1	1.811
4	0.65	128.4	28.4	85.9	2.285
5	0.85	133.6	33.6	95.2	2.461
6	1.05	139.5	39.5	100.0	2.660
7	1.25	145.4	45.4	103.5	2.753
8	1.45	150.9	50.9	107.2	2.852
9	1.65	156.1	56.1	110.6	2.942
10	1.85	161.2	61.2	113.6	3.022
11	2.05	166.0	66.0	116.7	3.104

Table 2. Elasticity module E in the transversal direction of the fabric

N_0	P , kg	l , cm	Δl , cm	E , kg/cm ²	EF , kg
1	0	100.0	0	—	—
2	0.25	118.9	18.9	50.0	1.330
3	0.45	124.2	24.2	70.0	1.862
4	0.65	130.2	30.2	81.0	2.155
5	0.85	136.0	36.0	88.7	2.359
6	1.05	141.7	41.7	94.6	2.516
7	1.25	147.0	47.0	100.0	2.660
8	1.45	152.6	52.6	105.0	2.793
9	1.65	156.4	56.4	110.0	2.926
10	1.85	160.5	60.5	115.0	3.059
11	2.05	164.2	64.2	120.0	3.192

In Fig. 12, curves of the elasticity module of the reflecting mesh structure in longitudinal and transversal directions are shown. As can be seen, there is non-linear dependence between the load (P) and elasticity module (E). Apparently, the elasticity modules of the longitudinal and transversal directions slightly differ from each other and it is possible to draw an average elasticity module curve (Fig. 13). It should be noted that two characteristic areas (I – $P=0\div0.45\text{kg}$ and II – $P=1.05\div2.05\text{kg}$) can be marked on the curve, where the elasticity (rigidity) coefficients are constant values and are calculated by the formula (1)

$$K = \frac{P}{\Delta l} = \frac{EA}{l}, \quad (3)$$

Then from equation (2) we receive that

$$E = 3760K. \quad (4)$$

For the area I ($E_{\text{mean}}=57.4 \text{ kg/cm}^2$, $l=100\text{cm}$, $A=0.0266 \text{ kg/cm}^2$) $K_I=0.015 \text{ kg/cm}$, and for the area II ($E_{\text{mean}}=107.8 \text{ kg/cm}^2$, $l=100\text{cm}$, $A=0.0266 \text{ kg/cm}^2$) $K_{II}=0.029 \text{ kg/cm}$.

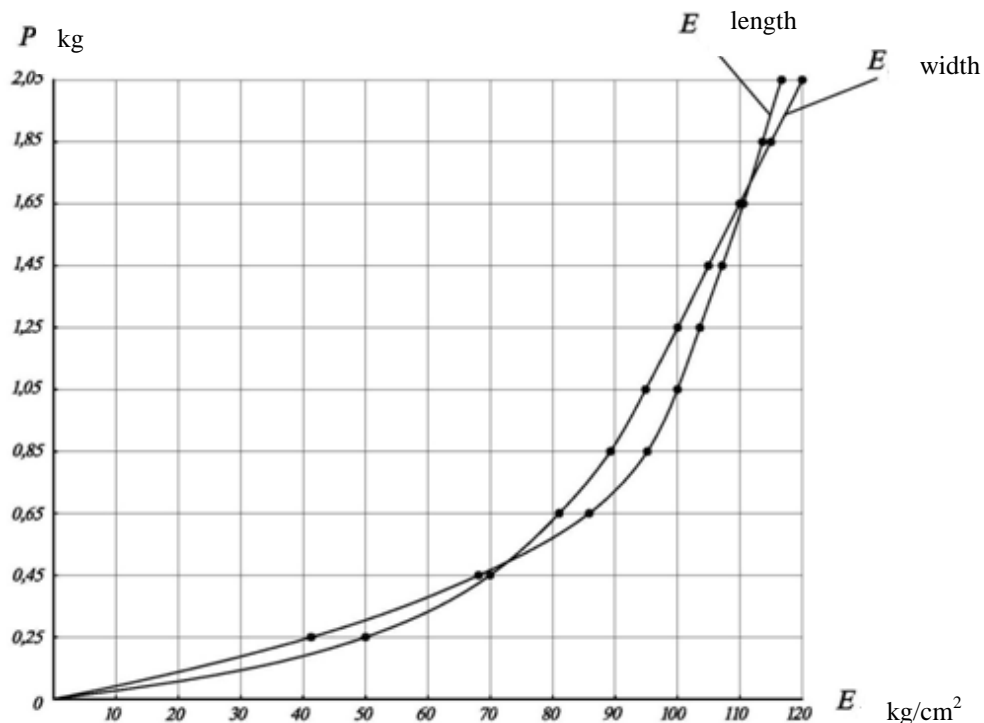


Fig. 12. Curve of dependence of the reflecting mesh elasticity module on load in longitudinal and transversal directions

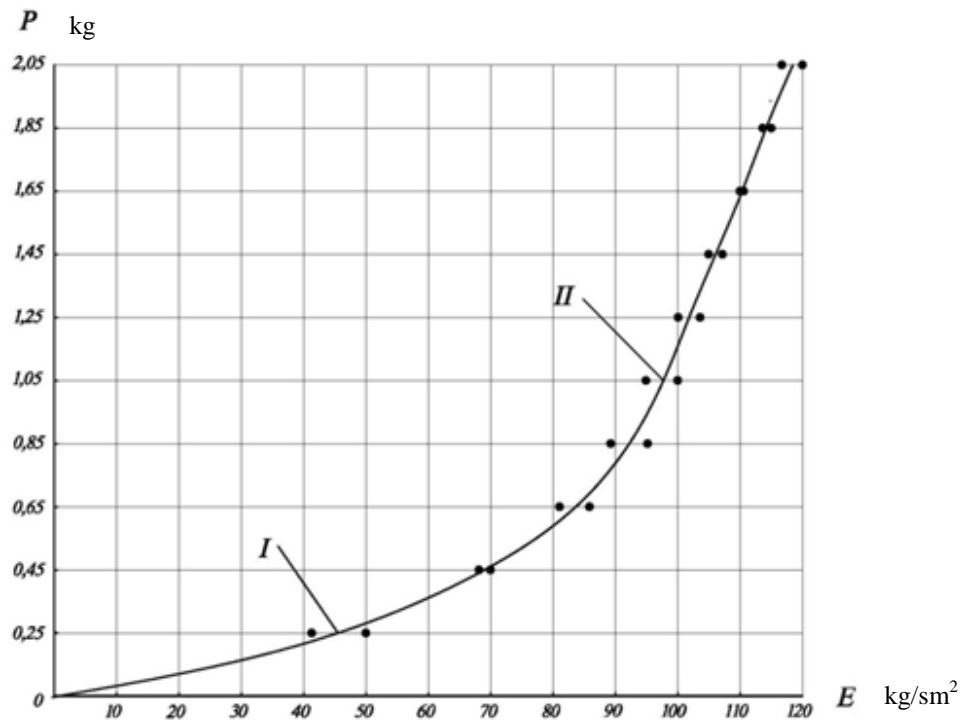


Fig. 13. Curve of dependence of the reflecting mesh elasticity module on load

Based on the experimental studies it can be concluded the elasticity modules of the present reflecting mesh are the same in longitudinal and transversal directions of the knitted structure.

4.2. EXPERIMENTAL STUDY OF THE TENSIONERS ARRANGED ON THE REFLECTOR TECHNOLOGICAL KNITTED FABRIC TYPE WIRE MESH

The testing bench (Fig. 14) consists of two rigidly connected parallel frames. On one frame (1) contour, a reflecting mesh (3) (see Fig. 10, 11) of the sizes of 1540×1820×2350 cm that was prepared for testing purposes is stretched by the force of 1.8 kg/m, and rollers (4) are arranged on another frame (2), whereon tensioners (5) fixed in the mesh are hanged over for stretching the mesh, and loads (P) are hanged on the ends of the tensioners (Fig. 15, Fig. 16).

The mesh was tested on static loads vertical to the mesh plane, which were applied in longitudinal and transversal directions of the mesh in points (6) arranged in every 25 centimeters (44 points) (Fig. 14). Initially, (tension force $P=0$) the above mentioned points were fixed above the tested mesh (3) with respect to the bench frame (1) plane (Fig. 15). The initial load was $P=20$ g and the displacements of the points were measured. Maximum displacement was observed in 3-6 points and was $\Delta l=52$ mm. In Fig. 16 a, distribution diagram (3_1), of the displacement of the points arranged on the 5th vertical (Fig. 14) is shown. It can be seen that 3-5 points were displaced to a maximum degree ($\Delta l=49$ mm) with respect to the non-stretched mesh (3).

At the further stages of the experiment, the load of $P=80$ g were applied in 9 points (2-3, 2-4, 2-5, 2-6), (3-3, 3-4, 3-6), (4-4, 4-5), and in the tenth 3-5 point, the load was increased by the steps of 20 g, from $P=20$ g to $P=160$ g.

Dynamics of increase in the displacement values observed at each step of loading does not have any regularity for the point 3-5. By way of example, in case of increase of the load from 20 g to 40 g $\Delta l=4$ mm, from 40 g to 60 g $\Delta l=8$ mm, from 60 g to 80 g $\Delta l=5$ mm, from 80 g to 100 g $\Delta l=4$ mm, from 100 g to 120 g $\Delta l=14$ mm, from 120 g to 140 g $\Delta l=8$ mm, and from 140 g to 160 g $\Delta l=1$ mm.

In Fig. 16 b, distribution diagram (3_2), of the displacement of the points arranged on the 5th vertical is shown, where the load of $P=80$ g is applied to all of the ten points. Like as in the previous case, maximum displacement was observed in 3-5 point $\Delta l=106$ mm, and when $P=160$ g, $\Delta l=133$ mm (Fig. 16 c). From $P=80$ g to $P=160$ g, the 3-5 point was displaced by 27 mm.

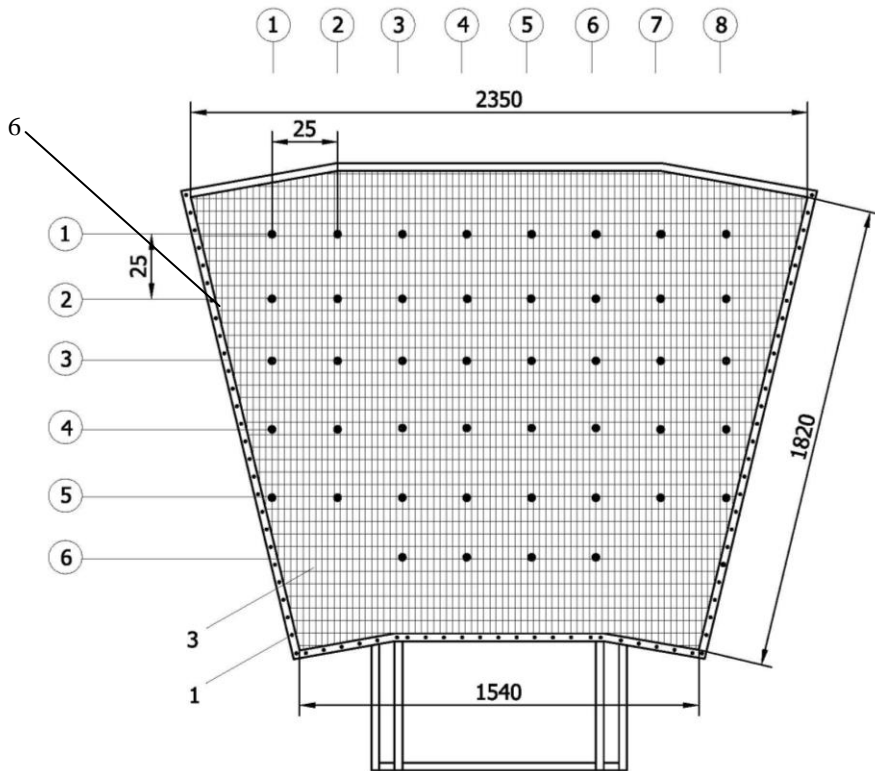


Fig. 14. Test bench

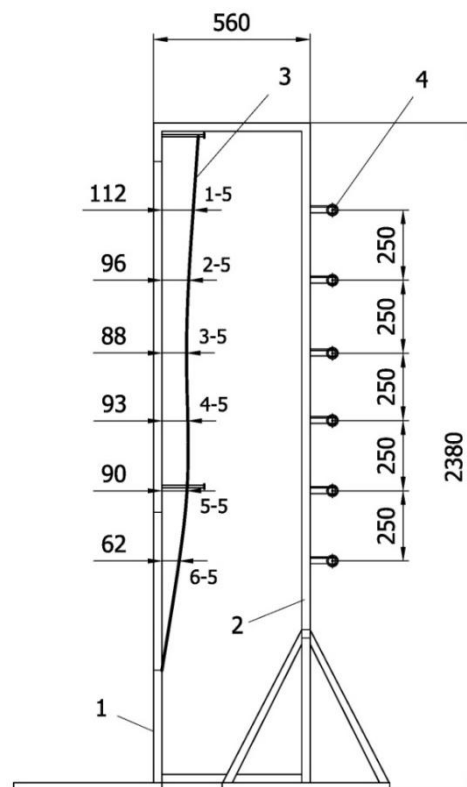


Fig. 15. Distribution diagram of the mesh stretch in non-loaded state

It should be noted that some “bosoms” are created in the engagement points (6) (Fig. 14) of the tensioners (5), on time of load influence (Fig. 16).

During the experiment, influence on neighboring points was observed when the load of $P=100-160g$ was applied on the 3-5 point, and the same was observed on second degree neighboring points when $P=160g$.

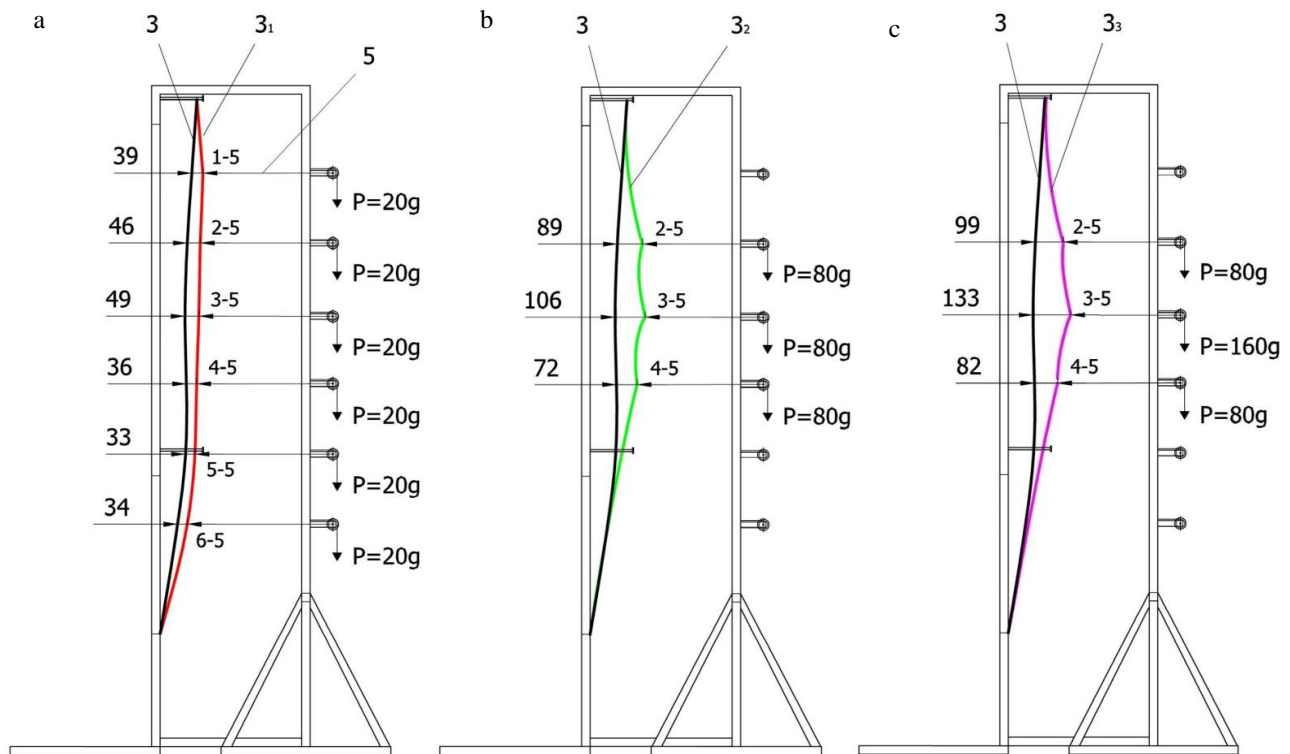


Fig. 16. Distribution diagrams of the mesh stretch in loaded (a, b, c) states

5. CONCLUSION

Due the application of new technological method of receiving considered in the paper reflecting surface of reflector is reaching reflecting antenna screen higher design precision in comparison with current methods.

On the bases of results received from experimental researches we can conclude that elasticity modulus of reflecting mesh is similar for longitudinal and lateral directions of knitted structure. The mesh elasticity coefficient is established. Within the particular loads they are constant magnitude. Increment dynamic of fixed motion magnitude in tensioners joints are nonlinear. Tensioning force was determined. In case of load influencing in tensioning points arises so called convexities.

6. REFERENCES

- [1]. E. Medzmariashvili. Transformable systems. Academy of science USSR, scientific production association “prognostics and perspective R/D”, Tbilisi, 1990, -106 p. (In Russian).
- [2]. E. Medzmariashvili. The Technology Which Has No Analog. Transformable Space and Ground-Based Constructions. Special Issue of Magazine. Valemar S&T, Liechtenstein-Germany-Georgia, 1994. 36 p.
- [3]. Medzmariashvili E. Transformable structures in space and ground. Germany – Georgia, “Vallemar”, 1995, - 447 p. (In Russian).

- [4]. E. Medzmariashvili, G. Bedukadze, K. Chkhikvadze, M. Sanikidze. Theoretical and experimental study of reflector antenna. "Problems of Mechanics". Tbilisi, 2012, № 4(49). pp. 71-83.
- [5]. E. Medzmariashvili. Mechanical Supporting Ring Structure. CEAS Space Journal of European Aerospace Societies. ISSN 1868-2502. Published online: June 2013. 10 p.
- [6]. E. Medzmariashvili. The possible options of conical v-fold bar ring's deployment with flexible pre-stressed center. CEAS Space Journal of European Aerospace Societies. ISSN 1868-2502. Published online: June 2013. 9 p.
- [7]. Space Deployable Reflector E&GM-1. Georgia, Certificate of invention patent # P 5298. Priority 29.03.2007. E. Medzmariashvili, G. Medzmariashvili. Date of issue 27.04.2011. (In Georgian).
- [8]. E. Medzmariashvili, O. Tusishvili, M. Sanikidze, N. Tsignadze, G. Gratiashvili. Experimental research reflecting mesh of reflector// "Problems of Mechanics", Tbilisi, 2011, № 4(45), pp. 58-64.

STRUCTURE OF LIGHTWEIGHT REFLECTOR USING THE PRINCIPLE OF “TENSION ARCHITECTURE”

Nikoloz Medzmariashvili⁽¹⁾, George Medzmariashvili⁽¹⁾

⁽¹⁾*Institute of Constructions, Special Systems and Engineering Maintenance of Georgian Technical University
#68b Kostava St. 0172 Tbilisi, Georgia
Email: icssem@gtu.ge*

ABSTRACT

Optimal approach in an attempt to drop a deployable apace reflector antenna weight can be deemed designing it on the principle of “tensioned construction”. According to this principle, constructions, and in the given case, the structure of a deployable reflector antenna, are based on the use of as much elastic members – cables and as less rigid members as possible. Just this approach is outlined in the present paper describing a novel ring of deployable reflector antennas that is provided with V-fold bars, the central portion of the ring being formed as a geometrically unchangeable precision system owing to the completely tensioning thereof.

1. DEPLOYABLE SPACE REFLECTOR WITH CABLE ROD RING AND FLEXIBLE TENSIONED CENTER

The preliminary testing diagram of the mentioned modification was realized in a deployable reflector antenna, during testing of the deploying ring having springs and “V-fold bars” as one of the possible modifications of the structural design [1]. After the successful test, the new ring, which is provided with “V-fold bars”, electric drive and cables and, which has a prismatic, or truncated pyramid shape forming circular or oval outline in projection was applied by the European Space Agency for obtaining the European patent.

Ideas realized in mentioned constructions creates optimal possibilities of its rigidity, lightness and accuracy [2][3][4][5][6][7].

The ring, which is provided with “V-fold bars”, electric drive and a deployable cable has been revealed to be challenging as a result of the conducted experiments.

Just for this reason, 6 meter diameter prismatic reflector antenna has been designed and created, its full-scale tests as well as improvements of its respective units conditioned creation of new, light and rigid deployable space reflector.

Experimental option of 6 meter prismatic deployable reflector consists from two basic blocks – deployable load bearing ring and flexible-tensioned center, which creates unified constructional structure of reflector. Herewith, according the model that is fabricated according the experimental option, without changes in joints, can be manufactured deployable rings as with offset oval – elliptic outline, also with truncated pyramid shape.

Also, it should be explained that in presented case deployable V-fold bars are unfolded with cable systems and not with springs located in joints.

The main function is carried by the cable that passes over the rollers on the upper and lower ends of a post and the rollers that are disposed in the “V-fold bar”, which deploys the ring by coiling on the electric drive drum. During the entire process of deployment as well as after the deployment, i.e. in a so called operational state, the load-bearing stretched cable is not an “operational element” of the system and is not directly involved in its operation. The load-bearing cable exerts influence on the ring structure only by concentrated forces, in the form of external loads (fig. 1), and leads to the deployment of the ring and pre-stressing the diagonal rods.

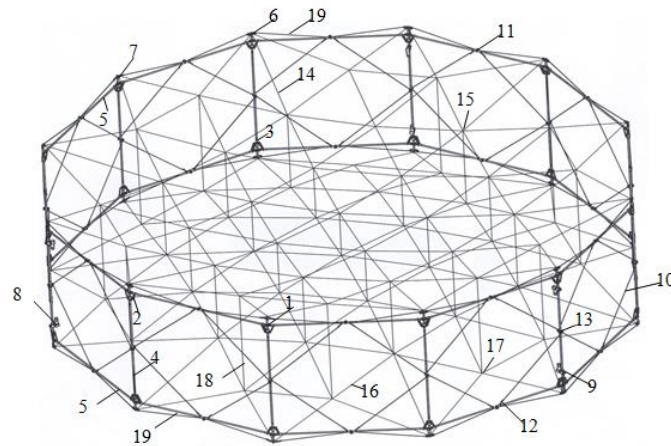


Fig 1. Deployable space reflector with cable rod ring and with flexible tensioned center

1 - cylindrical upper articulation with spatial orientation; 2 – levers of umbrella type synchronizers; 3 - “sliding” joint; 4 – vertical bar; 5 - Levers of upper and lower chords; 6 – rollers placed on ends of vertical bar; 7 – deployable cable; 8 – motor; 9 – rolling drum located on the motor; 10 – cable to reach geometrically unchangeable condition of deployable ring; 11 – cylindrical articulation; 12 – joint for cable affixion; 13 – cable rolling drums; 14 – tensioned rod of upper mesh located with flexible, triangular shape of center; 15 – joint with flexible, tensioned rods of upper mesh; 16 – tensioned rod of lower mesh located with flexible, triangular shape of center; 17 – joint of lower mesh; 18 – tensioning cables; 19 – deployable load bearing cable of upper and lower ring.

Wholly, presented scheme is a pre-stressed, cable –rod, geometrically unchanged structure – transformable spatial truss, which is created by spatial truss with round cable-rod form, by ring and wires attached to it with spatial cable truss. The levers of upper and lower chord that in deployable ring is located between the vertical rods, uniting in cylindrical articulation. The roller is installed on vertical rod, and deployable cable is coiled on it. Tensioning force produced in cables forming equal force that in upper chords are directed up, and in lower chord – directed bottom. Equal force, with variable size, but constantly actuates until correction of adjacent levers – until cable rod affixed with one end close to the uniting joint with second end affixed to the post (vertical bar). Thus, creating triangle from pressed and tensioned rods, which’s formation and its form fixation is conditioned by equal force produced in joints by tension of deployable cable (fig2; fig. 3; fig. 4).



Fig 2 Adjacent levers of upper chord unifying in central articulation



Fig 3. Photo of adjacent levers of chord in unfolding moment

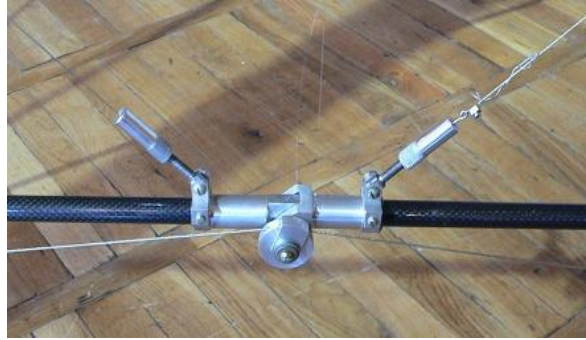


Fig. 4 Photo of adjacent levers of lower chord in unfolded state

Deployable cables coiled on rollers that are affixed on adjacent levers of chord is directed to the rollers that are affixed on the ends of vertical bar. Load bearing cable is coiled on it as on upper also on lower ends of vertical bar (fig. 5 and fig. 6).



Fig 5 Photo pf connection of vertical bar to the upper chord of deployable ring, load-bearing cable coiled on joint, folding and unfolding synchronization of levers and joint affixed on flexible center, it also shows upper joint for cable subdivided panel



Fig 6 Photo pf connection of vertical bar to the lower chord of deployable ring, load-bearing cable coiled on joint, folding and unfolding synchronization of levers and joint affixed on flexible center, it also shows upper joint for cable subdivided panel

Joints presented on photos are mainly performed according the project (fig 1). The chord of deployable ring is manufactured from 12 mm carbon fiber pipes, and vertical bars from 14 mm carbon fiber pipes. Joints are performed from aluminum alloy. The joint end bushes are attached all carbon fiber pipes as on vertical bars also on chord.

Different constructional elements are gathered in discussed joints. First of all should be mentioned structure of movable cylindrical joints having spatial orientation and are affixed with vertical bar of levers of chord. Using the mentioned joint it also gives possibility to perform ring with truncated pyramid shape, thus the outline of ring in both cases can be as circular also elliptic.

Two pair of short levers with cylindrical articulations with one end is connected on the end of adjacent levers close to the construction of cylindrical articulation and with another end is affixed with sliding joint. Mentioned construction serves to the simultaneous deployment of adjacent levers that is performed from the same corner, and it causes synchronization of chord levers deployment during the ring deployment.

Thus, in mentioned constructional determination, liner moveable bearing is located in its "sliding" joint, which causes change of sliding friction with rolling friction. It significantly reduces obstructions conditioned by the friction caused during the movement of joint. The cable rods of flexible center are fixed on a very upper point of vertical bar.

In every third section of deployable cable instead of roller is fixed in bushes. Thus, its affixion in joint is performed with springs as in upper also in lower joints (fig 7).

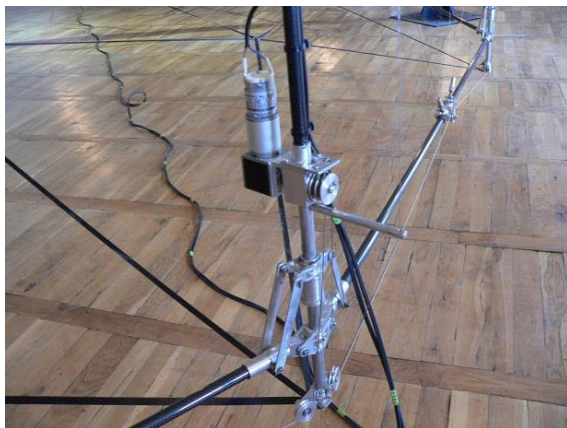


Fig 7. Joints located at the end of vertical bar

Affixion of load bearing cable of deployable ring using the length compensating springs are important for the compliance of the length of all cables during the roll on a drum, even with fewer sizes.

Its necessity in given specific determination is conditioned with that the after the length compensating springs on every third post the deployable cable from two side is rolled on two drums rolling with one axis of electric motor (fig 8).

a)



b)



Fig 8. The roll of bearing cable of deployable ring on two drum located on the rolling drum of the motor
a) general view; b) The roll of two deployable cables on the drum of the motor

The length of mentioned joint are restricted with distinct requirements and its maximum size is gained from the constructional requirements (fig 9 a), Also we should take in to account an installation of electric motors in mentioned joints, which should cause minimum length of metal joint (fig 9 b).

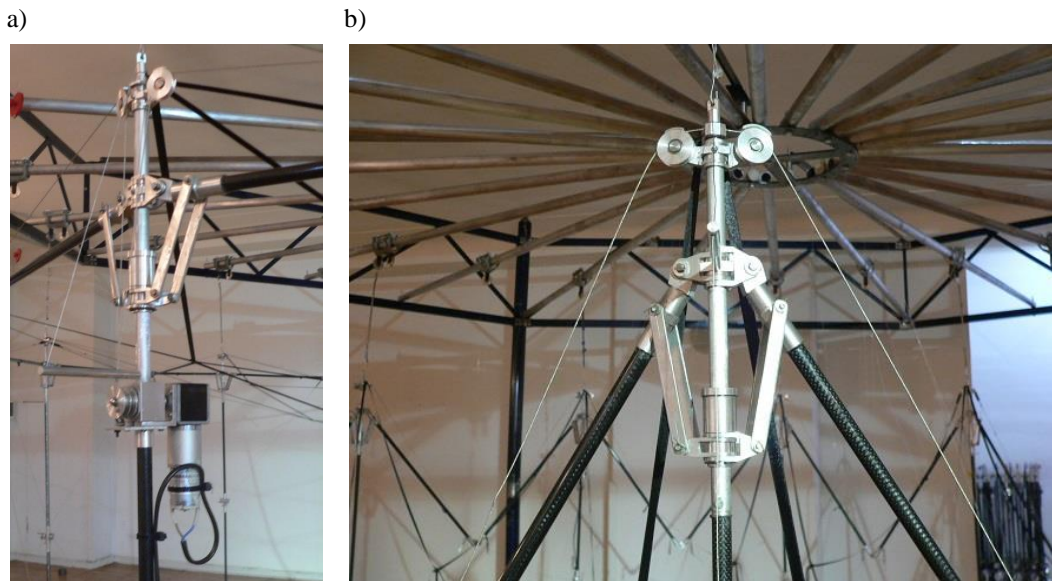


Fig 9. The maximum size requirements of aluminum elements of unifying joints.

a. for the joints with motors; b. joints without motors

As we can see from the photos the length of metal joints are determined from that condition when the roller folds the package.

The flexible and tensioned center mounted in deployable ring – in geometrically unchangeable supporting joint creates geometrically unchangeable construction with accurate geometry. Reflecting mesh – screen is installed on it (fig 10).



Fig 10. Tension of flexible center of reflector

Let's discuss spatial sample to protect tension of all flexible thread and cable in the structure of reflector.

Let us consider the deployment kinetics. The main function is carried by the cable that passes over the rollers on the upper and lower ends of a post and the rollers that are disposed in the "V-fold bar", which deploys the ring by coiling on the electric drive drum. During the entire process of deployment as well as after the deployment, i.e. in a so called operational state, the load-bearing stretched cable is not an "operational element" of the system and is not directly

involved in its operation. The load-bearing cable exerts influence on the ring structure only by concentrated forces, in the form of external loads (fig. 11), and leads to the deployment of the ring and pre-stressing the diagonal rods.

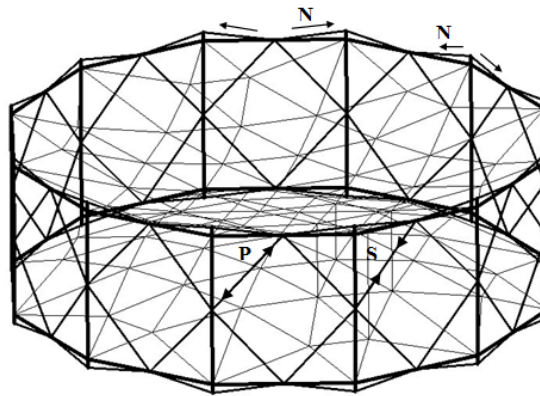


Fig. 11. General diagram of the forces acting on the reflector antenna structure and of the produced forces.

N – Force in the load-bearing cable; S – stretching forces in the cables;
P – contracting force in the cables

Deployment of 6 meter experimental construction of deployable space reflector with cable rod ring and flexible tensioned center was carried out on mechanical stand of weightlessness (fig 12).



Fig 12 - Deployment of 6 meter experimental construction of deployable space reflector

Numerous experimental deployments showed that the process of deployment of reflector with cable rod ring and motors is stable. All process of deployment went under the control, safely and what is important it was prognostic.

Deployment time varied between from 2 till 7 minutes, it was depended on the speed of roll of cable on rolling drum of motor.

2. Conclusions

1. A super lightweight deployable space reflector antenna provided with “V-fold bars” and an electric drive has been created.
2. The creation of the new type super lightweight reflector antenna was conditioned by optimal structural solution of the deploying load-bearing ring and by fitting of the later logically to the central stretched part.
3. Choosing the optimal version was conditioned by the use of truss type, geometrically unchangeable and statically definable elements therein that operate on contracting and stretching only.
4. The created stressed and deformed picture of the ring construction determines minimum number of contracted elements, arrangement the elements made of stretched elastic rods and cables according to the new design.
5. The number of stretched elements is also minimal in the ring, which is necessary for ensuring geometrical unchangeability of the system, and its stretching force in the structural system is represented as concentrated external force acting on the cable-rod system units.
6. The system is super lightweight, rigid and it has precise geometrical parameters, which is necessary condition for attaining the operation shape of the reflector antenna reflecting screen.
7. The reflector system has capability to adjust accuracy of reflecting surface.

Should be mentioned that the weight of discussed experimental option of 6 meter deployable space reflector with cable rod ring and with flexible tensioned center became 12kg, at that time when there are views for its constructional optimization and lightening of its weight.

3. REFERENCES

- [1]. E. Medzmariashvili, N. Medzmariashvili, O. Tusishvili, N. Tsignadze, J. Santiago-Prowalds, C. Magenot, H. Baier, L. Scialino, L. Philipenko. The possible Options of Conical V-fold Bar Ring's Deployment with Flexible Pre-Stressed Center. *CEAS Space Journal of European Aerospace Societies*. ISSN 1868-2502. Published online. June 2013;
- [2]. E. Medzmariashvili. Transformable Space and Ground Structures. *Monograph. Pub.* Georgia-Germany-Liechtenstein. 1995;
- [3]. E. Medzmariashvili, N. Medzmariashvili. Constructive Logic of Reflector Created with Double Pantograph Deployable Load-Bearing Ring. *Proceedings of ESA Antenna Workshop on Large Deployable Antennas*. 2-3 October 2012. ESTEC, Noordwijk, The Netherlands;
- [4]. E. Medzmariashvili, Sh. Tserodze, O. Tusishvili, N. Tsignadze, J. Santiago-Prowald, C.G.M. Van't Klooster, N. Medzmariashvili. Mechanical Supporting Ring Structures *CEAS Space Journal of European Aerospace Societies*. ISSN 1868-2502. Published online. June 2013;
- [5]. E. Medzmariashvili, J. Santiago-Prowald, C. MAnogenot, H. Baier, L. Scialino, L. Philipenko, N. Medzmariashvili. The Possible Options of Conical V-fold Bar Ring's Deployment with Flexible Pre-Stressed Center. *Proceedings of ESA Antenna Workshop on Large Deployable Antennas*. 2-3 October 2012. ESTEC, Noordwijk, The Netherlands.
- [6]. Инженерные Конструкции. Под редакцией В.В. Ермолова. Высшая школа. Москва. 1991.
- [7]. Frei Otto. Zugbeanspruchte Konstruktionen. Bauwelt Verlag. Berlin 1966

CONICAL V-FOLD BAR RING WITH FLEXIBLE PRE-STRESSED CENTER

E. Medzmariashvili⁽¹⁾, N. Tsignadze⁽¹⁾, J. Santiago Prowald⁽²⁾,
L. Datashvili⁽³⁾, O. Tusishvili⁽¹⁾, G. Phavlenishvili⁽¹⁾

⁽¹⁾*Institute of Constructions, Special Systems and Engineering Maintenance of GTU;
q 68b Kostava St. 0175, Tbilisi, Georgia;
Emails: Tserodze@gtu.ge, Tsignadze@gtu.ge, pavlenagio@gmail.com*

⁽²⁾*European Space Agency, ESTEC – Structures Section,
Keplerlaan 1, 2200 AG, Noordwijk, The Netherlands.
Email: Julian.santiago.prowald@esa.int*

⁽³⁾*Munich Technical University - Institute of Lightweight Structures
Boltzmannstr. 1585748 Garching
Email: datashvili@llb.mw.tum.de*

ABSTRACT

The paper presents the basic scheme of the deployment of a conical ring, based on V-folding bars. The designs follow recent ESA patents and have been implemented in a demonstrator model, showing good results. The main options investigated include spring and electric motor actuation. The installation of springs in V-fold joints and the stabilization and drive using a release cable was the first option investigated. The demonstrator model also included the use of three electric motors. The latter deployment actuation method was shown at the Large Deployable Antenna Workshop in ESTEC, demonstrating thus the performances that can be obtained from this architecture, in view of the low mass, the high deployed stiffness, the scalability to large dimensions and to some extent the potential of modularity.

1. CONSTRUCTIONAL PART

The overall views of the reflector in deployed and transportable states are illustrated in Fig. 1. It consists of the following parts [1, 2, 3]:

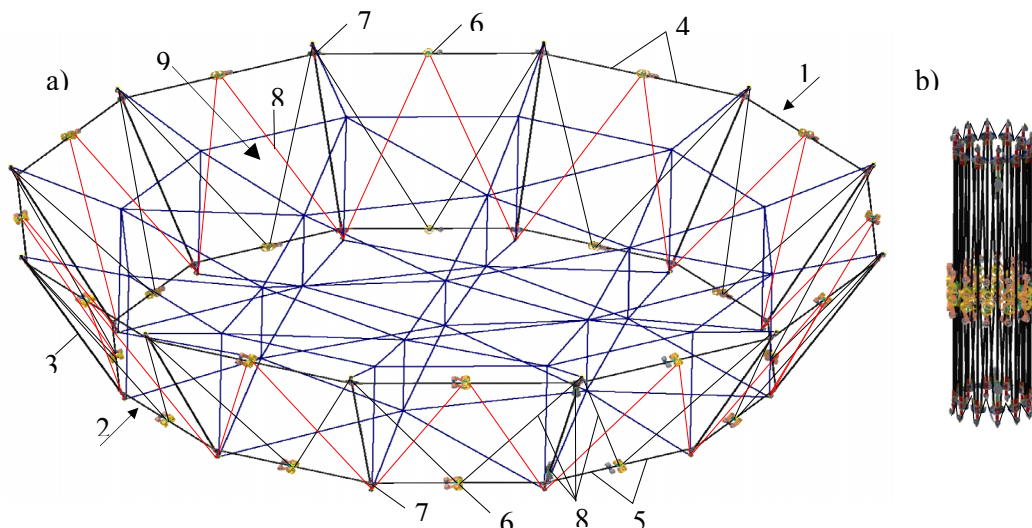


Fig. 1. Overall view of the construction in a) deployed state and b) folded state
1-upper ring; 2-lower ring; 3-post; 4-V-fold bars in the upper ring; 5-V-fold bars in the lower ring; 6- a hinge with permanent force spring mechanism that connects the V-fold bars; 7- synchronization mechanism connecting the sections hingedly; 8-deployment stabilization system; 9-central part.

1. A transformable conical load-bearing ring having V-fold bars, that comprises:

- Upper and lower rings connected by posts;
- Hinges intended for connecting the V-fold bars and having constant moment deploying spring mechanisms;
- Sections connecting hinges with synchronization mechanisms;
- Deployment stabilizing system.

2. A central part that comprises:

- Functional and technological flexible meshes;
- Vertical and inclined ties for connecting them;
- Let us consider principal diagrams of each space antenna component.

2. TRANSFORMABLE CONICAL LOAD-BEARING RING HAVING V-FOLD BARS

The load-bearing ring of the conical reflector antenna is a frame having the shape of a truncated cone with an upper ring of 6000mm in diameter and a lower ring of 4480mm in diameter, with distance between the ring planes being 1316.36mm and with lengths of the posts being 1520mm. See Fig. 2.

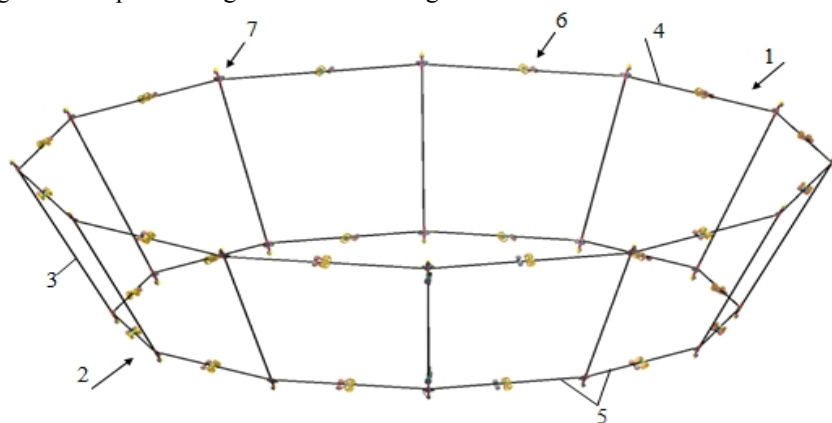


Fig. 2. The load-bearing ring construction in deployed state

1-upper ring; 2-lower ring; 3-post; 4-V-fold bars in the upper ring; 5-V-fold bars in the lower ring; 6-a hinge that connects the V-fold bars; 7- hinges connecting the sections.

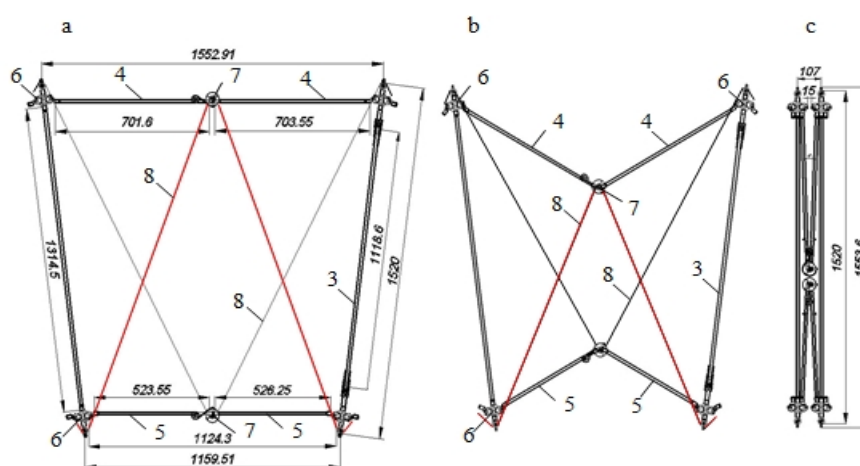


Fig. 3. Kinematical diagram of deployment-folding one section of the load-bearing ring

a)- deployed state; b)-partially folded state; c)-folded state; 3 – post; 4-V-fold bars in the upper ring; 5-V-fold bars in the lower ring; 6 – synchronization mechanism; 7- a hinge with permanent force spring mechanism;

The frame is divided into 12 equal parts. Each part is a trapezium shape flat frame made of carbon (carbonplastic) tubular rods (Fig. 2. reference numerals 3, 4, 5). The diameter of the posts is 14mm, and of the V-fold bars is 12mm. A kinematical diagram of deployment and folding of the load-bearing ring one section and its geometrical parameters are illustrated in Fig. 3. The section width in its folded state is 107mm, and its height is 1553.6mm. Folding and unfolding cinematic scheme of one section of load-bearing ring and its geometrical parameters are given in fig 3. the wids in folded state is 107mm and haight – 1553.6mm.

3. V-FOLD BARS CONNECTING HINGES HAVING CONSTANT MOMENT DEPLOYING SPRING MECHANISM

The load-bearing ring is deployed by flat constant moment springs (Fig. 4). The characteristics of the spring have been chosen taking the loads acting on a single section into the consideration. In particular, the V-fold bars weights, spring weight and stretching forces in the mesh have been taken into account. As has been defined by calculations, the acting force equals 46 N, the spring thickness is 0.4mm, width – 25mm, length - 700mm and weight – 54.6g. The spring is rolled up on a drum 2 movably mounted on a rod 4 at the V-fold bar 3 side.

The spring 1 is clamped around the small drum 2 because the outer diameter of the drum exceeds the inner diameter of spring in its free state by 10%. The end of the spring is attached to the drum by a bolt 5. At the V-fold bar 6 side, the drum is fixedly mounted on the axis 7 which in turn is fixedly mounted on the V-fold bar 6. The spring rolls on the drum 5 when folding and elongates by 60.84 mm. The spring is tensioned when the antenna is in a folded state.

Due to the symmetrical distribution of forces, pairs of constant moment spring mechanisms are used on each pairs of the V-fold bars (Fig. 4, (d), (e)).

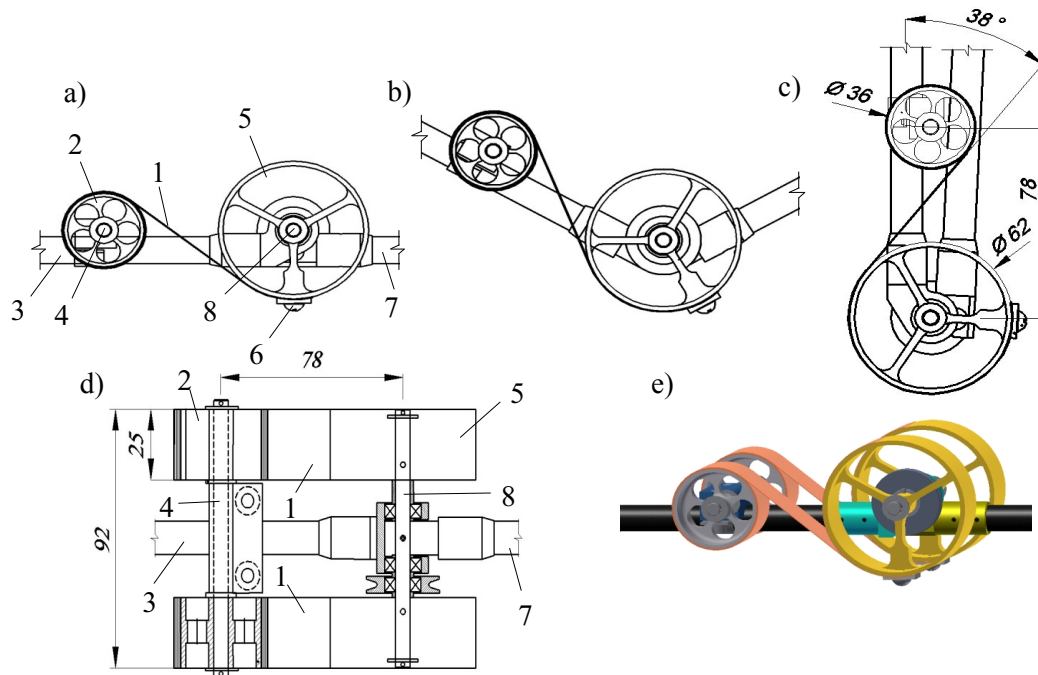


Fig. 4. Constant moment spring deployment mechanism

a)-deployed state; b)-partially folded state; c)-folded state; d) top view; e) axonometric view.

4. SECTION CONNECTING HINGES WITH SYNCHRONIZATION MECHANISMS

The horizontal rods are interconnected by means of synchronous transmission mechanisms (Fig. 5 (a), (b), (c)) to enable synchronous displacement of levers in the upper and lower rings. The operation principle of the synchronizer lies in cross like arrangement of the cables 1 on the guide rollers 2. Such arrangement of the cables enables synchronous turning of the levers. The tension of the cables is regulated by a tensioner 3 (Fig. 5 (e)). The angle between the sections changes within the range of $150^0 - 154.4^0$ from the folded state to the full deployment (Fig. 5 (d)).

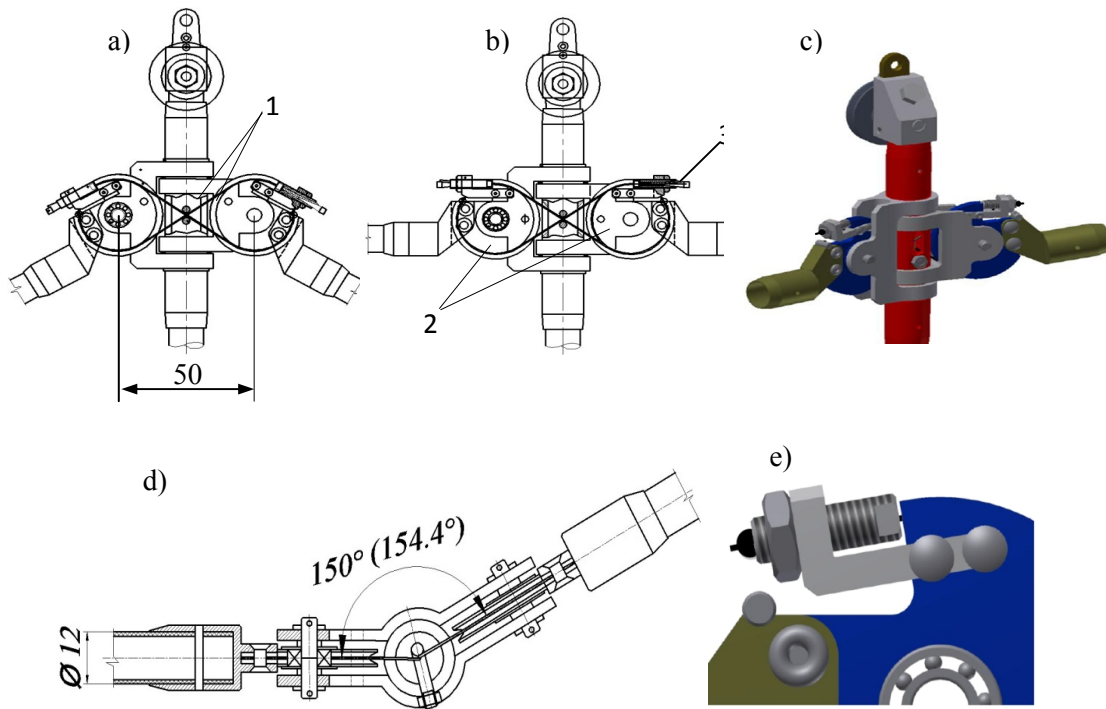


Fig. 5. Synchronization mechanism

a) - partially folded state; b), c)- deployed state; d) – top view; e)- stretching device.

1 – cable; 2 – guide roller; 3 – cable stretching device.

5. DEPLOYMENT STABILIZATION SYSTEM

Rapid turning of the levers and the blowing effect at the final moment is expected during the deployment. This can be prevented by use of a system 1 of cables for restraining the levers opening, that is operated by gear-motor drives 2, IG-32RGM 50 (Fig 6. a.). The gear-motor drives are permanent current engines with planetary conical reduction gears having the following characteristics: voltage 12V; drive ratio 1:721; torque 12kg.sm; rotation number 9.6r/pm. Two gear-motor drives are used in the antenna, one being intended for restraining the rotation of the upper ring levers, and another one being intended for restraining lower levers (Fig 6. b.). After attaining the horizontal disposition, the motors are switched off. The stretching forces produced in the cable can be compensated by use of a spring 3.

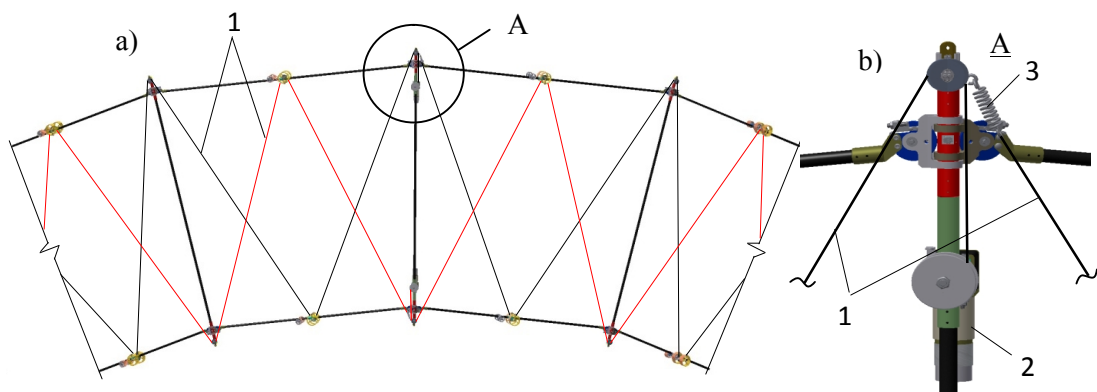


Fig. 6. Deployment stabilization system

a) – ring fragment; b) – unit for connecting the cables and motor
1 - cable; 2 – motor; 3 – stretching force compensating spring

6. CENTRAL PART

The central part consists of two interconnected triangular cell meshes disposed on paraboloidal surfaces and consisting of elastic linear elements [4, 5, 6].

The geometrical parameters of the upper functional mesh are as follows: aperture diameter $D = 6000$ mm.; focal distance $F = 3750$ mm.; lifting height $f = 600$ mm.

The geometrical parameters of the lower technological mesh are as follows: aperture diameter $D = 4480$ mm.; focal distance $F = 4181, 3(3)$ mm.; lifting height $f = 334.5$ mm. Distance between the central units of the meshes is 381.86 mm.

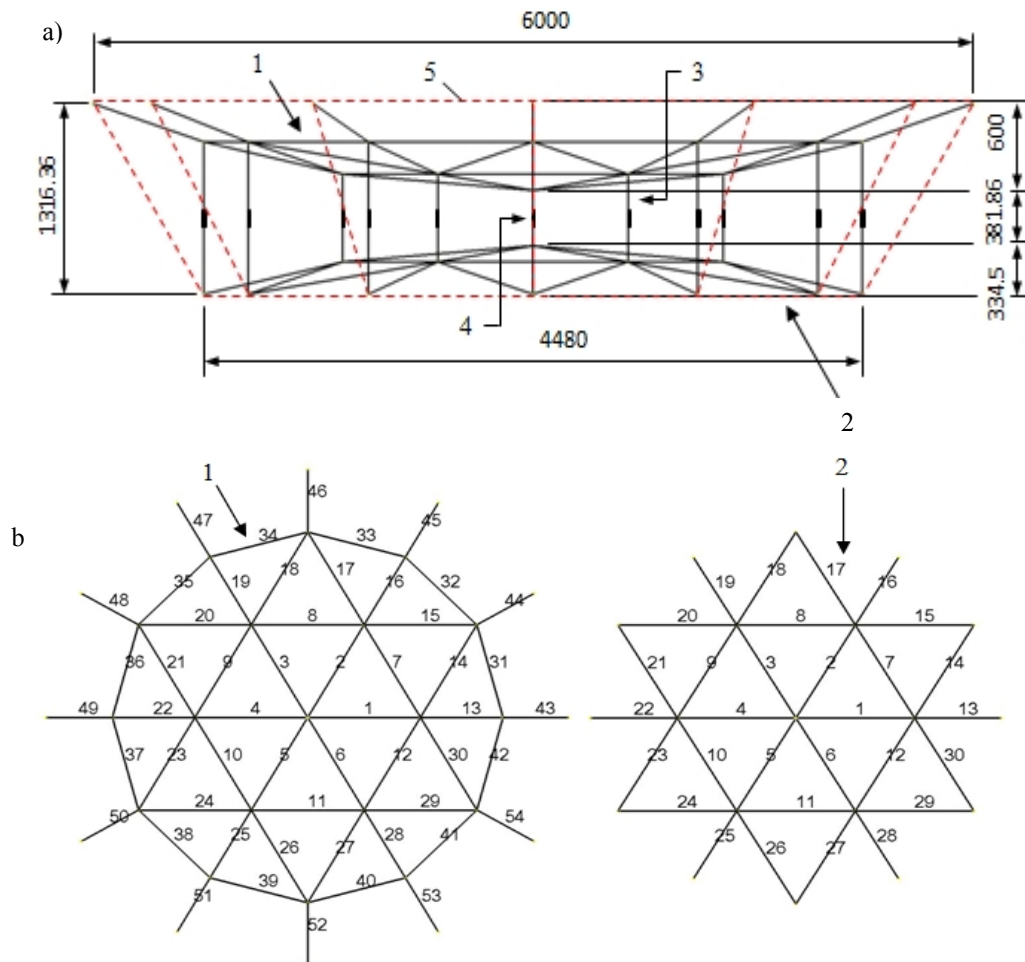


Fig. 7. Central part with vertical ties

a) Side view; b) Top view

1-functional mesh; 2-technological mesh; 3-ties; 4 – flexible elements; 5 – load-bearing ring.

Two embodiments of the central part – with vertical and inclined ties are discussed in the present article.

In the first case (Fig.7), the functional mesh is identical to the technological mesh with the exception of the inclined ties and peripheral circular elements, i.e. it consists of 19 units (units references are not shown) and 30 elements. Therefore the ties disposed between the meshes are parallel, and stretching of their all component parts are ensured. The cells are equilateral triangles in plan with sides of 1293.26 mm.

Due to the conical shape of the ring, the upper mesh, in contrast to the lower mesh, requires additional circular elements 31-43 and inclined elements 43-54 for attaching to the ring. The inclined elements are 805.04 mm in length, i.e. peripheral cells of the functional mesh have trapezium outline.

In the second case (Fig. 8), the functional and technological meshes are identical.

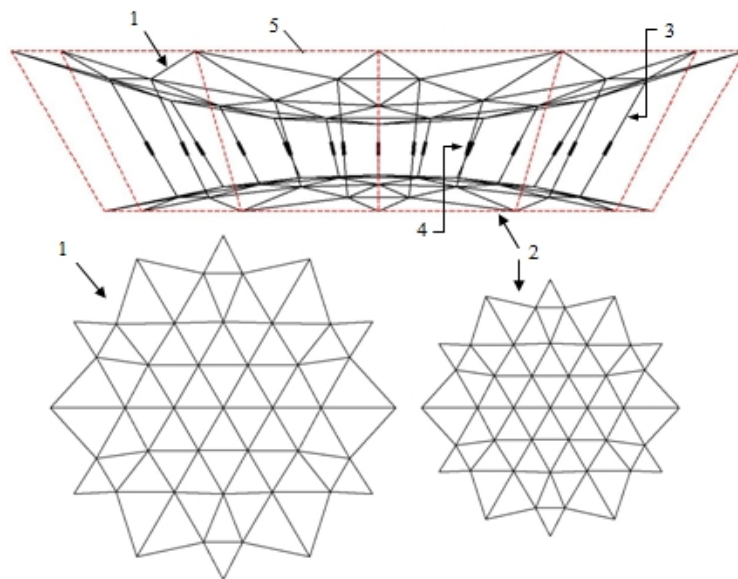


Fig. 8. Central part with inclined ties

1-functional mesh; 2-technological mesh; 3-ties; 4 – flexible elements; 5 – load-bearing ring.

Difference is in the scale only, due to the diameters of the upper and lower rings. As differed from the first modification, the ties are inclined. However, the stretching forces in all elements of the meshes can be ensured by distributing the stretching forces proportionally in the ties.

In both cases, the attachment of the meshes to the ring and inclination angles of the mesh peripheral elements with respect to horizontal planes are shown in Fig. 9.

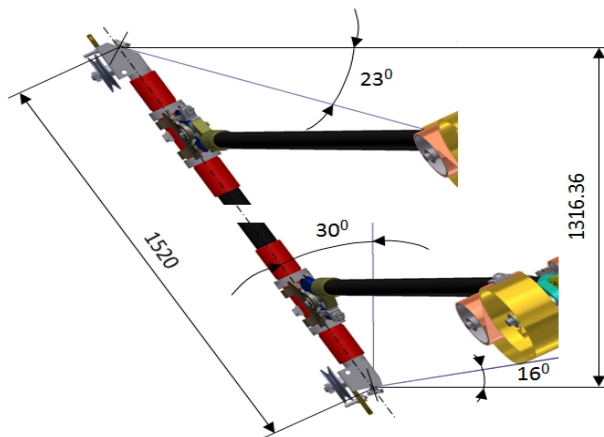


Fig. 9. Units for connecting the central part with the ring

1-functional mesh; 2-technological mesh; 3-ties;
4 – flexible elements; 5 – load-bearing ring.

7. CONSTRUCTION WEIGHTS AND ITS TRANSPORT PACKAGE

The transport package is cylindrical. Its dimensions are shown in Fig. 10.

Duraluminum and steel alloys are used for the parts contained in the load-bearing ring units.

The six meter diameter reflector antenna weights 13.925kg in total according to the data assumed in result of designing, which is a sum of the following data:

1. Carbon plastic tubes – 2,549kg;

2. Antenna metal part – 6,036kg;
3. Constant moment springs – 48 items (1 item – 54.6g) 2.62kg in total;
4. Gear-motor drives IG-32RGM – 2 items (1 item – 320g) – 0.64kg in total;
5. Reflecting mesh (1m² – 52g) 30m² – 1.560kg in total;
6. Technological mesh – 0.520 kg.

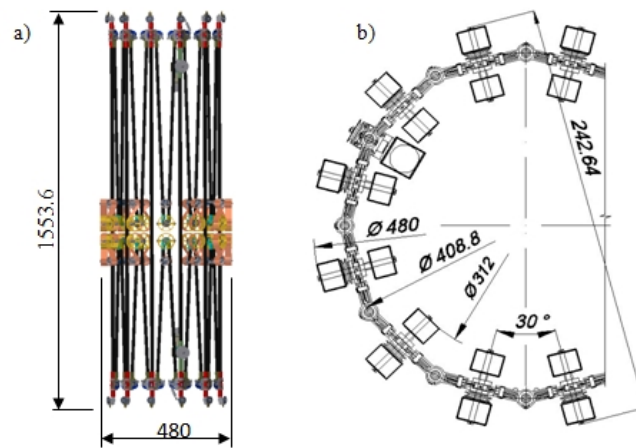


Fig. 10 Transport package.

- a)– lateral view of the transport package;
b)– top view of the transport package in enlarged scale

8. THEORETICAL ESTIMATION OF CONSTRUCTION.

Estimation performed using the computer software LIRA WINDOWS. This software is the system where the methods of finite elements are realized, and determined static and dynamic influence to calculate construction (Figs. 11, 12, 13).

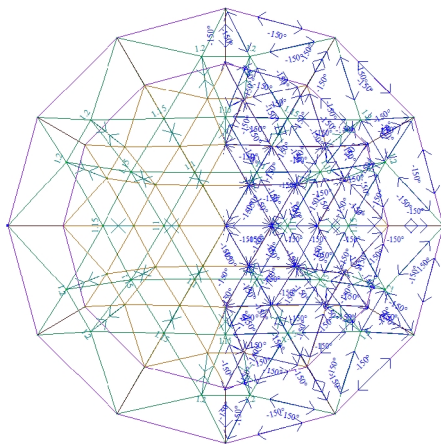


Fig.. 11. Temperature load scheme of 6 meter conical reflector.

Temperature load is spread in half construction (T=-150C, in tension system – 1N, 1.1N, 1.2N).

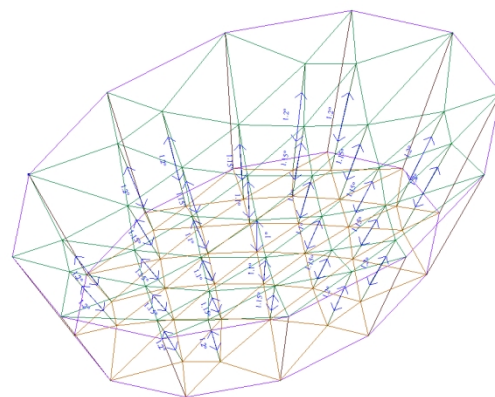


Fig. 12. Calculation scheme of 6 meter conical reflector on sustainability.

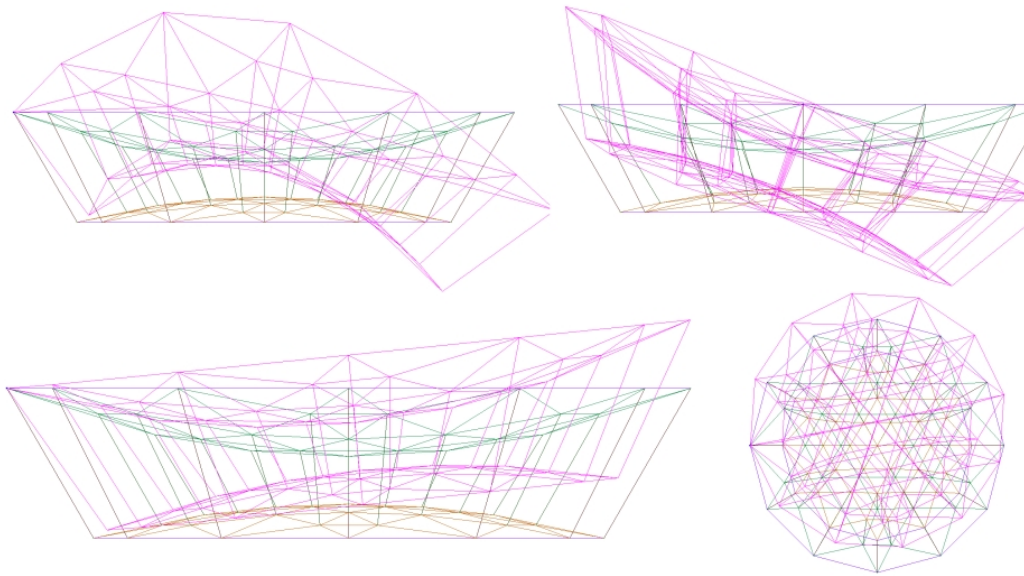


Fig 13. Model analyses are performed to determine eigenfrequencies and form of 6 meter conical reflector.

4.20-4.23 drawings are showing the first 4 form of reflector's eigenfrequencies and the periods of corresponding eigenfrequencies. The meanings of periods: : $T_1 = 1.6013$. $T_2 = 1.3472$. $T_3 = 0.6934$. $T_4 = 0.2274$ sec.

9. FOLDING AND UNFOLDING EXPERIMENT OF CONICAL ANTENNA AND SPECIFIC CONCLUSIONS

Constant torque flat springs are used as unfolding asset for the deployment of load-bearing ring. The thickness of spring is 0.3mm. The number of springs according the project is 48 pcs and overall weight is 3264 gr. During the experiment we had to increase the number of springs, it was caused from the influence of gravitational force on the deployment of load-bearing ring. Two constant torque springs with 14106mm.sec. moment were inserted in each v-folded bar of reflector. The deployment result showed that this moment was not enough to overcome the rolling and sliding frictions. That is why the number of springs was doubled in upper V-fold bar. The common moment in each joint of V-fold bar became 28206 mm.sec. After this deployment became easier. The overall weight of spring reached 6528 gr. Here should be mentioned that it is possible to minimize the length of spring from 1100 mm to 600mm, after what the weight of each spring will be minimized with 47% and the overall weight of springs will be 3456 gr. with same moment.

The fast turn of levers is possible during the deployment. To avoid them we used cable system to detain deployment of levers, which are actuated by motors IG-32RGM 50. Motor-reducers are presenting reverse collecting constant power motors with planetary conical reducers, which characters are: power 12v; transmitting number 1:721; torque moment 12kg.cm number of rotate 9.6 turn in sec. From the beginning we used two motors in ring. One of them served to the deployment of joints of upper V-fold bar and another to the lower ones. But finally we had to increase the number of motors to 6 pcs. Three motors served to the upper part and another 3 to the lower part. The weight of reflector with motors became ≈ 10 kg.

The structure started normal deployment after partial reduction of defects that rose during the deployment. The hooks in central part were the one defect that was not reduced. Existence of mentioned hooks according the given scheme is inevitable. It is caused from that the component cables of upper mesh are not covered by net. Also, the mesh during the deployment is lowered and freely follows to the deployment process. It has no separate hanging components for the gravity. To salve all of this the hook will no longer exist.

Finally, it can be said that the conical V fold bar reflector performed according the given scheme by European Space Agency is real. It deploys, reaches design form, is light, has accuracy, is sustainable and has enough rigidity.

10. CONCLUSION

On the bases of done work we can formate the following:

1. The deformed condition and displacements during the tension (forces in tensioning system – 1N, 1.1N, 1.15N, 1.2N) in 6 meter conical reflector is in range. The maximum vertical displacement in upper mesh is 0.77mm. I comparison with upper mesh the displacement in lower mesh is much bigger and equals 1.38mm.
2. The all elements of upper mesh is tensioned by result of reflector's tension and maximum meaning equals to 4.86N. The elements of lower mesh are also tensioned and maximum meaning equals to 7.27N.
3. Calculation on sustainability of the construction of reflector showed that the safety coefficient from tensioning forces is $K_{safety}=14.81$
4. The periods and forms of eigenfrequencies of reflector are determined. Construction is enough rigid and the first frequency of eigenfrequencies is $f_1=0.6245\text{Hz}$ (period $T_1= 1.6013$ sec).
5. Calculation on temperature loads ($T= -150\text{ }^{\circ}\text{C}$, $T= +150\text{ }^{\circ}\text{C}$) showed that the forces (forces in tensioning system – 1N, 1.1N, 1.15N, 1.2N) in upper mesh are all tensioners.
6. From the above mentioned we can conclude that the structure of 6 meter conical reflector is acceptable and father researches should be continued.
7. There are numerous novel features in the mechanical construction intended for designing the space parabolic reflector antennas.
8. First of all it should be noted very little weight of the antenna which is attained owing to its overal conical shape. It means that minimum cross sections and quantity of its component elements can be used due to high dynamic characteristics and stiffness reserve of the overal structure. Moreover, the central part is made of cables and, in the stretched state, it is a surface consisting of triangular flat cells which is characterized by sfficiently high accuracy apart from little weight.
9. Hence a hinge system provided with V-fold bars connected by posts has been chosen as a load-bearing part wherein an original diagram has been suggested in order to make its kinematical motion degree equal to one, i.e. the principle of operation of the synchronization mechanism is accomplished by cross like disposition of the cable on the guide rollers, making it sufficiently simple and reliable.
10. Constant moment springs disposed in V-fold hinges of each pair of the bars are used as the system drive. To avoid the dynamic blow at the final moment of deployment, a restraining cable system controlled by two motors is used in the structure. These motors can be used also for controlling the deployment speed. This means that kinetic energy accumulated by the springs is used for deploying the reflector antenna, which is controlled by the cables and two electric motors.
11. Thus the load-bearing part ensures designed stress of the central part and production of stretching forces in all its elements. Eventually, high stiffness and accuracy light weight construction is assumed that is characterized by reliable deployment and completely satisfies all technical requirements inposed to the antenna technology.

REFERENCES

- [1]. **van't Klooster C.G.M., E. Medzmariashvili, Sh.Tserodze, L. Datashvili, N. Tsignadze** "Large Deployable Reflector Configuration for Spacebased Applications in Telecom muni cations, Science and Remote Sensing". Proceedings of International Scientific Conference "Advanced Lightweight Structures and Reflector Antennas". 14-16 Octo ber 2009 Tbilisi Georgia, p. 75-82.
- [2]. **E. Medzmariashvili, Sh. Tserodze, N. Tsignadze, K. Chkhikvadze, M. Sanikidze, M. Djanikashvili, N.Khatiashvili, M. Adeishvili, V. Medzmariashvili, N. Siradze.** "New Types of High-Precision Deployable Space Reflectors" Proceedings of International Scientific Conference "Advanced Lightweight Structures And Reflector Antennas". 14-16 October 2009 Tbilisi Georgia, p. 111-116.
- [3]. Ozawa S, Shintate K., Tsujihata A.: tri-fold deployable reflectorfor communication satellites, In: AIAA 29th International CommunicationsSatellite Systems Conference (ICSSC-2011), AIAA 2011–8082
- [4]. **E. Medzmariashvili, Sh. Tserodze, N. Siradze, A. Sarchimelia, N. Tsignadze, M. Sanikidze.** New space reflex structures // "Problems of mechanics". Tbilisi, 2008, №1(30), p.24-30, (Eng.).
- [5]. **E. Medzmariashvili, V. Gogilashvili, Sh. Tserodze, N. Tsignadze, N. Siradze.** Structure and kinematics of reflector's transformed mechanical systems // "Problems of mechanics". Tbilisi, 2008, № 3(32), p. 23-33 , (Eng.)
- [6]. **Sh. Tserodze, C.G.M. van 't Klooster, N. Tsignadze, M. Sanikidze, G. Medzmariashvili, J. Chapodze, D. Sxiladze.** "Spatial double conical ring-shaped reflector concepts for spacebased application" 31nd ESA Antenna Workshop on Antennas for Space Applications – From technologies to Ar-chitectures. 5-8 October 2010, ESA/ESTEC, Noordwijk, The Netherlands